Fundamental study on 3D particle tracking, flow stability and particle dynamics relevant to Taylor-Couette reactors

Am Fachbereich Maschinenbau
der Technischen Universität Darmstadt
zur
Erlangung des Grades eines Doktor-Ingenieurs (Dr.-Ing.)
genehmigte

Dissertation

vorgelegt von

Philipp Maximilian Josef Hermann Brockmann, M.Sc.

aus Oberhausen

Berichterstatter:	Prof. Dr.-Ing. J. Hussong
Mitberichterstatter:	Prof. Dr.-Ing. C. Egbers
Tag der Einreichung:	25.01.2022
Tag der mündlichen Prüfung:	19.04.2022

Darmstadt 2022

D 17

Philipp Maximilian Josef Hermann Brockmann:
Fundamental study on 3D particle tracking, flow stability and particle dynamics relevant to Taylor-Couette reactors

Darmstadt, Technische Universität Darmstadt
Jahr der Veröffentlichung der Dissertation auf TUprints: 2023
Tag der mündlichen Prüfung: 19.04.22

Bitte zitieren Sie dieses Dokument als:
URN: urn:nbn:de:tuda-tuprints-232265
URL: https://tuprints.ulb.tu-darmstadt.de/id/eprint/23226

Dieses Dokument wird bereitgestellt von TU Prints, E-Publishing-Service der Technischen Universität Darmstadt http://tuprints.ulb.tu-darmstadt.de tuprints@ulb.tu-darmstadt.de

"Die Familie ist das Wichtigste."

J.V.B

Abstract

Combining axial and rotational flow between two concentric cylinders, Taylor-Couette Reactors (TCRs) bear huge potential for both mixing and separation of particle laden flows. In such flows, the particle dynamics are affected by the structure of the flow, gravitational and centrifugal forces and interaction of particles with the fluid and themselves. However, these effects are not completely understood on their own such that their combined effect on the particle dynamics in TCRs is far from being predictable. Therefore, in the present thesis, the major physical effects relevant in such scenarios are investigated separately to provide a foundation for future potential applications.

As particle trajectories differ significantly for laminar, bifurcated or turbulent flow, precise knowledge of the flow stability of the carrier liquid is required to set the process parameters. Given that, a comparative study of the linear stability behavior of the laminar flow in a TCR with rotation of the inner cylinder and with rotation of the outer cylinder is performed by means of swirl and curvature parameter. It is revealed that the stability behavior for both the rotating inner as well the rotating outer cylinder case strongly depends on the curvature parameter. While rotation of the inner cylinder generally has a destabilizing effect, it is revealed that rotation of the outer cylinder can stabilize but also destabilize the flow depending on swirl and the curvature parameter.

Until now, the direct observation and characterization of suspensions by means of optical methods bears large potential but is highly challenging especially in small geometries such as in the gap of a TCR. In the present study, different methods are developed to apply Astigmatism Particle Tracking Velocimetry (APTV) on suspension flows for dilute, semi-dilute, mono- and polydisperse suspensions. Using these techniques, the dynamics of mono- and tridisperse suspensions are investigated in pressure driven square duct flows at volume fractions up to 9.1%. It is discovered that interaction of small and large particles can lead to strikingly different concentration patterns in tridisperse compared to monodisperse suspensions depending on Reynolds number, volume fraction and channel height.

While particle interaction is usually associated with higher particle volume fractions, it is known that dilute suspension flows in horizontally aligned rotating cylinders could give rise to formation of band shaped particle accumulations. In this thesis, it is investigated how an additional inner cylinder, which is present in a TCR, affects this band formation. To reduce the complexity, a Taylor Couette flow with solid body rotation without axial flow is considered. Different particle patterns are discovered including three types of bands, which are periodic in axial direction, and two types of bands that are periodic in azimuthal direction. It is shown, that the presence of the inner cylinder can significantly alter the particle trajectories and stabilize the particle bands.

Kurzfassung

Taylor-Couette Reaktoren (TCRs) zeichnen sich durch eine Axialströmung mit zusätzlicher Drallkomponente zwischen zwei konzentrischen Zylindern aus und bergen großes Potential für Misch- und Trennprozesse von partikelbeladenen Strömungen. Die Partikeldynamik in solchen Systemen unterliegt dem Einfluss des Strömungszustandes, Gravitations- und Zentrifugalkräften sowie Wechselwirkungen der Partikel untereinander und mit dem Fluid. Jedoch sind diese Effekte nicht vollständig verstanden und die Partikeldynamik in TCRs daher kaum zu antizipieren. In der vorliegenden Arbeit werden die Phänomene daher separat untersucht, um ein Wissensfundament für die gezielte Entwicklung von TCRs zum Mischen und Trennen von Suspensionen zu schaffen.

Da laminare Strömungen Potential für die Partikelfraktionierung haben, während turbulente Strömungen ein Mischen von Partikeln fördern, ist Kenntnis des Strömungszustandes in TCRs Vorrausetzung um die Prozessparameter einzustellen. Es wird daher eine vergleichende Studie des Stabilitätsverhaltens bei rotierendem Außen- und Innenzylinder in Bezug auf Drall und Krümmungsparameter durchgeführt. Dabei zeigt sich, dass das Stabilitätsverhalten bei rotierendem Innen- sowie Außenzylinder stark vom Krümmungsparameter abhängt. Während Rotation des Innenzylinders generell einen destabilisierenden Effekt hat, zeigt sich, dass sich eine Aussenzylinderrotation mit steigendem Drall in Abhängigkeit vom Krümmungsparameter sowohl destabilisierend als auch stabilisierend auf die Strömung auswirken kann.

Die Charakterisierung von Suspensionen mithilfe optischer Messtechniken birgt großes Potenzial, ist jedoch besonders in kleinen Geometrien wie dem Spalt eines TCRs eine große Herausforderung. In dieser Arbeit werden verschiedene Methoden entwickelt um Astigmatismus Particle Tracking Velocimetry (APTV) auf dilute, semi-dilute, mono- und polydisperse Suspensionen anzuwenden. Mithilfe dieser Methoden, wird die Dynamik von mono- und tridispersen Suspension in rechteckigen Kanalströmungen bis zu Volumenfraktionen von 9.1% untersucht. Dabei wird gezeigt, dass die Interaktion von kleinen und großen Partikeln in Abhängigkeit von Reynoldszahl, Volumenfraktion und Kanalhöhe, zu signifikant unterschiedlichen Konzentrationsverteilungen in tridispersen und monodispersen Suspensionen führen kann.

Während Partikelinteraktionen generell bei höheren Volumenfraktionen auftreten, ist bekannt, dass dilute Suspensionen in rotierenden, horizontal ausgerichteten Zylindern bandartige Strukturen ausbilden können. In dieser Arbeit, wird untersucht, wie ein zusätzlicher Innenzylinder, welcher beim TCR vorliegt, diese Strukturbildung beeinflusst. Zur Vereinfachung wird dazu die Strömung bei Festkörperrotation ohne zusätzliche Axialströmung untersucht. Es werden verschiedene Partikelstrukturen entdeckt, darunter

auch Bandstrukturen die periodisch in Axialrichtung aber auch welche die periodisch in Azimutalrichtung sind. Es wird gezeigt, dass der Innenzylinder die Partikeltrajektorien beeinflussen und zu einer Stabilisierung der Bandstrukturen beitragen kann.

Erklärung

Ich versichere hiermit, dass zu einem vorherigen Zeitpunkt noch keine Promotion versucht wurde. In diesem Fall sind nähere Angaben über Zeitpunkt, Hochschule, Dissertationsthema und Ergebnis dieses Versuchs mitzuteilen.

Hiermit erkläre ich, dass ich die vorliegende Arbeit, abgesehen von den in ihr ausdrücklich genannten Hilfen, selbständig verfasst habe.

Die Arbeit hat bisher noch nicht zu Prüfungszwecken gedient.

Datum: 25.01.22, Frankfurt am Main

Acknowledgments

Without the help, feedback and motivation of great people, i would not have succeeded the challenges of my doctoral studies. I experienced the opportunity of working at two great chairs at two different universities and many kind people accompanied me on my way.

First of all, I would like thank Prof. Dr.- Ing. Jeanette Hussong as my supervisor for her endless support, inspiration, patience, encouragements, trust in my skills and the scientific freedom I enjoyed during my time at the RUB and the TUDa. Thank you! Also would like to thank Prof. Dr.-Ing. Christoph Egbers for refereeing my thesis. I would like to thank Prof. Dr.-Ing. Venkatesa Iyengar Vasanta Ram for unforgettable discussions, insipiration, historical stories about fluid mechanics and for always being welcome in his office. Prof. Dr.-Ing. Franz Peters for his support in building the experimental setups for investigation of pattern formation in rotating suspensions. I thank Apl. Prof. Dr.-Ing. habil. Suad Jakirlic for inspiring discussions, providing valuable literature and advices.

I am thankful for having nice colleges at the RUB. Thank you Martin, Ali, Phillip, Nicolas, Markus, Steffen, Pascal, Kevin, Felix, Philip, Andreas, Stephan, Arnulf, Artem and Helmuth. I always enjoyed the lunch break with you. This also accounts for the great colleges at the TUDa who made me feel comfortable from the beginning on. Thank you: Niklas, Maximilian, Johannes, Johannes, Lingxi, Amandine, Benedikt, Jan, Killian, Marija, Hatim, Lu, Sebastian, Sebastian, Mark, Louis, Markus, Klaus, Andreas, Fabian, Sebastian, Bastian, Max, Till, Patrick and Ivan.

Undoubtly, the insights presented in this thesis would have never been acomplished without the full-hearted support of great students. Thank you: Cihan Acer, Zhichao Deng, Xulan Dong, Frankziska Schindler, Christoph Symanczyk, Martin Tvarozek and Zihao Zhang. It was a pleasure to work with you.

The setups utilized for the experiments would have never been realized without the support of two excellent workshops and their teams. Thanks to Christian Gramann and his team at the RUB. Thanks also to Ilona, Timm, Joachim, Manolo and Kevin at the SLA. For instant support in technical questions I would like to thank Martin Stenger, Alexander Beck and Martin Weiß. It was always a joy working with you. Thanks also to Johannes Kissing for fruitful and amusing discussions on scientific and not-so scientific topics.

I would like to thank Claudia, Birgit, Monika and Susanne for bureaucratic and organizational support.

Special thanks go out to Christoph Symanczyk, Niklas Apell, Maximilian Lausch and Hamid Tabaei Kazerooni for proof reading the thesis.

The foundation for my doctoral studies was founded during bachelor and master studies, which I would have never accomplished without the support, fun and long discussions about the next days exam I had with my friends Marcel, Sebastian and Basti!

No word can express my gratitude to my collaborator and friend Hamid Tabaei Kazerooni, who influenced me on personal, cultural as well on professional level. It was so much fun with you, I will never forget. Hamid, I owe you a lot!

Finally, I would like to thank my beloved ones for the motivation, fun and support during the last years. I love you from the bottom of my heart.

Philipp

Contents

1 Introduction

1.1 Background and motivation

Suspension flows of rigid particles are found in various natural flows and technological applications on the microscale as well as on the macroscale. These are for instance the flow of blood cells, sediment transport in rivers, mudslides or inkjet printing (Morris 2020). These flows are a fertile ground for a variety of different phenomena such as shear induced migration, inertial migration, shear thinning and shear thickening (Leighton and Acrivos 1987, Ho and Leal 1974, Stickel and Powell 2005). It is known that such effects occur in monodisperse suspensions, which solely contain one particle size. However, when multiple particle sizes are present in a suspension, viz. a polydisperse suspension, additional effects can occur within the flow. These are for instance size segregation, formation of structures and mutual repellence of large and small particles (Lyon and Leal 1998b; Batchelor and Van Rensburg 1986; Semwogerere and Weeks 2008; Gao et al. 2019). In fact, the vast majority of suspension flows found in nature and technical enviroments are polydisperse, while monodisperse suspensions are rather an exception. In addition, particles usually have a different density than the suspending fluid and are rarely neutrally buoyant. Furthermore, in industrial applications suspension flows are often subjected to rotation. Such situations are found for example in slurry pumps, gas turbines operating with particle laden working fluids or induced fans for cleaning the ducts in a room (Pan et al. 2001).

One device which explicitly combines an axial through flow with a rotational flow is the Taylor-Couette Reactor (TCR), which basically consists of two concentric cylinders of which one or both rotate and an additional pressure driven axial flow (Fig. 1.1). In the laminar regime, the flow composes of an Annular Poiseuille Flow (APF) and a Taylor-Couette flow resulting in spiral-shaped streamlines, often referred to as Spiral Poiseuille Flow (SPF). TCRs are used for rotating filtration applications including blood filtration and other biological separation processes (Wereley and Lueptow 1999) or mixing applications (Dusting and Balabani 2009; Nemri et al. 2016). One advantage of a TCR is that the ratio of axial and rotational flow can be tailored specifically to the process and hence enhances mixing and dispersion as required (Schrimpf et al. 2021).

In rotating systems, such as a TCR, particle trajectories are affected by coriolis and centrifugal forces, resulting in complex dynamics and sharp particle concentration gradients (Pan et al. 2001). Even slow rotation induces centrifugal hydrodynamic instabilities that initiate the transition in a TCR and give rise to Taylor vortices. Higher rotation rates can easily lead to turbulence. In such scenarios the particle

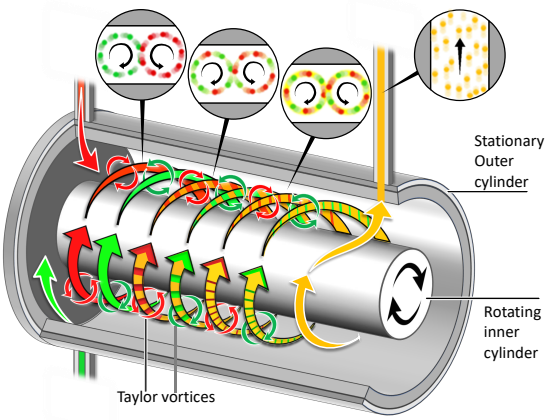

Figure 1.1: Principle of Taylor-Couette Reactor for steady processing of fluid (adapted from: https://www.uni-muenster.de/MEET). Here, rotational flow is induced by rotation of the inner cylinder. Axial flow is induced by a pressure gradient.

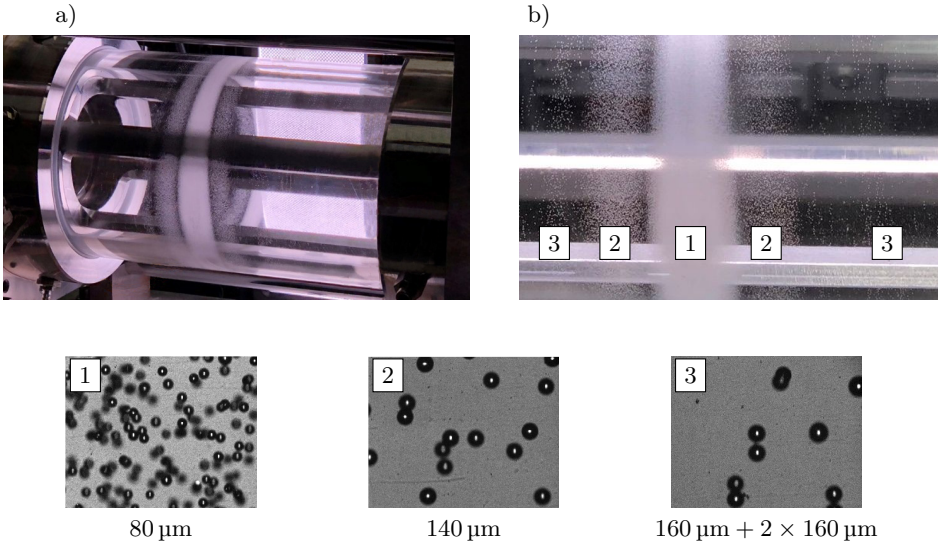

Figure 1.2: Recently discovered particle sorting phenomena in a polydisperse suspension of Polystyrene (PS) particles. Particle characteristics of each band are 1: 80 µm PS particles, 2: 140 µm PS particles and 3: 160 µm single and 140 µm doublet PS particles. a) Macro view of system; b) close up; 1-3 are microscopic images taken in the bands.

dynamics get even more complex (Majji et al. 2018; Fornari et al. 2018). Recently, it was discovered that in a horizontally oriented TC flow with a gap of 1 mm, the particles in a monodisperse suspension form a single particle band so that the rest of the system

is devoid of particles. An unexpected phenomenon in case of a tridisperse suspension is the formation of five symmetric and distinct particle bands as depicted in Fig. 1.2. Each band consists thereby of particles of same size. This observation is an outstanding example of the complexity of the particle dynamics in TC suspension flows.

Hence, to process mono- and polydisperse suspensions using a TCR more efficiently, a deeper understanding of all involved physical effects is required. This includes the hydrodynamic stability behavior of the SPF, the effect of rotation acting on (non-neutrally buoyant) particles as well as particle migration and segregation mechanisms that occur in mono- and polydisperse suspensions. In the present thesis, these aspects are addressed.

1.2 Theory and state of the art

As stated in the previous section, the overall goal of the present thesis is to improve our understanding of the basic physical effects one encounters in TCRs. In the following sections, we first perform a literature review of related topics and then build the foundation of our investigations. In particular, we review the basic principles as well as the state of the art of linear stability analysis in Spiral Poiseuille Flows (section 1.2.1), suspension flows of rigid particles (section 1.2.2), particle banding in rotating flows (section 1.2.3) and measurement techniques in suspension flows (section 1.2.4).

1.2.1 Linear stability analysis in spiral Poiseuille flows

For processing suspensions in TCRs, it is crucial to know the transitional behavior of the flow, as the particle trajectories differ significantly for laminar, transitional and turbulent flow regimes. It is important to understand how kinematic boundary conditions (inner and outer cylinder rotation speed, ratio of azimuthal and axial velocity) and geometrical boundary conditions (radius ratio) affect the stability of the flow. Indeed the number of particles in a flow is another parameter, which influences the flow stability. However, the transitional behavior of the Spiral Poiseuille Flow (SPF) especially with rotating outer cylinder is far away from being explored even for a pure liquid. Therefore, the first logical step is to thoroughly explore the stability behavior of the pure liquid case, before considering the effect of added particles. Hence, in this work we will investigate the stability of the SPF in the absence of particles with a special focus on the effect of the outer cylinder rotation. This will be done by means of linear stability analysis, which will be explained in the following.

1.2.1.1 Linear hydrodynamic stability theory

In hydrodynamic stability theory, the flow is considered as system whose reaction to small disturbances is analyzed. If the system is disturbed and all disturbances gradually die down, the system is considered as stable. Otherwise, if the disturbances grow in amplitude and the system progressively departs from the initial state, the system is considered as unstable. The prime aim of hydrodynamic stability analysis is to determine the locus in the parameter space which separates the unstable and the stable states of the system. This defines the curve of marginal stability of the system (Chandrasekhar 2013). Such a curve, also known as curve of neutral stability, will be presented later in the text. Two types of instabilities are distinguished based on the development of the perturbation. A flow is considered absolutely unstable if the perturbation growths at a fixed point in the flow, while the flow is considered as convective unstable if the perturbation grows at a moving point within the flow (Drazin and Reid 2004). Within this work, we solely consider absolute instabilities. From a mathematical point of view, the equations describing the stationary base flow are superimposed with disturbances (i.e. velocity disturbances u_i' and pressure disturbances p'). The linear stability theory assumes that the disturbances are infinitesimal and hence the nonlinear terms in the governing equations can be neglected. This simplification results in linearized disturbance equations describing the motion of disturbances in dependence of the base flow properties (i.e. Reynolds number, streamwise velocity, spanwise velocity). The disturbances are then substituted by ansatz functions. Thereby, it is essential to expand the disturbance, viz. the ansatz function, in a suitable set of normal modes to capture all possible waveforms for the problem, which may require several spatial wavenumbers (Roy and Govindarajan 2010; Chandrasekhar 2013). The system is only considered as stable if it is stable against all possible modes. For numerous flows, such as the plane channel flow, the boundary layer flow over a flat plate or the Taylor-Couette flow, at least one unstable mode can be found if the Reynolds number is sufficiently high. However, some flows are stable for all possible modes, even at high Reynolds numbers. These are for instance the plane Couette flow (parallel plate shear flow) or the Hagen-Poiseuille flow (pipe flow) (Gallagher 1974; Salwen et al. 1980). Such flows are termed as linear stable flows.

Within this work, where we restrict ourselves to the flow between two concentric cylinders, we consider modes which are periodic in azimuthal as well as in axial direction. With the axial wavenumber $\lambda \in \mathbb{R}$, the azimuthal wavenumber $n \in \mathbb{Z}$ and the amplitude A the disturbances are described by the following ansatz function, which is substituted into the disturbance equations (here exemplary for the radial velocity fluctuation u_r'):

$$u_r' = A_r(r)\, e^{i(\lambda x + n\varphi - \omega t)} \tag{1.1}$$

A schematic sketch of the disturbance, described by the ansatz function, is given in Fig. 1.3a. Fig. 1.3b exemplary depicts a computed visualization of such a disturbance u_r'. Here r, x, φ are the radial, the axial and the azimuthal coordinate, respectively. t is

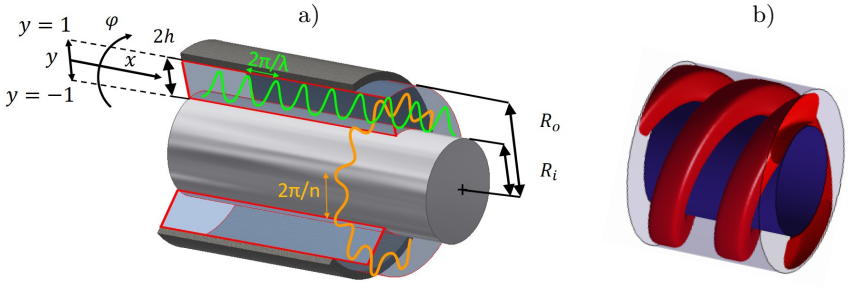

Figure 1.3: a) Schematic sketch of the infinitesimal disturbances within two concentric cylinders. R_o = outer cylinder radius, R_i = inner cylinder radius, h = half gap width, n = azimuthal wavenumber, λ = axial wavenumber. b) Example for a disturbance described by equation 1.1 ($n = 2$, $\lambda = 0.86$). Depicted over two periods ($4\pi/\lambda$).

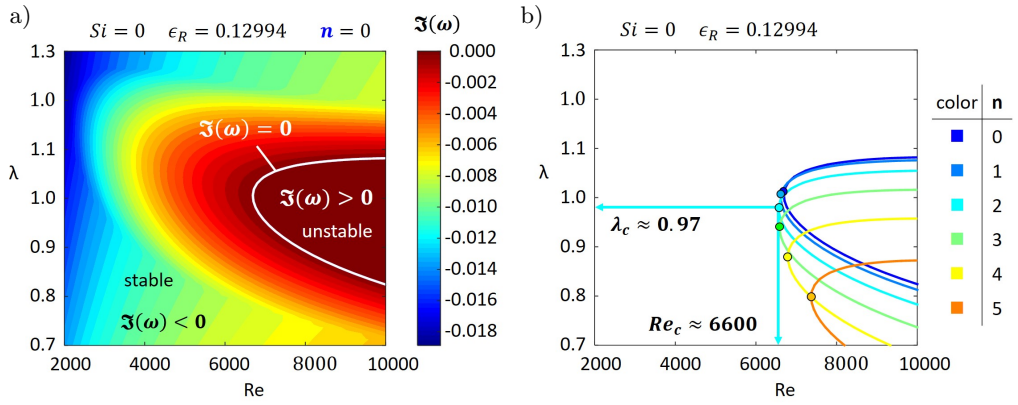

Figure 1.4: a) Curve of neutral stability. Unstable regions correspond to $\Im(\omega) > 0$, while stable regions correspond to $\Im(\omega) < 0$. b) Finding the disturbance associated with the lowest Reynolds number. The disturbance with $n = 2$ and $\lambda = 0.97$ is critical here, as it gets unstable at the lowest Re. S_i is the swirl parameter and defined as ratio of inner cylinder angular velocity and axial reference velocity. The curvature parameter is defined as $\epsilon = \epsilon_R = (1 - R_i/R_o)/(1 + R_i/R_o)$.

the time and $\omega \in \mathbb{C}$ denotes the complex frequency. The wave speed is given by the real part of ω as $c = \Re(\omega)/\sqrt{n^2 + \lambda^2}$. The temporal behavior of the disturbance amplitude depends on the imaginary part of ω. The disturbance grows when $\Im(\omega) > 0$ and decays if $\Im(\omega) < 0$. The system is only considered as stable if it is stable against all possible combinations of λ and n. In fact, the disturbance equations containing ansatz function (1.1) pose an eigenvalue problem which yields $\Im(\omega)$ as function of Re, λ and n. Hence, for a reasonable range of λ, n and Re the value of $\Im(\omega)$ has to be computed as shown exemplary in Fig. 1.4a for an annular Poiseuille flow. If $\Im(\omega) > 0$ for any combination of Re, n and λ the flow is considered unstable as indicated in Fig. 1.4a. The line where

$\Im(\omega(Re, \lambda, n)) = 0$ defines the curve of neutral stability as shown as a white line in Fig. 1.4a. For each n such a curve can be defined. The combination of n and λ which gets unstable at a lower Reynolds number than all other possible combinations, is the most "dangerous" for the stability of the flow and is considered as critical mode or critical disturbance. This is illustrated exemplary in Fig. 1.4b where the disturbance associated with $n = 2$, $\lambda = 0.97$ gets unstable at a lower Re than any other disturbance. When $n = 0$ the disturbance is symmetric in azimuthal direction and consequently denoted as symmetric disturbance. Analogous disturbances associated with $n \neq 0$ are referred to as non-axisymmetric disturbances.

1.2.1.2 Instability mechanisms

Hydrodynamic instabilities can be caused by thermal effects (Rayleigh-Bénard convection), stratification (Rayleigh-Taylor instability), centrifugal effects (Taylor-, Dean-, and Görtler instability), surface tension (Rayleigh-Plateau instability), viscous effects (Tollmien-Schlichting instability) or due to shear layers in the flow profile (Kelvin-Helmholtz instability) (Drazin and Reid 2004, Roy and Govindarajan 2010). From a theoretical perspective, flows, which can get unstable when the viscosity is neglected, are denoted as inviscid unstable. Contrary, flows, which are unstable only when viscosity is considered, are termed as viscous unstable. An inviscid flow can get unstable if the velocity profile exhibits an inflection point (Rayleigh's inflection point criterion) or if the angular momentum decreases outward in a flow with curved streamlines (Rayleigh's criterion). It should be mentioned, that in the case of inviscid stability the viscosity is only neglected in the stability considerations, but still necessary for generating the velocity profile. For the Spiral Poiseuille flow (SPF) investigated in this work, the relevant transition mechanisms are the viscous Tollmien-Schlichting instability and the inviscid centrifugal Taylor instability. These are briefly discussed hereafter.

Rayleigh criterion and Taylor instability: Flows along curved streamlines or in a rotating system can exhibit instabilities resulting from adverse angular momentum gradients (Chandrasekhar 2013). For inviscid flows, Rayleigh's criterion states that a stratification of angular momentum is only stable if it increases monotonically outward, such that the radial distribution of angular velocity $\Omega(r)$ fulfills the condition $d/dr(r^4\Omega^2) > 0$ everywhere. This criterion can be explained by considering the mass transfer between two neighboring elementary fluid rings at radial positions $r = r_1$ and $r = r_2$ ($r > 0$). It can be shown that the change in centrifugal potential energy associated with this mass exchange is proportional to:

$$\Delta E \propto \left(r_2^4\Omega_2^2 - r_1^4\Omega_1^2\right)\left(\frac{1}{r_1^2} - \frac{1}{r_2^2}\right) \tag{1.2}$$

Hence, if $d/dr(r^4\Omega^2) > 0$ no interchange of fluid between the rings can occur without a source of external energy and the flow is stable (Chandrasekhar 2013). Applied to a flow between two rotating concentric cylinders (TC-flow) as displayed in Fig. 1.5a the Rayleigh criterion yields the following conditions:

$$\mu = \frac{\Omega_o}{\Omega_i} > \eta^2 = \frac{{R_i}^2}{R_o} \quad \text{(stable)} \quad \text{and} \quad \mu = \frac{\Omega_o}{\Omega_i} < \eta^2 = \frac{{R_i}^2}{R_o} \quad \text{(unstable)} \qquad (1.3)$$

Where Ω_i, R_i and Ω_o, R_o denote the angular velocity and the radius of the inner and outer cylinder, respectively. Synge (1938) theoretically investigated the flow between two concentric cylinders with no axial flow by means of linear stability analysis. He showed that these conditions (1.3) also apply to the viscous case. It should be mentioned that for the inviscid case equation (1.3) is valid for arbitrary disturbances ($n \in \mathbb{Z}$, Chandrasekhar 2013), while it is only valid for axisymmetric disturbances ($n = 0$) in the viscous case (Synge 1938). However, recently it was shown by Deguchi (2017), that viscous TC-flow where $\mu > \eta^2$ can get linear unstable at very high Reynolds numbers ($O(10^5)$) due to non-axisymmetric disturbances. Deguchi assumed that a viscous type of instability is responsible here. For simplicity, in the following we will refer to azimuthal flow components where $\mu > \eta^2$ or $\mu < \eta^2$ as "Rayleigh stable" or "Rayleigh unstable", respectively.

The experimental work of Taylor (1923) revealed that the viscosity has a slight stabilizing effect on equation (1.3) as can be seen schematically from Fig. 1.5b. Moreover, the presence of viscosity leads to stable regions in the counter rotating regime (Fig. 1.5b). The centrifugal instability in the TC flow is associated with standing waves and results

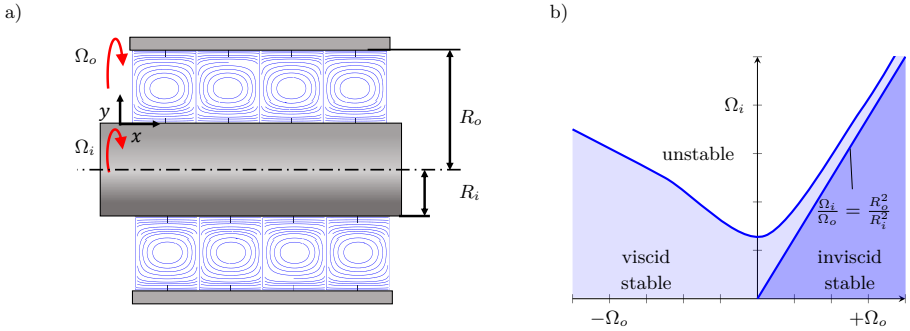

Figure 1.5: a) Geometry of Taylor Couette flow. Taylor vortices are visualized based on disturbance velocities obtained with linear stability computations. b) Stable and unstable parameter regions Taylor 1923 (schematic results for $R_o/R_i \approx 1.3$ and $R_o/R_i \approx 1.1$). Negative values of Ω_o denote counter rotation of cylinders, while positive values denote co-rotation.

in the formation of the well-known stationary Taylor vortices as indicated in Fig. 1.1a.

It should be mentioned, that both, the inviscid Rayleigh criterion and its viscous extension by Synge, do not account for axial flow. Nevertheless, it is sometimes inferred that rotating flows which are stable according to equation (1.3), must be equally stable or unstable when a (slight) axial flow component is added (Pedley 1968). In fact, the influence of centrifugal effects on the stability of a spiral flow, which features both axial and azimuthal components, is far more complicated. Ludwieg (1961) showed that a slight axial flow can destabilize Rayleigh stable azimuthal flow ($\Omega_o = \Omega_i$). In turn, the works of Ludwieg (1960); Kiessling (1963) and Mackrodt (1966) revealed that annular flows can be destabilized when Rayleigh-stable rotational flow is superimposed. In fact, Hagen-Poiseuille flow - which is linearly stable - can become linear unstable when superimposed with Rayleigh stable azimuthal flow (Mackrodt 1976). The works of Cottrel and Pearlstein (2004) as well as Meseguer and Marques (2005) further showed that also Spiral Poiseuille flow can be destabilized by a Rayleigh stable azimuthal flow component.

A generalization of Rayleigh's criterion under consideration of an additional axial shear flow was given by Howard and Gupta (1962) for the case of axisymmetric disturbances. According to Howard and Gupta (1962) the spiral flow is stable if the local Richardson number $J = \Psi / V_x^{'2}$ fullfills $J \geq 1/4$ everywhere. Here V_x is the axial flow component. With V_φ being the azimuthal flow component Ψ is defined as $r^{-3} \frac{d}{dr}(r^2 V_\varphi(r))$. Howard and Gupta (1962) were not able to define such a critera for non-axissymmetric disturbances. This was later achieved by Maslowe (1974). For the case of the Hagen-Poiseille flow with an imposed solid body rotation (rotating pipe flow) Maslowe showed that a necessary condition for instability is that the azimuthal wavenumber n is negative. Therefore, Joseph (1976) assumed that spiral flows whichs azimuthal flow component is Rayleigh stable ($\mu > \eta^2$) or Rayleigh unstable ($\mu < \eta^2$) feature negative or positive critical values of n, respectively. However, later works refuted Joseph's assumption. Cottrel and Pearlstein (2004) showed for a SPF with a Rayleigh stable azimuthal flow component ($\mu > \eta^2$) that both negative and positive values of n lead to an instability at different rotation rates (swirls). In chapter 3 we will show that a Rayleigh stable azimuthal flow component ($\mu \to \infty$) can trigger both negative as well positive n in the SPF. Also, we show that a Rayleigh unstable azimuthal flow component can trigger both both negative as well positive n in a SPF.

Overall, the interplay between axial and azimuthal velocity component results in a complex instability behavior, such that it is not possible to entirely anticipate the stability of the flow with simple criteria.

The Tollmien-Schlichting instability: As described centrifugal instabilities are related to flows in rotating systems or curved streamlines. The Tollmien-Schlichting instability (TSI) instead is primarily found in planar shear flows such as the boundary layer flow over a flat plate, as well as (axial) flows in annular gaps or plane channels. Those flows are linearly stable in the inviscid case, as their velocity profile exhibits no

inflection point, which is a necessary condition for instability according to Rayleigh's inviscid inflection point criterion Drazin and Reid 2004; Schmid and Henningson 2000. Tollmien (1930) showed that the viscosity is essential for the correct treatment of such flows. In fact, the TSI is based on the effect of viscosity, which induces a phase shift to the velocity fluctuations, such that their products (the Reynolds stresses) are nonzero when spatially averaged. This phase shift occurs in the "critical layer", a thin layer parallel to the walls. From a mathematical perspective, the critical layer is located where the pressure eliminated and linearized disturbance equation exhibits a singularity when $Re \to \infty$ (Tollmien 1930; Schlichting and Kestin 1961; Vasanta Ram 2019). This equation is well known as Orr-Sommerfeld equation (Schmid and Henningson 2000). For shear flows the singularity occurs at the location where the base flow velocity equals the disturbance velocity ($U = c$) (Maslowe 1986; Schmid and Henningson 2012). The TSI is associated with travelling waves of spatial or temporal increasing amplitude, inducing the formation and decay of vortices and finally resulting in a fully turbulent flow. It should be mentioned that the "classical" Tollmien-Schlichting instability is associated with a planar flow and features solely a streamwise wavenumber (= axial wavenumber λ) while the spanwise wavenumber is $n = 0$. For the Annular Poiseuille Flow (APF) instead, disturbances which are periodic in axial as well in azimuthal direction can become critical (Cottrel and Pearlstein 2004; Cottrel et al. 2004; Cotrell and Pearlstein 2006). In such cases where $n \neq 0$ the instability is spiral shaped and is also referred to as "Tollmien-Schlichting-like" instability (Cottrel and Pearlstein 2004). For simplicity, we use the terminology TSI for both axisymmetric as well as non-axisymmetric disturbances.

1.2.1.3 Works considering linear stability of Spiral Poiseuille Flow (SPF):

The Spiral Poiseuille Flow (SPF) is a combination of the Annular Poiseuille Flow (APF), driven by an axial pressure gradient and the Taylor-Couette Flow (TCF), driven by the rotation of the cylinder walls. This type of flow allows to adjust the amount of axial and rotational velocity present in the flow. Hence, it can smoothly merge a flow associated with a centrifugal instability (induced by TCF) and a flow associated with a shear instability (induced by APF). This renders it a unique tool to investigate instability mechanisms. As shown before, the interplay of axial and azimuthal flow components results in a complex instability behavior. Thereby, even a Rayleigh stable azimuthal flow component can induce an instability in a spiral-shaped flow. In the following, we will review the literature considering the SPF. As will be shown, the stability behavior of the SPF where the azimuthal flow is Rayleigh unstable has been subject to numerous studies. This includes the rotation of the inner cylinder ($\mu = 0$), counter-rotation ($\mu < 0$) and co-rotation where $\mu < \eta^2$ (Takeuchi and Jankowski 1981; Ng and Turner 1982; Meseguer and Marques 2000; Mesequer and Marques 2002; Cottrel and Pearlstein 2004; Cottrel et al. 2004; Cotrell and Pearlstein 2006). Several studies further considered the case of Rayleigh stable co-rotation (Mesequer and Marques 2002;

Cottrel and Pearlstein 2004; Cottrel et al. 2004; Meseguer and Marques 2005; Cotrell and Pearlstein 2006). However, to the authors best knowledge, only a single study considered a SPF where the inner cylinder is at rest ($\mu \to \infty$) (Meseguer and Marques 2005). In the following the curvature parameter $\epsilon = (1 - R_i/R_o)/(1 + R_i/R_o)$ is used for describing the geometry and all values from literature have been transferred accordingly. The ratio of azimuthal to axial flow component is hereafter referred to as swirl. Details about the parametrization, utilized to study the stability of the SPF in chapter 3, are described in detail in section 2.2.

The seminal work of Taylor (1923), in which he experimentally and theoretically analyzed the stability of the flow between two concentric cylinders, can be considered as the beginning of the linear stability analysis of annular gap flows. While Taylor's work dealed with the classical TCF, with no axial pressure gradient present, soon after the more complex SPF was investigated both experimentally (Cornish 1933; Fage 1938) and theroretically (Goldstein 1937). Subsequently, the SPF became the subject of further experimental works (Kaye 1958; Donnelly and Fultz 1960; Snyder 1962) as well as theroretical works (DiPrima 1960; Chandrasekhar 1960a,b; Krueger and Di Prima 1964). Following works started to add complexity to the problem by accounting for non-axissymmetric disturbances (Chung and Astill 1977) or reconsidering modifications and approximations of the velocity profile using alternative numerical methods (Hasoon and Martin 1977).

For an extensive review of the aforementioned works, the reader is referred to DiPrima and Pridor (1979). DiPrima and Pridor investigated the SPF with $\mu = 0$ for the small-gap approximation $\epsilon \to 0$ as well as curvature parameters of $\epsilon = 0.0256$ and 0.0526. While considering merely axisymmetric disturbances, they found that decreasing swirl has a stabilizing effect on the flow and further discovered the existence of two minima (two modes) in the neutral stability curve. The existence of this two minima leads to a jump of the critical wavenumber when the ratio of axial flow and azimuthal flow exceeds a certain threshold. This wavenumber jump was later associated with a change in the instability mechanism for axisymmetric (Ng and Turner 1982) and non-axisymmetric disturbances (Cottrel and Pearlstein 2004). Takeuchi and Jankowski (1981) presented the first time correct results considering non-axissymmetric disturbances for a wide gap SPF ($\epsilon = 0.333$, $\mu = 0; 0.2; -0.5$). Their results showed that non-axisymmetric disturbances become dominant and the Rayleigh unstable rotational flow is non-monotonous stabilized as the axial flow velocity increases (or vice versa). The aforementioned work of Ng and Turner (1982) instead considered both axissymmetric and non-axisymmetric disturbances for $\epsilon = 0.0256; 0.129$ and covered significantly higher values of Re compared to previous works. Ng and Turner confirmed the existence of the two minima discovered by DiPrima and Pridor (1979) and associated them to a Tollmien-Schlichting-type instability (TSI) and a "rotational" instability, respectively. However, they stated the importance of these modes dimishes when non-axisymmetric modes are considered. Mesequer and Marques (2002) investigated the SPF for the

co-rotation case for $\epsilon = 0.333$ and focused on the transition from an axial induced shear instability to a centrifugal instability. Meseguer & Marques concluded that solid-body rotation (Rayleigh stable, $\mu > \eta^2$), induces centrifugal instabilities in the SPF which are associated with positive azimuthal wavenumbers $1 \leq n \leq 6$. However, Cottrel and Pearlstein (2004) later noted, that Mesequer and Marques (2002) covered an unsufficient range of n and showed that for $\mu = 1$ increasing swirl triggers negative modes ($-6 \leq n \leq -1$). For co-rotating cylinders ($\mu > 0$), Mesequer and Marques (2002) further concluded that the centrifugal instability is characterized by an increase of the gradient of the azimuthal disturbance velocity u_φ towards the inner cylinder, while for the shear instability the disturbance exhibits a spiral pattern which is almost parallel to the rotation axis. Furthermore, they discovered discontinuities in the critical Reynolds number, which are related to disconnected closed curves of neutral stability.

Cottrel and Pearlstein (2004) numerically connected the linear stability behavior of the APF and the TC flow considering $\epsilon = 0.333$. Besides the case of rotating inner cylinder ($\mu < 0$), they also investigated co-rotation ($\mu = 0.2, 0.5, 1$) and counter-rotation ($\mu = -0.5$). The main focus of the investigations was on the transition between the TSI induced by the pressure gradient and the centrifugal instability induced by the rotational flow component. They identified this transition at the critical Reynolds number Re^*, where a discontinuity in the slope of Ta versus Re occurs. Also, they noted that the disturbance speed undergoes a jump. In fact, they concluded for Rayleigh unstable ($\mu = -0.5; 0; 0.2$) as well as for Rayleigh stable azimuthal flows ($\mu = 0.5; 1$) that there is a transition from a TSI to a centrifugal instability. In agreement with the (extended) Rayleigh criterion, for $\mu > \eta^2$ they where not able to find linear instability when the axial flow deceeds a certain threshold. Similar results and conclusions were obtained by Cottrel et al. (2004) for $\epsilon = 0.1299$ and $\epsilon = 0.0256$. Meseguer and Marques (2005) investigated a SPF with $\epsilon = 0.333$ and focused their analysis on the co-rotation regime ($\mu > 0$) also capturing Rayleigh stable azimuthal flow components. They also considered the case where only the outer cylinder is rotating (ORSPF, $\mu \to \infty$) and discovered that an instability associated to the rotating outer cylinder can destabilize the SPF and supersedes the TSI above a certain swirl threshold. At this point Meseguer and Marques (2005) denote the instability associated with the outer cylinder rotation as "outer rotation instability mechanism". Further, Meseguer and Marques (2005) observed a slight stabilization associated with the outer cylinder rotation at higher swirl values. Cotrell and Pearlstein (2006) investigated the linear stability boundaries of the SPF at several rotation rate ratios $\mu = -1; -0.5; -0.25; 0; 0.2$ and $\epsilon = 0.818$ and found that the flow is linearly stable if no rotation is present. In fact, their results show that the critical Reynolds number blows up for $\epsilon \to \approx 0.793$ in the absence of rotation and conclude that the flow is linearly stable for larger values of ϵ. Furthermore, they found no linear instability for the case of co-rotation $\mu > \eta^2$ (Rayleigh stable) in the absence of axial flow. However, their results showed that the SPF ($\mu > \eta^2$) was linear unstable at swirls inbetween those extremes. Increasing swirl both destabilized and stabilized the flow. Cotrell and Pearlstein (2006) further extensively investigated the phenomenon of

multi-valued stability boundaries induced by formation of closed (disconnected) stability curves which occur for $\mu < \eta^2$ as well as for $\mu > \eta^2$. While Cotrell and Pearlstein (2006) came to the conclusion that SPF is linearly stable for $\epsilon \to\gtrapprox 0.793$ if no rotation is present, Heaton (2008) showed there exists linear instability for all $0 < \epsilon < 1$ if sufficiently high Reynolds numbers and axissymmetric disturbances are considered.

An important fact considering the stability of the azimuthal flow component was recently revealed by Deguchi (2017) who performed a comprehensive analysis on the behavior of Rayleigh stable TCF in absence of axial flow ($\mu > \eta^2$). Deguchi observed that the flow can get unstable at $Re > 2.4 \times 10^4$ and discovered a previously unkown non-axissymmetric "long-wavelength" wavelength mode. He assumes that this long wavelength mode is not associated with the centrifugal instability explained by Rayleigh and that the viscosity acts as a destabilizing mechanism analoguous to a TSI.

Recently, Vasanta Ram (2019) reconsidered the transition from a TSI to a centrifugal instability in the SPF with increasing swirl. To identify a TSI, Vasanta Ram developed an expression to calculate the position of the critical layer and reformulates the SPF problem by means of ϵ and the swirl parameter S_i. Deriving a generalized Orr-Sommerfeld and Squire equation by eliminating the pressure in the Navier-Stokes equations, he obtains an expression for the location of the critical layer as function of the critical axial wavenumber (λ_c), the critical azimuthal wavenumber (n_c) and the critical complex frequency (ω_c). In the present thesis, this expression will be employed to verify the existence of a critical layer in the SPF and calculate its theoretical position.

1.2.1.4 Need for research in linear stability of the Spiral Poiseuille Flow (SPF)

Overall, the above-mentioned literature shows, that the SPF has been extensively studied for the Rayleigh unstable azimuthal flow ($\mu < \eta^2$) for fixed curvature parameters of $\epsilon = 0.0256; 0.1299; 0.333; 0.818$. However, till date no work considered ϵ as a quasi-continuous variable to uncover the linear stability behavior when ϵ is smoothly varied within $0 < \epsilon < 1$. Such information, depicted as a phase map, would provide a more complete picture. Phase maps covering the whole range of $0 < \epsilon < 1$ are further interesting for the design of TCRs as here arbritary values of ϵ can occur. Besides TCRs, in technical applications often ϵ is significantly smaller than $\epsilon < 0.0256$. This is, for example, the case in sealing gaps of hydraulic turbo machinery. Hence, it is of particular interest to uncover the linear stability behavior of the SPF ($\mu < \eta^2$) when ϵ approaches 0. This should be performed first for the Spiral Poiseuille Flow with Rotation of the Inner cylinder (IRSPF, $\mu = 0$) as is it is the most simple case but also the most common case in industrial applications.

Also, the SPF with a Rayleigh stable azimuthal flow ($\mu > \eta^2$) has been investigated for $\epsilon = 0.0256; 0.1299; 0.333; 0.818$. However, the case where only the outer cylinder rotates ($\mu \to \infty$) has solely considered by Meseguer and Marques (2005). Thereby Meseguer did

only consider $\epsilon = 0.333$ and restricted their computation to low and intermediate swirls. Hence, the linear stability behavior of the Spiral Poiseuille flow with outer cylinder rotation (ORSPF) is unexplored with respect to different values of ϵ and high swirls. Therefore, it is desirable to have a phase map, which fully covers the linear stability behavior of the ORSPF by means of ϵ and swirl.

So far, the transition from a Tollmien-Schlichting instability (TSI) to a centrifugal instability was identified by aprubt changes in the critical modes (λ, n, c) and an associated rapid decrease of the critical Reynolds number when the swirl increased. However, besides this indirect method of identification, to our knowledge, no work so far provided a quantitative method to determine wether a shear instability or a centrifugal instability is dominant. Further, while it was assumed that there exists a critical layer in the SPF in the low swirl limit (Cottrel and Pearlstein 2004) its existence has not been confirmed yet. While the instabilities in pressure driven flows such as the annular Poseuille flow (Mott and Joseph 1968b), or flows along curved streamlines (Guaus and Bottaro 2007) have been discussed based on the distribution of shear stresses or the budget of the disturbance energy, such a deep discussion has never been made for the SPF. To the authors best knowledge, no clear quantitative criteria have been formulated to clearly identify the onset of a centrifugal instability in a SPF. This accounts especially for the cases with Rayleigh stable azimuthal flow where the centrifugal effect of the azimuthal flow seems to develope a stabilizing as well as a destabilizing effect depending on the swirl. From literature it is still unclear how a centrifugal effect induced by the rotation of the outer cylinder can both destabilize and stabilize the flow. Hence, there is a need for a methodology to precisely identify and quantify centrifugal as well as shear instabilities.

1.2.2 Suspension flows of rigid particles - shear flows

As mentioned, it is unclear which mechanism leads to the separation of particles in the observed phenomena in the small gap TC setup (Fig. 1.2). Therefore, we perform an extensive study on particle segregation and migration in mono- and polydisperse suspension shear flows within this study. In this section we discuss the basics as well as the state of the art of suspension dynamics with a special focus on migration phenomena.

1.2.2.1 Governing equations, dimensionless numbers and effective viscosity

Whereas most theories and experiments have been developed for single particle dynamics, the majority of industrial processes involves large numbers of particles interacting with each other and the fluid (Crowe 2005). These interactions define the particle dynamics and become increasingly pronounced as the particle volume fraction is increased. The particle volume fraction, also referred to as solid volume fraction, is defined as $\Phi = V_s/(V_s+V_f)$ where V_s and V_f are the volume of the solid and the fluid phase, respectively (Stieß 2008, Crowe 2005). In general, flows with solid volume fractions up to $\Phi =$

0.5% (Mewis and Wagner 2012) or $\Phi = 5\%$ (Crowe 2005) are referred to as dilute suspensions. In dilute suspensions particle-particle interactions as well as particle induced disturbances to the flow field are negligible. In flows with particle volume fractions up to $\Phi \approx 20\%$ ($\Phi \approx 15\%$; Mewis and Wagner 2012), which are known as intermediate or semi-dilute suspensions, particle-particle interactions become as important as particle-fluid interactions. Ultimately, at volume fractions beyond $\Phi \approx 20\%$, the flow is referred to as dense suspension and particle-particle interactions become dominant while particle-fluid interactions are of lesser importance (Crowe 2005). Due to the presence of particles and the associated interactions, the viscous dissipation rate in a suspension is increased compared to a pure liquid. Neglecting hydrodynamic particle-particle interactions and collisions, Einstein showed theoretically, that the effective bulk viscosity μ_{eff} of a dilute suspension increases linearly as Φ increases (Einstein et al. 1905; Einstein 1911):

$$\mu_{\text{eff}} = \mu_{\text{fluid}}(1 + 2.5\Phi) \tag{1.4}$$

Due to the simplifications Einsteins equation is only valid for $\Phi < 0.5\%$ (Mewis and Wagner 2012). The work of Batchelor and Green (1972) accounted for this limitation and considered pair-wise particle interactions in suspensions of up to $\Phi = 20\%$ resulting in the following quadratic expression:

$$\mu_{\text{eff}} = \mu_{\text{fluid}}(1 + 2.5\Phi + 5.2\Phi^2) \tag{1.5}$$

To predict the effective viscosity at even higher volume fractions where complex particle-particle collisions are hampering the analytical treatment numerous empirical and semi-empirical models such as the Eilers fit (Ferrini et al. 1979) have been developed up to date (Zarraga et al. 2000; Stickel and Powell 2005). Furthermore, while the aforementioned works presuppose Stokes flow regime ($Re << 1$), recent numerical and experimental works revealed, that inertial effects can also increase the effective bulk viscosity (Kulkarni and Morris 2008; Haddadi and Morris 2014; Lashgari et al. 2014; Picano et al. 2013). For polydisperse suspensions, the effective viscosity is usually lower compared to monodisperse suspensions. At the same time, the maximum attainable volume fraction, which is about 64% for monodisperse suspensions (close random packing limit), is found to be higher in polydisperse suspensions (Shapiro and Probstein 1992; Chang and Powell 1994; Krishnan and Leighton Jr 1995; Santiso and Müller 2002).

In a suspension flow the ratio of inertial forces and viscous forces, known as the Reynolds number, can be described on the characteristic length scale of the bulk flow, as well as on the length scale of the particles. With the bulk velocity U_b, the hydraulic diameter D_h, the viscosity μ_{fluid} and the density ρ_f of the liquid phase, the bulk Reynolds number is defined as $Re_b = \rho_f U_b D_h / \mu_{\text{fluid}}$. Within this work U_b is defined as the mean velocity, which is the ratio of volume flow rate and cross-sectional area $\dot{V}/A$. When investigating pressure driven shear flows of neutrally buoyant suspensions, the particle Reynolds number is usually defined based on the local shear rate $\dot{\gamma}$ and the particle diameter d_p

as $Re_p = \rho_f \dot{\gamma} d_p^2 / \mu_{\text{fluid}}$. Re_p can be estimated, by using the average shear rate, that is for instance $\dot{\gamma} = U_b / D_h$ for a Poiseuille flow or $\dot{\gamma} = U_{\text{wall}} / H$ for a linear shear flow. For the pressure driven suspension flows investigated within this work, the particle Reynolds number is hence estimated based on the average shear gradient which can be written as $Re_p = Re_b (d_p / D_h)^2$ as utilized by Asmolov 1999; Chun and Ladd 2006; Di Carlo et al. 2007; Miura et al. 2014; Shichi et al. 2017; Pan et al. 2018; Chun et al. 2019; Morris 2020; Chun and Jung 2021. According to Bhagat et al. (2009) inertial effects emerge at $Re_p \gtrapprox 0.1$, while Abbas et al. (2014) observed inertial migration for $Re_p \approx O(10^{-4})$. Within this work, inertial effects are observed at $Re_p \approx 0.05$.

The research in describing the dynamics of suspended particles goes back to the works of Basset (1888), Boussinesq (1903) and Oseen (1927) who investigated the motion of a settling sphere in quiescent flow at vanishing particle Reynolds numbers. In general the equation of motion of a spherical particle in a fluid is:

$$m_p \frac{du_{pi}}{dt} = m_p g_i + \oint_s \sigma_{ij} n_j dS \quad \text{with} \quad \sigma_{ij} = p\delta_{ij} + \mu_{\text{fluid}} \left(\frac{\partial u_i}{\partial x_j} + \frac{\partial u_j}{\partial x_i} \right) \tag{1.6}$$

Here m_p and u_{pi} denote the particle mass and velocity, respectively. p and u_i are the pressure and the velocity components of the fluid. The challenging part here is to evaluate the fluid stress tensor $\oint_s \sigma_{ij} n_j dS$ on the right. Tchen (1947) proposed the first equations for spheres in unsteady and non-uniform flows, that was later corrected by Corrsin and Lumley (1956) who emphasized the role of the pressure gradient of the base flow. Using the Faxén correction to account for finite size effects of the particle, the first correct expansions of the fluid stress tensor in an non-uniform and unsteady flow where developed independently by Maxey and Riley (1983) and Gatignol et al. (1983) for the Stokes flow regime:

$$\underbrace{m_p \frac{d\vec{u}_p}{dt}}_{\vec{F}_I} = \underbrace{-\frac{18\mu_{\text{fluid}}}{\rho_p d_p^2} m_p (\vec{u}_p - \vec{u}_f - \frac{d_p^2}{24}\nabla^2 \vec{u}_f)}_{\vec{F}_D} + \underbrace{m_f \frac{D\vec{u}_f}{Dt}}_{\vec{F}_P} \underbrace{- 0.5 m_f \frac{d}{dt}(\vec{u}_p - \vec{u}_f - \frac{d_p^2}{24}\nabla^2 \vec{u}_f)}_{\vec{F}_{VM}}$$
$$\underbrace{-9\sqrt{\frac{\rho_f \mu_{\text{fluid}}}{\pi}} \frac{m_p}{\rho_p d_p} \int_{t_0}^{t} \frac{\frac{d}{d\tau}(\vec{u}_p - \vec{u}_f - \frac{d_p^2}{24}\nabla^2 \vec{u}_f)}{(t-\tau)^{1/2}} d\tau}_{\vec{F}_B} + \underbrace{(m_p)\vec{g}}_{\vec{F}_G} + \underbrace{(-m_f)\vec{g}}_{\vec{F}_{\text{Buo}}} \tag{1.7}$$

Here D/Dt is the derivative following a fluid element, while $\frac{d}{dt}$ is the temporal derivative following the particle, which are approximately the same for $Re_p << 1$ (Maxey and Riley 1983). $\frac{d_p^2}{24}\nabla^2 \vec{u}_f$ represents the Fax'en terms which account for the fluid velocity disturbance caused by the presence of the particle, where $\nabla^2 u_f$ is the curvature of the flow. m_f denotes the mass of the fluid displaced by the particle. In their derivation, Maxey and Riley (1983) separate the fluid stress tensor in two parts for the undisturbed fluid velocity and the velocity disturbance. The pressure force $\vec{F}_p = m_f \frac{D\vec{u}_f}{Dt}$ and

the Archimedes buoyancy force $\vec{F}_{\text{Buo}}$ originate from the fluid stress tensor $\oint_s \sigma_{ij} n_j dS$ associated with the undisturbed fluid velocity. The pressure force in laminar linear shear flows or Poiseuille flows equals zero as $\frac{D\vec{u}_f}{Dt} = 0$ in these cases. Furthermore, for neutrally buoyant particles the buoyancy force $\vec{F}_{\text{Buo}}$ gets canceled out by the gravity force $\vec{F}_G$ acting on the particle. The drag force $\vec{F}_D$, the virtual mass force $\vec{F}_{VM}$ and the Basset force $\vec{F}_B$ emerge from the fluid stress tensor of the disturbed velocity. The drag force given in equation (1.7) arises from viscous friction and is the corrected Stokes drag, which is known as the Fax'en law. This expression for $\vec{F}_D$ already considers that a neutrally buoyant particle deviates from the fluid velocity in the order of $\frac{d_p^2}{24}\nabla^2\vec{u}_f$ (Guazzelli and Morris 2011).

The virtual mass force is the inertia force induced by surrounding fluid that is accelerated by the moving particle. The Basset or history force accounts for the temporal developement of the viscous region near the particle.

Due to the Stokes flow approximation equation (1.7) only holds for $Re_p << 1$ where $Re_p = \frac{\rho_f |\vec{u}_p - \vec{u}_f| d_p}{\mu_{\text{fluid}}}$. Equation (1.7) further does not account for lift forces that would arise from the surface integral in (1.6) for example in the presence of channel walls. To account for inertial effects and lift forces, the equation has to be extended by empirical expressions, based on numerical simulations or experiments as discussed for instance in Zhang et al. (2016).

1.2.2.2 Forces on the particle and inertial migration in shear flows of suspensions

With increasing particle Reynolds number Re_p, a particles movement in a suspension is increasingly affected by inertial effects, which alters the forces acting on the particle along both the streamwise direction and the cross-sectional direction. The forces in cross-sectional direction can be combined to the effective lift force, which depends on the particles distance to the walls and induces a lateral movement of the particle (Zhang et al. 2016). At a certain wall distance, the effective lift force reaches zero and the particle attains its equilibrium position. This phenomena, known as inertial migration, was first observed by Segre and Silberberg (1961) in a circular pipe and is till date investigated in numerous flow geometries such as rectangular channels (Hood et al. 2016), square ducts (Shichi et al. 2017, Kazerooni et al. 2017), laminar as well as supercritical Taylor-Couette flows (Majji et al. 2018) and recently also in pulsating channel flows (Vishwanathan and Juarez 2021). In fact, inertial migration also referred to as inertial focusing is used widely in microfluidic particle separation processes (Zhang et al. 2016). The effective lift force composes of the shear gradient force, the wall force as well as Magnus force and the Saffman force.

It is important to understand that a neutrally buoyant particles exhibits a relative velocity compared to the local fluid velocity. In case of a Poiseuille flow the particle center lags the flow in the order of approximately $(d_p/D_h)^2$ as shown by Brenner (1966)

for Stokes flow and indicated by the numerical results of Feng et al. (1994) for $Re_p > 2.5$. A lag velocity in approximately the same order is also indicated by the experimental results of Pan et al. (2018) who additionally observed that the relative lag velocity decreases slightly as Re_p increases beyond $Re_p \gtrapprox 16.8$. In contrast, in a plane shear flow the particle center leads the flow (Feng et al. 1994). This velocity difference is also known as slip velocity. The combination of slip velocity and velocity profile of the base flow, leads to different distributions of the relative velocity and hence the pressure distribution around the particle. If the velocity profile in a (pressure driven) channel flow would be linear, a lagging of the particle would result in higher relative velocities on the side that is opposed to the channel wall, as depicted in Fig. 1.6a (Feng et al. 1994). As the pressure would drop accordingly on this side, the resulting force would push the particle away from the wall. However, in a laminar channel flow the velocity profile is curved such that the relative velocities are higher on the side thats directed towards the wall (Feng et al. 1994). Hence, according to the Bernoulli equation, the pressure is lower on this side and the particle is drawn towards the wall (Fig. 1.6b). The associated force is referred to as the shear gradient lift force, which approximately scales as $F_{SG} \sim \rho_f U_b^2 d_p^3 / D_h$ (Martel and Toner 2014; Zhang et al. 2016). As the particle approaches the wall, pressure builds up in the constriction between particle and wall, while the pressure drops at the opposed side of the particle resulting in a repulsive force that is inversely proportional to the normalized wall distance (Zeng et al. 2009; Martel and Toner 2014). Fig. 1.6c shows a sketch of these effects close to the wall. This force is commonly termed as wall (repulsive) force and scales with $F_{\text{wall}} \sim \rho_f U_b^2 d_p^6 / D_h^4$ (Martel and Toner 2014). It is mainly the balance of shear gradient lift force and wall repulsive force which are both of inertial origin, that determine the equilibrium position of a particle. In contrast, the Magnus force originates from a streamline asymmetry and associated pressure distribution that is caused by rotation of the particle (Rubinow and Keller 1961). The Saffman force arises from the interaction of the Stokeslet velocity field and the velocity gradient of the bulk flow, independently of the particle rotation (Saffman 1965). The direction of both, the Magnus force as well as the Saffman force depends on the sign of the slip velocity and is directed towards the channel centerline for a Poiseuille flow. However, both forces are negligible compared to the shear gradient lift and the wall repulsive force which are considered as the dominant effects for inertial migration (Amini et al. 2014).

1.2.2.3 Works considering inertial migration in dilute particle laden square duct flows

The rising interest in using inertial migration for particle separation has lead to numerous studies among which several have been performed in squared microchannels (Di Carlo et al. 2009). Since the work of Chun and Ladd (2006) who performed lattice-Boltzmann simulation at moderate to high Reynolds numbers ($Re_b = 100...1000$, $Re_p = 1...10$) and Di Carlo et al. (2007) who performed experiments at moderate Reynolds numbers

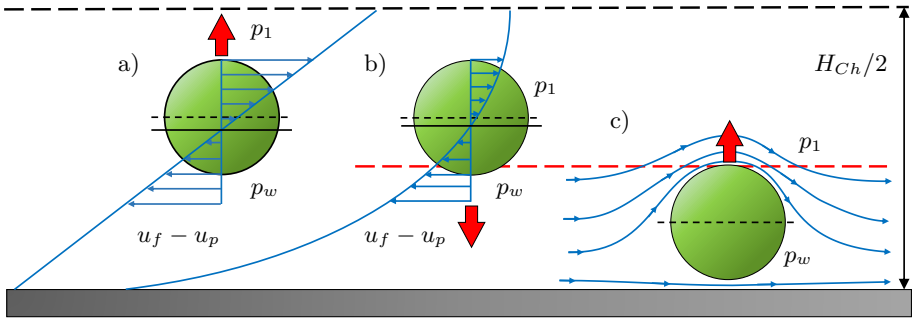

Figure 1.6: Schematic of the shear gradient lift force and the wall (repulsive) force adapted from Feng et al. (1994) and Martel and Toner (2014). Red line=equilibrium position where wall force and shear gradient lift force are equal. a) In a linear velocity profile a lagging particle would experience higher relative velocities on the upper side and hence get sucked away from the wall ($p_1 < p_w$). As the particle lags the flow the relative velocity is zero below the particle's centerline (indicated with dashed a solid line). b) Shear induced lift force in a laminar channel flow: The curvature of a parabolic velocity profile leads to higher relative velocities on the lower side of the (lagging) particle and the particle is sucked in direction of the wall ($p_1 > p_w$). c) Wall repulsive force: Close to the wall the relative velocities are higher on the upper side of the particle resulting in a force, directed away from the wall ($p_1 < p_w$).

($Re_b = 45$, $Re_p = 1.45$), it is known that in such geometries neutrally buoyant particles of dilute suspensions ($\Phi \lessapprox 0.5\%$) migrate across the streamlines to four equilibrium positions at the center of the channel faces. These four equilibrium positions are also referred to as Channel Face Equilibrium positions (CFE) (Fig. 1.7b) (Shichi et al. 2017). Choi et al. (2011) performed similar experiments with Re_b ranging from 2.35 to 60. While the particles where randomly distributed at low Re_b, with increasing Re_b they first migrated laterally forming an Pseudo Segré Silberberg Annulus (PSSA) (Fig. 1.7a) and subsequently migrate cross-laterally attaining the four equilibrium positions (CFE) as observed by Di Carlo et al. (2007). They further found the lateral as well as the cross-lateral focussing to be fully developed when the focussing number ($F_c = 2 \cdot Re_{max}(d_p/H)^2 L/H$) attained values of $\Pi/0.02$ and $\Pi/0.01$, respectively. It should be mentioned, that the Reynolds numbers are converted here for the sake of comparison. Using a macroscopic square duct of 6 mm width, Miura et al. (2014) achieved bulk Reynolds numbers ranging from 100 up to 1200 and particle Reynolds numbers up to $Re_p = 14$. They observed four additional equilibrium positions in the duct corners, denoted as channel corner equilibrium positions (CCE), which coexist with the CFE positions observed by Di Carlo et al. (2009) (Fig. 1.7d). Covering a range of $1 \leq Re_b \leq 800$ Shichi et al. (2017) observed the existence of Intermediate Equilibrium Positions (IME) in addition to the Channel Corner Equilibrium positions

(CCE) and Channel Face Equilibrium positions (CFE) (Fig. 1.7c). Sichi et al. defined four regimes associated with these position and showed that the range of Re_b related to these regimes strongly depends on d_p/H.

Besides these lateral focussing effects, particles where also observed to arrange axially into particle trains as a result of hydrodynamic particle interaction (Gao et al. 2017; Humphry et al. 2010). In fact, numerical and experimental studies revealed that even at very dilute conditions the presence of particles can induce secondary flows and signifcantly alter the flow profile such that inertial migration can be affected (Humphry et al. 2010; Kazerooni et al. 2017; Pan et al. 2018; Yuan et al. 2018). Further Nakagawa et al. (2015) revealed that rotation induced lift forces can play a role in migration from the point when particles collect at the annulus and shear- and wall-induced forces are balanced. For more details regarding inertial migration in microfluidic geometries the interested reader is referred to the comprehensive works of Di Carlo et al. (2009); Zhou and Papautsky (2013); Martel and Toner (2014); Zhang et al. (2016); Bazaz et al. (2020).

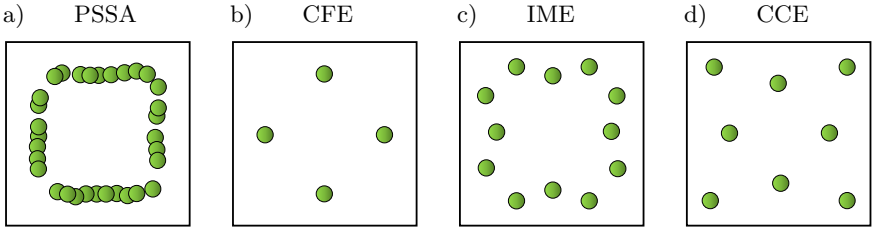

Figure 1.7: Equilibrium Positions adapted from Shichi et al. (2017) ($H/d_p = 8$). a) $Re_b = 100$, $L/H = 125$ b) $Re_b = 100$, $L/H = 1500$ c) $Re_b = 280$, $L/H = 1500$ d) $Re_b = 450$, $L/H = 1500$

1.2.2.4 Shear induced migration

In contrast to inertial migration, denoting the inertial interaction of individual particles and ambient fluid at high Reynolds numbers, the term shear induced migration refers to the irreversible collective particle drift from regions of high to low shear rates at vanishing particle Reynolds numbers in semi-dilute or dense suspensions. In a Taylor-Couette device with rotating inner cylinder shear induced migration leads to a particle depletion close to the inner cylinder (high shear rate) and an accumulation of particles at the outer cylinder (low shear rate) (Leighton and Acrivos 1987; Abbott et al. 1991). In pressure driven flows in pipes or rectangular channels, particles migrate to the channel center while they deplete at the walls, as a consequence of the shear rate distribution (Leighton and Acrivos 1987; Abbott et al. 1991).

The underlying mechanism of shear induced migration is irreversible particle interactions (Leighton and Acrivos 1987; Buyevich 1996). These can be classified into two-body and three-body particle collisions, whereby in the former case the irreversibility emerges from surface roughness, while in the latter case irreversibility persist also in the presence of perfect surfaces (Leighton and Acrivos 1987). However, it was shown in experiments that in real flows the effect of three-body collisions is approximately three orders lower compared to two-body collisions and therefore negligible (Leighton and Acrivos 1987; Phillips et al. 1992). For the onset of shear induced migration in experiments a sufficient solid volume fraction is required, which is for instance about $5\% < \Phi < 10\%$ in a rectangular channel flow (Gao et al. 2009). Hampton et al. (1997) observed the onset of shear induced migration at $\Phi \geq 20\%$ in a circular conduit. Based on the shear-induced-migration hypothesis developed by Leighton and Acrivos (1987), the minimum concentration required for shear induced migration to be observable can be estimated based on the shear Peclet number (Nott and Brady 1994, Dinther et al. 2013):

$$P_{shear} = \left(\frac{H}{d_p}\right)^2 \frac{1}{12 D_\Phi} \frac{H}{L} \tag{1.8}$$

Where $D_\Phi = \frac{1}{3}\Phi^2(1 + 0.5e^{8.8\Phi})$ is the non dimensionalized diffusion coefficient, H is the channel height and L the development length. For $P_{shear} < 1$ a stationary concentration profile should have developed, such that shear-induced migration can be observed. Interestingly, some studies report shear-induced migration at much lower solid volume fractions than $\Phi = 5\%$. Abbas et al. (2014) seemingly observed shear induced migration at solid volume fractions of $\Phi = 0.2\%$ and $\Phi = 0.8\%$ at $L/H \approx O(10^3)$ while eq. 1.8 yields ($L/H > O(10^5)$). Further, Brown et al. (2009) reported the phenomena in a (brownian) suspension at $\Phi = 0.5\%$. In this study we report shear induced migration at a volume fraction of $\Phi = 9.1\%$ in a square duct.

The model of Phillips et al. (1992) provides a good overview, which parameters affect the rate of shear induced migration. Based on the analysis of Leighton and Acrivos (1987), they developed their well-known "diffusive flux model" which accounts for the flux induced by spatial gradients of the collision frequency and the flux induced by spatial gradients of the effective viscosity, which both scale with d_p^2:

$$\frac{D\Phi}{Dt} = \underbrace{d_p^2 K_c \nabla \cdot (\Phi^2 \nabla\dot{\gamma} + \Phi\dot{\gamma}\nabla\Phi)}_{\text{interaction frequency effect}} + \underbrace{d_p^2 K_{\mu_{\text{eff}}} \nabla \cdot (\dot{\gamma}\Phi^2 \frac{1}{\mu_{\text{eff}}} \frac{\partial \mu_{\text{eff}}}{\partial \Phi} \nabla\Phi)}_{\text{viscosity gradient effect}} \tag{1.9}$$

As can be seen gradients in $\dot{\gamma}$, Φ and μ_{eff} induce migration. The model further does not depend on the absolute value of the viscosity. The coefficients K_c and $K_{\mu_{\text{eff}}}$ are constants that need to be determined experimentally. The effect of the interaction frequency is visualized schematically in Fig. 1.8a. When two particles embedded in adjacent shearing surfaces pass each other, collisions occur which displace the particles with a magnitude of $O(d_p)$. When these collisions are irreversible, the particle is displaced from its original streamline. Hence, if a particle experiences a higher frequency of

collisions from one direction, it will travel to the opposite direction (Phillips et al. 1992). As mentioned, regarding equations (1.4) and (1.5), the presence of particles alters the effective viscosity. The effect of a gradient in the effective viscosity, induced by gradients in particle concentration, is visualized in Fig. 1.8b. In case of a gradient in viscosity one particle experiences a higher resistance to motion. As a result, the center of rotation of the particle pair is shifted in the direction of higher viscosity. Hence, when the particle pair rotates during the collision, both spheres are displaced in the direction of lower viscosity (Phillips et al. 1992). This model is used in chapter 6 to explain particle

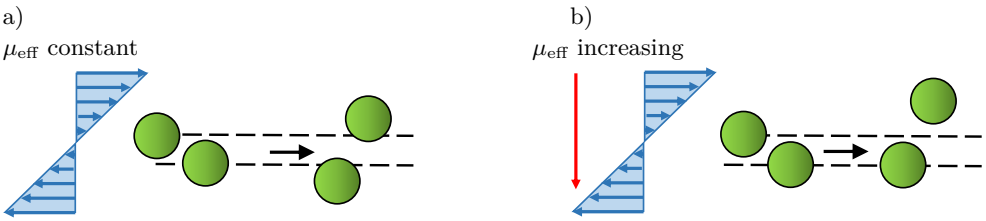

Figure 1.8: Schematic of the effects considered in the "diffusive flux model" (adapted from Phillips et al. 1992). a) Irreversible two body collision with constant viscosity b) Irreversible two body collision with viscosity gradient

migration phenomena which we observe in pressure driven suspension flows through square capillaries. In the following section, we review the literature on shear-induced migration in mono- and bidisperse suspensions.

1.2.2.5 Works considering shear induced migration of mono- and bidispersed suspensions

Up to date, it has been shown that monodispersed particles migrate to regions of minimum shear rate when suspended in non-homogenous shear flows (Leighton and Acrivos 1987; Hampton et al. 1997). While for monodisperse suspensions it is known that the particle fluxes scale with d_p^2 (Phillips et al. 1992), the situation is more complex in polydisperse suspensions. Even though studies concerning bidisperse suspensions indicate that large particles migrate faster than smaller particles (Husband et al. 1994; Lyon and Leal 1998b; Semwogerere and Weeks 2008), the overall migration behavior is altered by bimodal particle size distribution and several studies indicate that small particles hinder the migration of large particles (Lyon and Leal 1998b; Gao et al. 2009; Dinther et al. 2013; Chun et al. 2019). Further, the rate of migration of individual species not only depends on d_p but also on Φ such that smaller particles can migrate faster if their volume fraction is higher than that of the large species (Semwogerere and Weeks 2008). In the following, an overview on works concerning mono- and polydisperse suspension flows associated with shear induced migration in pressure driven flows is given.

One of the first works considering pressure driven flows of dense suspensions is the work of Karnis et al. (1966), who measured velocity profiles in monodisperse suspensions up to 41% solid volume fraction. While they found no direct evidence for particle migration towards the channel center, they observed a significant blunting of the velocity profile. This blunting is a result of high particle concentration in the center, which can lead to the formation of a plug as for instance shown by Oh et al. (2015).

The first clear experimental proof for shear induced migration in monodisperse pressure driven suspension flows was presented in the work of Koh et al. (1994), who measured velocity and concentration profiles in a rectangular channel at volume fractions ranging from 10% to 30%. Considering different ratios of particle diameter and channel heigth ($H/d_p = 9...50$), they observed the particles to migrate to the channel center, resulting in prominent concentration peaks at the channel centerline and concentration minimums at the walls. Further, they observed a significant blunting of the velocity profile which became pronounced with increasing Φ and decreasing H/d_p. Hampton et al. (1997) investigated monodispersed suspension flows in a pipe at $10\% \leq \Phi \leq 45\%$. No shear induced migration could be observed for $\Phi = 10\%$. However, for $\Phi \geq 20\%$ a clear concentration peak, which became less pronounced with increasing Φ, and a blunting of the velocity profile was observed. Lyon and Leal (1998a) investigated shear induced migration of monodisperse suspensions up to $\Phi = 50\%$ in a rectangular channel flow. They showed that increasing Φ results in an increased concentration of particles in the channel center, leading to a blunting of the velocity profile. Regarding both velocity and concentration profiles no dependence on H/d_p could be observed. The aforementioned work of Oh et al. (2015) investigated pressure driven pipe flows at solid volume fractions up to $\Phi = 55\%$. The migration of particles to the centerline resulted in the formation of a center plug, consisting of jammed particles, leading to blunted velocity profiles. Within the plug, which radius increased with increasing Φ, the solid volume fraction reached the random close packing limit of 64%.

As mentioned, while in monodisperse suspensions the vast majority of studies agree that particles migrate from high to low shear regions with Φ being the dominant parameter, in polydisperse suspensions the behavior depends also on the volume fraction ratio of the different species (Φ_s/Φ_L), as well as on the size ratio $d_{p,\mathrm{L}}/d_{p,\mathrm{s}}$, where the indices "L" and "s" denote the larger and smaller species, respectively. Lyon and Leal (1998b) investigated bidisperse suspensions in a rectangular channel flow for total volume fractions of 30% and 40% at different volume fraction ratios Φ_s/Φ_L. They observed that the concentration of large particles always increased towards the channel center regardless of Φ and amount of small particles. Contrary, the migration of small particles was found to be dependent on Φ_s/Φ_L as well as the total volume fraction. Further, they found the rate of migration to be reduced in the bidisperse case compared to the monodisperse case. This finding was confirmed by Gao et al. (2009) who investigated the mixing and segregation of settling mono- and bidisperse suspensions in microchannels at low bulk and particle Reynolds numbers ($Re_b = O(10^-3)$, $Re_p = O(10^-5)$). Their

results showed that at $\Phi \geq 20\%$ polydispersity inhibits shear induced migration in a straight channel. Dinther et al. (2013), who investigated bidisperse suspension flows in a rectangular microchannel at various volume fractions ($\Phi = 9\%$, 19% and 38%) of different ratios of Φ_s/Φ_L, came to a similar conclusion. While increasing Φ led to increased migration, increasing Φ_s at a fixed total volume fraction ($\Phi = 38\%$) hindered the migration of large particles. Dinther et al. (2013) focused in their work on the migration induced separation of species (segregation). They concluded that, even though migration of large particles was found to be pronounced at smaller Φ_s, the maximum segregation of both species occurs at high volume fractions (e.g. 38%) with equal volume fractions of small and large particles ($\Phi_s = \Phi_L$). Here small particles were found to accumulate at the wall while larger particles migrated to the channel center. When Φ_s was lower than Φ_L ($\Phi_s \approx 0.5\Phi_L$) small particles did not exhibit concentration peaks on the wall.

The link between segregation and the individual particle size and concentration, was deduced by Semwogerere and Weeks (2008). They investigated the shear-induced particle migration of binary suspensions in a rectangular microchannel for different volume fractions of small and large species up to a total volume fraction of $\Phi = 35\%$. Depending on the individual volume fraction, either the small or the large species exhibited concentration peaks at the center, leading to the conclusion that the species with the shorter entrance length ($L/H \sim 1/(12d(\Phi))(H/d_p)^2$) (Nott and Brady 1994) migrates to the center and screens off the other species. The role of the entrance length, or rather the effects of a not yet fully developed concentration profile, were also topic of the recent studies of Chun et al. (2019) who numerically investigated the shear induced segregation of binary suspensions in a plane channel flow. Chun et al. (2019) considered $\Phi = 30\%$ as well as various volume fraction ratios (Φ_s/Φ=0.13-0.67) and particle size ratios ($d_{p,\mathrm{L}}/d_{p,\mathrm{s}} = 1.4 - 2.4$). They observed the accumulation of large particles at the mid plane region while smaller particles depleted from this region. This observation was shown to be independent of Φ_s/Φ or $d_{p,\mathrm{L}}/d_{p,\mathrm{s}}$. They further emphasized that no significant depletion of small particles is observed when the particle concentration profile is not sufficiently developed. Also, a bidisperse suspension took 5-8 times longer to develope a steady concentration profile which is in agreement with findings of Lyon and Leal (1998b); Gao et al. (2009); Dinther et al. (2013).

1.2.2.6 Works considering mixed migration mechanisms in dilute to semi dilute suspensions

In laminar dilute suspensions flows through rectangular channels (see section 1.2.2.2 to 1.2.2.3), inertial effects lead to the migration of particles across streamlines to different equilibrium positions given a sufficient channel length and Reynolds number. These effects result in different particle concentration patterns in the crossectional plane. This

requires that particle-particle interactions are negligible, which is only the case for dilute suspensions. With increasing volume fraction the frequency of particle-particle interactions increases, giving rise to shear induced migration (section 1.2.2.4 to 1.2.2.5).

The competition of these effects was investigated by Han et al. (1999) in a tube flow of a suspension of neutrally buoyant particles at volume fractions ranging from 6% to 40%. For $\Phi \leq 10\%$ they observed that particles accumulate at 0.5-0.6 times the tube radius attaining a parabolic velocity profile, while at $\Phi = 40\%$ the particles migrated to the centerline and a blunted velocity profile was observed. For $10\% < \Phi < 40\%$ the competition of shear induced migration and inertial migration resulted in two distinct concentration peaks whose prominence is dependend on Re_p and Φ. While the work of Han et al. (1999) was restricted to $Re_b < 3.14$, Kazerooni et al. (2017) considered Re_b up to 550. Using Direct Numerical Simulations (DNS) they investigated the effect of Re_b, Re_p and particle size ratio H/d_p in a laminar monodisperse suspension flow through a square duct for $0.4\% \leq \Phi \leq 20\%$. For $\Phi \leq 5\%$ and $Re_b = 550$, they showed that Re_b is the key parameter in defining particle migration, while Re_p has just a slight influence. Further, for $Re_b = 550$ they find particle distributions to be similar for volume fractions between $5\% < \Phi \leq 20\%$ and conclude that inertial forces dominate over particle interaction effects. However, at $Re_b = 144$ the particle distribution was found to strongly depend on Φ which lead to the conclusion that particle interaction play a significant role at lower Re_b. While in the aforementioned works significant particle-particle interactions where observed for $\Phi > 5\%$, the study of Abbas et al. (2014) indicates that shear induced migration and inertial migration can coexist even at $\Phi = 0.2\%$. For a monodisperse suspension flow in a square duct they observed inertial migration towards the walls at $Re_b \geq 10$, while at $Re_b < 1$ particles migrated to the channel center which was related to shear-induced migration. Both mechanisms were found to coexist in the range of $1 < Re_b < 10$ resulting in multiple peaks in the concentration distribution. An explanation why they were able to observe shear induced migration at this low values of Φ may be the fact that Abbas et al. (2014) realized relative channel lengths of L/H up to 7215. However, according to the equation of Nott and Brady (1994) L/H should be in the order of $O(10^5)$ for fully developed shear induced migration in their case. Tatsumi et al. (2019) investigated the concentration distribution of rigidized red blood cells (RBCs) and monodispersed particles in a rectangular channel at volume fractions of $\Phi = 9\%$ to $\Phi 16.6\%$. With $Re_p \approx 0.02$ they observed concentration peaks close to the channel center and at the walls, which were found to primarily result from interparticle collisions. Incorporating the effect of collisions and inertia on the diffusive flux in their model they were able to obtain a qualitative agreement between experimental and numerical results up to $\Phi = 16.6\%$.

Up to date studies, on suspension flows at higher volume fractions ($\Phi \geq 10\%$) and significant particle Reynolds numbers were mostly exclusively restricted to monodisperse cases. Recently, Chun and Jung (2021) observed that inertial effects as well as shear

induced effects lead to particle segregation in bidisperse flows. Chun and Jung (2021) numerically investigated the particle distribution of mono- and bidisperse suspensions resulting from the interplay of shear induced and inertial migration for $0.003 \leq Re_p \leq 0.94$ at $\Phi = 20\%$ in linear shear flow. At $Re_p \geq 0.078$ smaller particles enriched in the mid plane in agreement with findings from Ho and Leal (1974) while larger particles maintained a uniform distribution which the authors related to their larger self diffusivity ($D \sim d_p^2 \Phi \dot{\gamma}$). While the distribution of small particles was found to be unchanged in bidisperse suspensions, their presence lead to a strikingly different distribution of large particles compared to the monodisperse case that became pronounced with increasing Re_p.

1.2.2.7 Need for research in shear flows of suspensions

The particle separation phenomena depicted in Fig. 1.2, occurred at operations points where the shear particle Reynolds number was estimated as $Re_p \approx 0.16...0.9$. Further, preliminary/similar experiments strongly indicate that local particle concentrations are beyond the dilute regime within the particle bands (Schröer et al. 2017). Hence, according to estimated particle Reynolds number and solid volume fraction, it is likely that both inertia as well as shear induced migration play a role in separating the species. Up to now there is no understanding how these mechanisms interact and lead to a size separation.

As clear from the previously mentioned literature, extensive research has been performed on inertial migration in dilute monodisperse suspensions ranging from low to high Reynolds numbers. Thereby, it was revealed that the particle size as well as the Reynolds number are key parameters which determine the rate of migration. On the other hand, shear induced migration has been investigated at vanishing Reynolds numbers for both mono- and bidisperse suspensions. It was revealed that shear-induced migration could lead to a size segregation of particles. However, the behavior of semi-dilute or dense suspensions at higher Reynolds numbers, where both migration mechanisms are relevant, has scarcely been investigated both for mono- and bidisperse suspensions. To our knowledge, the numerical study of Chun and Jung (2021) is the only work considering bidisperse suspensions at finite Reynolds numbers beyond the dilute regime. Also, no experimental work has been performed in shear flows at finite Reynolds numbers comparable to direct numerical simulations as performed by Kazerooni et al. (2017). In fact, no experimental work so far considered bi- or even tridisperse suspensions at higher Reynolds numbers and suspensions beyond the dilute regime. The lack of such experimental works may be related to the opaque nature of suspension flows at higher volume fractions, so that usually sophisticated measurement techniques such as Magnetic Resonance Imaging are employed, which makes the experiments costly and time consuming. Further, as will be discussed in section 1.2.4 most measurement techniques are not suitable for polydisperse suspensions. Moreover, for shear-induced as well as for inertial migration long developement lengths (L/H) are required which

leads to large setups when performed on the macroscale. This may be another factor which hinders experimental works. Therefore, it is easier to perform the experiments in the microscale.

Hence, a measurement technique is required, which is easy-to-implement, inexpensive and can be applied to polydisperse suspensions on the microscale. Most significantly, the measurement technique has to be realiable at solid volume fractions beyond the dilute regime. In this thesis, we conclude that Astigmatism Particle Tracking Velocimetry (APTV) together which a refractive index matching (RIM) technique is a promising method for such a purpose. Therefore, a discussion on the application of different non-intrusive measurement techniques is given in section 1.2.4. Hence, different aspects on the application of APTV on suspension flows will be investigated in chapter 4 to chapter 6. Also, in chapter 6 we will successful apply APTV to polydisperse suspensions at 9.1% volume fraction.

1.2.3 Supsension flows of rigid particles - rotating flows

In the previous sections, the properties of suspensions and the phenomena of particle migration in shear flows are discussed, considering only neutrally buoyant particles. In this section the dynamics of isolated settling particles in a rotating fluid are reviewed briefly. Subject to Coriolis, centrifugal and gravitational forces, these types of particles are undergoing motion relative to the fluid, even when the fluid is quiescent. Thus, using the difference between the particle velocity ($\vec{u}_p$) and the fluid velocity ($\vec{u}_f$) to define the particle Reynolds number $Re_p = d_p(|\vec{u}_p - \vec{u}_f|)\rho_f/\mu_{\text{fluid}}$ is a frequently chosen option. As in macroscopic experiments the local slip velocity usually is unkown, the Reynolds number can be approximated based on the estimated settling velocity of a particle in a quiescent flow.

1.2.3.1 Single Particle dynamics in rotating flows - Governing equation

In this section, a simplified equation of motion for particles suspended in a horizontally aligned Taylor-Couette flow will be presented. For this, equation (1.7) is extended by empircal expressions to account for the drag force ($\vec{F}_D$) at higher values of Re_p and the Saffman force ($\vec{F}_{\text{Saff}}$). Further, due to the rotation the pressure field is changed by centrifugal effects (Roberts et al. 1991), which is not considered in equation (1.7) explicitely. Hence, we reevaluate the integral of the pressure over the particle surface and derive an expression for $\vec{F}_P$ that accounts for the centrifugal pressure. Further, we assume stationary flow ($d\vec{u}_f/dt = 0$) and we neglect the Basset force such that the equation attains the following form:

$$\underbrace{m_p \frac{d\vec{u}_p}{dt}}_{\vec{F}_I} = -\vec{F}_D \underbrace{- \oint_S p dS}_{\vec{F}_P} \underbrace{- 0.5 m_f \frac{d}{dt}\vec{u}_p}_{\vec{F}_{VM}} + \underbrace{m_p \vec{g}}_{\vec{F}_G} + \vec{F}_{\text{Saff}} \tag{1.10}$$

Because equation (1.10) is formulated in Cartesian coordinates, it does not contain a special term for the centrifugal force acting on the particle. Instead, the centrifugal force arise from $\vec{F}_I$ when the particle moves along a curved streamline or the cylinder walls. In the following we present approximations for $\vec{F}_D$, $\vec{F}_{\text{Saff}}$ as well an analytical solution for $\vec{F}_P$. All forces are assumed to be independent of each other.

For the Stokes regime ($0 < Re_p < 0.2$) the Faxén law is employed for F_D as given in (1.7).

$$\vec{F}_D = \frac{18\mu_{\text{fluid}}}{\rho_p d_p^2} m_p (\vec{u}_p - \vec{u}_f - \frac{d_p^2}{24}\nabla^2 \vec{u}_f) \tag{1.11}$$

For higher values of Re_p several correlations can be found in literature for determination of F_D based on empirical drag coefficients. For $Re_p > 0.2$ we employ an empirical expression developed by Khan and Richardson which applies for $0 < Re_p < 10^5$ (Richardson et al. 2002) and yields $\vec{F}_D$ in the following form:

$$\vec{F}_D = (1.84 Re_p^{-0.31} + 0.293 Re_p^{0.06})^{3.45} \rho_f \pi d_p^2 \frac{1}{4} |\vec{u}_p - \vec{u}_f| (\vec{u}_p - \vec{u}_f) \tag{1.12}$$

Equation (1.12) assumes the sphere moving through theoretically infinite, unbounded fluid, which deviates from a rotating flow in TC system (Khan and Richardson 1987). However, as will be shown later, equation (1.12) is sufficient for the considered scenario. The Saffman force is a lift force, which results from the interaction of the Stokeslet velocity field of the particle and the velocity gradient of the bulk flow. It is independent of the particle rotation and is also referred to as a shear slip force (Zhang et al. 2016). The Saffman force is considered using the empirical expression of Mei (1992) which is valid for $Re_p \leq 100$:

$$\vec{F}_{\text{Saff}} = \frac{\rho_f}{2} \frac{\pi}{4} d_p^2 C_{LS} d_p \left((\vec{u}_f - \vec{u}_p) \times \vec{\omega}_f \right) \tag{1.13}$$

Thereby the lift coefficient C_{LS} is calculated as follows:

$$C_{LS} = \frac{4.1126}{Re_s^{0.5}} f(Re_p, Re_S)$$

The factor $f(Re_p, Re_s)$ is defined for two regions of Re_p:

$$\begin{aligned} f(Re_p, Re_s) =& (1 - 0.3314\beta^{1/2}) \exp\left(-\frac{Re_p}{10}\right) + 0.3314\beta^{1/2} \quad \text{for} \quad Re_p \leq 40 \\ f(Re_p, Re_s) =& 0.0524(\beta Re_p)^{1/2} \quad \text{for} \quad 40 < Re_p \leq 100 \end{aligned}$$

with $\beta = 0.5 \cdot Re_s / Re_p$ and the Reynolds number based on the vorticity of the flow Re_s defined as:

$$Re_s = \frac{\rho_f d_p^2 |\vec{\omega_f}|}{\mu_{\text{fluid}}} \quad \text{with} \quad \vec{\omega_f} = \text{rot}(\vec{u_f}) = \nabla \times \vec{u_f} \tag{1.14}$$

The Saffman force deviates from zero only if the particle velocity differs from the local fluid velocity such that $\vec{u}_f - \vec{u}_p \neq 0$. Furthermore, the direction of the Saffman force depends on the sign of the expression $\vec{u}_f - \vec{u}_p$, which is also referred to as slip velocity. When a particle lags the fluid in a simple shear flow, the Saffman force is perpendicular to the slip velocity and directed towards the moving wall. Contrary, when the particle leads the flow the Saffman force is directed towards the stationary wall.

As mentioned for equation (1.7) the pressure force $\vec{F}_P$ arises from the pressure distribution around the particle. In linear shear flows or Poiseuille flows $\vec{F}_P$ consists solely of the buoyancy term $V_p \rho_f \vec{g}$ as $D\vec{u}_f/Dt$ is zero. However, in rotating flows $\vec{F}_P$ is also affected by the centrifugal pressure (Roberts et al. 1991). Hereafter, we derive an expression for the pressure force in a generalized Taylor-Couette flow with independently rotating cylinders. For this, the azimuthal velocity profile $W(r)$ for a general Taylor Couette device is required, as given for instance by Takeuchi and Jankowski (1981) for $R_i < r < R_o$:

$$W(r) = Ar + B/r \quad \text{with} \quad A = \frac{\Omega_o R_o^2 - \Omega_i R_i^2}{R_o^2 - R_i^2} \quad B = \frac{R_i^2 R_o^2 (\Omega_i - \Omega_o)}{R_o^2 - R_i^2} \tag{1.15}$$

With equation (1.15) the pressure change in radial direction due to the centrifugal acceleration is:

$$\frac{\partial p}{\partial r} = \frac{W(r)^2}{r} \rho_f = \frac{(Ar + B/r)^2}{r} \rho_f \tag{1.16}$$

By integrating for r, we obtain the following pressure field $p(x, y)$ where $r^2 = x^2 + y^2$:

$$p(x,y) = p_0 + \frac{\rho_f}{2} \left(4AB \ln(r) + A^2 r^2 - \frac{B^2}{r^2} \right) - \rho_f g y \quad \text{with} \quad r^2 = x^2 + y^2 \tag{1.17}$$

Hence, the Gauss theorem is used for integrating the surface integral and the pressure force attains the following form:

$$\vec{F}_p = -\int_V \nabla p dV = \rho_f V_p \begin{pmatrix} -\frac{\left(\frac{4ABx}{x^2+y^2} + \frac{2B^2 x}{(x^2+y^2)^2} + 2A^2 x \right)}{2} \\ -\frac{\left(\frac{4ABy}{y^2+x^2} + \frac{2B^2 y}{(y^2+x^2)^2} + 2A^2 y \right)}{2} + g \end{pmatrix} \tag{1.18}$$

Equation (1.18) is valid for a general Taylor-Couette flow where both cylinders have a rotary degree of freedom with individual frequencies ($\Omega_o \neq \Omega_i$). However, in chapter 7 we solely consider rotating flows at solid body rotation ($\Omega_o = \Omega_i = \Omega$). For such a scenario (1.18) reduces to (1.19) which is identical with the expression obtained by Roberts et al. (1991) for a drum flow with no inner cylinder:

$$\vec{F}_p = -\int_V \nabla p dV = \rho_f V_p \begin{pmatrix} -\Omega^2 x \\ -\Omega^2 y + g \end{pmatrix} \tag{1.19}$$

For this case Roberts et al. (1991) derived an analytical expression for the trajectory $(x(t), y(t))$ of a settling particle:

$$x(t) = x_0 + \alpha e^{dt}\cos(\Omega t + \Theta) \quad \text{and} \quad y(t) = \alpha e^{dt}\sin(\Omega t + \Theta) \tag{1.20}$$

This expression describes a spiral whose radius increases with the growth rate d. The coefficients c, d as well as the spiral center $x_0 + iy_0$ are obtained as follows:

$$c = \frac{18\mu_{\text{fluid}}}{\rho_p (d_p)^2} \quad d = \frac{(\rho_p - \rho_f)\Omega^2}{\rho_p c} \quad x_0 + iy_0 = \frac{g d_p^2 (\rho_p - \rho_f)}{18\mu_{\text{fluid}}\Omega} \tag{1.21}$$

The spiral radius α and the phase shift Θ can be determined by the initial displacement of a particle with respect to the spiral center (Roberts et al. 1991). Hereafter, equation (1.10) is utilized for analyzing the dynamics of particles in drum flow as well as co-rotating TC flow at solid body rotation. For this, equation (1.10) is integrated numerically using Matlab (*ode15s*). Interaction with the inner and outer cylinder walls is realized by introducing a perfectly elastic spring force with a spring constant of $c_{\text{Spr}} = 10g(m_{eff}/m_{bes})(1/0.125d_p)$.

1.2.3.2 Single Particle dynamics in rotating flows - Validation and parametric study

In this section equation (1.10) and the numerical implementation is validated by comparing obtained results to the analytical solution of Roberts et al. (1991) (equation 1.20) for Stokes conditions. Additionally, numerical results of Seiden et al. (2007) are considered, who developed an approximation for trajectories of particles in drum flow (no inner cylinder) at finite Reynolds numbers. Furthermore, the numerical obtained trajectories are compared to experimental results obtained in the present work. Hence, we utilize the code to perform an analysis of the particle trajectories at finite Reynolds numbers and work out the basic differences between double cylinder system (co-rotating TC flow) and single cylinder system (drum flow). These simulations provide the base for understanding the particle dynamics in the conducted experiments presented in chapter 7.

An initial test considers the case given in Seiden et al. (2007) with $d_p = 50\,\mu\text{m}$, $R_o = 50\,\text{mm}$, $n = 3.82\,\text{min}^{-1}$ ($\Omega = 0.4\,\text{rad}\,\text{s}^{-1}$) and $\rho_p = 1.5\,\text{g}\,\text{cm}^{-3}$. As can be seen from Fig. 1.9a for the given parameters the numerical solution is in excellent agreement with the analytical solution (1.20). For validating the code at higher Re_p, the second test case given in Seiden et al. (2007) is considered. They compared their simulations to an experiment with $d_p = 1.59\,\text{mm}$, $R_o = 55.8\,\text{mm}$, $n = 46.8\,\text{min}^{-1}$ ($\Omega = 4.9\,\text{rad}\,\text{s}^{-1}$). The particle material was Nylon. As no value for the density could be found in their work, the density of Nylon balls reported in Seiden et al. (2005) is employed ($\rho_p = 1.11\,\text{g}\,\text{cm}^{-3}$). Figure 1.9b shows the obtained numerical results of the present work (blue line) in comparison to the numerical (black line) and experimental results of Seiden et al. (2007) (circles). As can be seen in Fig. 1.9b, besides a small

offset in the upper portion of the trajectory, the numerical results are in good agreement. It is assumed that this slight offset is because Seiden et al. (2007) employed a slightly different expression for the drag force. For further validation, numerical simulations are compared to experiments performed in Setup 6 (see section 2.1.4). For this, a single fluorescent particle ($d_p \approx 450\,\mu m$, $\rho_p \approx 2.5\,g\,cm^{-3}$) was injected into single cylinder systems of $R_o = 16\,mm$, $R_o = 23\,mm$, filled with destilled water. Hence, high speed image recordings were performed as described in section 2.1.4 and the particle trajectory was extracted with a binarization procedure. The measured and the computed trajectories are displayed in Fig. 1.9c,d for different values of n. The numerical results are in good agreement with the experimental data for all values of n. Solely, for n_1 a slight offset becomes evident, while the diameter of the trajectory matches with the experimental results. We assume that the underlying reason for this deviation is a error in determining the cylinder wall, which was determined based on the averaged image. As only single particles were illuminated the contrast of the cylinder walls is low, which hamperes the cylinder wall detection in this case. Furthermore the single particle in this case was located in a cylinder section which was opposed to the camera, such that slight perspective errors occured. Overall, it is assumed that the numerical implementation of equation (1.10) sufficiently captures the basic particle dynamics within the system. Further, from the numerical results it is also possible to estimate the particle forces in equation (1.10). The dominant forces are drag force, gravitation and the pressure force, while the effect of Saffman force on the particle trajectory is negligible. The maximum particle Reynolds number achieved in the simulations is $Re_p \approx 40...60$ such that the approximations used in equation (1.10) are valid.

The validated code is then used to investigate the difference in steady state particle trajectories between a single cylinder system (drum flow) and double cylinder system (TC flow) at solid body rotation ($\Omega_i = \Omega_o = 2\pi n/60$). For this, in Fig. 1.10a we show the computed single particle trajectories in a rotating drum flow for n ranging from $10\,min^{-1}$ to $140\,min^{-1}$. For $n \leq 30\,min^{-1}$ the drag force does not overcome the gravity and the particle attains a static position on the cylinder wall. For $n \geq 35\,min^{-1}$ the particle rises up the left cylinder wall, detaches at point A and travels along a circular orbit, until it hits the opposed cylinder wall at point D (exemplary shown for $120\,min^{-1}$). The radius of the orbit increases as n increases and the point D is shifted towards the right cylinder wall.

As can be seen from Fig. 1.10b the trajectories in a double cylinder system are identical to the single cylinder system for $n \leq 30\,min^{-1}$ and $n \geq 80\,min^{-1}$. These rotation rates are termed as "region $R0$" and indicated with the black line in Fig. 1.10a,b. For intermediate rotation rates the particle hits the inner cylinder wall which leads to three types of strikingly different particle orbits. These rotation rates are denoted as regions R1, R2 and R3 and indicated with purple, cyan and magenta bars in Fig. 1.10b, respectively. In region R1, which occurs for ($45\,min^{-1} \leq n \leq 47.5\,min^{-1}$) , the particle oscillates between the outer cylinder (point A) and the inner cylinder (point B) in the left half

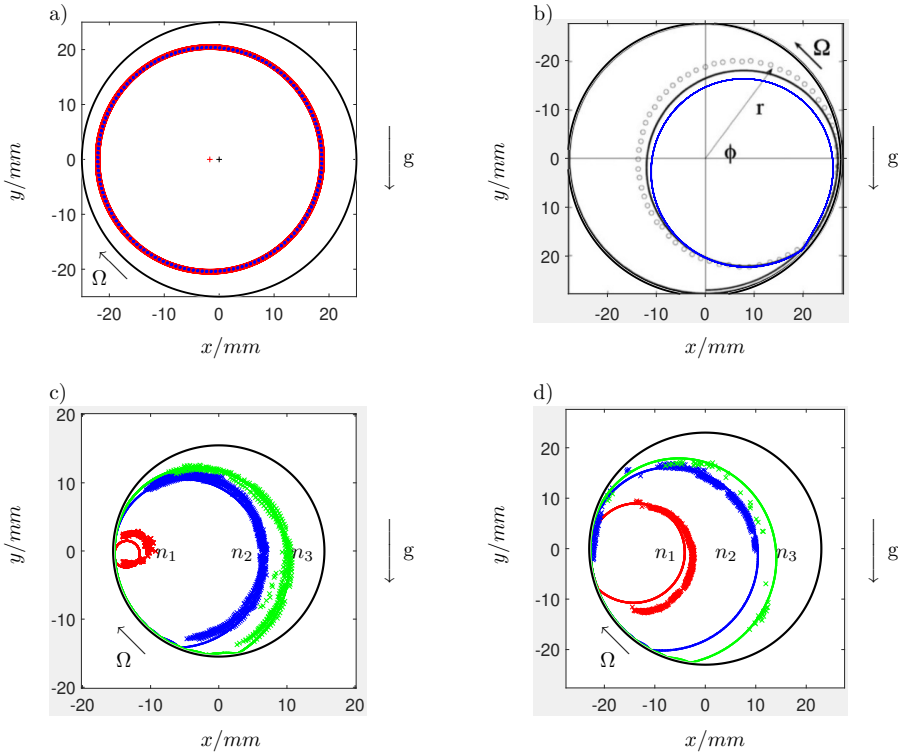

Figure 1.9: Validation of numerical obtained particle trajectories. a) $d_p = 50\,\mu m$, $R_o = 50\,mm$, $n = 3.82\,min^{-1}$, $\rho_p = 1.5\,g\,cm^{-3}$, red line = theoretical solution (1.20), red cross = spiral center, blue dots = trajectory obtained by numerical integration of (1.10). b) $d_p = 1.59\,mm$, $R_o = 55.8\,mm$, $n = 46.80\,min^{-1}$ and $\rho_p \approx 1.1\,g\,cm^{-3}$, blue line = trajectory obtained by numerical integration of (1.10), black line = numerical results of Seiden et al. 2007, circles = experimental results of Seiden et al. 2007 c) $d_p = 450\,\mu m$, $R_o = 16\,mm$, $\rho_p \approx 2.5\,g\,cm^{-3}$, $n_1 = 46\,min^{-1}$, $n_2 = 82\,min^{-1}$, $n_3 = 99\,min^{-1}$ d) $d_p = 450\,\mu m$, $R_o = 23\,mm$, $\rho_p \approx 2.5\,g\,cm^{-3}$, $n_1 = 47\,min^{-1}$, $n_2 = 112\,min^{-1}$, $n_3 = 143\,min^{-1}$

of the system (Fig. 1.10b). If n is slightly increased ($50.0\,min^{-1} \leq n \leq 55\,min^{-1}$) the particle performs a circular movement in the left side of the system thereby periodically hitting the inner cylinder at point B but not the outer cylinder wall (region R2). If n is further increased to $57.5\,min^{-1} \leq n \leq 70\,min^{-1}$, the third scenario occurs (R3) where the particle hits the outer cylinder wall at point E, then travels to point A where it detaches from the outer cylinder followed by a fall, until hitting the inner cylinder at point C. Hence, the particle travels along around the inner cylinder, until it detaches at point F and falls back to the outer cylinder (point E).

As can be seen in Fig. 1.10, the single particle trajectories in a double cylinder system differ significantly from the single cylinder case for rotation rate ranges associated with R1, R2 and R3 ($45\,min^{-1} \leq n \leq 70\,min^{-1}$). In particular in scenario R3, the particle

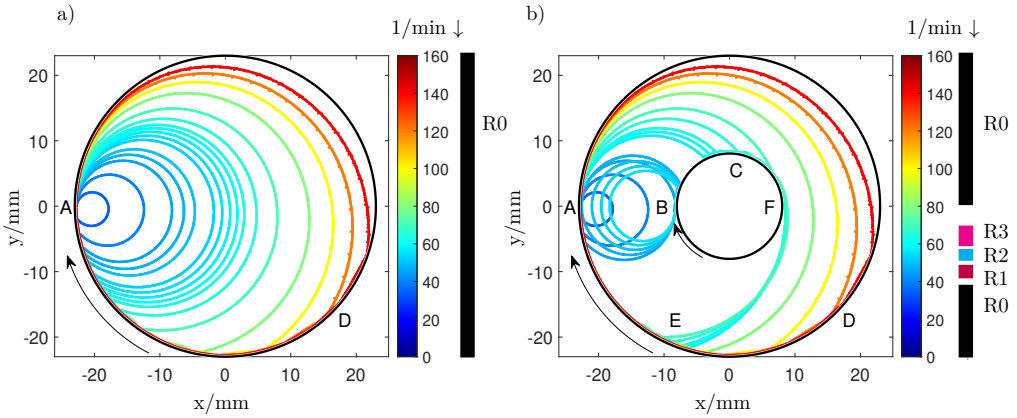

Figure 1.10: Numerical study of single particle trajectories in single and double cylinder system at solid body rotation ($d_p = 500\,\mu m$, $\rho = 2.5\,g\,cm^{-3}$). a) Single cylinder system, $R_o = 23\,mm$, b) Double cylinder system, $R_o = 23\,mm$, $R_i = 8\,mm$, $\Omega_1 = \Omega_2$

spends significantly more time in contact with the cylinder walls compared to a single cylinder setup. As is shown in chapter 7, the inner cylinder also affects the particle trajectories in suspensions and leads to a stabilization of particle band structures within a double cylinder system compared to a single cylinder system.

1.2.3.3 Literature on Banding and structure formation of rotating suspension flows

In the previous section (1.2.3.2) it was shown that the governing equation for an isolated (non-neutrally buoyant) particle in a rotating flow features additional terms compared to a shear flow. The associated forces lead to a circular motion of the particle in a rotating drum flow where the particle undergoes a periodic movement along the wall and across the cylinder. Through numerical simulations it was further demonstrated that an additional cylinder in the rotating system leads to different particle orbits as function of the rotation rate of the system. This observation gives rise to the question: How does the additional inner cylinder affect the dynamics of a suspension in a TCR? This question is addressed with the conducted experimental study in chapter 7 where the structure formation in drum flows and TC flows at solid body rotation is investigated. In this section, we will review the current state of research dealing with rotating suspensions of rigid particles in cylindrical systems to build the foundation for our experimental work. In the review, we will focus on non-neutrally buoyant particles and exclusively consider horizontally aligned systems.

In general, rotating systems are a fertile ground for the formation of structures and patterns. This applies for pure granular flows as well as for flows of pure liquids. Famous examples include the size segregation in granular drum flows or fingering wave patterns

in partially filled liquid drum flows (Williams 1976; Thoroddsen and Mahadevan 1997). Hence, it is not surprising that a combination of solid particles and liquid gives rise to various unique structures when subjected to rotation and gravity (Seiden and Thomas 2011). Probably the most striking phenomena is the so-called banding, where initially homogenously suspended particles arrange into periodic, axially well separated bands. The first observation of band formation was performed by Tirumkudulu et al. (1999) in a neutrally buoyant suspension within a partially filled horizontal Taylor-Couette (TC) flow. With the outer cylinder fixed and the inner cylinder rotating, the free surface developed a wavy pattern and a segregation of particles in areas of high and low concentration was observed underneath the crest and troughs. Tirumkudulu et al. did not observe particle segregation for the case of a fully filled cylinder. Almost at the same time Boote and Thomas (1999) who investigated the effect of settling particles on the behavior of rimming flows in partially filled drums, observed the formation of bands above a certain particle concentration threshold. While they found the band wavelength to be independent of the solid volume fraction, they observed an increase in wavelength with increasing cylinder rotation rate. Subsequently, in analogy to their initial work, Tirumkudulu et al. (2000) investigated the band formation of a neutrally buoyant suspension in a partially filled horizontal rotating drum. Similar to their previous work they observed the formation of a wavy front along the free surface associated with the band formation. Like Tirumkudulu et al. (1999) and Boote and Thomas (1999) Tirumkudulu et al. (2000) suspected the banding to be caused by shear induced migration (Leighton and Acrivos 1987).

Initially assuming that banding is exclusively associated with partially filled systems (as observed by Tirumkudulu et al. 2000), Lipson (2001) and Lipson and Seiden (2002) observed the formation of bands with a wavelength of $\lambda^*/R_o \approx 3.5...3.9$ during the crystallization process of a horizontally rotating NH_4Cl solution and in an aqueous suspension with settling spherical particles, respectively. Breu et al. (2003), who focused on the transition from granular bed to banding in a low viscosity suspension drum flow, observed a hysteretic transition behavior during the band formation. The bands attained wavelengths of $\lambda^*/R_o \approx 3.5$ and $\lambda^*/R_o \approx 1.66$ for an increasing or decreasing rotation rate, respectively. They concluded that the transitions can be considered as subcritical bifurcations. The saw tooth like dependence of the tube length and the wave length, which was discovered later by Seiden et al. (2004), led to the conclusion that inertial waves are the driving mechanism of band formation in the low viscosity case. These waves are internal waves, which occur in a rotating incompressible fluids due to Coriolis forces (Landau and Lifshitz 1987). This was later supported by a comparison of experimentally and theoretically determined velocity fields (Seiden et al. 2004, 2005, 2007).

While the experiments of Seiden et al. focused on axial banding in low viscosity suspensions, Matson et al. (2003, 2005, 2006) performed an extensive phase mapping of a high viscosity suspension considering a wide range of viscosity and rotation rate at

a volume fraction of $\Phi = 2.3\%$. Besides an axial band pattern with $\lambda^*/R_o \approx 2.6$ they observed a total number of ten distinct particle patterns (viz ten different phases) and divided the phase diagram of a suspension into the high-, the low- and the intermediate rotation rate regime. This distinction is based on different ratios of the forces acting on the particles. In a subsequent work Matson et al. (2008) performed an extensive study on the effect of particle size and cylinder radius on resulting pattern formation with different volume fractions ranging from $\Phi = 1\%$ to $\Phi = 3\%$. This led to scaling laws for the high viscosity case. They further observed that the particle concentration affects the phase transition boundaries but does not alter the character and the number of the phases. According to their conclusions this is rather an effect of increased gravitational forces, as the particle mass increases with increasing volume fraction, than an increase in effective viscosity. In analogy to Matson et al. (2003, 2006, 2008) et al. Kalyankar et al. (2008) performed a phase mapping for high viscosity liquid and settling (negatively buoyant) as well as floating (buoyant) particles. Their experiments show, that in gravitationally dominated flows the buoyant and the settling particles suspension behave similar, while they behave different in centrifugally dominated flows. The axial patterns observed in their experiments contradict the differential centrifuging explanation of Lee and Ladd (2002) that axial patterns are an exclusive feature of settling particles as they attract each other while positively buoyant particles repel themselves.

Nasaba and Singh (2020) investigated the radial patterns and the velocity field of monodisperse suspensions containing floating particles of spherical shape or settling particles of spherical or cylindrical shape. Similar to the works of Konidena et al. (2018) they found a resemblance of the buoyant and the settling suspensions particle pattern phases at low rotation rates. They concluded that the fluid behavior is guided by the suspension particle behavior, which indicates that fluid-particle interaction is the key to pattern formation (Nasaba and Singh 2020).

Apart from monodisperse systems also bidisperse or bidensity suspension drum flows became subject to investigation. Kumar and Singh (2010) investigated the segregation of a bidisperse suspension of a low viscosity liquid for various filling fractions and angular speeds at a total volume fraction of 8.08%. They observed the particle specimen to segregate into alternating bands with the band width increasing while the number of bands decreases with increasing rotation rate. Nasaba and Singh (2018) experimentally investigated the pattern formation in a suspension composed of spherical floating particles together with spherical or cylindrical settling particles. They observed the phase transitions to occur at lower speeds compared to a pure settling suspension. They concluded that the presence of floating particles locally enhances the concentration of settling particles. This in turn alters the sedimentation behavior of the settling particles, and hence affect the phase boundaries.

Besides the summarized experimental studies, several numerical studies have been performed to improve understanding of the band inducing mechanisms in monodisperse and bidisperse systems. Assuming that banding is caused by attractive hydrodynamic forces between particles Lee and Ladd (2002, 2005, 2007) performed Stokesian dynamics simulations on the low Reynolds number regime ($Re_p = O(0.01)$) in analogy to the experiments of Matson et al. (2003). Lee and Ladd obtained banding patterns with a wavelength approximately equal to the tube diameter, which is in agreement with the results of Matson et al. who observed a band spacing of 1.2 times the tube diameter. From their results they concluded that the cylinder walls screen off the hydrodynamic particle interactions (see Brenner 1999) and hence restrict the growth of density perturbations (particle bands) to wavelengths less than $2R_o$. Besides having a distinct Ekman number, the numerical simulations by Hou et al. (2014) intended to mimic the experiments of Lipson and Seiden (2002); Seiden et al. (2004, 2005). Varying rotation rate, number of particles and the aspect ratio of the rotating pipe Hou et al. obtained wavenumbers of $\lambda^*/R_o \approx 2.7 - 3.5$ while finding no evidence for the presence of inertial waves in their fluid velocity fields. They concluded that the band formation is mainly caused by the hydrodynamic interaction of the particles themselves. Using a similar simulation approach as Lee and Ladd (2007), Konidena et al. (2018) performed a Stokesian dynamics simulation of monodisperse positive buoyant particles. They successfully reproduced the axial and radial patterns observed in the experimental work of Kalyankar et al. (2008) except for the discontinuous banding phase. In agreement with Kalyankar et al. (2008) their simulations revealed that axial patterns also occur for buoyant suspensions, which contradicts the differential centrifuging theory of Lee and Ladd (2002). Konidena et al. (2019) who extended the simulations of Konidena et al. (2018) to a bidensity system of floating and settling particles at different particle density ratios, observed that both phases behave identical at low but behave contrasting at high rotation rates. By nondimensionalization of the settling velocity U_s with the circumferential velocity ΩR they were able to unify the transition boundaries of different density ratios for settling and floating particles within the low rotation rate regime.

1.2.3.4 Need for research in banding and structure formation of rotating suspension flows

Despite the thorough research performed on the band formation in rotating drums, the underlying mechanism is not yet completely understood. Furthermore, thorough phase mapping was solely performed for the high viscosity regime and for small cylinder diameters (Matson et al. 2005, 2006; Kalyankar et al. 2008). Moreover, despite its technical relevance, just a few studies investigated completely filled suspension TC flows. In fact, most works focus on the particle dynamics in the presence of spiral, wavy and steady Taylor vortices (Ashwin and King 1997; Rudman 1998; Wereley and Lueptow 1999; Henderson et al. 2007; Majji and Morris 2018) or on the effect of the particles on the transition behavior of the flow (Majji et al. 2018; Ramesh et al. 2019) while

only a few works investigate the behavior of neutrally buoyant particles in laminar TC flows (Majji and Morris 2018; Kang and Mirbod 2020). However, to the authors best knowledge, no works investigated the behavior of suspensions with settling particles in completely filled horizontally aligned TC devices to date.

Therefore, in chapter 7 we present a thorough phase mapping for a low viscosity drum flow as well as for a low viscosity TC flow. In order to work out how the additional inner cylinder of the TC flow affects the particle dynamics in contrast to a drum flow, we investigate the case where both cylinders rotate with the same frequency (corotating TC flow). In this manner, the velocity profile of drum flow and TC flow attain solid body rotation which enables us to perform a direct comparison.

1.2.4 Measurement techniques for mono- and polydisperse suspension flows [1]

As discussed in section 1.2.2, migration phenomena in suspension flows usually become pronounced with increasing solid volume fraction or increasing flow velocity. Hence, in order to investigate those phenomena, it is desirable to keep those parameters as high as possible. However, besides practical problems such as jamming of particles at higher volume fractions, it is a challenging task to measure suspension properties such as velocity and concentration distribution especially in polydisperse suspensions. In the following, different non-intrusive measurement techniques are briefly reviewed, which are potentially suitable for investigating particle migration in suspension flows. It is elaborated whether different particle sizes can be distinguished with the individual techniques. It is also investigated whether the techniques can be applied to small geometries such as microchannels. As will be shown, this is not possible for some methods. Subsequently, the basics of astigmatism particle tracking velocimetry (APTV) will be discussed, which is considered as the most suitable technique for the present study.

In general, measurement techniques for suspension flows can be divided into non-optical and optical techniques. While non-optical techniques can be applied to opaque suspensions, for the application of optical methods the suspension has to be rendered transparent by refractive index matching (RIM) such that the latter methods are usually restricted to model suspensions (Van Dinther et al. 2012).

1.2.4.1 Non-optical techniques

Nuclear Magnetic Resonance (NMR) or Magnetic Resonance Imaging (MRI) is considered as one of the most promising and versatile measurement technique for suspension flows (Powell 2008; Van Dinther et al. 2012). In NMR an external magnetic field is

[1] Parts of this section are adopted from Brockmann et al. (2020) and Brockmann and Hussong (2021) published under https://creativecommons.org/licenses/by/4.0/

applied, and the resonance frequency of protons and relaxation time of the signal is measured. The amplitude can then be related to the proton density and hence a certain component (Windt 2007). Till date NMR has been employed in numerous studies to measure both velocity and particle concentration in monodisperse suspensions of up to $\Phi = 55\%$ (Abbott et al. 1991; Sinton and Chow 1991; Hampton et al. 1997; Han et al. 1999; Brown et al. 2009; Oh et al. 2015). Furthermore, the distribution of different particle sizes present in polydisperse flows could be determined by using different particle materials (Van Dinther et al. 2012). However, different particle materials usually are associated with different densities, such that achiving a polydisperse neutrally buoyant suspension is difficult. Further, drawbacks of MRI are the enormous costs of the associated equipment, complex postprocessing and the requirement for highly specialized staff. Further, the experimental body must be void of ferromagnetic materials (Poelma 2017).

Based on ultrasonic principles Ultrasonic Pulsed Doppler Velocimetry (UPDV) (Jensen et al. 2016) and Ultrasound Imaging Velocimetry (UIV) (Poelma 2017) both methods are capable to provide velocity information in suspension flows beyond the dilute regime in opaque systems. Examples include blood flow in rats or in hearts of humans (Qian et al. 2010; Hong et al. 2008). While UPDV utilizes the Doppler effect for velocity information, in UIV the velocity information is generated based on the correlation of subsequent ultrasound images. Due to multiple scattering and low spatial resolution determining concentration profiles with UPDV is difficult. Further, simultaneously determining the spatial position of large and small particles exceeds the capabilities of UPDV (Van Dinther et al. 2012). While UIV typically solely provides velocity information, Gurung and Poelma (2016) showed that the relative particle distribution can be indirectly measured by the signal intensity. However, distinguishing between different particle sizes of the same material appears to be not possible using UIV.

Electrical impedance tomography (EIT) is based on measuring differences in electrical conductivity to determine the distribution of dispersed and continuous phase (Cheney et al. 1999). Electrodes, which are distributed along the walls, detect changes in the electrical signal when particles are passing by that have different dielectric properties than the fluid. Butler and Bonnecaze (1999) applied it successfully to investigate shear induced migration of $d_p \approx 150\,\mu m$ particles in a flow through a pipe of 2 cm diameter. While the required hardware is relatively cheap, a major drawback is that no velocity information can be obtained and the technique has a relatively low resolution such that individual particles or bubbles cannot be resolved (Poelma 2020). Further, for the differentiation of particle sizes, particles of different electrical conductivities are required, which complicates composing a neutrally buoyant suspension.

In X-ray imaging X-rays of a source radiate through a sample and are detected on the other side. The signal at the detector depends on the density of the matter that is penetrated by the rays. As a shadowgraphy technique, the 3D flow information is collapsed onto a single 2D plane. 3D information can be received by tomographic

reconstruction (CT), which in turn requires more sophisticated hardware and usually yields only a poor temporal resolution (Heindel 2011). To overcome this issue, fast X-ray CT systems have been developed, which require even more sophisticated hardware. Furthermore, realizing neutrally buoyant suspensions is problematic as the method is primarily based on density differences. For creating neutrally buoyant particles different materials have to be combined; for example lead shots and polyurethane foam (Drake et al. 2011).

Positron emission particle tracking (PEPT) is a method, where single radioactively labelled tracer particles are tracked with a positron camera. Till date, the method has been applied to numerous industrial and scientific problems (Parker et al. 1993, 1997). A shortcoming of the technique is that solely up to three particles can be tracked simulatenously (Parker and Fan 2008) such that only sparse velocity information is provided (Poelma 2020). Further, a minimum particle size of approximately 60 µm is required to provide a sufficient radioactive load (Fan et al. 2006) which limits the particle sizes investigated in polydisperse suspensions.

Overall, while all presented techniques have the advantage of being compatible with opaque flow devices as well as relatively dense suspensions, they all provide either low temporal or spatial resolutions. Further, different sized particles in polydisperse suspensions need to be made of different materials to be distinguished for most of the methods. This makes it difficult to realize neutrally buoyant suspensions. More importantly, they require expensive hardware, safety equipment and highly specialized operators which is hardly affordable for most fluid mechanic laboratories.

1.2.4.2 Optical techniques

In comparison, optical methods facilitate high temporal and spatial resolution at relative low cost and are available in virtually all laboratories (Poelma 2020; Tropea et al. 2007). However regarding suspensions, the problem with optical measurement techniques is that the turbidity of the flow renders them useless for volume fractions beyond around $\Phi = 0.5\%$ up to $\Phi = 4\%$, depending on the flow geometry and particle size (Deen et al. 2002; Poelma et al. 2006). Furthermore, the flow geometry needs to be transparent and should not exhibit curvature to avoid distortions, which is usually referred to as “optical access” (Poelma 2020). A solution for this issue is refractive index matching (RIM), where the refractive index of solid and liquid phase is adjusted to the same value, such that the resulting suspension becomes transparent. RIM can also be applied to the exterior of the geometry, to eliminate the distortions induced by the geometry surface, allowing optical access even to very complex geometries (Song et al. 2015). Extensive reviews of the RIM technique, with an overview of numerous solid-liquid combinations is provided by Budwig (1994); Wiederseiner et al. (2011); Wright et al. (2017).

Laser Doppler Velocimetry (LDV) or Laser Doppler Anemometry (LDA) is a point-wise measurement technique based on the Doppler effect of a particle passing two crossed laser beams. It provides directional sensitivity, high spatial and temporal resolution as well as high accuracy. It also allows to determine particle concentration profiles, by measuring the time between two particles entering the probe volume (Tropea et al. 2007; Lyon and Leal 1998b). LDA measurements were performed in dense suspension flows of up to 50% solid volume fraction (Koh et al. 1994; Lyon and Leal 1998b; Shapley et al. 2002, 2004). Phase Doppler Anemometry (PDA) is an extension of LDA where additionally the phase shift, induced by the particle, is measured. This allows to simultaneously measure particle size and velocity (Brenn et al. 1998). Furthermore, Ferrand et al. (2001) presented a technique where PDA is combined with Laser induced Fluorescence (LIF) to improve the reliability of measuring particle concentrations in dense two phase flows. This renders it an interesting technique for polydisperse suspension flows of spherical particles. While LDA provides high spatial accuracies, as a point wise technique, measuring the whole flow field is a time consuming process, which makes it less attractive for extensive parameter studies. In contrast, Particle image velocimetry (PIV) which will be explained hereafter, allows to measure entire velocity fields.

Over the past four decades, Particle image velocimetry (PIV) became a powerful tool and certainly the most popular measurement technique in the field of fluid dynamics (Adrian and Westerweel 2011; Raffel et al. 2018; Scharnowski and Kähler 2020). In PIV, the velocity field in a plane, or volume, is measured based on the displacement Δx of particle (groups) in a time interval Δt, such that the velocity can be estimated as $\Delta x/\Delta t$. For this, two images at t and $t+\Delta t$ are recorded with a digital camera. For illumination usually a light sheet, generated by a pulsed laser, is employed which facilitates short time intervals and high intensities. In the post-processing the image pair is divided into interrogation windows which are correlated with the other image. The particle displacement Δx is then given by the position of the correlation maximum. PIV is usually applied on small tracers to measure the motion of the carrier liquid in suspension flows. For instance, recently Medhi et al. (2019) applied PIV on small tracer particles to investigate the fluid velocity during shear induced migration of larger unlabeled suspension particles in bifurcating channels and found a good agreement to numerical simulations. Also recently, PIV was successfully applied to measure the fluid motion on refractive index matched suspensions of up to 20% solid fraction composed of water and hydrogel particles (Zade et al. 2018, 2019; Zhang and Rival 2018). Nevertheless, PIV has also been applied directly on the suspension particles such as in the work of Fock and Rasmuson (2008), who investigated pulp suspension flow up to 2.7% (mass fraction) in a square channel flow ($40\times40\,\mathrm{mm}^2$) and used the fibers as tracers.

While classical PIV (planar PIV), with a single camera and a light sheet, yields 2D2C (two-dimensional, two-components) velocity fields, different volumetric variants of PIV have been developed. In Scanning PIV the laser sheet is rapidly translated through

the flow domain with double frame images recorded at different positions (Brücker 1995). While this method is restricted to stationary or relatively slow instationary flows, it is able to provide 3D2C velocity information (Schröder and Willert 2008; Raffel et al. 2018). In Stereo PIV and Tomographic PIV, discussed in more detail below, threedimensional velocity information is reconstructed from recordings simultaneously obtained at different viewing angles.

As we are preliminary interested in small geometries in the millimeter and submillimeter range, we restrict our further review on such geometries. In such environments the PIV is referred to as μPIV which was introduced by Santiago et al. (1998) and is considered as a separate technique due to its different mechanical and optical constraints (Wereley and Meinhart 2010). While in planar PIV the measurement plane is commonly defined by a thin light sheet (Adrian 1991), in μPIV, due to the resctricted optical access and small dimensions, usually a volume illumination is employed (Meinhart et al. 2000) such that the measurement plane is defined by the depth of focus (Olsen and Adrian 2000). In the following we will discuss the basic principles of μPIV before we review its application on suspension flows. For further information on μPIV the reader is referred to the reviews of Lindken et al. (2009) and Wereley and Meinhart (2010). In μPIV problems arise from the fact, that defocused particles contribute to the cross correlation and hence can bias the results, especially in case of strong velocity gradients in depth direction. The out-of-plane range along which defocused particles contribute to the correlation is known as depth of correlation (DOC), which should be as low as possible to reduce bias of the cross correlation. The DOC strongly depends on d_p as well as the numerical aperture NA as can be seen from the model of Olsen and Adrian (2000) as rewritten by Rossi et al. (2012):

$$\mathrm{DOC} = \frac{n_w}{n_0}\sqrt{\frac{1-\sqrt{\epsilon}}{\epsilon}\left(\frac{n_0^2}{NA^2}-1\right)\left(d_p^2+1.49{\lambda_L}^2\left(\frac{n_0^2}{NA^2}-1\right)\right)} \tag{1.22}$$

Here n_w, n_0, denote the refractive index of liquid and air while λ_L is the wavelength of the light emitted by particles with a gaussian light intensity distribution. The parameter ϵ is a threshold value, above which a particle contributes to the cross correlation and usually set to 0.01 (Olsen and Adrian 2000). To decrease the DOC usually microscope objectives with large values of NA are employed. Further, the use of small tracers can decrease the DOC at the cost of reducing the signal to noise ratio (Cierpka and Kähler 2012). Thereby, tracers should be bigger than $\approx 500\,\mathrm{nm}$ to avoid Brownian motion (Santiago et al. 1998; Nguyen et al. 2019). However, especially close to the wall, the effect of DOC leads to bias even when small tracer particles are used ($d_p \leq 2\,\mu\mathrm{m}$) (Kähler et al. 2012b). Hence, significant errors are to be expected for large suspension particles ($d_p \geq 10\,\mu\mathrm{m}$). Consequently, when dealing with suspension flows μPIV is usually applied on small tracer particles to measure the motion of the fluid.

For instance, Ali et al. (2016) performed 2D μPIV measurements at different planes to capture the 3D2C flow induced by rotating particles of 4 µm and 8 µm using 200 nm tracers. Also, Pan et al. (2018) successfully measured the secondary flow induced by single particles and particle trains in microscopic channel flows of 152 µm×275 µm cross-section using 1 µm tracers. They achieved good agreement with numerical results. Nevertheless, μPIV has also applied for measuring the dynamics of larger suspension particles. Bitsch et al. (2005) investigated suspension flows of spherical 1.02 µm particles of up to 3% volume fraction as well as of red blood cells (RBC) at hematocrit (Hct) of about 60%. Besides achieving plausible velocity profiles, in both cases significant out of focus effects (due to the DOC) were observed. Hood et al. (2016) utilized a hybridized μPIV/μPTV (Micro Particle Tracking velocimetry) procedure to determine the lateral migration velocities of particles ranging from 2.4 µm to 9.5 µm in a square channel with a cross-sectional area of 45 µm×90 µm. While they determined the single particle displacement with sub-pixel accuracy by a correlation method, they reconstructed the 3D position of particles indirectly by their streamwise velocity. Very recently, Blahout et al. (2021) simultaneously applied μPIV on large "surface labeled" fluorescent particles (60 µm) as well as on small fluorescent tracers (1.19 µm). As a result of the surface labeling the images of the large particles where ring-shaped which was found to improve the accuracy and reliability of cross-correlations. Their technique is a promising approach, to deal with larger particles, which potentially could decrease the effect of DOC.

Besides using conventional microscopes for image acquisition, Confocal Laser Scanning Microscopy (CLSM) can be employed for imaging which can significantly reduce the DOC. In CLSM the field of view is illuminated successively point by point such that a single image is composed of several scanning points across the sample. By this out-of-focus signals are eliminated, resulting in optical slices of 1 µm to 2 µm and enhancing the contrast as well as the resolution in the confocal image (Cierpka and Kähler 2012; Bayguinov et al. 2018). For maximizing the scanning speed, the laser light is directed through patterns of micro lenses and apertures on a spinning disk ("Nipkow-disk"), allowing to record full-field images at frame rates up to the kilohertz range (Tanaami et al. 2002; Kinoshita et al. 2007). Compared to conventional epi-fluorescent microscopy, CLSM greatly reduces the background noise and can therefore handle larger solid volume fractions. Therefore, CLSM μPIV has been successfully applied to investigate the dynamics of microscopic in-vitro blood flows with red blood cells (RBC) at Hematocrits of up to 20% (Lima et al. 2006, 2007, 2008). Besides its significant advantages, the downsides of CLSM are the expensive lab equipment and the relatively low temporal resolution which depends on the time required for a full field scan (Cierpka and Kähler 2012).

Mutliple camera approches: Stereoscopic and tomographic μPIV/μPIV While for many flow problems two-dimensional velocity information is sufficient, numerous flow scenarios require full three-dimensional information of all three velocity components (3D3C). This accounts also for suspension flows, where knowledge of the three-dimensional particle velocities with respect to the carrier liquid is important for the physical interpretation. Also, the 3D distribution of particles is an important information in the context of investigating particle migration. For measuring 3D3C velocity fields, different particle-based imaging methods have been developed which will be presented in the following. Thereby, the particle velocity can be determined either by correlation (PIV) or by tracking of individual particles, termed as Particle Tracking Velocimety (PTV). Besides providing the volumetric velocity field data, these imaging methods also can reduce the problem of DOC (Raffel et al. 2018) and can be used to obtain information about the particle distribution. In stereoscopic imaging the out-of-plane movement of particles is reconstructed by simultaneous observation from two different perspectives under an angle such that 2D3C information is obtained (Lee and Kim 2009). This is commonly realized by two cameras sharing a common microscope objective (CMO design) (Lee and Kim 2009; Cierpka and Kähler 2012). In general, in typical stereoscopic setups (CMO) only small viewing angles can be realized which introduce errors in the out-of-plane velocity. At the same time the DOC is large due to the use of CMO lenses, biasing the measured out-of-plane gradients. Further, the focal planes of both cameras mismatch due to aberrations and imperfections of the microscope, which leads to systematic errors (Cierpka et al. 2012). While in stereoscopic imaging the third component is reconstructed from the in-plane velocities, Tomographic imaging (tomo μPIV) is a fully volumetric method (3D3C) where the volume distribution of particles is reconstructed from at least four different perspectives (Elsinga et al. 2006). A major problem of tomographic imaging is the appearance of so-called ghost particles arising during the iterative particle position reconstruction procedure (Elsinga et al. 2011). Therefore, the particle concentration should be one order lower than in planar μPIV such that particle tracking velocimetry (PTV) is often better suited for the data analysis compared to correlation based methods (Cierpka et al. 2013). However, Kim et al. (2012) performed a comparison of 3D μPTV and Tomographic μPIV on identical images, found that Tomographic μPIV yields more accurate data over a larger measurement depth. Tomographic imaging has been successfully applied to different microfluidic flow problems such as drop impact on liquid films (Steinmann et al. 2019), internal flows in droplets and drop coalescence (Ortiz-Dueñas et al. 2010; Kim et al. 2011), or to resolve small scale structures in turbulent flows (Fiscaletti et al. 2014). Drawbacks are the complexity of the setup (implementation of four cameras in the optical path) and the required complex calibration procedure within the common field of view (Cierpka and Kähler 2012). Furthermore, the computational cost of Tomographic PIV are four to five orders of magnitude higher than in planar PIV (Scarano 2012). Single camera techniques instead allow three dimensional tracking of particles with a single camera, which eases the calibration and reduces the costs, especially when

high-speed cameras are employed. This applies especially for Astigmatism Particle Tracking Velocimetry (APTV) which is utilized within this thesis and is thoroughly reviewed at the end of this section. It should be mentioned, that in the following, techniques where two cameras share the same perspective (e.g. multi-plane imaging), are also classified as single camera techniques.

Single camera approaches make use of the relation between the particle image and the particle's out-of-plane position to reconstruct the three-dimensional particle position. In general, in a stigmatic microscopic optical system the particle image diameter a_{st} increases with the particles distance to the focal plane. This can be described with the following equation under the assumption of a particle with Gaussian intensity distribution (Olsen and Adrian 2000; Rossi et al. 2012):

$$a_{st}(z) = M \sqrt{\underbrace{d_p^2}_{\text{geometry}} + \underbrace{1.49{\lambda_L}^2 \left(\frac{n_0^2}{NA^2} - 1\right)}_{\text{diffraction}} + \underbrace{4(z)^2 \left(\frac{n_0^2}{NA^2} - 1\right)^{-1}}_{\text{defocusing}}} \tag{1.23}$$

Here, d_p, λ_L, n_0, M and NA denote the particle diameter, the wavelength of the emitted light, the index of refraction of the immersion medium of the lens, the magnification and the numerical aperture of the microscope objective, respectively. For large magnifications and numerical apertures, it is reported that equation (1.23) significantly overestimates the increase in diameter (Kloosterman et al. 2011; Rossi et al. 2012) while for small magnification and long working distances a significant underestimation is observed (Kähler et al. 2012a). However, with an appropriate calibration the particle image diameter can be used to determine the particle's out of plane position (Cierpka and Kähler 2012). A critical point is here that $a(z)$ increases symmetrically to the focal plane in a stigmatic system as can also be seen from equation (1.23). The defocusing term contains z^2. Hence, only the absolute distance to the focal plane can be reconstructed by a particle image, but not if the particle is located in front or behind the focal plane as schematically depicted in Fig. 1.11. This problem of ambiguity is a challenge for single camera techniques. A straightforward approach is here to arrange the system components in such a way that particles are only visible on one side of the focal plane. Stolz and Köhler (1994) for instance used a thick light sheet which solely illuminated particles on one side of the focal plane. Leister et al. (2021) instead positioned their entire geometry on one side of the focal plane. Besides their simplicity, these methods do only use half the range over which a particle is detectable. Furthermore, the latter method is restricted to small geometries as no scanning is possible. To overcome the problem of ambiguity different methods have been established. One way is using stigmatic optics with several staggered focal planes (Towers et al. 2006; Toprak et al. 2007; Ram et al. 2009; Dalgarno et al. 2010). Using this technique, multiple images are generated for each particle and compared to determine the sign of the particles out-of-plane position. Another positive effect is that the measurement volume depth can be increased. Murata and Kawamura (1999) were among the first applying the

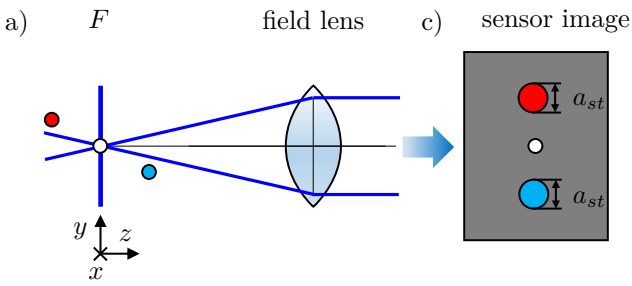

Figure 1.11: Principle sketch of the problem of ambiguity when reconstructing the out-of-plane positions of particles in stigmatic optical systems. a) Optical system. c) Resulting image. As can be seen, the particle image diameter of both the red particle (in front of the focal plane) and blue particle (behind the focal plane) are identical.

multiplane technique for measuring the 3D position of small particles. They realized multiple focus planes by using a color-camera and a color filter system. Recently, Zhou et al. (2020a) modified the method for measuring the size and position of droplets in a spray using two staggered cameras resulting in two distinct focal planes. More recently, Zhou et al. (2021) further showed that the method can potentially be applied to measure size and 3D position of non-spherical particles. This renders the technique a promising tool for the investigation of polydisperse suspensions of particles of arbitrary shape.

Digital holography microscopy (DHM) is based on the interference pattern (Fresnel diffraction pattern) which results from the interaction of a coherent reference beam and the object. While conventional microscopy only yields 2D focused images, in a single DHM recording the object can be refocused in the postprocessing and a hologram can be obtained which contains all the object's 3D structures and its position (Yu et al. 2014). Thereby, the problem of ambiguity is solved by the reconstruction procedure applied to the diffraction pattern. In general, DHM shows a great potential and has been successfully applied to various microscopic flows like microchannels (Coëtmellec et al. 2001) and backward-facing steps (Yang and Chuang 2005). Kühn et al. (2008) demonstrated that the technique can provide sub nanometer accuracies. A great advantage of DHM is that it can be applied to objects of arbitrary shape such as living cancer cells (Kemper et al. 2006; Langehanenberg et al. 2009) and animal sperm (Di Caprio et al. 2010). This makes it a promising technique for investigating polydisperse suspension flows with non-uniform shaped particles. DHM is also compelling because of its compact and relatively low-cost design, which consists of a laser, collimating optics, and only one camera (Discetti and Coletti 2018). Unfortunately, the technique is limited to very low seeding densities to avoid excessive overlapping of interference patterns (Hinsch 2002). Another problem is that, due to the limited resolution of the digital recording array, particles appear elongated in the depth direction which reduces the depth resolution. For overcoming this problem DHM has been combined

with tomographic imaging (Soria and Atkinson 2008; Buchmann et al. 2012), which in turn greatly increases the complexity of the method. DHM is also sensitive to noise and limited to low seeding densities (Cierpka and Kähler 2012). Moreover, the reconstruction procedure is computationally expensive and often relies on user defined thresholds (Toloui and Hong 2015).

Another technique to achieve unambiguous depth coding in a single camera system is to mount a three-pinhole aperture into the optical path as first proposed by Willert and Gharib (1992). By this, every particle image appears as an image triplet, whose orientation depends on whether the particle is located before or behind the focal plane. The particles distance to the focal plane can be reconstructed by the diameter of the triplet (Willert and Gharib 1992; Pereira et al. 2000). A great advantage of the technique is that it is easy to implement and no additional optical elements such as lenses or diffraction gratings are introduced which would induce optical aberrations (Cierpka and Kähler 2012). Furthermore, the technique can be easily applied to highly non-spherical particles as recently demonstrated by Troutman and Dabiri (2018). As the method yields two separate information, the image of the particle and the diameter of the triplet, it could potentially be applied for measuring the out of plane position and size of particles at the same time. This makes it potentially suitable for measuring polydisperse suspensions. However, the mask blocks most of the laser light, such that usually a background illumination must be employed. In fact, the presence of the pinhole-mask decreases the signal-to-noise ratio about a factor of 20 compared to standard stigmatic imaging (Cierpka and Kähler 2012). The light intensity can be increased by employing a three-camera arrangement, which also increases the accuracy but in turn increases the complexity and costs of the setup (Chamorro et al. 2013). Furthermore, the technique is restricted to low seeding rates and identifying the images corresponding to individual triplets is often difficult (Cierpka and Kähler 2012).

By far the most common method for obtaining a unambigous depth-coding is the use of an astigmatic imaging system where the associated measurement technique is known as Astigmatism Particle Tracking Velocimetry (APTV) (Zhou et al. 2019). Sometimes it is also referred to as “wavefront sensing” (Angarita-Jaimes et al. 2006; Towers et al. 2006). A standard microscope may easily be converted into an APTV setup by introducing a cylindrical lens in front of the camera sensor. In contrast to the 3-pinhole method, no mask is used such that no background illumination is required. As no mask blocks the aperture, APTV provides significantly higher SNRs than the 3-pinhole method (Cierpka and Kähler 2012). Moreover, in APTV the problem of identifying triplets is removed. Furthermore, compared to stereoscopic μPIV APTV yields two times lower uncertainties in determining the out-of-plane velocity and avoids the problems of aligning two focal planes (Cierpka et al. 2012). Due to these advantages, we utilize APTV in this thesis to measure the motion of particles in dilute as well as semi-dilute suspensions up to 20% solid volume fraction. The APTV method employed within this work will be based on calibration functions, where the particle image information is reduced to few parameters,

viz the particle image width (a_x) and height (a_y), as function of the depth position. This is a well-established and probably the most common approach. Besides this calibration function-based approach, recently the method of General Defocusing Particle Tracking (GDPT) was independently developed by Barnkob et al. (2015) and Taute et al. (2015). The technique generalizes the aforementioned single camera approaches which rely on deformation of the particle image due to diffraction, pinhole-mask or astigmatism. In fact, the technique can be applied to any optics or image type and basically compares detected particle images to reference particle images stored in lookup tables. The image comparison can be achieved for instance by cross-correlation or use of neural networks (Barnkob et al. 2021). A great advantage of GDPT is, that it can be applied also to non-spherical objects such as bacteria (Taute et al. 2015). For further information on this technique the reader is referred to the detailed work of Barnkob and Rossi (2020).

1.2.4.3 Astimatism particle tracking velocitmetry (APTV):

The principle of APTV is based on a cylindrical lens which is placed in the optical path of a microscope and generates two spatially separated focal planes F_{xz} and F_{yz}. The images of particles which are located at a depth position midway between these planes appear circular and transform to a horizontally or vertically aligned ellipse when the particles are located closer to F_{yz} or F_{xz}, respectively (see Fig. 1.12 and Fig. 1.13). Hence, the horizontal axis length a_x and the vertical axis length a_y of the particle image are a function of the particle's depth position, which will be hereafter also referred to as z position or out-of-plane position. The evolution of a_x and a_y can be described by equation (1.24) as given by Cierpka et al. (2010a) and based on the model of Olsen and Adrian (2000):

$$a_i(z_i) = M\sqrt{d_p^2 + 1.49{\lambda_L}^2\left(\frac{n_0^2}{NA^2} - 1\right) + 4(z_i)^2\left(\frac{n_0^2}{NA^2} - 1\right)^{-1}} \quad i = x, y \quad (1.24)$$

with $z_i = z - F_{iz}$ being the distance between particle and respective focal plane. In fact, equation (1.24) is identical to equation (1.23), but accounts for the staggered focal planes in an astigmatic system.

Since its first application to a fluid mechanics problem by Kao and Verkman (1994), APTV has been applied and developed further by various authors (Angarita-Jaimes et al. 2006, Chen et al. 2009, Cierpka et al. 2010b,a, Rossi and Kähler 2014). For a detailed report of the history of APTV and its different fields of application, the reader is referred to Cierpka and Kähler (2012). Till date, APTV has been succesfully applied to geometries at various length scales to investigate a wide spectrum of physical phenomena while exhibiting a remarkable accuracy in reconstructing the depth position of (tracer) particles. A short overview of different applications and aspects of APTV is given hereafter. An overview of the reconstruction accuracies and measurement volume depths achieved in different publications is given in the appendix (see Table A.9).

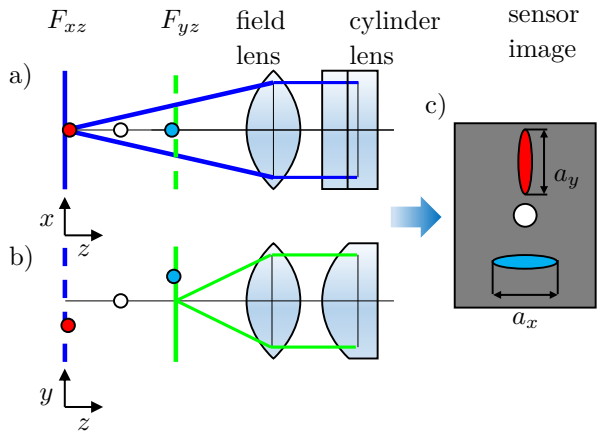

Figure 1.12: Principle sketch of APTV. a) Optical system in x-z plane b) Optical system in y-z plane c) Resulting image

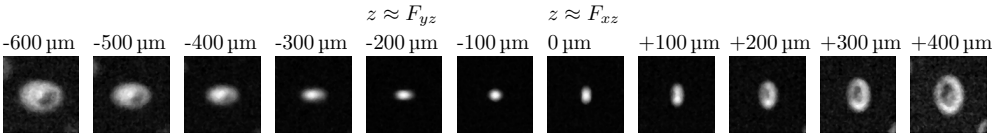

Figure 1.13: Images of labeled particles for different depth positions z (d_p=60 µm, PMMA, z corrected for refractive index of RIM-liquid ($n_{\mathrm{RIM}} = 1.488$)). The particle is located close to F_{yz} at $z \approx -200$ µm and located in F_{xz} at $z = 0$ µm.

Ragan et al. (2006) applied APTV to measure the motion of living kidney cells with a measurement volume depth of Δz=2.5 µm. Huang et al. (2008) applied the technique in a nanoscale environment. Using stochastic optical reconstruction microscopy, they reconstructed the position of 200 nm beads labeled with photo-switchable molecules with a resolution of 60 nm in the depth direction within a measurement volume of 600 nm depth. Huang et al. (2016) could resolve the protein structures in a 9 µm spermatocyte with a depth resolution of 10-20 nm and a measurement volume depth of 1200 nm, by using a dual objective 4Pi-microscope system with deformable mirrors to compensate for aberrations as well as an improved scanning technique. Another example of the application of APTV is the work of Müller et al. (2013). Investigating the ultrasound-induced acoustophoretic motion of microparticles, they utilized APTV in a channel with a rectangular cross section of 377×157 µm^2 and captured the trajectories of 0.5 µm and 5 µm particles to validate their analytical results. Apart from microfluidic applications, increasing efforts are undertaken to apply APTV to larger flow domains. Fuchs et al. (2014b,a) showed that APTV is suitable for measuring volumetric velocity fields in

macroscopic domains of up to 40 mm measurement volume depth. Likewise, Buchmann et al. (2014) measured the motion of 110 µm particles in a supersonic, impinging jet flow, over a measurement volume depth of 5100 µm.

Apart from utilizing APTV in combination with small tracer particles to measure the motion of liquids or resolve microscopic structures, in recent years the technique is more and more applied to measure the dynamics of the particles themselves in situations where particles undergo their own dynamics and do not follow the flow streamlines. Rossi et al. (2019) used APTV to measure particle velocity and concentration of an electrokinetically induced particle pattern in a suspension with a solid volume fraction of $\Phi = 0.05\%$ inside a channel of $350 \times 30\,\mu m^2$ cross section. They used a mixture of labeled particles with different dyes ($d_p = 0.245\,\mu m$) with the majority of them being invisible during the APTV measurement to allow for higher solid volume fractions. They concluded that APTV is capable of measuring the concentration profile with a better resolution compared to classical segmentation approaches. Using APTV Blahout et al. (2020) investigated the fractionation of $d_p = 3.55\,\mu m$ and $d_p = 9.87\,\mu m$ particles in a serpentine channel with a crossection of $200 \times 50\,\mu m^2$. They observed that a transition of particles from four to two equilibrium trajectories takes place at particle size dependent bulk Reynolds numbers. Distinguishing large and small particles by their individual astigmatism characteristics, they were able to simultaneously measure the motion of both particle species.

Recently, APTV is also combined with special particles to measure properties other than velocity. Segura et al. (2015) utilized non-encapsulated thermochromic liquid crystals (TLC) particles, to measure the volumetric 3D velocity- and temperature field in an evaporating droplet with a measurement volume depth of 20 µm. Also, Massing et al. (2016, 2018) used luminescent polymer particles to measure the three-dimensional temperature and velocity field of a heated flow in a channel with a cross-section of $2 \times 2\,mm^2$. More recent works increasingly focus on using machine learning tools such as deep neural networks to further increase the degree of automatization of APTV (Rossi and Barnkob 2019) or to apply it on scenarios with low signal-to-noise ratios (Franchini et al. 2019). König et al. (2020) compared the performance of conventional and neural network supported APTV utilizing a bidisperse suspension in a laminar channel flow. While they achieved good results with both methods for the bidisperse suspension, they concluded that the neural network supported APTV is more robust against optical abberrations and can be of great use for investigating suspensions with different particles sizes, shapes and even with particle clusters. Furthermore, with conventional APTV they observed the calibration curve for both particle species to overlap close to the focal planes causing ambiguities and limiting the range of depth reconstruction. Efforts are also undertaken to further adapt and extend the classical APTV technique. For instance, Zhou et al. (2020b) introduced a modification utilizing Holographic imaging

principles to establish Holographic Astigmatic Particle Tracking Velocimetry (HAPTV). Using a nozzle flow as a test case, they could successfully validate their measurement technique.

As the performance of APTV strongly depends on the quality of defocused particle images, a central aspect is the correct selection of the imaging system and the tracer particles. Therefore, usually high-quality fluorescent particles are used, as they provide high-quality particle images, with acceptable signal to noise ratio (SNR) (Cierpka et al. 2010a). However, commercially available fluorescent particles are expensive and not all sizes or materials are available. Manually coated particles may be an alternative, nonetheless it is a challenge to ensure a sufficient, uniform and repeatable coating quality and to avoid bleaching. Furthermore, powerful monochromatic light sources such as lasers are required to excite fluorescent particles, which are an additional cost factor. Despite these challenges only very few studies report on the use of non-fluorescent particles for APTV. One is the aforementioned work of Buchmann et al. (2014), who used a pulsed high power LED for backlight-illumination to capture the 3D motion of 110 µm opaque polyamide particles. Their error in reconstructing the particle position was about σ_z=140 µm which was 2.74% of the measurement volume depth. However, compared to the particle diameter, the error was relatively large (σ_z/d_p=127%). The aformentioned authors Segura et al. (2015) used a white light source with a circular polarization filter to excite their TLC particles and reported a relative high uncertainty of $\sigma_z/\Delta z$=8.5% in reconstructing the z-position compared to laser based APTV. They concluded it was due to the less bright particle images obtained with a white light source. Using a backlight illumination, Franchini et al. (2019) performed APTV measurements with a calibration based on fitting a 2D, generalized Gaussian distribution to each particle image. They were able to resolve the velocity profile of a laminar flow in a 2x1.2x3 mm^3 channel covering a measurement volume depth of 240 µm. Due to a low SNR, an extensive calibration procedure, including measuring the background intensity of the channel in each measurement plane and sophisticated neural network algorithms were required in their study for a reliable reconstruction of the particles out-of-plane position.

1.2.4.4 Need for research in Astigmatism Particle Tracking Velocimetry (APTV)

As mentioned, in APTV high quality particle images are required and usually commercially produced small, fluorescent particles are utilized. However, these are expensive and not all sizes and materials are variable. Transparent particles in turn are inexpensive and available in various sizes as well as different materials. Some transparent materials such as acrylic can be labeled manually (Blahout et al. 2021), however still it is a challenge to achieve homogenous quality of the coating. Other particle materials such

as polystyrene, as utilized in the experiment displayed in Fig. 1.2, can hardly be dyed. Therefore, we will develop a method to apply microscopic APTV on large transparent particles in chapter 4.

Further, till date no work applied APTV to investigate the dynamics of suspensions beyond the dilute regime. In general, in most studies APTV was applied to very dilute suspensions ($\Phi << 1\%$). To our knowledge the highest volume fractions ($\Phi = 0.05\%$) were considered by the aforementioned work of Rossi et al. (2019). A reason is likely that APTV requires high quality images, which cannot be achieved at higher volume fractions when the flow becomes increasingly turbid. As previously explained, a solution for this issue is refractive index matching (RIM) which results in a transparent suspension. Then, a few particles can be labeled to make them visible for the camera. However in reality it is impossible to achieve a perfect index match such that slight mismatches remain at the particle-liquid interfaces which induce optical aberrations (Lyon and Leal 1998a,b). The effects of these aberrations on APTV are unclear. Hence, in this thesis we will investigate the application of APTV on fluorescent particles in refractive index matched suspensions at different solid volume fractions.

Lastly, the work of König et al. (2020) showed that calibration curves of different sized particles overlap close to the focal planes, leading to ambiguities. This is an issue when simultaneously tracking different particle species in polydisperse suspension flows. Furthermore, the particles investigated by König et al. (2020) were rather small ($d_p = 2.5\,\mu\text{m}; 5\,\mu\text{m}$) and its unknown how the calibration curves of significantly larger particles ($d_p \geq 30\,\mu\text{m}$) behave. Therefore, we will perform an extensive study on the effect of the particle size on the calibration curves.

1.3 Objectives and outline of the thesis

Understanding the particle dynamics in flows through Taylor-Couette reactors (TCRs) is a challenge from a fluid-dynamic perspective as well from a perspective of experimental techniques. The particle dynamics in dilute suspensions are determined by fluid forces such that the flow state (laminar or turbulent) must be known a priori. While it is known that the Spiral Poiseuille Flow in a TCR is destabilized by rotation of the inner cylinder, the effect of rotating outer cylinder was hardly studied. Moreover, the linear stability behavior was solely investigated for few fixed values of the curvature parameter, such that the effect of the curvature parameter on the flow stability is almost unexplored up to date. Particle migration due to inertial and particle interaction effects may lead to various particle distributions patterns and also induce particle separation in polydisperse suspensions. However to the authors best knowledge, experimental studies considering the simultaneous occurrence of both migration phenomena in the inertial regime are still rare and have not been reported for polydisperse suspensions. The underlying reason is certainly that measuring the three-dimensional particle dynamics in suspensions is a challenging task and often requires sophisticated equipment. Microscopic Astigmatism

Particle Tracking Velocimetry (APTV), which a low cost, simple-to-implement single camera measurement technique is a promising option. However, this technique is usually applied to small commercially coated fluorescent particles and it is unknown how the technique performs at larger transparent or manually coated particles in dilute or semi dilute suspensions. Besides the aforementioned migration phenomena it is known that settling suspensions in a horizontally aligned rotating cylinder can give rise to the formation of axially periodic band shaped particle accumulations. While this so-called banding phenomena has been subject to numerous studies in rotating cylinders, till date it is unknown how an additional inner cylinder, which is present in a TCR, affects the formation of such bands. These questions will be addressed within the present thesis in order to extend the basis for understanding the physical effects in particle laden flows in TCRs and building the foundation for more efficient processing in such reactors. For achieving this goal, the major effects, which are the hydrodynamic stability of the flow, the particle band formation in rotating flows and the particle migration in mono- and polydisperse suspensions, will be investigated separately.

In chapter 2 different setups are introduced to investigate the application of APTV on suspension flows, particle migration phenomena in suspensions and the particle band formation in rotating drums flows and TC flows at solid body rotation. In chapter 2 also the parametrization, governing equations and the numerical computation scheme are described, which are employed in the linear stability analysis.

Chapter 3 adresses the hydrodynamic stability of Spiral Poiseuille Flow (SPF) of a pure liquid with rotating inner ($\mu = 0$) or rotating outer cylinder ($\mu = \infty$), by means of linear stability analysis. These two cases allow to investigate the effect of radial increasing or decreasing momentum on the stability of the flow. First a thorough mapping of the linear stability behavior of the SPF is performed, covering a wide range of curvature parameters and swirl parameters of both the rotating inner and the rotating outer cylinder case. Hence, two approaches are developed to characterize of the instability mechanisms encountered in SPFs. One approach uses the concept of the critical layer for the identification of a Tollmien-Schlichting instability. The second approach is to analyze the production terms of the Reynolds Shear Stress Transport Equations (RSSTE) as well as the budget of the kinetic disturbance energy, which enables distinguishing between shear instabilities and centrifugal instabilities. Hence, utilizing these approaches, we perform a profound characterization of the instability mechanisms encountered in the investigated parameter range.

To date, it is not clear which mechanism leads to the separation of species in the observed phenomena in the small gap TC setup (Fig. 1.2). Hence, in chapter 4 to chapter 6 migration phenomena in shear flows of mono- and polydisperse suspensions are investigated experimentally. For this, we develope measurement techniques for large suspension particles based on Astigmatism Particle Tracking Velocimetry (APTV). First an APTV technique is developed which utilizes the ball lens effect and can be applied to large transparent suspension particles (chapter 4). Subsequently, an APTV

technique is developed that uses fluorescence labeled tracer particles in combination which a Refractive Index Matching (RIM) technique and can be applied to suspensions of up to 20% volume fraction (chapter 5). This technique is then further developed to be applied on polydisperse suspensions beyond the dilute regime (chapter 6). Finally using the fluorescence APTV technique the particle migration in bi- and tridisperse suspensions is investigated for both low and high Reynolds numbers at different volume fractions (0.08% and 9.1%) in a square duct. In contrast to chapter 7, here neutrally buoyant particles are used to exclude sedimentation effects and isolate the migration effects. A laminar square duct flow is chosen as flow geometry because it facilitates a comparison to numerous works found in the literature (Abbas et al. 2014; Kazerooni et al. 2017; Shichi et al. 2017).

In chapter 7 the particle band and particle structure formation in rotating suspensions is investigated, to generate a basic understanding of the particle dynamics in TC flows. At first an extensive phase mapping is performed for a low viscosity drum flow as well as for a low viscosity TC flow with settling particles. In order to work out how the additional inner cylinder of the TC flow affects the particle dynamics in contrast to a drum flow, we investigate the case where both cylinders rotate with the same frequency ($\mu = 1$, corotating TC flow). In this manner, the velocity profile of drum flow and TC flow attain solid body rotation, which enables a direct comparison. As solid body rotation is expected to be centrifugally stable in absence of axial flow, no Taylor vortices and hence no secondary flows are expected to occur in the base flow (Esser and Grossmann 1996). This configuration allows for an isolated investigation of the additional cylinders influence and presents the simplest case of a TC flow such that its investigation is the logical first step in untangling the dynamics of such systems.

2 Experimental and numerical Setups

In this chapter, the experimental test stands, measurement systems, the calibration procedures and post-processing strategies are presented which where employed within the experimental investigations conducted at the Ruhr University Bochum (RUB) and TU Darmstadt (TUD). Furthermore, the govering equations, the discretization, the minimization algorithm and the strategies for identifying the instability mechanisms utilized in our linear stability investigations will be introduced. The microscopic setup utilized for investigating the ball lens effect of large transparent particles in astigmatic optics located at the RUB is described in section 2.1.1. For investigating the optical behavior of large fluorescent particles in suspensions of volume fractions up to $\Phi = 20\%$ this microscopic setup was modified which is described in section 2.1.2. Investigations of the optical behavior of large fluorescent particles of different size and migration phenomena in polydisperse suspensions were investigated in two different custom built microscopic setups at the TUD which are described in section 2.1.3. The experimental setups for the investigations of the pattern formation in rotating suspensions of settling particles conducted at the TUD are described in section 2.1.4. In section 2.2.1 to section 2.2.4 we describe the geometry, the governing equations, the numerical implementation and the minimization algorithm used for performing the linear stability analysis. Strategies for identifying the instability mechanisms are presented in section 2.2.5. Parts of this chapter were published in Brockmann et al. 2020 and Brockmann and Hussong 2021.

2.1 Experimental setups [1]

In the following a total number of six different experimental setups is presented of which the first four where utilized to investigate and apply APTV on suspension flows while the latter two where utilized to perform investigation on rotating suspension flows.

2.1.1 Setup 1 - investigation of the application of APTV to large, transparent particles in dilute suspensions

The setup for investigating the application of APTV to large transparent particles, utilizes a backlight illumination. By this particles act as ball lenses and yield a bright signal for the tracking procedure as described later in section 4.

[1] Parts of this section are adopted from Brockmann et al. (2020) and Brockmann and Hussong (2021) published under https://creativecommons.org/licenses/by/4.0/.

The measurement system consists of a microscope (Nikon Eclipse LV100) with a continuous backlight illumination. For image-recording, two cameras are used for a comparative study. These are a 12-bit, 1280×800 pixel CMOS high-speed camera (Phantom Miro Lab 110, Vision Research) with 20 µm pixel size, as well as a 12-bit, dual frame, CCD camera (Imager ProSX 5M, LaVision GmbH) with 2456×2058 pixel and a pixel size of 3.45 µm. A shematic drawing of the full experimental setup is shown in Fig. 2.1. Measurements are performed with two Nikon Cfi60 objective lenses of $M = 20\times$ and $M = 10\times$ magnification. To introduce astigmatism, a cylindrical lens with a focal length of $f_{cyl} = 200\,\text{mm}$ is placed in front of the camera sensor. To investigate the influence of the magnification, the light intensity, the processing parameters and the properties of particles and liquid on the calibration curves, we build a test-chamber which allows us to easily change particles or liquid. To validate the accuracy of BLAPTV for macroscopic flow applications, a plane channel flow is realized with a rectangular cross sectional area of h×w = 2.305×30 mm^2 and a length of 150 mm.

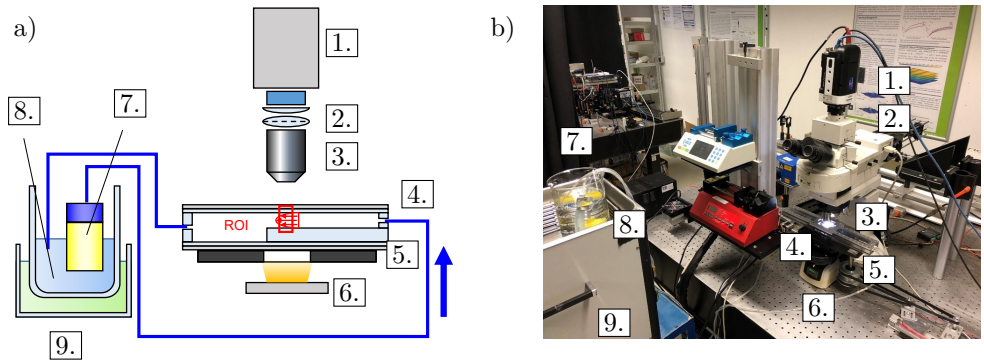

Figure 2.1: Sketch of Setup 1: a) Sketch. b) Photograph. 1) Camera, 2) Cylindrical lens and field lens, 3) Microscope objective, 4) Transparent Channel, 5) x,y,z-Traverse, 6) Mercury lamp, 7) Pump, 8) Tank, 9) Cooling Unit.

2.1.2 Setup 2 - investigation of the application of APTV to fluorescent particles in semi-dilute and dense suspensions

For investigating the applicability of APTV to large fluorescent particles in dense suspensions up to $\Phi = 20\%$ the microscopic setup described in 2.1.1 was modified and equipped with a with a 15 W continuous green laser of 532 nm wavelength. The laser is operated at 1.5 W. For image-recording a 12-bit, 1280×800 pixel CMOS high-speed camera (Phantom Miro Lab 110, Vision Research) with $20 \times 20\,\mu\text{m}^2$ pixel size is used. A shematic drawing of the experimental setup is shown in Fig. 2.2a. Measurements are performed with a Nikon Cfi60 objective lens of $M = 10\times$ magnification. To introduce astigmatism, a cylindrical lens with a focal length of $f_{cyl} = 200\,\text{mm}$ is placed in front of the camera sensor, generating two spatially separated focal planes with a measured

distance of approximately 192 µm. For the present experiments a plane channel with a cross sectional area of h×w = 2.55×30 mm^2 and a length of 300 mm was realized. Velocity profiles were measured 150 mm downstream of the channel entrance. The flow is generated with a high pressure syringe pump (LA-800, Landgraf HLL GmbH) and a 100 mL syringe (Braun GmbH). For obtaining a density and refractive index matched suspension with $d_p = 60\,\mu m$ PMMA particles we have used the receipe proposed by Bailey and Yoda 2003 with a ternary mixture of 24.85wt% water, 36.03wt% glycerin and 39.12 wt% ammonium thiocyanate that has a refractive index of $n_{\mathrm{RIM}} = 1.4867$, a density of $\rho_{\mathrm{RIM}} = 1.19\,\mathrm{g\,m^{-3}}$ and a dynamic viscosity of $\eta_{\mathrm{RIM}} = 4.99\,\mathrm{cP}$.

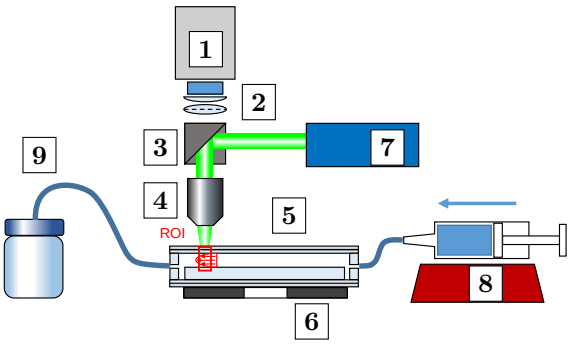

Figure 2.2: Sketch of Setup 2: 1) Camera, 2) Cylindrical lens and field lens, 3) Dichroic mirror, 4) Microscope objective, 5) Transparent Channel, 6) x,y,z-Traverse, 7) Laser, 8) Syringe Pump, 9) Bottle.

2.1.3 APTV setups utilized for investigating migration phenomena in suspension flows (setup 3 and 4)

We employ two experimental configurations for investigating particle migration in mono- and polydisperse suspensions by means of APTV. In setup 3 the optical path is perpendicular to the main flow direction (see Fig. 2.3), while in setup 4 the optical path is parallel to the main flow direction as shown in Fig. 2.4. Setup 3 and setup 4 will be hereafter referred to as Lateral View Setup (LVS) and Front View Setup (FVS), respectively. As in APTV the largest position reconstruction error occurs in the out-of-plane direction, the LVS allows to perform the experiments with a high accuracy in the velocity profile reconstruction. In contrast, the FVS faciliates a high accuracy in determining the cross sectional particle distribution. Additionally, to the astigmatic measurements we perform stigmatic measurements without a cylindrical lens in the FVS for validation of particle distributions reconstructed over the cross-sectional area by means of APTV.

2.1.3.1 Setup 3: Lateral View APTV Setup (LVS)

Setup 3 consists of a custom built microscope based on a tube (Infinity Photo Optical InfiniTube Special) illuminated with a 2.4 W High Power LED (Thorlabs SOLIS-525C) featuring a peak wavelength of $\lambda = 525\,\mathrm{nm}$. For directing the light through the objective and filtering the fluorescence signal, a filtercube (Thorlabs DFM1/M) with a dichroic mirror and two band-pass filters is installed in the optical path. For image-recording a 12-bit, 1280×800 pixel CMOS high-speed camera (Phantom Miro Lab 110, Vision Research) with $20 \times 20\,\mu\mathrm{m}^2$ pixel size is used. A schematic drawing of the experimental setup is shown in Fig. 2.3. Measurements are performed with a Nikon Cfi60 objective lens of $M = 10\times$ magnification. Using a resolution of 512×384 pixels the field of view spans $992\times744\,\mu\mathrm{m}^2$. To introduce astigmatism, a cylindrical lens with a focal length of $f_{cyl} = 150\,\mathrm{mm}$ is placed in front of the camera sensor, generating two spatially separated focal planes with a measured distance of approximately 110 µm for a refractive index of air ($n_o = 1$). This configuration is similar to the microscopic setup described in section 2.1.1 and section 2.1.2. For the suspension flow experiments square duct capillaries (VitroCom) with a cross sectional area of H×W = $400\times400\,\mu\mathrm{m}^2$ and $600\times600\,\mu\mathrm{m}^2$ and a length of $L = 500\,\mathrm{mm}$, 600 mm, respectively were utilized. Velocity profiles were measured 450 mm downstream of the channel entrance such that a minimum ratio of $x/L \approx 750$ was ensured. The flow is generated with a high pressure syringe pump (LA-800, Landgraf HLL GmbH) and a 10 mL syringe (Braun GmbH). For reducing the reflections by the curved channel corners of the capillary, the capillary is submerged into glycerol. For obtaining a density and refractive index matched suspension with PMMA particles of 30 µm, 40 µm and 60 µm diameter (Microbeads), the composition of the RIM liquid was slightly adjusted to 26.46wt% water, 32.30wt% glycerin and 41.24 wt% ammonium thiocyanate to obtain a slightly better optical quality compared to the liquid utilized in section 2.1.2. This mixture has a refractive index of $n_{\mathrm{RIM}} = 1.4882$, a density of $\rho_{\mathrm{RIM}} = 1.19\,\mathrm{g\,m^{-3}}$ and a dynamic viscosity of $\eta_{\mathrm{RIM}} = 4.99\,\mathrm{cP}$. The refractive index was checked with a digital refractometer (DR301-95 KRUESS Optronic GmbH). The tracer particles are labeled with Rhodamine B (Carl Roth).

2.1.3.2 Setup 4: Front View APTV Setup (FVS)

APTV Setup 4 is schematically depicted in Fig. 2.4. It incorporates the identical camera, tubus, filter cube, objectiv and syringe pump as in setup 3 but the measurement section is illuminated with a 7 W high power LED (7) (ILA iLA.LPS v3) equipped with a green LED chip ($\lambda \approx 532\,\mathrm{nm}$). The measurements are performed with $M = 10\times$ at a resolution of 512×512 pixel resulting in a field of view of $992\times992\,\mu\mathrm{m}^2$ such that the whole cross-sectional area of the capillary is captured. Measurements are performed with and without a cylindrical lens of $f_{cyl} = 150\,\mathrm{mm}$ placed in front of the camera sensor. The camera and corrsponding optics are aligned on the capillary centerline axis. Images are taken through a bososilicate glass coverslip (Marienfeld) with a thickness

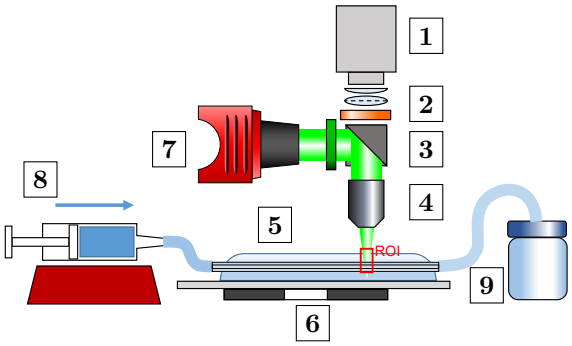

Figure 2.3: Sketch of setup 1 (LVS): 1) Camera, 2) Cylindrical lens and field lens, 3) Dichroic mirror with band-pass filters, 4) Microscope objective, 5) Square capillary submerged in glycerol, 6) x,y,z-Traverse, 7) High power LED, 8) Syringe Pump, 9) Bottle.

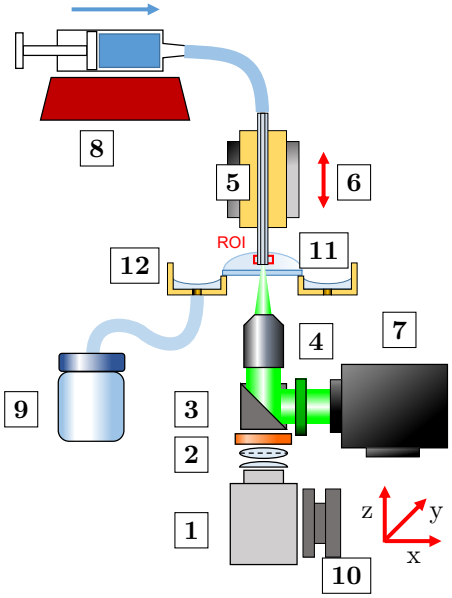

Figure 2.4: Sketch of Setup 4 (FVS): 1) Camera, 2) Cylindrical lens and field lens, 3) Dichroic mirror with band-pass filters, 4) Microscope objective, 5) Square capillary, 6) z-Traverse, 7) High power LED, 8) Syringe Pump, 9) Bottle 10) x,y,z-Traverse 11) Coverslide 12) Tub with drainage.

of approximately 0.13 mm and a diameter of 30 mm as depicted in Fig. 2.4. The camera together with LED and optical components can be precisely traversed in x,y,z direction in steps of 1.25 µm. The capillary is mounted on a traverse and can be positioned in steps of 2.5 µm in z-direction such that the distance with respect to the glass coverslip can be adjusted. The fluid driven through the capillary is collected in a

tub and drains into a container. In setup 4 experiments are performed within a square capillary of $600 \times 600\,\mu m^2$ and a length of $L = 600\,mm$. Velocity profiles were measured approximately 250 µm to 500 µm upstream of the capillary outlet such that a ratio of flow length to duct height of $L/H \approx 750$ was obtained. The RIM liquid and particles used in setup 3 and 4 are identical.

2.1.4 Setups for investigating pattern formation in rotating suspensions

Two different setups have been established for recording the particle patterns in rotating suspensions from the front or side view as discussed later in chapter 7. The front view experiment (setup 5) is depicted in Fig. 2.5, while the side view experiment (setup 6) is depicted in Fig. 2.6. The main body of the experiments consists of a horizontal rotating device equippable with acrylic single cylinders or cylinder pairs of different diameters and a length of $L = 480\,mm$ (see Fig. 2.5 and Fig. 2.6). With a tail-stock spindle (front view experiment) or threaded rods (side view experiment) the cylinders are pressed into the grooves of endcaps and are axially sealed with flat silicone rings. For the side view experiments a transparent endcap is employed (Fig. 2.6). The system is filled through four radial holes drilled in each cylinder.

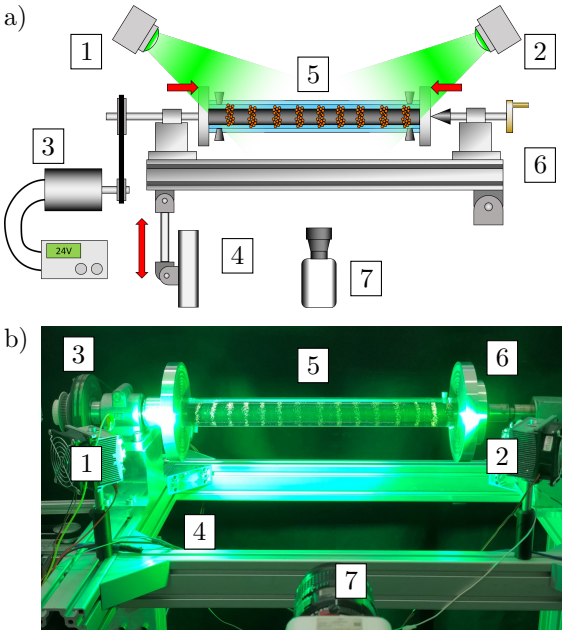

Figure 2.5: Setup 5: Exemplary configuration of the Experimental setup for the observation of the axial particle distribution - "front view experiment" (cylinder pair mounted): a) Sketch b) Foto. 1,2) High Power LED, 3) 24V DC motor, 4) Pivotable frame with inclination system 5) Cylinder system, 6) Spindle stock, 7) Camera

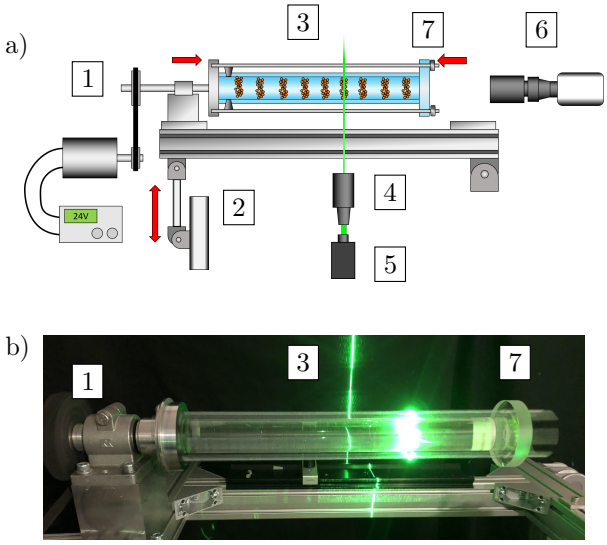

Figure 2.6: Setup 6: Exemplary configuration of the Experimental setup for the observation of the radial particle distribution - "side view experiment" (single cylinder mounted): a) Sketch b) Foto. 1) 24V DC motor, 2) Pivotable frame with inclination system, 3) Cylinder system, 4) Light sheet optics, 6) 5 Continuous wave laser, 6) Camera 7) Transparent endcap

In the TC system the inner radius of the outer cylinder and the outer radius of the inner cylinder are referred to as R_o and R_i as illustrated in Fig. 2.7a. The resulting gap height is denoted as $H = 2h = R_o$-R_i (see Fig. 2.7a). Both cylinders rotate with the same rotation rate such that the angular frequency of the inner cylinder (Ω_i) equals that of the outer (Ω_o). As both cylinders are fixed in the endcaps this is achieved by simply rotating the endcaps at the desired rotation rate. The geometry of the TC flow will be hereafter described in a nondimensionalized form by the ratio H/R_o. In the case of the drum the geometry is defined by the inner radius of the cylinder, which rotates with Ω_o (Fig. 2.7b). By definition, for the drum flow the gap height is $H = R_o$, such that H/R_o is equal to one.

A 300 W 24 V DC Motor (Motor Co. Ltd, MY1016), connected to a laboratory power supply, is used to rotate the system. The rotation rate (0-540 rpm) is controlled by adjusting the voltage of the power supply and measured by an optical rotation rate sensor (TESTO 470) with an uncertainty of 0.02%. The suspension for the experiments is composed of distilled water with a dynamic viscosity of 1 cP and 500 µm glass beads (CarlRoth, density 2.5 g/cm^3) at a volume fraction of 0.11%. A small amount of sodium dodecyl sulfate (CarlRoth) is added to avoid clustering of particles. The particles are coated with Rhodamine B (CarlRoth). In the front view experiments two LEDs with a wavelength of 532 nm are used to excite the particles by means of a volume illumination

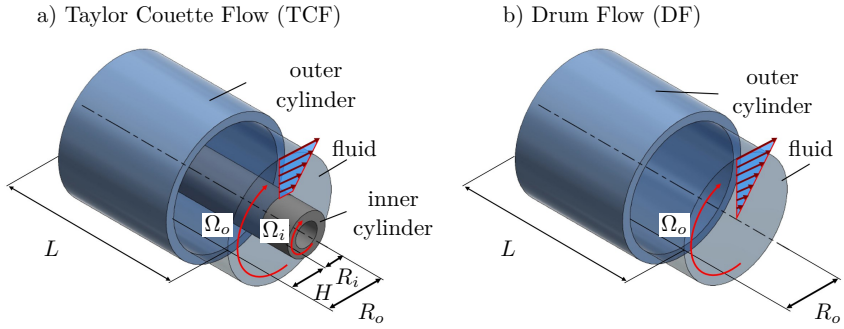

Figure 2.7: a) Geometry of the corotating Taylor-Couette flow (TCF) b) Geometry of the drum flow (DF). Both flow types exhibit a solid body rotation.

(Fig. 2.5). In contrast, for the side view experiments a 200 mW continuous wave laser (CNI Optoelectronics Tech. Co.) with a wavelength of 532 nm is utilized to generate a light sheet in the radial plane of the cylinder(s) (Fig. 2.6).

To enhance the image contrast, the inner cylinder is blackened for the TC flow configuration. Recordings are performed with a high-speed camera (Phantom MiroLAB 110) at a resolution of 1280×800px at different frame rates (60fps, 250fps, 500fps). By mounting a red longpass filter in front of the objective, only the excited particles are visible to the camera.

2.1.5 Experimental procedure

For phase mapping, the rotation rate of the cylinder is increased successively in small steps, rarely more than 2 to 5 rpm. Between each increment the system is given time to stabilize (ranging from about 3 min up to 90 min) and reach a steady state. Once a phase transition is observed at a given rotation rate, it is tested bidirectionally to ensure that no hysteresis affects the phase boundaries. To extract the axial wavelengths of particle bands the grayscale intensity of the images is summed up along the cylinder centerline and the distance of the peaks is computed. For estimating the azimuthal wavelength the space-time diagrams are extracted across two staggered horizontal lines close to the cylinder center. A cross-correlation of the space-time diagrams is performed to determine the band speed and hence to estimate the distance between individual azimuthal particle bands.

2.2 Governing equations and numerical setup for linear stability analysis [2]

Section 2.2.1 to section 2.2.4 considers the geometry and the governing equations as well as the computation strategy used in the linear stability investigations in chapter 3. Furthermore, the strategies for identifying the character of instabilities as also utilized in chapter 3, will be presented (section 2.2.5).

2.2.1 Governing equations and basic flow profile

In our linear stability analysis the flow of an incompressible fluid with the kinematic viscosity ν and the density ρ in the annular gap of two concentric cylinders is considered. The flow is assumed to be laminar and fully developed. The inner and outer cylinder radii are denoted as R_i and R_o, while the gap height is defined as $H = 2h = R_o - R_i$ (see Fig. 2.8a and Fig. 2.8b). Here h denotes the half gap height. The inner and outer cylinder rotate with the angular velocities Ω_i and Ω_o, respectively. Also an axial pressure gradient dp/dx is present, which induces a flow in axial direction. The radius ratio of the cylinders equals $\eta = R_i/R_o$, which can be translated into the curvature parameter $\epsilon = \frac{1-\eta}{1+\eta}$ (Vasanta Ram 2019). The curvature parameter describes the curvature of the gap in azimuthal direction, which can also be expressed as the ratio of the gap height to the mean diameter ($\epsilon = 2h/(R_o + R_i)$). In the following, we consider the case where either the inner or the outer cylinder of the system is rotating. The first case will be referred hereafter to as Spiral Poiseuille Flow with Rotation of the Inner cylinder (IRSPF) (Fig. 2.8a), whereas the second case will be referred to as Spiral Poiseuille Flow with Rotation of the Outer cylinder (ORSPF) (Fig. 2.8b).

For the IRSPF and the ORSPF, we define the corresponding rotational reference velocities as $U_\varphi = R_i\Omega_i$ and $U_\varphi = R_o\Omega_o$, respectively. The axial reference velocity is defined as $U_x = \frac{h^2}{2\mu_{\text{fluid}}}\frac{dp}{dx}$. In the following, the ratio of axial and azimuthal reference velocities will be described by the swirl parameters $S_i = \frac{U_\varphi}{U_x}$ (IRSPF) and $S_o = \frac{U_\varphi}{U_x}$ (ORSPF), respectively (Vasanta Ram 2019). With these parameters we define the reference velocity as $U_{ref} = \sqrt{U_x^2 + U_\varphi^2} = U_x\sqrt{1 + S_i^2}$ or $U_{ref} = U_x\sqrt{1 + S_o^2}$ and the Reynolds number as $Re = U_{ref}h/\nu$. Utilizing the swirl parameter together with this definition of Re enables us to operate our computations at defined ratios of the azimuthal and axial velocity and then determine Re_c. Hence, we are enabled to determine Re_c at defined ratios of the azimuthal and axial velocity, such that the parameter space is captured uniformly for all ϵ. This parametrization poses the base for the generation of the phase maps in chapter 3. The Navier-Stokes equations are non-dimensionalized

[2] Parts of this section are adopted from "Comparison of the instability mechanisms of inner and outer rotating spiral Poiseuille flow." written by Philipp Brockmann, V.I. Vasanta Ram, Suad Jakirlić and Jeanette Hussong, to be submitted. Parts of it are also adopted from "Stability characteristics of the spiral Poiseuille flow induced by inner or outer wall rotation" written by Philipp Brockmann, V.I. Vasanta Ram, Suad Jakirlić and Jeanette Hussong to be submitted.

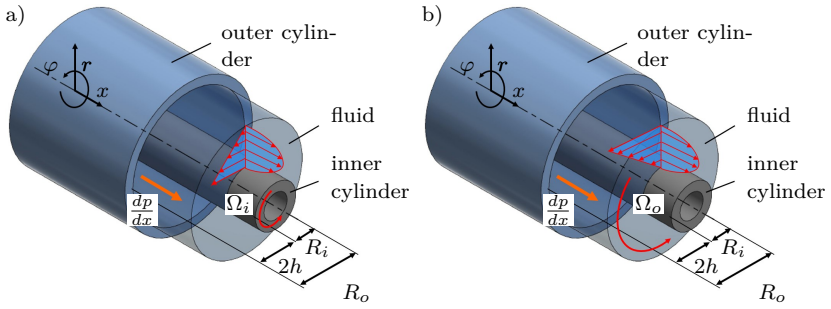

Figure 2.8: Illustration of the two flow cases considered within this study. a) Spiral Poiseuille Flow with Rotation of the Inner Cylinder (IRSPF) b) Spiral Poiseuille Flow with Rotation of the Outer Cylinder (ORSPF)

using h, U_{ref}, ρU_{ref}^2 and h/U_{ref} for space, velocity, pressure and time, respectively. In the following, v_x, v_φ, v_r denote the non-dimensionalized velocity components in cylindrical coordinates. Here x, φ and r are the axial, the azimuthal and the radial coordinate, respectively. The radial coordinate r ($R_i < r < R_o$) is translated into the gap coordinate y ($-1 < y < 1$).

$$r = \frac{R_o + R_i}{2} + \frac{R_o - R_i}{2} y \quad \text{with} \quad -1 \leq y \leq 1 \tag{2.1}$$

The analytical solution for the normalized axial flow profile can be expressed as:

$$\frac{V_x^*}{U_{ref}} = V_x = \frac{1}{\sqrt{1+Si^2}} \frac{A\ln(1-\epsilon) + B\ln(1+\epsilon) + 4\ln(1+\epsilon y)}{2\epsilon(\ln(1-\epsilon) - \ln(1+\epsilon))}, \tag{2.2}$$

with $A = -2(1-y) + (-1+y^2)\epsilon$ and $B = -2(1+y) + (1-y^2)$. Whereas the analytical solution for the normalized azimuthal flow profile of IRSPF and ORSPF can be expressed as:

$$\frac{V_\varphi^*}{U_{ref}} = V_\varphi = \frac{S_i}{\sqrt{1+S_i^2}} \frac{(\epsilon-1)}{4} \frac{2+\epsilon(1+y)}{1+\epsilon y}(1-y) \tag{2.3}$$

$$\frac{V_\varphi^*}{U_{ref}} = V_\varphi = \frac{S_o}{\sqrt{1+S_o^2}} \frac{\left(\frac{(\epsilon\, y+1)}{\epsilon} - \frac{(\epsilon-1)^2}{\epsilon\,(\epsilon\, y+1)}\right)(\epsilon+1)}{4} \tag{2.4}$$

Here V_x^*, V_φ^* and V_x, V_φ refer to the dimensionalized and non-dimensionalized velocity components of the base flow, respectively. The velocity profiles as function of ϵ are given in the appendix A.1.4.

2.2.2 Disturbance equations

The laminar base flow is perturbed by a small disturbance:

$$u_x{=}V_x(y){+}u_x'; \quad u_r{=}0{+}u_r'; \quad u_\varphi{=}V_\varphi(y){+}u_\varphi'; \quad p{=}P(x,y) + p' \tag{2.5}$$

By substituting equations (2.5) into the Navier-Stokes equations (see section A.1.1 in the appendix) nonlinear equations are obtained which describe the motion of the disturbances (A.6 to A.9). By neglecting nonlinear terms a linearized set of equations for describing the movement of the disturbance is obtained (cylindrical coordinates) (Gonzales 2013):

- x-momentum of the disturbance

$$\begin{aligned}&\frac{\partial u_x'}{\partial t} + V_x\frac{\partial u_x'}{\partial x} + u_r'\frac{dV_x}{dr} + \frac{V_\varphi}{r}\frac{\partial u_x'}{\partial \varphi} + \frac{\partial p'}{\partial x}\\ &-\frac{1}{Re}\left(\frac{\partial^2 u_x'}{\partial x^2} + \frac{1}{r}\frac{\partial u_x'}{\partial y} + \frac{\partial^2 u_x'}{\partial y^2} + \frac{1}{r^2}\frac{\partial^2 u_x'}{\partial \varphi^2}\right) = 0\end{aligned} \tag{2.6}$$

- r-momentum of the disturbance

$$\begin{aligned}&\frac{\partial u_r'}{\partial t} + V_x\frac{\partial u_r'}{\partial x} + \frac{V_\varphi}{r}\frac{\partial u_r'}{\partial \varphi} - \frac{2V_\varphi u_\varphi'}{r} + \frac{\partial p'}{\partial y}\\ &-\frac{1}{Re}\left(\frac{\partial^2 u_r'}{\partial x^2} + \frac{1}{r}\frac{\partial u_r'}{\partial y} + \frac{\partial^2 u_r'}{\partial y^2} + \frac{1}{r^2}\frac{\partial^2 u_r'}{\partial \varphi^2} - \frac{u_r'}{r^2} - \frac{2}{r^2}\frac{\partial u_\varphi'}{\partial \varphi}\right) = 0\end{aligned} \tag{2.7}$$

- φ-momentum of the disturbance

$$\begin{aligned}&\frac{\partial u_\varphi'}{\partial t} + V_x\frac{\partial u_\varphi'}{\partial x} + u_r'\frac{dV_\varphi}{dy} + \frac{V_\varphi}{r}\frac{\partial u_\varphi'}{\partial \varphi} + \frac{V_\varphi\, u_r'}{r} + \frac{1}{r}\frac{\partial p'}{\partial \varphi}\\ &-\frac{1}{Re}\left(\frac{\partial^2 u_\varphi'}{\partial x^2} + \frac{1}{r}\frac{\partial u_\varphi'}{\partial y} + \frac{\partial^2 u_\varphi'}{\partial y^2} + \frac{1}{r^2}\frac{\partial^2 u_\varphi'}{\partial \varphi^2} - \frac{u_\varphi'}{r^2} + \frac{2}{r^2}\frac{\partial u_r'}{\partial \varphi}\right) = 0\end{aligned} \tag{2.8}$$

- Continuity equation for the disturbance

$$\frac{\partial u_x'}{\partial x} + \frac{u_r'}{r} + \frac{\partial u_r'}{\partial y} + \frac{1}{r}\frac{\partial u_\varphi'}{\partial \varphi} = 0 \tag{2.9}$$

Where $\frac{1}{r}$ can be expressed as function of y and ϵ as $\frac{1}{r} = \frac{\epsilon}{1+\epsilon\cdot y}$. The disturbance is assumed to be periodic in the azimuthal and axial coordinates and is described with the following ansatz functions:

$$u_j' = A_j(y)\, e^{i\Theta} + \tilde{A}_j(y)\, e^{-i\Theta} \tag{2.10}$$

$$p' = A_p(y)\, e^{i\Theta} + \tilde{A}_p(y)\, e^{-i\Theta} \tag{2.11}$$

with $\Theta = (\lambda x + n\varphi - \omega t)$, $j = x$, φ, r and the azimuthal wavenumber $n \in \mathbb{Z}$, the axial wavenumber $\lambda \in \mathbb{R}$ and the temporal complex wavenumber $\omega \in \mathbb{C}$. A_j and $\tilde{A}_j$ denote the complex and the complex conjugated amplitude of the velocity disturbance, which holds analogous for A_p and $\tilde{A}_p$.

By substituting u_x', u_r' and u_φ' with the ansatz functions (2.10)-(2.11) the following eigenvalue problem is obtained:

- x-momentum:

$$\underbrace{V_x A_x\, i\, \lambda_x + \frac{V_\varphi}{r} A_x\, i\, n_\varphi - \frac{1}{Re}\left(A_x\,(+i)^2\,\lambda_x^2 + \frac{1}{r}\frac{dA_x}{dy} + \frac{d^2A_x}{dy^2} + \frac{1}{r^2}A_x\,(+i)^2\,n_\varphi^2\right)}_{M_{1x}} + \\ + \underbrace{A_r \frac{dV_x}{dy}}_{M_{1r}} + \underbrace{0}_{M_{1\varphi}} + \underbrace{A_p\, i\, \lambda_x}_{M_{1p}} = \underbrace{0}_{L_{1r}} + \underbrace{0}_{L_{1\varphi}} + \underbrace{A_x\, i\, \omega}_{L_{1x}} + \underbrace{0}_{L_{1p}} \tag{2.12}$$

- φ-momentum:

$$\underbrace{A_r \frac{dV_\varphi}{dy} + \frac{V_\varphi}{r} A_r - \frac{1}{Re}\left(+\frac{2}{r^2} A_r\, i\, n_\varphi\right)}_{M_{2r}} + \underbrace{V_x A_\varphi\, i\, \lambda_x + \frac{V_\varphi}{r} A_\varphi\, i\, n_\varphi}_{M_{2\varphi}} \\ \underbrace{- \frac{1}{Re}\left(A_\varphi\,(+i)^2\,\lambda_x^2 + \frac{1}{r}\frac{dA_\varphi}{dy} + \frac{d^2A_\varphi}{dy^2}\right)}_{M_{2\varphi}} + \underbrace{\frac{1}{r^2}A_\varphi\,(+i)^2\,n_\varphi^2 - \frac{A_\varphi}{r^2}\Big)}_{M_{2\varphi}} + \underbrace{0}_{M_{2x}} + \underbrace{\frac{1}{r} A_p\, i\, n_\varphi}_{M_{2p}} \\ = + \underbrace{0}_{L_{2r}} + \underbrace{A_\varphi\, i\, \omega}_{L_{2\varphi}} + \underbrace{0}_{L_{2x}} + \underbrace{0}_{L_{2p}} \tag{2.13}$$

- r-momentum:

$$\underbrace{V_x A_r\, i\, \lambda_x + \frac{V_\varphi}{r} A_r\, i\, n_\varphi}_{M_{3r}} \underbrace{- \frac{1}{Re}\left(A_r\,(+i)^2\,\lambda_x^2 + \frac{1}{r}\frac{dA_r}{dy} + \frac{d^2A_r}{dy^2} + \frac{1}{r^2}A_r\,(+i)^2\,n_\varphi^2 - \frac{A_r}{r^2}\right)}_{M_{3r}} \\ + \underbrace{- \frac{2V_\varphi}{r} A_\varphi - \frac{1}{Re}\left(-\frac{2}{r^2} A_\varphi\, i\, n_\varphi\right)}_{M_{3\varphi}} + \underbrace{0}_{M_{3x}} + \underbrace{\frac{dA_p}{dy}}_{M_{3p}} \\ = + \underbrace{A_r\, i\, \omega}_{L_{3r}} + \underbrace{0}_{L_{3\varphi}} + \underbrace{0}_{L_{3x}} + \underbrace{0}_{L_{3p}} \tag{2.14}$$

- continuity:

$$\underbrace{\frac{A_r}{r} + \frac{dA_r}{dy}}_{M_{4r}} + \underbrace{\frac{1}{r} A_\varphi\, i\, n_\varphi}_{M_{4\varphi}} + \underbrace{A_x\, i\, \lambda_x}_{M_{4x}} + \underbrace{0}_{M_{4p}} = \underbrace{0}_{L_{4r}} + \underbrace{0}_{L_{4\varphi}} + \underbrace{0}_{L_{4x}} + \underbrace{0}_{L_{4p}} \tag{2.15}$$

This can be composed into the following system of equations:

$$\underbrace{\begin{pmatrix} M_{1r} & M_{1\varphi} & M_{1x} & M_{1p} \\ M_{2r} & M_{2\varphi} & M_{2x} & M_{2p} \\ M_{3r} & M_{3\varphi} & M_{3x} & M_{3p} \\ M_{4r} & M_{4\varphi} & M_{4x} & M_{4p} \end{pmatrix}}_{\boldsymbol{M}} \underbrace{\begin{pmatrix} A_r \\ A_\varphi \\ A_x \\ A_p \end{pmatrix}}_{\boldsymbol{A}} = \omega \underbrace{\begin{pmatrix} L_{1r} & L_{1\varphi} & L_{1x} & L_{1p} \\ L_{2r} & L_{2\varphi} & L_{2x} & L_{2p} \\ L_{3r} & L_{3\varphi} & L_{3x} & L_{3p} \\ L_{4r} & L_{4\varphi} & L_{4x} & L_{4p} \end{pmatrix}}_{\boldsymbol{L}} \underbrace{\begin{pmatrix} A_r \\ A_\varphi \\ A_x \\ A_p \end{pmatrix}}_{\boldsymbol{A}} \tag{2.16}$$

The boundary conditions for A_x, A_φ, A_r, that need to be satisfied are:

$$A_r(y{=}\pm1){=}0 \quad \frac{d}{dy}A_r(y{=}\pm1){=}0 \quad A_x(y{=}\pm1){=}0 \quad A_\varphi(y{=}\pm1){=}0 \tag{2.17}$$

whereas for $A_p(y{=}\pm1)$ no boundary condition is needed. The boundary conditions also apply for the complex conjugated amplitudes.

2.2.3 Discretization

To obtain a discretized eigenvalue problem in the following form:

$$\boldsymbol{MA} = \omega \boldsymbol{LA} \quad \text{with} \quad \boldsymbol{A}{=}[A_r; A_\varphi; A_x; A_p] \tag{2.18}$$

we use a Chebyshev collocation method to discretize the coordinate y on $N{+}1$ Gauss Lobatto Points (Trefethen 2000). The continuous derivations of $\boldsymbol{A}$ are discretized using the Chebyshev Differentiation Matrix with dimension $(N{+}1){\times}(N{+}1)$, such that $\boldsymbol{M}$ and $\boldsymbol{L}$ consist of four submatrices and have the dimension $(N{+}4){\times}(N{+}4)$. The boundary conditions (2.17) are implemented by replacing the respective rows of the submatrices. To ensure a sufficient number of collocation points we performed a convergence study on N. All results presented within this work are obtained with $N = 100$.

2.2.4 Computation of critical Reynolds- and wavenumbers

The temporal eigenvalues $\omega = \omega_i + \omega_r$ ($\omega_i = \Im(\omega)$, $\omega_r = \Re(\omega)$) of (2.18) are computed using MATLAB (eig(a, b)). As briefly explained in section 1.2.1.1, we seek the combination of λ and n for a given pair of ϵ, λ which provide the point on the neutral stable surface $\omega_i(\lambda, Re) = 0$ associated with the smallest Re. The corresponding Re is hereafter referred to as the critical Reynolds number Re_c. The corresponding values of the axial and azimuthal wavenumber are referred to as critical wavenumbers λ_c, n_c, respectively. A simple, straight forward approach to solve this multi dimensional minimization problem is to compute all ω_i on a fine grid in the Re-λ space to derive the neutral stable curve along which $\omega_i = 0$. However, as all eigenvalues need to be computed for each grid point, this strategy is not practicable, expecially when a high number of collocation points is used, which is required for high Re. For high Re the terms associated with

$\frac{1}{Re}$ become small and a high resolution is required to solve the eigenvalue problem correctly. This was observed in preliminary computations and also reported for the APF by Heaton (2008).

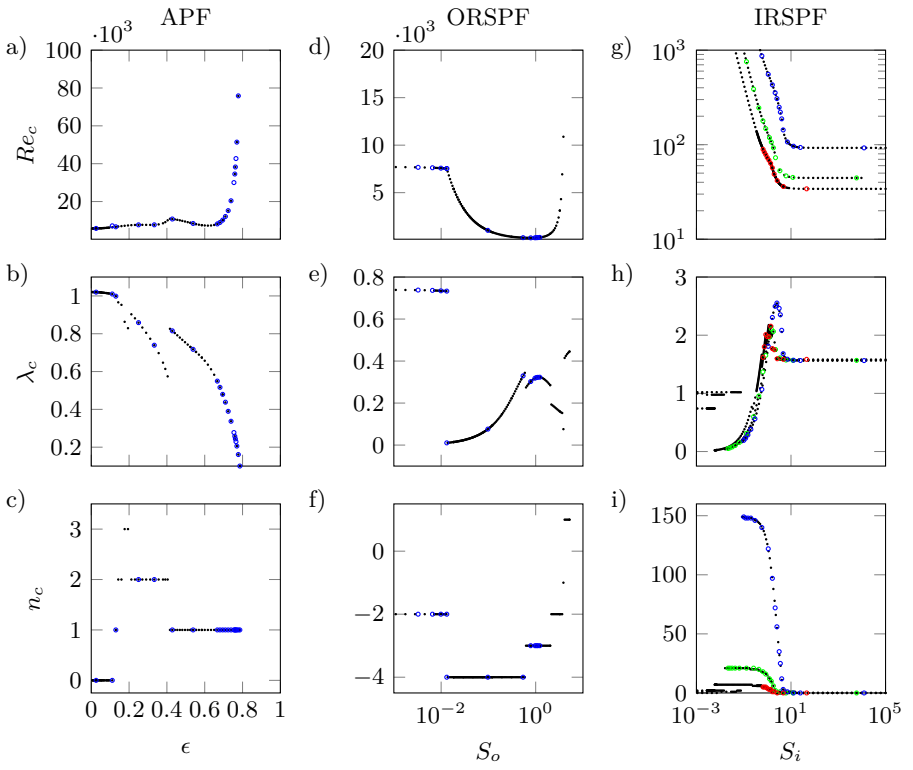

Figure 2.9: Comparison of numerically obtained values for Re_c, λ_c, n_c to reference data. Black dots refer to data of the current authors, circles refer to reference data. a) Re_c over ϵ, blue circles: Cotrell and Pearlstein (2006) b) λ_c over ϵ, blue circles: Cotrell and Pearlstein (2006) c) n_c over ϵ, blue circles: Cotrell and Pearlstein (2006) d) Re_c over S_o, blue circles: Meseguer and Marques (2005) e) λ_c over S_o, blue circles: Meseguer and Marques (2005) f) n_c over S_o, blue circles: Meseguer and Marques (2005) g) Re_c over S_i, blue circles: Ng and Turner (1982) ($\epsilon = 0.0256$), green circles: Ng and Turner (1982) ($\epsilon = 0.1299$), red circles: Takeuchi and Jankowski (1981) h) λ_c over S_i, blue circles: Ng and Turner (1982) ($\epsilon = 0.0256$), green circles: Ng and Turner (1982) ($\epsilon = 0.1299$), red circles: Takeuchi and Jankowski (1981) i) n_c over S_i, blue circles: Ng and Turner (1982) ($\epsilon = 0.0256$), green circles: Ng and Turner (1982) ($\epsilon = 0.1299$), red circles: Takeuchi and Jankowski (1981)

To perform an extensive parametric study, we developed a procedure which computes Re_c, λ_c, n_c at a very low computational effort, such that the computations can easily be performed on a desktop workstation. The basic features of the procedure are as follows. First, $\omega_i(\lambda, Re)$ is computed on a non-equidistant coarse grid in the $Re \times \lambda$ space. If a change of sign of ω_i is detected, a zero search is initiated at λ=const., providing the first point on the neutral stability curve. Hence, the algorithm increases or decreases λ

by $\Delta\lambda$ and repeats the zero search till three points that bracket the minimum of the stability curve are captured. Subsequently, a minimizing algorithm based on bisection and parabola fit is used to determine the minimum point and hence the Re_c of the stability curve. After the minimum has been determined a vertical scan at constant $Re = Re_c - 0.1$ is performed in the range of $0.01 < \lambda < 14$, with λ beeing step-wise increased by $\Delta\lambda$. This is necessary to ensure, that the global minima is detected, as the stability curve for a given n may exhibit several local minima. If a change of sign of ω_i is detected in this vertical scan, there exists a second branch and the computed Re_c is only a local minimum. The aforementioned zero search and minimization procedure is then repeated, which provides the global minimum and hence the global Re_c. This procedure is performed for all n considered, resulting in a global Re_c for every n. Finally, the Re_c of all n is compared to find the lowest Re_c and the associated n_c, λ_c. Within our calculation we restrict the axial wavelength to $\lambda > 0$ while n_c is allowed to assume both positive and negative values, which provides a sufficent range as discussed by Takeuchi and Jankowski (1981).

In order to validate the code for the IRSPF, the ORSPF, as well as for Annular Poiseuille Flow (APF) we compared the results to those available in literature. In Fig. 2.9a-c we present the computed values of Re_c, λ_c and n_c as function of ϵ in comparison to the results obtained by Cotrell and Pearlstein (2006) for the APF. In Fig. 2.9d-f we compare our results for the ORSPF with $\epsilon = 0.333$ as provided by the work of Meseguer and Marques (2005). As can be seen, all computed values of Re_c, λ_c and n_c are in excellent agreement for both the APF and the ORSPF. Finally, for the validation of the IRSPF we compare our results with those obtained by Ng and Turner (1982) for $\epsilon = 0.1299$ and $\epsilon = 0.0256$ and those obtained by Takeuchi and Jankowski (1981) for $\epsilon = 0.333$ as depicted in Fig. 2.9g-i. As clearly can be seen from the plots our results coincide well with reference data.

2.2.5 Identification of instability mechanisms

In this section we develope approaches to identify and characterize centrifugal and shear instability mechanisms. For, this we formulate the transport equation of the kinetic disturbance energy for the SPF. The amplification of the disturbance motion is related to an increase in disturbance energy which is transmitted from the base flow to the disturbance mostly by shear. As the shear distribution and hence the energy transfer along the gap changes when the velocity profile is changed, we expect significant differences between the ORSPF and the IRSPF with increasing ϵ and swirl. The analysis of those processes gives a more differentiated picture of the instability mechanisms than that obtained by soley dicussing the critical values of Re_c, λ_c, n_c and ω_c. The transport equation is obtained by scalar multiplication of the (nonlinear) momentum equation of the disturbance (see section A.1.2 in the appendix) and the disturbance velocity vector $\vec{u'} = (u'_x\ u'_r\ u'_\varphi)^T$ (Schmid and Henningson 2012). With the kinetic disturbance energy defined as $K = \frac{1}{2}u_r'^2 + \frac{1}{2}u_\varphi'^2 + \frac{1}{2}u_x'^2 = \frac{1}{2}q$ the transport

equation is obtained as (Gonzales 2013):

$$
\begin{aligned}
&\underbrace{\frac{\partial K}{\partial t}}_{\text{rate of change}} + \underbrace{V_x\frac{\partial K}{\partial x} + \frac{V_\varphi}{r}\frac{\partial K}{\partial \varphi}}_{\text{convection}} \underbrace{- \frac{V_\varphi u_r' u_\varphi'}{r}}_{Z_K(V_\varphi)=\text{centr. production}} \\
&\underbrace{+u_\varphi' u_r' \frac{dV_\varphi}{dr} + u_x' u_r' \frac{dV_x}{dr}}_{P_K(V_\varphi)+P_K(V_x)=\text{shear production}} = \underbrace{-\left(\frac{\partial u_x' p'}{\partial x} + \frac{1}{r}\frac{\partial r u_r' p'}{\partial r} + \frac{1}{r}\frac{\partial u_\varphi' p'}{\partial \varphi}\right)}_{\text{velocity pressure gradient}} \\
&\underbrace{+p'\left(\frac{\partial u_r'}{\partial r} + \frac{1}{r}\frac{\partial u_\varphi'}{\partial \varphi} + \frac{\partial u_x'}{\partial x}\right)}_{\text{velocity pressure gradient}} \underbrace{-\frac{1}{2}\left[\frac{\partial u_x' q}{\partial x} + \frac{1}{r}\frac{\partial r u_r' q}{\partial r} + \frac{1}{r}\frac{\partial u_\varphi' q}{\partial \varphi}\right]}_{\text{triple terms}} \\
&+\frac{1}{Re}\Bigg[\underbrace{u_r'\frac{\partial^2 u_r'}{\partial x^2} + u_\varphi'\frac{\partial^2 u_\varphi'}{\partial x^2} + u_x'\frac{\partial^2 u_x'}{\partial x^2} + u_r'\frac{1}{r}\frac{\partial}{\partial r}\left(r\frac{\partial u_r'}{\partial r}\right) + u_\varphi'\frac{1}{r}\frac{\partial}{\partial r}\left(r\frac{\partial u_\varphi'}{\partial r}\right)}_{\text{viscous terms}} \\
&\underbrace{+u_x'\frac{1}{r}\frac{\partial}{\partial r}\left(r\frac{\partial u_x'}{\partial r}\right) + \left(\frac{u_r'}{r^2}\frac{\partial^2 u_r'}{\partial \varphi^2}\right) + \frac{u_\varphi'}{r^2}\frac{\partial^2 u_\varphi'}{\partial \varphi^2} + \frac{u_x'}{r^2}\frac{\partial^2 u_x'}{\partial \varphi^2}}_{\text{viscous terms}} \\
&\underbrace{-\frac{2u_r'}{r^2}\frac{\partial u_\varphi'}{\partial \varphi} + u_\varphi'\frac{2}{r^2}\frac{\partial u_r'}{\partial \varphi} - \frac{u_r' u_r'}{r^2} - \frac{u_\varphi' u_\varphi'}{r^2}}_{\text{viscous terms}}\Bigg]
\end{aligned}
\tag{2.19}
$$

Where $\frac{1}{r}$ can be expressed as $\frac{1}{r} = \frac{\epsilon}{1+\epsilon \cdot y}$. Equation (2.19) will be later referred to as kinetic energy transport equation (KTE). This equation is also known as the Reynolds-Orr energy equation (Drazin and Reid 2004; Schmid and Henningson 2012). The first term is the temporal change of K. In the neutral stable scenario, the disturbance does neither grow nor decay such that $\partial K/\partial t$ must be zero when averaged over the wavelengths. The convection term describes the convection of kinetic energy by the base flow. This term is zero when averaged over the disturbance wavelengths and hence is not relevant for the present considerations. The velocity pressure gradient term describes the rate of work done by the pressure disturbance on the velocity disturbance (Drazin and Reid 2004). The triple terms account for the convection of kinetic disturbance energy by the disturbance velocities. They are zero when averaged over the wavelengths. The viscous terms account for the viscous dissipation of kinetic disturbance energy and the transport of kinetic energy due to viscous effects (Rotta 1951; Drazin and Reid 2004; Moser 1984). Apart from the aforementioned terms different types of production terms can be identified in equation (2.19). The total shear production consists of the production due to azimuthal shear (2.20) of the base flow:

$$
P_K(V_\varphi) = u_\varphi' u_r' \frac{dV_\varphi}{dy} \tag{2.20}
$$

and the production due to axial shear (2.21) of the base flow:

$$P_K(V_x) = u'_x\, u'_r \frac{dV_x}{dy} \tag{2.21}$$

These terms represent the energy that is transferred from the base flow to the velocity pertubations (Rotta 1951; Drazin and Reid 2004). We further identify a curvature related production term in analogy to the work of Guaus and Bottaro (2007):

$$Z_K(V_x) = -\frac{V_\varphi u'_r u'_\varphi}{r} \tag{2.22}$$

Guaus and Bottaro (2007) investigated the instabilities in curved channel flows and termed this term as centrifugal production term. Terms of such a structure arise from the tranformation to cylindrical coordinates and are also referred to as "extra terms" (Bradshaw 1973; Moser 1984; Moser and Moin 1987). For the sake of simplicity the term in equation 2.22 is referred to as centrifugal production term within this work. To analyze and identify the onset and the characteristics of different instability mechanisms we evaluate the averaged values of equations (2.20)-(2.22). The averaged distribution of the production terms as function of y is obtained by spatial averaging over the wavelengths λ and n (2.23-2.25):

$$\overline{P_K(V_x)} = \frac{\lambda}{2\pi}\frac{n}{2\pi}\int_0^{\frac{2\pi}{\lambda}}\int_0^{\frac{2\pi}{n}} u'_x\, u'_r \frac{dV_x}{dy} dx d\varphi \tag{2.23}$$

$$\overline{P_K(V_\varphi)} = \frac{\lambda}{2\pi}\frac{n}{2\pi}\int_0^{\frac{2\pi}{\lambda}}\int_0^{\frac{2\pi}{n}} u'_\varphi\, u'_r \frac{dV_\varphi}{dy} dx d\varphi \tag{2.24}$$

$$\overline{Z_K(y)} = \frac{\lambda}{2\pi}\frac{n}{2\pi}\int_0^{\frac{2\pi}{\lambda}}\int_0^{\frac{2\pi}{n}} -\frac{V_\varphi\, u'_r\, u'_\varphi}{r}\, dx\, d\varphi \tag{2.25}$$

As can be seen from equations (2.23)-(2.25), the production terms contain the products of $u'_r u'_\varphi$ and $u'_r u'_x$. They are, when averaged over the wavelengths, the Reynolds shear stresses τ_{rx} and $\tau_{r\varphi}$:

$$\tau_{ij} = \overline{u'_i u'_j} = \frac{\lambda}{2\pi}\frac{n}{2\pi}\int_0^{\frac{2\pi}{\lambda}}\int_0^{\frac{2\pi}{n}} u'_i u'_j\, dx d\varphi = \left(\tilde{A}_j\, A_i + \tilde{A}_i\, A_j\right) \quad j,i = x,r,\varphi \tag{2.26}$$

In order to gain a deeper insight, we also analyse the production terms of the Reynolds Shear Stress Transport Equations (RSSTE) (see Appendix A.1.3). For the sake of concision, we soley consider the transport equations for $u_\varphi u_r$ and $u_r u_x$ as they contribute to equations (2.23-2.25). The azimuthal shear production (2.28) and the centrifugal production (2.27) of $u'_r u'_\varphi$ are defined as:

$$P_{\varphi r}(V_\varphi) = u'_r\, u'_r \frac{dV_\varphi}{dy} \tag{2.27}$$

$$Z_{\varphi r,1} = -\,u'_\varphi\, \frac{2V_\varphi u'_\varphi}{r} \tag{2.28}$$

In the $u'_r u'_\varphi$ transport equation also a convection term arises, which has a similar structure as equation (2.28):

$$Z_{\varphi r,2} = +u'_r \frac{V_\varphi \, u'_r}{r} \tag{2.29}$$

However, the contribution of this term is negligible as will be shown in section 3.2. The centrifugal production (2.30) and the axial shear production of $u'_r u'_x$ (2.31) are defined as:

$$Z_{xr} = -u'_x u'_\varphi \frac{2V_\varphi}{r} \tag{2.30}$$

$$P_{xr}(V_x) = u'_r u'_r \frac{dV_x}{dy} \tag{2.31}$$

As in equation (2.19), these terms, arise from the transformation from Cartesian to cylindrical coordinates. They are also referred to as "extra production terms". For simplicity, we denote them as centrifugal terms in analogy to equation 2.19. Equations (2.27)-(2.31) are evaluated analogous to equations (2.20)-(2.22) and averaged over the wavelengths.

Besides utilizing the distributions of K, the distribution of the shear stresses and the distribution of the associated production terms, we further employ the concept of the critical layer for the identification of instability mechanisms. The existence of a critical layer is associated with a TSI and known as the location where the coefficient of the second derivative in the non-viscous Orr-Sommerfeld equation exhibits a singularity when $Re \to \infty$. For plane shear flows this is the location where the disturbance velocity equals the base flow velocity ($V_x = c_x$). To our knowledge, investigations of the location of the critical layer have not been performed yet for the SPF. So far, investigations of the critical layer in the flow between concentric cylinders were restricted to the case where no rotation is present and only axisymmetric disturbances were considered ($n = 0$) (Sadeghi and Higgins 1991a; Mott and Joseph 1968a). In these works the location of the critical layer was determined as the location where the disturbance velocity equals the base flow velocity ($V_x = c_x$). Recently, Vasanta Ram (2019) derived a generalized Orr-Sommerfeld equation for the SPF as function of ϵ and the swirl parameter. For $\epsilon \to 0$ this generalized equation merges into the classical Orr-Sommerfeld equation associated with straight and parallel streamlines. In analogy to the classical Orr-Sommerfeld equation, the coefficients of the second derivative of the Amplitude of u'_r exhibit a singularity when $Re \to \infty$. Based on these coefficients an expression of the critical layer is obtained as function of S_i, λ_c, n_c and ϵ (Vasanta Ram 2019):

$$1 - \frac{\lambda}{\omega} \frac{1 - y_c^2}{\sqrt{1 + S^2}} - \epsilon \left(\frac{\lambda}{\omega} \frac{1}{\sqrt{1 + S^2}} \frac{y_c(1 - y_c^2)}{3} + \frac{n}{\omega} \frac{S}{\sqrt{1 + S^2}} \frac{(1 - y_c)}{2} \right) = 0 \tag{2.32}$$

Here y_c terms the position of the critical layer. This equation hold only for small values of ϵ, because Vasanta Ram (2019) neglected terms of the order $O(\epsilon^2)$. In the present study also large values of ϵ are considered for which equation (2.32) is not valid.

Hence, the steps described by Vasanta Ram (2019) were performed in order to derive an equation where higher order terms of ϵ are included. The resulting equation takes the following form:

$$-V_x(y_c)\lambda - V_\varphi(y_c)n\frac{\epsilon}{1+\epsilon\cdot y_c} + \omega = 0 \tag{2.33}$$

It should be mentioned, that the equation is evaluated for the critical values λ_c, n_c, Re_c and ω_c such that $\omega_i = 0$ and equation (2.33) can be expressed as follows.

$$-V_x(y_c)\lambda_c - V_\varphi(y_c)n_c\frac{\epsilon}{1+\epsilon\cdot y_c} + \omega_r = 0 \tag{2.34}$$

Equations (2.33) and (2.34) hold for the ORSPF and the IRSPF case as well. As can be seen when $\epsilon \to 0$, $V_\varphi = 0$ or $n_\varphi = 0$ equation (2.34) yields $V_x(y_c) = \frac{\omega_r}{\lambda} = c_x$ which coincides with the classical case with straight parallel streamlines. Here, the disturbance velocity equals the base flow velocity at the critical layer. However, when $n_\varphi \neq 0$, $V_\varphi \neq 0$ and $\epsilon > 0$ this relation does not hold anymore. Further, if $V_x \to 0$ and $V_\varphi > 0$, n has to be nonzero and positive to yield a location of the critical layer.

3 Comparison of the instability mechanisms of inner and outer rotating spiral Poiseuille flow [1]

Here, it is revealed, that the stability behavior of the Spiral Poiseuille Flow with Rotating Inner cylinder (IRSPF) and the Spiral Poiseuille Flow with Rotating Outer cylinder (ORSPF) exhibit a striking similarity at low and intermediate swirls, while both cases differ significantly at higher swirls. Details on the parametrization can be found in section 2.2. In the present chapter an extensive parameter study is performed to unravel the interplay between curvature parameter, swirl parameter, the critical Reynolds number and the change in the critical wavenumbers. Results will be presented in detailed phase maps for both the IRSPF and the ORSPF.

In section 3.1 the phase maps are presented and discussed which display the critical Reynolds number and the critical wavenumbers as function of ϵ and swirl parameter for the IRSPF (section 3.1.1) and for the ORSPF (section 3.1.2). Subsequently, in section 3.2 different instability mechanisms are identified which occur in the IRSPF and the ORSPF by analyzing the distribution of shear stresses and kinetic disturbance energy as well as associated production terms based on the equations presented in section 2.2.5. To benchmark the method, the Annular Poiseuille Flow (APF) and the Taylor-Couette Flow (TCF) are analyzed to show that the method is suitable for the identification of shear instabilities as well as centrifugal instabilities (section 3.2.1). Hence, in section 3.2.2 to section 3.2.5 the distributions of shear stresses and kinetic disturbance energy found in the different regions are analyzed to work out differences regarding the instability mechanisms found in the IRSPF and the ORSPF. Next, in section 3.2.6, it is analyzed how the integrated production terms of K change for different regions as function of the swirl in the IRSPF and the ORSPF. Finally, in section 3.3 the results and conclusions are summarized. The theoretical background and state of the art relevant for this chapter can be found in section 1.2.1 (fundamentals of linear stability analysis). The parametrization, the governing equations and the numerical implementation are given in section 2.2. The description of the methods for characterization of instability mechanisms are given in section 2.2.5.

[1] This chapter is adopted from "Comparison of the instability mechanisms of inner and outer rotating spiral Poiseuille flow." written by Philipp Brockmann, V.I. Vasanta Ram and Jeanette Hussong, to be submitted.

3.1 Discussion of phase maps

3.1.1 Re_c, λ_c, n_c on ϵ for the Inner Rotation Spiral Poiseuille Flow (IRSPF)

The problem is formulated by means of the curvature parameter $\epsilon = (1 - \frac{R_i}{R_o})/(1 + \frac{R_i}{R_o})$, where R_i and R_o are the inner and outer cylinder radii and the swirl parameters S_i and S_o defined as the ratios of the corresponding rotational and axial reference velocities. The rotational reference velocities are $U_\varphi = R_i\Omega_i$ and $U_\varphi = R_o\Omega_o$ while the axial reference velocity is $U_x = \frac{h^2}{2\mu_{\text{fluid}}}\frac{dp}{dx}$ as illustrated in Fig. 3.1. The reference velocities are combined to a resulting reference velocity $U_{ref} = (U_x^2 + U_\varphi^2)^{1/2}$ such that the Reynolds number is given as $Re = U_{ref}h/\nu$. In this section we discuss the evolution of the critical Reynolds number (Re_c), the critical axial wavenumber (λ_c), the critical frequency (ω_c) and the critical azimuthal wavenumber (n_c) with increasing swirl parameter S_i and varying curvature parameter ϵ for the IRSPF.

First, the general behavior of Re_c will be discussed. For this, we present Re_c as a function of S_i for ϵ ranging from 0.0025 to 0.785 in Fig. 3.2a. To reduce the computation time, we restricted our computations to $Re < 1.5 \cdot 10^5$. Figure 3.2b represents a close-up showing Re_c in the range of $0.0025 \leq \epsilon \leq 0.1$. As can be seen from Fig. 3.2a the phase map covers a range of $10^{-5} \leq S_i \leq 10^5$ and thus connects the Annular Poiseuille Flow (APF) where azimuthal flow is negligible ($S_i = 10^{-5}$) and the Taylor-Couette flow ($\mu = 0$) where axial flow is negligible ($S_i = 10^5$). For every ϵ Re_c shows a similar behavior as function of S_i. For low values of the swirl parameter ($10^{-5} \leq S_i \leq O(10^{-2})$) Re_c is approximately constant for fixed values of ϵ and remains at $O(10^4)...O(10^5)$. Hence, at intermediate values of S_i ($O(10^{-2} \leq S_i \leq O(10^1))$ Re_c dreceases down to $Re_c \approx O(10^2)$. Finally, at high swirls ($S_i > O(10^1)$) Re_c remains almost constant at $Re_c \approx O(10^2)$. Therefore, in the following, we divide the S_i space into three regions, indicated with red and magenta lines. These are denoted as Tollmien-Schlichting instability region (I), region II and region III. Henceon, a phase transition from region I to II is denoted as first transition and a transition from region II to III will be referred to as second transition. Thus, in the context of this chapter transition refers to a change

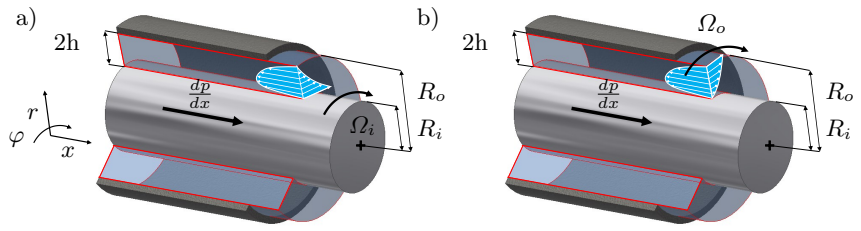

Figure 3.1: Sketches of the flow configurations. a) Spiral Poiseuille Flow with Rotating Inner cylinder (IRSPF) b) Spiral Poiseuille Flow with Rotating Outer cylinder (ORSPF)

of the region when S_i is varied and should not be confused with the flow transiting from laminar to turbulent. The corresponding S_i values are referred to as $S_{i,T1}$ and $S_{i,T2}$, respectively. Furthermore, the superscripts "-" and "+" refer to a state just before and just behind the transition, respectively. As will be shown later in section 3.2, the first and second transition lead to changes of the radial distribution of the Reynolds shear stresses, the kinetic disturbance energy and the associated production terms and are related to the onset of different instability mechanisms. We recall here, that all presented values of Re_c are associated with the neutral stable state of the flow. This means the flow is laminar but neutrally stable due to the "most unstable mode". In region I the most unstable mode refers to Tollmien-Schlichting instabilities which render the flow neutrally stable. Instead, in region II and III centrifugal instabilities are the most unstable modes (which will be explained in detail in section 3.2) and therefore render the flow neutrally stable. Transition from I to II means that the swirl is increased such that the flow situation is now located in region II and the SPF would become unstable due to centrifugal instabilities. In section 3.2 we show, why we classify the instabilities as centrifugal or Tollmien-Schlichting instabilities within the different regions.

Before discussing the evolution of Re_c as function of ϵ and S_i in detail, the behavior of the region boundaries with respect to ϵ is briefly discussed. As can be seen from the red line in Fig. 3.2a $S_{i,T1}$ decreases with increasing ϵ and assumes values inbetween $1.89 \cdot 10^{-4} \leq S_i \leq 0.95$ for the ϵ considered within this work. Thereby, the change of $S_{i,T1}$ is most pronounced at low and high values of ϵ. Obviously, $S_{i,T1}$ increases sharply for $\epsilon \to 0$ and decreases sharply as ϵ approaches to 0.785. This reveals that ϵ is a key parameter which strongly affects the swirl parameter at which the transition from a Tollmien-Schlichting to a centrifugal instability occurs. The underlying reason is that a increase in ϵ leads to an increase of centrifugal effects in the flow ($\sim \epsilon$) and vice versa. The second phase transition (II to III) occurs at S_i values of $S_{i,T2} \approx 2.27$ for $0.356 \leq \epsilon \leq 0.6$ up to $S_{i,T2} = 156.27$ for $\epsilon = 0.0025$ (see magenta line in Fig. 3.2a). In general, $S_{i,T2}$ increases sharply for $\epsilon \to 0$, but changes only little for larger epsilon.

3.1.1.1 Evolution of Re_c

Re_c in region I ($10^{-5} \leq S_i \leq S_{i,T1}^-$): In general, within region I there is just a slight variation of Re_c for all ϵ considered which can hardly be seen from Fig. 3.2a. This also applies to Fig. 3.2c-l where Re_c is presented as function of S_i for selected values of ϵ. Therefore, in Fig. 3.2m we show the relative change within region I. The relative change is defined as $(Re_c(S_{i,T1}^-) - Re_c(S_i = 10^{-5}))/Re_c(S_i = 10^{-5}) \times 100$. In Fig. 3.2m it can be seen that Re_c is decreased by about -10% at $\epsilon \approx 0.6$. For $\epsilon \leq 0.0256$ however, an increase of Re_c becomes evident that increases with decreasing ϵ and is about +31.5% for $\epsilon = 0.0025$. In Fig. 3.3a we show a close up of Re_c over S_i for $\epsilon = 0.0025$, where

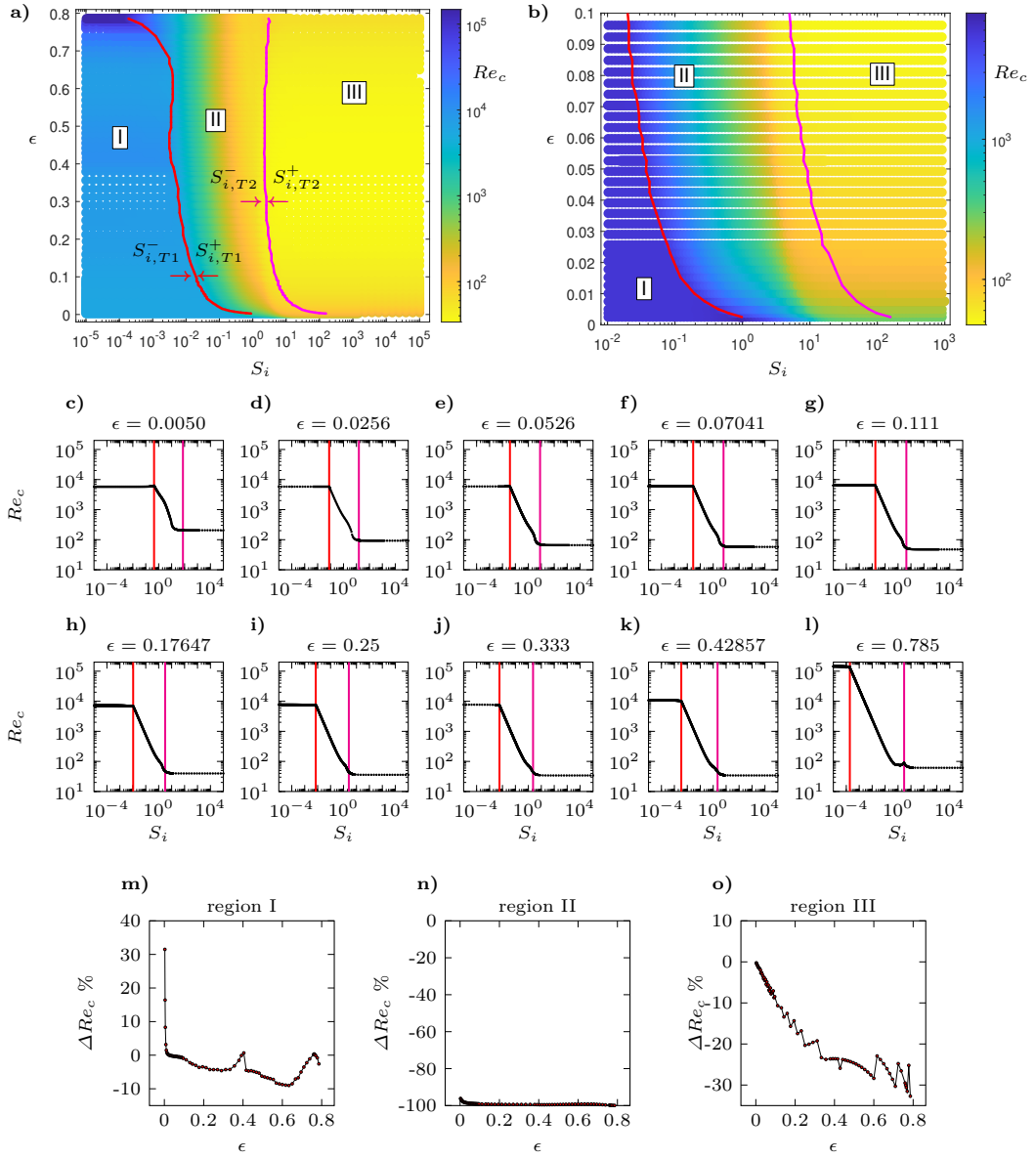

Figure 3.2: Re_c as function of ϵ and S_i for the IRSPF. Red line: Transition from I to II where $S_i = S_{i,T1}$, magenta line: transition from II to III where $S_i = S_{iT2}$. a) Re_c as function of ϵ and S_i for $0.005 \leq \epsilon \leq 0.78$. b) Re_c as function of ϵ and S_i for $0.005 \leq \epsilon < 0.1$. c-l) Re_c as function of S_i for selected values of ϵ. m) Percentage change of Re_c in region I. n) Percentage change of Re_c in region II. o) Percentage change of Re_c in region III.

this stabilization becomes evident. As can be seen Re_c increases monotously as S_i approaches $S^-_{i,T1}$. Hence, in region I increasing swirl is destabilizing for larger ϵ, while it is stabilizing for smaller ϵ.

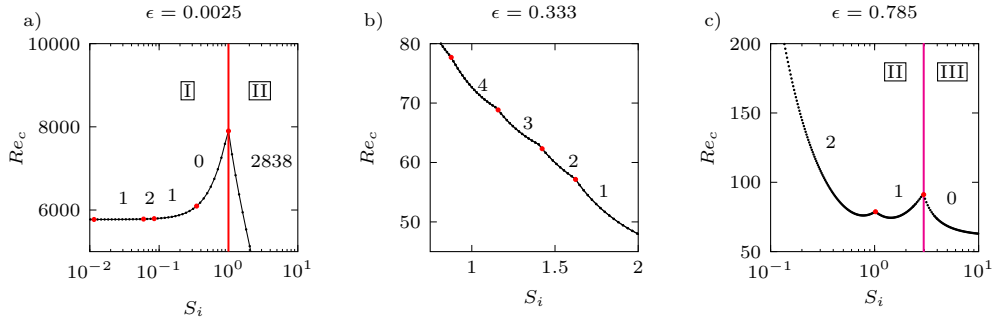

Figure 3.3: Close up showing details in Re_c over S_i for different ϵ and S_i. Changes in n_c are highlighted as red dots and labeled with the associated wavenumber (integers). a) Re_c over S_i for $\epsilon = 0.0025$ in the range of $10^{-2} \leq S_i \leq 10^{1}$. b) Re_c over S_i for $\epsilon = 0.333$ in the range of $0.75 \leq S_i \leq 2$. c) Re_c over S_i for $\epsilon = 0.78$ in the range of $0.1 \leq S_i \leq 10$.

Re_c in region II ($S^+_{i,T1} \leq S_i \leq S^-_{i,T2}$): In region II Re_c collapses sharply with increasing S_i, which is clearly evident from Fig. 3.2c-l. Re_c remains continuous during the transition from I to II. Within region II Re_c decreases monotously for $\epsilon < 0.6$. Thereby, towards the end of region II the slope increases, resulting in a slight bump which is pronounced in Fig. 3.2e-k. Around this bumb slight kinks become visible in Re_c which are related to changes in n_c as can be seen in Fig. 3.3b, where we exemplarily show Re_c for $0.75 \leq S_i \leq 2$ and $\epsilon = 0.333$. These kinks have been described firstly by Takeuchi and Jankowski (1981) in Fig. 1 of their work. It may be noted here that Takeuchi and Jankowski (1981), Mesequer and Marques (2002) and Cottrel and Pearlstein (2004) observed a non-monotonous decreases for the critical Taylor number with increasing Re for $\epsilon = 0.333$ ($\eta = 0.5$) at the same point. In our case Re_c decreases monotonously for $\epsilon = 0.333$ because we employ a definition of the Reynolds number which contains both axial and azimuthal flow components as described in section 2.2.1. Nevertheless, the numerical results obtained with our method are in excellent agreement with those of Takeuchi and Jankowski (1981) as shown in section 2.2.4. For $\epsilon > 0.6$ first decreases monotously in region II but then a stabilization becomes evident in the region where the kinks occur as can be seen from Fig. 3.3c for $\epsilon = 0.785$. Here it can be seen clearly, that Re_c increases first around $S_i \approx 10^0$ and then again when S_i approaches $S^-_{i,T2}$. Overall, the change of Re_c within region II, defined as $(Re_c(S^-_{i,T2}) - Re_c(S^+_{i,T1}))/Re_c(S^+_{i,T1}) \times 100$ is well over 90% for all ϵ considered (see Fig. 3.2n).

Re_c in region III ($S_i \geq S^+_{i,T2}$): When the flow transits from region II to region III there is no significant change in the behavior of Re_c for $\epsilon < 0.6$. For $\epsilon \geq 0.6$ however a kink in Re_c over S_i occurs which can be clearly seen in Fig. 3.2l and Fig. 3.3c for $\epsilon = 0.785$. This kink becomes increasingly severe, when ϵ increases from 0.6 to 0.785. As will be shown later in section 3.2.4 this kink is associated with a (slight) change of the production terms in the transport equation of the kinetic

energy. Afterwards, througout region III Re_c decreases as S_i increases. In Fig. 3.2o, we show the relative change of Re_c in region III from $S^+_{i,T2}$ to $S_i = 10^5$ defined as $(Re_c(S_i = 10^5) - Re_c(S^+_{i,T2}))/Re_c(S^+_{i,T2}) \times 100$. The change of Re_c within region III is 0% for $\epsilon = 0.0025$ but increases as ϵ increases, up to 32.7% for $\epsilon = 0.78$ here (Fig. 3.2o).

3.1.1.2 Evolution of λ_c

λ_c in region I ($10^{-5} \leq S_o \leq S^-_{o,T1}$): In Fig. 3.4a we present λ_c as a function of S_i for $0.0025 \leq \epsilon \leq 0.78$. Fig. 3.4b represents a close-up showing λ_c in the range of $0.0025 < \epsilon < 0.1$. Overall, within region I the axial wavenumber λ_c remains approximately constant for fixed values of ϵ and undergoes no significant changes as S_i increases, as can be seen from Fig. 3.4a. However, with variation of ϵ λ_c changes significantly and assumes values between 1.02 for $\epsilon = 0.0025$ and 0.1 for $\epsilon = 0.78$.

λ_c in region II ($S^+_{i,T1} \leq S_i \leq S^-_{i,T2}$): When the flow transits from I to II λ_c undergoes a jump at $S^+_{i,T1}$ which can be seen from Fig. 3.4a and Fig. 3.4c-l. The behavior of λ_c at this wavenumber jump is summarized in Fig. 3.4n, where we present λ_c over ϵ for $S^-_{i,T1}$ and $S^+_{i,T1}$. As can be seen $\lambda_c(S^+_{i,T1})$ assumes values close to zero for $0.25 \leq \epsilon \leq 0.78$ but increases significantly for $\epsilon \to 0$. In fact, for $\epsilon = 0.005$ $\lambda_c(S^-_{i,T1}) = 1.021$ is approximately equal to $\lambda_c(S^+_{i,T1}) = 0.988$. For $\epsilon < 0.005$ $\lambda_c(S^+_{i,T1})$ is even significantly higher than $\lambda_c(S^-_{i,T1})$. This behavior of λ_c is caused by a different type of curves of neutral stability which become critical at $S^+_{i,T1}$. For a visualization of this process, Fig. 3.5a shows the critical neutral stability curves for $S^-_{i,T1}$ and $S^+_{i,T1}$ for selected values of $\epsilon \geq 0.0526$. As can be seen for $S^-_{i,T1}$ wide curves, associated with large values of λ are critical. Instead for $S^+_{i,T1}$ narrow curves associated with small values of λ are critical (indicated with $S^-_{i,T1}$ and $S^+_{i,T1}$ in Fig. 3.5a). However, as ϵ decreases, the shape and position of the neutral stability curves at $S^+_{i,T1}$ significantly changes which is shown in Fig. 3.5b. For $\epsilon = 0.010$ the curve at $S^+_{i,T1}$ (thin red line) is significantly closer to the curve at $S^-_{i,T1}$ (thick red line) compared to the curves in Fig. 3.5a. For $\epsilon = 0.005$ the curve at $S^+_{i,T1}$ (thin orange line) attains almost the same shape and position as the curve at $S^-_{i,T1}$ (thick orange line). For $\epsilon = 0.0025$ the curve at $S^+_{i,T1}$ is even located at significantly higher values of λ_c compared to that of $S^-_{i,T1}$.

As S_i increases further within region II λ_c increases up to a global maximum and then decreases again, as can be seen in Fig. 3.4c-l. Thereby λ_c shows a non-continous behavior exhibiting several jumps which result in a fan shaped pattern, that becomes more pronounced for larger values of ϵ (Fig. 3.4i-l) and is associated with jumps in n_c. This fan-shaped pattern, can be seen more clear in Fig. 3.4m, where we show a close up of λ_c over S_i for $\epsilon = 0.333$. These fan-shaped pattern and jumps become also visible for ω_c as will be discussed later in the text. This behavior of λ_c, related to jumps in n_c, has been reported by Cottrel and Pearlstein (2004) (for $\epsilon = 0.33$), Cottrel et al. (2004) (for ϵ =0.129). As concluded by Cottrel and Pearlstein (2004) this behavior becomes less

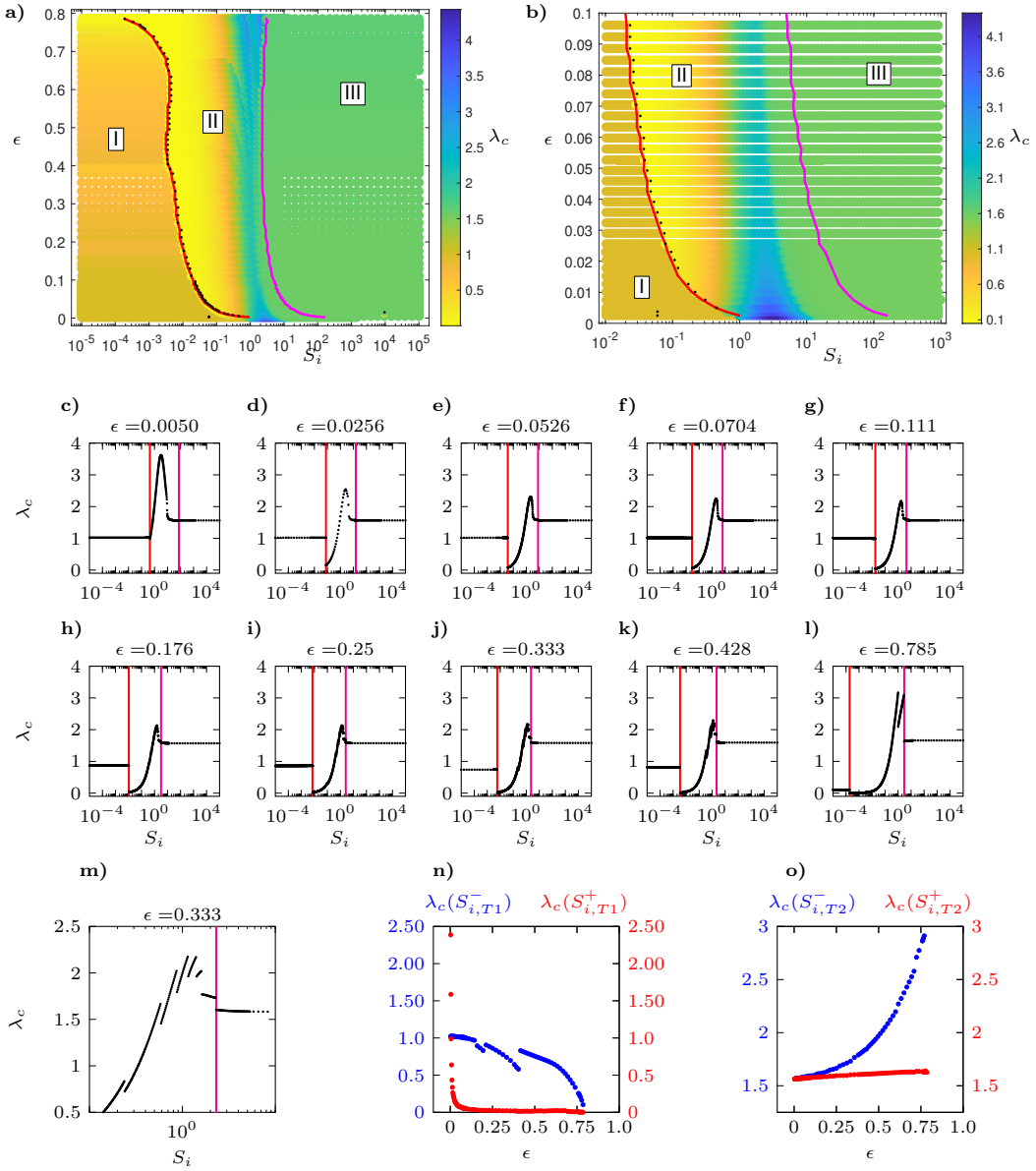

Figure 3.4: λ_c as function of ϵ and S_i for the IRSPF. Red line: Transition from I to II where $S_i = S_{i,T1}$, magenta line: transition from II to III where $S_i = S_{iT2}$. a) λ_c as function of ϵ and S_i for $0.005 \leq \epsilon \leq 0.78$. b) λ_c as function of ϵ and S_i for $0.005 \leq \epsilon < 0.1$. c-l) λ_c as function of Si for selected values of ϵ. m) Close up of λ_c over S_i for $\epsilon = 0.333$ in II. n) Change of λ_c during the transition from I to II. o) Change of λ_c during the transition from II to III.

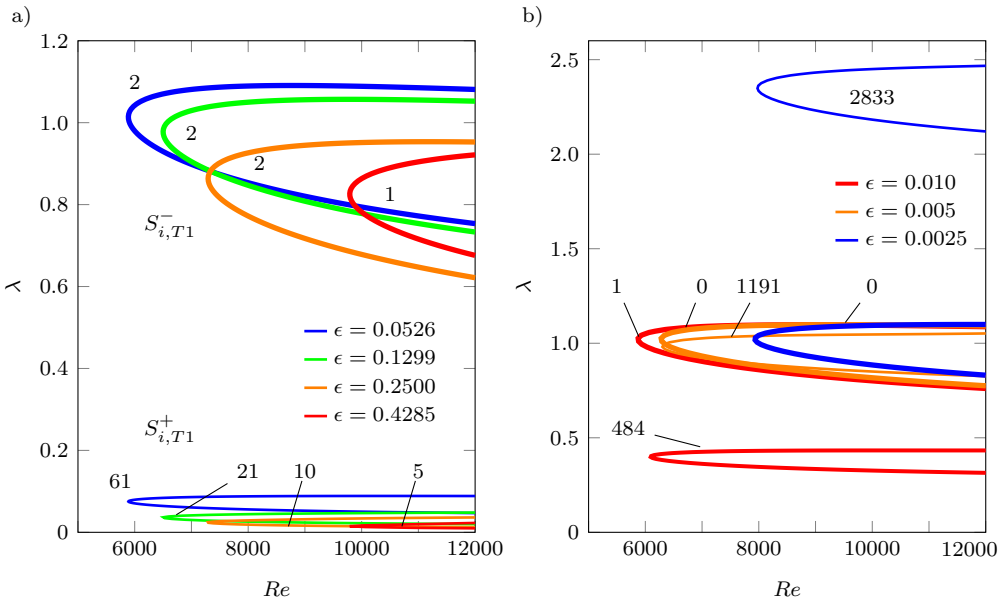

Figure 3.5: Shapes of the critical curves of neutral stability at the first wavenumber jump for $S^-_{i,T1}$ and $S^+_{i,T1}$. Thick lines indicate neutral stability curves at $S^-_{i,T1}$, while thin lines indicate neutral stability curves at $S^+_{i,T1}$. Associated values of n_c are indicated with the integer numbers. a) Neutral stability curves for $\epsilon \geq 0.0526$ b) Neutral stability curves for $\epsilon < 0.0526$

apparent for smaller ϵ as here n_c assumes higher values and thus the relative changes ($\sim \frac{n_c+1}{n_c}$) of the n_c dependent terms in the disturbance equations are less pronounced when n_c decreases by 1.

λ_c in region III ($S_i \geq S^+_{i,T2}$): At the transition from II to III λ_c undergoes a jump to lower values which can be seen clearly from Fig. 3.4o where $\lambda_c(S^-_{i,T2})$ and $\lambda_c(S^+_{i,T2})$ are presented as function of ϵ. The amplitude of the wavenumber jump thereby decreases with decreasing ϵ. In fact, for $\epsilon < 0.07$ λ_c remains approximately constant during the region transition at $S_{i,T2}$. It is noteworthy that for all ϵ considered $\lambda_c(S^+_{i,T2})$ assumes values of $1.56 < \lambda_c < 1.62$ in III. Subsequently, througout region III λ_c remains approximately constant for increasing values of S_i.

3.1.1.3 Evolution of ω_c

ω_c in region I ($10^{-5} \leq S_i \leq S^-_{i,T1}$): Fig. 3.6a and Fig. 3.6b show ω_c over S_i for $0.0025 \leq \epsilon \leq 0.78$ and $0.005 < \epsilon < 0.1$, respectively. Similar to λ_c, ω_c remains approximately constant within region I (Fig. 3.6a) for fixed values of ϵ, thereby assuming values inbetween $\omega_c \approx 0.269$ for $\epsilon = 0.0025$ and $\omega_c \approx 0.020$ for $\epsilon = 0.78$.

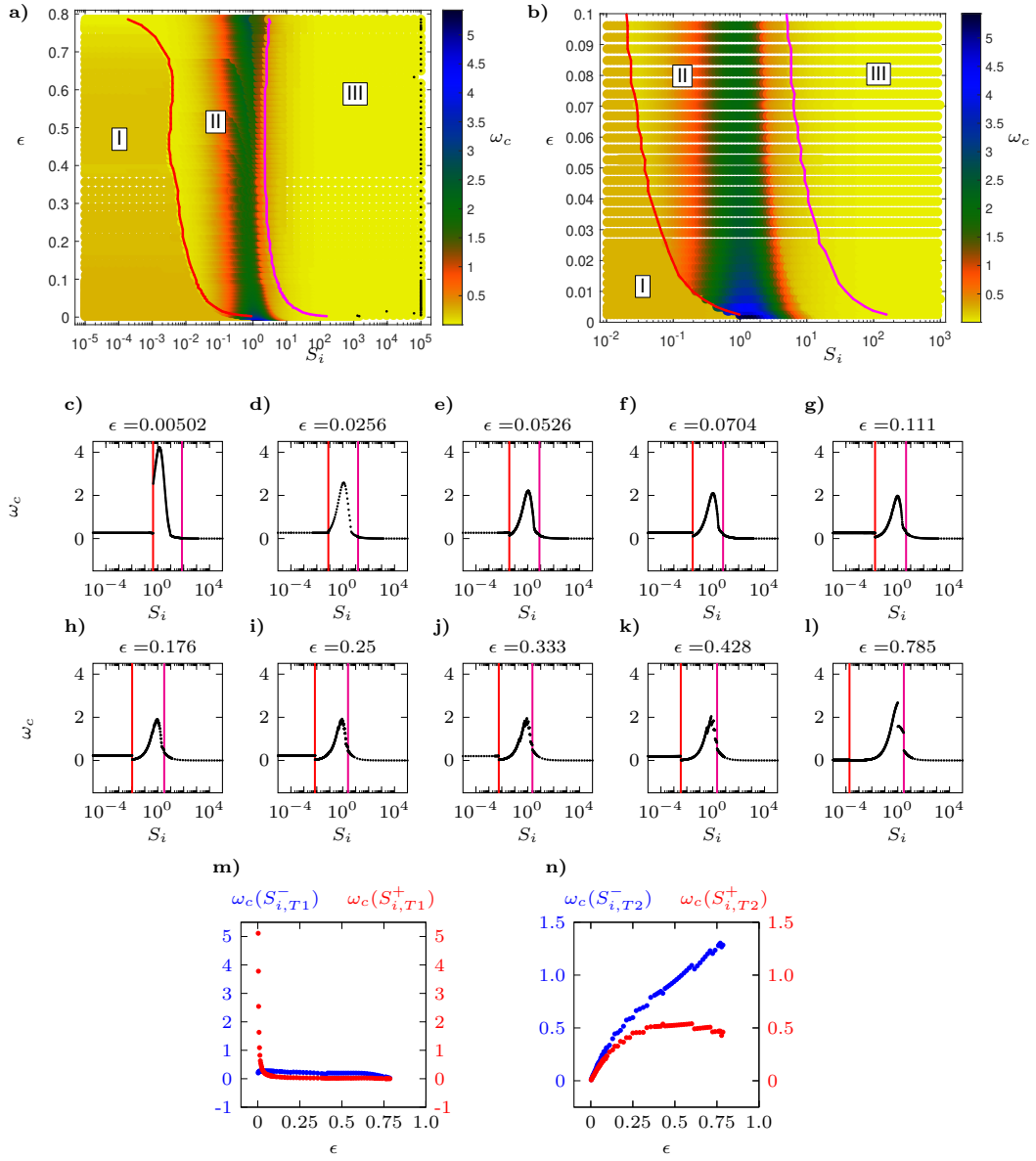

Figure 3.6: ω_c as function of ϵ and S_i for the IRSPF. Red line: Transition from I to II where $S_i = S_{i,T1}$, magenta line: transition from II to III where $S_i = S_{iT2}$. a) ω_c as function of ϵ and S_i for $0.005 \leq \epsilon \leq 0.78$. b) ω_c as function of ϵ and S_i for $0.005 \leq \epsilon < 0.1$. c-l) ω_c as function of S_i for selected values of ϵ. m) Change of ω_c during the transition from region I to II. n) Change of ω_c during the transition from region II to III.

ω_c in region II ($S_{i,T1}^{+} \leq S_o \leq S_{i,T2}^{-}$): As can be seen from Fig. 3.6a and Fig. 3.6b during the transition to II ω_c undergoes a jump as well. Fig. 3.6m, displays $\omega_c(S_{i,T1}^{-})$ vs $\omega_c(S_{i,T1}^{+})$ as function of ϵ. Here ω_c drops to lower values at $S_{i,T1}^{+}$ for $\epsilon > 0.0323$ and remains approximately constant for $\epsilon = 0.0323$. For $\epsilon < 0.0323$ instead ω_c jumps to higher values (Fig. 3.6m). Fig. 3.6m further reveals that $\omega_c(S_{i,T1}^{+})$ increases sharply as ϵ decreases. With S_i further increasing in region II ω_c increases up to a global maximum and then decreases again (Fig. 3.6c-l). During the decrease ω_c jumps several times as S_i increases, resulting in a fan shaped pattern as described for λ_c. These jumps are associated with jumps in n_c and are more pronounced for larger values of ϵ (see Fig. 3.6j,k,l).

ω_c in region III ($S_i \geq S_{i,T2}^{+}$): During the transition from II to III ω_c drops to lower values with the magnitude of the jump increasing with increasing ϵ as shown in Fig. 3.6n. Hence, with increasing S_i, ω_c approaches 0 within region III for all ϵ considered (Fig. 3.6a). This means the critical disturbance becomes steady within region III for all ϵ, which is consistent with the well kown time independent Taylor Couette instability as also concluded from Cottrel and Pearlstein (2004) for $\epsilon = 0.333$. As will be shown in the next section the disturbance also becomes axissymmetric here as $n_c = 0$, such that the disturbance motion attains the shape of the well known torodial Taylor-Couette vortices.

3.1.1.4 Evolution of n_c

n_c in region I ($10^{-5} \leq S_i \leq S_{i,T1}^{-}$): Fig. 3.7a and Fig. 3.7b show n_c over S_i for $0.0025 \leq \epsilon \leq 0.78$ and $0.0025 < \epsilon < 0.1$, respectively. Fig. 3.7c-q show n_c as function of S_i for selected values of ϵ, with Fig. 3.7h-l being a close up of Fig. 3.7c-g. For $\epsilon \geq 0.1429$ the azimuthal wavenumber n_c remains constant for fixed values of ϵ within region I for $S_i < S_{i,T1}^{-}$. Thereby ω_c assumes values in the range of $-2 < n_c < 3$ for different ϵ (Fig. 3.7a). It is remarkable that $n_c = -1$ for $0.762 \leq \epsilon \leq 0.785$ and $n_c = -2$ for $\epsilon = 0.403$ while n_c is positive for all other ϵ. To our knowledge, it was never reported before that negative azimuthal wavenumbers become critical for SPF with $\mu = 0$ (Rayleigh unstable azimuthal component). Instead, negative wavenumbers have solely been reported for SPF with $\mu > \eta^2$ (Rayleigh stable azimuthal component) (Cottrel and Pearlstein 2004; Cottrel et al. 2004; Meseguer and Marques 2005). For smaller values of ϵ ($\epsilon < 0.1429$), n_c exhibit jumps as S_i increases thereby exhibiting a stair step behavior (Fig. 3.7a,b). For $0.0230 \leq \epsilon \leq 0.0526$ n_c jumps in a pattern of $n_c = 0, 1, 2$ for increasing S_i (Fig. 3.7d,e,i,j). This has been reported by Cottrel et al. (2004) for $\epsilon = 0.0256$. However for $0.0075 \leq \epsilon \leq 0.0230$ n_c jumps in a pattern of $n_c = 0, 1, 2, 1$ and for $\epsilon \leq 0.005$ n_c even exhibits a pattern of $n_c = 0, 1, 2, 1, 0$ (Fig. 3.7b and Fig. 3.7c,h). The fact that n_c drops back to 0 is a remarkable observation. Hence, obviously for $\epsilon \leq 0.005$ increasing swirl first triggers non-axissymmetric disturbances ($n_c \leq 2$) but then damps those non-axissymmetric disturbances such that axissymmetric disturbances become critical again as S_i increases further within region I.

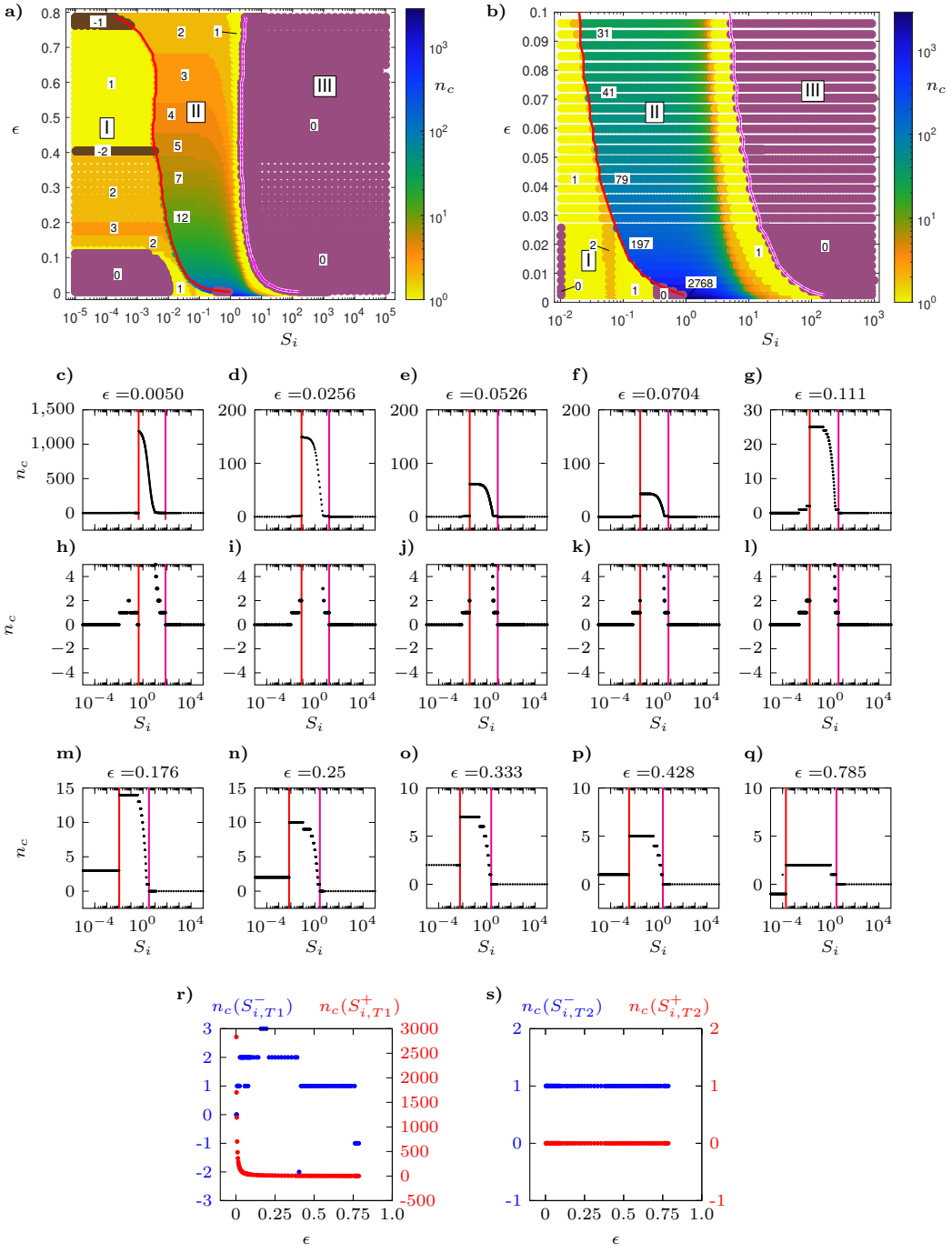

Figure 3.7: n_c as function of ϵ and S_i for the IRSPF. Red line: Transition from I to II where $S_i = S_{i,T1}$, magenta line: transition from II to III where $S_i = S_{iT2}$. a) n_c as function of ϵ and S_i for $0.005 \leq \epsilon \leq 0.78$. b) n_c as function of ϵ and S_i for $0.005 \leq \epsilon < 0.1$. c-q) n_c as function of S_i for selected values of ϵ. r) Change of n_c during the transition from region I to II. s) Change of n_c during the transition from region II to III.

n_c in region II ($S^+_{i,T1} \leq S_o \leq S^-_{i,T2}$:) During the transition from I to II n_c jumps to higher positive values. Here the wavenumber behind the jump increases sharply with decreasing ϵ as can be seen from (Fig. 3.7r), where we show $n_c(S^-_{i,T1})$ and $n_c(S^+_{i,T1})$ as function of ϵ. In particular n_c jumps from 0 to 2838 for $\epsilon = 0.0025$ while it jumps from -1 to 2 for $\epsilon = 0.78$ at $S^+_{i,T1}$ (Fig. 3.7r,q). Previous works reported maximum n_c values of 7, 21 and 149 for $\epsilon = 0.0256$, 0.129 and 0.333, respectively (Cottrel and Pearlstein 2004; Cottrel et al. 2004). The results in Fig. 3.7r reveal there is a clear trend when $\epsilon \to 0$. An explanation for this behavior is, that the narrower the gap, the more spiral shaped disturbances (with an aspect ratio of $O(1)$) can arrange in azimuthal direction. As discussed before λ_c and ω_c also increase sharply as $\epsilon \to 0$. In fact, at S^+_{iT1} λ_c, ω_c and n_c increase in the same manner when $\epsilon \to 0$ such that the speed of the disturbance wavefront $c_s = |\omega_c/\sqrt{n_c^2 + \lambda_c^2}|$ is in the order of $O(10^{-3})$ for all ϵ considered. At the same time the axial wavespeed ($c_x = \omega_c/n_c$) increases monotonously and then decreases again as $\epsilon \to 0$ (see Fig. A.5) in the appendix. For all ϵ n_c assumes a global maximum at $S^+_{i,T1}$. As S_i increases further within II n_c drops in steps of 1 till n_c reaches 1 at the end of region II. This step-wise decrease can be seen clearly in Fig. 3.7m-q. These jumps of n_c are associated with a fan-shaped pattern of λ_c and ω_c as mentioned previously.

n_c in region III ($S_i \geq S^+_{i,T2}$): For all ϵ considered n_c jumps from $n_c = 1$ to $n_c = 0$ at $S^+_{o,T2}$ during the region transition from II to III (Fig. 3.7s) and remains constant afterwards in region III (Fig. 3.7a). As will be shown in section 3.21, this is associated with toriodial disturbances, that move with an axial speed which decreases to approximately 0 as S_i increases to 10^5. This coincides with the finding of Cottrel and Pearlstein (2004); Cottrel et al. (2004) for $\epsilon = 0.0256$, 0.1299 and 0.333.

3.1.1.5 Intermediate conclusions for phase maps of the IRSPF

Using the swirl parameter S_i and a Reynolds number based on the resulting velocity, 2D phase maps of the stability behavior of the IRSPF were generated in a swirl range of $10^{-5} \leq S_i \leq 10^5$. While till date only point-wise information at fixed values of ϵ (0.0256, 0.1299 and 0.333, Cottrel and Pearlstein 2004; Cottrel et al. 2004) over the full swirl range was available, the present results show the influence of ϵ as a quasi continuous variable. Three regions (I, II, III) were identified for all values of ϵ, associated with a TSI (I) and centrifugal instabilities (II, III) in agreement with previous works for individual values of ϵ. It was revealed, that the boundaries change up to four orders of magnitude (in S_i) depending on ϵ as centrifugal effects are pronounced with increasing curvature. Previously unknown details were uncovered in regions I and II. It was shown that negative azimuthal wavenumbers can be triggered in the first region for $\epsilon = 0.403$ and for $\epsilon \geq 0.762$. Further, while it was known before that n_c jumps from 0 to 1 to 2 for $\epsilon = 0.0256$ in region I (Cottrel et al. 2004), the present results revealed that n_c jumps from 0 to 1 to 2 and then back to 1 and finally to 0 for $\epsilon \leq 0.005$ as S_i increases. This shows, that increasing swirl triggers non-axisymmetric modes and then damps non-axisymmetric modes compared to axisymmetric modes within region I. It

was discovered, that at the transition to II n_c increases sharply for decreasing values of ϵ. This is consistent with the appearance of an increasing number of spiral shaped disturbances (which similar aspect ratio) within the gap in azimuthal direction. It was shown that for $\epsilon < 0.005$ λ_c jumps to significant higher values behind the transition and increases sharply as $\epsilon \to 0$. A similar behavior was also discovered for ω_c. In fact, the ratio of ω_c, λ_c and n_c directly behind the first transition is such that the resulting speed of the disturbance wavefront $c_s = \omega_c/\sqrt{n_c^2 + \lambda_c^2})$ is in the order of $\approx O(10^{-3})$ for all ϵ considered. Thereby, the axial wavespeed $c_x = \omega_c/\lambda_c$ increases monotously and then decreases for $\epsilon \to 0$ behind the first transition.

3.1.2 Re_c, λ_c, n_c on ϵ for the Outer Rotation Spiral Poiseuille Flow (ORSPF)

In this section we consider the evolution of Re_c, λ_c, ω_c and n_c as function of ϵ and S_o for the ORSPF analogous to the IRSPF in section 3.1. First, the general behavior of Re_c will be shown. For this, Fig. 3.8a shows the evolution of Re_c as a function of S_o and ϵ in the range of $0.005 < \epsilon < 0.78$. Fig. 3.8b complementary shows a close-up for ϵ ranging from 0.005 to 0.1 and S_o ranging from 10^{-1} to 10^1. In contrast to the IRSPF case, we did not consider $\epsilon < 0.005$ here, because for such low values of ϵ Re_c increases sharply beyond values of $Re_c > 1.5 \cdot 10^5$ with increasing S_o. As mentioned in section 3.1.1, in order to reduce the computational effort we restricted our computations to $Re_c < 1.5 \cdot 10^5$.

From Fig. 3.8a it becomes evident, that at low values of S_o ($O(10^{-5}) \leq S_o \leq O(10^{-2})$) the behavior of Re_c is approximately similar for all ϵ considered and Re_c remains constant at values of $O(10^4)...O(10^5)$. However, at intermediate swirls ($O(10^{-2}) \leq S_o \leq O(10^0)$) for $\epsilon \gtrapprox 0.07$ Re_c drops sharply as S_o increases and then increases again as S_o increases further. For $\epsilon < 0.07$ Re_c increases monotonously at intermediate swirls with increasing S_o. At larger swirls ($S_o \gtrapprox O(10^1)$) Re_c increases strongly for all ϵ considered. This increase is pronounced for $\epsilon < 0.55$ such that no data is presented here at larger S_o as Re_c exceeds the values considered in the computations.

Similar to the IRSPF, the evolution of Re_c, λ_c, ω_c and n_c for the ORSPF can be divided into three regions, which are indicated by the red and the magenta lines in Fig. 3.8a,b and denoted as IO, IIO and IIIO. Thereby, the red line indicates the S_o value where the phase transition from IO to IIO occurs. The corresponding S_o value, where the transition occurs, will be hereafter referred to as $S_{o,T1}$. Analogous, the magenta line indicates the transition from IIO to IIIO and the corresponding S_o value is hereafter referred to as $S_{o,T2}$. In the following, the superscripts "-" and "+" refer to a state just before and just behind the transition, respectively.

In section 3.2 it will be shown, that in I, IO a Tollmien-Schlichting instability (TSI) is present while in II, III and IIO centrifugal instabilities are present. In IIIO the instability features different characteristics compared to all other regions. Before discussing details

on the evolution of Re_c as function of S_o, here the dependence of $S_{o,T1}$ and $S_{o,T2}$ on ϵ will briefly be discussed. The red line in Fig. 3.8a shows that $S_{o,T1}$ behaves similar to $S_{i,T1}$ as discussed for the IRSPF in Sect. 3.1. Like $S_{i,T1}$, $S_{o,T1}$ decreases with increasing ϵ, thereby assuming a similar "S"-shape, but generally attains higher values than $S_{i,T1}$, ranging from $S_{o,T1} = 0.000284$ for $\epsilon = 0.785$ to $S_{o,T1} = 0.889$ for $\epsilon = 0.0513$. Thereby, for $\epsilon \leq 0.4$ the difference between $S_{i,T1}$ (IRSPF) and $S_{o,T1}$ (ORSPF) is up to one order of magnitude. This reveals, for the first time, that the transition from a TSI to a centrifugal instability occurs at much higher swirl parameters in the ORSPF for $\epsilon \gtrapprox 0.4$. For $\epsilon > 0.4$ $S_{i,T1}$ and $S_{o,T1}$ exhibit a significant similarity, which can be seen from Fig. 3.9a where a direct comparison of $S_{i,T1}$ and $S_{o,T1}$ is performed. For smaller ϵ, the ORSPF features a striking difference compared to the IRSPF. Namely, the transition from IO to IIO solely occurs for $\epsilon \geq 0.0513$ for the ORSPF. For $\epsilon < 0.0513$ a direct transition from IO to IIIO is observed for the ORSPF, which also can be seen clearly in Fig. 3.8b.

The swirl parameter at the second transition (IIO to IIIO, magenta line in Fig. 3.8a) assumes a minimum of $S_{o,T2} = 1.26$ at $\epsilon = 0.0615$ and increases for both decreasing or increasing values of ϵ. The maximum value of $S_{o,T2} = 37.605$ is attained at $\epsilon = 0.785$ for the ϵ considered in this work. Fig. 3.8a reveals that the S_o range associated with IIO increases monotously with increasing ϵ thereby covering four orders of magnitude. Hence, the swirl range over which a centrifugal instability is dominant depends strongly on ϵ. In Fig. 3.9b a comparison of $S_{i,T2}$ (red dots) and $S_{o,T2}$ (blue dots) is performed. It shows that for $\epsilon < 0.23$ $S_{o,T2}$ is smaller than $S_{i,T2}$ while $\epsilon > 0.23$ $S_{o,T2}$ is larger than $S_{i,T2}$.

3.1.2.1 Evolution of Re_c

Re_c in region IO ($10^{-5} \leq S_o \leq S_{o,T1}^-$): In general, for most values of ϵ ($0.088 \leq \epsilon \leq 0.66$) there is just a slight variation of Re_c in region IO as can be seen from Fig. 3.8a,b. For each ϵ in the range of $0.035 < \epsilon \leq 0.0704$ the flow assumes a global minimum in region IO around $10^{-2} < S_o < 10^{-1}$ (see black dots in Fig. 3.8a) and is stabilized as S_o increases further. However, the aforementioned minima are not prominent, and not visible for instance in Fig. 3.8e. For $0.005 \leq \epsilon \leq 0.035$, the outer rotation has a purely stabilizing effect. This can be seen clearly by position of the minimum value of Re_c (black dots) in Fig. 3.8a which is at the lowest computed S_o value ($S_o = 10^{-5}$). This means with increasing swirl the flow is stabilized in region IO for $0.005 \leq \epsilon \leq 0.035$. This stabilization is signficant and clearly visible at the end of region IO in Fig. 3.8c,d. To the authors best knowledge this is the first time such a stabilizing effect was revealed for the ORSPF. Figure 3.8m, shows the relative change of Re_c. The relative change is defined analogous as for the IRSPF as $(Re_c(S_{o,T1}^-) - Re_c(S_o = 10^{-5}))/Re_c(S_o = 10^{-5}) \times 100$. Here, it can be clearly seen that the change of Re_c remains below 5% for $0.088 \leq \epsilon \leq 0.66$

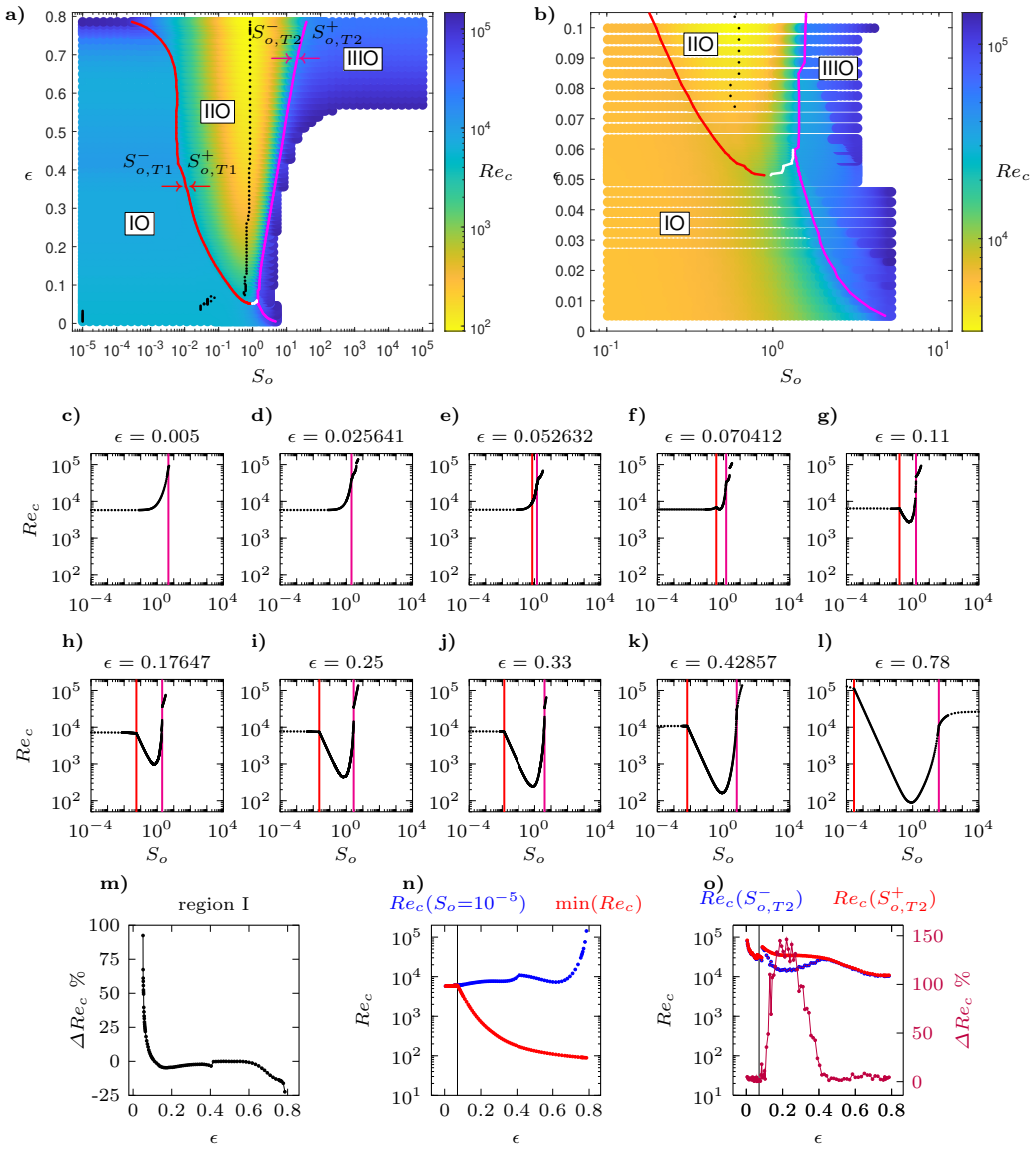

Figure 3.8: Re_c as function of ϵ and S_o for the ORSPF. Red line: Transition IO to IIO where $S_o = S_{o,T1}$, magenta line: transition IIO to IIIO where $S_o = S_{o,T2}$. Black dots in a,b indicate minimum Re_c for fixed values of ϵ. a) Re_c as function of S_o and $0.005 \leq \epsilon \leq 0.78$. b) Re_c as function of S_o and $0.005 \leq \epsilon \leq 0.1$. c-l) Re_c over S_o for selected values of ϵ. m) Percentage change of Re_c in region I. n) $Re_c(10^{-5})$ vs $min(Re_c)$, solid line: $\epsilon = 0.07041$. o) $Re_c(S_{o,T2})^-$ vs $Re_c(S_{o,T2})^+$ and percentage change of Re_c during the transition from IIO to IIIO, solid line: $\epsilon = 0.07041$.

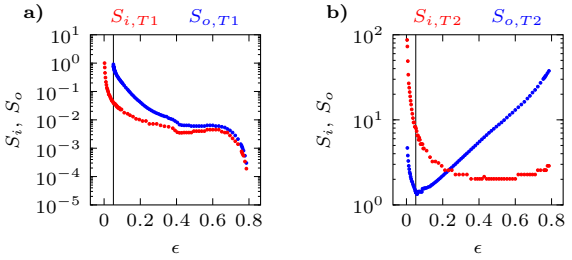

Figure 3.9: Comparison of phase boundaries between the IRSPF and the ORSPF. a) $S_{i,T1}$ (red dots) vs $S_{o,T1}$ (blue dots), solid line: $\epsilon = 0.0513$. b) $S_{i,T2}$ (red dots) vs $S_{o,T2}$ (blue dots), solid line: $\epsilon = 0.0513$.

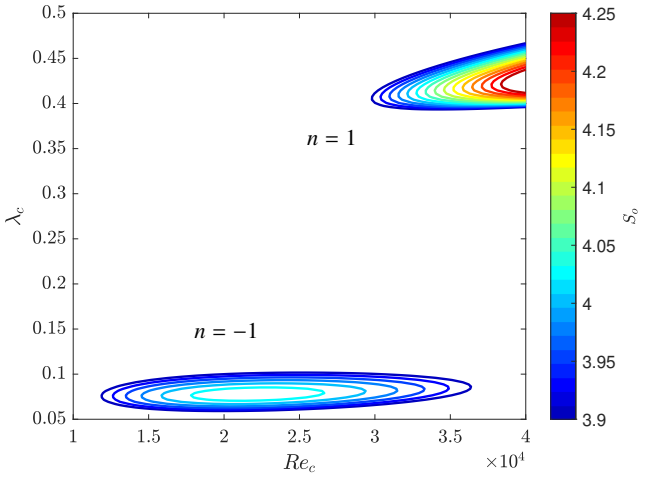

Figure 3.10: Shrinking and disappearance of an island of stability for $\epsilon = 0.333$ in the swirl range of $3.9 \geq S_o \geq 4.25$.

at the end of region IO. In contrast, for smaller or larger values of ϵ we observe a significant stabilization or destabilization, respectively. As can be seen Re_c increases by about 92% within IO for $\epsilon = 0.005$ and is decreased by about 22.23 % for $\epsilon = 0.785$.

Re_c in region IIO ($S^+_{o,T1} \leq S_o \leq S^-_{o,T2}$): At $S_{o,T1}$ the flow transits from IO to IIO and Re_c collapses for $\epsilon \geq 0.0739$ as S_o increases further (see red lines in Fig. 3.8a,b). The collapse is also clearly visible from Fig. 3.8g-l. For $\epsilon \geq 0.0739$ Re_c decreases in region IIO until reaching its minimum value as can be seen from the black dots in Fig. 3.8a,b. Thereby, the minimum value of Re_c decreases with increasing ϵ, which can be seen clearly by comparing Fig. 3.8g-l. The destabilization that occurs in region IIO is visualized in Fig. 3.8n where we show the minimum Re_c achieved within $10^{-5} \leq S_o \leq 10^5$ (red line) vs. the critical Reynolds number at $S_o = 10^{-5}$ (blue line) as a function of ϵ. Here it

can be seen, that for $\epsilon \geq 0.0739$ $\min(Re_c)$ (red line) attains significantly lower values compared to Re_c at $S_o = 10^{-5}$ (blue line). Further it is revealed that the minimum Re_c decreases monotonously with increasing ϵ. In fact, the decrease of the Reynolds number within region IIO, defined as $(\min(Re_c) - Re_c(S^+_{oT1}))/Re_c(S^+_{oT1}) \times 100$ is well over 90% for $\epsilon > 0.2$ (see Fig. A.4 in the appendix). This reveals two interesting details about the outer rotation within region IIO. First, outer rotation is capable of tremendously destabilizing the flow. Second, ϵ is the key parameter which determines the minimum critical Reynolds number that can be achieved. For all $\epsilon \geq 0.0739$ Re_c assumes its minimum value at swirl parameters inbetween $0.58 < S_o < 0.83$ (see black dots in Fig. 3.8a). This reveals that for $\epsilon \geq 0.0739$ the minimum Re_c occurs at similar values of S_o, where the axial and the azimuthal velocity component are at comparable magnitudes. As S_o increases further within IIO Re_c starts to increase again for $\epsilon \geq 0.0739$ as can be seen from Fig. 3.8f-l. As will be shown in section 3.2.3.3 this increase is related to an increased retransfer of kinetic disturbance energy to the base flow. For $0.0632 \geq \epsilon \geq 0.0704$ Re_c first decreases slightly in region IIO, however Re_c does not drop below $Re_c(S_o = 10^{-5})$ which can be seen exemplary for $\epsilon = 0.0704$ in Fig. 3.8f. After assuming a local minimum Re_c increases sharply for $0.0632 \geq \epsilon \geq 0.0704$ as S_o increases further.

For $0.0513 \leq \epsilon \leq 0.0632$, there is no drop in Re_c within region IIO such that Re_c increases monotonously here (see $\epsilon = 0.0526$ in Fig. 3.8e). For $0.0513 \leq \epsilon \leq 0.059$, there is a transition to IIO but then the flow switches back to IO. This transition back to IO is indicated with the white line in Fig. 3.8a,b. For $0.0513 \leq \epsilon \leq 0.0526$ the flow even switches several times between IO and IIO before falling back to IO. However, the behavior of Re_c is not affected significantly by these multiple region transitions, except for exhibiting slight kinks, which are associated with jumps in n_c. This multiple switching behavior that can be solely observed for $0.0513 \leq \epsilon \leq 0.0526$ will be discussed later in detail for λ_c, ω_c and n_c. For $\epsilon < 0.0513$ there is no transition to region IIO (see Fig. 3.8b).

Re_c in region IIIO ($S_o \geq S^+_{o,T2}$): With S_o increasing further the ORSPF transits from IIO to region IIIO. As there is no region IIO for $\epsilon < 0.0513$ the ORSPF directly transits from IO to region IIIO.

In region IIIO for $\epsilon \geq 0.569$ Re_c increases up to $Re_c = O(10^5)$ and assumes a plateau around $S_o = O(10^3)$ as shown exemplary for $\epsilon = 0.785$ in Fig. 3.8l. This is in agreement with the work of Deguchi (2017) who found there exists a linear stability for Rayleigh stable Taylor Couette flow ($S_o \to \infty$, $\mu \to \infty$). As described in section 1.2.1.1 the extended Rayleigh criterion (Synge 1938) states that viscous TC flow is stable for $\mu > \eta^2$ such that there would exist no finite Re_c ($Re_c \to \infty$). However, this criterion only accounts for axissymmetric disturbances ($n_c = 0$). Later it will be shown that $n_c = 1$ for $\epsilon \geq 0.569$ in region IIIO such that the criterion of Synge, which only holds for $n_c = 0$, does not apply. For smaller curvature parameters ($\epsilon < 0.569$), Re_c quickly

grows to values beyond $Re_c = 1.5 \cdot 10^5$ in region IIIO (see Fig. 3.8a). Thereby, with decreasing ϵ Re_c blows up at much lower values of S_o, which becomes evident from comparing Fig. 3.8h-k. This can be also seen clearly in Fig. 3.8a, by looking at the right side of the magenta line in the range of $0.059 \leq \epsilon < 0.569$. As ϵ decreases, the area where no data is available ($Re_c > 1.5 \cdot 10^5$) is shifted to the left (Fig. 3.8a). For $0.08859 \leq \epsilon \leq 0.41$ Re_c undergoes a discontinuity during the transition from IIO to IIIO and jumps to significantly higher values at $S^+_{o,T2}$ which can be seen from Fig. 3.8g-j. These jumps are caused by the formation and the decay of islands of instability, which are illustrated in Fig. 3.10. As can be seen in Fig. 3.10 the closed bottom neutral stability curve ($n_c = -1$) associated with a lower Re shrinks as S_o increases and ultimatively disappears for S_o values greater than 4.103. Hence, the top curve ($n_c = 1$), which is associated with a much higher Re, becomes critical. This process induces jumps in Re_c. These islands have been described also as disconnected branches by Mesequer and Marques (2002); Meseguer and Marques (2005) and Cottrel and Pearlstein (2004) for the co-rotation case ($\epsilon = 0.333$, $\mu > \eta^2$). Our results reveal that these phenomena can also appear if only the outer cylinder rotates. Hence, the disconnected branches appear to be associated with the outer cylinder rotation. Please note that these islands of instability are associated with multiple-valued stability boundaries such that for the case depicted in Fig. 3.10 three values for Re_c can be found as described by Mesequer and Marques (2002) and Cotrell and Pearlstein (2006). However, automatized tracking of multiple valued stability boundaries greatly increases the complexity of the computer code and increases the computational effort. In order to uncover a wide parameter range, we neglect those hidden branches which simplifies the computation procedure and soley consider the lowest Re_c associated with those "islands of instability'. Nevertheless with the present results the parameter space where those phenomena occur is precisley known, such that follow up works can properly track those hidden branches. From tests performed for selected ϵ we conclude that complete tracking would yield triple-valued Re_c here.

In Fig. 3.8o we show $Re_c(S^-_{o,T2})$ and $Re_c(S^+_{o,T2})$ as well as the percentage difference as function of ϵ. This plot reveals, that the difference between $Re_c(S^-_{o,T2})$ and $Re_c(S^+_{o,T2})$ increases systematically with increasing ϵ, till reaching a maximum of 150% at $\epsilon = 0.185$ and then decreases again with ϵ increasing further. We recall here that the numerical computations are restricted to $Re_c < 1.5 \cdot 10^5$ within the present work such that no data is obtained for the S_o-ϵ combinations in the lower right corner of Fig. 3.8a,b.

3.1.2.2 Evolution of λ_c

λ_c in region IO ($10^{-5} \leq S_o \leq S^-_{o,T1}$): Fig. 3.11a and Fig. 3.11b depict λ_c over S_o for $0.005 \leq \epsilon \leq 0.78$ and $0.005 \leq \epsilon \leq 0.1$, respectively. For fixed values of ϵ λ_c just varies slightly within region IO (Fig. 3.11c). In particular, for smaller values of ϵ ($\epsilon < 0.212$) an increase in S_o leads to slight jumps in λ_c that can be seen from Fig. 3.11f-h. These jumps are associated with small jumps of n_c within region IO as will

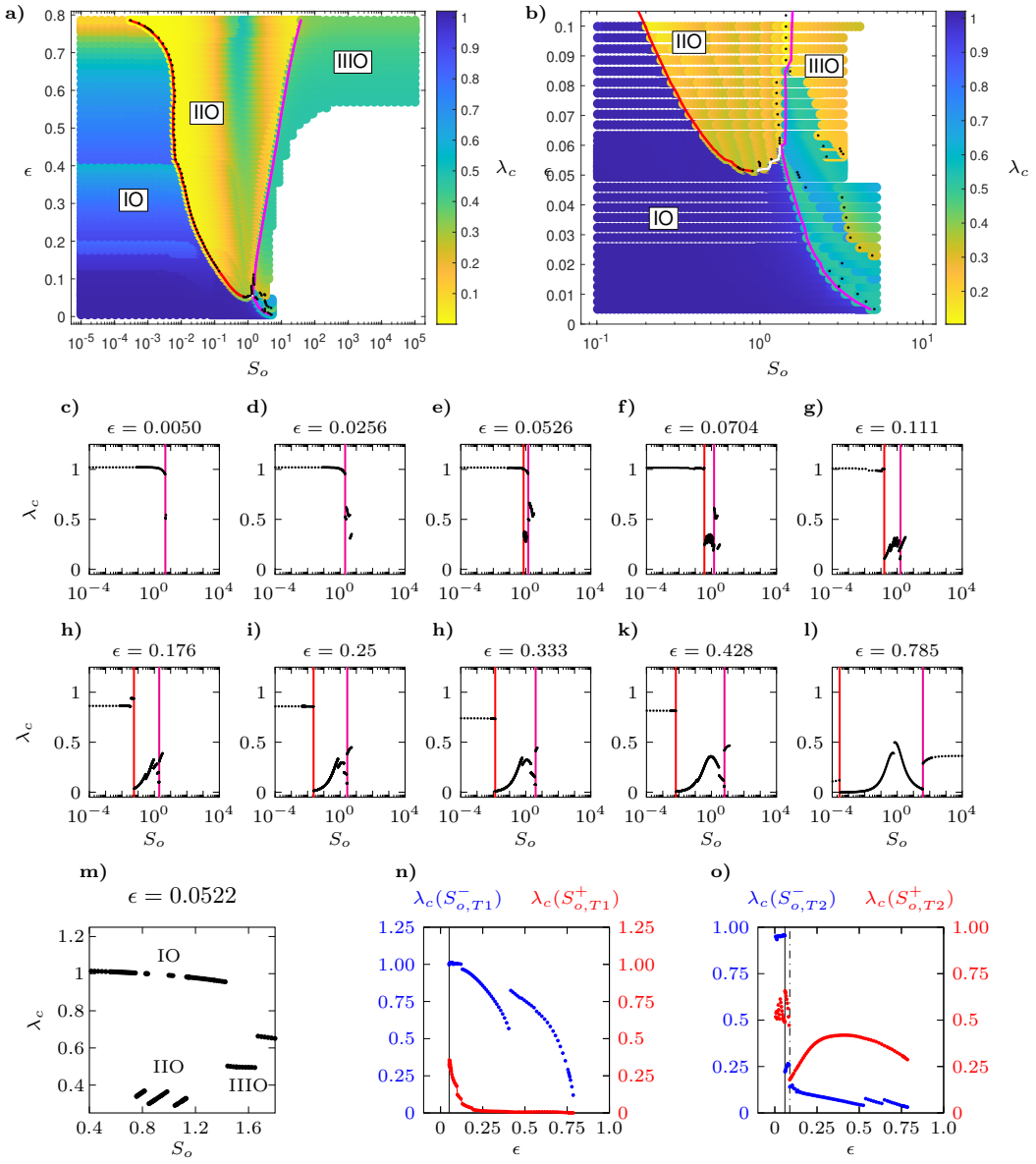

Figure 3.11: λ_c as function of ϵ and S_o for the ORSPF. Red line: Transition IO to IIO where $S_o = S_{o,T1}$, magenta line: transition IIO to IIIO where $S_o = S_{o,T2}$. a) λ_c as function of ϵ and S_o for $0.005 \leq \epsilon \leq 0.78$ b) λ_c as function of ϵ and S_o for $0.005 \leq \epsilon \leq 0.1$ c-l) λ_c over S_o for selected values of ϵ. m) λ_c over S_o for $\epsilon = 0.0526$ n) $\lambda_c(S_{o,T1})^-$ vs $\lambda_c(S_{o,T1})^+$, solid line: $\epsilon = 0.05094$ o) $\lambda_c(S_{o,T2})^-$ vs $\lambda_c(S_{o,T2})^+$, solid line: $\epsilon = 0.05974$, dash dot line: $\epsilon = 0.08859$

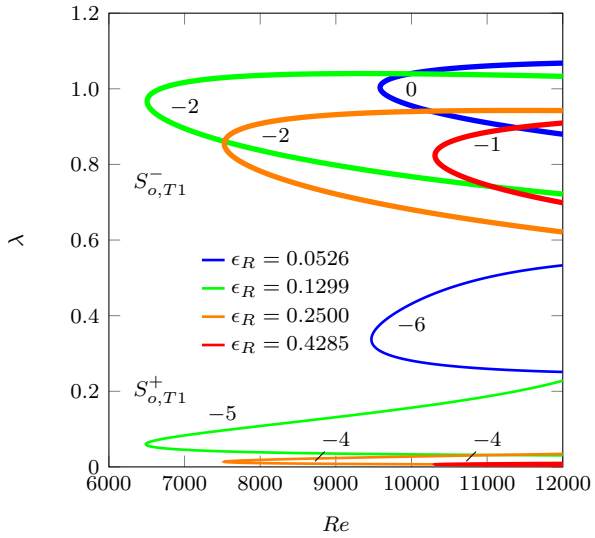

Figure 3.12: Shapes of the critical curves of neutral stability at the first wavenumber jump for $S^-_{o,T1}$ and $S^+_{o,T1}$. Thick lines indicate neutral stability curves at $S^-_{o,T1}$, while thin lines indicate neutral stability curves at $S^+_{o,T1}$. Associated values of n_c are indicated with the integer numbers.

be discussed later on. Furthermore, for small values of ϵ a slight decrease of λ_c at the end of IO becomes evident. This effect becomes more significant as ϵ decreases and is visible in Fig. 3.11c,d.

λ_c in region IIO ($S^+_{o,T1} \leq S_o \leq S^-_{o,T2}$): The transition from IO to IIO is accompanied with λ_c dropping to significantly lower values (see Fig. 3.11a,b). In Fig. 3.11n, where we show $\lambda_c(S^-_{,T1})$ and $\lambda_c(S^+_{,T1})$ as function of ϵ it can be seen that λ_c increases sharply for decreasing values of ϵ behind the jump ($\lambda_c(S^+_{,T1})$). However in contrast to the IRSPF, $\lambda_c(S^+_{,T1})$ is always less than $\lambda_c(S^-_{,T1})$. Similar to the IRSPF these jumps in λ_c are associated with different curves of neutral stability becoming critical at $S^+_{o,T1}$, which is illustrated in Fig. 3.12. As can be seen at $S^+_{o,T1}$ narrow stability curves, associated with lower values of n_c become critical. Thereby the curves become wider as ϵ increases. As S_o increases in region IIO, λ_c increases up to a local maximum with the corresponding S_o value matching approximately with that of the minimum Re_c (see Fig. 3.11a). With S_o increasing further λ_c decreases again. Thereby λ_c exhibits a piecewise continuous behavior and jumps several times as S_o increases. This behavior results in a fan shaped λ_c curve which can be clearly seen in Fig. 3.11g-l and has been discussed for the IRSPF in Sect. 3.1. Also here, these jumps are associated with jumps of n_c.

As mentioned before for $0.0513 \leq \epsilon \leq 0.059$ the flow transits back to IO as S_o increases further and λ_c jumps accordingly as can be seen from the white line in Fig. 3.11a,b. For $0.0513 \leq \epsilon \leq 0.0526$, the flow even switches several times between IO to IIO before falling back to IO. These switches are associated with a finger like pattern in λ_c as function of S_o and ϵ which becomes visible only with a further close up than given in Fig. 3.11b. Such a close up will be given later for n_c. In Fig. 3.11m we show a detailed plot of λ_c for $\epsilon = 0.0522$ in the range of $0.4 < S_o < 1.8$ to visualize this behavior. As can be seen with increasing S_o λ_c jumps multiple times between values associated with IO and IIO. These jumps are associated with radical changes of the budgets of K and the shear stresses which is related to changes of the instability mechanism and hence allows for a clear assigment to region IO and IIO. Typical distributions found in IO and IIO are discussed in section 3.2.3. The changes in the production terms are later visualized as function of S_o in section 3.2.6. The transition from IIO to IO means that increasing swirl damps centrifugal instabilities such that TSI instabilities become critical again. Finally for $\epsilon < 0.0513$, no transition from IO to IIO and hence no jump in λ_c occurs. Instead the flow directly transits from IO to IIIO (see Fig. 3.11b).

λ_c in region IIIO ($S_o \geq S^+_{o,T2}$): While the flow transits to IIIO λ_c jumps again as can be seen from Fig. 3.11a,b. In Fig. 3.11o we show λ_c before ($\lambda_c(S^-_{o,T2})$) and behind the jump ($\lambda_c(S^+_{o,T2})$. The plot reveals that, λ_c undergoes a positive jump for $\epsilon > 0.088$. Thereby $\lambda_c(S_{o,T2})^+$ attains a maximum of 0.418 at $\epsilon = 0.428$. For $0.059 < \epsilon \leq 0.088$ λ_c also undergoes a jump with $\lambda_c(S^-_{o,T2})$ and $\lambda_c(S^+_{o,T2})$ being significantly higher than for $\epsilon > 0.088$. For $0.005 < \epsilon \leq 0.059$ there is direct a transition from IO to IIIO (Fig. 3.11b) and λ_c drops from $\lambda_c \approx 0.95$ to $0.489 < \lambda_c < 0.613$ as can be seen from Fig. 3.11o.

For $\epsilon \geq 0.569$ λ_c quickly assumes values around $0.36 < \lambda < 0.47$ as S_o reaches $O(10^3)$ in region IIIO (Fig. 3.11l). For $0.0811 < \epsilon < 0.569$ with increasing S_o λ_c increases slightly within the range that is captured by our computations, as can be seen for $\epsilon \geq 0.11$ in Fig. 3.11g-k. For $0.0513 < \epsilon \leq 0.0811$ λ_c jumps several times assuming values inbetween $0.3 \leq \lambda_c \leq 0.7$ resulting in a piece wise continuous pattern (Fig. 3.11b). These jumps are associated with jumps of n_c that occur in IIIO as will be discussed hereafter. For $\epsilon < 0.0513$ the flow directly transits from IO to IIIO, hence λ_c drops from $\lambda_c \approx 0.95$ to $\lambda_c \approx 0.50$ (see Fig. 3.11b,c,d). With S_o further increasing within region IIIO λ_c undergoes jumps between values of $0.3 \leq \lambda_c \leq 0.7$ that are associated with jumps in n_c (see Fig. 3.11b).

3.1.2.3 Evolution of ω_c

ω_c in region IO ($10^{-5} \leq S_o \leq S^-_{o,T1}$): In Fig. 3.13a and Fig. 3.13b we present λ_c over S_o for $0.005 \leq \epsilon \leq 0.78$ and $0.005 \leq \epsilon < 0.1$, respectively. For for $\epsilon \geq 0.11$, ω_c just shows slight variations at fixed values of ϵ in region IO. Thereby, ω_c assumes

values between $0.0208 \geq \omega_c \geq 0.269$ with a maximum decrease of 7% in this region. For $\epsilon < 0.11$ a significant decrease becomes evident at the end of IO which becomes increasingly severe as ϵ decreases and can be clearly seen from Fig. 3.13c,d.

ω_c in region IIO ($S^+_{o,T1} \leq S_o \leq S^-_{o,T2}$): During the transition from IO to IIO, there is a jump in ω_c (see Fig. 3.13a,b). Our results show here that for $\epsilon \geq 0.739$ ω_c jumps to positive values, while for $\epsilon \leq 0.724$ assumes negative values behind the jump. In Fig. 3.13n we show ω_c before ($\omega_c(S_{o,T1^-})$) and behind the transition from I to II ($\omega_c(S_{o,T1^+})$). As can be seen the discrepancy between $\omega_c(S_{o,T1^-})$ and $\omega_c(S_{o,T1^+})$ increases as ϵ decreases. Further, as ϵ increases the magnitude of $\omega_c(S_{o,T1^+})$ grows, thereby exhibiting a similar behavior as $\lambda_c(S_{o,T1^+})$ except for attaining negative values (see Fig. 3.13n, Fig. 3.11n). Within region IIO for large values of ϵ, ω_c first remains almost constant and then drops sharply as S_o increases (see Fig. 3.13l). Hence, ω_c decreases further with increasing S_o and assumes a global minimum for each ϵ within region IIO (see black dots in Fig. 3.13a). This behavior is more pronounced for larger values of ϵ and the value attained at the minimum decreases with increasing ϵ (see Fig. 3.13h-l).

As mentioned above for $0.0513 \leq \epsilon \leq 0.059$ with S_o increasing the flow transits to region IIO and falls back to region IO before it finally reaches region IIIO. For $0.0513 \leq \epsilon \leq 0.0526$ there are even multiple region transitions and the flow switches several times between IO and IIO before falling back to IO and finally switching to IIIO. Thereby ω_c jumps accordingly as can be seen clearly in Fig. 3.13m where we show ω_c for $\epsilon = 0.0522$ in the range of $0.4 \geq S_o \geq 1.8$. For $\epsilon < 0.0513$ there is a direct transition from IO to IIIO and hence no jump in ω_c occurs which can be associated with a transition to IIO (see Fig. 3.13b).

ω_c in region IIIO ($S_o \leq S^+_{o,T2}$): While the ORSPF transits from IIO to IIIO for $\epsilon > 0.059$, ω_c jumps from negative values to positive values (see Fig. 3.13a,b). Fig. 3.13o compares ω_c before ($\omega_c(S^-_{o,T2})$) and behind the second transition ($\omega_c(S^+_{o,T2})$) as function of ϵ. The plot reveals that $\omega_c(S^-_{o,T2})$ decreases while $\omega_c(S^+_{o,T2})$ increases with ϵ increasing. In sum, the discrepancy between $\omega_c(S^-_{o,T2})$ and $\omega_c(S^+_{o,T2})$ increases with increasing ϵ. For $\epsilon \leq 0.059$ flow transits from region IO to IIIO and ω_c remains positive while exhibiting a slight jump, as can be seen from Fig. 3.13o.

As the swirl parameter reaches $S_o = O(10^2)$ ω_c assumes a plateau within IIIO for $\epsilon \geq 0.569$ (see Fig. 3.13a). Thereby ω_c attains values ranging from $\omega_c = 0.062$ ($\epsilon = 0.569$) to $\omega_c = 0.2043$ ($\epsilon = 0.785$).

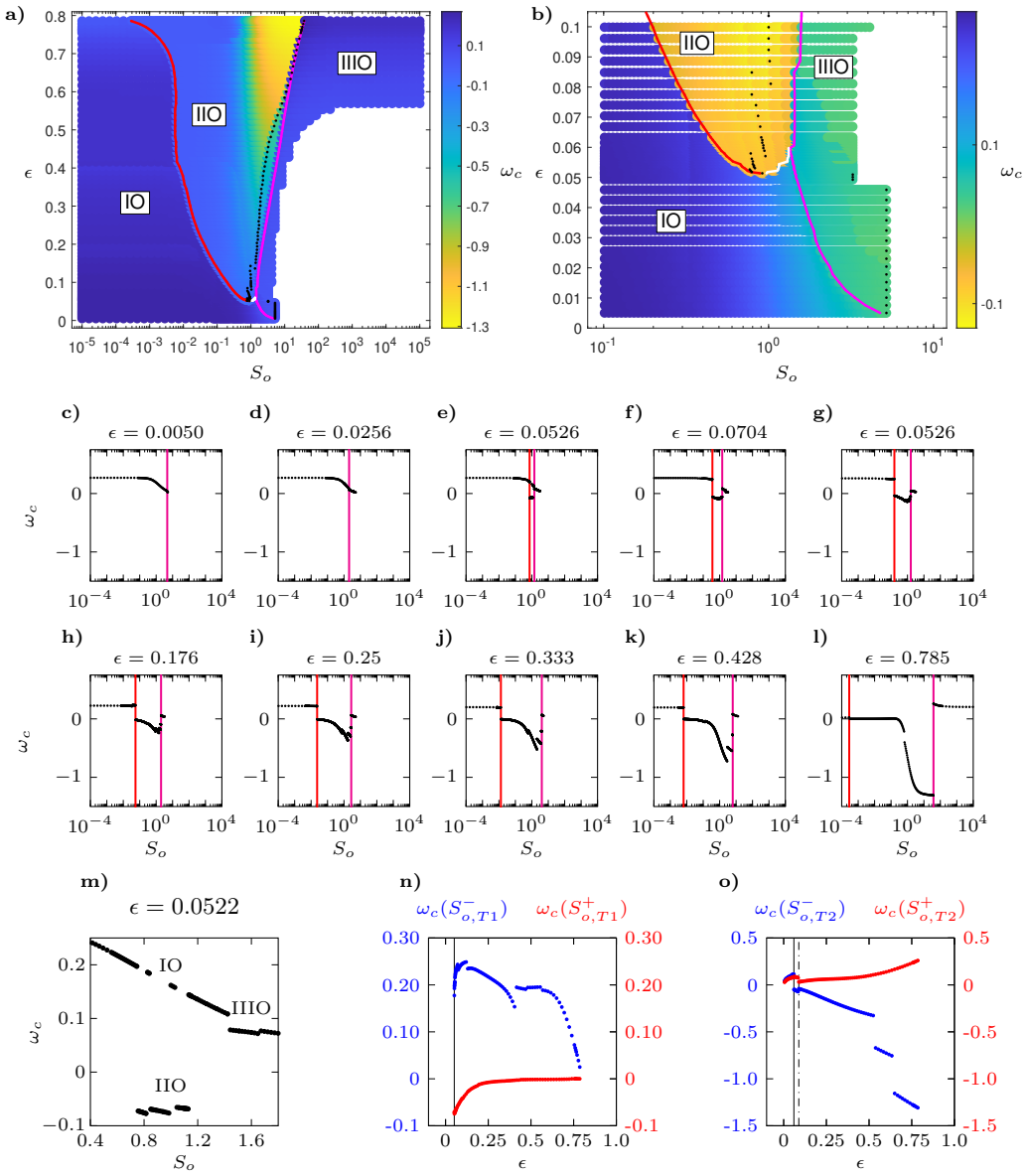

Figure 3.13: ω_c as function of ϵ and S_o for the ORSPF. Red line: Transition IO to IIO where $S_o = S_{o,T1}$, magenta line: transition IIO to IIIO where $S_o = S_{o,T2}$. a) ω_c as function of ϵ and S_o for $0.005 \leq \epsilon \leq 0.78$ b) ω_c as function of ϵ and S_o for $0.005 \leq \epsilon \leq 0.1$ c-l) ω_c over S_o for selected values of ϵ. m) ω_c over S_o for $\omega = 0.0526$ n) $\omega_c(S_{o,T1})^-$ vs $\omega_c(S_{o,T1})^+$, solid line: $\epsilon = 0.05094$ o) $\omega_c(S_{o,T2})^-$ vs $\omega_c(S_{o,T2})^+$, solid line: $\epsilon = 0.05974$, dash dot line: $\epsilon = 0.08859$

3.1.2.4 Evolution of n_c

n_c in region IO ($10^{-5} \leq S_o \leq S^-_{o,T1}$): Fig. 3.14a and Fig. 3.14b depict n_c over S_o for $0.005 \leq \epsilon \leq 0.78$ and $0.005 \leq \epsilon \leq 0.1$, respectively.

For $\epsilon \geq 0.212$ n_c does not change as S_o increases within IO and assumes values of $n_c = \{-2, -1, 1\}$ (see Fig. 3.14a). It is remarkable that for $0.481 \leq \epsilon \leq 0.553$ $n_c = 1$ while n_c attains negative values for all other ϵ (or zero for few small ϵ) within region IO. Similary, as mentioned before, for the IRSPF we found that $n_c = -1$ for $0.762 \leq \epsilon \leq 0.785$ and $n_c = -2$ for $\epsilon = 0.403$ while n_c is positive for all other ϵ. For $\epsilon < 0.212$, n_c jumps between different values of n_c $-3 \leq n_c \leq 0$ as S_o increases in IO (see Fig. 3.14a,b). Analogous to the IRSPF the number of jumps increases with ϵ decreasing: In particular, for $\epsilon = 0.2032$ n_c assumes $n_c = -3, -2$, for $\epsilon = 0.1299$ n_c assumes $n_c = -1, -2$, for $\epsilon = 0.1203$ n_c assumes $n_c = 0, -1, -2, -1$, and for $\epsilon \leq 0.07041$ n_c even assumes $n_c = 0, -1, -2, -1, 0$ (see Fig. 3.14c-f). Obviously, similar to the IRSPF different azimuthal modes are triggered within region IO for small ϵ. Negative and positive modes are associated with spirals which are inclined in the same and opposite direction as the streamlines of the base flow, respectively (Ng and Turner 1982). In general, the IRSPF triggers positive n_c for most values of ϵ, while the ORSPF triggers negative n_c for most values of ϵ. However, the present results show, that both negative and positive n_c occur for both the IRSPF and ORSPF such that no generalization can be made.

n_c in region IIO ($S^+_{o,T1} \leq S_o \leq S^-_{o,T2}$): When the flow transits to IIO n_c jumps to lower negative values (see Fig. 3.14a,b). A more detailed picture of the wavenumber jump is given in Fig. 3.14n where we present $n_c(S^-_{o,T1})$ and $n_c(S^+_{o,T1})$ as function of ϵ. As can be seen $n_c(S^+_{o,T1})$ decreases with decreasing ϵ, reaching a minimum of $n_c = -7$ at $0.0553 \leq \epsilon \leq 0.096$ and then again increases up to $n_c = -5$ for $\epsilon = 0.0513$ (indicated with the black vertical bar in Fig. 3.14n). As S_o increases within region IIO for $\epsilon > 0.059$ n_c increases in steps by +1 till n_c reaches -2 ($0.059 < \epsilon < 0.088$) or -1 ($\epsilon \geq 0.088$) (Fig. 3.14b).

For $0.053 < \epsilon < 0.059$ throughout region region IIO n_c increases step wise to $n_c = -3$ or $n_c = -2$ but then jumps back to $n_c = 0$ associated with a transition to region IO as indicated with the white line in Fig. 3.14b. For $0.0513 \leq \epsilon \leq 0.0526$ the behavior is even more complex and there are multiple switches between IO and IIO with n_c jumping between -6, -5, -4 and 0 and finally jumping back to IO ($n_c = 0$) as S_o increases. This is shown exemplary for $\epsilon = 0.0522$ in Fig. 3.14m. As can be seen, after the first transition where $n_c = -6$, n_c jumps back to zero and then to -5 and so on. In fact, n_c forms a finger-like pattern for $0.0513 \leq \epsilon \leq 0.0526$ as can be seen in Fig. 3.15a where we present a further close up of Fig. 3.14b showing n_c for $0.3 \leq S_o \leq 1.8$ and $0.048 < \epsilon < 0.065$. In the area associated with the finger-like pattern, different neutral stability curves compete which is depicted for $\epsilon = 0.0522$ and $S_o = \{0.71; 0.779; 0.8264; 0.9158\}$ in Fig. 3.15b-e. As highlighted by the black dot, the neutral stability curves for n_c = -6, 0 and

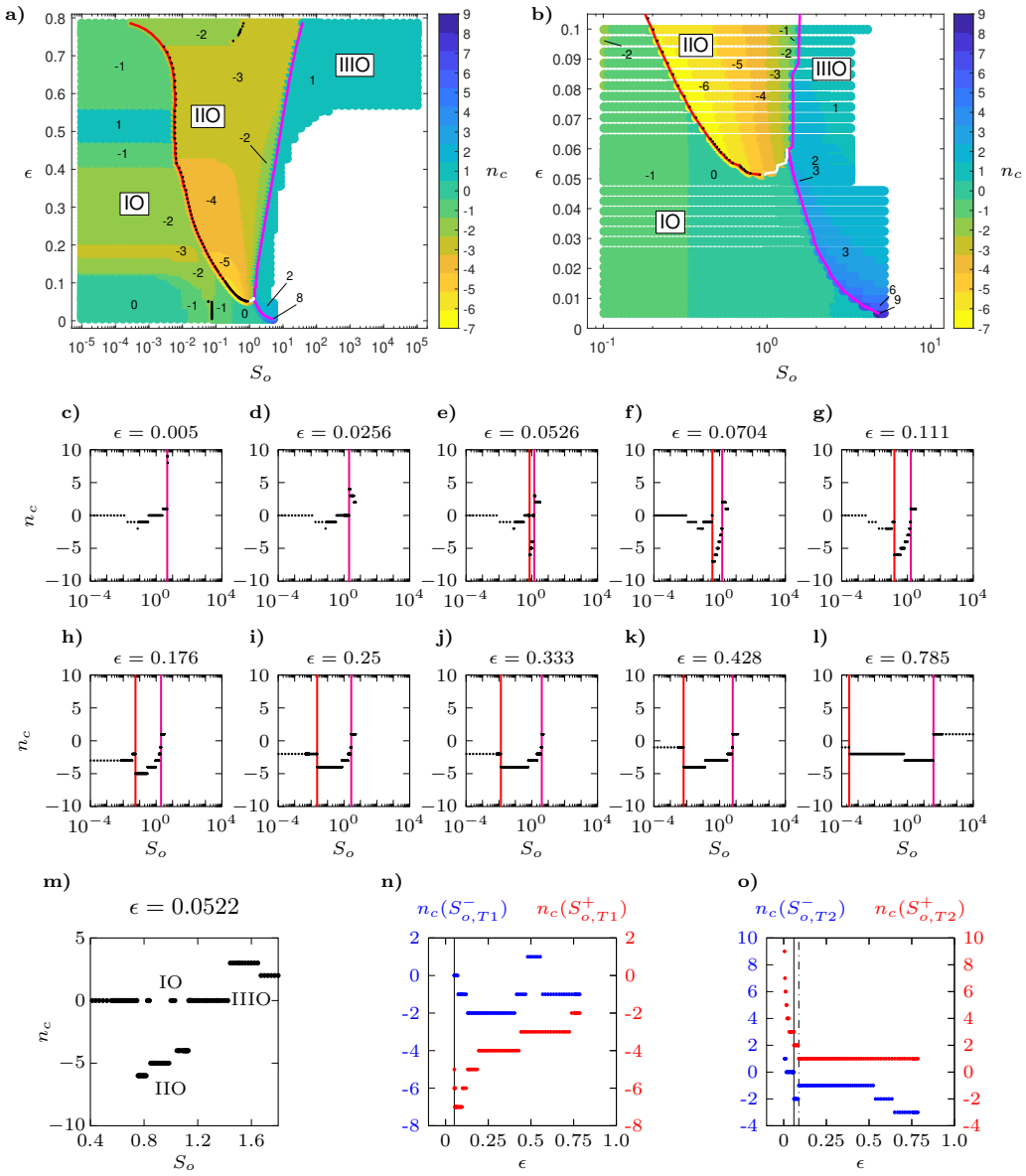

Figure 3.14: n_c as function of ϵ and S_o for the ORSPF. Red line: Transition from IO to IIO where $S_o = S_{o,T1}$, magenta line: transition IIO to IIIO where $S_o = S_{o,T2}$, black dots: minimum of n_c for fixed ϵ, white line: transition from IIO to IO. a) n_c as function of ϵ and S_o for $0.005 \leq \epsilon \leq 0.78$ b) n_c as function of ϵ and S_o for $0.005 \leq \epsilon \leq 0.1$ c-l) n_c over S_o for selected values of ϵ. m) n_c over S_o for $n = 0.0522$ n) $n_c(S_{o,T1})^-$ vs $n_c(S_{o,T1})^+$, solid line: $\epsilon = 0.05094$ o) $n_c(S_{o,T2})^-$ vs $n_c(S_{o,T2})^+$, solid line: $\epsilon = 0.05974$, dash dot line: $\epsilon = 0.08859$

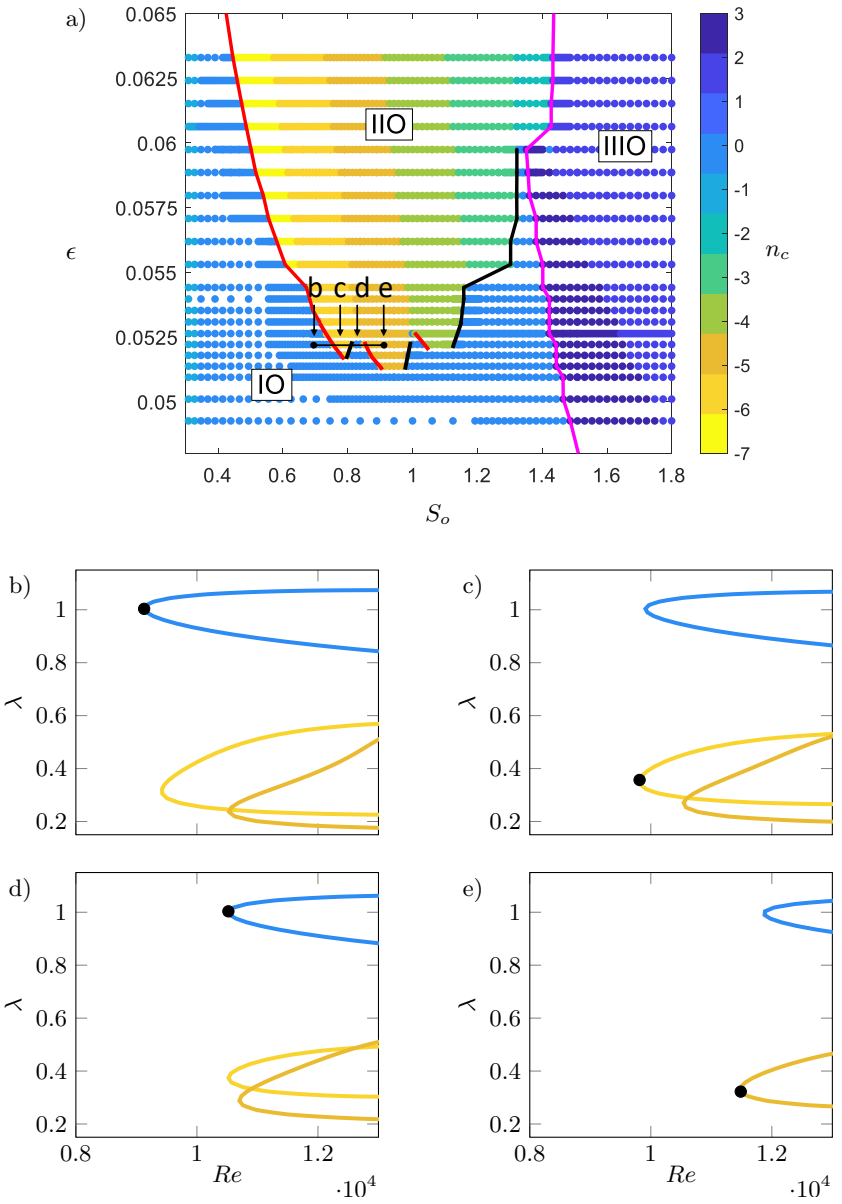

Figure 3.15: Details on the transition from IO to IIO. Colorbar holds for all subfigures (a-e). a) n_c for $0.048 < \epsilon < 0.065$ and $0.4 \leq S_o \leq 1.8$. Red line: transition from IO to IIO, black line: transition from IIO to IO, magenta line: transition from IIO to IIIO. Labels b-e in a correspond to subfigures b-e. b-e) Neutral curves for $\epsilon = 0.0522$ showing the switching between IO and IIO that can be observed for $0.05125 < \epsilon < 0.060$: b) $S_o = 0.71$ c) $S_o = 0.7793$ d) $S_o = 0.8264$ e) $S_o = 0.9158$

-5 sequentially become critical as S_o increases (Fig. 3.15b-d). As we will show later, this means increasing swirl in the ORSPF can damp a centrifugal instability and force the flow back into a TSI instability.

n_c in region IIIO ($S_o \geq S^+_{o,T2}$): As the flow transits to IIIO n_c jumps to a higher positive value for all ϵ considered as can be seen from Fig. 3.14a,b. Detailed information about n_c before and behind the jump is given in Fig. 3.14o where we plot $n_c(S^-_{o,T2})$ and $n_c(S^+_{o,T2})$ as function of ϵ. Here it can be seen, that for $\epsilon \geq 0.088$ $n_c(S^-_{o,T2})$ assumes negative values, while $n_c(S^+_{o,T2})$ is constant at 1. For $0.059 < \epsilon < 0.088$ instead n_c jumps from $n_c = -2$ before the jump to $n_c = 2$ behind the jump. For $\epsilon < 0.059$ where there is a transition from IO to IIIO n_c jumps from $n_c(S^-_{o,T2}) = 0, 1$ to $n_c(S^+_{o,T2}) = \{3, ..., 9\}$ with $n_c(S^+_{o,T2})$ increasing as ϵ decreases (Fig. 3.14o).

As S_o increases further within IIIO different behavior can be observed depending on ϵ. Within IIIO, n_c remains constant at 1 for $\epsilon \geq 0.0885$. For $0.056 < \epsilon \leq 0.088$ n_c drops from $n_c = 2$ to $n_c = 1$ as S_o increases within IIIO. For $\epsilon < 0.056$ our results show that n_c decreases in steps of 1 througout region IIIO (see Fig. 3.14b), however as we restrict our computations to $Re_c < 1.5 \cdot 10^5$ we do not cover sufficiently high S_o values to see if n_c drops back to $n_c = 1$ for S_o further increasing in IIIO.

3.1.2.5 Intermediate conclusions for phase maps of the ORSPF

Previously, to the authors best knowledge, the ORSPF ($\mu \to \infty$) has solely been investigated for $\epsilon = 0.333$ for low and intermediate swirls (Meseguer and Marques 2005). Here, results for the ORSPF are presented for 107 values in the range of $0.005 \leq \epsilon \leq 0.785$ extending the available data more than hundredfold. Thereby, for all ϵ for the first time higher swirls were investigated. The presented phase maps revealed that three regions (IO, IIO, IIIO) associated with different instability mechanisms exist for the ORSPF. The S_o value associated with these regions changes up to four orders of magnitude depending on ϵ. In region IO Re_c does not change significantly for $\epsilon > 0.0704$. Instead, in region IIO drops sharply with increasing swirl and attains a minimum value, which decreases monotonously with increasing ϵ. It was revealed, that in contrast to the IRSPF, the ORSPF gets stabilized sharply towards the end of region IIO, as the swirl increases further. Discontinuities in Re_c were discovered for $0.00885 < \epsilon < 0.41$ at the transition from IIO to IIIO, associated with a formation and decay of islands of instability. At the end of region IIIO, we find that a finite critical Reynolds number exists for large swirls ($S_o = 10^5$, $\epsilon \geq 0.569$), which coincides with the findings of Deguchi (2017) for $S_o \to \infty$. Curvature parameters of $\epsilon < 0.0513$ are a special case and region IIO does not exist such that increasing swirl is strongly stabilizing. To the authors best knowledge, such a monotonous stabilization with increasing swirl has not been reported for any configuration of the SPF before. For $\epsilon < 0.0513$ region IO, associated with a TSI, persists up to significantly larger swirl parameters compared to the IRSPF (up to one order of magnitude). Further, it was discovered for $0.0513 \leq \epsilon \leq 0.0526$, that the flow switches several times between IO and IIO as the swirl increases. Hence, for

certain ϵ increasing swirl inhibits centrifugal instabilities and can force the flow back to a TSI. Interesting details were discovered for λ_c, ω_c and n_c. Similar to the IRSPF the amplitude n_c jumps to higher absolut values at the transition to IIO, with the amplitude increasing as ϵ decreases. However, the amplitude remains smaller than in the IRSPF (i.e. for $\epsilon = 0.074$, $n_c = -7$ for ORSPF, $n_c = 43$ for IRSPF). Similar to the IRSPF, at $S^+_{i,T1}$, ω_c, λ_c and n_c are in balance such that for all ϵ the wave front attains a speed ($c_s = \omega_c/\sqrt{\lambda_c^2 + n_c^2}$) in the order of $O(10^{-3})$. Similar to the first transition, at the transition to IIIO n_c increases monotonously with decreasing ϵ and attains maximum values of $n_c = 9$ for $\epsilon = 0.005$. In region IIIO n_c is constant at 1 for all $\epsilon \geq 0.569$ up to $S_o = 10^5$.

3.2 Identification of the involved instability mechanisms in the different regions

In this section we use the production terms of the Reynolds Shear Stress Transport Equations (RSSTE, see section A.1.3) for the identification and characterization of the instability mechanisms involved in the Spiral Poiseuille Flow with Rotating Inner cylinder (IRSPF) as well as the Spiral Poiseuille Flow with Rotating Outer cylinder (ORSPF).

3.2.1 Analysis of the benchmark flows

Before investigating and identifying the different instability mechanisms of the IRSPF and the ORSPF, we apply our identification strategy on the two benchmark cases, viz the Annular Poiseuille flow (APF) and the Taylor-Couette flow (TCF). While the former flow is associated with a Tollmien-Schlichting type shear instability (TSI) the latter is associated with a centrifugal instability (CI). For these two cases, we determined Re_c, λ_c, ω_c and n_c for $S_i = 10^{-5}$ (APF) and $S_i = 10^5$ (TCF) and computed the distribution of K, the shear stresses and associated production terms as presented in Sect. 2.2.5. In Fig. 3.16a we show the distribution of K (normalized) as a function of the annular gap height y for $S_i = 10^{-5}$ and $\epsilon = 0.005$. The coordinate $y = -1$ represents the inner cylinder wall while $y = 1$ represents the outer cylinder wall. The theoretical position of the critical layer, whose concept was described in section 2.2.5 and 1.2.1.2, is determined by equation (2.33) and indicated by the dash dot vertical lines. As can be seen, K assumes peak values close to the critical layer, while for the major part of the channel significantly lower values of K become evident (see Fig. 3.16a). The reason for this distribution is revealed in Fig. 3.16b, which shows the distribution of the production terms $\overline{P_K(V_\varphi)} = \tau_{r\varphi} dV_\varphi/dy$, $\overline{P_K(V_x)} = \tau_{rx} dV_x/dy$ and $\overline{Z_K} = -V_\varphi \tau_{r\varphi}(1/r)$ as a function of the gap height. These are normalized by the maximum of the production term that has the highest amplitude. In Fig. 3.16b it can be seen, the production of K due to $\overline{P_K(V_x)}$ is restricted to a region close to the theoretical position of the critical layer. This is in agreement with the concept of the critical layer as the location where the most energy is transferred between disturbance and base flow (Maslowe 1986) and explains while the highest values of K are found at the critical layer. As K contains the squared disturbance velocities it is always positive. A negative sign of $\overline{P_K(V_x)}$ is associated with a production (gain) of kinetic disturbance energy. A positive sign of $\overline{P_K(V_x)}$ means that energy is transferred back to the base flow (loss), such that the base flow is stabilized (Mott and Joseph 1968a; Sadeghi and Higgins 1991a; Nouar and Frigaard 2009). As already explained in Sect. 2.2.5, $\overline{P_K(V_x)}$ depends on the distribution of τ_{xr}. Consequently, the distribution of $\overline{P_K(V_x)}$ is similar to the distribution of τ_{xr}, which is depicted in Fig. 3.16c. A peak of production terms close to the maximum of shear stresses has also been described by Mott and Joseph (1968a); Sadeghi and Higgins (1991a) for APF and by Nouar and Frigaard (2009) for Couette Poiseuille flow.

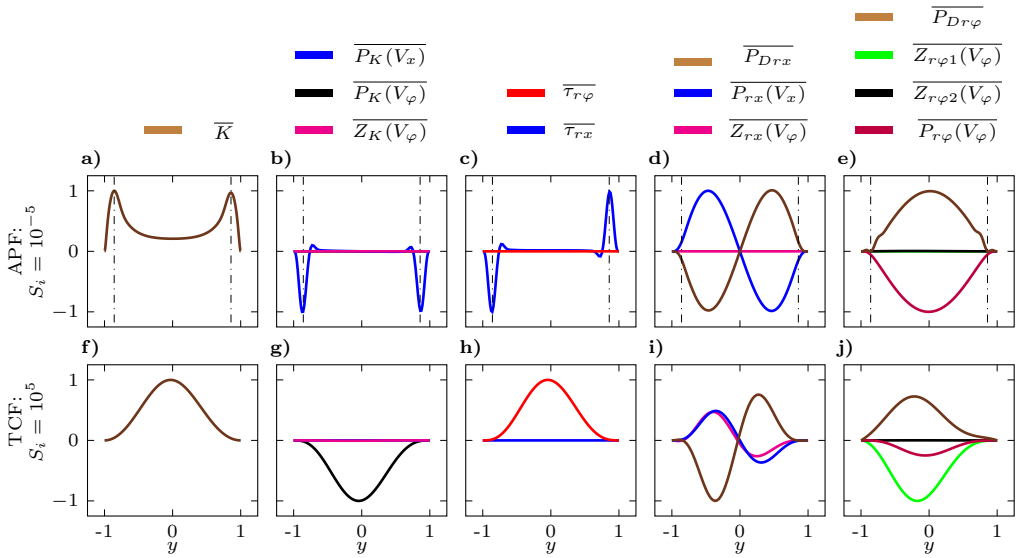

Figure 3.16: Normalized radial distributions of kinetic energy, production terms and shear stresses for $\epsilon = 0.005$ in the Annular Poiseuille flow (a-e, APF, $S_i = 10^{-5}$, $Re_c = 5773.45$, $\lambda = 1.0205$, $n_c = 0$, $\omega_c = 0$) and the Taylor Couette Flow (f-j, TCF, $S_i = 10^5$, $Re_c = 206.02$, $\lambda = 1.563$, $n_c = 0$, $\omega_c = 1.21 \cdot 10^{-5}$).) Dash dot lines = critical layer. a, f) K as function of y. b, g) K production terms as function of y. c, h) τ_{rx} and $\tau_{r\varphi}$ as function of y. d, i) τ_{rx} production terms as function of y. e, j) $\tau_{r\varphi}$ production terms as function of y.

As can be seen, τ_{xr} is zero except close to the locations of the critical layer and attains opposite signs at both sides of the channel. It should be noted, that even though τ_{rx} assumes both positive and negative values, $P_K(V_x) = \tau_{rx} dV_x/dy$ is always negative for this flow configuration as dV_x/dy switches its sign in the channel center.

Figure 3.16d shows the distribution of the production of τ_{rx}. The graph reveals that, the production of τ_{rx} is solely due to the axial shear production $\overline{P_{rx}(V_x)}$, which spans over the whole gap and undergoes a sign change close to the middle of the gap. Unlike the shear stresses, the amplitude of $\overline{P_{rx}(V_x)}$ assumes large values distant from the critical layer and assumes a maximum and a minimum in the left and right half of the channel, respectively. Hence, there is a significant discrepancy between the distribution of τ_{rx} and $\overline{P_{rx}(V_x)}$. The shape of τ_{rx} can be explained by the velocity pressure gradient $\overline{P_{Drx}}$ (see appendix A.1.3), which is almost reversed to $\overline{P_{rx}(V_x)}$, but not excatly identical. Therefore, τ_{rx} is cancelled for the most part of the gap, except close to the critical layer which results in the distribution of τ_{rx} as depicted in Fig. 3.16c. We computed the sum of $\overline{P_{rx}(V_x)}$ and $\overline{P_{Drx}}$ for the APF for different values of ϵ (see appendix A.1.7), which in fact revealed peaks close to the critical layer. Distant from the critical layer slight deviations, were observed for smaller ϵ which are related to numerical errors in approximating the derivatives (see appendix A.1.7). The viscous terms of the budget of

τ_{rx} (not shown here) are very small here compared to $\overline{P_{rx}(V_x)}$ and $\overline{P_{Drx}}$. The centrifugal production $\overline{Z_{rx}(V_\varphi)}$ is zero over the whole gap. Finally, Fig. 3.16e shows the production of $\tau_{r\varphi}$. As can be seen $\overline{P_{r\varphi}(V_\varphi)}$ spreads over the whole gap and assumes a minimum at the channel center. As before, $\overline{P_D}$ is approximately reversed to $\overline{P_{r\varphi}(V_\varphi)}$. $\overline{Z_{r\varphi,1}(V_\varphi)}$ and $\overline{Z_{r\varphi,1}(V_\varphi)}$ are zero. The dissipation and viscous dissipation of $\tau_{r\varphi}$ also exhibit a small amplitude here (not shown). It should be noted, that the overall production of $\tau_{r\varphi}$ here arises from the small amount of rotation 10^{-5} and is negligible. It is solely visible from Fig. 3.16 due to normalization to one. The presented distributions clearly identify the instability of the APF as a shear instability as the production of the Reynolds stress τ_{rx}, as well as the production of K is due to shear production terms. Furthermore equation (2.33) yields a location of the critical layer, which matches with the maxima of K and the maxima of τ_{rx}. Hence, we consider the instability present here, as a Tollmien-Schlichting type shear instability (TSI). Hereafter, the term Tollmien-Schlichting type instability and shear instability will be used synonymously.

Now we analogously characterize the centrifugal instability of the TCF ($\mu = 0$, $S_i \to \infty$). For this, the second row of Fig. 3.16f-j displays the distribution of K, the production of K, the Reynolds stresses τ_{rx}, $\tau_{r\varphi}$ and the associated production terms for $S_i = 10^5$. For $S_i = 10^5$ the Reynolds number is $Re_c = 206$ while for $Si = 10^{-5}$ $Re_c = 5773.45$. Hence, the assumption of large values of Re_c, on which the equation (2.33) is based, is not valid. Therefore, the concept of the critical layer, and equation (2.33) will not be applied here. As can be seen from Fig. 3.16f in contrast to the APF the distribution of K is not restricted to a critical layer and spreads over the whole gap width assuming a maximum close to the channel center. The distribution of $\overline{P_K(V_x)}$, $\overline{P_K(V_\varphi)}$ and $\overline{Z_K}$ is displayed in Fig. 3.16g. As can be seen, solely $\overline{P_K(V_\varphi)}$ contributes to the production of K, while the centrifugal production of K is zero ($\overline{Z_K}$). Hence, while the instability present in a Taylor-Couette flow for $\mu = 0 < \eta^2$ is a centrifugal instability, all the production of K stems from azimuthal shear. In fact, for increasing values of ϵ $\overline{Z_K}$ increases, but remains always smaller than $\overline{P_K(V_\varphi)}$ (not shown here). This finding is comparable to that of Moser and Moin (1987) who investitgated curved turbulent channel flow by means of DNS. They concluced that the transport equation for the (turbulent) kinetic energy is insensitive to curvature effects. Similarily, Guaus and Bottaro (2007), who performed a linear stability analysis on curved channel flow noted that the magnitude of the centrifugal K production term is small. Because for $S_i = 10^5$ the axial velocity profile V_x is approximately zero also $\overline{P_K(V_x)}$ is approximately zero. As discussed in Sect. 2.2.5 $\overline{P_K(V_\varphi)}$ is proportional to the distribution of $\tau_{r\varphi}$ as can be seen from Fig. 3.16h. Fig. 3.16j, in which we present the production of $\tau_{r\varphi}$ as function of y, reveals that the production of $\tau_{r\varphi}$ is mostly due to the centrifugal term $\overline{Z_{r\varphi,1}}$ which spans over the whole channel and assumes a minimum close to the channel center. $\overline{P_{r\varphi}(V_\varphi)}$ attains a similar shape but exhibits a significantly smaller amplitude. It should be mentioned that negative shear stress production terms result in positive shear stresses and vice versa as can be seen from the RSSTE in section A.1.3.

The velocity pressure gradient is reversed to $\overline{Z_{r\varphi,1}}$ and $\overline{P_{r\varphi}(V_\varphi)}$. The viscous terms (not shown) attain a similar shape as $\overline{P_D}$ such that the sum of $\overline{P_D}$ and viscous terms is equal to the sum of $\overline{Z_{r\varphi,1}}$ and $\overline{P_{r\varphi}(V_\varphi)}$ (see Fig. in A.14 in the appendix). By comparing Fig. 3.16h and j it can be seen, that the distribution of $\tau_{r\varphi}$ is similar to the magnitude of the production terms $\overline{Z_{r\varphi,1}}$ and $\overline{P_{r\varphi}(V_\varphi)}$.

Overall, the distributions presented in Fig. 3.16g show that in the case of the TCF the production of K is mostly due to azimuthal shear ($\overline{P_K(V_\varphi)}$). Hence, from the budget of K it is not possible to identify the instability present in the TCF as a centrifugal instability. For identification of the instability a closer look on the budget of $\tau_{r\varphi}$ which contributes to $\overline{P_K(V_\varphi)} = \tau_{r\varphi} dV\varphi/dy$ is required. As mentioned $\tau_{r\varphi}$ stems from the centrifugal production term $\overline{Z_{r\varphi 1}}$ in the TCF. Only a neglibigle amount arises from azimuthal shear $P_{r\varphi}$. Hence, the production of K indirectly depends on $\overline{Z_{r\varphi 1}}$. We conclude, that a centrifugal instability cannot be identified by the production terms of the KTE (equations 2.20-2.22) but by the centrifugal production terms of the RSSTE (equations 2.27-2.31). This finding can be put in analogy to the aforementioned work of Moser and Moin (1987). They stated that curvature dependent terms have little effect in the budget of turbulent kinetic energy but are important and not negligible in the shear stress transport equations in the context of turbulence modelling.

In the following, a TSI will be identified based on the following criteria. First, the shear stresses must reveal the position of a critical layer in accordance with equation (2.33). Second, the production of the shear stress, which contributes to the dominant K production term, stems from shear production. A centrifugal instability will be identified based on the shear stress, which contributes to the dominant production term stemming from centrifugal production. While the K production terms seem to be not suitable for identifying instabilities, it will be shown that they show striking similarities at the first transition but also differences at higher swirls for the IRSPF and the ORSPF.

3.2.2 Analysis of the first transition for the IRSPF

Here, we characterize the instability as the flow transits from I to II for the IRSPF analogous to Sect. 3.2.1. The situation before and behind the transition is referred to as $S^-_{i,T1}$ and $S^+_{i,T1}$, respectively, as described in section 3.1.1 and indicated in Fig. 3.2. The associated critical values of Re_c, λ_c, n_c and ω_c can be found in the appendix A.1.8. As Re_c attains values of $O(10^3)...O(10^3)$ before and directly behind the transition the condition for equation (2.33) is assumed to be valid. As will be shown, before the transition a Tollmien-Schlichting instability is dominant while behind the transition a centrifugal instability is dominant.

3.2.2.1 Region I: Distributions at $S^-_{i,T1}$

From Fig. 3.17a-d which shows the distribution of K before the transition from I to II ($S^-_{i,T1}$) it can be seen that K attains sharp peaks at the position of the critical layer (dash dots lines). In fact, for $S^-_{i,T1}$ the distribution of K for $\epsilon = 0.005$ is essentially identical with that of the APF presented in Fig. 3.16a. For increasing ϵ it can be seen that the peak close to the outer cylinder shrinks and the area where K is nonzero reduces. This is associated to the skewing of the axial velocity profile, that comes apparent at larger values of ϵ (see Fig. A.1 in section A.1.4).

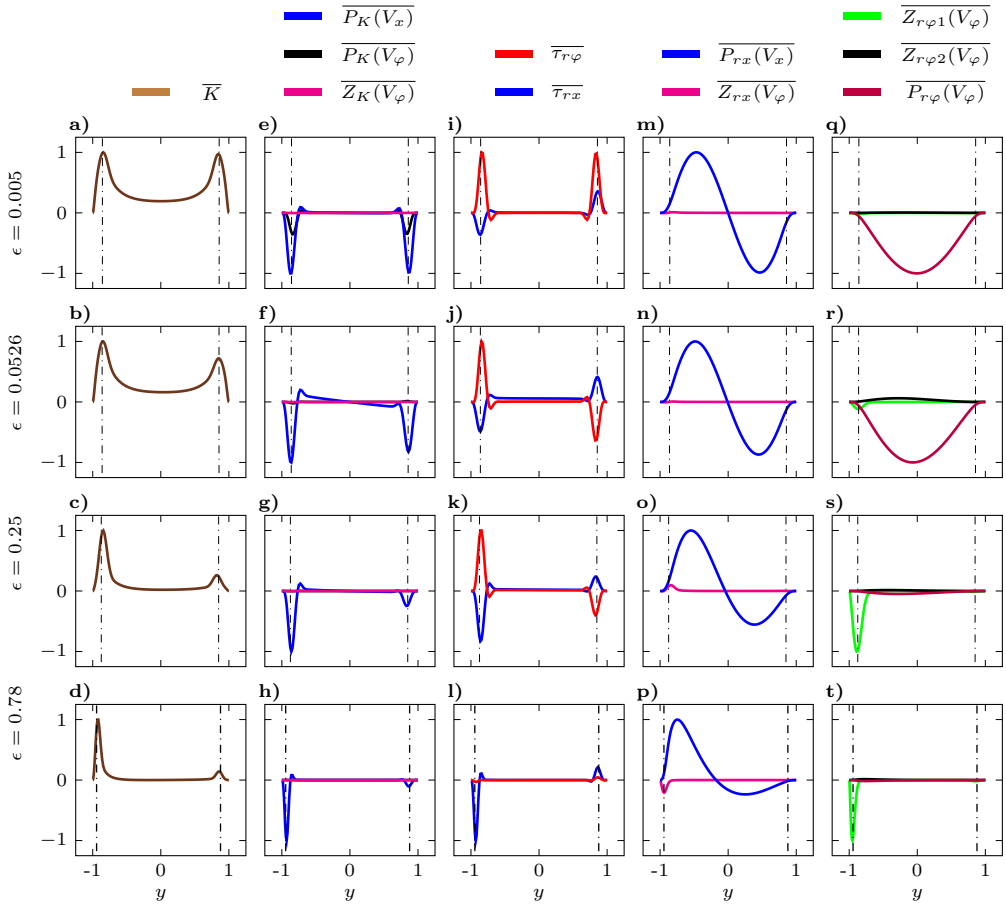

Figure 3.17: Normalized radial distributions of kinetic energy, production terms and shear stresses found in the IRPSF before the first transition (end of I) at $S^-_{i,T1}$ for $\epsilon = \{0.005; 0.0526; 0.25; 0.78\}$. Dash dot line = position of critical layer according to equation (2.33) at $S^-_{i,T1}$. a-d) K over y. e-h) Production of K over y. i-l) τ_{rx}, $\tau_{r\varphi}$ over y. m-p) Production of τ_{rx} over y. q-t) Production of $\tau_{r\varphi}$ over y.

For $\epsilon = 0.005$ the distribution of $\overline{P_K(V_x)}$ for $S^-_{i,T1}$ (blue line in Fig. 3.17e) is essentially identical with that of the APF flow (Fig. 3.16b). For increasing values of ϵ, as the velocity profile gets increasingly skewed, the right peak of $\overline{P_K(V_x)}$ shrinks, similar to the distribution of K (Fig. 3.17f-h). An asymmetric distribution of production terms for skewed velocity profiles was also reported by Mott and Joseph (1968a) for the APF. For $\epsilon = 0.005$ $\overline{P_K(V_\varphi)}$ is nonzero and attains a similar distribution as $\overline{P_K(V_x)}$ with a smaller amplitude (Fig. 3.17e). For ϵ smaller than $\epsilon = 0.005$ the magnitude of $\overline{P_K(V_\varphi)}$ becomes even larger than that of $\overline{P_K(V_x)}$ (see Fig. A.6 in the appendix). The underlying reason is that $S_{i,T1}$ increases sharply as ϵ decreases as shown in section 3.1.1. For $\epsilon \geq 0.0526$ $S_{i,T1}$ is less than 0.037 while for $\epsilon = 0.005$ $S_{i,T1}$ is 0.439 and for $\epsilon = 0.0025$ $S_{i,T1}$ is 0.99 so that V_φ is about the same value as V_x. Hence at $S^-_{i,T1}$ the azimuthal velocity component is significantly larger for small ϵ, which consequently affects the azimuthal shear production $\overline{P_K(V_\varphi)}$. This is a remarkable difference to the classical Tollmien-Schlichting instability in a flow with parallel streamlines where the production of P_K can only emerge from $\overline{P_K(V_x)}$. For larger values of ϵ instead, $S_{i,T1}$ is small and $\overline{P_K(V_\varphi)}$ remains zero (Fig. 3.17f-h). From comparing Fig. 3.17i and Fig. 3.16c, it can be seen that for $\epsilon = 0.005$ the shear stress τ_{rx} for $S^-_{i,T1}$ (blue line) exhibits a similar shape as for the APF. However, while $\tau_{r\varphi}$ is zero for the APF (Fig. 3.16c) its amplitude is even larger than that of τ_{rx} for the IRSPF with $\epsilon = 0.005$ at $S^-_{i,T1}$ (Fig. 3.17i). This is induced by the significant amount of rotation that is present for $\epsilon = 0.005$ at $S^-_{i,T1} = 0.439$. As can be seen from Fig. 3.17j-l $\tau_{r\varphi}$ is nonzero as well for ϵ =0.0526, 0.25, 0.78 at $S^-_{i,T1}$. However, for these values of ϵ this is related to azimuthal wavenumbers of $n_c \neq 0$ being dominant, while for $\epsilon = 0.005$ $n_c = 0$ (see table A.1). As further can be seen, as ϵ increases the right peak of τ_{rx} and $\tau_{r\varphi}$ decrease, as already stated for K.

For all considered ϵ the distribution of $\overline{P_{rx}(V_x)}$ exhibits the same characteristics as the APF (Fig. 3.16d) but gets skewed towards the inner cylinder as ϵ increases (Fig. 3.17m-p). The contribution of $\overline{Z_{rx}(V_\varphi)}$ is negligible for all considered ϵ (see Fig. 3.17o,p).

Fig. 3.17q-t reveals that the budget of $\tau_{r\varphi}$ strongly depends on ϵ. For small ϵ $\overline{P_{r\varphi}(V_\varphi)}$ is dominant and spreads over the whole gap with a peak close to the channel center (Fig. 3.17q,r). As ϵ increases, its magnitude decreases significantly (Fig. 3.17s,t). Contrary, with increasing ϵ the magnitude of $\overline{Z_{r\varphi,1}(V_\varphi)}$ increases and a sharp peak developes close to the inner cylinder (Fig. 3.17q-t). The contribution of $\overline{Z_{r\varphi,2}(V_\varphi)}$ is insignificant.

Overall, the distributions presented in Fig. 3.17 for $S_i < S^-_{i,T1}$ feature similar characteristics as those presented in Fig. 3.16a-e. The production of the Reynolds stress (τ_{rx}) which is contained in the dominant K production term ($\overline{P_K(V_x)}$) is due to the shear production term $\overline{P_{rx}(V_x)}$. For $\epsilon = 0.0025$ the dominant K production term is $\overline{P_K(V_\varphi)}$ and the associated Reynolds stress $\tau_{r\varphi}$ stems from azimuthal shear production $\overline{P_{r\varphi}(V_\varphi)}$ (see Fig. A.6 in the appendix). Furthermore, a critical layer becomes evident from both the distribution of the shear stresses as well as equation (2.33) as predicted by Cottrel and Pearlstein (2004). Hence, based on the criterias defined in section 3.2.1,

it is concluded that in region I ($S_i < S^-_{i,T1}$) a TSI is dominant in the IRSPF. This is in agreement with the presumption of Cottrel and Pearlstein (2004). Furthermore, for all $\epsilon \geq 0.0526$ in Fig. 3.17 $n_c \neq 0$ (see table A.1). To the authors best knowledge, the existence of a critical layer for non-axisymmetric disturbances in accordance with equation (2.33) was proven for the first time for a SPF. Moreover, it was revealed that a TSI can exist in scenarios where axial and azimuthal flow component attain comparable magnitudes, such that K production stems also from azimuthal shear production.

3.2.2.2 Region II: Distributions at $S^+_{i,T1}$

In fact, equation (2.33) yields two roots for each ϵ at $S^+_{i,T1}$ and even three for $\epsilon > 0.735$. However, as will be shown with Fig. 3.18 here, the shear stresses and the production terms, drastically get redistributed behind the wave number jump during the transition I to II. Hence, no TSI is present here, and we consider the roots of equation (2.33) as meaningless in this context.

As obvious from Fig. 3.18a-d, for $S^+_{i,T1}$, K spreads widely over the inner half of the channel, rather than being restricted to a critical layer. This distribution of K results from the altered distribution of $\overline{P_K(V_x)}$, which now spreads over the inner gap half as well (see Fig. 3.18e-h). As can be seen for $S^+_{i,T1}$ the production of K is exclusively due to axial shear ($\overline{P_K(V_x)}$) whereas $\overline{Z_K}$ is approximately zero. By comparing the blue lines in Fig. 3.18e-h and the blue lines in Fig. 3.18i-l it can be seen, that for $S^+_{i,T1}$ the distribution of the dominant K production term $\overline{P_K(V_x)}$ is almost directly proportional to the distribution of τ_{rx}.

The distributions of $\overline{Z_{rx}}$ and $\overline{P_{rx}(V_X)}$, as depicted in Fig. 3.18m-p reveal, that for $S^+_{i,T1}$ a centrifugal instability is dominant in the IRSPF. As can be seen clearly from Fig. 3.18m-p the production of τ_{rx} is mostly due to the centrifugal production $\overline{Z_{rx}}$ and spreads over the inner half of the gap, thereby assuming a similar shape as τ_{rx} and $\overline{P_K(V_x)}$ (but with a positive sign) for all ϵ considered.

Figure 3.18q-t shows that $\overline{P_{r\varphi}(V_\varphi)}$, $\overline{Z_{r\varphi,2}(V_\varphi)}$ as well as $\overline{Z_{r\varphi,1}(V_\varphi)}$ spread over the left side of the channel and form a peak close to the inner cylinder. Thereby the magnitude $\overline{Z_{r\varphi,1}(V_\varphi)}$ is significantly larger than that of the other components, which also shows that $\tau_{r\varphi}$ emerges from centrifugal production.

Overall, because the shear stress τ_{rx} which contributes to the dominant K production term ($\overline{P_K(V_x)}$) emerges from centrifugal production $Z_{rx}(V_\varphi)$, we conclude that a centrifugal instability is present at $S^+_{i,T1}$. This is in agreement with the findings of Cottrel and Pearlstein (2004) and Cottrel et al. (2004) for $\epsilon = 0.0265; 0.1299$ and 0.3333, who concluded there is a onset of a centrifugal instability at $S^+_{i,T1}$. The fact that the K production stems from axial shear production ($\overline{P_K(V_x)}$) is a remarkable difference to the centrifugal instability of the TC flow where the production of K emerges from the azimuthal shear ($\overline{P_K(V_\varphi)}$). This reveals an interesting feature about the interplay of

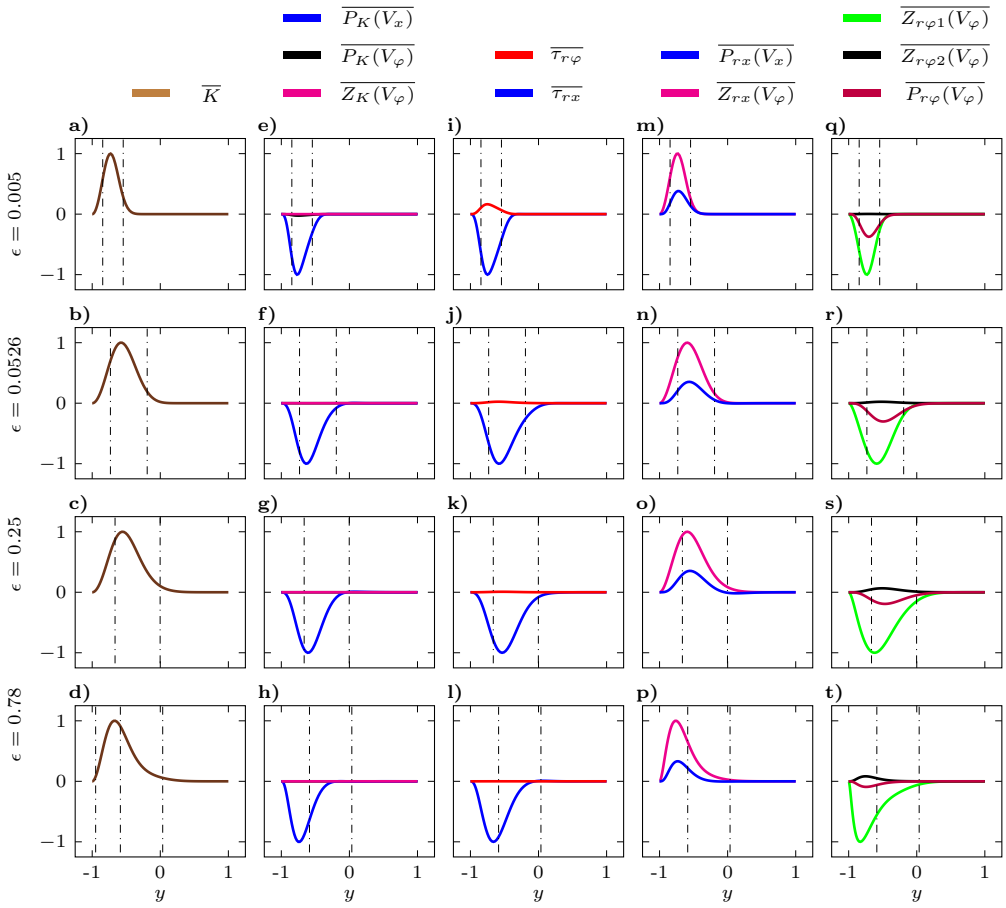

Figure 3.18: Normalized radial distributions of kinetic energy, production terms and shear stresses found in the IRPSF behind the first transition (beginning of II) at $S^+_{i,T1}$ for $\epsilon = \{0.005; 0.0526; 0.25; 0.78\}$. Dash dot line = position of critical layer according to equation (2.33) at $S^+_{i,T1}$. a-d) K over y. e-h) Production of K over y. i-l) τ_{rx}, $\tau_{r\varphi}$ over y. m-p) Production of τ_{rx} over y. q-t) Production of $\tau_{r\varphi}$ over y.

axial and azimuthal flow at low swirls. While the azimuthal flow plays a dominant role in the budget of the shear stresses, the axial flow plays a dominant role here in the K budget. As will be shown in section 3.2.3.3 as the swirl increases within region II, the azimuthal production of K increases as well and finally becomes dominant at higher swirls.

3.2.3 Analysis of the first transition for the ORSPF

Analogous to the IRSPF, it will be shown here that before the transition from IO to IIO a Tollmien-Schlichting instability is dominant while behind the transition a centrifugal instability is dominant. By this, the authors best knowledge, for the first time a direct connection between the effect of rotating inner and rotating outer cylinder is revealed. The situation before and behind the transition is referred to as $S^-_{o,T1}$ and $S^+_{o,T1}$, as described in section 3.1.2 and indicated in Fig. 3.8. The associated critical values of Re_c, λ_c, n_c and ω_c can be found in the appendix A.1.8.

3.2.3.1 Region IO: Distributions at $S^-_{o,T1}$

Analogous to Fig. 3.17, in Fig. 3.19 we show the distributions of K and the production of K, the distribution of τ_{rx} as well as the production of τ_{rx} before the transition from IO to IIO for the ORSPF. We point out here, as thoroughly discussed in Sect. 3.1.2, that for the ORSPF no transition to IIO takes place for $\epsilon < 0.0513$.

From Fig. 3.19a-c, where we show K as function of y, it can be seen that at $S^-_{o,T1}$ the distribution of K is almost identical with that of the IRSPF in Fig. 3.17a-d. This applies also for the production terms $\overline{P_K(V_x)}$, $\overline{P_K(V_\varphi)} = \tau_{r\varphi} dV_\varphi/dy$ and $\overline{Z_K(V_\varphi)}$ which are shown in Fig. 3.19d-f. However, the magnitude of $\overline{P_K(V_\varphi)}$ for $\epsilon = 0.0526$ is signifcantly higher for the ORSPF compared to the IRPSF (compare Fig. 3.17f and Fig. 3.19d). This is because the transition for $\epsilon = 0.0526$ in the ORSPF takes place at $S^-_{o,T1} = 0.7349$ while it takes place at $S^-_{i,T1} = 0.0419$ for the IRSPF. Hence, for the ORSPF the azimuthal velocity component is significantly larger at the transition than that for the IRSPF. The distributions of τ_{rx} and $\tau_{r\varphi}$, depicted in Fig. 3.19g-i, are essentially identical with that of the IRSPF (Fig. 3.17i-l) except for $\tau_{r\varphi}$ being vertically flipped for the ORSPF. This is a result of the negative wavenumbers which are dominant for the ORSPF. For $\epsilon = 0.785$ negative modes are dominant for both the ORSPF and the IRPSF, resulting in the same sign for $\tau_{r\varphi}$.

Next, also the distribution of $\overline{P_{rx}(V_x)}$ as well as the distribution $\overline{Z_{rx}(V_\varphi)}$ is similar to the IRSPF as can be seen from Fig. 3.19j-l. For smaller values of ϵ however $\overline{Z_{rx}(V_\varphi)}$ is nonzero here and exhibits a peak close to the outer cylinder, as can be seen exemplary for $\epsilon = 0.0526$. This is induced by the large amount of rotation which is present at $S_{o,T1}$ for smaller ϵ. As mentioned before for $\epsilon = 0.0526$ the transition takes place at $S^-_{o,T1} = 0.7349$.

Finally, looking at Fig. 3.19m-o differences can be identified for $\overline{Z_{r\varphi,1}(V_\varphi)}$ in the ORSPF compared to the IRSPF. For $\epsilon = 0.0526$ $\overline{Z_{r\varphi,1}(V_\varphi)}$ is nonzero and exhibits a sharp peak close to the outer cylinder, which is related to the high amount of rotation at $S^-_{o,T1} = 0.7349$. For intermediate values of ϵ two peaks become evident for $\overline{Z_{r\varphi,1}(V_\varphi)}$, while for the IRSPF there was only one. For $\epsilon = 0.785$ instead $\overline{Z_{r\varphi,1}(V_\varphi)}$ feature a remarkable similarity to the IRSPF except for being horizontally flipped (Fig. 3.19o

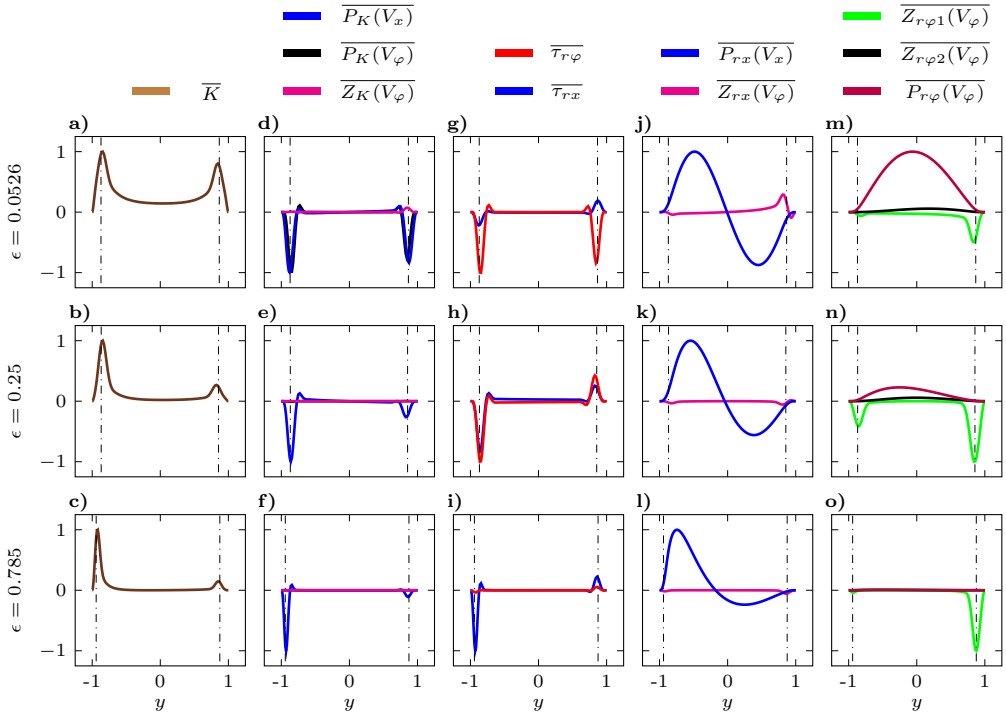

Figure 3.19: Normalized radial distributions of kinetic energy, production terms and shear stresses found in the ORPSF before the first transition (end of IO) at $S^-_{o,T1}$ for $\epsilon = \{0.0526; 0.25; 0.78\}$. Dash dot line=position of critical layer according to equation (2.33). a-c) K over y. d-f) Production of K over y. g-i) τ_{rx}, $\tau_{r\varphi}$ over y. j-l) Production of τ_{rx} over y. m-o) Production of $\tau_{r\varphi}$ over y.

and Fig. 3.17t). $\overline{P_{r\varphi}(V_\varphi)}$ shows essentially the same distribution except for having a positive sign while it is negative in the IRSPF (Fig. 3.19o). $\overline{Z_{r\varphi,2}(V_\varphi)}$ is approximately zero for all ϵ. For all ϵ $\overline{Z_{r\varphi,1}(V_\varphi)}$ counteracts $\overline{P_{r\varphi}(V_\varphi)}$.

Overall, the distributions of the shear stresses and the budgets associated with $S^-_{o,T1}$ in Fig. 3.19 (ORSPF) are almost identical with those of Fig. 3.17 at $S^-_{i,T1}$ (IRSPF) and the same conclusions apply here. As a critical layer becomes evident and the shear stress in the dominant K production terms emerges from shear production, it is concluded that analogous to the IRSPF a TSI is dominant for the ORSPF at $S^-_{o,T1}$. This is in agreement with Meseguer and Marques (2005) who concluded for $\epsilon = 0.333$, based on n_c and the behavior of Re_c, that here a TSI dominant. In addition, our results provide a detailed insight in the production of kinetic disturbance energy, the production of shear stresses and confirm the existence of a critical layer for the first time for both axisymmetric and non-axisymmetric disturbances. The main difference compared to the IRSPF is that negative azimuthal modes are triggered for the ORSPF and the transition takes place at significantly higher swirl parameters (for $\epsilon = 0.0526$ factor 14)

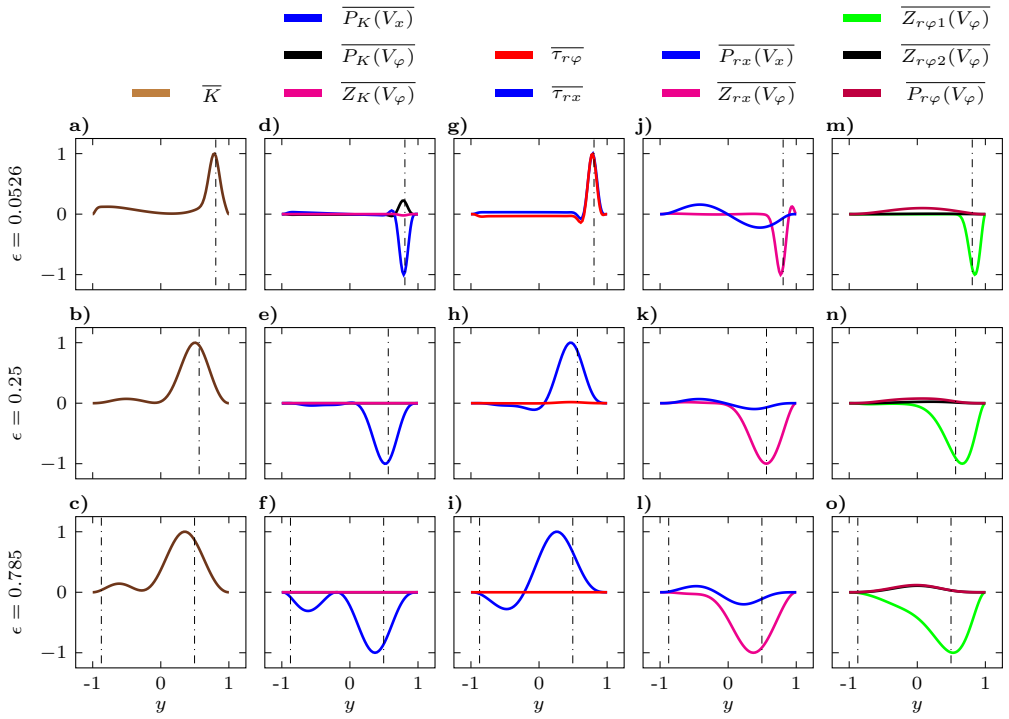

Figure 3.20: Normalized radial distributions of kinetic energy, production terms and shear stresses found in the ORPSF behind the first transition (beginning of IIO) at $S^+_{o,T1}$ for $\epsilon = \{0.0526; 0.25; 0.78\}$. Dash dot line = position of critical layer according to equation (2.33). a-c) K over y. d-f) Production of K over y. g-i) τ_{rx}, $\tau_{r\varphi}$ over y. j-l) Production of τ_{rx} over y. m-o) Production of $\tau_{r\varphi}$ over y.

which significantly affects $\overline{P_K(V_\varphi)}$ and $\overline{Z_{rx}(V_\varphi)}$ for smaller ϵ. This shows that in the ORSPF the TSI persists at significantly larger swirls where axial and azimuthal velocity profile attain similar magnitudes. As will be shown in section 3.2.5 for $\epsilon < 0.0513$ the TSI persists even at swirls of $S_o = 4.67$ for the ORSPF in region IO.

3.2.3.2 Region IIO: Distributions at $S^+_{o,T1}$

Analogous to Fig. 3.18, Fig. 3.20 depicts the distributions of the production terms and the shear stresses for $S^+_{o,T1}$ behind the transition IO to IIO. Similar to the IRSPF case, equation (2.33) yields one root for $0.0513 \geq \epsilon < 0.73$ and two roots for $0.73 \geq \epsilon < 0.785$, which are indicated with the dash dot lines here. However, as will be shown in the following the instability shows evidences of a centrifugal instability and hence we consider the results of equation (2.33) not as relevant here.

Obviously, for the ORSPF the distribution of K at $S^+_{o,T1}$ is similar to that of the IRSPF at $S^+_{i,T1}$ except for having its peak in the outer gap half (see Fig. 3.18a-d, Fig. 3.20a-c). Furthermore, for larger values of ϵ a second small peak becomes evident in the left half of the gap (Fig. 3.20c). The distribution of $\overline{P_K(V_x)}$ attains a similar shape as for the IRSPF except for being horizontally flipped (Fig. 3.20d-f).

Also the distribution of τ_{rx} assumes a similar shape with the peak being at the outer gap half. The only remarkable difference to the IRSPF is, that τ_{rx} exhibits a small second negative peak whose amplitude increases with increasing ϵ (Fig. 3.20g-i). The distribution of $\tau_{r\varphi}$ is similar to the IRSPF. $\tau_{r\varphi}$ is almost zero for most ϵ but increases with decreasing ϵ as can be seen for $\epsilon = 0.0526$ where the magnitude of $\tau_{r\varphi}$ is approximately equal to that of τ_{rx}.

From Fig. 3.20j-l it can be seen that $\overline{Z_{rx}(V_\varphi)}$ is dominant in the budget of τ_{rx} and features a strong similarity to the IRSPF case besides being at the outer gap half rather than at the inner gap half. Further, the sign is opposed to that of the IRSPF. This shows an analogy to direct numerical simulations of turbulent flows in curved channels where curvature dependent terms in the RSSTE attain opposed signs at concave and convex walls, which are here the outer and inner cylinder wall, respectively (Moser and Moin 1987). The distribution of $\overline{P_{rx}(V_x)}$ is slightly different for the ORSPF. Instead of being zero in one side of the gap $\overline{P_{rx}(V_x)}$ features a small minimum and maximum in the left and the right side of the channel, respectively (Fig. 3.20j-l). As can be seen from Fig. 3.20m-o for the ORSPF at $S^+_{o,T1}$ the production terms of $\tau_{r\varphi}$ also exhibits a remarkable similarity to the IRPSF. For larger values of ϵ $\overline{Z_{r\varphi,1}(V_\varphi)}$ occupies a wide area and exhibits a peak on the right side of the gap (Fig. 3.20n,o) while it is restricted to a sharp peak for smaller ϵ (Fig. 3.20m). Like in the IRSPF case $\overline{Z_{r\varphi,2}(V_\varphi)}$ and $\overline{P_{r\varphi}(V_\varphi)}$ are negligible at $S^+_{o,T1}$.

Overall, Figs. 3.20d-f and Figs. 3.20j-l reveal, that in the ORSPF for $S^+_{o,T1}$ the dominant K production term is $\overline{P_K(V_x)}$, while the production of the associated shear stress τ_{rx} is due to the centrifugal production term ($\overline{Z_{rx}(V_\varphi)}$). The latter identifies the instability as centrifugal instability according to our criteria defined in section 3.2.1. Hence, the same centrifugal instability mechanism is present at $S^+_{i,T1}$ and $S^+_{o,T1}$ for the IRSPF and the ORSPF, respectively. To our knowledge, this is the first time a direct connection between the centrifugal effect of rotating inner and outer cylinder has been made. The destabilizing effect of the outer cylinder, observed by Meseguer and Marques (2005) for $\epsilon = 0.333$ could be clearly identified as centrifugal instability mechanism.

The similarity of the instabilities present in the IRSPF and the ORSPF becomes also evident from the instantaneous shapes of the disturbances before and behind the first transition, which are presented in Fig. 3.21 for $\epsilon = 0.25$. In Fig. 3.21a,b we show the disturbance spirals for the IRSPF at $S^-_{i,T1}$ and $S^+_{i,T1}$, visualized by isosurfaces of u'_r. From comparing Fig. 3.21a and Fig. 3.21b it can be seen that the number of spirals increases and the inclination is significantly reduced across the first transition. From

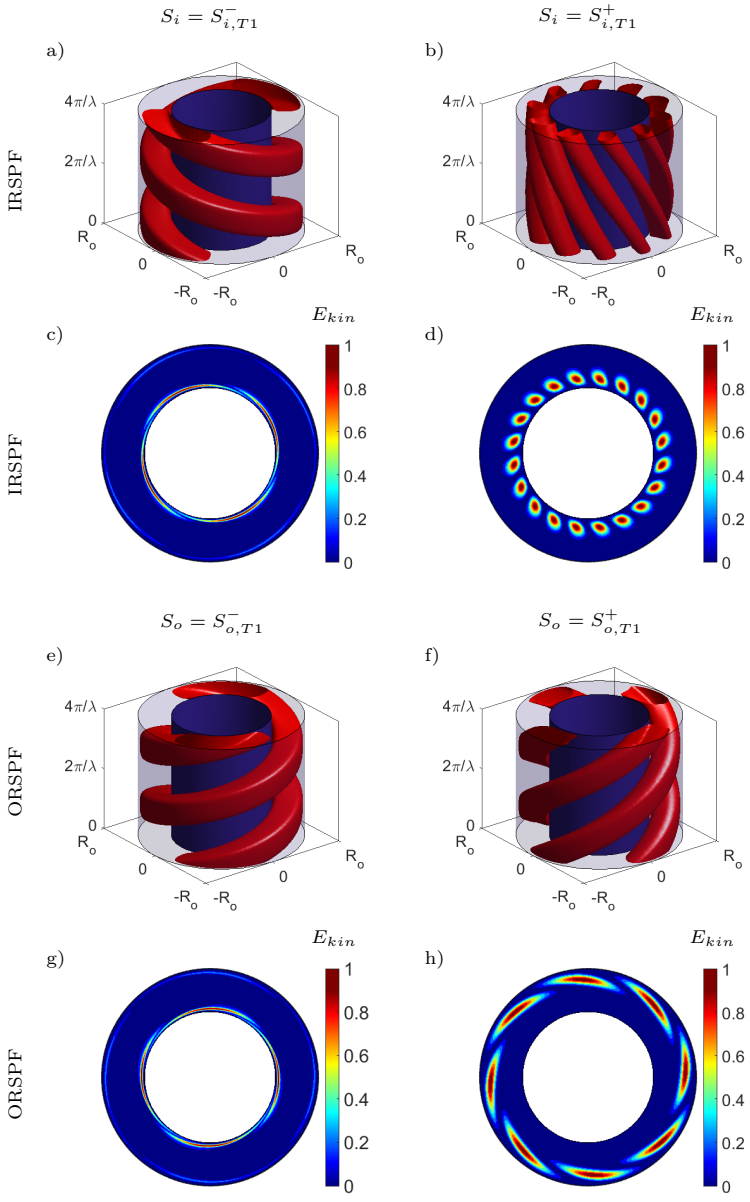

Figure 3.21: Visualization of critical disturbances for the IRSPF and the ORSPF before and behind the first transition at $S_{i,T1}$ and $S_{o,T1}$. a, b, e, f) Isosurfaces indicate 10% of the maximum value of u'_r (depicted over two periods) c, d, g, h) Distribution of kinetic disturbance energy K, normalized by its maximum value.

Fig. 3.21c it becomes evident, that the kinetic disturbance energy is restricted to the

critical layer close to the inner cylinder and outer cylinder at $S^-_{i,T1}$. Thereby, the peaks at the outer cylinder are almost not visible from Fig. 3.21c. For $S^+_{i,T1}$ instead, the kinetic energy spreads over a significantly wider area close to the inner cylinder (Fig. 3.21d). It should be mentioned, that the number of peaks Fig. 3.21c,d is twice the number of spirals in Fig. 3.21a,b as the kinetic energy contains the squares of the disturbance velocity components. Similar to the IRSPF the spirals get more inclined for the ORSPF at $S^+_{o,T1}$ compared to $S^-_{o,T1}$ (Fig. 3.21e,f). However, for the ORSPF negative modes are triggered ($n_c(S^-_{o,T1}) = -2$, $n_c(S^+_{o,T1}) = -4$) and the inclination of the spirals is opposed to that of the IRSPF. At $S^-_{o,T1}$ the distribution of kinetic energy is around the critical layers and almost identical to the IRSPF (Fig. 3.21g). At $S^+_{o,T1}$ similar to the IRSPF the kinetic energy distributes over a wide area, but close to the outer cylinder (Fig. 3.21h and Fig. 3.21d).

3.2.3.3 Effect on increasing swirl in region II and IIO

In section 3.1.1 and section 3.1.2 it was shown, that both the IRSPF and the ORSPF get destabilized with increasing swirl in the second region (II and IIO). This changes towards the end of the second region where the ORSPF is sharply stabilized with increasing swirl, while the IRSPF is destabilized further as the swirl increases. The underlying reason is, that the production of K develops striking differences for IRSPF and ORSPF as the swirl increases within region II and IIO. For illustration of this differences Fig. 3.22a-c shows the distribution of the K production terms for the IRSPF with $\epsilon = 0.25$ for different values of S_i within region II. As can be seen the magnitude of $\overline{P_K(V_\varphi)}$ increases with increasing swirl, while that of $\overline{P_K(V_x)}$ decreases (Fig. 3.22a-c). In between, for $S_i = 1$, $\overline{P_K(V_x)}$ and $\overline{P_K(V_\varphi)}$ are approximately equal as both flow components have a similar amplitude. For the IRSPF, all production terms destabilize the flow in region II, as they attain negative signs (Fig. 3.22a-c). In contrast, in the ORSPF $\overline{P_K(V_\varphi)}$ attains a positive amplitude (stabilizing) which increases compared to $\overline{P_K(V_x)}$ as the swirl increases towards the end of IIO (Fig. 3.22d-f). In the ORSPF, due to $\overline{P_K(V_\varphi)}$ energy is transferred back to the base flow which results in a stabilization of the base flow as shown similarly for APF by Mott and Joseph (1968b) and Sadeghi and Higgins (1991b). Hence, the azimuthal shear production has a stabilizing effect in the ORSPF in region IIO. This is the underlying reason why the critical Reynolds number of the ORSPF increases as the swirl increases towards the end of region IIO. For both the IRSPF and the ORSPF the production of the shear stresses, which contribute to the dominant K production terms, is due to the centrifugal production terms, such that a centrifugal instability is dominant throughout region II and IIO. For the interested reader the distribution of K and the shear stresses with associated production terms corresponding to Fig. 3.22 is given in the appendix in Fig. A.7.

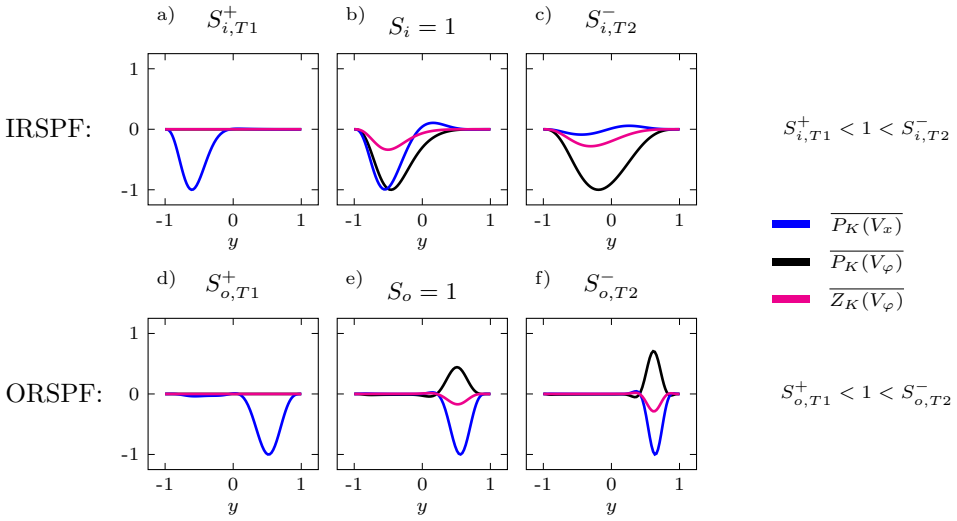

Figure 3.22: Normalized distributions of the K production terms for IRSPF and ORSPF for increasing swirl within region II and IIO, respectively. Legend holds for all plots. a) IRSPF: $S^+_{i,T1}$ b) IRSPF: $S_i = 1$ c) IRSPF: $S^-_{i,T2}$ d) ORSPF: $S^+_{o,T1}$ e) ORSPF: $S_o = 1$ f) ORSPF: $S^-_{o,T2}$

3.2.4 Analysis of the second transition for the IRSPF

As shown in section 3.2.2, the transition from I to II results in a drastical redistribution of K, the shear stresses and the production terms. Instead, the transition from II to III is less sharp for the IRSPF. From Fig. 3.23a,b,c,d it can be seen, that the distribution of the production terms remains almost unchanged across the second transition for small and intermediate ϵ (0.005 and 0.25). However, as ϵ increases, the change across the transition becomes more pronounced, which can be seen exemplary for $\epsilon = 0.785$ in Fig. 3.23f,e. As can be seen, at $S^-_{i,T2}$ all production terms ($\overline{P_K(V_\varphi)}$, $\overline{Z_K(V_\varphi)}$ and $\overline{P_K(V_x)}$) attain a similar amplitude and shape for $\epsilon = 0.785$. At $S^+_{i,T2}$ $\overline{P_K(V_x)}$ drops to zero, while $\overline{P_K(V_\varphi)}$ and $\overline{Z_K(V_\varphi)}$ spread over a significantly wider area. In fact, $\overline{P_K(V_x)}$ is always approximately zero for all ϵ considered in region III. This is the most significant feature of region III. For smaller ϵ $\overline{P_K(V_x)} = \tau_{rx} dV_x/dy$ is (close to) zero because the transition takes places at higher swirl parameters, such that V_x is negligible compared to V_φ. For larger values of ϵ instead the distribution of τ_{rx} changes at $S^+_{i,T2}$ as n_c drops to zero. This results in $\overline{P_K(V_x)}$ dropping to zero. The production of shear stresses before and behind the jump is due to centrifugal terms, such that the instability at $S^-_{i,T2}$ and $S^+_{i,T2}$ is a centrifugal instability. Detailed plots of K, shear stresses and production terms are provided in the appendix (Fig. A.8 and Fig. A.9)

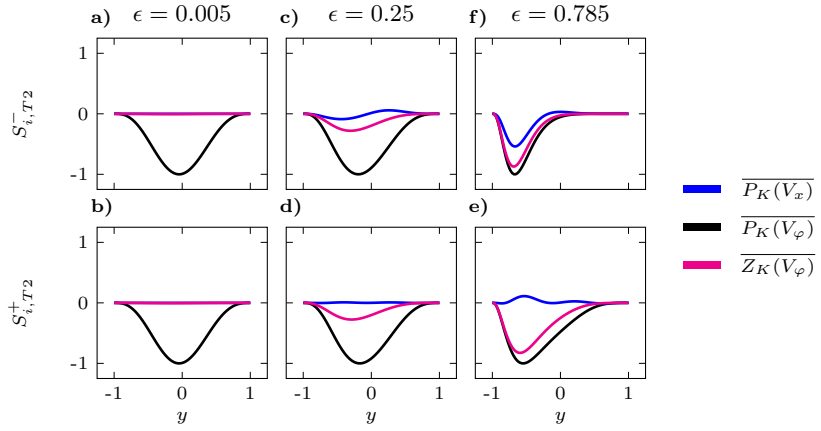

Figure 3.23: Normalized radial distributions of K production terms in the IRSPF before ($S^-_{i,T2}$) and behind ($S^+_{i,T2}$) the second transition for $\epsilon = \{0.005; 0.25; 0.78\}$. a, c, f) K production at $S^-_{i,T2}$ b, d, e) K production at $S^+_{i,T2}$

3.2.5 Analysis of the second transition for the ORSPF

Here, the distribution of shear stresses, K and associated production terms before and behind the transition from IIO to IIIO is discussed for the ORSPF. The situation before and behind the second transition is referred to as $S^-_{o,T2}$ and $S^+_{o,T2}$, as described in section 3.1.2 and indicated in Fig. 3.8. The associated critical values of Re_c, λ_c, n_c and ω_c can be found in the appendix A.1.8.

3.2.5.1 Region IIO: Distributions at $S^-_{o,T2}$

The distribution of shear stresses, K and associated production terms at $S^-_{o,T2}$ are depicted in Fig. 3.24. As analyzed in section 3.2.3 there is a TSI dominant in IO, which will be confirmed here for $\epsilon = 0.005$ and $\epsilon = 0.0526$. The roots of equation (2.33) are indicated with the dash dot vertical lines in Fig. 3.24. As Re_c attains values of $Re_c \approx 10^4$ here (see appendix, table A.7) the condition for equation (2.33) is assumed to be valid.

Figures 3.24a-e show the distribution of K for selected values of ϵ. As can be seen from Fig. 3.24a,b at $S^-_{o,T2}$ for $\epsilon < 0.059$ the distribution of K is similar to the APF and features sharp peaks at the critical layers which indicates a Tollmien-Schlichting instability. As previously mentioned for $\epsilon < 0.059$ there is a direct transition from IO to IIIO such that the distributions at $S^-_{o,T2}$ differ significantly for $\epsilon < 0.059$ and $\epsilon \geq 0.059$. For $\epsilon > 0.059$ the peaks of K are similar to those at $S^+_{o,T1}$ but less wide (see Fig. 3.24c-e).

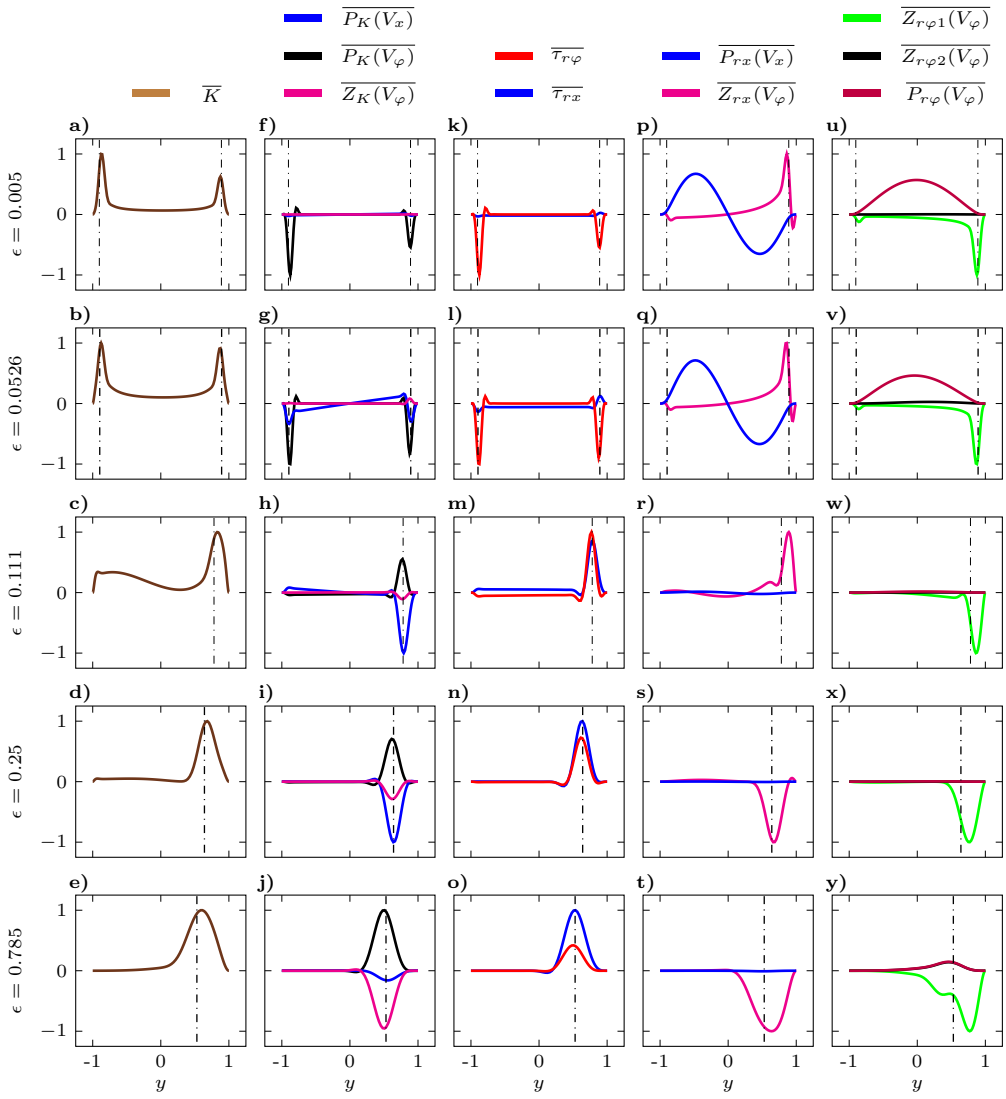

Figure 3.24: Normalized radial distributions of kinetic energy, production terms and shear stresses found in the ORPSF before the second transition at $S^-_{o,T2}$ (IO to IIIO for $\epsilon < 0.059$, IIO to IIIO for $\epsilon > 0.059$) for $\epsilon = \{0.005; 0.0526; 0.11; 0.25; 0.78\}$. Dash dot line = position of critical layer according to equation (2.33). a-e) K over y. f-j) Production of K over y. k-o) τ_{rx}, $\tau_{r\varphi}$ over y. p-t) Production of τ_{rx} over y. u-y) Production of $\tau_{r\varphi}$ over y.

As can be seen the production terms of the K budget, exhibit sharp peaks close at the theoretical position of the critical layer, which indicates a TSI $\epsilon < 0.059$ (Fig. 3.24f,g). A remarkable feature is, that the major part of K production stems from azimuthal shear $\overline{P_K(V_\varphi)}$. As described before, a significant magnitude of $P_K(V_\varphi)$ is also observed for the ORSPF ($\epsilon = 0.0526$) at $S^-_{o,T1}$ and the IRSPF at $S^-_{i,T1}$ ($\epsilon = 0.0025$, 0.005). However, here for $\epsilon = 0.005$ $\overline{P_K(V_\varphi)}$ provides approximately 100% of the kinetic disturbance energy. This is a sharp contrast to the "classical" TS instability in a flow with straight streamlines where the production of K is solely due to axial shear $P_K(V_x)$. This is because, here V_x is much smaller compared to V_φ as $S^-_{o,T2} = 4.67$ for $\epsilon = 0.005$ (see table A.7 and Fig. A.3). This reveals that in a ORSPF a TSI can even persists at relatively large swirls where the azimuthal component is significantly larger than the axial flow component. As the TSI in a SPF is usually associated with the axial flow, this is counter-intuitive. The existence of a TSI will by confirmed by the shear stresses and production terms in the following.

For $\epsilon > 0.059$ $\overline{P_K(V_\varphi)}$, $\overline{Z_K(V_\varphi)}$ and $\overline{P_K(V_x)}$ are nonzero only close to the outer cylinder where they exhibit a symmetric peak (Fig. 3.24h-j). Thereby, $\overline{P_K(V_\varphi)}$ stabilizes the flow, as it attains a positive sign, while $\overline{Z_K(V_\varphi)}$ and $\overline{P_K(V_x)}$ attain negative signs as explained in Sect. 3.2.3.3. With increasing ϵ the magnitude of $\overline{Z_K(V_\varphi)}$ increases while $\overline{P_K(V_x)}$ decreases, such that for $\epsilon = 0.785$ $\overline{Z_K(V_\varphi)}$ is the dominant destabilizing production term (Fig. 3.24h-j). As both $\overline{Z_K(V_\varphi)}$ and $\overline{P_K(V_\varphi)}$ depend on V_φ this shows, that the effect of the azimuthal velocity is ambivalent in the ORSPF and has both destabilizing and stabilizing effects.

The shape of the K production terms is determined by the distribution of τ_{rx} and $\tau_{r\varphi}$ which are different for $\epsilon \leq 0.059$ and $\epsilon > 0.059$ as can be seen in Fig. 3.24k-o. For $\epsilon \leq 0.059$ τ_{rx} and $\tau_{r\varphi}$ exhibit peaks close to both critical layers with τ_{rx} having a negiglibe amplitude compared to $\tau_{r\varphi}$ (Fig. 3.24k-l). For $\epsilon > 0.059$ instead τ_{rx} and $\tau_{r\varphi}$ both assume a peak at the outer gap width, whereby the magnitude of $\tau_{r\varphi}$ decreases with increasing ϵ (solid lines, Fig. 3.24m-o). In contrast to $\epsilon \leq 0.059$ for $\epsilon > 0.059$ $\tau_{r\varphi}$ attains positive values. When compared to the shear stress distributions at $S^+_{o,T1}$ (Fig. 3.20g-i) it can be seen that at $S^-_{o,T2}$ the shear stresses are restricted to a significantly narrower area. This also illustrates an ambivalent effect of outer rotation. While at S^+_{oT1} the interaction of axial flow and azimuthal shear lead to a wide distribution of shear stresses. At larger swirls the outer rotation seems to supress shear stresses over a large area of the gap. This can be seen clearly from comparing Fig. 3.20i and Fig. 3.24o.

For $\epsilon < 0.059$ $\overline{P_{rx}(V_x)}$ exhibits a similar distribution as for the APF (Fig. 3.24p-q and Fig. 3.16d). In contrast to the APF $\overline{Z_{rx}(V_\varphi)}$ is nonzero, increases from left to right and exhibits a significant positive peak close to the outer cylinder. As clear from Fig. 3.24p-q $\overline{Z_{rx}(V_\varphi)}$ attains a positive sign and counteracts $\overline{P_{rx}(V_x)}$ in the right channel half. However, this centrifugal term does not significantly affect the overall production of τ_{rx} and gets cancelled by the velocity pressure gradient (not shown). For $\epsilon > 0.059$

$\overline{P_{rx}(V_x)}$ is approximately zero, while $\overline{Z_{rx}(V_\varphi)}$ assumes a peak in the right gap half (Fig. 3.24r-t). For $\epsilon > 0.059$ 100% of the τ_{rx} production is due to the centrifual term $\overline{Z_{rx}(V_\varphi)}$. It should be mentioned that at the end of region IIO for $0.0509 \leq \epsilon \leq 0.111$ a slightly different distribution of $\overline{Z_{rx}(V_\varphi)}$ was observed. This can be exemplary seen for $\epsilon = 0.111$ in Fig. 3.24r. As can be seen here $\overline{Z_{rx}(V_\varphi)}$ acts as a sink for τ_{rx}. The source here is the velocity pressure gradient (not depicted) which balances $\overline{Z_{rx}(V_\varphi)}$ and has essentially the same shape. However, this distribution is observed only very close to the end of region IIO. For instance, for $\epsilon = 0.111$ a distribution as depicted in Fig. 3.24r can be observed in the range of $1.55 \leq S_o \leq 1.58 = S^-_{o,T2}$, while for $S_o < 1.55$ the distribution is similar to those in Fig. 3.24s,t. These cases represent an exception in IIO, which does not fall into the criteria defined in section 3.2.1. Hence, they cannot be identified. This indicates that the velocity pressure gradient should be also considered for identification in some cases.

For $\epsilon < 0.059$ the major part of $\tau_{r\varphi}$ emerges from $\overline{P_{r,\varphi}(V_\varphi)}$ which spreads symmetrically across the gap and assumes positive values (Fig. 3.24u,v). Similar to $\overline{Z_{rx}(V_\varphi)}$, $\overline{Z_{r\varphi,1}(V_\varphi)}$ exhibits a sharp negative peak for $\epsilon < 0.059$ at $S^-_{o,T2}$ (Fig. 3.24p,q,u,v) and counteracts $\overline{P_{r\varphi}(V_\varphi)}$. For $\epsilon > 0.059$ instead $\overline{P_{r\varphi}(V_\varphi)}$ is approximately zero and $\tau_{r\varphi}$ emerges from $\overline{Z_{r\varphi 1}(V_\varphi)}$ which assumes a peak at the right channel half (Fig. 3.24w-y). Obviously at $S^-_{o,T2}$ $\tau_{r\varphi}$ is mostly produced by azimuthal shear for $\epsilon < 0.059$ while it is produced by centrifugal effects for $\epsilon > 0.059$.

Overall, the results show that for $\epsilon < 0.059$ up to $S^-_{o,T2}$ a TSI is present. This becomes evident from the fact that the shear stress that contributes to the K dominant production term emerges from shear production and a critical layer exists. However, as the azimuthal flow component is significantly larger than the axial flow component at $S^-_{o,T2}$, striking differences to the "classical" TS instability associated with an axial flow occur. In contrast to the "classical" TS instability associated with an axial flow, here the production of K and the shear stress $\tau_{r\varphi}$ emerges mostly from the azimuthal flow component. As described in section 3.2.2.1 for the IRSPF similar observation were made for $\epsilon < 0.005$ at $S^-_{i,T1}$ where most of the K production emerges from azimuthal shear. This shows, for the first time that in a SPF a Tollmien Schlichting instability can persist when the azimuthal flow component is significantly larger than the axial flow component given a sufficiently small ϵ. In the ORSPF the first region (associated with a TSI) persists up to significantly larger swirls for small ϵ (no transition to IIO). Hence, the TSI can be observed at much higher swirls, compared to the IRSPF.

For $\epsilon > 0.059$ at $S^-_{o,T2}$ the production of shear stresses which contribute to the dominant destabilizing K production terms emerges exclusively from centrifugal terms which indicates that a centrifugal instability is present. Here $\overline{Z_K(V_\varphi)}$ and $\overline{P_K(V_x)}$ are destabilizing the flow while $\overline{P_K(V_\varphi)}$ is stabilizing the flow. This is a major difference to the IRSPF here, where $\overline{P_K(V_\varphi)}$ is destabilizing at $S^-_{i,T2}$ and throughout region II as illustrated in section 3.2.3.3. Remarkably, the roots of equation (2.33) approximately coincide

with the peaks of the shear stresses and associated production terms for $\epsilon > 0.059$. However, as shear stresses clearly emerge from centrifugal production terms here, they are assumed to be meaningless.

3.2.5.2 Region IIIO: Distributions at $S^+_{o,T2}$

Here it will be shown that behind the transition to IIIO at $S^+_{o,T2}$, K, the shear stresses and the associated production terms assume a strikingly different distribution compared to $S^-_{o,T2}$ and show a similar distribution for all ϵ. As shown here, a critical layer becomes evident and the shear stresses, which contribute to the dominant K terms arise from shear production terms which act as a source. Instead centrifugal terms act as sink here. Thus, the instability present in region IIIO at $S^+_{o,T2}$ is considered as a TSI. In contrast to a TSI which is present at low swirls, here only one layer exists close to the inner cylinder. The distributions of K, shear stresses and associated production terms are depicted in Fig. 3.25 for selected ϵ at $S^+_{o,T2}$ at the beginning of IIIO. As the Reynolds number is in the order of $O(10^4)$ the underlying assumption of equation (2.33) is justified. One root for each ϵ is found and indicated with the dash dot lines in Fig. 3.25.

Figure 3.25a-e reveals that for $S^+_{o,T2}$ the peak of K is located near the inner cylinder wall and exhibits a peak close to the theoretical position of the critical layer obtained by equation (2.33) for all ϵ considered. The distribution of K results from the distribution of $\overline{P_K(V_\varphi)}$, $\overline{Z_K(V_\varphi)}$, $\overline{P_K(V_x)}$, which also attain a sharp peak at the theoretical position of the critical layer (Fig. 3.25f-j). This indicates the existence of a critical layer. Depending on ϵ either $\overline{P_K(V_\varphi)}$ or $\overline{P_K(V_x)}$ is the dominant destabilizing term (Fig. 3.25f-j). The shear stresses concentrate on a small area close to the theoretical position of the critical layer and assume peaks with different signs depending on ϵ (Fig. 3.25k-o). Compared to the shear stresses before the transition, the peaks are narrower here for $\epsilon = 0.111$, 0.25 and 0.785 (Fig. 3.25k-o and Fig. 3.24k-o).

By comparing the signs of the shear stresses with those of the production terms of the RSSTE in Fig. 3.25p-y, it can be seen that for the shear stresses, that contribute to the dominant K production term, the shear production terms act as a source. For $\epsilon = 0.005$, 0.25 and 0.785 this is $\tau_{r\varphi}$ (negative) stemming from (positive) shear production $\overline{P_{r\varphi}(V_\varphi)}$ (Fig. 3.25k,n,o and Fig. 3.25p,s,t). For $\epsilon = 0.111$ this is τ_{rx} (negative) stemming from (positive) shear production $\overline{P_{rx}(V_x)}$ (Fig. 3.25m,r). For $\epsilon = 0.0526$, where both $\overline{P_K(V_x)}$ and $\overline{P_K(V_\varphi)}$ are about the same order, both shear stresses τ_{rx} and $\tau_{r\varphi}$ (negative) arise from shear production terms ($\overline{P_{r\varphi}(V_\varphi)}$, $\overline{P_{rx}(V_x)}$, both positive close to critical layer) as a source (Fig. 3.25l,q,v). Instead for all ϵ, the centrifugal production terms $\overline{Z_{r\varphi,1}(V_\varphi)}$ and $\overline{Z_{rx}(V_\varphi)}$ act as a sink for these shear stresses as they attain the same sign as $\tau_{r\varphi}$ and τ_{rx}. Thereby, the magnitude of these centrifugal production terms exceeds that of the shear production terms locally, but get balanced by the velocity pressure gradient, which also acts as a source (brown lines in Fig. 3.25p-t and Fig. 3.25u-y). In fact,

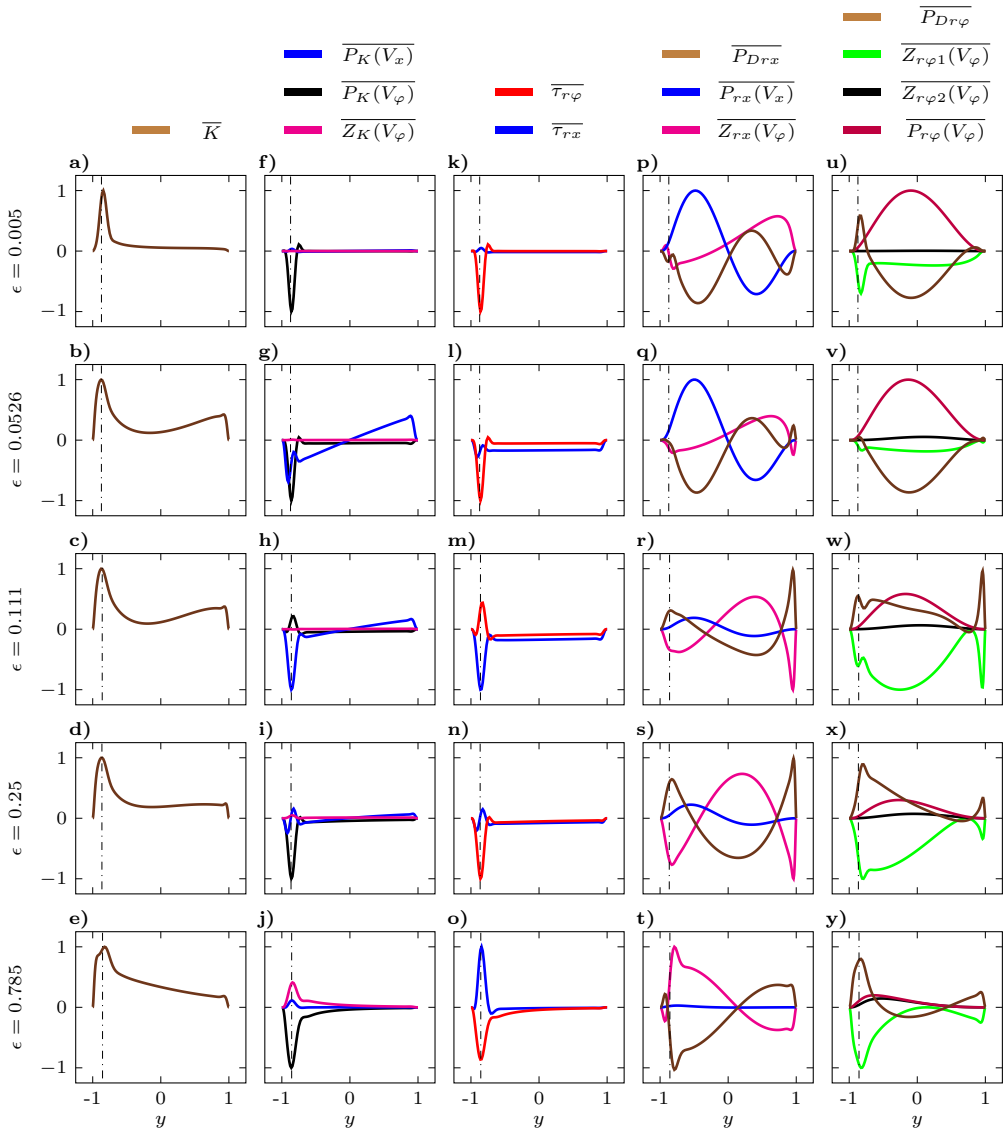

Figure 3.25: Normalized radial distributions of kinetic energy, production terms and shear stresses found in the ORPSF behind the second transition at $S^+_{o,T2}$ (IO to IIIO for $\epsilon < 0.059$, IIO to IIIO for $\epsilon > 0.059$) for $\epsilon = \{0.005; 0.0526; 0.11; 0.25; 0.78\}$. Dash dot line = position of critical layer according to equation (2.33). a-e) K over y. f-j) Production of K over y. k-o) τ_{rx}, $\tau_{r\varphi}$ over y. p-t) Production of τ_{rx} over y. u-y) Production of $\tau_{r\varphi}$ over y.

distant from the critical layer the velocity pressure gradient balances both shear and centrifugal terms, such that effective shear stress production is limited to the critical layer, resulting in the shape of the shear stresses as can be seen from Fig. 3.25k-o. The viscous effects are very small here and not depicted.

As defined in section 3.2.1, within this thesis a TSI is identified by the shear stress, which contributes to the dominant K production term, stemming from shear production. Furthermore a critical layer must become evident. A centrifugal instability instead, is characterized by the shear stress in the dominant K production term stemming from centrifugal production. Hence, the instability present in region IIIO at $S^{+}_{o,T2}$ is considered as a TSI here. In contrast to a TSI which is present at low swirls, here only one layer exists close to the inner cylinder. The presence of one critical layer is typical for boundary layer flows with monotonically increasing velocity profiles (Craik 1988). Also for the ORSPF the velocity profile is monotonically increasing at higher swirls as depicted exemplary in Fig. A.2 in the appendix. These evidences and conclusions are in agreement with Deguchi (2017) who investigated Rayleigh-stable Taylor Couette flow ($\mu \to \infty$ and $S_o \to \infty$) and assumed that a instability similar to a TSI drives the flow instability. Deguchi observed the magnitude of the disturbance velocity to be approximately zero over the most part of the gap except for a small area close to the wall of the inner cylinder. This is similar with our finding, that there is just one critical layer close to the inner cylinder wall. Nevertheless, the velocity-pressure gradient act as a source here as well and attains large magnitudes. The criteria defined in section 3.2.1 does not consider the velocity pressure gradient. However, it would be interesting to reveal, the underlying effects that affect the pressure gradient. For instance, from turbulent flows in curved channels it is known, that the curvature can affect the velocity pressure gradient (Moser and Moin 1987). However, this is beyond the scope of the present thesis.

In the next section, 3.2.5.3, it will be shown that the characteristics of the instability unify for all ϵ considered such that $\overline{P_K(V_\varphi)}$ becomes the dominant production term.

Next, briefly the instantaneous structures of the critical disturbances across the second transition are discussed, which display features of the instability present in IIIO. Figure 3.26 therefore presents the instantaneous disturbance structure of both the IRSPF and the ORSPF for $\epsilon = 0.25$ analogous to Fig. 3.21. As can be seen from Fig. 3.26a,b before the jump at $S^{-}_{i,T2}$ spirals exist, while at $S^{+}_{i,T2}$ the disturbance attains an axisymmetric vortical shape as $n_c = 0$. At $S^{+}_{i,T2}$ these vortical structures travel in axial direction with the speed $c = \omega_r/\lambda$. When $S_i \to \infty$ $\omega \to 0$ such that the disturbances become stationary and turn into the well known axisymmetric Taylor instability as also concluded by Cottrel and Pearlstein (2004). From comparing Fig. 3.26c and Fig. 3.21c it becomes evident, that the kinetic energy spreads over a significantly wider area at $S^{-}_{i,T2}$ compared to the beginning of region II at $S^{+}_{i,T1}$. At $S^{+}_{i,T2}$ the kinetic energy distributes asymmetrically over the gap Fig. 3.26d. For the ORSPF it can be seen that the spirals change their orientation as n_c jumps from -1 to 1 across the second

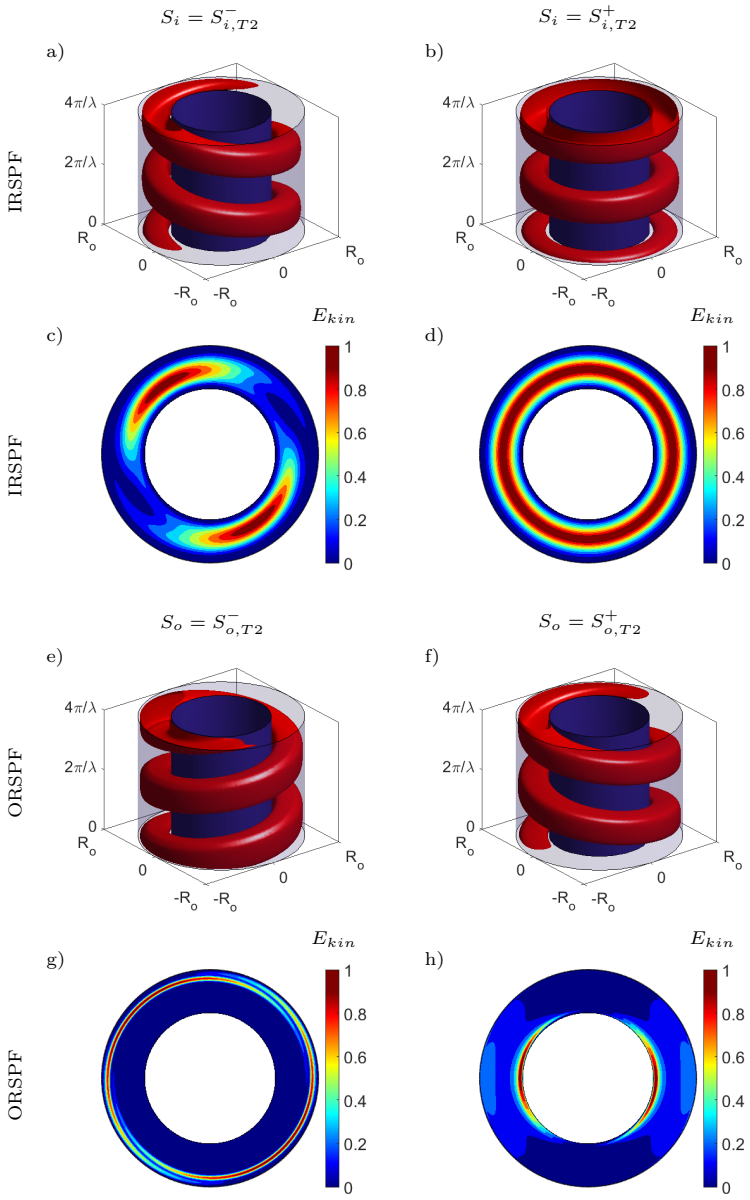

Figure 3.26: Visualization of critical disturbances for the IRSPF and the ORSPF before and behind the first transition at $S_{i,T2}$ and $S_{o,T2}$. a,b,e,f) Isosurfaces where the radial disturbance velocity (u'_r) attains 10% of their maximum value (depicted over two periods). c,d,g,h) Distribution of kinetic disturbance energy K, normalized by its maximum value.

wavenumber jump (Fig. 3.26e,f). From Fig. 3.26g it can be seen that the kinetic energy is restricted to significantly narrower region at $S^-_{o,T2}$ at the outer cylinder compared to $S^+_{o,T1}$ in Fig. 3.21h and especially to the IRSPF at $S^-_{i,T2}$ (Fig. 3.26c). At $S^+_{o,T2}$ the kinetic energy exhibits sharp peaks close to the inner cylinder, but also exhibits a slight plateau across the gap (Fig. 3.26h). In fact, the distribution of K found in region IIIO Fig. 3.26h resembles that of Fig. 3.21c,g associated with a TSI. The major difference compared to the distribution of K in Fig. 3.21c,g is that there are no peaks close to the outer cylinder, as there is only one critical layer.

3.2.5.3 Region IIO: Distributions for $S_o > S^+_{o,T2}$

As discussed previously for $0.088 \leq \epsilon \leq 0.111$ for $S^+_{o,T2}$ the production of K is mostly due to axial shear $\overline{P_K(V_x)}$ while for $\epsilon \leq 0.059$ and $\epsilon > 0.111$ the production of K is mostly due to azimuthal shear $\overline{P_K(V_\varphi)}$. Moreover, $\tau_{r\varphi}$ and τ_{rx} exhibit different signs for different ϵ. However, with increasing S_o in region IIIO, all the distributions unify as demonstrated exemplarily for $\epsilon = 0.0526$ and $\epsilon = 0.111$ in Fig. 3.27. As can be seen K, the K production terms and the shear stresses concentrate on the critical layer and are zero across the rest of the gap when the swirl increases from $S^+_{o,T2}$ to 3.37 (Fig. 3.27a-l). Thereby, $\overline{P_K(V_\varphi)}$ becomes the dominant K production term which destabilizes the flow (Fig. 3.27e-h). Also the shear stress $\tau_{r\varphi}$ attains a negative sign when S_o increases to 3.37 (Fig. 3.27i-l). It should be mentioned, that for these values of ϵ S_o higher than 3.37 have not been computed since Re_c strongly increases with increasing S_o. In general, as S_o increases, for all ϵ the magnitude of $\overline{Z_{r\varphi,1}(V_\varphi)}$ increases, while the amplitude of $\overline{P_{r\varphi}(V_\varphi)}$ decreases. Thereby, $\overline{Z_{r\varphi,1}(V_\varphi)}$ attains the same sign as $\tau_{r\varphi}$ such that it acts as a sink. Hence, the source terms for $\tau_{r\varphi}$ are $\overline{P_{r\varphi}(V_\varphi)}$ and $P_{Dr\varphi}$. This shows, that the production of $\tau_{r\varphi}$ is increasingly hindered by the centrifugal production term $\overline{Z_{r\varphi,1}(V_\varphi)}$ at higher swirls. This observation, that centrifugal effects increasingly hinder the production of shear stresses in region IIIO could explain the stabilizing effect that is observed for increasing swirl. This can be illustrated in analogy to the Rayleigh criterion. According to this criterion, an increase of radial momentum hinders transfer of mass across the streamlines and hence the generation of velocity fluctuations resulting in shear stresses (see section 1.2.1.1). This hindering effect is represented here by the centrifugal production $\overline{Z_{r\varphi,1}(V_\varphi)}$. Overall, Fig. 3.27 shows exemplary that the distributions for all ϵ attain a similar distribution at higher values of S_o. These results show that, in the budget of $\tau_{r\varphi}$ the centrifugal production term acts as a sink, while the azimuthal shear production acts as source. At the same time the shear stresses and budgets confirm a critical layer in region IIIO associated with a TSI. Hence, to the criteria defined in section 3.2.1 the instability observed in region IIIO is considered as a TSI as concluded in the previous section. As mentioned before in section 3.2.5.2, the velocity-pressure gradient acts as a source here as well. In fact, the magnitude of $\overline{P_{r\varphi}(V_\varphi)}$ is small here, compared to that of $\overline{Z_{r\varphi,1}(V_\varphi)}$ and that of the

velocity pressure gradient. As mentioned, it would be interesting to investigate the underlying effects leading to the distribution of the velocity pressure gradient, but this is beyond the scope of this thesis.

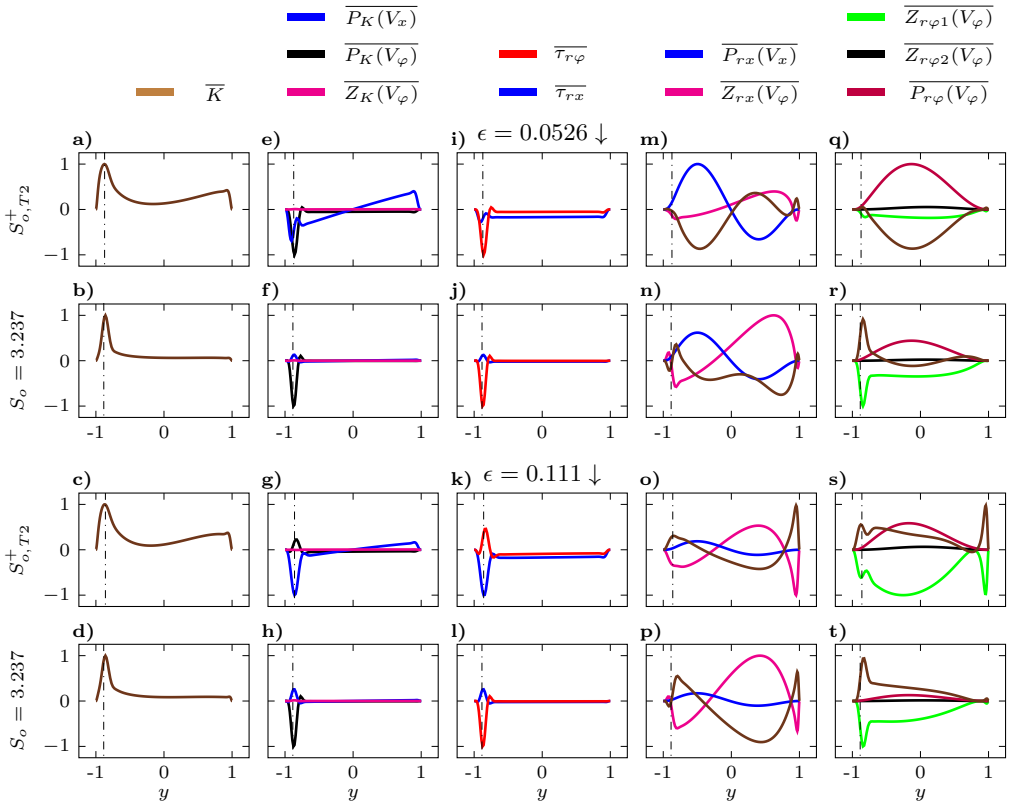

Figure 3.27: Normalized radial distributions of kinetic energy, production terms and shear stresses found in the ORPSF in region IIIO for $\epsilon = 0.0526$ and $\epsilon = 0.111$ for $S_o = S^+_{o,T2}$ and $S_o = 3.237$ ($S^+_{o,T2} < 3.237$). First two rows: $\epsilon = 0.0526$. Last two rows: $\epsilon = 0.111$. a-d) K over y. e-h) Production of K over y. i-l) τ_{rx}, $\tau_{r\varphi}$ over y. m-p) Production of τ_{rx} over y. q-t) Production of $\tau_{r\varphi}$ over y.

3.2.5.4 Intermediate conclusions identification of instability mechanisms

In the previous sections, the instability mechanisms associated with the different regions were analyzed and identified for the IRSPF and the ORSPF. For this, the budget of the kinetic disturbance energy (K) and the shear stresses as well as the concept of the critical layer for a generalized SPF as proposed by Vasanta Ram (2019) were employed. From two benchmark cases (TC-flow and plane Poiseuille flow), it was concluded that a centrifugal instability can be identified by a centrifugal production of the shear stress which contribute to the dominant K production term. A Tollmien-Schlichting

instability instead can be identified by the existence of a critical layer and the shear stress, which contributes to the dominant K production term, stemming from shear production. Using this approach it was shown that within the first region a TSI is present for the IRSPF and ORSPF. The results clearly confirmed the existence of a critical layer as assumed by Cottrel and Pearlstein (2004) for the IRSPF. To the authors best knowledge, for the first time the existence of a critical layer is shown for non-axisymmetric disturbances. Further, it was revealed that for both the IRSPF and the ORSPF at small ϵ a TSI can persist at large values of swirl ($O(1)$) where the axial and azimuthal velocity component are about the same value. For the ORSPF the TSI can persist even at swirls where the azimuthal component is significantly larger than the axial component (about factor four) if ϵ is sufficiently small. At such high swirls the major part of the K production stems from azimuthal shear.

In the second region, the production terms are drastically redistributed and spread in the left and right half of the gap for the ORSPF and the IRSPF, respectively. At the beginning of this region, for all ϵ the production of K stems from axial shear $P_K(V_x)$ and the corresponding shear stress emerges from centrifugal production. Hence, the associated instability is identified as a centrifugal instability for both the IRSPF and the ORSPF. By this, to the best authors knowledge, for the first time a link between the instability induced by a Rayleigh unstable (IRSPF) and a Rayleigh stable azimuthal flow component (ORSPF) was created. Moreover, it was shown that in the second region the IRSPF gets monotonously destabilized with increasing swirl for all considered ϵ. Instead, the ORSPF is first destabilized in the beginning of the second region but then stabilized as the swirl increases further. This is related to the azimuthal production of K, which continuously increases in the second region and stabilizes the ORSPF while it destabilizes the IRSPF. By this a striking difference between the IRSPF and the ORSPF was revealed for the first time.

It was shown for the IRSPF that in the third region the distribution of the K budgets and shear stress budgets are similar to the second region. The most prominent feature of the third region is that the production of K is solely due to azimuthal shear and clearly a centrifugal instability is present for the IRSPF as expected and also concluded for individual values of ϵ by Cottrel and Pearlstein (2004), Cottrel et al. (2004) and Mesequer and Marques (2002). In the ORSPF within the third region, K, the shear stresses and the associated production terms attain a shape which is strikingly different compared to the second region. Here, the shear stresses and production terms locate on a region close to the inner cylinder, which indicates the existence of a critical layer. Furthermore, the shear stresses which contribute to the dominant production terms are generated by shear production. The centrifugal terms act as sink here and inhibit the production of the shear stresses which contribute to the dominant K production term. These terms get balanced by the velocity pressure gradient. It is concluded that a TSI instability is present in region IIIO, which coincides with the conclusions of Deguchi (2017) for Rayleigh stable Taylor Couette flow ($S_o \to \infty$).

3.2.6 Integral production terms as function of Si and S_o

In the previous sections the distributions of kinetic disturbance energy, shear stresses and associated budgets were analyzed as function of the gap height. It was revealed that the distributions in region I and IO concentrate on the proximity of a critical layer while they spread across the inner and outer gap half in region II and IIO, respectively. Investigating the production terms of the shear stresses, the former regions could be associated with a Tollmien-Schlichting instability while the latter ones were associated with a centrifugal instability. Based on the shear stress production terms, region III could be associated with a centrifugal instability. In region IIIO the distributions of the budgets focused on a small area on the inner cylinder and indicated a critical layer here. By analyzing the budgets of shear stresses and kinetic energy is was concluded a TSI is present in region IIIO.

While the presentation along the gap height provides a detailed picture for individual values of the swirl parameter, it does not provide a picture how the production terms change when the swirl parameter is varied continuously. This can be achieved by considering the integral values of $\overline{P_K(V_x)}$, $\overline{P_K(V_\varphi)}$, $\overline{Z_K(V_\varphi)}$ as function of the swirl parameter. For this, equations (2.23)-(2.25) are integrated over $-1 \leq y \leq 1$ for each S_i and S_o.

In Fig. 3.28 we show Re_c and n_c (Fig. 3.28a,c,e) as well as $\int \overline{P_K(V_x)}$, $\int \overline{P_K(V_\varphi)}$, $\int \overline{Z_K(V_\varphi)}$ (Fig. 3.28b,d,f) as function of S_i for the IRSPF. For comparability we plot $\int \overline{P_K(V_x)}$ (blue dots), $\int \overline{P_K(V_\varphi)}$ (red dots), $\int \overline{Z_K(V_\varphi)}$ (green dots) normalized with the absolute value of their sum ($P_{sum} = |\int \overline{P_K(V_x)} + \int \overline{P_K(V_\varphi)} + \int \overline{Z_K(V_\varphi)}|$). Negative values of $\int \overline{P_K(V_x)}$, $\int \overline{P_K(V_\varphi)}$ and $\int \overline{Z_K(V_\varphi)}$ indicate destabilization, while positive values stabilize the flow.

In general, for intermediate and larger values of ϵ $\int \overline{P_K(V_\varphi)}$, $\int \overline{Z_K(V_\varphi)}$ remain constant at zero, while $\int \overline{P_K(V_x)}$ remains at approximately -1 throughout region I for the IRSPF (see Figs. 3.28d,f). However, for smaller ϵ towards the end of I the amplitude of $\int \overline{P_K(V_\varphi)}$ increases while that of $\int \overline{P_K(V_x)}$ decreases (see Figs. 3.28b). This is because for smaller ϵ the transition to II occurs at relatively high values of S_i associated with a relativley high magnitude of the azimuthal velocity profile, as already explained in connection with Fig. 3.17e.

With the transition to II $\int \overline{P_K(V_x)}$ jumps back to -1 while $\int \overline{P_K(V_\varphi)}$, $\int \overline{Z_K(V_\varphi)}$ drop to zero, which is pronounced for $\epsilon = 0.005$ (Fig. 3.28b,d,f). This is remarkable and shows that the distribution of τ_{rx} together with the axial shear provides approximately 100% of the production of K at $S^+_{i,T1}$. Subsequently as S_o increases further within II the magnitude of $\int \overline{P_K(V_x)}$ decreases, while that of $\int \overline{P_K(V_\varphi)}$, $\int \overline{Z_K(V_\varphi)}$ increase at the same time (Fig. 3.28b,d,f). Thereby, the magnitude of $\int \overline{P_K(V_\varphi)}$ is always larger than that of $\int \overline{Z_K(V_\varphi)}$. As worked out in section 3.2.3.3, it is characteristic for the

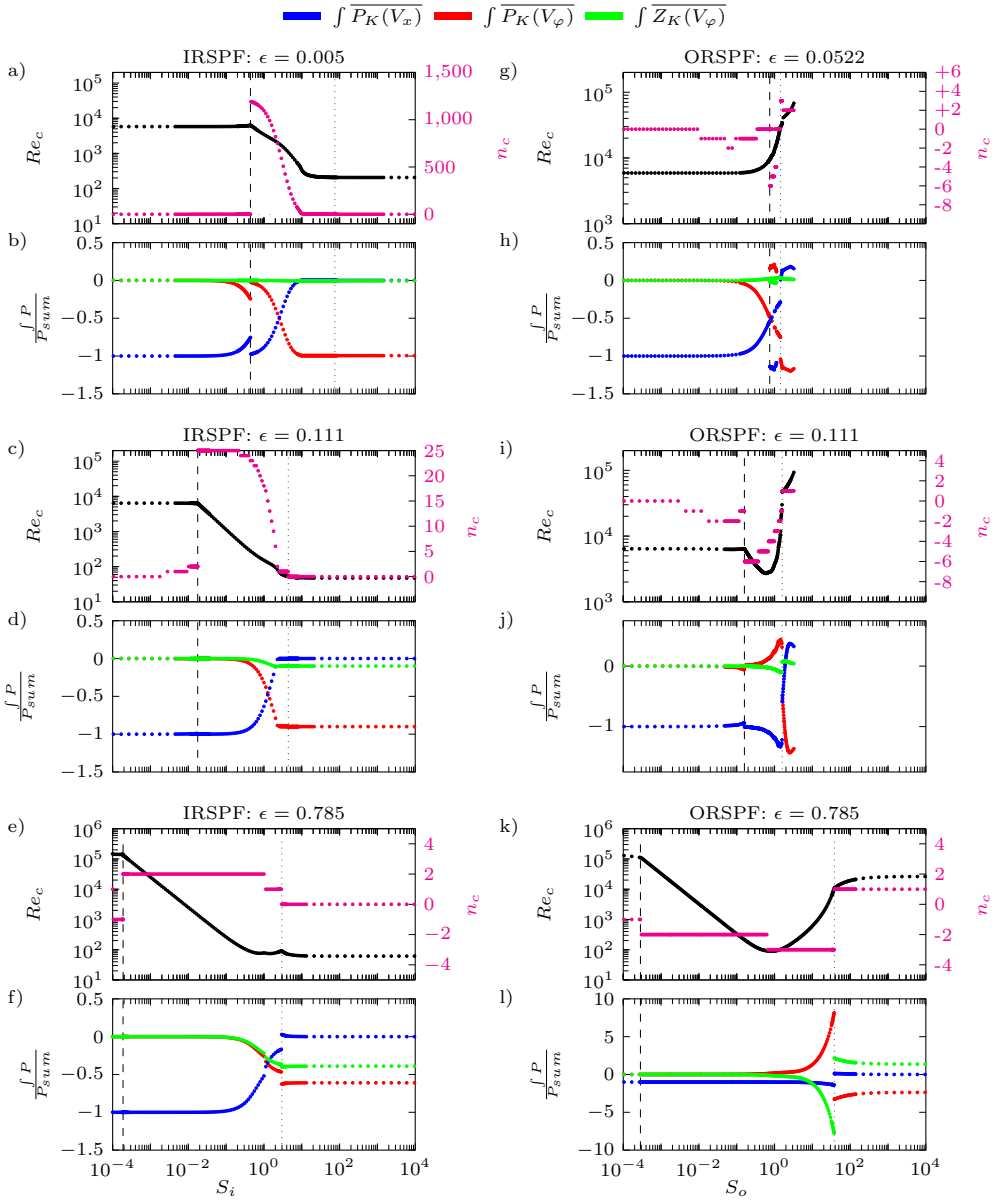

Figure 3.28: a, b) Re_c, n_c (a) and $\frac{P}{P_{sum}}$ (b) over S_i for $\epsilon = 0.005$ and IRSPF c, d) Re_c, n_c (c) and $\frac{P}{P_{sum}}$ (d) over S_i for $\epsilon = 0.111$ and IRSPF e, f) Re_c, n_c (e) and $\frac{P}{P_{sum}}$ (f) over S_i for $\epsilon = 0.785$ and IRSPF g, h) Re_c, n_c (g) and $\frac{P}{P_{sum}}$ (h) over S_o for $\epsilon = 0.0526$ and ORSPF i, j) Re_c, n_c (i) and $\frac{P}{P_{sum}}$ (j) over S_o for $\epsilon = 0.111$ and ORSPF k, l) Re_c, n_c (k) and $\frac{P}{P_{sum}}$ (l) over S_o for $\epsilon = 0.785$ and ORSPF

IRSPF, that all production terms within region II are destabilizing the flow as they attain negative signs (Fig. 3.28b,d,f). Therefore, the flow is destabilized with increasing swirl and Re_c drops continuously throughout region II.

It can further be seen that the increase of $\int \overline{P_K(V_x)}$ and the decrease of $\int \overline{P_K(V_\varphi)}$ and $\int \overline{Z_K(V_\varphi)}$ are both synchronous with the decay of n_c for $\epsilon = 0.005$ and $\epsilon = 0.111$ (see Figs. 3.28a,b,c,d). This is less clear for $\epsilon = 0.785$ where n_c undergoes a lower number of jumps (see Figs. 3.28e,f). Fig. 3.28e,f further reveal a strong dependency of $\int \overline{P_K(V_x)}$, $\int \overline{P_K(V_\varphi)}$ and $\int \overline{Z_K(V_\varphi)}$ on n_c. As clear from the graph the jumps in n_c are accompanied by jumps of $\int \overline{P_K(V_x)}$, $\int \overline{P_K(V_\varphi)}$ and $\int \overline{Z_K(V_\varphi)}$. For $\epsilon = 0.005$ and $\epsilon = 0.111$ the change of $\int \overline{P_K(V_\varphi)}$, $\int \overline{Z_K(V_\varphi)}$ stops at higher S_i values and reaches a plateau within region II (see Figs. 3.28b,d). In contrast, for $\epsilon = 0.785$ the production terms change till the end of region II and undergo a significant jump as the flow transits from II to III (see Figs. 3.28e,f). In fact, for $\epsilon = 0.78$ the axial shear production $\int \overline{P_K(V_x)}$ abruptly drops to approximately zero at the transition from II to III. In fact, $\int \overline{P_K(V_x)}$ dropping to zero is the most prominent characteristic of region III and could be observed for all considered ϵ. We observe at this stage, that the change of the production terms associated with the transition from II to III is smoothly for smaller values of ϵ, while it is aprubt for larger values of ϵ.

In region III $\int \overline{P_K(V_x)}$, $\int \overline{P_K(V_\varphi)}$, $\int \overline{Z_K(V_\varphi)}$ remain essentially constant for all ϵ considered (see Figs. 3.28b,d,f). The major production of K in this region is from azimuthal shear ($\int \overline{P_K(V_\varphi)}$). However the contribution of $\int \overline{Z_K(V_\varphi)}$ increases with increasing ϵ as can be seen from comparing Figs. 3.28b,d,f.

In Fig. 3.28g,i,k we show Re_c and n_c as function of S_o for the ORSPF. In Fig. 3.28h,j,l we show corresponding $\int \overline{P_K(V_x)}$, $\int \overline{P_K(V_\varphi)}$ and $\int \overline{Z_K(V_\varphi)}$ as function of S_o. As can be seen from Fig. 3.28h,j for $\epsilon = 0.0526$ and $\epsilon = 0.111$ the magnitude of $\int \overline{P_K(V_x)}$ decreases at the end of IO while that of $\int \overline{P_K(V_\varphi)}$ increases. This behavior is more pronounced for $\epsilon = 0.0526$ than for $\epsilon = 0.111$ and in general more pronounced for smaller values of ϵ. This increase of $\int \overline{P_K(V_\varphi)}$ occurs simultaneously to the increase of Re_c, which can be seen clearly for $\epsilon = 0.0526$ (see Fig. 3.28g,h). As revealed in section 3.2.3 and 3.2.5 in region IO, a TSI associated with a critical layer is dominant for the ORSPF. The increase in Re_c that comes visible in Fig. 3.28g is accompanied with the critical layer moving closer to the wall with increasing S_o. This effect becomes pronounced with decreasing ϵ. This is shown exemplarily in Fig. 3.29 for $\epsilon = 0.005$, where this effect is most prominent. As can be seen the increase in Re_c (Fig. 3.29b) is synchronous to the critical layer moving closer to the inner and outer cylinder wall (Fig. 3.29a). Closer to the wall the viscous dissipation of K increases which could explain the stabilization. Sadeghi and Higgins (1991b) also observed, for axisymmetric modes, that a stabilization of the flow goes along with the critical layer moving closer to the wall (see Fig. 5 and Fig. 14 in their work). They considered an APF with the inner cylinder sliding in axial direction in addition to the pressure gradient. Fig. 3.29 reveals that the rotation of the outer cylinder has a similar effect on the flow (in region IO).

For $\epsilon = 0.785$ throughout region IO the integral terms $\int \overline{P_K(V_\varphi)}$ and $\int \overline{P_K(V_x)}$ remain constantly at 0 and -1, respectively (see Fig. 3.28l). When the flow transits from IO to IIO the behavior of the terms drastically changes. As can be seen from Fig. 3.28h and Fig. 3.28j for $\epsilon = 0.0526$ and $\epsilon = 0.111$ $\int \overline{P_K(V_\varphi)}$ and $\int \overline{P_K(V_x)}$ undergo a jump at $S^+_{o,1}$, which is more pronounced for $\epsilon = 0.0526$.

For $\epsilon = 0.0526$ $\int \overline{P_K(V_x)}$ drops from -0.5 to approximately -1.2. $\int \overline{P_K(V_\varphi)}$ instead jumps from a negative (-0.5) to a positive value (0.25) and hence stabilizes the flow at $S^+_{o,T2}$ (Fig. 3.28h). As discussed in Sect. 3.1.2 the flow switches several times between IO and IIO after the first transition to IO. This behavior is clearly visible from the production terms here for $\epsilon = 0.0526$. By comparing n_c in Fig. 3.28g and $\int \overline{P_K(V_\varphi)}$ and $\int \overline{P_K(V_x)}$ in Fig. 3.28h it can be seen that jumps of n_c are coupled with the jumps of the production terms. Thereby, $\int \overline{P_K(V_\varphi)}$ switches between negative and positive values and hence a stabilizing and a destabilizing effect, while the magnitude of $\int \overline{P_K(V_x)}$ switches between approximately -0.5 and -1.0. This switching behavior illustrates that during the TSI in IO the azimuthal shear production is destabilizing while it is stabilizing in region IIO where a centrifugal instability is present.

For $\epsilon = 0.111$ $\int \overline{P_K(V_x)}$ jumps from -0.95 back to approximately -1.00 while $\int \overline{P_K(V_\varphi)}$ jumps from -0.05 back to zero during the transition to IIO at $S^+_{o,T1}$ (Fig. 3.28j). As S_o increases further within region IIO for $\epsilon = 0.111$ $\int \overline{P_K(V_\varphi)}$ assumes positive values and increases continously with increasing S_o, simultanously $\int \overline{P_K(V_x)}$ decreases to negative values below -1. Compared to $\int \overline{P_K(V_x)}$ and $\int \overline{P_K(V_\varphi)}$ $\int \overline{Z_K(V_\varphi)}$ is insignificant for $\epsilon = 0.111$.

For $\epsilon = 0.785$ a different behavior becomes apparent. During the transition from IO to IIO $\int \overline{P_K(V_\varphi)}$ and $\int \overline{P_K(V_x)}$ remain constantly at 0 and -1, respectively Fig. 3.28l. At higher values of S_o $\int \overline{P_K(V_\varphi)}$ starts to increase sharply while simultaneously $\int \overline{P_K(V_\varphi)}$ decreases with approximately the same slope. Thereby the magnitude exceeds 5 for both terms at higher values of S_o (Fig. 3.28l). At the same time $\int \overline{P_K(V_x)}$ decreases slightly. It is remarkable, that for $\epsilon = 0.785$ $\int \overline{Z_K(V_\varphi)}$ reaches a significantly higher magnitude as $\int \overline{P_K(V_x)}$. However as $\int \overline{P_K(V_\varphi)}$ is counterbalanced by $\int \overline{Z_K(V_\varphi)}$ the effective destabilization still results from the axial flow profile ($\int \overline{P_K(V_x)}$).

As mentioned, in region IIO the flow is destabilized by $\int \overline{P_K(V_x)}$ and $\int \overline{Z_K(V_\varphi)}$ where the latter only plays a role at higher values of S_o. The azimuthal shear production term $\int \overline{P_K(V_\varphi)}$ instead stabilizes the flow throughout IIO. As the flow transits to IIIO, this relation is reversed and henceon $\int \overline{P_K(V_x)}$ and $\int \overline{Z_K(V_\varphi)}$ assume positive values and stabilize the flow, while $\int \overline{P_K(V_\varphi)}$ drops to negative values and destabilizes the flow (Fig. 3.28h,j,l). For $\epsilon = 0.0526$ and $\epsilon = 0.111$ it can be seen that within region IIIO the magnitude of $\int \overline{P_K(V_x)}$ as well as $\int \overline{P_K(V_\varphi)}$ increases and then decreases again as S_o increases (Fig. 3.28h,j). Thereby for $\epsilon = 0.0526$ both terms exhibit kinks that are associated with jumps in n_c as S_o increases (Fig. 3.28g,h). For $\epsilon = 0.785$ $\int \overline{P_K(V_\varphi)}$, $\int \overline{Z_K(V_\varphi)}$ $\int \overline{P_K(V_x)}$ first decreases at the beginning of IIIO and then remain constant

afterwards (Fig. 3.28l). In region IIIO a remarkable feature is observed. As discussed in section 3.25 the results indicate the existence of a critical layer in accordance with equation (2.33) within region IIIO and it was concluded that a TSI is present here. When the position of the critical layer is plotted against S_o, it can be seen that the increase of Re_c at the beginning of IIIO is accompanied with the critical layer moving towards the inner cylinder wall. This is depicted exemplary for $\epsilon = 0.55$ in Fig. 3.29c,d. This is similar to the behavior of Re_c and y_c observed at the end of region IO for small ϵ and is considered as a further evidence, that here a TSI is dominant.

Overall, the integral presentation provided a complete picture of the production terms as function of the swirl parameter. For both the IRSPF and the ORSPF it was shown, that the azimuthal shear production of K increases smoothly towards the end of the first region for smaller ϵ. For the IRSPF it was revealed that within section II the decrease of n_c goes along with a increase of $\int \overline{P_K(V_\varphi)}$ and a decrease of $\int \overline{P_K(V_x)}$. For the ORSPF it was revealed, that within region IIO the increase of the stabilizing effect $\int \overline{P_K(V_\varphi)}$ goes along with an increase of Re_c. Throughout region III for the IRSPF there is no change in the production terms and the ratio of the production terms remains constant. In III the production of K is solely due to the azimuthal flow ($\int \overline{P_K(V_\varphi)}$, $\int \overline{Z_K(V_\varphi)}$). Instead, for the ORSPF the ratio of the production terms changes within region IIIO for smaller ϵ.

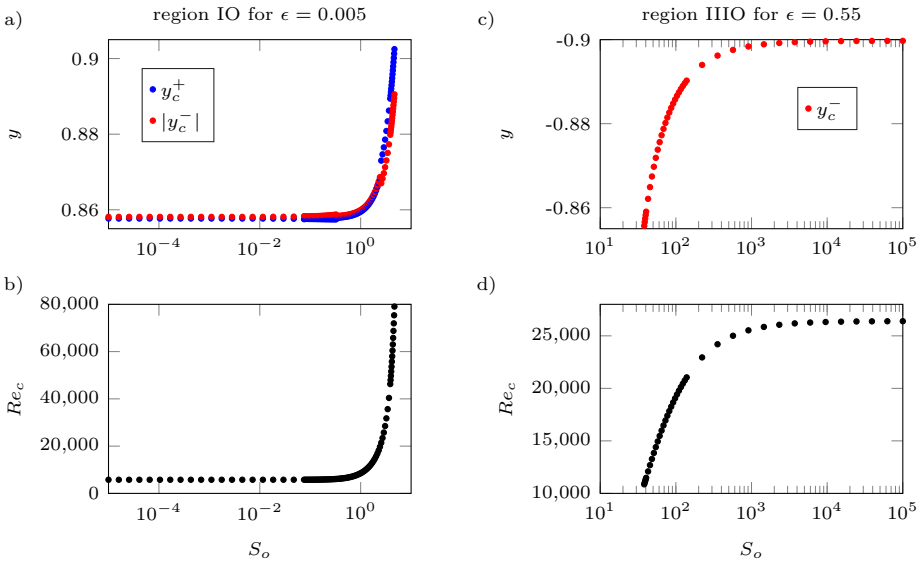

Figure 3.29: Location of critical layers and Re_c in region IO and IIIO. a) Critical layers y_c^+ (at outer cylinder wall) and $|y_c^-|$ (at inner cylinder wall) in region IO for $\epsilon = 0.005$. b)Re_c in region IO for $\epsilon = 0.005$. c) Critical layer y_c^- (at inner cylinder wall) in region IIIO for $\epsilon = 0.55$. d) Re_c in region IIIO for $\epsilon = 0.55$.

3.3 Discussion and Conclusion

We present a thorough comparison of the linear stability behavior the Spiral Poiseuille Flow with Rotation of the Inner cylinder (IRSPF) which features Rayleigh unstable azimuthal flow and the Spiral Poiseuille Flow with Rotation of the Outer cylinder (ORSPF) which features a Rayleigh stable azimuthal flow. The problem is formulated by means of the curvature parameter $\epsilon = (1 - \frac{R_i}{R_o})/(1 + \frac{R_i}{R_o})$, where R_i and R_o are the inner and outer cylinder radii, as well by means of the swirl parameters (S_i, S_o), defined as the ratio of rotational (U_φ) and axial reference velocity (U_x). The Reynolds number is defined with the resulting velocity $U_{\text{ref}} = (U_\varphi^2 + U_x^2)^{1/2}$ and the half gap width. We performed a complete phase mapping of the critical Reynolds number Re_c space, the critical wavenumber space (λ_c, n_c) and the critical frequency space (ω_c) for a huge range of swirl and curvature parameters. For the IRSPF 77 different values of ϵ ranging from 0.0025 to 0.785 have been explored, capturing a swirl range of $10^{-5} < S_i < 10^5$. For the ORSPF we provide numerical results for 108 different values of ϵ in the range of 0.005 to 0.785 and the swirl parameter in a range of up to $10^{-5} < S_o < 10^5$. We significantly extend the data range for the IRSPF for which only results for $\epsilon = 0.0256$, 0.1299 and 0.333 were available up to date in the literature. More significantly, we extend the data range for the ORSPF more than hundredfold, which was before solely investigated for low and intermediate swirls for $\epsilon = 0.333$ by Meseguer and Marques (2005). With the data we generate phase maps of Re_c, λ_c, n_c and ω_c in the ϵ-S_i and ϵ-S_o space. For the IRSPF, we identify three regions denoted as I, II and III and associated with low, intermediate and large swirls, respectively. We discover that the phase maps significantly depend on ϵ and reveal that for $\epsilon \geq 0.0513$ for the ORSPF, also three regions can be identified (IO, IIO and IIIO) which are associated with low, intermediate and large swirls, respectively. To identify and analyze the instabilities in the different regions (I; II; III and IO; IIO; IIIO), we evaluate the budget of the kinetic disturbance energy K, the Reynolds shear stresses as well as the production terms of the Reynolds Shear Stress Transport Equations (RSSTE). To the authors knowledge, this is the first time the RSSTEs were utilized for the interpretation of linear stability analysis results.

In region I and IO the critical Reynolds number does only change slightly for both the IRSPF and the ORSPF. We show, that here the production of K as well as the production of the shear stress τ_{rx} is mostly due to axial shear and there exists a critical layer according to the definition of Vasanta Ram (2019). Hence, a shear instability associated with a critical layer is dominant as already assumed by Cottrel and Pearlstein (2004) and Cottrel et al. (2004) for $\epsilon = 0.0256$, 0.1299 and 0.333. We further show, that in the second region (II, IIO) the same centrifugal instability mechanism is present for both the IRSPF and the ORSPF. The onset of this centrifugal mechanism is associated with a jump of the critical wavenumbers and leads to a sharp collapse in the critical Reynoldsnumber (Re_c) with increasing swirl within the second region. This centrifugal instability mechanism is characterized by a radical redistribution of kinetic disturbance

energy and a centrifugal production of the shear stress τ_{rx}. A characteristic feature within the beginning of the second region is that the shear stresses, K and the associated production terms assume a striking similarity for both the IRSPF and ORSPF. Further, at the beginning of the second region, the production of the kinetic disturbance energy K mostly emerges from axial shear $\overline{P_K(V_x)}$ of the base flow. By revealing this similarities, to the authors best knowledge, here for the first time a direct connection between the instability mechanism found in the IRSPF and the ORSPF is made. However, when the swirl increases in the second region, the azimuthal shear production of K ($\overline{P_K(V_\varphi)}$) increases which leads to a further destabilization of the IRSPF. Contrary, $\overline{P_K(V_\varphi)}$ attains a different sign in the ORSPF which leads to a strong stabilization associated with a sharp increase of Re_c. This reveals striking differences between the IRSPF and ORSPF and uncovers an ambivalent effect of outer cylinder rotation on the stability of the flow.

For the IRSPF in the third region (III), the shear stresses, K and the associated production terms attain a similar distribution as in II and still a centrifugal instability is present which further leads to a destabilization with increasing swirl. The onset of III is associated with the axial shear production of K ($\overline{P_K(V_x)}$) dropping to zero. In contrast, for the ORSPF in the third region (IIIO) the distributions of shear stresses, K and associated production terms change strikingly. The position of their maxima switches from close to the outer cylinder to close to the inner cylinder, where a critical layer becomes evident. While the shear production acts as a source here for the shear stresses, the centrifugal production acts as a sink and hinders production of shear stresses. It is concluded that a Tollmien-Schlichting instability is dominant which coincides with the assumptions of Deguchi (2017).

Besides the aforementioned observations for the IRSPF and the ORSPF, significant differences are found for the ORSPF for smaller curvature parameters of $\epsilon \leq 0.0513$. For $\epsilon \leq 0.0509$ there is no transition from region IO to region IIO and the flow transits directly from region IO to region IIIO as S_o increases. For $\epsilon \leq 0.0509$ it is discovered, that region I associated with a TSI persists up to swirl parameters where the azimuthal flow component is significantly larger than the axial flow component. To the authors knowledge, this has never been observed before for any configuration of the SPF. Moreover, for $\epsilon \leq 0.0509$ outer rotation stabilizes the flow monotonously in region I and III and the critical Reynolds number quickly increases monotously up to values beyond $Re_c > 1.5 \cdot 10^5$ as S_o increases. Thereby, in region IO the stabilization is associated with the critical layer moving closer to the wall. Furthermore, we discover that for $0.0513 < \epsilon \leq 0.059$ the flow transits to IIO and then falls back to IO before finally transiting to IIIO as the swirl increases. For $0.0513 \leq \epsilon \leq 0.0526$ the flow even switches multiple times between IO and IIO before falling back to IO and ultimately transiting to IIIO as the swirl increases. These switches are associated with radical redistributions of the shear stresses which clearly confirm the competition of two instability mechanisms

here. This drastically shows the ambivalent effect of outer cylinder rotation, which can both trigger and damp centrifugal instabilities depending on curvature parameter and swirl.

4 Applying APTV to suspension flows with transparent particles [1]

In this chapter a method is developed to apply Astigmatism Particle Tracking Velocimetry (APTV) to transparent particles utilizing backlight illumination. Here, a particle acts as ball lens and bundles the light to a focal point, which is used to determine the particle's out-of-plane position. Compared to conventional APTV additional features have to be considered in Ball Lens Astigmatism Particle Tracking Velocimetry (BLAPTV) due to the distance between the focal point and the particle. All required calibration steps are described and it is analyzed how the autorrelation coefficient and the light intensity affect the accuracy of the method. We further extend the Euclidean calibration approach (Cierpka et al., Meas Sci Technol 21 (045401): 13, 2010a) by additional considering the particle's light intensity, which is found to increase the accuracy and robustness of the depth reconstruction. In addition, we study the influence of the particle diameter and the refractive index jump between liquid and particles on the calibration curves and the accuracy. In this way, particles of the same size, but different material, can be distinguished by their calibration curve. Furthermore, an approach is presented to account for shape changes of the calibration curve along the depth of the measurement volume.

The chapter is structured as follows: In section 4.1 the measurement principle is elaborated and the special features of BLAPTV are discussed. Section 4.2 adresses the procedure of calibration measurements. It is explained which properties of the particle and its focal point are extracted during the calibration procedure. Based on these calibration measurements 2D and 3D Euclidean calibration curves are generated, which is explained in section 4.3. Subsequently, in section 4.4 and section 4.5 it is discussed how image processing parameters and the intensity of the light source affect the accuracy of the depth position reconstruction procedure, respectively. In section 4.6, it is shown how particle size, refractive index of material and liquid as well as the magnification affect the shape of the calibration curves and the reconstruction accuracy. In section 4.7 BLAPTV is validated by measuring a laminar rectangular channel flow. A summary and conclusion is given in section 4.8. The theory and state of the art relevant for this chapter are given in section 1.2.2 (fundamentals of suspension flows) and section 1.2.4.3 (theory and state of the art of APTV). The setup utilized to obtain the results presented in the present chapter is described in section 2.1.1.

[1] This chapter is adopted from "Utilizing the ball lens effect for astigmatism particle tracking velocimetry." Experiments in Fluids 61.2 (2020): 1-19, written by Philipp Brockmann, Hamid Tabaei Kazerooni, Luca Brandt and Jeanette Hussong. Published under `https://creativecommons.org/licenses/by/4.0/`.

4.1 Measurement principle

In BLAPTV transparent particles are illuminated in bright-field mode as illustrated in Fig. 4.1. As the particle's refractive index differs from the surrounding liquid they act as ball lenses and focus the light, forming a focal point at some distance between particle and objective. A cylindrical lens, placed in front of the camera sensor, alters the light

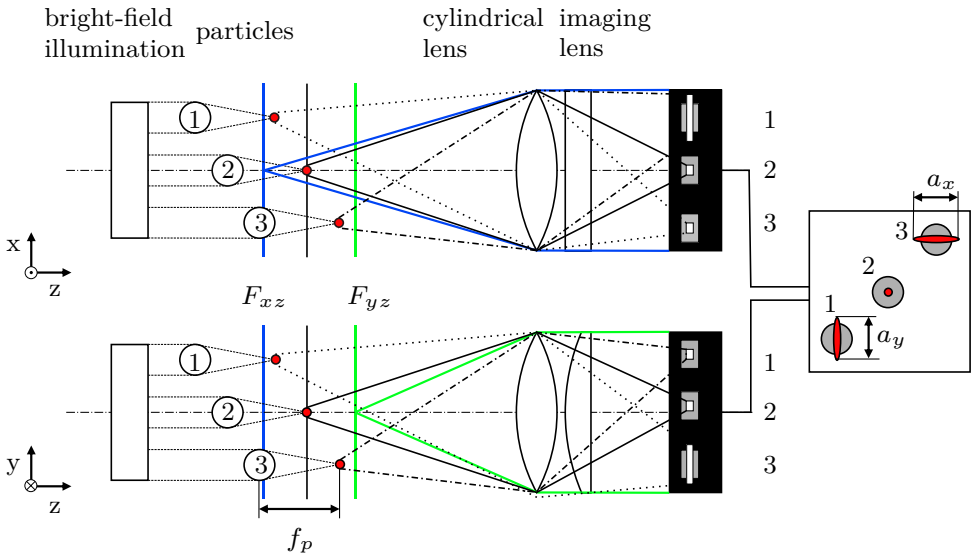

Figure 4.1: Illustration of the measurement principle: The particle's focal point (red dots) deforms in the image plane to a vertically or horizontally deformed ellipsoid depending on the particle's out-of-plane position (f_p=focal length of particle).

path resulting in two different focal planes for rays travelling in the xz and the yz plane. This induces astigmatism to the image of the particle's focal point (highlighted as red dots in Fig. 4.1), henceforth called "focal image". The shape of the focal image changes based on the z-location of the focal point with respect to the focal planes, denoted as F_{xz} and F_{yz} in the object plane (see Fig. 4.1). The shape of the focal image is circular when the particle's focal point is located approximately in the middle between both focal planes (see label "2" in Fig. 4.1) and it deforms to a vertically or horizontally stretched ellipsoid when the focal point is located closer to F_{xz} or F_{yz}, respectively (see label "1" and "3" in Fig. 4.1). In comparison to the focal image, the shape change of the particle image is not significant. In fact, the particle silhouette remains almost circular as it can be seen in Fig. 4.2a. Hence, it is the deformation of the focal image that will be used to determine the out-of-plane position of the particles. This shape change can be quantified by extracting the information of the length of the horizontal $a_x(z)$ and the vertical axis $a_y(z)$ of the ellipsoid (see Fig. 4.1). Hereafter, the ratio of

the major axis max[a_x, a_y] and minor axis min[a_x, a_y] of the focal image, is referred to as aspect ratio $a(z)=\frac{\max[a_x, a_y]}{\min[a_x, a_y]}$. Due to this definition the aspect ratio is always greater than one.

As mentioned before, there is a distance between a particle and its focal point, viz. the particle's focal length, which has to be considered for reconstructing the out-of-plane position of a particle. Measuring this distance is not a difficult task in a non-astigmatic (stigmatic) imaging system, as the system has only one focal plane. This can be done by scanning a stationary particle in z-direction to determine the scanning position at which the particle and its focal point are in focus. As there is no shape change of the focal image in the stigmatic case, the focal point is located in the focal plane when the focal image diameter is minimum. Note that the focal image always appears as a round bright spot in a stigmatic imaging system. For both stigmatic and astigmatic systems, the particle position along the scanning path can be found where the particle center plane is located in the focal plane (F_{xz}=F_{yz}). Hence the focal length can be calculated as the difference between the particle and its focal point position, hereafter referred to as ΔF_{yz}=ΔF_{xz}.

However, in the presence of a cylindrical lens, the imaging system features two focal planes and hence the particle's "focal length" can be determined with respect to both focal planes (F_{xz} and F_{yz}). To determine the out-of-plane position of a particle with respect to its focal point, one can choose either ΔF_{xz} or ΔF_{yz} as a reference length. Preferably, the reference length should be considered which can be determined more accurately. Theoretically ΔF_{yz} and ΔF_{xz} should be identical. Nonetheless, because different methods are used to determine the particle's position and its focal points position, measured values of ΔF_{yz} and ΔF_{xz} may slightly differ, depending on the refractive index of liquid and particles or the magnification. Hereinafter, the particle's focal length measured in an astigmatic system is referred to as $\Delta F_{yz}\approx\Delta F_{xz}$. Similar to the stigmatic optical system ΔF_{xz} and ΔF_{yz} can be deducted from a scanning procedure. Here, the focal point is located in F_{xz} or F_{yz} when the axis length a_x or a_y is minimum, respectively. The particle itself is in focus when either F_{xz} or F_{yz} pass the particle's center plane during the scanning procedure. Knowing these positions in the depth direction, the focal length of a particle ($\Delta F_{xz}\approx\Delta F_{yz}$) can be defined in an astigmatic optical system. The particle's focal length is approximately linearly proportional to the particle diameter and can be estimated by the lensemaker's equation (see section 4.6).

4.2 Calibration measurement procedure

To determine the particle's focal length $\Delta F_{xz}\approx\Delta F_{yz}$ as well as the change of the aspect ratio $a(z)$ of the focal image, wall-attached particles are scanned in 1 µm steps typically over a range of 500 µm such that the shape change of the focal image and the focusing and defocusing of the particle itself is fully captured, as shown in Fig. 4.2 for a 60 µm

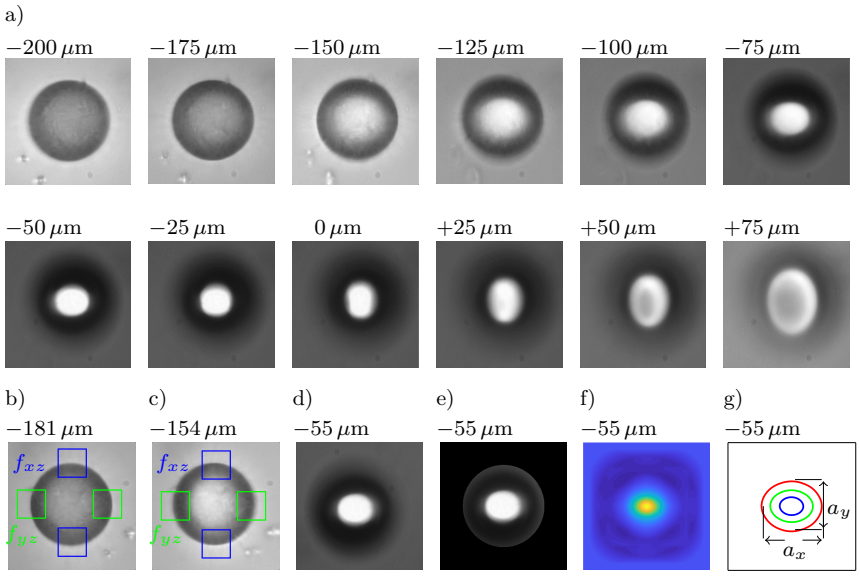

Figure 4.2: a) Particle images for different depth positions z (d_p=60 µm, PMMA, z corrected for 25wt% glycerol-water solution). b,c) ROI for focus measures f_{xz}, f_{yz}. b) Particle is focused in F_{yz}. c) Particle is focused in F_{xz}. d) Raw particle image. e) Cropped particle image. f) Autocorrelation map of Fig. 4.2e. g) Autocorrelation iso-contours (red line c_a=0.7, green line c_a=0.4, blue line c_a=0.155).

PMMA particle with M=20× magnification in a 25wt% glycerol-water solution. Figures 4.2b and 4.2c show the particle located in the focal planes F_{yz} and F_{xz}, respectively. To determine ΔF_{xz} and ΔF_{yz} a focus detection algorithm based on the Tenengrad variance is applied in four regions of interest (ROI) at the edge of the particle image and delimited by the green and blue squares in Fig. 4.2b,c according to Pertuz et al. (2013). The computed values of the Tenengrad variance are a measure for the sharpness of an object image, henceon referred to as f_{xz} and f_{yz}. The maximum values of f_{xz} (blue ROI) and f_{yz} (green ROI) show that the focal planes F_{xz} and F_{yz} are located at the center plane of the particles, respectively. Please note that the maxima of f_{xz} and f_{yz} can be used to detect the particle center during a scanning procedure to define the absolute coordinate system with respect to the channel wall as will be described in section 4.7. If the scanning procedure is continued, the particle image defocusses and the focal image is characterized by varying axis lengths a_x and a_y (Fig. 4.2a,−75 µm<z<75 µm). It can be seen that the shape change of the focal image is much more pronounced than the shape change of the particle itself, which almost remains circular. $a_x(z)$ and $a_y(z)$ and their ratio $a(z)$ are determined with an autocorrelation method as indicated in Figs. 4.2d-g. First, the image of the detected particle (Fig. 4.2d) is cropped out by the particle radius (see Fig. 4.2e). Hence, an autocorrelation is applied to the image section and the aspect ratio of the auto-correlation peak is determined by extracting

isocontours at a fixed threshold (see Fig. 4.2f,g). This procedure was found to be insensitive to light intensity fluctuations (Cierpka et al. 2010a). The threshold at which the aspect ratio is determined will hereafter be referred to as autocorrelation threshold c_a.

To illustrate the influence of the particle image size and induced astigmatism on the calibration procedure, a 60 µm PMMA particle is dispersed in water and the same scanning procedure is repeated four times at M=20× and M=10× with (astigmatic case) and without cylindrical lens (stigmatic case) (see Fig. 4.3). The z-position where $a_x(z)$ assumes its minimum value, is chosen as the reference position, referred to as z_0 such that $a_x(z{=}z_0)$ assumes a minimum. As expected and shown in Fig. 4.3a and c, without cylindrical lens, the focal planes F_{xz} and F_{yz} collapse onto each other. This is why the evolution of the particle image sharpness measures f_{xz} and f_{yz} is identical for both magnifications (see Fig. 4.3a,c). f_{xz} and f_{yz} attain their maximum where the focal plane reaches the center of the particle (highlighted with $F_{xz}{=}F_{yz}$), hence the particle itself is focused (see Fig. 4.3a,c). As the scanning procedure is continued further, the focal plane ($F_{xz}{=}F_{yz}$) passes the particle and consequently f_{xz} and f_{yz} decrease again, as the particle itself gets defocused. As z-z_0 increases more, the focal planes now get closer to the focal point of the particle. This is illustrated in the insets I1-I3 of Figs. 4.3a,c with the respective z-z_0 positions highlighted by the crosses in the plots. As the focal plane moves towards the particle's focal point, the axis lengths of the focal image $a_y(z\text{-}z_0)$, $a_x(z\text{-}z_0)$ shown in Fig. 4.3a,c, decrease till the focal point is located at $F^*_{xz}{=}F^*_{yz}$ (z-z_0=0). As no astigmatism is involved in the results presented in Fig. 4.3a,c, the aspect ratio $a(z\text{-}z_0)$ is constantly one. The distance between the particle and its focal point is given by $\Delta F_{xz}{=}\Delta F_{yz}$ (see Fig. 4.3a,c), which is 130 µm and 119 µm for the particle in Fig. 4.3a and Fig. 4.3c. The distance between a particle and its focal point can be estimated by the lensemaker's equation for thick lenses. With the refractive index of the liquid n_L and of the particle n_p the focal length f_p of a ball lens, that is the particle in the present case, can be expressed as (4.1):

$$\frac{1}{f_p} = \frac{4\,(n_p - n_L)}{n_L} \frac{\left(n_p - \frac{n_p - n_L}{n_L}\right)}{n_p\, d_p} \tag{4.1}$$

For a PMMA particle with d_p=60 µm (n_p=1.49) in water (n_L=1.333) the lensemaker's equation (4.1) results in f_p=138 µm. This approximates the measured values quite well.

As mentioned before, if astigmatism is involved two focal planes coexist ($F_{xz}{\neq}F_{yz}$). In this case F_{yz} is shifted closer towards the camera (see Fig. 4.1). Thus, f_{yz} assumes its peak value at a lower z-z_0 compared to f_{xz} (see Fig. 4.3b,d) and the aspect ratio $a(z\text{-}z_0)$ shows its characteristic M-shape (see black curves in Fig. 4.3b,d). As mentioned before, the focal image appears circular in the image plane only when the focal point in the object plane is located inbetween the focal planes F_{yx} and F_{zx}, that is when $a_x{=}a_y$ (see Fig. 4.3b,d). The distance between both focal planes can be determined from Fig. 4.3b,d. This is equal to the distance F_{xz}-F_{yz} which equals F^*_{xz}-F^*_{yz} (see Fig. 4.3b,d).

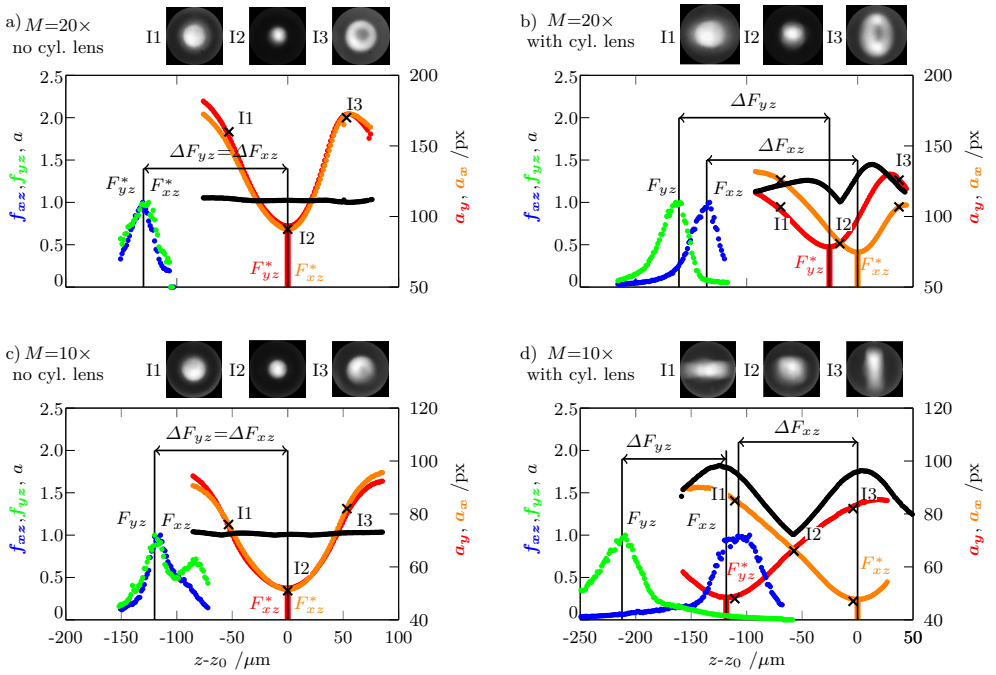

Figure 4.3: Calibration measurements in water with PMMA particles of d_p=60 µm (c_a=0.4095). The z-position where a_x is minimum (F^*_{xz}) is taken as reference position z_0. a) Without cylindrical lens for M=20×. b) With cylindrical lens for M=20×. c) Without cylindrical lens for M=10×. d) With cylindrical lens for M=10×. Symbols: black dots=a, blue dots=f_{xz}, green dots=f_{yz} (see Fig. 4.2b,c), red dots=a_y and orange dots=a_x.

For M=10× (Fig. 4.3d) this distance is significantly larger than for M=20× (Fig. 4.3b). The distance between the particle and its focal point is given by $\Delta F_{xz} \approx \Delta F_{yz}$ that is ΔF_{xz}=136 µm≈ΔF_{yz}=135.6 µm for M=20× and ΔF_{xz}=107.33 µm≈ΔF_{yz}=94 µm for M=10× as depicted in Fig. 4.3b and d, respectively. Thus, there is a good agreement with equation (4.1) for M=20×. However, the discrepancy observed for M=10× requires further investigations to be explained in future.

For an overview on the effect of magnification, the properties of the cylindrical lens, the distance of the focal planes on the measurement range in the context of conventional APTV, the reader is referred to Chen et al. (2009), Cierpka et al. (2010a) and Rossi and Kähler (2014). Figs. 4.4a and b display the evolution of the light intensity of the focal image for a d_p=60 µm PMMA particle in water for M=20× and M=10×, with and without cylindrical lens. For M=20× the evolution of the light intensity with and without cylindrical lens remains similar (Fig. 4.4a). In contrast, for M=10× the light intensity exhibits two peaks close to F^*_{yz} and F^*_{xz} when a cylindrical lens is mounted in the system (Fig. 4.4b). This is because the distance between the focal planes F_{yz}-F_{xz} is significantly larger for M=10× than for M=20× (see Fig. 4.4a,b). Please note that

the effective magnification is higher in the stigmatic case, as the distance between field lens and camera sensor is altered ($M_{stig}/M_{astig} \approx 125\%$). This is why for M=20× the maximum light intensity is higher in the astigmatic case (see Fig. 4.4a). Figures

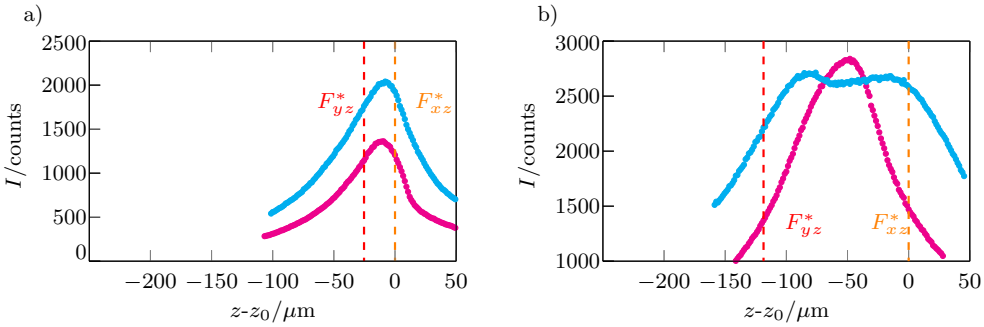

Figure 4.4: Maximum light intensity of the focal image for a d_p=60 µm PMMA particle in water. Pink dots=without cylindrical lens, light blue dots=with cylindrical lens a) M=20×. b) M=10×. The focal planes are highlighted by the dashed lines.

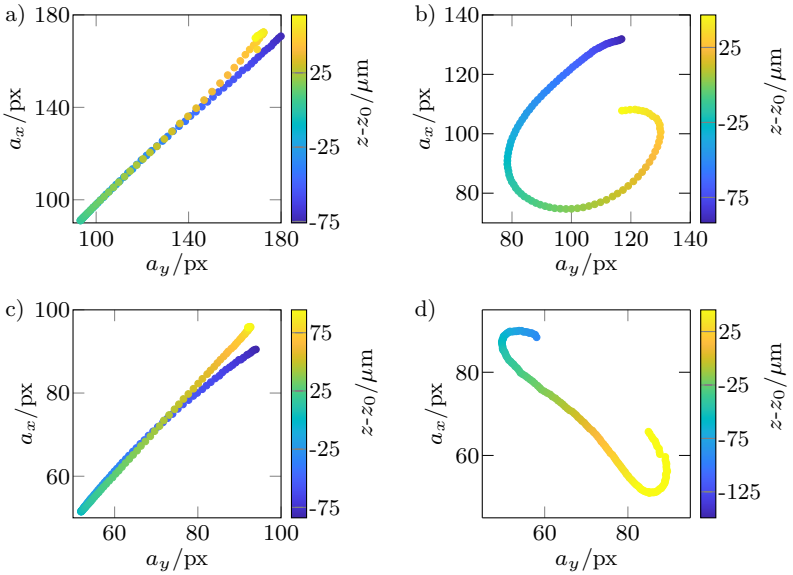

Figure 4.5: a_x as function of a_y for a d_p=60 µm PMMA particle in water (corresponding to Fig. 4.3) (c_a=0.4095). The color map indicates the out-of-plane position z-z_0. a) M=20×, without cylindrical lens. b) M=20×, with cylindrical lens. c) M=10×, without cylindrical lens. d) M=10×, with cylindrical lens.

4.5a-d show a_x as function of a_y for a d_p=60 µm PMMA particle in water with M=20× and M=10×, each with and without cylindrical lens. As can be seen, a_x is directly proportional to a_y in the stigmatic case (Fig. 4.5a,c). When astigmatism is introduced,

a_x plotted over a_y shows a characteristic curled curve (Fig. 4.5b,d). Thus, every a_y, a_x pair is associated with just one z-z_0 value (Fig. 4.5b,d). This form of representation is the base for the out-of-plane reconstruction based on the Euclidean calibration approach which will be discussed and utilized in the next section.

4.3 Reconstruction of the out-of-plane particle position and outlayer detection

The calibration procedure described in section 4.2 is repeated for several particles randomly distributed over the field of view. The major steps to generate a calibration function from which the out-of-plane particle positions can be determined are illustrated in Fig. 4.6 for a total number of 36 calibration particles. In fact, for all results presented later in this work at least ten calibration particles have been used. In the first step, $a_x(z\text{-}z_0)$, $a_y(z\text{-}z_0)$ and the maximum intensity $I(z\text{-}z_0)$ of all focal images that are taken at different out-of-plane positions (z-z_0) are superimposed. Hence, the median curve of I is generated, denoted as $\overline{I}$ (see Fig. 4.6a). From the median intensity curve $\overline{I}$ the maximum value $\overline{I}_{max}$ is determined (see Fig. 4.6a). The out-of-plane measurement volume depth Δz is determined by only considering data that fullfills the following criterion: $\mathrm{I} \geq \overline{I}_{max} \cdot c_I$ (see vertical dashed lines in Fig. 4.6a). c_I is herafter referred to as the intensity coefficent and its influence on the relative measurement accuracy will be discussed in section 4.4. In the next step a polynominal of 14th order is fitted to the a_x and a_y scatter data. The resulting fitting curves $\overline{a_x}(z\text{-}z_0)$ and $\overline{a_y}(z\text{-}z_0)$ are shown in Fig. 4.6b. The actual calibration function now consists of three data sets, $\overline{a_x}$, $\overline{a_y}$ and z-z_0 which can be represented as one calibration curve with $\overline{a_x}$ plotted as function of $\overline{a_y}$, see Fig. 4.6c. This is known as the 2D calibration curve in APTV. For the sake of clarity, we divide the calibration curve into three equal sections A, B and C with respect to the depth position z-z_0. The section borders are indicated with white dots in Fig. 4.6b-f.

As mentioned before, z_0 is the relative z-position where a_x assumes its minimum value. With this data at hand we can reconstruct the z position of the focal point of a particle with respect to z_0. Fig. 4.6c shows the scatter data of a_x plotted as a function of a_y and the calibration curve obtained from $\overline{a_x}$ plotted over $\overline{a_y}$. To determine the z-z_0 position, measured a_x, a_y values are associated to a point on the calibration curve that is given by the minimum Euclidean distance (see Fig. 4.6c). Henceon, this method is referred to as Euclidean method and is described in detail by Cierpka et al. (2010a). If the Euclidean distance of a pair of a_x, a_y values exceeds a certain threshold the measurement data is rejected. This threshold will be henceon referred to as a_D and is defined as the mean Euclidean distance of all a_x and a_y pairs of all calibration particle images multiplied by the factor c_D (4.2):

$$a_D = \frac{c_D}{N} \sum_{i=1}^{N} \min \sqrt{(\overline{a_x}\text{-}a_{x,i})^2 + (\overline{a_y}\text{-}a_{y,i})^2} \tag{4.2}$$

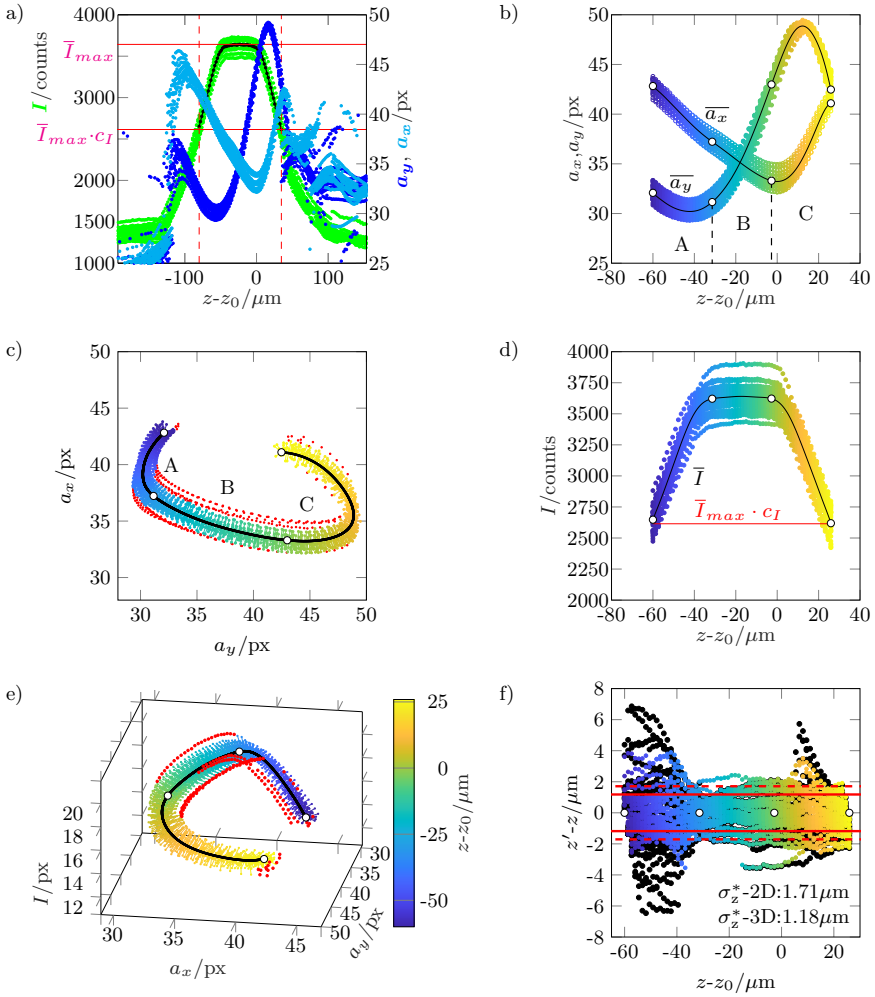

Figure 4.6: Procedure of generating a calibration function. Scale of colormap in Fig. 4.6b-f is given in 4.6e. z-z_0 data is corrected for refractive index of a 25wt% glycerol-water solution (d_p=30 µm, M=20×, c_a=0.7, c_I=0.7, c_D=2). a) Selecting z-z_0 range of scattered data by light intensity I (light dots=a_x, dark blue dots=a_y, green dots=I, black line=$\overline{I}$). b) Fitting polynomials of degree 14 to a_x and a_y (black line=polynomials $\overline{a_x}$, $\overline{a_y}$). c) Reconstruction of z-z_0 of scattered a_x-a_y data (colored dots) by Euclidean distance with the 2D calibration curve (black line=polynomial, red dots=outliers). d) Fitting polynomials of degree 14 to I (black line=polynominal $\overline{I}$). e) Reconstruction of z-z_0 of scattered a_x-a_y-I data (colored dots) by Euclidean distance with the 3D calibration curve in the a_y-a_x-I space (black line=polynomials). f) Position reconstruction error z'-z plotted over z-z_0 obtained with the 3D calibration curve (colored dots) and the 2D calibration curve (black dots). The uncertainty of the 2D and 3D position reconstruction procedure is σ_z^*=1.71 µm and σ_z^*=1.18 µm, respectively.

with N being the total number of the calibration particle images. For the given case the factor is set to c_D=2 with the detected outliers indicated as red dots in Fig. 4.6c.

Particles may differ in terms of shape, roughness and refractive index such that their a_x, a_y, I or z-z_0 data deviates from the majority of the particles. Moreover, we noticed that the change of the particles light intensity can be used as additional information to encode the particles depth position. It is also observed that the calibration curve may intersect in the a_y, a_x space resulting in a large uncertainty in estimating the depth position of a particle (see section 4.4). To reduce such problems, we use the information of the particles light intensity as an extra parameter to increase the accuracy and robustness of the calibration procedure. In fact, using a polynomial fit of 14th degree to the I scattered data $\overline{I}(z\text{-}z_0)$ (see Fig. 4.6d) we extend the 2D (a_y-a_x) calibration curve to 3D a_y-a_x-I space (see Fig. 4.6e). As for the 2D case, the z-z_0 position of scattered data is determined by assigning measured a_x-a_y-I values to a point on the calibration curve that is given by the minimum 3D Euclidean distance (see Fig. 4.6e). To facilitate computation of the 3D Euclidean distance, the light intensity is transformed to the same order of magnitude as a_y and a_x by normalization with $\overline{I}_{max}$ and multiplication with the maximum width or height of the 2D calibration curve. Data points which are too far away from the 3D-calibration curve are rejected as indicated with red dots in Fig. 4.6e. Similar to the 2D case, the threshold a_D for rejecting data is defined as the mean Euclidean distance of all a_x, a_y and I pairs of the calibration set multiplied by a factor c_D (4.3):

$$a_D = \frac{c_D}{N} \cdot \sum_{i=1}^{N} \min \sqrt{(\overline{a_x}\text{-}a_{x,i})^2 + (\overline{a_y}\text{-}a_{y,i})^2 + (\overline{I}\text{-}I_i)^2} \tag{4.3}$$

For the given case the factor is set to c_D=2.

From Fig. 4.6c a strong increase in the 2D calibration curve curvature becomes evident in regions A and C, while the curve is almost linear in region B. Furthermore, the arclength of A is small compared to B and C. These topoligical differences result in different depth position reconstruction accuracies in A,B,C as depicted with the black dots in Fig. 4.6f. Here we show the difference of the reconstructed depth position z'-z_0 and the true scanning position z-z_0 (z'-z) as a function of z-z_0 (Fig. 4.6f). As can be seen the out of plane reconstruction error with the 2D calibration curve sharply increases in regions A and C where the curvature assumes maximum values. In contrast to this, the 3D calibration curve enables a more accurate assignment of data and significantly reduces the error in regions A and C (see colored dots in Fig. 4.6f). This leads to a total reduction of 30% in the reconstruction uncertainty for the 3D calibration procedure in comparison to the 2D one (σ_z^*=1.71 µm for 2D vs σ_z^*=1.18 µm for 3D). Furthermore, the 3D reconstruction procedure increases the number of valid data points which are N_{valid}=1995 and N_{valid}=2120 (+6%) for the 2D and the 3D case, respectively.

With the steps mentioned above we reconstruct the out-of-plane position of the particle's focal point relative to z_0 with σ_z^* being the associated uncertainty. To determine the absolute uncertainty in reconstructing the particle's out-of-plane position, the uncertainty in determining the particle's focal length $\Delta F_{yz} \approx \Delta F_{xz}$ has to be considered: $\sigma_z = \sqrt{\sigma_z^{*2} + \sigma(\Delta F_{xz})^2}$. Therefore, the overall reconstruction accuracy of the out-of-plane particle position of a 30 µm PMMA particle in the given example is σ_z=3.11 µm and σ_z=2.85 µm for the 2D and the 3D calibration curve, respectively. A detailed analysis of the out-of-plane reconstruction accuracy for different particle sizes is given in section 4.6.

4.4 The influence of the autocorrelation threshold c_a on the relative out-of-plane reconstruction accuracy

The relative out-of-plane reconstruction uncertainty $\sigma_z^*/\Delta z$ depends on the choice of the threshold values c_a and c_I. Therefore, an optimization study is performed for both threshold values c_I of the focal image light intensity and c_a of the autocorrelation. The optimization study is done with M=20× and PMMA particles of d_p=60 µm diameter in water. To account for the aberrations of particle images at different in-plane positions, calibration particles (here 14 particles) are randomly distributed over the whole field of view. As, the signal strength of the focal image depends on the light sensitivity of a camera, the same measurements are performed with a light sensitive CCD camera (LaVision Imager Pro SX) and a CMOS camera (Miro 110 Phantom). To ensure comparability of both cameras the same group of particles is used for both calibrations. For both parameter sets, we determine the optimum combination of c_a and c_I that leads to a minimum relative out-of-plane reconstruction uncertainty $\sigma_z^*/\Delta z$ ($0<c_a<1$ and $0<c_I<1$). The resulting uncertainties are plotted in Figs. 4.7a and b as function of c_a, for the optimum value of c_I for both camera types. As c_I only affects Δz, whereas c_a affects σ_z^* as well, we focus on discussing c_a for fixed c_I.

Different light intensities are used, given here as ratio of the median image intensity of the whole image c_{med} and the maximum camera intensity c_{max}, which is 8-bit (4096 counts) for both the CCD and the CMOS camera. Tests showed that the median of the whole image c_{med} is equal to the median of the background intensity without the particles. Hence, c_{med}/c_{max} describes the normalized background illumination intensity. As we use backlight-illumination, the background intensity is directly proportional to the illumination intensity. Hence, the parameter c_{med}/c_{max} can be easily adjusted prior to the measurements by simply increasing the illumination intensity. The influence of the light intensity will be discussed in section 4.5 in further detail.

Four characteristic regions of c_a can be identified in Figs. 4.7a and b denoted as A-D. Obviously, a range of c_a values between $0.40<c_a<0.75$ (denoted with C) leads to uncertainties $\sigma_z^*/\Delta z$ below 2% for both camera types. The corresponding, optimized

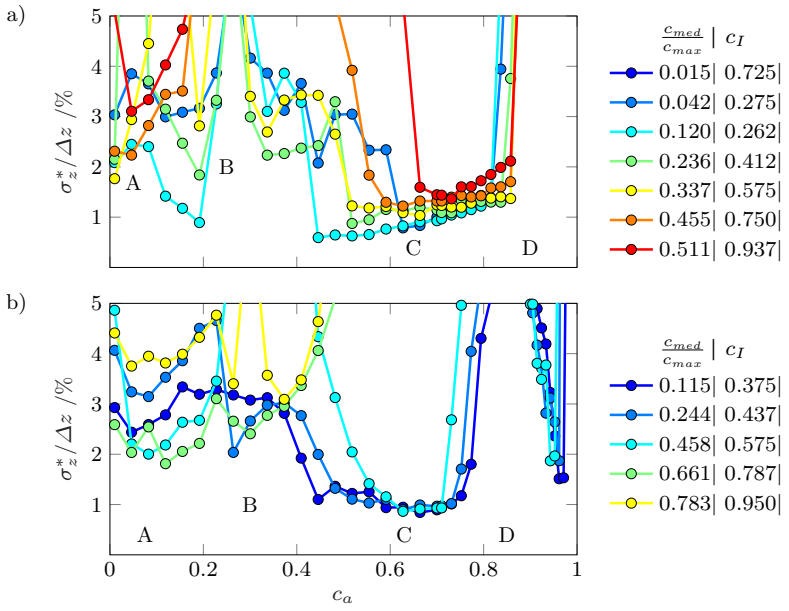

Figure 4.7: $\sigma_z^*/\Delta z$ over c_a for different c_{med}/c_{max}. All data is presented using optimal c_I (M=20×, d_p=60 µm, water, c_D=3). a) CCD camera. b) CMOS camera.

c_I values are given in the legend. For lower or higher values of c_a (regions denoted with A, B and D in Fig. 4.7) the relative out-of-plane reconstruction uncertainty sharply increases due to ambiguities in the corresponding calibration curves. This can be better understood from the calibration curves in the a_y-a_x-I-space as plotted in Figs. 4.8a-d. Here, where we report the 3D calibration curves (Figs. 4.8a-d II) and their projections onto the a_y-a_x plane (Figs.4.8a-d I). Please note that Figs. 4.8a-d correspond to regions A-D in Figs. 4.7a and b. While the calibration curves shown in Figs. 4.8a and c are continuous without intersections, those corresponding to regions B and D in Figs. 4.7a and b, exhibit a sharp kink (see Fig. 4.8b) or intersect in the a_x-a_y-I-space (see Fig. 4.8d). These characteristics lead to local ambiguities during the Euclidean reconstruction procedure and hence a sharp increase in the relative out-of-plane reconstruction uncertainty $\sigma_z^*/\Delta z$. It may be noted, that the a_x and a_y data are typically used in fluorescence APTV. In the present study, informations on I are additionally utilized to derive 3D calibration curves for BLAPTV. Fig. 4.8c I and II reveal that ambiguities in the 2D a_x-a_y space can be avoided by this extended calibration, giving rise to an improvement evaluation accuracy with a stable c_a range of low relative out-of-plane reconstruction accuracies $\sigma_z^*/\Delta z$ as mentioned earlier (see region C in Figs. 4.7a,b). Furthermore, preliminary tests (not shown here) indicate, that significant improvements in the reconstruction accuracy may also be realized for fluorescence APTV by utilizing calibration curves in a_x-a_y-I-space. Finally, Figs. 4.7a and b indicate that lower light intensities corresponding to lower values of c_{med}/c_{max}<0.45

lead to a reduction of the relative out-of-plane reconstruction uncertainty $\sigma_z^*/\Delta z$. For

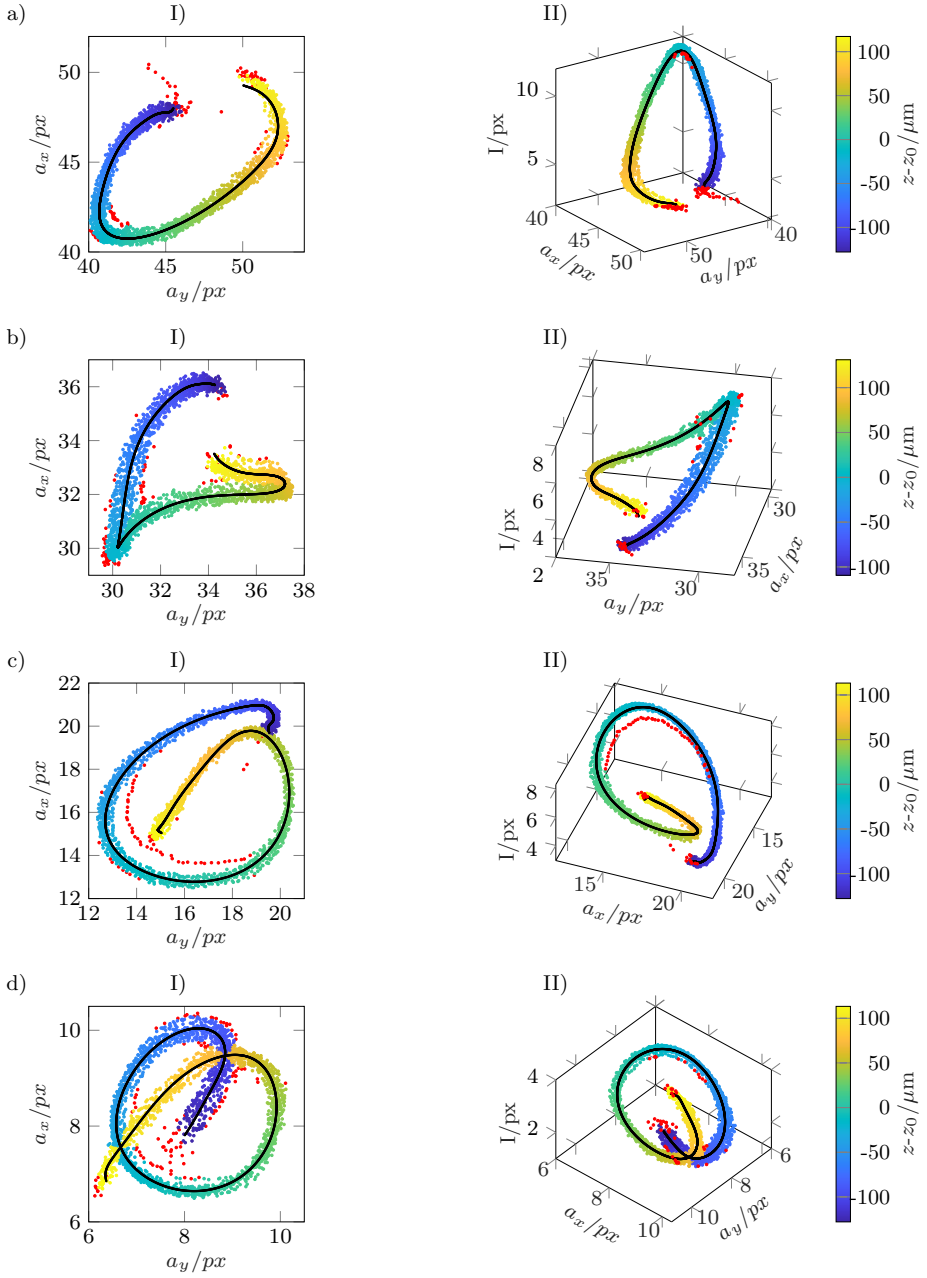

Figure 4.8: Calibration curves in a_x-a_y-space (I) and a_x-a_y-I-space (II) corresponding to A,B,C,D in Fig. 4.7b (CMOS, c_{med}/c_{max}=0.115, c_I=0.375, M=20×, d_p=60 µm, c_D=3, z-z_0 corrected for water). a) c_a=0.11 (A) b) c_a=0.33 (B) c) c_a=0.6637 (C) d) c_a=0.85 (D)

the cases under investigation, the in-plane position of particles has a negligable effect on the reconstruction accuracy compared to other parameters such as c_a, c_I and c_D. As said before, in this study each calibration is performed using particles that are randomly distributed across the field of view. Hence the resulting calibration curve can be considered as an averaged calibration curve. For all calibration measurements the mean value of the depth position reconstruction error for all individual particles is monitored. Results show a negligible difference in the reconstruction accuracy with respect to the in-plane particle position and associated aberrations. However, if the 3D calibration is applied to situations where a strong gradient of I is present across the image or a_x and a_y depend on the in-plane particle position, the in-plane position of particles has to be taken into account aswell in the calibration.

4.5 The effect of the light intensity

Due to the ball-lens effect, the light intensity of the focal image is much higher compared to the background light intensity. Thus the ratio of focal image and background intensity, denoted here as signal to noise ratio, varies for different particle materials, magnifications, particle sizes and liquid-particle combinations. It even varies with the depth position of a particle (see section 4.7). Thus, in pratice it may not be feasable to adjust the light intensity for each particle species, especially in a polydisperse suspension.

In the present section we investigate how the relative light intensity, defined here as the ratio between median image intensity c_{med} and the grayscale depth (maximum counts) of the camera c_{max}, influences the minimum achievable relative out-of-plane reconstruction uncertainty of a particle $\sigma_z^*/\Delta z$ (Fig. 4.9a). Henceon, the signal to noise ratios SNR, the measurement volume depths Δz, the number of valid data points N_{valid} and the c_I and c_a values that result from the optimization study (shown in Figs. 4.9b-f) are discussed. From Fig. 4.9a it can be seen that $\sigma_z^*/\Delta z$ assumes a minimum around $c_{med}/c_{max}\approx 0.1$. Please note, that $\sigma_z^*/\Delta z$ assumes just slightly larger values for the CMOS camera in comparison to the CCD camera for $c_{med}/c_{max}<0.5$. This is remarkable, as the resolution of the CMOS camera is significantly lower than the resolution of the CCD camera, that is 1.78 µm and 0.29 µm per pixel at $M=20\times$, respectively. For larger relative intensity values c_{med}/c_{max}, the relative uncertainty $\sigma_z^*/\Delta z$ increases.

The increase in $\sigma_z^*/\Delta z$ is accompanied with a decrease in the maximum signal to noise ratio (SNR) as shown in Fig. 4.9b. Here, the SNR is defined as the maximum intensity of the focal image ($\overline{I}_{\max}$) divided by the median of the background light intensity. As can be seen from Fig. 4.9b the SNR increases with decreasing intensity c_{med}/c_{max}. This trend is counterintuitive and is reversed for very low values of c_{med}/c_{max}. As c_{med}/c_{max} drops below $c_{med}/c_{max}<0.042$ for the CCD camera, the SNR decreases again due to the vanishing image contrast (Fig. 4.9b). On the other hand, it can be understood easily why the SNR decreases for $c_{med}/c_{max}>0.2$ and $c_{med}/c_{max}>0.4$ for the CCD and

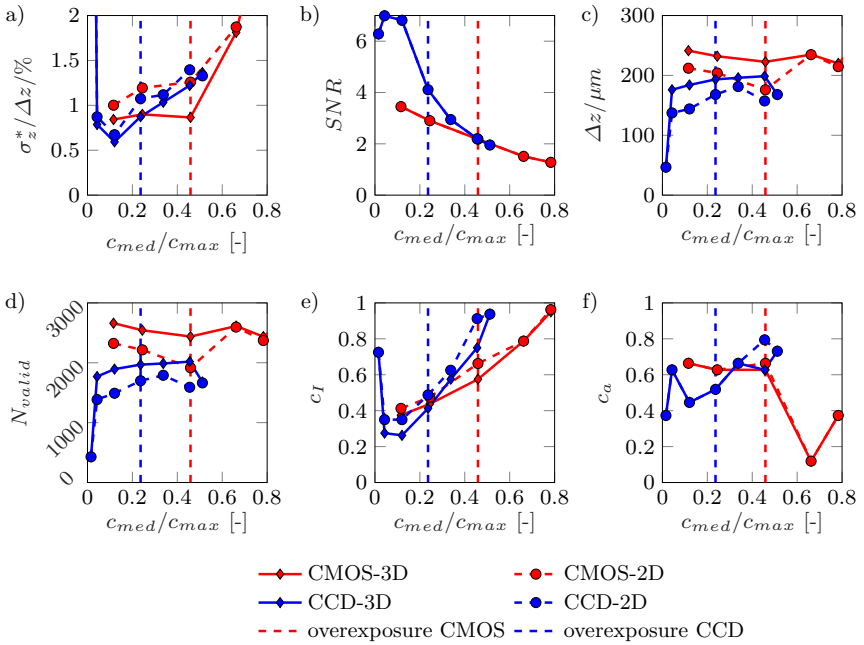

Figure 4.9: Optimized parameter values associated with minimum $\sigma_z^*/\Delta z$ plotted over c_{med}/c_{max} obtained with the 3D (solid lines) and the 2D (dashed lines) calibration procedure (M=20×, d_p=60 µm, water, c_D=3). a) Influence of c_{med}/c_{max} on $\sigma_z^*/\Delta z$. b) Maximum SNR as a function of c_{med}/c_{max}. c) Influence of c_{med}/c_{max} on Δz. d) Influence of c_{med}/c_{max} on valid particle images N_{valid}. e) Influence of c_{med}/c_{max} on c_I. f) Influence of c_{med}/c_{max} on c_a.

the CMOS camera, respectively. This is related to an overexposure of the focal image as indicated in Fig. 4.10a and b in which we display the evolution of the median light intensity of the focal image of all 14 particles $\overline{I}(z\text{-}z_0)$ for the CCD and CMOS camera. As the light intensity exceeds c_{med}/c_{max}>0.236 for the CCD and c_{med}/c_{max}>0.45 for the CMOS camera, the curve peak transforms into a plateau. Thus, the maximum exposure of the camera chip is reached. These limits are also indicated in Figs. 4.9a-f with vertical dashed lines for the CCD (blue) and CMOS (red) camera. Overall, for $c_{med}/c_{max}\leq$0.6 uncertainties $\sigma_z^*/\Delta z$ stay below 2%, thus the measurement technique is also applicable outside the optimal range of illumination, though loosing accuracy.

From Fig.4.9a a strong increase in $\sigma_z^*/\Delta z$ also becomes evident for the CCD camera when c_{med}/c_{max}<0.1. This can be better understood from Fig. 4.9c where the effective measurement volume depth Δz for BLAPTV is plotted as function of the relative light intensity. Here, Δz drops sharply for c_{med}/c_{max}<0.042, leading to an increase in relative uncertainty $\sigma_z^*/\Delta z$. We assume that the decrease of Δz originates from weaker signals of focal images with a focal point located behind or in front of the reference plane. In addition we observed that with decreasing c_{med}/c_{max}<0.1 the detection of particle

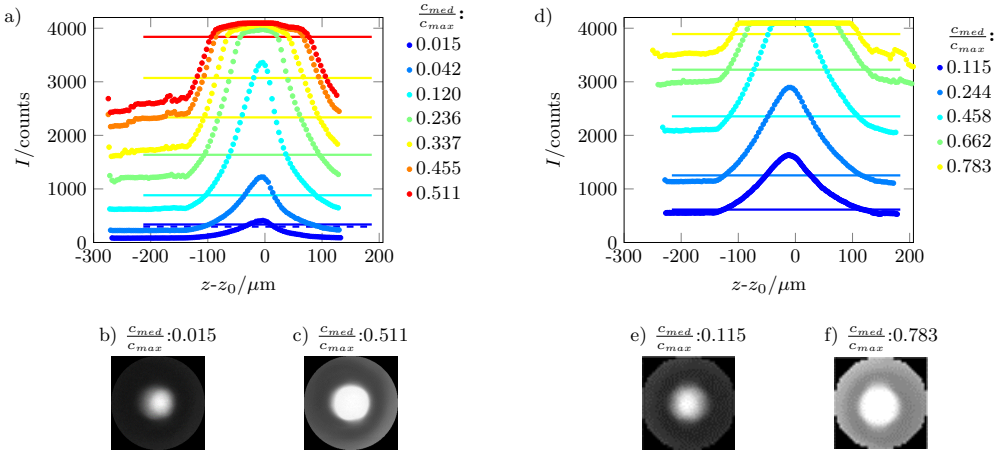

Figure 4.10: Median of I ($\overline{I}$) over z-z_0 for different c_{med}/c_{max}. Horizontal lines: $c_I \cdot \overline{I}_{max}$. M=20×, d_p=60 µm, z-z_0 corrected for refractive index of water. a) $\overline{I}$ over z-z_0 (CCD). b) Particle image at c_{med}/c_{max}=0.015 (CCD). c) Particle image at c_{med}/c_{max}=0.511 (CCD). d) $\overline{I}$ over z-z_0 (CMOS) e) Particle image at c_{med}/c_{max}=0.115 (CMOS). f) Particle image at c_{med}/c_{max}=0.783 (CMOS).

centers is increasingly erroneous. This leads to false a_x and a_y data and hence creates high uncertainties. The increasing number of misdetections for low values of c_{med}/c_{max} also leads to large standard deviations of the measured particle's focal length as will be discussed later in this section. Figs. 4.9a and c display the evolution of the relative uncertainty and effective measurement volume depth for a 3D calibration procedure in a_x-a_y-I space (solid lines) and the 2D calibration in a_x-a_y space (dashed lines). It may be noted that the 3D calibration procedure decreases the relative uncertainty and increases the effective measurement volume depth. Furthermore, utilizing a 3D calibration procedure increases the number of valid data points N_{valid} up to 26% (see Fig. 4.9d). The minimum relative uncertainty is determined based on an optimization of the c_I and c_a combinations for all tested light intensities. These values are plotted in Figs. 4.9e and f. Overall, the optimal values of c_I decrease, hence Δz increases, if 3D calibration curves are utilized instead of 2D calibrations in the a_x-a_y plane. Moreover, from Fig. 4.9f it can be seen that the optimal values of c_a differ for the CCD and CMOS camera depending on c_{med}/c_{max} and they are in the range of $0.38<c_a<0.7$ (CCD) and $0.6<c_a<0.7$ (CMOS) for c_{med}/c_{max} values below the onset of overexposure.

As discussed above the relative light intensity has a significant influence on the accuracy of the out-of-plane particle reconstruction. This can be better understood when the effect of c_{med}/c_{max} on the shape of the calibration curves is analyzed. For this, Fig. 4.11 depicts the calibration curves for selected values of c_a and Δz for both the CCD and the CMOS camera. As can be seen from Fig. 4.11a-d an increase in light intensity leads to an overall decrease of the calibration curve length. Furthermore, it can be observed

that the significance of this shape change depends on c_a. Comparing Fig. 4.11a and b, a much higher deformation of the calibration curve can be seen for c_a=0.118 in comparison to c_a=0.7. Here we conclude, that if the light intensity varies significantly across the image, the particle in-plane position has to be taken explicitly into account during the calibration procedure.

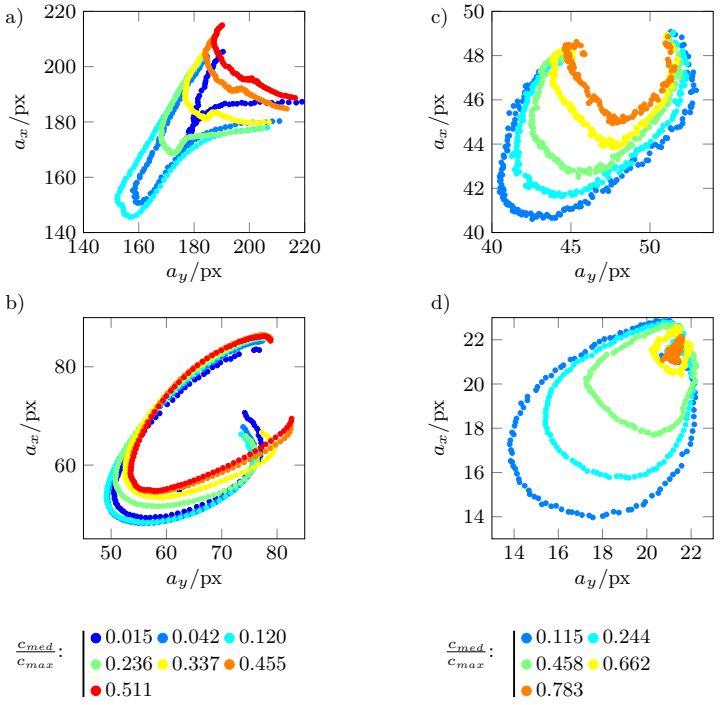

Figure 4.11: Influence of light intensity (c_{med}/c_{max}) on the calibration curve shape in the a_x-a_y plane for a single particle and fixed c_a and Δz. a) CCD, c_a=0.118, Δz=130 µm b) CCD, c_a=0.7, Δz=112 µm c) CMOS, c_a=0.118, Δz=217 µm d) CMOS, c_a=0.627, Δz=180 µm

As the light intensity affects the calibration curves, the question arises if it also affects the measured focal length of the particle, which is considered to be constant in theory. Fig. 4.12 shows the measured values of ΔF_{xz} and ΔF_{yz} plotted versus c_{med}/c_{max} for both the CCD and the CMOS camera. As can be seen for $0.015<c_{med}/c_{max}<0.5$ the measured values of ΔF_{xz} and ΔF_{yz} are in good agreement with the lensemaker's equation (black horizontal line). In particular, the values obtained with the CMOS camera show an excellent agreement.

As already stated before, for $c_{med}/c_{max}<0.015$ the detection of the particle centers becomes increasingly erroneous, leading to a sharp increase in ΔF_{xz} accompied by large standard deviations of ΔF_{xz} and ΔF_{yz} (vertical error bars). For $c_{med}/c_{max}>0.6$ (CMOS) measured values for ΔF_{xz} show signifcant deviations from the lensemaker's equation, yet for ΔF_{yz} there is still a good agreement. Overall, we conclude that

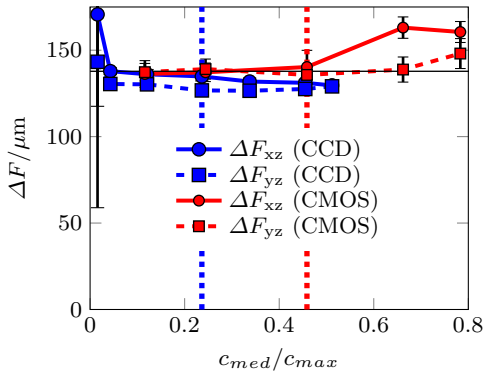

Figure 4.12: Effect of increasing light intensity $c_{\mathrm{med}}/c_{\mathrm{max}}$ on the measured focal length of d_p=60 µm PMMA particles in water for CCD and CMOS camera (M=20×, c_a=0.7 (CCD), c_a=0.6274 (CMOS)). The horizontal black line indicates the focal length calculated by the lensemaker's equation (4.1). The vertical blue and red dotted lines highlight the onset of overexposure for the CCD and the CMOS camera, respectively.

changes in c_{med}/c_{max} have a significant effect on the shape of the calibration curves, whereas the measured focal length of the particle, as a intrinsic feature of the particle itself, remains approximately constant. We will reconsider this observation in section 4.7.

4.6 Influence of particle size, material, liquid and magnification on the calibration properties

As BLAPTV is based on light being focused by particles, the optical properties of the system and the particles have an influence on the measurement technique. In this section we present a parametric study to understand the influence of the particle diameter d_p, the refractive index jump between particle and surrounding fluid Δn=n_p-n_L and the magnification M. From the lensemaker's equation (4.1) we conclude that the particle's focal length and hence $\Delta F_{xz} \approx \Delta F_{yz}$ will increase linearly with increasing d_p and decreasing refractive index jump between particle and liquid (Δn=n_p-n_L). As these parameters determine the aperture of the focused light behind a particle, they are expected to affect I_{max}, a_x, a_y and hence the aspect ratio $a(z\text{-}z_0)$ as a function of the out-of-plane position z-z_0. For the sake of comparison, the threshold for the autocorrelation and the threshold for the light intensity are kept constant in the following (c_a=0.4095, c_I=0.77). These values are found to provide satisfactory accuracy for the particle sizes and liquids discussed in this section. In Fig. 4.13a-c calibration measurements for single PMMA particles of d_p=30 µm, 60 µm and 124 µm are presented for a 25wt% glycerol-water solution at a magnification of M=20×. With increasing d_p a wider range of z-z_0 is covered by $a_y(z\text{-}z0)$ and $a_x(z\text{-}z0)$ (red and orange dots in

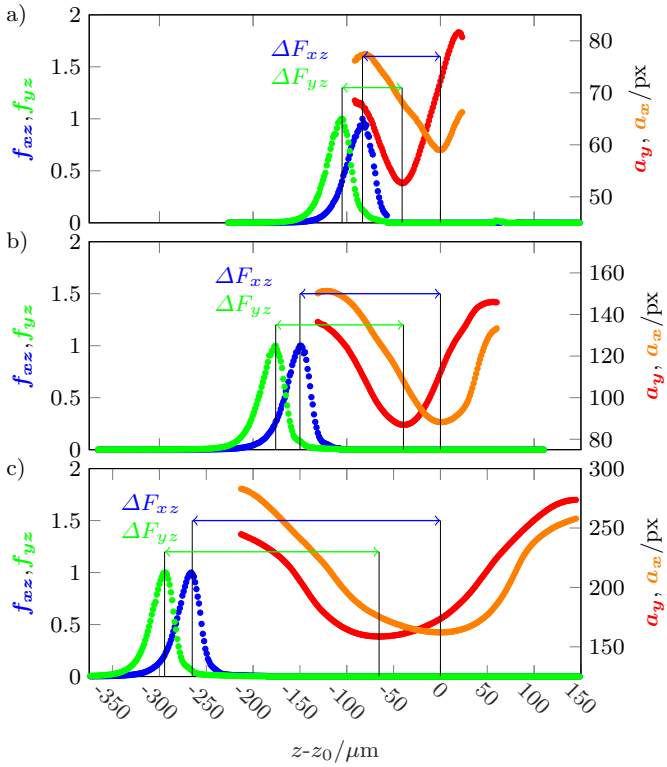

Figure 4.13: The effect of particle size on the axis lengths $a_y(z\text{-}z_0)$, $a_x(z\text{-}z_0)$ and measured particle focal lengths ΔF_{yz}, ΔF_{xz}. $z\text{-}z_0$ is corrected for the refractive index of a 25wt% glycerol-water solution (M=20×, c_a=0.4095, c_I=0.77, CCD camera). Symbols: red dots=a_y, orange dots=a_x, green dots=f_{yz}, blue dots=f_{xz}. a) d_p=30 µm b) d_p=60 µm c) d_p=124 µm

Fig. 4.13a-c). This leads to an increase in measurement volume depth Δz as given in Fig. 4.14a, which can be understood from Fig. 4.14b. Here, the maximum focal image intensity is plotted as function of the out-of-plane position $z\text{-}z_0$. For increasing particle sizes a larger Δz is determined, as a larger particle provides a sufficiently strong focal image signal over a bigger $z\text{-}z_0$ range (indicated by dashed lines). It may be noted that, for large particles the measurement volume depth Δz exceeds the distance between the focal planes by far (F_{yx}-F_{xz}=21 µm in Fig. 4.13 and Fig. 4.14). This is a significant difference to conventional APTV with small particles where it is assumed that the measurement range is primarily defined by the distance of the focal planes (Cierpka et al. 2010a).

Figures 4.13a-c indicate a linear increase in the measured particle's focal length with increasing d_p, as also depicted in Fig.4.14c: ΔF_{yz} (dashed lines with filled squares) and ΔF_{xz} (bold lines with filled circles). This is in agreement with the lensemaker's equation (4.1), where the particles focal length increases linearly with d_p. However, as

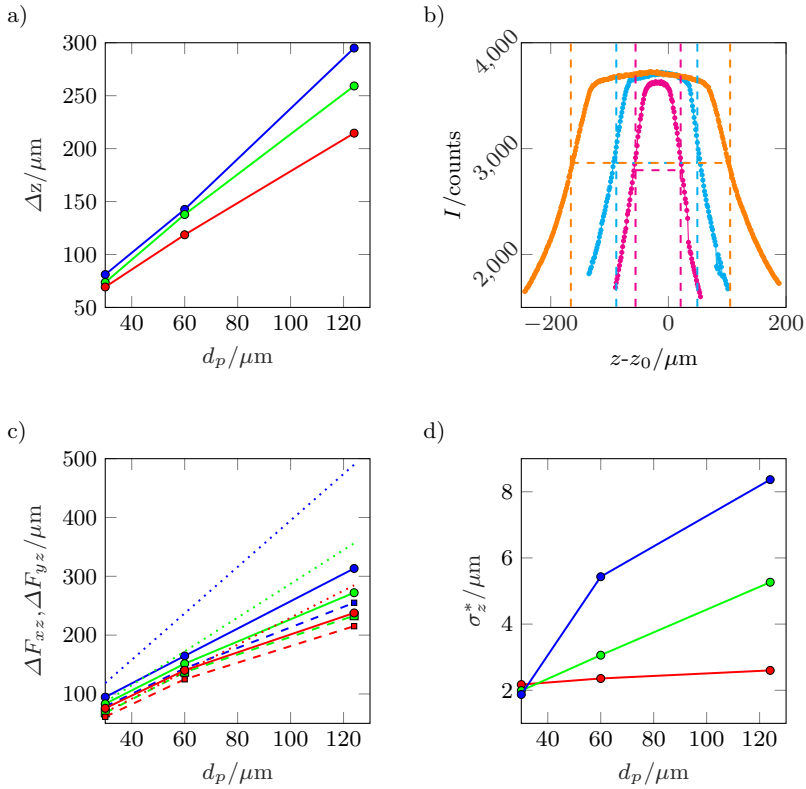

Figure 4.14: Effect of d_p on the calibration data (M=20×, c_a=0.4095, c_I=0.77, c_D=3, CCD camera). Symbols: red dots=0wt% (n_L=1.333), green dots=25wt% (n_L=1.364), blue dots=50wt% (n_L=1.398) glycerol-water solution, pink dots=d_p=30 µm, light blue dots=d_p=60 µm, orange dots=d_p=124 µm. a) Effect of d_p and refractive index of liquid on Δz. b) Effect of d_p on $I(z\text{-}z_0)$ (z-z_0 corrected for refractive index of 25wt% glycerol-water solution). c) Effect of d_p on ΔF_{xz} (solid line with filled circles), ΔF_{yz} (dashed line with filled squares) and on the focal length f_p of a particle according to the Lensemaker's equation (4.1) (solid dotted line). d) Effect of d_p on σ_z^*.

can be seen from Fig. 4.14c ΔF_{yz} and ΔF_{xz} deviate from the particle's focal length obtained by the lensemaker's equation (solid thin lines) as the refractive index of the liquid increases. While for water the agreement of measured and calculated values is quite good (red lines), obviously this is not the case when the refractive index difference between particle and liquid is increased (see Fig. 4.14c). As already stated in section 4.1, here further investigations are required to understand the reasons for this discrepancy.

In general we observe, that the shape change and hence the change of the aspect ratio as function of the out-of-plane position is more pronounced with decreasing focal image size. As the size of the focal image increases with the particle size, it can be understood that the uncertainty of the out-of-plane particle reconstruction σ_z^* grows with the particle

size as shown in Fig. 4.14d. Also a decrease in $\Delta n{=}n_p{-}n_L$ is associated with a decrease in focal angle of light rays that are bundled by the particle. Hence a decreased focal image deformation is observed when moving along the out-of-plane direction. Therefore, σ_z^* grows when $\Delta n{=}n_p{-}n_L$ decreases, as seen from Fig. 4.14d. A further overview of measured values of σ_z^*, σ_z, ΔF_{yz} and ΔF_{xz} for different particle sizes and different ratios of glycerol and water is provided in the Appendix (see Table A.11).

The effect of particle size and refractive index jump on the calibration curves in the a_y-a_x plane is illustrated in Figs. 4.15a-f. Overall, an increase in particle size, shown here for PMMA particles in a 25wt% glycerol-water solution for two magnifications (Figs. 4.15a and b), leads to an increase in a_x and a_y. Therefore, calibration curves are strongly shifted without any overlapping region. Please note, that this characteristics may be utilized to assign particles to one calibration curve. Thus, it is possible to determine both the out-of-plane position of the particles and at the same time perform a size classification, if particles of the same shape and material are used. Figures 4.15c and d reveal, that a reconstruction of out-of-plane particle positions can be also combined with a classification of particles according to their refractive index. Here, calibration curves for PS and PMMA are shown with a refractive index difference of $\Delta n{=}n_p{-}n_L{=}0.258$

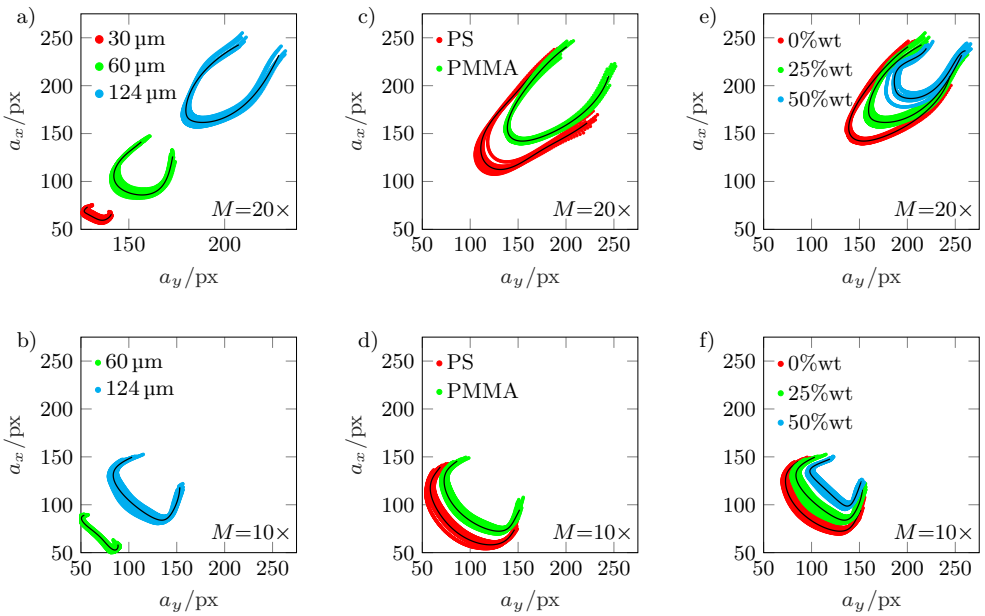

Figure 4.15: Effect of d_p and refractive index jump on the calibration curves (c_a=0.4095, c_I=0.77, CCD camera). For d_p=30 µm and M=10× the particle and focal image size and quality are not sufficient enough for evaluating. a) M=20×, PMMA, 25wt% (n_L=1.364). b) M=10×, PMMA, 25wt% (n_L=1.364). c) M=20×, 0wt% (n_L=1.333), d_p=124 µm. d) M=10×, 0wt% (n_L=1.333), d_p=124 µm. e) M=20×, PMMA, d_p=124 µm. f) M=10×, PMMA, d_p=124 µm.

and Δn=n_p-n_L=0.154, respectively. It may be noted that more stringent outlier criteria are required when calibration curves move closer together as it is the case for Figs. 4.15c and d compared to 4.15a and b. A change in refractive index jump can also occur when the refractive index of the liquid is varied. Figs. 4.15e and f show how changes of the refractive index affect the calibration curves. Different refractive indices are realized by creating different water-glycerine mixtures. When the refractive index jump between particle and fluid increases with decreasing glycerol fraction, a_x and a_y decrease. In the present study refractive index changes of the liquid of Δn=0.0307 (for 25wt%) and Δn=0.064 (for 50wt%) are realized. Overall, it can be seen that the differences between the individual calibration curves are more pronounced for M=20× compared to M=10× under the depicted experimental conditions. In the present section only an excerpt of the whole parameter study is presented. An overview of Δz, ΔF_{xz}, ΔF_{yz}, σ_z^*, σ_z for all investigated parameter combinations of d_p, M, material of the particles and wt% of the glycerol-water solution is given in Table A.11 of the Appendix. For the investigated cases, $\sigma_z/\Delta z$ is around 0.7-5.2% for BLAPTV (except for two cases) which is comparable to the accuracies obtained by Cierpka et al. (2010b), Buchmann et al. (2014) and Franchini et al. (2019). In the present study, the uncertainty relative to the particle diameter is in the range $1.8\% \leq \sigma_z/d_p \leq 16\%$ (except for two cases), see Table A.11 in the Appendix. This is even below the values reported in earlier studies which are also given in Table A.10 in the Appendix.

4.7 Validation measurements

To demonstrate the capability of BLAPTV for flow domains with a depth beyond the submillimiter range, measurements in a plane channel flow with 2305 µm channel height are performed. For this, a 25wt% glycerol and 75wt% deionized water solution was seeded with 10^{-4}%wt polystyrene particles of diameter d_p=80 µm. The solution is density matched to the particles at 20 °C. As particles are two orders of magnitude smaller compared to the channel height, we expect them to behave as neutrally buoyant fluid tracers (Lindken et al. 2009). Despite the fact that the density of liquid and particles is matched, few particles float and stick to the top or settle at the bottom channel walls, due to small variations of the individual particle density as a result of the manufacturing process. These particles are used to determine the absolute position of the channel walls prior to the experiments. For this, the whole channel is scanned in steps of 1 µm, to record particles that are located at the top and the bottom wall within the field of view, acting as "wall markers". As mentioned in Section 4.2, the evolution of the Tenengrad sharpness measure (f_{xz}) is used to detect the particle center and hence the walls of the channel by considering the particle radius. The origin of the scanning coordinate, is set to zero at the bottom channel wall. Hence, a volume flow rate of $3.75\times10^{-4}\mathrm{m}^3\,\mathrm{s}^{-1}$ is created using a submerged rotary pump (Barwig). The liquid is continuously recirculated and temperature regulated at 19-20 °C, see Figs. 2.1a and

b. To measure the flow rate, we repeatedly measured the weight of the liquid pumped during a defined time interval. Herafter, the massflow rate was calculated based on the density of the glycerol-water mixture (Cheng 2008). An in situ-total gap height of H=2305 µm was determined.

Prior to the actual flow measurement calibrations are performend. The resulting calibration curves and the associated scattered a_x, a_y and I-values are presented in Fig. 4.16a. For particles located at the top wall (z=2305 µm), a_x, a_y, I and hence the calibration curve differ from those of particles located at the bottom wall (z=0 µm). As shown in section 4.5, different light intensities result in different calibration curves for the same particle. Therefore, we assume that the shape difference of the calibration curves, is a result of a change in the light intensity along the gap height.

Due to the different shape of the calibration curves, the challenge is to find a calibration function which is valid for particles located at any z-position in between the bottom and top channel wall. To overcome this difficulty we interpolate the coefficients of the $\overline{a}_x$, $\overline{a}_y$ and $\overline{I}$ polynomials of the calibration curves as a linear function of z. In this way, intermediate calibration curves are computed, see Fig. 4.16b. In the present case, the measurement volume depth of the interpolated calibration curves is set to Δz=173.22 µm. In addition to the calibration curve, the threshold for the Euclidean distance a_D is also interpolated linearly.

Also the measured particle's focal length $\Delta F_{yz} \approx \Delta F_{xz}$ differs for particles located at the top and bottom, see Table A.12 in the Appendix. As discussed in section 4.5 the measured particle's focal length is almost constant as light intensity is increased. Therefore, we assume the difference is related to the refractive index jump at the top channel wall. Hence, the particle's focal length is assumed to be constant for the major part of the channel ($\Delta F_{xz} \approx \Delta F_{yz}$=const.), as the refractive index jump at the top wall comes only into play for particles closer than ΔF_{yz}=177.32 µm$\approx\Delta F_{yz}$=196.29 µm (see Table A.12) to the channel walls. The out-of-plane position reconstruction uncertainties for the top and the bottom calibration curve are given in Table A.12. As can be seen, the uncertainty of determining the particle's z-position is decreased by 15% and 10% with a 3D calibration in comparison to a 2D calibration, while the number of valid particles is increased by 2.5% and 4.8% for the top and bottom calibration curve, respectively. It should be mentioned, that a maximum position error of 0.488% of the total channel height and 14% of d_p is achieved for the 3D calibration.

During the actual flow measurements the gap is scanned in steps of 136 micron and at each measurement plane 5300 images with a resolution of 512×384 pixel, covering a 0.93×0.82 mm^2 field of view, are recorded at 1000fps. Hence, the out-of-plane positions of particles, based on the a_y, a_x and I data of the flow measurement has to be determined. For this, each of the 3D calibration curves displayed in Fig. 4.16b, is compared with the a_x, a_y and I-values from the corresponding measurement planes. In this way a suitable calibration curve with associated out-of-plane particle positions along the curve can be associated to the scatter data of each measurement plane. To find the most suitable

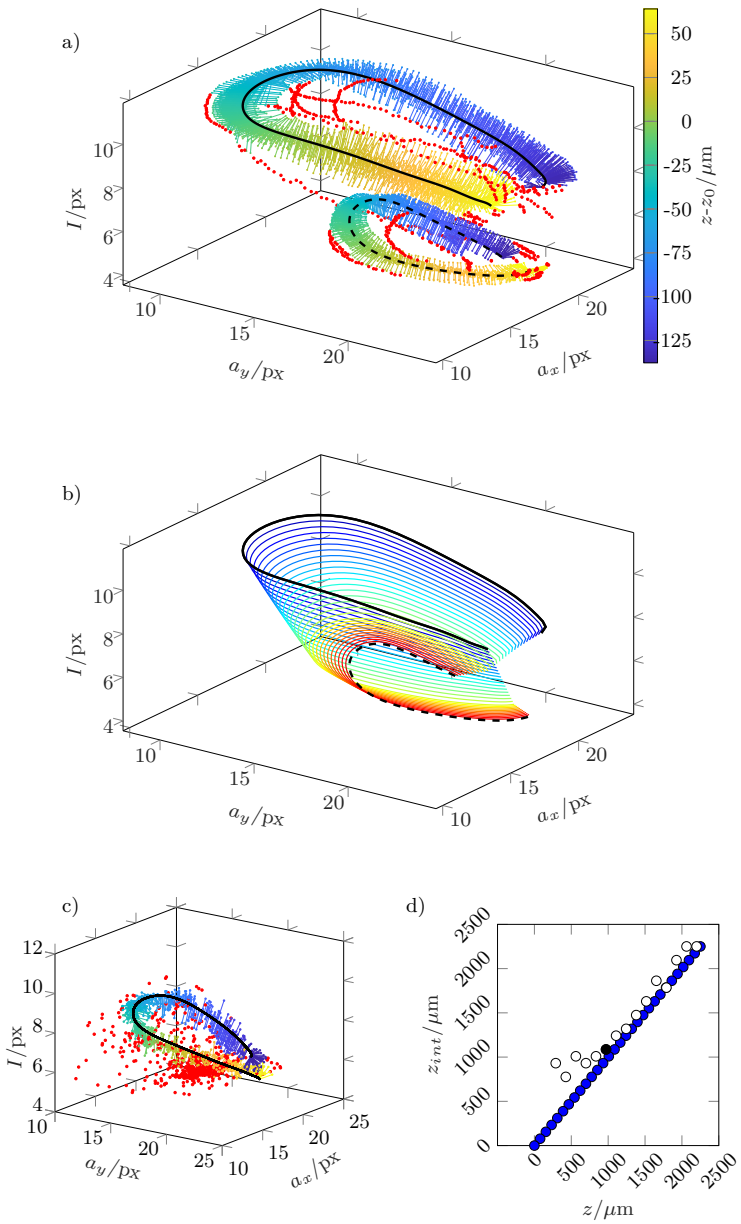

Figure 4.16: Linear interpolation of calibration curves. Dashed line=0 µm (bottom), solid line=2305 µm (top), colored dots=valid data, red dots=rejected data. M=20×, d_p=80 µm, c_D=2, c_a=0.7, c_I=0.575, z-z_0 corrected for n_L of 25wt% glycerol-water solution. a) Scattered a_x-a_y-I data and resulting 3D calibration curves. b) Interpolated 3D calibration curves. c) Best matching interpolated calibration curve for z=971 µm d) z_{int} of best matching 3D calibration curves vs. measurement plane position z (blue dots=interpolated, white dots=best matching, black dots=shown in Fig. 4.16c).

calibration curve, it is checked how many pairs of a_y, a_x and I are valid, i.e. their minimum Euclidean distance to the calibration curve is smaller than a_D, as described in section 4.3. The curve that yields the largest number of valid particles is considered as a match and selected for determining the z-z_0 of the a_y, a_x and I pairs in the respective measurement plane. Figures 4.16c displays the best matching calibration curve (black solid line) and corresponding scatter data with valid measurement points (colored markers) and outliers (red markers) for the measurement plane located at z=971 µm. Note that, the interpolated a_D value corresponding to the depicted calibration curve have been used for outlier detection. Here an interpolation of a_D is crucial as the scattering of a_x-a_y-I data varies along the gap height (compare the scattering distance of the top and bottom curve in Fig. 4.16a).

This procedure is applied to the a_x, a_y and I data of all measurement planes, such that for each measurement plane the out-of-plane positions of the focal points are computed. Hence, the absolute particle positions can be computed with respect to the channel wall by summing up the focal points out-of-plane positions, the particles focal length (ΔF_{xz}) and the associated measurement plane position. In Fig. 4.16d the interpolated coordinate z_{int} of the calibration curve is plotted vs. the z where the curve showed the most valid pairs, hence is considered as a match (white dots). As can be seen z vs. z_{int} of the matching curves (white dots) approximately shows a linear behavior. This confirms the previous assumption that the shape of the calibration curves can be described as a linear function.

Figure 4.17a shows a scatterplot of the position of all valid (green dots) and invalid (red dots) data in the x-y measurement plane.

As can be seen the accepted data points are well distributed across the image (Fig. 4.17a). This means that any in-plane particle position effect is already included in the result data, as particles across the whole field of view are accepted. Hence the influence of the in-plane position on the Euclidean distance to the calibration curve and thus on the particle's out-of-plane reconstruction accuracy is not signifcant here. It may be noted, that data points at the very corners of the images are rejected as particle images intersect with the image borders and do not provide the complete focal image. Therefore, particle center points close to the FOV border do not enter the statistics.

Fig. 4.17b shows the measured velocity profile of the plane channel flow that is obtained with the aforementioned extended calibration procedure. The velocities are calculated using a simple nearest neighbors algorithm. As is it clear from Fig. 4.17b, the experimentally determined velocity profile matches very well the analytical solution (red line). It may be noted that particles assume a minimum z-distance of approximately 200 µm to both top and bottom channel walls which might be due to to wall-induced lift forces, which push particles away from the walls towards the channel center. Utilizing a 3D calibration procedure 7996 valid data points are obtained while in-plane velocities u, v as well as the out-of-plane velocity w could be determined with standard deviations of σ_u=0.75%, σ_v=0.28% and σ_w=2.29% of the maximum

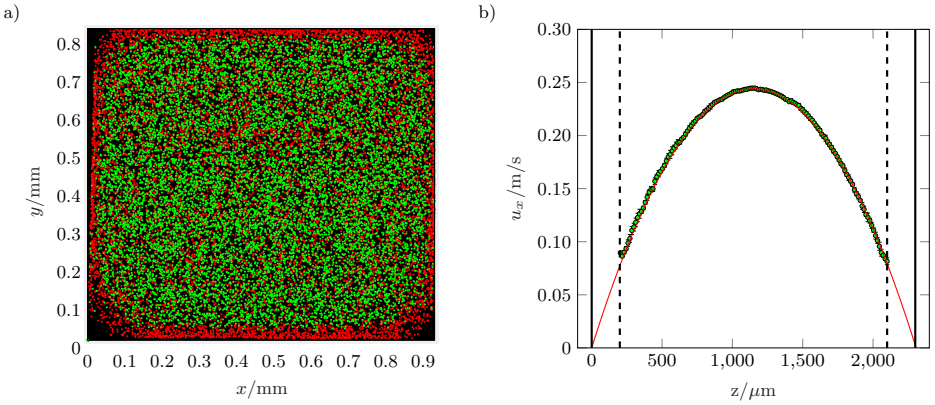

Figure 4.17: a) Particle image centroids detected within the field of view during the measurement. Green dots denote valid particle images, red dots denote outliers. b) Experimental results and analytical solution for laminar channel flow. red line= analytical solution, green dots (with errorbar)= measurement, black straight line= channel walls, black dashed line= particle depletion area). The dashed lines indicate the minimum distance particles assume relative to the walls. The mean value of the streamwise velocity standard deviation along z is σ_u=0.75% of $U_{\max}$ (c_D=2)

streamwise velocity u_{max}, respectively. The same procedure with a 2D calibration and reconstruction yields $N_{\text{valid}}(2D)$=7267 (-10%) data points and uncertainties of σ_u=0.80% (+6.1%), σ_v=0.27% (-3%) and σ_w=2.66% (+16%) for u, v and w, respectively. If c_D is reduced to c_D=1.75 for the 3D calibration such that the number of valid particles is approximately equal ($N_{\text{valid}}(2D)$=7267≈$N_{\text{valid}}(3D)$=7298) uncertainties of σ_u=0.73% (-8%), σ_v=0.25% (-8%) and σ_w=2.05% (-30%) for u, v and w are achieved. This shows that the 3D calibration procedure provides a better accuracy and more reliable data in comparision to the 2D calibration procedure.

Overall the accuracies obtained with the 3D as well as the 2D calibration procedure are comparable to the uncertainties obtained by Cierpka et al. (2010a), which are σ_u=0.9% and σ_w=3.72% of u_{max}. Thus, BLAPTV shows comparable measurement accuracies compared to fluorescence based APTV, if a proper calibration procedure as presented here is utilized.

4.8 Discussion and Conclusion

In this chapter, a method is presented to apply APTV to large transparent particles, using bright-field illumination. As particles act here as ball lens, we referred to this method as Ball Lens Astigmatism Particle Tracking Velocimetry (BLAPTV). Based on a parameter study on the role of the background light intensity, the particle size and the refractive index jump between particle and fluid, it was shown that

BLAPTV achieves comparable measurement accuracies as conventional APTV where fluorescent particles are typically utilized. We showed how the evaluation procedure, in particular the autocorrelation coefficient c_a and the light intensity coefficient c_I affect the accuracy of the method. Furthermore, we showed that BLAPTV may be utilized to combine measurements of the 3D displacement of particles with a particle classification by either size or refractive index due to different shapes of the corresponding calibration curves. Given a proper calibration procedure, BLAPTV can provide high reconstruction accuracies with respect to the particle diameter even for large particles. To reduce the particle depth position reconstruction uncertainty, we proposed an extended calibration procedure in which the focal image intensity is used an additional parameter to the Euclidean method of Cierpka et al. (2010a) resulting in a 3D calibration curve. Uncertainties of the out-of-plane particle position reconstruction of σ_z=2.5 µm for d_p=60 µm (σ_z/d_p=4.16%) with M=20× and σ_z=2.26 µm for d_p=124 µm (σ_z/d_p=1.8%) and M=20× were reported using the 3D calibration procedure. We observed, that the measurement depth Δz depends on the particle diameter and can exceed the distance of the focal planes significantly (up to 11.1-13.4 times for a 124 µm particle, while it is typical of the same order of magnitude in conventional APTV with small particles. We also developed a method to compensate for shape changes of the calibration curve inside a large measurement volume without the need to place a calibration target inside the measurement volume. Instead, linearly interpolated calibration curves are assigned to the measurement data in a best fit procedure to determine the out-of-plane position of particles.

Finally we validated BLAPTV successfully by measuring a planar Poiseuille flow in a rectangular channel. Utilizing a 3D calibration procedure we showed that the uncertainty of the measured streamwise and out-of-plane velocity can be reduced by 6.1% and 16%, respectively. Overall, the accuracies obtained in the measurement are comparable to those obtained by Cierpka et al. (2010a) for both the 2D and the 3D calibration.

As BLAPTV is an adapted version of APTV, the same postprocessing code can easily be applied to both fluorescent and transparent particles. Also measurements can be performed with the same optical setup if the light source is adapted. This is an advantage, when measurements should be performed with small fluorescent tracer particles ($d_p \leq 3$ µm) combined with larger transparent suspension particles ($d_p \geq 30$ µm) with the same magnification. We conclude our observations can be transferred to conventional, fluorescent APTV, as from some experiments we know, that the choice of c_a affects the reconstruction accuracy σ_z as well in the case of fluorescent particles. Furthermore, using a 3D calibration curve has the potential to increase accuracy and robustness of conventional fluorescent APTV, because here outliers appear due to deviations in shape or coating and overlapping particles.

The next chapter considers the application of APTV on large fluorescent particles in suspensions at solid volume fractions up to 20% using a refractive index matching method. As will be shown, slight refractive index differences between particles and

liquid lead to shape changes of the calibration curve similar to those described in this chapter. The interpolation method presented in this chapter is used to compensate these shape changes.

5 Applying APTV to suspension flows at high volume fractions [1]

In this chapter it is demonstrated how Astigmatism Particle Tracking Velocimetry (APTV) can be utilized to measure suspensions dynamics beyond the dilute regime. Measurements were successfully performed in monodisperse, refractive index matched suspensions of up to a volume fraction of $\Phi = 19.9\%$. For this, a small percentage ($\Phi < 0.01\%$) of the particles is labeled with fluorescent dye acting as tracers for the particle tracking procedure. Calibration results show, that a slight deviation of the refractive index of liquid and particles leads to a strong shape change of the calibration curve with respect to the unladen case. This effect becomes more severe along the channel height. To compensate the shape change of the calibration curve we adapt the interpolation method presented in chapter 4. Using this technique, the interpolation procedure is applied to suspensions with different volume fractions of $\Phi < 0.01\%$, $\Phi = 4.73\%$, $\Phi = 9.04\%$, $\Phi = 12.97\%$, $\Phi = 16.58\%$ and $\Phi = 19.9\%$. To determine the effect of volume fraction on the perfomance of the method, the depth reconstruction error σ_z and the measurement volume depth Δz, obtained in different calibration measurements, are estimated. Finally, the measurement technique is validated for a laminar flow in a straight rectangular channel with a cross-sectional area of $2.55 \times 30\,\mathrm{mm}^2$.

This chapter is structured as follows: First in section 5.1 the calibration procedure, which differs to that described in chapter 4, is explained for large fluorescent particles. In doing so, the effect of slight abberrations is considered which are induced by refractive index differences between RIM-liquid and particles. Hence, in section 5.2 a method to compensate shape changes of the calibration curves, resulting from these aberrations is developed. Then the technique is validated in a laminar channel flow at different particle volume fractions up to 20%. Finally, a summary of the observations and results is given in section 5.3. The theory and state of the art relevant for this chapter are given in section 1.2.2 (fundamentals of suspension flows) and section 1.2.4.3 (theory and state of the art of APTV). The setups utilized to obtain the results presented in the present chapter are given in section 2.1.2.

[1] This chapter is adopted from "On the calibration of Astigmatism particle tracking velocimetry for suspensions of different volume fractions." Experiments in Fluids 62.1 (2021): 1-11, written by Philipp Brockmann and Jeanette Hussong. Published under `https://creativecommons.org/licenses/by/4.0/`.

5.1 Calibration procedure

Here, a 2D Euclidean calibration procedure is presented similar to that described in chapter 4. The main difference is that we utilize fluorescent particles for the investigations in this chapter. Therefore, the aberrated particle image itself is used here for particle out-of-plane position reconstruction. Furthermore, in contrast to chapter 4 we do not use the 3D Euclidean calibration procedure hereafter, as the distribution of the light intensity is not sufficiently homogenous to improve the accuracy through a 3D procedure, here. This is because in setup 2 a continuous wave laser was used for illumination (see Fig. 2.2 in section 2.1.2).

The major steps of the calibration procedure are summarized in the following, where we also outline the differences in the calibration curves for a labeled particle in a dilute ($\Phi < 0.01\%$) and in a dense refractive index matched suspension ($\Phi = 19.9\%$). To capture the change of a_x and a_y for different out-of plane positions of particles, labeled and wall attached particles in a suspension of $\Phi < 0.01\%$ and $\Phi = 19.9\%$ are scanned in steps of 1 µm over a distance of 1000 µm such that the deformation of the particle image is entirely captured. Fig. 5.1 shows particle images of such a scan of a 60 µm PMMA particle labeled with Rhodamin B and located at the bottom channel wall. A magnification of $M = 10\times$ for $\Phi < 0.01\%$ (Fig. 5.1a) and $\Phi = 19.9\%$ (Fig. 5.1b) is chosen. The particle shown in Fig. 5.1a is submerged in a dilute suspension where only labeled tracer particles of $d_p = 60\,\mu\text{m}$ are present in the RIM-liquid such that $\Phi < 0.01\%$. The change of a_x and a_y is determined as a function of $z - z_0$. Results are displayed in Fig. 5.2a (large colored dots). The coefficient c_a at which the isolines of the autocorrelation map are extracted to measure a_x and a_y will be denoted as autocorrelation coefficient as introduced and described in chapter 4. The autocorrelation coefficient is set to $c_a = 0.5547$ for the results presented within this work. In Fig. 5.2b a_y is plotted as a function of a_x. This presentation poses the base for the Euclidean calibration method as developed by Cierpka et al. (2010a) and adapted in chapter 4. The labeled particle displayed in Fig. 5.1b is submerged in a suspension of RIM-liquid and additional unlabeled particles such that the total volume fraction is $\Phi = 19.9\%$. In fact, the suspension was at rest for 24 hours, such that the particle shown in Fig. 5.1b is covered with appoximately 11 layers of unlabeled, transparent PMMA particles. From Fig. 5.1a and b it is obvious that the images of the particle in a suspension of $\Phi = 19.9\%$ (Fig. 5.1b) are slightly blurred and also exhibit a speckle pattern for relative out-of plane positions ranging between $200\,\mu\text{m} < z - z_0 < 400\,\mu\text{m}$. The blurriness and the speckle patterns are a result of slight deviations of the refractive index of individual transparent particles and the RIM liquid. The refractive index deviation of transparent particles which are located in the optical path between the labeled calibration particle and the objective, induces these distortions of the particle image affecting the values of $a_x(z - z_0)$ and $a_y(z - z_0)$. These deviations become evident in Fig. 5.2a (small

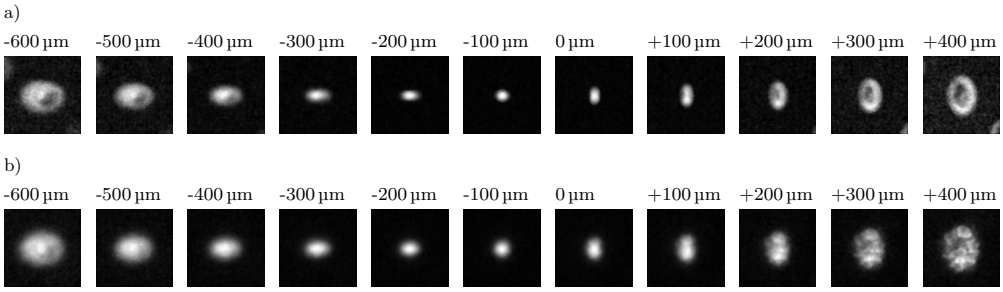

Figure 5.1: Images of labeled particles for different depth positions z (d_p=60 µm, PMMA, z corrected for refractive index of RIM-liquid ($n_{\mathrm{RIM}} = 1.488$)). The particle is located close to F_{yz} at $z \approx -200$ µm and located in F_{xz} at $z = 0$ µm. a) Labeled particle in a suspension with $\Phi = 0.01\%$. b) Labeled particle in a suspension with $\Phi = 19.9\%$.

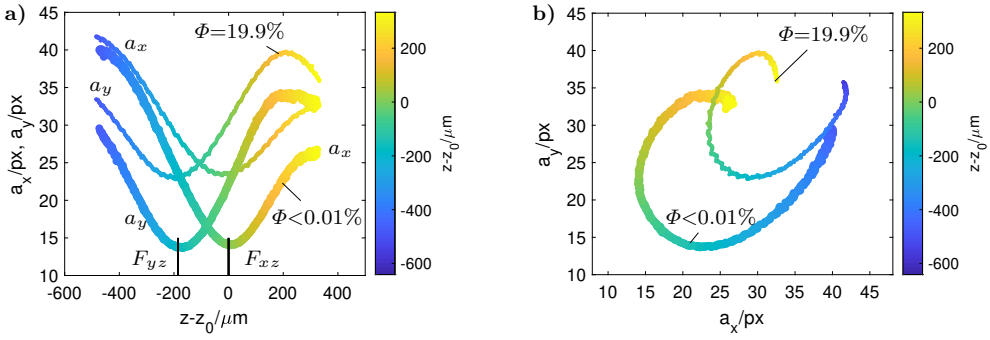

Figure 5.2: Calibration data of $d_p = 60$ µm particles in RIM-Liquid for Φ<0.01% (large dots) and Φ=19.9% (small dots) ($M = 10\times$). The position where a_x is minimum (F_{xz}) is taken as reference position z_0. a) a_x and a_y as function of $z - z_0$ b) a_y as function of a_x.

colored dots) and Fig. 5.2b (small colored dots), respectively. Obviously the volume fraction affects the a_x and a_y values and particles displayed in Fig. 5.1a and b can not be treated with the same calibration curve.

To obtain a proper calibration function for both the dilute and the dense suspension the previously described calibration scans are repeated for several labeled particles randomly distributed over the field of view. This results in a data set of a_x, a_y and I as function of $z - z_0$ for several particles, where I denotes the maximum light intensity within the particle image. An exemplary set of such scattered a_x, a_y and I data for $d_p = 60$ µm particles submerged in a suspension at $\Phi < 0.01\%$ is given in Fig. 5.3a. In a first step the median of I as a function of $z - z_0$ is computed, denoted as $\overline{I}$. For the following steps only data points associated with $I \geq c_I \cdot \overline{I}_{\max}$ are considered, where c_I is defined as the intensity coefficient. The value of $c_I \cdot \overline{I}_{\max}$ will be hereafter referred to as intensity threshold I_{thr}. For further information on c_I the interested reader is referred to chapter 4. In the following step, a polynomial of 14th order is fitted to the scattered a_x and a_y

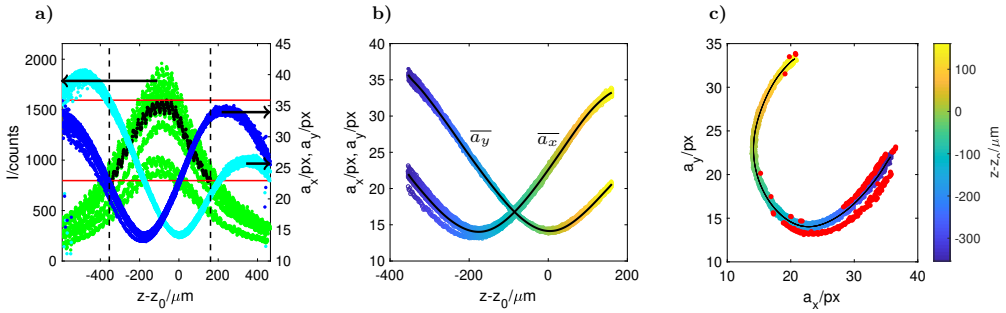

Figure 5.3: Procedure of generating a calibration function ($c_a = 0.5547$, $c_I = 0.5$, $c_D = 2$, $M = 10\times$, $d_p = 60\,\mu\text{m}$, $\Phi < 0.01\%$). Scale of colormap in b and c is given in c. $z - z_0$ data is corrected for the refractive index of the RIM-liquid ($n_{\text{RIM}} = 1.488$). a) Selecting $z - z_0$ range of scattered data by light intensity I (light blue dots=a_x, dark blue dots=a_y, green dots=I, black dots=$\overline{I}$). b) Fitting polynominals of degree 14 to a_x and a_y (black line=polynomials $\overline{a_x}$, $\overline{a_y}$). c) Reconstruction of $z - z_0$ of scattered a_x-a_y data (colored dots) by Euclidean distance (black line=polynomials, red dots=outliers).

data as shown in Fig. 5.3. Preliminary tests on fluorescent particles revealed, that the a_x-a_y-calibration curves assume a wide spectrum of different shapes depending on d_p, c_a and the optical properties of the setup. In order to provide a general procedure here, which can adapt to such a wide range of shapes high order polynomials are required. Polynomials of 14th order are found to be suitable here, as lower order polynomials do not adapt well to the data, while higher order polynomials do not provide a better fit. When the polynomial fit of a_y (denoted as $\overline{a_y}$) is plotted as a function of the polynomial fit of a_x (denoted as $\overline{a_x}$) the 2D calibration curve is obtained. The z-position of a particle can now be reconstructed by assigning its measured a_x, a_y values to a point on the calibration curve that is given by the minimum Euclidean distance and then reading out the associated $z - z_0$ value. Pairs of a_x, a_y where the Euclidean distance exceeds a certain threshold are rejected as an outlier. This threshold is referred to as a_D and defined as the mean Euclidean distance of the a_x, a_y data of all calibration particles multiplied by the factor c_D as described in chapter 4. For the case depicted in Fig. 5.3 c_D is set to a value of $c_D = 2$, resulting in an out-of-plane reconstruction accuracy of $\sigma_z = 4.67\,\mu\text{m}$ for $d_p = 60\,\mu\text{m}$ particles. The measurement volume depth for the given example equals $\Delta z = 514.84\,\mu\text{m}$ for $c_I = 0.5$, such that the relative reconstruction accuracy, hence referred to as relative error, equals $\sigma_z/\Delta z = 0.90\%$. With $c_I = 0.4$ the measurement volume depth is increased to $\Delta z = 606.28\,\mu\text{m}$ whereas σ_z increases slightly to $4.92\,\mu\text{m}$ resulting in a relative error of $\sigma_z/\Delta z = 0.80\%$.

5.2 Validation measurements

To validate the applicability of APTV to dense suspensions, measurements are carried out in a plane channel flow with 2550 µm channel height. The suspension is a ternary liquid mixture proposed by Bailey and Yoda (2003) and PMMA particles of diameter d_p=60 µm (Microbeads). The channel is filled with the RIM-liquid and a small amount of labeled particles such that $\Phi < 0.01\%$. Due to a slight density variation of the RIM-liquid and the particles, the particles settle to the channel bottom when rested over night, while a few are stuck to the top channel wall. Settled particles are used to determine the absolute position of the bottom and the top channel wall prior to the experiments. For this, the whole channel is scanned in steps of 1 µm, to record particles that are located at the top and the bottom wall within the field of view. The evolution of a_x is used to detect the particle center and thereby the channel walls by considering the particle radius. In fact the particle center is focused in F_{xz} when a_x assumes a minimum. The origin of the scanning coordinate, is set to zero at the channel bottom. Hence, a constant suspension flow rate of 20 mL min^{-1} is induced by a high pressure syringe pumpe (LA-800, Landgraf HLL GmbH). A container is used to collect the liquid driven from the syringe through the channel.

Before the actual flow measurement is started, calibrations measurements are performed with particles located at the bottom channel wall to generate calibration curves for $\Phi < 0.01\%$ as shown in Fig. 5.4 (solid line). Hence, flow measurements for suspensions with six different volume fractions ranging from $\Phi < 0.01\%$ to $\Phi = 19.9\%$ are performed. After the final measurements at $\Phi = 19.9\%$ the setup is rested over night such that particles settle to the channel bottom. Then, calibration measurements are performed with settled and labeled particles to generate a calibration curve for $\Phi = 19.9\%$ as shown in Fig. 5.4 (dashed line). As already discussed in section 5.1 both curves differ significantly due to particle image distortions. Test calibrations performed on particles located at the top and bottom of the channel revealed that this effect does not occur for a dilute suspension ($\Phi < 0.01\%$) in the present case. While for low volume fractions no effect can be noticed, for volume fractions larger than $\Phi \geq 4.73\%$, we observed that the calibration curve changes with the z-coordinate and hence is an implicit function of the channel height. This is because the number of particles that disturb the light path is higher for labeled particles located closer to the bottom than for labeled particles located closer to the top of the channel. The challenge is to find a calibration function which is valid for labeled particles located at any z-position in between the bottom and top channel wall and for volume fractions in the range from $\Phi < 0.01\%$ to $\Phi = 19.9\%$. To solve this problem we adapt the interpolation method developed in chapter 4. For this, we interpolate and extrapolate the polynomial coefficients of $\overline{a}_x$, $\overline{a}_y$ based on the calibration curves for $\Phi < 0.01\%$ and $\Phi = 19.9\%$. In this way, we compute 30 intermediate calibration curves. These are presented as colored lines in Fig. 5.4. The extrapolation allows us to generate calibration curves which are even more skewed than the calibration curve for $\Phi = 19.9\%$ (see orange to red lines in Fig. 5.4). As we

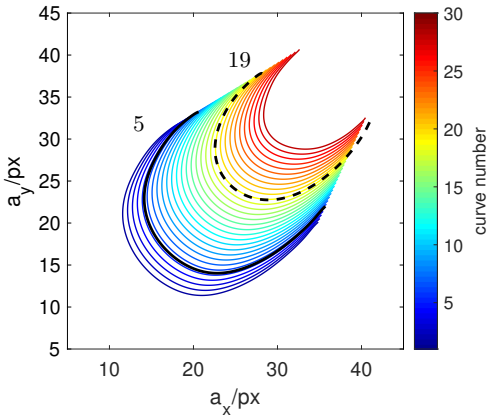

Figure 5.4: Inter- and extrapolated calibration curves as used in section 5.2. The dotted line equals the calibration curve for Φ=19.9% (curve number 19), the solid line corresponds to the calibration curve for Φ=0.01% (curve number 5).

will show later these extrapolated curves are required at higher volume fractions. The z-range of all interpolated calibration curves is set to Δz=514 µm. In addition to the calibration curve, which consists of $\overline{a}_y$ as function of $\overline{a}_x$, the threshold for the maximum allowed Euclidean distance a_D is also interpolated linearly. The out-of-plane position reconstruction uncertainties of particles of d_p=60 µm diameter for $\Phi < 0.01\%$ and $\Phi = 19.9\%$ are $\sigma_z = 4.67$ µm and $\sigma_z = 15.64$ µm, respectively. The channel is scanned in steps of 223 µm during the flow measurements and at each measurement plane 2500 images with a resolution of 512×384 pixel, covering a 1.89×1.57 mm^2 field of view, are recorded at 100fps. In the post processing the image size is reduced to a region of interest of 300×300 pixel. By this, marginal areas of insufficient illumination are reduced and the computation time can be reduced significantly. After data acquisition, the particle positions and velocities need to be determined. To determine the out-of-plane positions of particles, based on their a_y, a_x values, each of the calibration curves displayed in Fig. 5.4, is compared with the a_x, a_y scatter data from the corresponding measurement planes. By this we can select an appropiate calibration curve for each measurement plane. To find the best fitting calibration curve, the number of valid a_y, a_x pairs that fulfill the Euclidean distance criterion is evaluated as described in section 5.1. In fact, the curve that yields the largest number of valid particles is considered as a match and selected to determine the z-z_0 of the a_y, a_x pairs in the respective measurement plane.

It should be mentioned that as the deformation of a particle's image depends on the layer of suspension on top of it and hence on its z-position, ideally a calibration curve should be generated individually for each particle based on its individual z-position. As the particle position is unkown in advance, this would have to be realized in a complex

iterative procedure. However, as we will show later we do not experience any significant bias by neglecting this effect. Therefore, we take the best fitting calibration curve for each measurement plane.

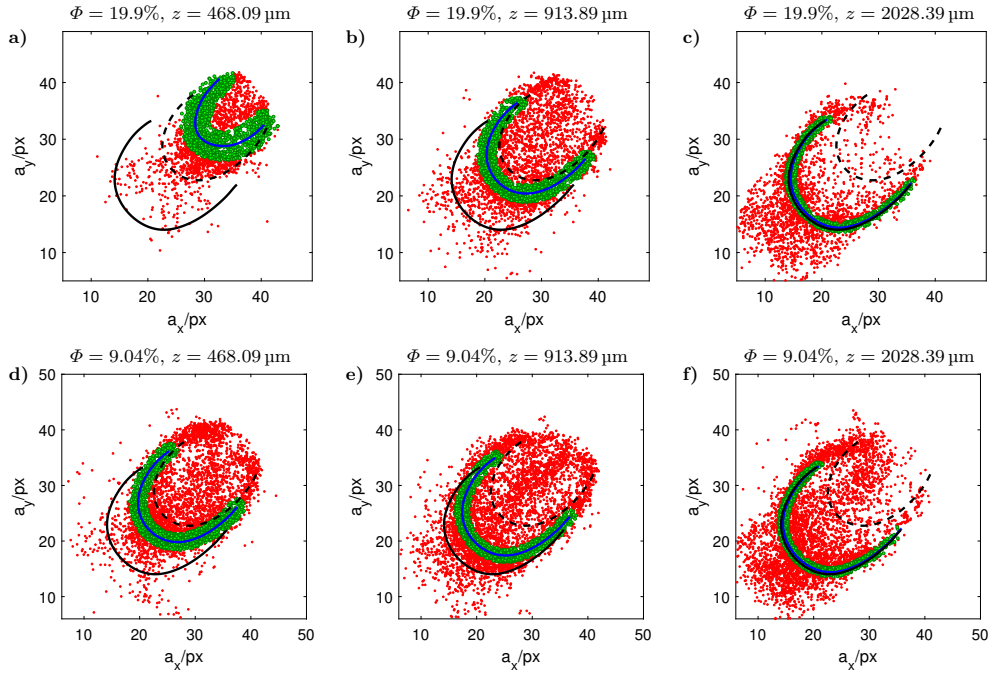

Figure 5.5: Best fitting calibration curve (blue line), valid a_x-a_y data (green dots) and rejected a_x-a_y data (red dots) for different measurement planes ($c_a = 0.5547$, $c_I = 0.5$, $c_D = 4$). The solid and the dashed line are the calibration curves as presented in Fig. 5.4 for a static suspension at Φ=0.01% and Φ=19.9%, respectively. a) $z = 468.09\,\mu m$, $\Phi = 19.9\%$, b) $z = 913.89\,\mu m$, Φ=19.9%, c) $z = 2028.39\,\mu m$, Φ=19.9%, d) $z = 468.09\,\mu m$, $\Phi = 9.04\%$, e) $z = 913.89\,\mu m$, $\Phi = 9.04\%$, f) $z = 2028.39\,\mu m$, $\Phi = 9.04\%$

Figures 5.5a-f display the best matching calibration curve (blue solid line) and corresponding valid data points (green dots) and outliers (red dots) as defined in section 5.1, for measurement planes located at z=468.09 µm, z=913.89 µm and z=2028.39 µm for $\Phi = 9.04\%$ and $\Phi = 19.9\%$ particle volume fraction, respectively. As can be seen in Fig. 5.5a it turns out for $\Phi = 19.9\%$ at a measurement position of $z = 468.09$ an extrapolated calibration curve (blue line) fits best to the measurement data. The reason for this is, that during the flow measurement the transparent particles are well distributed along the channel height and not settled to a bottom layer as during the calibration. We therefore conclude, that the distortion induced by a static bottom layer of transparent particles on top of a labeled particle is less intense than the distortion

created by homogenously distributed transparent particles at the same total volume fraction. Therefore an extrapolation of the calibration curve as displayed in Fig. 5.4 is needed to capture the calibration curve deformation during the flow measurement.

An interpolation of the maximum Euclidean distance threshold a_D as defined in section 5.1) is crucial as the scattering of a_x-a_y-I data varies along the gap height within the experiments as shown in chapter 4. In a suspension flow the scattering increases the closer labeled particles are located to the channel bottom. This can be seen from Figures 5.5a-c and d-e where the maximum distance of valid data points (green dots) with respect to the calibration curve (blue line) decreases when the measurement plane is shifted towards the channel top (increasing z values). In the present study we use the maximum light intensity I of the particle images for outlier detection. This is essential for the algorithm to reliably pick the best matching calibration curve. The importance of additionaly considering the light intensity as an outlier criterion can be better understood from Fig. 5.6, where we show the best fitting calibration curve and a typical distribution of I among the a_x and a_y scatter data. As can be seen, the light intensity increases close to the calibration curve. For using the light intensity as an additional outlier criterion we inter- and extrapolate the value of the intensity threshold I_{thr} analogous to a_D. Data points with $I < I_{thr}$ are rejected. The whole procedure is applied to the a_x, a_y and I data of all measurement planes, so that for every measurement plane the out-of-plane positions of the particles are computed. Hence, the absolute particle positions can be computed with respect to the channel wall by considering the particle out-of-plane positions and the corresponding measurement plane position. In Fig. 5.7 we show which interpolated calibration curve (see Fig. 5.4) matches best with respect to the z position of each measurement plane. As can be seen for the

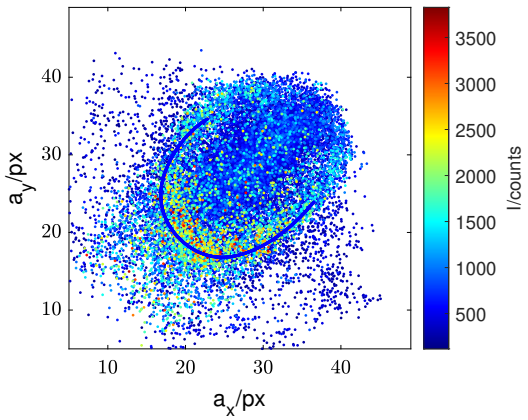

Figure 5.6: Typical distribution of scattered a_x, a_y and I data obtained in one measurement plane ($z = 1136.79\,\mu m$) during the flow measurement for Φ=12.97%. All data gathered in the measurement is displayed. Blue line=best fitting calibration curve.

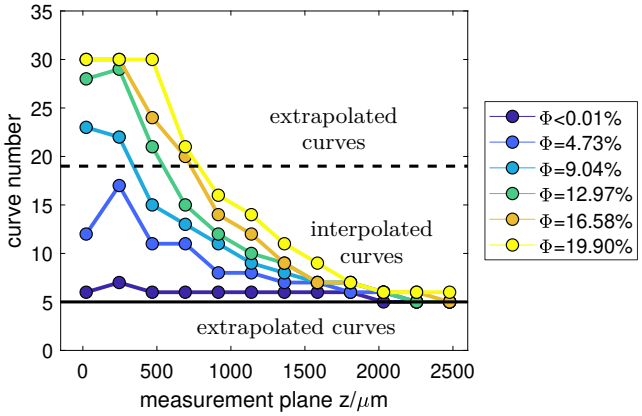

Figure 5.7: Number of best matching calibration curve as function of z-coordinate of measurement plane for the flow measurements presented in Fig. 5.8. Solid black line=calibration curve for ($\Phi < 0.01\%$) (curve number 5 in Fig. 5.4), dashed black line=calibration curve for ($\Phi = 19.9\%$) (curve number 19 in Fig. 5.4)

lowest volume fraction ($\Phi < 0.01\%$) the algorithm picks calibration curves 5, 6 and 7 for calculating the out-of-plane positions. For $z > 2000\,\mu m$ and $\Phi < 0.01\%$ the best fitting calibration curve matches with the calibration curve for $\Phi < 0.01\%$ (number 5). For lower values of z, curves 6 and 7 are selected for $\Phi < 0.01\%$. However, the differences between the best matching calibration curves for $\Phi < 0.01\%$ are small and it is sufficient to consider curve number 5 only for the whole measurement. On the contrary, the curve number changes significantly with increasing z for all flow measurements at higher particle volume fractions ($\Phi \geq 4.71\%$). This change becomes more pronounced with increasing volume fraction and appears to be nonlinear as can be clearly seen from Fig. 5.7. Obviously for $\Phi \geq 9.04\%$ extrapolated calibration curves are required, as the maximum curve number exceeds 19. For $\Phi = 19.9\%$ there is a plateau for $z \leq 468\,\mu m$, where the curve number is constant. It seems necessary here to extrapolate further to a higher curve number. However, the distortions of the scatter data for $z \leq 245\,\mu m$ at the highest volume fraction of $\Phi = 19.9\%$ are too strong to capture them by further extrapolation to higher curve numbers. Hence, for measurement planes $z \leq 245\,\mu m$ there is a lack of valid data points and the error of the calculated particle position and velocity increases sharply, as will be also discussed hereafter.

Fig. 5.8a-f show the measured velocity profile and the associated number of valid particles of the plane channel flow for six individual volume fractions between $\Phi \leq 0.01\%$ and $\Phi = 19.9\%$ obtained with the aforementioned procedure. Particle velocities are calculated using a simple nearest neighbour algorithm.

The scattered data of the particle velocity of each individual measurement plane is color coded according to the legend in Fig. 5.8.

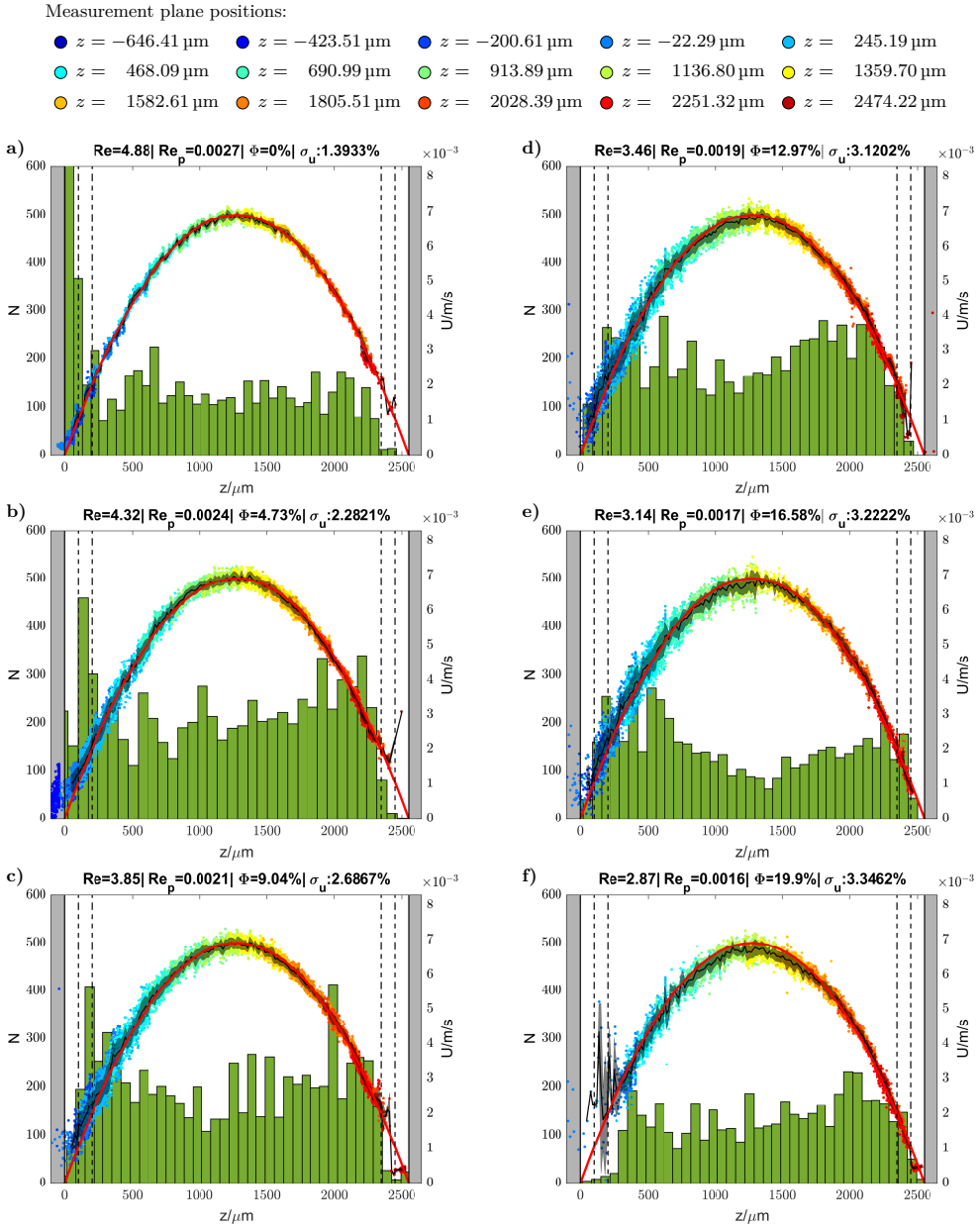

Figure 5.8: Measured velocity profile and number of valid particles for different particle volume fractions. Green bar plot = number of valid particles. Red line = analytical velocity profile. Colored dots = scatter data of measured velocity of individual measurement planes as given in the legend. Black line with shaded error marker = averaged velocity with standard deviation. The dashed vertical lines indicate a distance of 100 µm and 200 µm with respect to the wall. a) $\Phi < 0.01\%$, b) $\Phi = 4.73\%$, c) $\Phi = 9.04\%$, d) $\Phi = 12.97\%$, e) $\Phi = 16.58\%$, f) $\Phi = 19.9\%$

For comparison we show the velocity profile for a rectangular channel as given in Shah et al. (2014) as a red line. The bulk Reynolds number shown in Fig. 5.8a-f is defined as $Re = (U_{\mathrm{Bulk}} D_H \rho_{\mathrm{RIM}})/\nu_{\mathrm{eff}}$ with the effective viscosity estimated as $\nu_{\mathrm{eff}} = \nu_{\mathrm{RIM}}(1 + 2.5\Phi + 5.2\Phi^2)$ according to Batchelor and Green (1972). The particle Reynolds number is estimated as $Re_p = Re(d_p/D)^2$, where D denotes the gap height, as used for example by Shichi et al. (2017). In general, it can be seen that the measured velocity profile shows a good agreement with the analytical solution for all considered volume fractions. For higher volume fractions the maximum velocity is slightly lower than the velocity obtained from the analytical solution. This effect could be a result of particle-particle interactions. However the effect is small.

By comparing the scattered velocity data gathered in adjacent measurement planes (colored dots) it can clearly be seen that there is no signifcant mismatch of the data in the regions where the measurement planes overlap. The velocity data of the individual measurement planes merges together smoothly. Hence, choosing the best fitting calibration curve provides a sufficient reconstruction accuracy over the whole measurement volume depth. However, it should be mentioned that in different experimental setups the calibration curve may undergo a more pronounced shape change along the channel height. Hence individual particle images may deviate strongly from the calibration curves depending on their individual z-position relative to the measurement plane. In such scenarios it may be required to reduce the measurement volume depth in each measurement plane and simultaneously increase the number of measurement planes, or interpolate an individual calibration curve for each particle in an iterative procedure.

The uncertainty of determining the in-plane velocity increases from σ_u=1.39% to σ_u=3.34% with respect to the maximum streamwise velocity as the volume fraction increases from $\Phi \leq 0.01\%$ to $\Phi = 19.9\%$. The uncertainty for determining the out-of-plane velocity increases from σ_w=9.6% to σ_w=22.57% at the same time. We assume that the loss of accuracy with increasing volume fraction is related to two different effects. Firstly, the accuracy of determining the particles out-of-plane position decreases with increasing values of Φ as more layers of transparent particles inducing distortions to the images of the labeled particles. Secondly the accuracy of detecting the in-plane position of the particles centers decreases with increasing volume fractions due to the disturbances induced by the transparent particles. This effect becomes visible in the uncertainty in determining the span-wise velocity component which increases from σ_v=0.50% to σ_v=1.78% as the volume fraction increases from $\Phi \leq 0.01\%$ to $\Phi = 19.9\%$.

The accuracies obtained within this work are lower than those achieved in APTV with small particles and dilute suspensions. This accounts especially for the out-of-plane velocity. For instance Cierpka et al. (2010a) obtained uncertainties of σ_u=0.9% and σ_w=3.72% of u_{max}. We assume that the uncertainty is larger due to slight refractive index mismatches between the RIM-liquid and the transparent particles.

Regarding the number of detected particles it can be seen from Fig. 5.8, that there is no obvious lack of data visible among all the planes. Hence, we conclude that the described interpolation procedure is suitable for capturing the shape changes (a_x, a_y) and the mean Euclidean scattering distance a_D of the calibration curve. In Fig. 5.8c,d,e a slight decrease in the number of detected particles towards the middle of the channel becomes evident, which may be related to the measurement procedure and not to a physical phenomena. In fact, for all flow measurements the estimated particle Reynolds numbers are small ($Re_p << 0.1$) as can be seen from Fig. 5.8a-f. Baghat et al. (2009) showed that inertial migration of particles occurs for $Re_p > 0.1$. Hence we conclude that such effects can be neglected within our experiments.

Precisely measuring the particle concentration along the channel height is of great importance for the investigation of physical phenomena, however to developing an APTV based procedure to reliable measure the particle concentration is beyond the scope of this work.

As the particle Reynolds numbers are small and a good agreement could be observed between measured and theoretical velocity profile we conclude that the particle dynamics are negligible here. Thus, particles can approximately be considered as fluidtracers.

5.3 Discussion and Conclusion

In the present study we showed that APTV can be applied to measure the particle dynamics of suspensions of up to 19.9% volume fraction. Measurements have been performed at six different volume fractions ranging from $\Phi \leq 0.01\%$ to $\Phi = 19.9\%$.

To make the suspension optically accessible we use a refractive index matched liquid (RIM-liquid) and transparent particles of which just a small portion is labeled with a fluorescent dye. Firstly, we study the effect of remaining image aberrations due to slight refractive index mismatches. We observe that slight deviations of the refractive index of individual transparent particles induce optical distortions that result in a shape change of the calibration curve of a labeled calibration particle. Thus, at high volume fractions of transparent particles, images of labeled particles get increasingly distorted the closer they are located to the channel bottom as more transparent particles disturb the optical path. To overcome this effect we adapt the interpolation method presented in chapter 4. Inter- and extrapolated calibration curves for labeled particles are generated from calibration measurements at $\Phi \leq 0.01\%$ and $\Phi = 19.9\%$ and are related to the measurement data in a best fit procedure. In the present study, we used the light intensity as a simple outlier criterion. We found this additional outlier criterion to be crucial for a stable fitting procedure. Depth reconstruction accuracies of $\sigma_z/\Delta z = 0.90\%$ and $\sigma_z/\Delta z = 2.53\%$ were achieved for labeled static calibration particles of $d_p = 60\,\mu m$ and a magnification of $M = 10\times$ in a suspension of $\Phi \leq 0.01\%$ and $\Phi = 19.9\%$ volume fraction, respectively. Ultimately, we validated the interpolation

technique successfully by measuring the laminar velocity profile in a rectangular duct with a $2.550 \times 30\,\mathrm{mm}^2$ cross section for six individual volume fractions ranging from $\Phi \leq 0.01\%$ to $\Phi = 19.9\%$. The uncertainty of the measured in-plane velocity was found to be $\sigma_u = 1.39\%$ and $\sigma_u = 3.34\%$ while the uncertainty for the out-of-plane velocity was $\sigma_w = 9.06\%$ and $\sigma_w = 22.57\%$ for $\Phi \leq 0.01\%$ and $\Phi = 19.9\%$, respectively. These uncertainties are higher compared to those in APTV with small particles and dilute suspensions. However, we are convinced that by using a improved illumination technique and the use of a 3D calibration the uncertainties can be further reduced. Furthermore we only used two calibration curves generated at $\Phi \leq 0.01\%$ and $\Phi = 19.9\%$ for our interpolation technique. In future works the method could be improved by considering a higher number of volume fractions for generating inter- and extrapolated curves. In fact, preliminary tests (not shown here) indicate that it is benefitial to perform the calibration at solid volume fractions which are actually higher than those used during flow measurements. Finally, to date APTV has been scarcely applied to large fluorescent particles - following studies can help to gain further understanding of how particle size and properties of the optical system affect the measurement accuracy. In the following chapter 6 the latter issue will be adressed and the influence of the particle size on the calibration curves will be investigated extensively. Moreover, the refractive index matching technique will be utilized to measure the dynamics of mono- and tridisperse suspensions in square capillaries at volume fractions up to $\Phi = 9.1\%$.

6 Applying APTV to polydisperse suspensions beyond the dilute regime [1]

In this chapter, a method is developed which allows to measure the dynamics of polydisperse suspensions flows by means of APTV. Successful measurements are presented for both mono- and tridisperse suspensions flows in a square duct of up to $\Phi = 9.1\%$ particle volume fraction. Like in the previous chapter, few particles ($\Phi = 0.08\%$) of a refractive index matched suspension are labeled with fluorescent dye to make them visible for the camera. While the previous chapter considered the effect of increasing Φ on the calibration curves, in this chapter the effect of increasing the particle size is investigated. Calibration measurements are performed for ten different particles diameters d_p ranging from $d_p = 15\,\mu m$ to $d_p = 260\,\mu m$.

Section 6.1 adresses the effect of particle size on the calibration procedure. Thereby both theoretical calibration curves as well as measured calibration curves are discussed. Section 6.2 considers the application of the 3D euclidean calibration procedure on different particle sizes. In section 6.3 migration phenomena in mono- and tridisperse suspensions flows are investigated utilizing the 3D calibration procedure. In section 6.4 the results obtained in this chapter are summarized.

The theory and state of the art relevant for this chapter are given in section 1.2.2 (fundamentals of suspension flows) and section 1.2.4.3 (theory and state of the art of APTV). The setups utilized to obtain the results presented in the present chapter are given in section 2.1.3.

6.1 Calibration procedure

As described in section 1.2.4, the deformation of the particle image axis lengths (a_x and a_y) can be described by the following equation (Cierpka et al. (2010a)):

$$a_i(z_i) = M\sqrt{d_p^2 + 1.49{\lambda_L}^2\left(\frac{n_0^2}{NA^2} - 1\right) + 4(z_i)^2\left(\frac{n_0^2}{NA^2} - 1\right)^{-1}}\, i = x, y \qquad (6.1)$$

[1] This chapter is adopted from "Utilizing APTV to investigate the dynamics of polydisperse suspension flows beyond the dilute regime." written by Philipp Brockmann, Christoph Szymanczyk, Hatim Ennayar and Jeanette Hussong, submitted to “Experiments in Fluids” in November, 19th, 2021 (submission id: EXIF-D-21-00525)

Here $z_i = z - F_{iz}$ is the distance between particle and respective focal plane. The variables d_p, λ_L, n_0, M, NA are the particle diameter, the wavelength emitted by the particle, the refractive index of the liquid, the magnification and the numercial aperture of the objective, respectively.

In Fig. 6.1a we display a_x and a_y as function of $z - z_0$ obtained with equation (6.1) for different values of d_p. The reference position z_0 here refers to the scanning position where the particle is focused in F_{xz}. As can be seen, a_x and a_y first decrease down to a minimum and then increase again as $z - z_0$ increases. Thereby, the curves of a_y and a_x are staggered and the minimum values occur at F_{yz} and F_{xz}, respectively. With increasing d_p the values of a_x and a_y increase and the curvature close to the minimum decreases. Further, the total change of a_x and a_y becomes less pronounced as d_p increases. Hence, in theory, for a given optical setup the resolution for reconstructing the particle's depth position decreases with increasing particle diameter d_p.

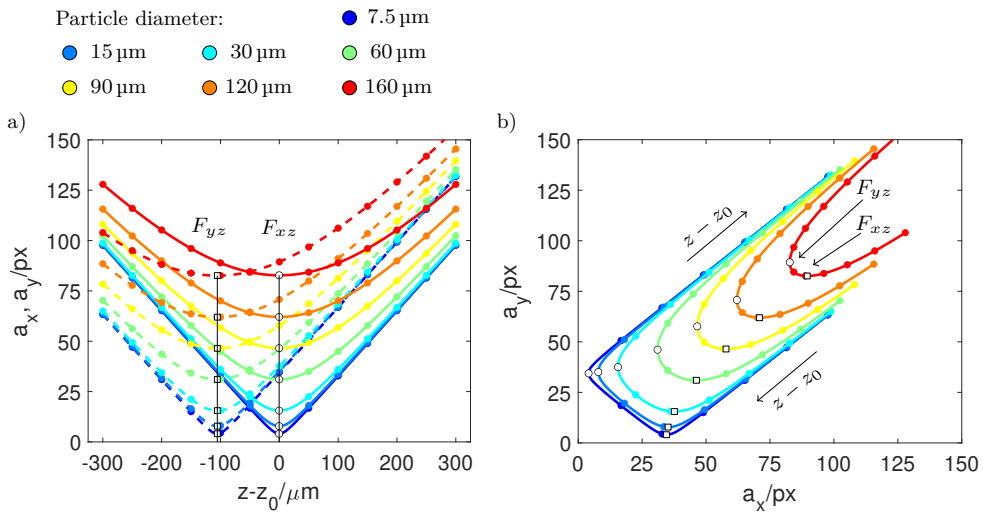

Figure 6.1: Plots of the axis lengths a_x and a_y obtained with equation (6.1) for $\lambda_L = 590\,\text{nm}$, $n_0 = 1$, $M = 10$, $NA = 0.3$ and selected values of d_p. White filled dots and squares indicate the a_x, a_y values at the focal planes F_{yz} and F_{xz}, respectively. Increasing z is associated with traversing the objective as depicted in Fig. 1.12. a) a_x (solid line) and a_y (dashed line) as function of $z - z_0$ b) a_y as function of a_x

The difference between small and large particles becomes more clear when a_y is plotted over a_x as depicted in Fig. 6.1b. This presentation is fundamental for the Euclidean calibration procedure, which will be described later in the text. As can be seen in Fig. 6.1b, with increasing d_p the curves are shifted towards larger values of a_x and a_y while at the same time the maximum change of a_x and a_y over the same z-range decreases significantly. Hence, the resolution of z-position reconstruction reduces for

increasing d_p as concluded from Fig. 6.1a. Furthermore, it becomes evident from Fig. 6.1b that, especially for smaller d_p, the curves collapse outside the focal planes which are highlighted as white filled dots and squares in Fig. 6.1b, respectively.

For reconstructing a real particles z position depending on its a_x and a_y values a calibration function, generated from recorded images, is needed. For this, we utilize the 3D Euclidean calibration procedure as developed in chapter 4. This calibration method requires a homogenous light distribution across the image to work properly, which we ensure by using a high power LED for illumination. In the following, we summarize the basic steps of the calibration procedure for an exemplary set of fluorescent PMMA particles of 30 µm and 60 µm.

To obtain the change of a_x and a_y for different particle depth positions, labeled and wall attached particles are scanned in steps of 1.25 µm over a distance of 1000 µm. Fig. 6.2 shows the result of such a scan for fluorescent PMMA particles located on a glass plate. In each recorded frame the individual particle centroids are detected by binarizing the image and applying the MATLAB function "regionprops". The threshold for binarizing the image within this step is defined as the median of the whole image intensity. For extracting the a_x and a_y from the individual particle images in the next step, we employ two different approaches, which will be compared in the following.

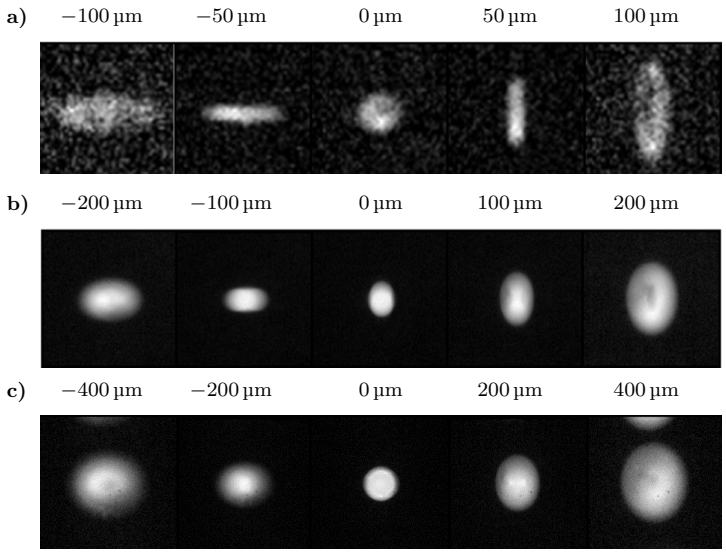

Figure 6.2: Particle images for different $z - z_0$ obtained in calibration measurements ($n_0 = 1$, $M = 10\times$). Particle images are not to scale. Increasing z is associated with traversing the objective as depicted in Fig. 1.12. a) d_p=15 µm b) d_p=60 µm c) d_p=155 µm.

In the binarization approach the particle image is cropped out by a rectangular section and binarized using MATLAB's "*imbinarize*". The a_x and a_y values are then extracted using matlab "*regionprops*" subfunctions "*major axis*" and "*minor axis*". For the autocorrelation method the particle image is cropped out by a circular section around the detected particle centroid at a defined radius of $3.6 \cdot d_p/px$. Hence, the cropped particle image is autocorrelated and the isoline where the autocorrelation coefficient is equal to c_a, is extracted. a_x and a_y are then given as the maximum x and y span of the isoline. c_a is denoted as the autocorrelation coefficient as introduced in chapter 4 and set to $c_a = 0.5184$ within this work.

a_x and a_y as function of z-z_0 obtained with the two aforementioned methods are displayed in Fig. 6.3a,b together with the theoretical curves calculated with equation (6.1). By comparing the data for d_p =30 µm (small dots) and d_p =60 µm (large dots) it can be seen that the measured a_x, a_y values increase with increasing particle size for both the autocorrelation method and the binarization approach. Obviously, the

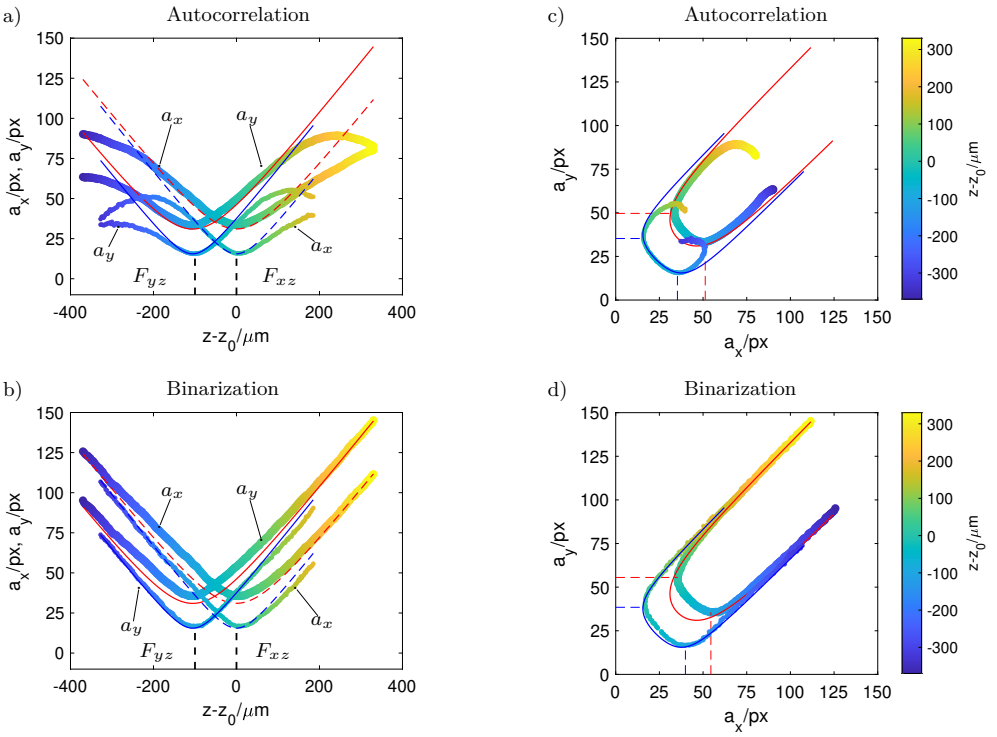

Figure 6.3: Axis lengths a_x and a_y over $z - z_0$ as well as a_y over a_x for particles of 30 µm (thin colored line) and 60 µm (bold colored line) for $n_0 = 1$ (air) and $M = 10\times$ (Setup 3). Dotted uni-color line= theoretical curve for a_x, solid uni-color line= theoretical curve for a_y, red= 60 µm particles, blue= 30 µm particles. a) a_x and a_y over $z - z_0$ b) a_x and a_y over $z - z_0$ c) a_y over a_x d) a_y over a_x

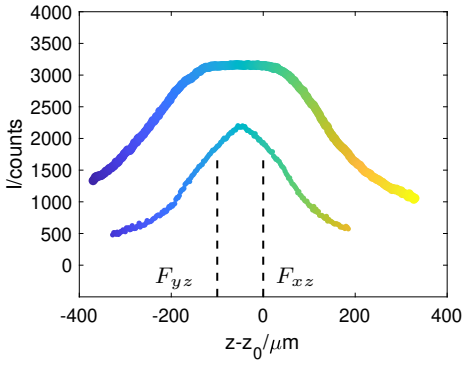

Figure 6.4: Maximum light intensity I of the particle image over $z - z_0$ for particles of diameter 30 µm (thin colored line) and 60 µm (thick colored line)

data obtained with the autocorrelation method coincides with equation (6.1) inbetween the focal planes but deviates significantly from the theroetical curves outside the focal planes (Fig. 6.3a). In contrast, the a_x, a_y data obtained with the binarization approach matches well with the theroretical data (Fig. 6.3b).

In Fig. 6.3c,d we show a_y plotted over a_x which is required for the Euclidean calibration (Cierpka et al. 2010a, Brockmann et al. 2020, Brockmann and Hussong 2021). Obviously here, for both the autocorrelation and the binarization approach, the curves for the small particles (small dots) and the large particles (large dots) intersect (Fig. 6.3c,d). Hence, if both curves are considered together they do provide ambiguous data in the a_x, a_y space. In contrast, the maximum particle light intensity $I(z - z_0)$ differs significantly for both particle sizes as can be seen in Fig. 6.4. Hence, by combining $I(z - z_0)$ and $a_x(z - z_0)$, $a_y(z - z_0)$ an unambiguous dataset is obtained. As we will show in section 6.2 we will use this combination of data to generate unambiguous 3D Euclidean calibration curves for polydisperse suspensions.

In general, to obtain a calibration curve we perform the procedure developed in chapter 4 and chapter 5. In the following, we present the basic steps of the procedure applied on our data. To generate a calibration curve to be used in a velocity measurement, the calibration data of several particles randomly distributed in the field of view is required. By this individual deviations in particle shape, labeling and minor optical aberrations are accounted for statistically. In Fig. 6.5a we show a set of scattered a_x, a_y and I data obtained from 25 60 µm particles. As first step, we determine the median of $I(z - z_0)$, which is represented by the black line in Fig. 6.5a and referred to as $\overline{I}$. Hereafter only data points associated with $I \geq c_I \cdot \overline{I}_{\max}$ are evaluated and c_I is referred to as the intensity coefficient. We define further an intensity threshold as $I_{thr} = c_I \cdot \overline{I}_{\max}$. A detailed discussion about the influence of c_I is provided in chapter 4. Subsequently, polynomials are fitted to the a_x and a_y scatter data (Fig. 6.5b). Here a polynomial degree of 14 has proven to be suitable for different types of particles and

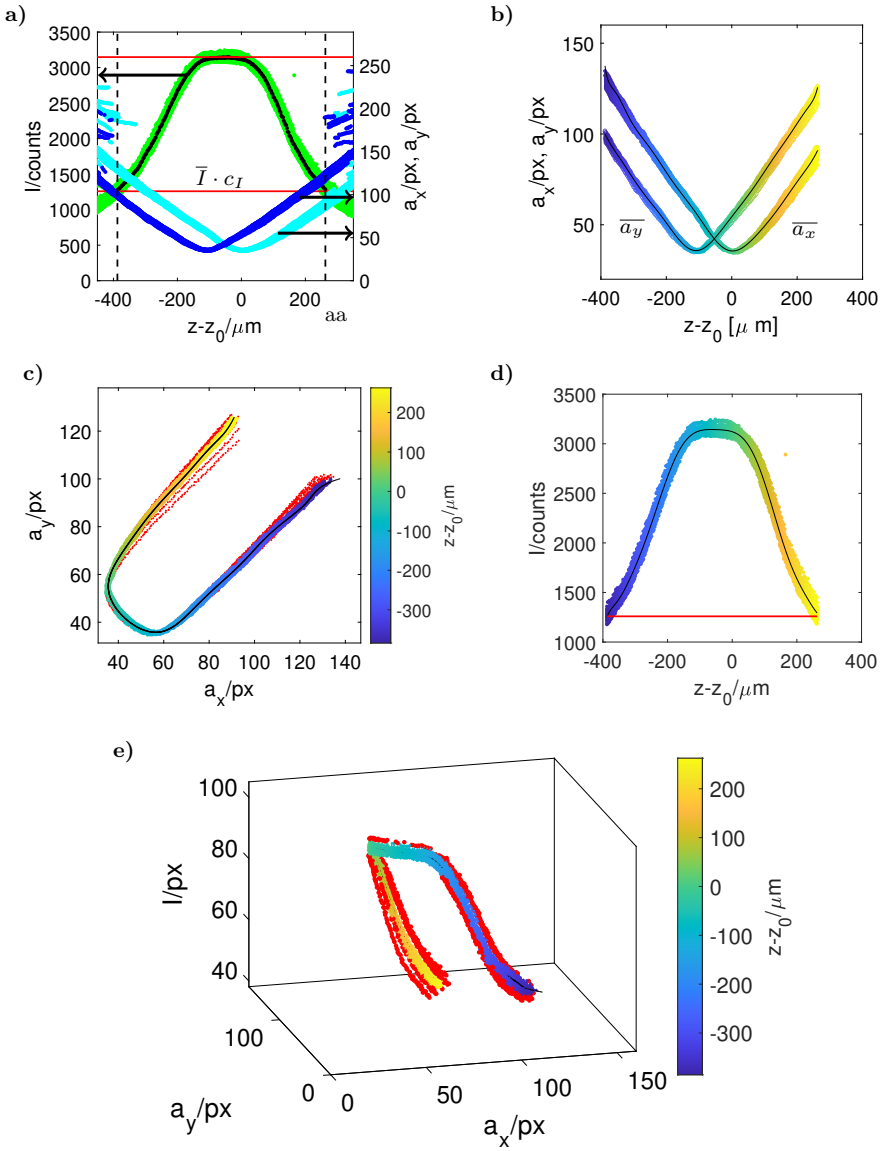

Figure 6.5: Procedure of generating a calibration function ($c_a = 0.518$, $c_I = 0.4$, $c_D = 2$, $M = 10\times$, $d_p = 60\,\mu$m). Scale of colormap is given in 6.5c. a) A $z-z_0$ range of scattered data is selected by light intensity I (light blue dots=a_x, dark blue dots=a_y, green dots=I, black dots=$\overline{I}$). b) A polynominal is fitted to a_x and a_y. c) The relative position $z-z_0$ of scattered a_x-a_y data (colored dots) is reconstructed by the 2D Euclidean distance method (black line=polynomials, red dots=outliers). d) A polynomial is fitted to I data. e) Reconstruction of $z-z_0$ of scattered a_x-a_y-I data (colored dots) by 3D Euclidean distance method (black line=polynomials, red dots=outliers).

optical properties as shown in chapter 5. By plotting the fits of a_y (denoted as $\overline{a_y}$) over the fit of a_x (denoted as $\overline{a_x}$) the 2D calibration curve is obtained (Fig. 6.5c). Now the depth position of a particle can be determined by relating its measured a_x, a_y values to a point on the calibration curve that is given by the minimum Euclidean distance and hence reading out the corresponding $z - z_0$ value (Cierpka et al. 2010a). If the Euclidean distance of a a_x, a_y pair exceeds the threshold a_D, which is defined as the mean distance of all a_x, a_y data multiplied by the factor c_D, it is rejected as an outlier (see chapter 4). In the results in Fig. 6.5 c_D is 2, which provides an overall depth reconstruction uncertainty of $\sigma_{z,2D} = 4.7\,\mu\text{m}$ and $N \approx 6200$ valid data points for $d_p = 60\,\mu\text{m}$ particles and the 2D reconstruction procedure. With $c_I = 0.5$ the measurement volume depth for the given example is $\Delta z = 650\,\mu\text{m}$ such that the ratio $\sigma_{z,2D}/\Delta z$ is 0.72%. If a polynom is fitted to the I scatter data as shown in Fig. 6.5d, it can be used to generate a 3D calibration curve as presented in Fig. 6.5e. a_x, a_y, I scatter data can now be assigned to this curve by means of the three-dimensional Euclidean distance. To ensure a_x, a_y and I are in the same order, I is normalized by $I_{\max}$ and multiplied by the maximum axis length as explained in chapter 4. Mathematically this factor, hereafter denoted as intensity scale factor, can be defined as:

$$c_s = \frac{\max[(\max(a_x) - \min(a_x)); (\max(a_y) - \min(a_y))]}{I_{\max}} \tag{6.2}$$

Using the 3D calibration an overall depth reconstruction uncertainty of $\sigma_{z,3D} = 3.95\,\mu\text{m}$ achieved for the given example such that $\sigma_z/\Delta z$ is 0.69%. If the autocorrelation method is applied the gain in accuracy when using 3D instead of 2D calibration is even more significant ($\sigma_{z,2D} = 8.25\,\mu\text{m}$ and $\sigma_{z,3D} = 5.45\,\mu\text{m}$).

6.2 3D calibration for different particle sizes

As discussed in section 6.1 the 2D calibration curves for particles of different size intersect outside the focal planes creating ambiguities. Hence, in a polydisperse suspension flow particles of different size can not be assigned correctly to the calibration curve. To overcome this problem König et al. (2020) successfully employed a cascaded convolutional neural network to distiuingish between particles of different size. We use a different approach here and utilize the 3D calibration to differentiate particle species thereby exploiting the fact that the particle light intensity increases sharply with increasing particle size. In Fig. 6.6 we present the 2D and the 3D calibration curves for different smaller ($15\,\mu\text{m} < d_p < 60\,\mu\text{m}$, Microbeads) and larger particles ($101\,\mu\text{m} < d_p < 256\,\mu\text{m}$, Altuglas). Due to slightly different material properties, the small particles (Microbeads) provide a higher light intensity in relation to their size than the large particles (Altuglas) such that we present them separately. Here we only present calibration curves obtained with the binarization method. Data based on the autocorrelation have shown similar trends but are not shown here for conciseness of the paper. It can be seen clearly, that the 2D calibration curves intersect each other outside the focal planes. In contrast, the

3D calibration curves are well separated from each other as the light intensity strongly correlates with d_p. Please note that we display the absolute value of I instead of the normalized I.

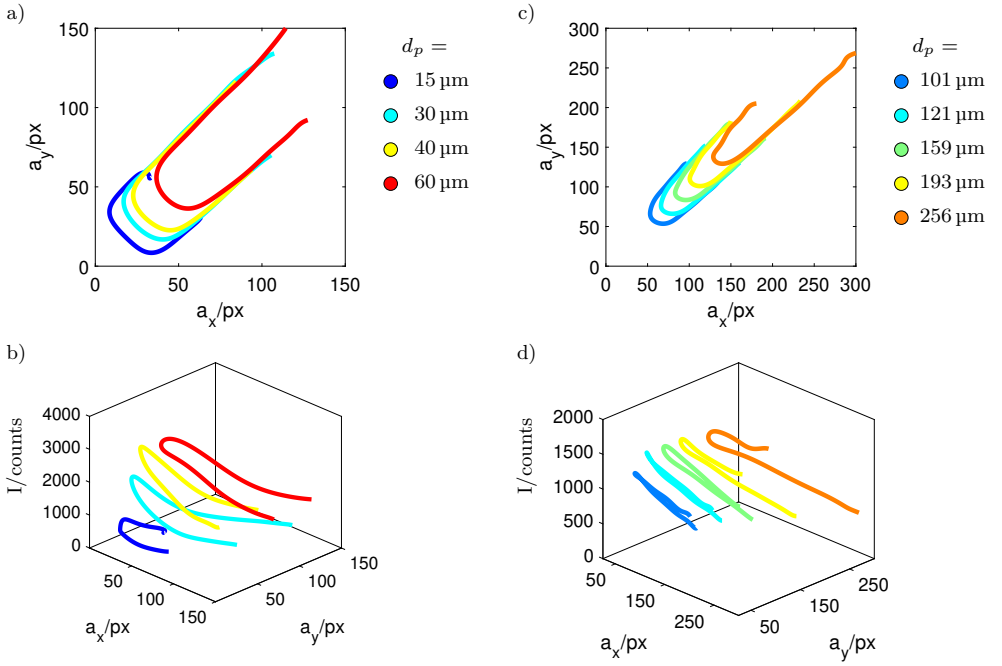

Figure 6.6: 2D and 3D calibration curves for particles of different diameters. a) 2D Calibration curves for 15 µm $< d_p <$ 60 µm. b) 3D Calibration curves for 15 µm $< d_p <$ 60 µm. c) 2D Calibration curves for 101 µm $< d_p <$ 256 µm. d) 3D Calibration curves for 101 µm $< d_p <$ 256 µm.

In the following, we will demonstrate the application of the 3D reconstruction procedure on mixed, scattered polydisperse calibration data with c_I set to zero. Hence, calibration data is included regardless of the light intensity over the full scanning range. By this we generate a test case close to measurement conditions by including a significant amount of erroneous a_x, a_y data, as can be seen exemplary for d_p=60 µm particles in Fig. 6.5a outside the dashed vertical bars. However, the calibration curves for the individual particle sizes are still obtained with $c_I = 0.4$ which corresponds to the calibration curve as shown in Fig. 6.5. As the calibration data is generated by a scanning procedure on static particles, the particle size as well as the out-of-plane position of each data point is known and we can evaluate the uncertainty in determining the particle size as well as the depth position. In Fig. 6.7a we present the 2D calibration curves for particles of d_p =15, 30, 40, 60 µm as shown in Fig. 6.6 together with the 2D calibration data. For this example the reconstruction procedure was applied to the curve for 60 µm particles (black and red line). Data that is assigned correctly to the calibration curve for 60 µm is

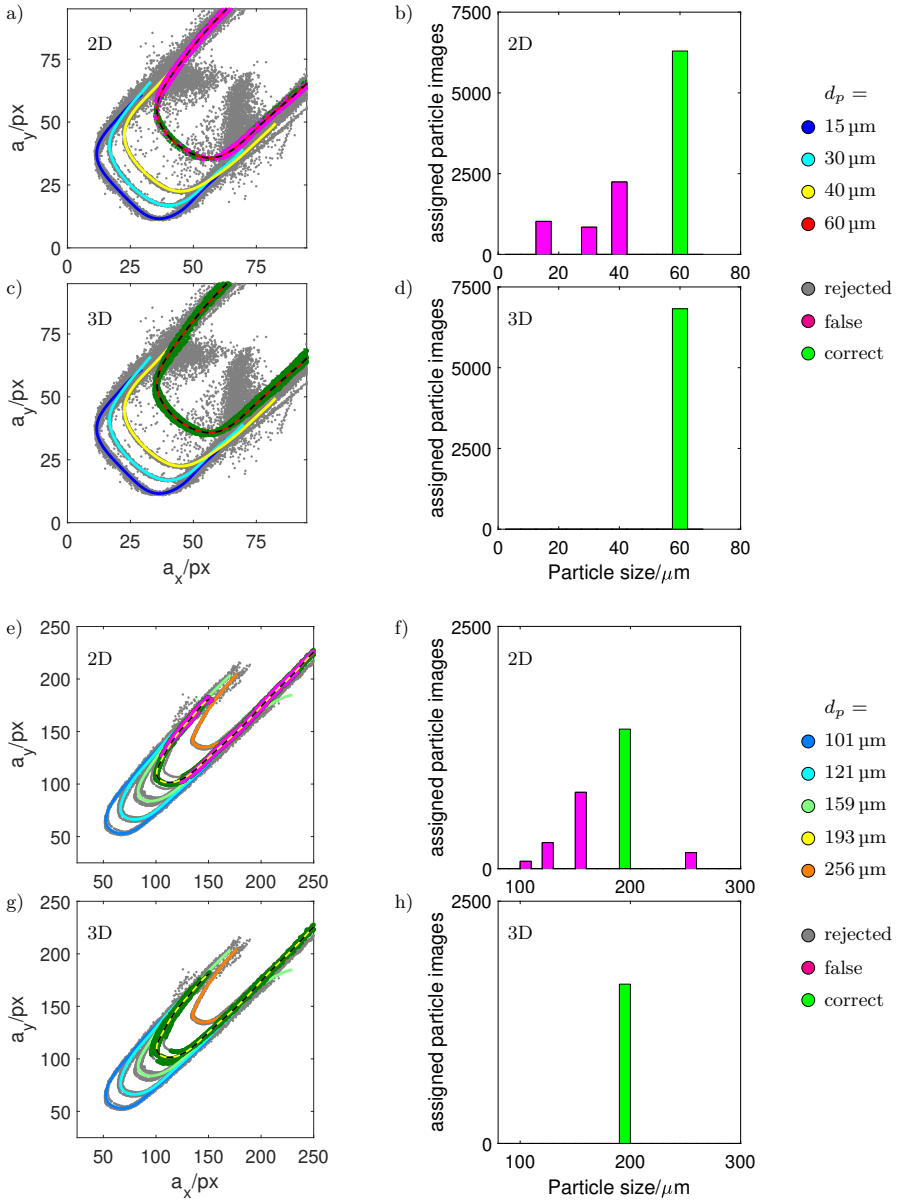

Figure 6.7: Applying the 3D Euclidean Calibration on mixed, scattered polydisperse calibration data. The reconstruction procedure is performed with the calibration curve for 60 µm particles in a-d (black and red line) and the calibration curve for 193 µm particles in e-h (black and yellow line). Symbols: Rejected data (gray), correct assigned data (green) and false assigned data (magenta). $c_a = 0.51$, $c_I = 0.4$, $c_D = 2$, $M = 10\times$. a,c) Calibration data for 15 µm $< d_p <$ 60 µm (a: 2D, c:3D). b,d) Histogram for 15 µm $< d_p <$ 60 µm (b: 2D, d:3D). e,g) Calibration data for 101 µm $< d_p <$ 256 µm (e: 2D, g:3D). f,h) Histogram for 101 µm $< d_p <$ 256 µm (f: 2D, h:3D).

plotted as green dots, while rejected data is grey. Data that is highlighted with magenta dots originates from d_p =15, 30 and 40 µm particles that were erroneously assigned to the calibration curve of 60 µm particles. From Fig. 6.7a it can be clearly seen, that the 2D calibration procedure yields a significant amount of erroneous detections outside the focal planes, where the calibration curves overlap. The amount of erroneously assigned 15, 30 and 40 µm particles is illustrated in the histogram in Fig. 6.7b. However, when the 3D calibration is used for the reconstruction procedure, it can be seen that almost all the data points are correctly assigned to the corresponding calibration curve (Fig. 6.7c and Fig. 6.7d). This observation also accounts for the 2D and the 3D reconstruction procedure applied on the data of larger particles (d_p =101, 121, 159, 193, 256 µm) when utilizing for instance the calibration curve for d_p =193 µm (black and yellow line), as can be seen from Fig. 6.7g and Fig. 6.7h. In fact, the 3D reconstruction procedure allows a reliable assignment of particle images to the correct calibration curve for all individual calibration curves depicted in Fig. 6.7a,c,e,g. In table 6.1 we provide an overview of correct and erroneously assigned particles using the 2D and 3D reconstruction for all depicted calibration curves, respectively. In table 6.1, erroneous detections are denoted as $N_{\mathrm{f,3D}}$ and $N_{\mathrm{f,2D}}$ for a 3D and 2D calibration, respectively. We further compare the efficiency of the 3D- and 2D reconstruction by computing the factor $\frac{N_{\mathrm{c,3D}}}{N_{\mathrm{c,2D}}}\frac{\sigma_{z,2D}}{\sigma_{z,3D}}$. This factor takes into account the number of correctly assigned particles as well as the uncertainty in determining the depth position of correctly assigned particles obtained with the 2D and 3D reconstruction, respectively. As can be seen, the factor assumes values higher than one for all particle sizes except for 15 µm which means that the 3D calibration provides more valid particles and/or a lower uncertainty in determining the z-position of valid particles for almost all cases. For 15 µm particles, the image quality as well the light intensity is not as homogenous as for larger particles which significantly affects the accuracy, especially of the 3D reconstruction ($\sigma_{z,2D} = 12.19$ µm, $\sigma_{z,3D} = 23.43$ µm for 15 µm particles). We recall here that a homogeneous light intensity is paramount for the accuracy of the 3D reconstruction. Even though the accuracy of the reconstructed depth position is reduced with the 3D reconstruction, no particle images are assigned incorrectly to the calibration curve of 15 µm particles.

6.3 Comparison of monodisperse and polydisperse Suspension dynamics

6.3.1 Experimental procedure

To investigate the migration behavior of mono- and tridisperse suspensions, flow measurements are performed in a square duct with 400×400 µm^2 and 600×600 µm^2 cross section. The suspensions are composed of RIM-liquid as proposed by Bailey and Yoda (2003) and PMMA particles (Microbeads) of 30 µm, 40 µm and 60 µm diameter. The square duct is filled with RIM-liquid and labeled particles such that the particle volume fraction is Φ = 0.08%. Due to slight density differences between RIM-liquid and

d_p	$\frac{N_{c,3D}}{N_{c,2D}} \frac{\sigma_{z,2D}}{\sigma_{z,3D}}$	$N_{c,2D}$	$N_{c,3D}$	$N_{f,2D}$	$N_{f,3D}$
15	0.699	6260	8408	1295	0
30	1.096	2598	2864	1709	0
40	1.210	5144	6203	1657	0
60	1.295	6297	6825	4106	0
101	1.132	743	894	615	1
121	1.424	1306	1645	951	61
159	1.043	2453	2747	1972	63
193	1.052	1440	1644	1297	0
256	1.190	838	944	1578	11

Table 6.1: Comparison of 2D and 3D reconstruction applied on polydipserse calibration data. $N_{c,2D}$ and $N_{c,3D}$ is the number of particles assigned to the correct curve with 2D and 3D calibration, respectively. Analogous, $N_{f,2D}$ and $N_{f,3D}$ are the number of incorrectly assigned particles.

particles, particles float to the top or settle to the bottom of the channel when the residence time in the square duct exceeds several minutes. In the absence of flow, these particles act as wall markers and are used to detect the absolute position of the duct and serve to set the origin of the z-coordinate as described in chapter 5. Subsequently, the syringe pump drives a constant suspension flow rate through the square duct into a container. Prior to the actual flow measurements, calibration measurements (as described in section 6.1) are performed on the particles at the bottom of the channel to generate calibration curves for the three particle sizes (30 µm, 40 µm, 60 µm). In the FVS the calibration was performed on particles located on the glass coverslip, as illustrated in section 2.1.3.

In chapter 5 it was shown that slight deviations of the refractive index of particles and RIM-liquid may lead to distortions of the particle images which become severe with increasing channel height. However, the height of the present ducts ($H = 400\,\mu m, 600\,\mu m$) is much less than that of the channel ($H = 2550\,\mu m$) used in chapter 5 such that the distortions can be neglected here. After calibration measurements are completed, the actual flow measurements are performed for the monodisperse and the polydisperse suspension for $\Phi = 0.08\%$ and $\Phi = 9.1\%$ for different bulk Reynolds numbers. In the polydisperse measurements the individual volume fraction of each single species is kept equal at 1/3 of $\Phi = 0.08\%$ and $\Phi = 9.1\%$.

During the flow measurements in the LVS the duct is scanned in steps of 74 µm or 148 µm and 21500 images with a resolution of 512×384 pixel (Lateral view) at 300 fps up to 8354 fps are recorded at each measurement plane. By this, depending on the duct height, data from 6 to 9 individual measurement planes is captured. In the FVS 4×16500 images with a resolution of 512×512 pixel are recorded at a single measurement plane located 250 µm to 500 µm upstream of the channel exit. To enhance the signal to

noise ratio a median filter with a kernel of a 5px×5px and a bandwidth filter filtering structures of 3 to 70 pixels in diameter is applied (Cierpka et al. 2010b). In the FVS defocussed particles in the background lead to a significant reduction of the signal to noise ratio. As the light intensity of 40 µm and 60 µm is significantly higher than that of the 30 µm particles, the backgroung noise affects the image quality of the latter ones the most. Therefore, we perform the polydisperse measurements in the FVS sequentially, with only one particle size labeled at the time. Further, an additional time series substract median filter is applied to the data recorded in the FVS. After image post-processing, the particle positions and velocities are reconstructed. Hence, the a_x, a_y and I of all detected particles from the different measurement planes is extracted using the autocorrelation method. While the binarization method provides a_x, a_y values close to the theoretical curves and in general yields a higher accuracy in the calibration measurements, the autocorrelation method is found to be more robust against fluctuations of the light intensity under measurement conditions as also concluded by Cierpka et al. (2010a).

Thereby, particle images of all particle sizes are cropped out at a fixed radius of 30 pixel. By comparing the I scatter data from the measurement with the I calibration curve we observe that the intensity level of I of the scattered data is slightly increased. The underlying reason is, that during the flow measurement a larger number of fluorescent particles is present in the picture. Furthermore, particles are distributed at different z-positions leading to superimposition of the light intensity. This effect is more pronounced for smaller particles and can be easily compensated by scaling the data with a constant factor. As the scattered data of I of the individual species is well separated (as shown in Fig. 6.9) this is sufficient for a proper differentiation between the species.

Hence the a_x, a_y, I scatter data of all measurement planes is assigned to the 3D calibration curves in order to determine the particles out-of-plane positions. In the polydisperse case, the data is compared to all three calibration curves (for 30 µm, 40 µm and 60 µm). Thereby, the a_x, a_y, I data is automatically assigned to the correct calibration curve with the 3D Euclidean reconstruction procedure as described in section 6.1 and section 6.2. Finally, the absolute particle positions are obtained by combining the measurement plane position and the particle-out-of-plane positions. Hence, the absolute particle positions can be computed with respect to the channel wall by considering the particle out-of-plane positions and the corresponding measurement plane position. Particle velocities are determined using a simple nearest neighbor algorithm. Outliers are removed with a median filter with a binning length of 10 µm in cross-sectional direction. For obtaining averaged velocity profiles the scattered velocity data is averaged across the horizontal center line with a binning length of 20 µm with data being considered in a lateral distance of 10 µm away from the centerline. The data is visualized in 2D histograms, with bins of 10 µm width in x and y direction and filtered by a Gaussian filter with a filtering length of 5 bins (Lansey 2021). For validation of the APTV measurements we further visualize the particle distributions

directly by performing stigmatic measurements in the FVS. For this, the cylindrical lens is removed from the optical path. Hence, 16197 images with a resolution 512×512 pixel at different frame rates up to 6200 fps are recorded. In the post processing, first the average of all images is computed. Hence the average is substracted from each individual image to remove the background. Then the contrast of the individual images is enhanced by MATLAB *imadjust*. All modified individual images are then summed up. Finally, the contrast of this summarized image is enhanced (MATLAB *imadjust*).

6.3.2 Validation of 3D reconstruction in dilute suspensions

For evaluating if the 3D calibration is suitable for determining the particle distribution of an individual species in a flowing tridisperse suspension, we performed several test cases at very dilute conditions. The results of such a test case are shown in Fig. 6.8 where we compare the particle distributions of three monodisperse suspensions and a tridisperse suspension (d_p =30 µm, 40 µm, 60 µm) at $\Phi = 0.08\%$ and all particles labeled in each case. For such a low volume fraction we assume that particle interaction does not play a role here, such that the distribution of each particle group is expected to be the same, both in the mono- and polydisperse case. In Fig. 6.8 the bulk Reynolds number is set to $Re_b \approx 20$ and defined as $Re_b = \rho_{\mathrm{RIM}} U_b H / \mu_{\mathrm{RIM}}$, where U_b denotes the average streamwise velocity. The distribution of detected particles is displayed in

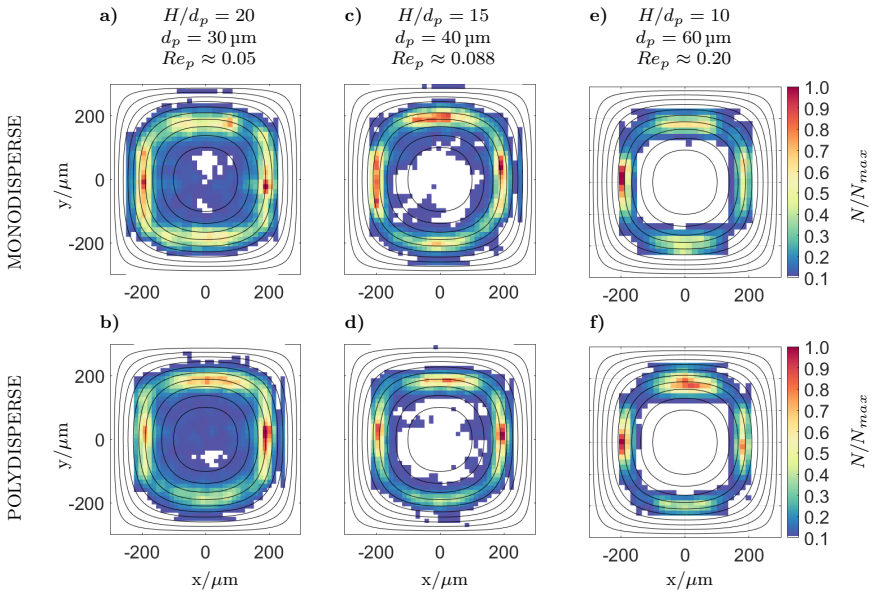

Figure 6.8: Distribution of particles in the cross sectional plane for monodisperse and polydisperse suspension at $\Phi = 0.08\%$, $Re_b = 20$ and $H = 600\,\mu m$ (measured in LVS). N/N_{max} = normalized number of detected particles.

normalized values and N/N_{max} denotes the number of particles in a bin normalized by the maximum number of particles found in all bins. The black lines represent isocontours of the theoretical velocity profile given in Shah and London (2014).

As can be seen in Fig. 6.8a-f particles collect along a Pseudo Segre Silberberg Annulus (PSSA) as described by Choi et al. (2011). Evidently, the particle distribution for the monodisperse cases (Fig. 6.8a,c,e) and tridisperse case (Fig. 6.8b,d,f) are the same. For all particles sizes, the highest particle concentration is located at the centers of the channel faces, which corresponds to the Channel Face Equilibrium (CFE) positions as discovered by Di Carlo et al. (2007). This is a result of cross-lateral migration (Choi et al. 2011). Thereby, Fig. 6.8a,c,e or Fig. 6.8b,d,f clearly show, that this cross lateral migration is more pronounced for larger particles as they have a significantly larger focusing number $F_c = 2Re_b(d_p/H)^2 L/H$ which is in accordance with the work of Choi et al. (2011).

Overall, the particle distributions of Fig. 6.8a,b and Fig. 6.8c,d and Fig. 6.8e,f show an excellent agreement such that we conclude that the 3D euclidean calibration is suitable for determining the 3D distribution of particles in polydisperse suspensions. Furthermore, for ensuring that the species are distinguished properly when being assigned to a calibration curve we perform an intrinsic check for all our measurements containing polydisperse tracers. Thereby, we compare the light intensity I of the individual species as a function of the reconstructed out of plane position $z - z_0$. Such a plot is exemplary shown in Fig. 6.9. As can be seen the calibration curve and the scattered data for $d_p = 40\,\mu\text{m}$ particles are well separated from the scattered data of $d_p = 30\,\mu\text{m}$ particles over a distance of $\approx 347\,\mu\text{m}$ which is almost twice the distance between the focal planes ($\Delta F \approx 166\,\mu\text{m}$). The data associated with the $d_p = 60\,\mu\text{m}$ particles covers a z-range of $\approx 452\,\mu\text{m}$ and has a much higher light intensity but is not displayed here for the sake of visualization. Please note that the data shown in Fig. 6.9 is multiplied with the intensity scaling factor c_s (6.2) for $d_p = 40\,\mu\text{m}$.

Before we discuss the results obtained for suspensions of $\Phi = 9.1\%$, we briefly demonstrate the principal difference in the accuracy of determining the particle distributions between LVS and FVS. For this in Fig. 6.10 we show the distribution of $30\,\mu\text{m}$ particles at $Re_b = 20$ and $\Phi = 0.08\%$ in a monodisperse suspension. Comparing Fig. 6.10 with Fig. 6.8a reveals that the detected particles scatter less around the lower and upper portion of the PSSA (labelled with 1 and 2) in the measurements performed in the FVS. This is because in APTV measurements the in-plane accuracy is higher than the out-of-plane accuracy (Cierpka et al. 2010a).

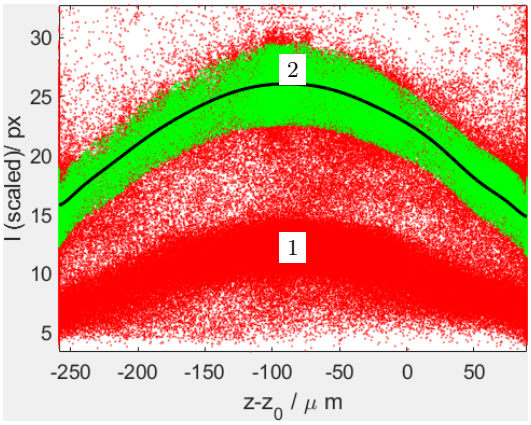

Figure 6.9: Light intensity as function of reconstructed $z - z_0$ of $d_p = 30\,\mu m$ and $d_p = 40\,\mu m$ particles corresponding to Fig. 6.8b,d,f. Symbols: 1=scattered data of $d_p = 30\,\mu m$ particles; 2=scattered data of $d_p = 40\,\mu m$ particles. Black line=calibration curve for $d_p = 40\,\mu m$. Green dots=valid data associated with $d_p = 40\,\mu m$ particles. Red dots=data that is rejected from the $d_p = 40\,\mu m$ calibration curve.

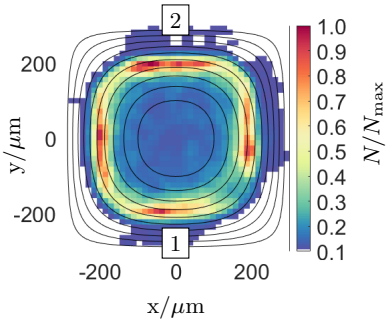

Figure 6.10: Particle distribution in a dilute monodisperse suspension obtained with FVS. d_p =30 µm, $\Phi = 0.08\%$, $Re_b = 20$, $H = 60\,\mu m$, $L/H \approx 1000$.

6.3.3 APTV measurements in suspensions of 9.1% volume fraction

Next, we discuss the particle distributions of mono- and tridisperse suspensions at $\Phi = 9.1\%$, determined by means of APTV in both setups. For this, Figs. 6.11a-f and Figs. 6.11g-l show the particle distributions for the mono- as well as tridisperse suspension cases for $Re_b \approx 20$ in a capillary of 600 µm height, obtained in setup 1 and setup 2.

As can be seen clearly, 30 µm particles are found to collect on a scattered PSSA with a significant lower concentration in the channel center in the monodisperse case (Fig. 6.11a,g). In the polydisperse case the PSSA gets widened towards the wall (Fig. 6.11b,h).

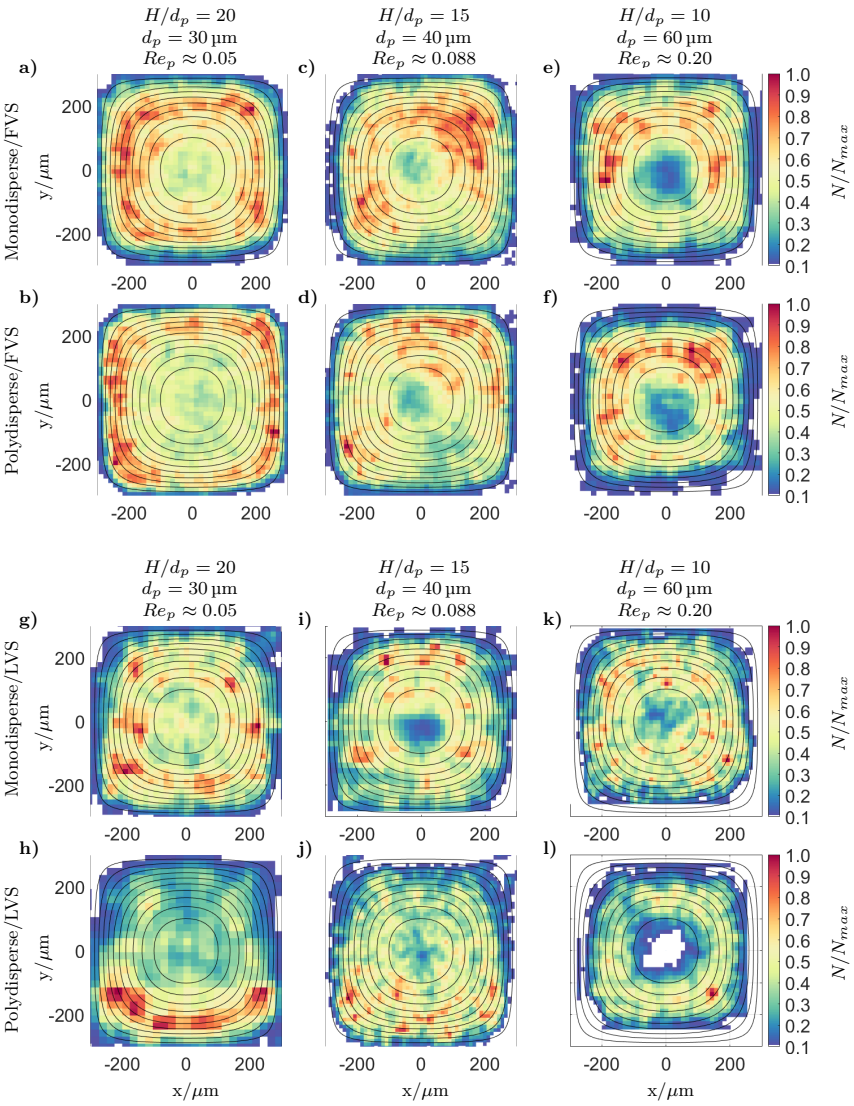

Figure 6.11: Comparison of particle distributions in the FVS (a-f) and the LVS (g-l). $Re_b \approx 20$, $H = 600\,\mu m$. The aspect ratio is $L/H \approx 750$.

This is more pronounced in the FVS which is likely because in APTV measurements the in-plane accuracy is higher than the out-of-plane accuracy as discussed in the previous section. A slight depletion of detected particles in vertical direction becomes evident in Fig. 6.11h. As the number of particles increases towards the channel bottom we exclude optical distortions to be the underlying reason, as these would be pronounced closer to the channel bottom and would lead to a depletion of detected particles here. This effect was described in chapter 5. Furthermore, as will be shown later on, a depletion of

detected particles towards the upper channel wall is also visible in the 400 µm capillary where optical distortions are expected to be less. Hence, we assume this depletion is induced by slight density mismatches leading to a sedimentation of particles. For 40 µm the reconstructed particle distributions (Fig. 6.11c,d,i,j) reveal that the particles are forced to the wall. As can be seen from Fig. 6.11e,f and Fig. 6.11k,l the particle distributions for 60 µm clearly show that the largest particles are more focused in the polydisperse case. This effect is more pronounced in Fig. 6.11l which is measured in the LVS. The aforementioned observations are confirmed by our visualization experiments shown in Sect 6.3.5.

Next we investigate the role of the aspect ratio (H/d_p) on the particle distribution by using a capillary with H=400 µm while keeping the particle sizes constant (30 µm, 40 µm, 60 µm). Further Re_b is adjusted to $Re_b \approx 20$ and $Re_b \approx 40$. As Re_p scales with $Re_b(d_p/H)^2$, this configuration allows us to achieve an estimated particle Reynolds number of up to $Re_p = 0.9$. In Fig. 6.12 we show particle distributions for monodisperse suspensions as well as polydisperse suspensions at $Re_b \approx 20$ and $Re_b \approx 40$.

At first, comparing corresponding mono- and polydisperse cases (Figs. 6.12a-f and Figs. 6.12g-l) confirm that smaller particles are closer to the wall in a polydisperse suspension compared to monodisperse suspensions while larger particles scatter less around the PSSA, as concluded for Fig. 6.11a,b,g,h and Fig. 6.11e,f,k,l. Comparing Fig. 6.11e,k and Fig. 6.12c further confirm that if Re_p and H/d_p are constant ($Re_p = 0.2$, $H/d_p = 10$) the particle distribution is essentially the same for the monodisperse case. However, as H/d_p is increased from $H/d_p = 10$ to $H/d_p = 13.33$ at constant Re_p ($Re_p = 0.2 \approx 0.22$) the particles shift closer to the wall and deplete in the center region (Fig. 6.12c,g). This effect becomes also evident when comparing Fig. 6.12e,i ($Re_p = 0.4 \approx 0.45$). Both, for monodisperse and polydisperse suspensions a simultaneous increase in Re_b and Re_p results in more pronounced particle focusing at fixed H/d_p. A comparison of Fig. 6.12b,d,f and Fig. 6.12h,j,l confirms that an increase in Re_b and hence Re_p also leads to a stronger particle focusing of a particle species in a polydisperse suspension.

6.3.4 Velocity profiles

In this section we discuss the velocity profiles measured in the LVS and FVS. In Fig. 6.13a,b and Fig. 6.13c,d we show the averaged velocity profiles for 30 µm and 60 µm particles measured in the FVS and LVS, respectively. The results reveal that the averaged velocity for both the monodisperse (blue dots) as well as the polydisperse suspensions (red dots) show an good agreement with the analytical solution as given by Shah and London (2014). Merely, the averaged velocity of the 60 µm particles exhibits slight deviations from the analytical solution closer to the channel center even though the mean error is low (visualized by the small error bars in Fig. 6.13a,c). The underlying reason is that there are much less 60 µm tracers than 30 µm tracers in the flow and furthermore the 60 µm particles deplete significantly in the center region. In

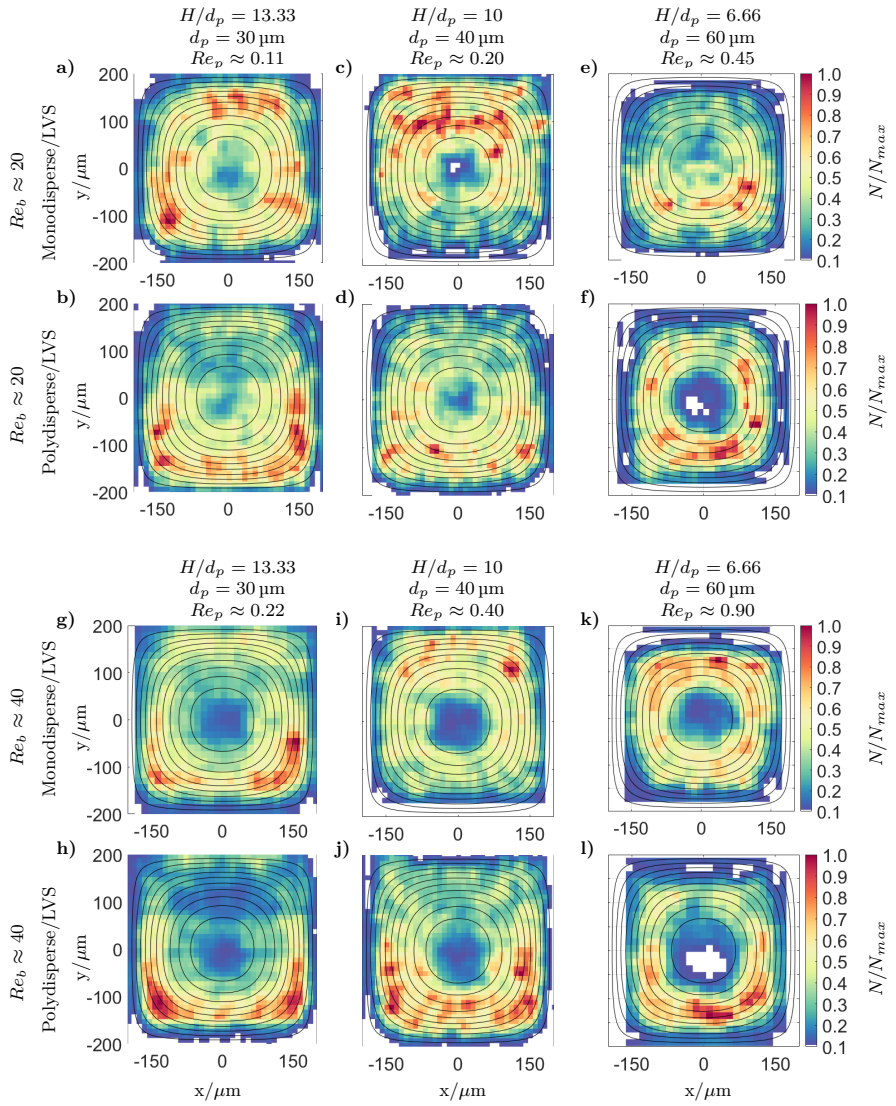

Figure 6.12: Distribution of particles in the cross sectional plane for 400 µm square duct $Re_b = 20$ and $Re_b = 40$ for monodisperse (Mono) and polydisperse suspensions (Poly) at 9.1% volume fraction. Measured in LVS at $L/H \approx 750$.

fact, the averaged data points close to the center result from one or a few 60 µm particles which were tracked across several frames. Hence, they enter the statistics several times. Depending on how their a_x a_y values deviate from the calibration curve they can bias the average. As can be seen clearly the standard deviation (visualized by the large error bars) for the FVS method is multiple times higher than for the LVS. This was expected as the uncertainty in determining the out-of-plane position and hence the

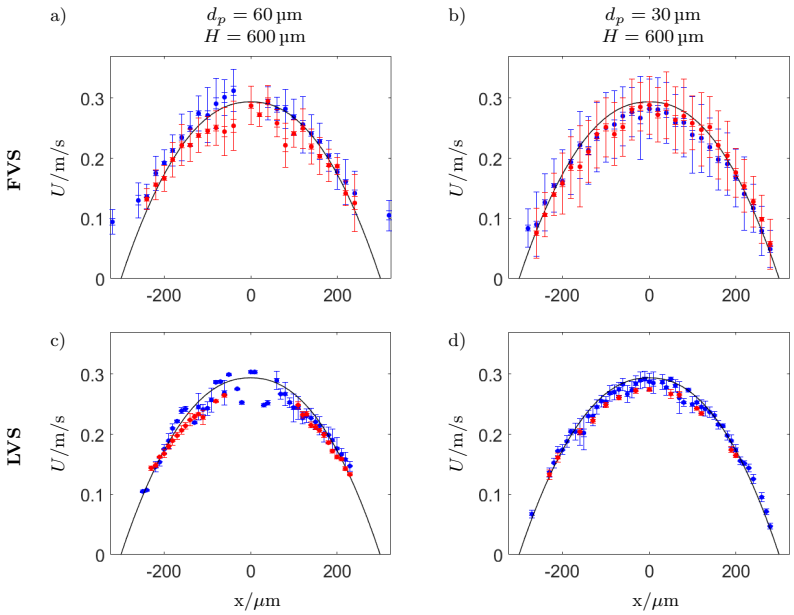

Figure 6.13: Comparison of measured streamwise velocity U for monodisperse (blue) and polydisperse (red) suspensions obtained in the FVS and LVS at a volume fraction of $\Phi = 9.1\%$. Standard deviation of velocity is indicated with vertical error bars. a) FVS, d_p=60 µm, b) FVS, d_p=30 µm, c) LVS, d_p=60 µm, d) LVS, d_p=30 µm,

out-of-plane velocity is usually one order larger than the in-plane position and velocity (Cierpka et al. 2010a). Overall, we conclude based on our results that no significant deformations of the velocity profile are induced within our parameter space for both mono- and polydisperse suspensions. For $\Phi = 10\%$ and $Re_b = 550$ Kazerooni et al. (2017) observed a slight blunting of the velocity profile, however significant deviations from the pure liquid flow were only observed for $\Phi = 20\%$. Our findings also coincide with the studies of Han et al. (1999) where no significant blunting of the velocity profile was observed for $\Phi = 10\%$ at comparable particle Reynolds numbers.

6.3.5 Visualization and physical interpretation

In this section we present results obtained with the visualization technique to validate the migration effects described before. Furthermore, the visualization technique faciliates to easily explore a larger range of Re_b, which allows us to gain some additional insights. For the APTV measurements increasing Re_b further is not possible with the current setup, as we need a minimum exposure time of $\gtrapprox 40\,\mu s$ to ensure a sufficient image quality for the 30 µm particles. This relative large exposure time leads to motion blur at larger Re_b skewing the a_x, a_y values and hence leads to bias in the velocity and the distribution information. It may be noted that the visualization technique needs

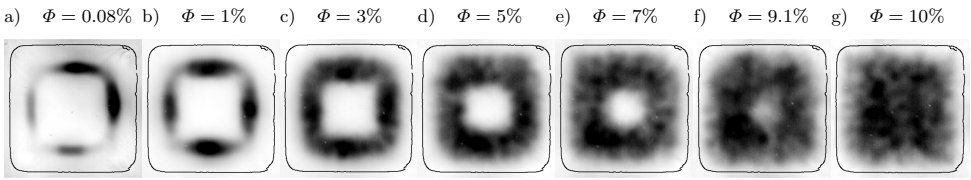

Figure 6.14: Particle distribution in a monodisperse suspension visualized by summarized image series ($Re_b \approx 20$, $H = 600\,\mu m$, $L/H \approx 750$, $d_p = 60\,\mu m$). Dark regions indicate particle positions. a-g) Particle concentration increasing from $\Phi = 0.08\%$ to $\Phi = 10\%$.

optical access from the face side of the geometry. In microfluidic devices, or macroscopic geometries this is rather an exception and optical access is mostly only available from a lateral direction.

Before discussing the effect of Re_b we briefly discuss the effect of increasing Φ on the particle distribution. For this, Fig. 6.14 shows the particle distributions in a monodisperse suspension ($d_p = 60\,\mu m$) at constant Re_b for Φ increasing from 0.08% to 10%. As can be seen, in Figs. 6.14a-g, particles scatter increasingly around the PSSA for increasing Φ.

In Fig. 6.15 we show particle distributions for mono- and polydisperse suspensions obtained from visualizations for $\Phi = 9.1\%$ and different Re_b ranging from 1 up to 72.86. At low Reynolds numbers ($0.99 \leq Re_b \leq 6.62$) 30 µm, 40 µm and 60 µm particles migrate to the center of the channel which can be attributed to shear induced migration for the monodispersed suspension. Thereby, the particles exhibit higher concentrations on the diagonal axis and the channel center. In contrast, in a polydisperse suspension 60 µm particles exihibt a more pronounced migration to the channel center compared to the corresponding monodisperse case. On the other hand, this effect seems to be reversed for 40 µm particles where less particles accummulate in the center in the polydisperse case compared to the monodisperse case. This observation coincides with the finding of Semwogerere and Weeks (2008) that at equal volume fractions larger particles migrate faster to regions of low shear and screen off smaller particles due to their lower developement length. For 30 µm particles, no migration to the center becomes evident for the polydisperse suspension in Fig. 6.15a.

For $Re_b \geq 19.87$ the particles distribute on a scattered PSSA in the monodisperse case which becomes more focussed as Re_b increases (Fig. 6.15c-g). This confirms the observations discussed with regard to Fig. 6.11 and Fig. 6.12. The focussing of the PSSA with increasing Re_b is pronounced for 40 µm where the squared void area around the channel center increases significantly with Re_b. For 30 µm, Fig. 6.15c-g reveal, that the area around the diagonal axis feature a lower particle concentration than the face centers resulting in a star shaped particle distribution, which was similarly observed by Kazerooni et al. (2017) for $Re_b = 550$ and $H/d_p = 18$. However, Kazerooni et al. found the highest concentration in the duct corners and not at the channel

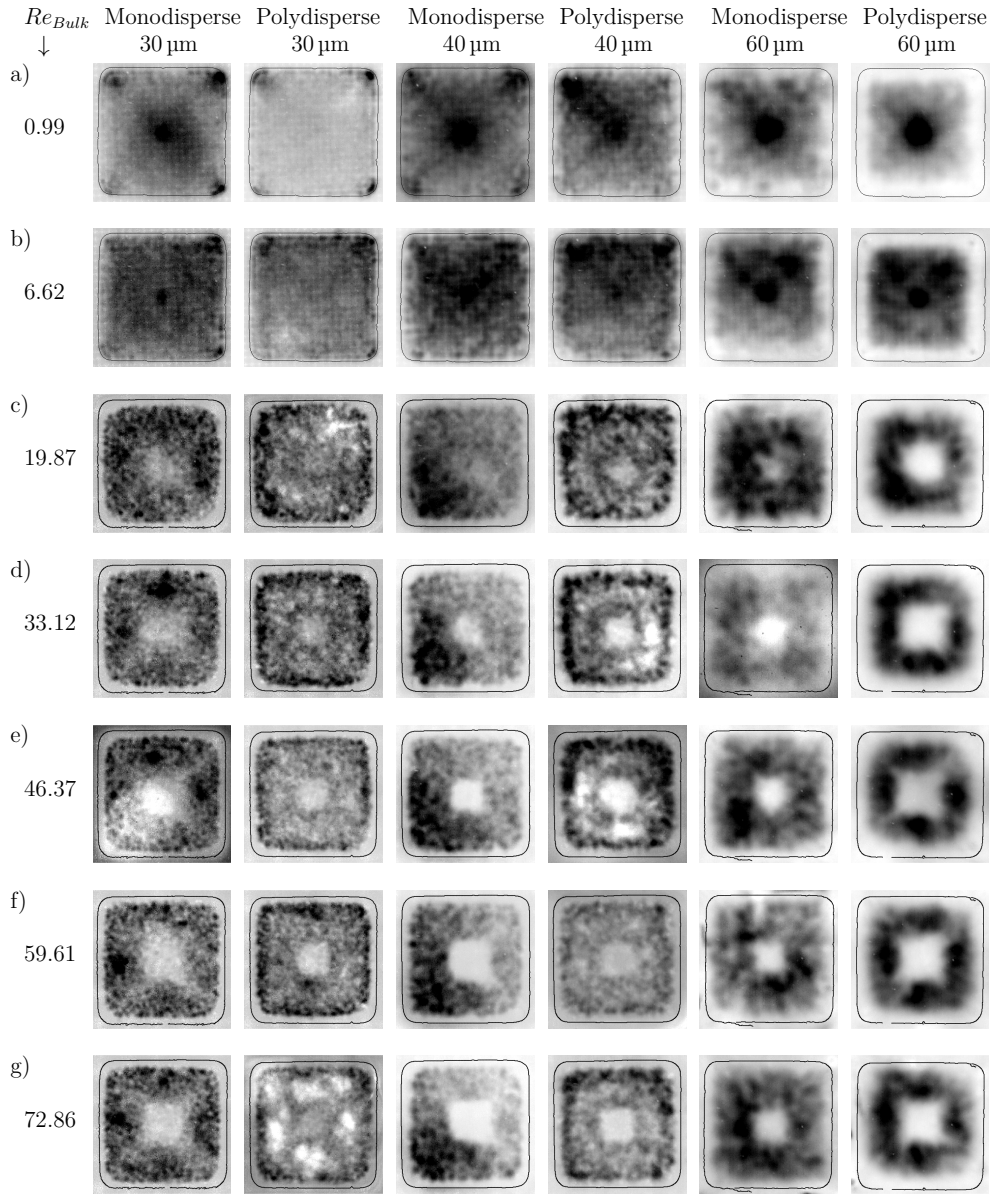

Figure 6.15: Particle distributions visualized by summarized image series for mono- and polydisperse suspensions at $\Phi = 9.1\%$ and different values Re_B for a square duct with $H = 600\,\mu\text{m}$ and $L/H \approx 750$.

faces, which we relate to the fact, that they simulated a square duct with perfectly sharp corners whereas the cappilaries used within this work exhibit round corners. The scattering around the PSSA visible in Fig. 6.14a-g and Fig. 6.15c-g result from a competition between inertial and shear induced migration forces. On the one hand inertial effects force particles to the equilibrium positions (EP) resulting in a high local particle concentration. On the other hand, shear induced migration leads to a migration away from these positions which can be explained as follows: According to the diffusive flux model of Phillips et al. (1992) for shear induced migration, particle migrate from regions of high collision frequency to regions of low collision frequency. The flux related to the collision frequency ($N_c \sim d_p^2(\Phi^2\nabla\dot{\gamma} + \Phi\dot{\gamma}\nabla\Phi)$) depends on both Φ and the shear rate $\dot{\gamma}$ and hence attains maximum values at the EP such that particles migrate away from these regions. As Φ is increased the collision frequency and hence shear induced migration is enhanced resulting in an increased scattering as can be seen from Fig. 6.14a-g. However, when the Reynolds number increases the inertial forces increase counteracting the shear induced migration such that the scattering is reduced as clearly visible for the 40 µm particles in Fig. 6.15c-g.

As observed in the APTV measurements, for all investigated particle sizes, corresponding particle distributions found for the polydisperse cases are strikingly different compared to those of the monodisperse cases. For 30 µm and 40 µm particles a significantly higher concentration close to the channel walls resulting in an outer annulus of high concentration is observed in the polydisperse case. Furthermore, a slight increase of concentration seems to exist for some Re_b close to the channel center forming an inner annulus of high concentration (6.15c-g) which was not visible in Fig. 6.11b,h,d,j. Similar to the APTV measurements, the 60 µm particles the PSSA appears to be more focused in the polydisperse case compared to the monodisperse case (Fig. 6.15c-g). As Re_b increases the PSSA formed by 60 µm particles breaks up at the corners which is a indicator for cross-lateral migration forcing the particles to the CFE positions (6.15c-g). The particle segregation observed in the tridisperse measurements at $\Phi = 9.1\%$ (Fig. 6.15c-g, Fig. 6.11b,d,f,h,j,l and Fig. 6.12b,d,f,h,j,l) can be explained in analogy to the work of Semwogerere and Weeks (2008) who found that in a bidisperse suspension the species that reaches its EP earlier (in their case region of lowest shear) screens of the other species. In our experiments large particles experience significantly higher inertial forces such that they attain their position at the PSSA at much lower values of z/H than the smaller species. We recall here that the focusing number scales with $F_c \sim (d_p/H)^2$. Hence, larger particles quickly exhibit high concentrations closely around the PSSA. As a result they are screening off smaller particles.

At the same time, large particles experience smaller displacements in the polydisperse case compared to the monodisperse case due to collisions as these scale with $O(d_p)$. Looking at the collision flux in the model of Philips et al. ($N_c \sim d_p^2(\Phi^2\nabla\dot{\gamma} + \Phi\dot{\gamma}\nabla\Phi)$) it is clear that suspensions of smaller particles exhibit smaller diffusive fluxes compared to large particles. Hence, using simple arguments, it can be assumed that the diffusive

fluxes and hence the rate of migration is decreased in a polydisperse suspension which contains solely 1/3 large particles, compared to a monodisperse suspension of large particles. Therefore the rate of shear induced migration is lower than in the monodisperse case, leading to a decreased scattering of large particles around the PSSA.

6.4 Discussion and Conclusion

In this chapter we utilize APTV to measure the particle dynamics in polydisperse suspensions containing three particles sizes of d_p =30 µm, 40 µm and 60 µm at volume fractions of $\Phi = 0.08\%$ to $\Phi = 9.1\%$. A refractive index matching technique is used to render the suspension transparent, while just a small portion of the particles is labeled with fluorescent dye to provide a signal for the tracking procedure.

First, an extensive study on the general effect of the particle size on the calibration curves is performed where we also compare two approaches for extracting the horizontal axis lenghts a_x and the vertical axis length a_y of the particle image. For both methods we observe the a_x, a_y values to increase, as the particle size increases as predicted by the expression derived by Cierpka et al. (2010a). Thereby, the data obtained with the binarizing approach is in excellent agreement with the theoretical data, while the data obtained with the autocorrelation deviates significantly from the theoretical curves beyond the focal planes. In agreement with König et al. (2020) it is observed that the 2D Euclidean calibration curves for different values of d_p intersect beyond the focal planes leading to ambiguities which lead to large errors when applying APTV to particles of different size. We overcome these ambiguities by utilizing a 3D calibration procedure, exploiting the fact that the maximum light intensity of the particles increases sharply with increasing particle size. Using calibration data of nine different particles sizes ranging from 15 µm to 256 µm we show that the 3D calibration procedure allows a reliable differentiation of particles of different sizes.

Ultimately, utilizing the 3D calibration technique, we investigate the particle migration behavior in mono- and tridisperse suspension flows in square ducts with cross-sectional areas of $400\times400\,\mu m^2$ and $600\times600\,\mu m^2$ at bulk Reynolds numbers of $Re_b \approx 20$ and $Re_b \approx 40$ and volume fractions of $\Phi = 0.08\%$ and $\Phi = 9.1\%$. At $\Phi = 0.08\%$ and $Re_b = 20$ we observe particles to collect onto a Pseudo Segre Silberberg Annulus (PSSA) with no signifcant differences between mono- and polydisperse suspensions beeing evident. At $\Phi = 9.1\%$ $Re_b = 20$ particles in monodisperse suspensions scatter around an annular shape with the scattering being pronounced as d_p decreases. When Re_b is increased to $Re_b = 40$ the scattering decreases for all d_p investigated leading to a square shaped depletion of particles close to the channel center. As H/d_p is increased at constant particle Reynolds number the particle distribution is shifted towards the channel walls and the depleted area in the channel center increases. For polydisperse suspensions, strikingly different particle migration behaviors are observed at the same values of Re_b and Φ. Compared to the monodisperse case large particles (60 µm) are

significantly more focused. In contrast, small and intermediate particles (30 µm and 40 µm) are repelled by larger particles resulting in a region of high concentration close to the channel walls. As Re_b increases from $Re_b = 20$ to $Re_b = 40$ these effects become pronounced such that the focusing of large particles (60 µm) is further enhanced while smaller and intermediate particles become more focused close to the walls. For both the mono- as well as the polydisperse measurements no significant blunting of the velocity profile become evident within our experiments which is in agreement for literature considering monodisperse suspensions.

7 Pattern formation in particle laden Taylor Couette flows at solid body rotation[1]

In this chapter, previously undescribed particle patterns are reported for suspensions of initially uniform dispersed non-Brownian particles in completely filled drum flows and in completely filled co-rotating Taylor-Couette (TC) flows under the influence of gravity at solid-body rotation. Extending previous studies, a thorough phase mapping is performed for the drum flow with a low viscosity working liquid (1 cP) and 500 µm glass beads at a solid volume fraction of $\Phi = 0.11\%$. Thereby, a wide range of cylinder radii is covered ($R_o = 7\,\text{mm}$ to $R_o = 145\,\text{mm}$). Moreover, for the first time, a phase mapping is performed for a co-rotating TC flow at several radius ratios. Overall 55 different geometrical combinations have been considered within the experiments.

The chapter is structured as follows: The different axial particle distributions, viz the phases, observed in both the drum flow as well as the TC flow are presented in section 7.1. In section 7.2 the radial particle distributions associated with different phases are described. The spatial and temporal behavior of axial and horizontal particle bands is discussed in section 7.3 based on space-time diagramms. Section 7.4 considers the effect of the particle volume fraction on the band formation. In section 7.5 it is adressed how the wavelength of the bands scales with the radius and the gap height. Finally, the results and conclusions are summarized in 7.6

The theory and the relevant state of the art for this chapter are given in section 1.2.3 (theory and state of the art of pattern formation in rotating flows). The experimental setups and the measurement procedure utilized to obtain the results presented in this chapter are given in section 2.1.4.

7.1 Axial particle distributions and pattern classification in centrifugally stable rotating drum and TC flow

In this section, different particle concentration patterns observed in the rotating drum and co-rotating TC flow are described. For both flows a solid body rotation velocity profile ($\Omega_i = \Omega_o$) without axial flow is considered (described in section 2.1.4). Hence, both systems are identical expect for the inner cylinder which is present in the TC

[1] This chapter is adopted from the manuscript "Pattern formation in particle laden Taylor Couette flows at solid body rotation" written by Philipp Brockmann, Martin Tvarozek and Jeanette Hussong to be submitted.

flow. This allows to study how the presence of the inner cylinder affects the particle patterns. As the flow is at solid body rotation, it is assumed to be centrifugally stable as described in section 1.2.1.2. We observed 10 different phases (GB, FF, UH, AX1, AZ, AX2, NP1-NP3, AX3, CLL, SQR) within our study in both systems of which 6 (AZ, AX2, NP1-NP3, AX3, CLL, SQR) are previously unreported to the best of our knowledge. The abbreviations will be clarified later. Before describing the different phases, the Reynolds numbers associated with the systems are briefly introduced. In the drum flow problem, there are two length scales (cylinder radius R_o, particle diameter d_p) and two velocity scales (particle settling velocity $u_p - u_f$, cylinder speed $U_\varphi = R_o\Omega_o$) involved (Matson et al. 2006, 2008). In the present thesis, the gap width of the system is considered as a length scale $H = R_o - R_i$ for both the drum flow and the TC flow. For the drum flow R_i is zero such that $H = R_o$. With these length and velocity scales four different Reynolds numbers can be defined in analogy to (Matson et al. 2006, 2008). The Reynolds number based on the particle settling velocity defined in section 1.2.3.2 is defined as $Re_1 = Re_p = d_p|(u_p - u_f)|\rho_{\text{fluid}}/\mu_{\text{fluid}}$. Based on the works of Dietrich (1982) and Bush et al. (2003), the particle Reynolds number based on the settling velocity is estimated to be in the range of $Re_1 = Re_p \approx 24...35$ for the experiments reported here. The Reynolds number based on the gap width ($H = R_o - R_i$) and the cylinder speed is defined as $Re_2 = R_o\Omega_o(R_o - R_i)\rho_{\text{fluid}}/\mu_{\text{fluid}}$ and ranges from 560 to 9300 for AX1, from 1100 to 4.7×10^4 for AZ and from 1500 to 9×10^4 for AX2. The Reynolds number based on the settling velocity and the gap height $Re_3 = |(u_p - u_f)|(R_o - R_i)\rho_{\text{fluid}}/\mu_{\text{fluid}}$ ranges from 238 to 10150 for the considered geometrical configurations. Finally, the Reynolds number based on the particle diameter and the outer wall speed $Re_4 = d_p R_o\Omega_o\rho_{\text{fluid}}/\mu_{\text{fluid}}$ ranges from 37 to 101 for AX1, from 61 to 163 for AZ and from 57 to 315 for AX2. Within this work, no unifying scaling was found to describe the phase boundaries of TC and drum flow for different radii and ratios of H/R_o. Hence all results are presented with their dimensions.

Figure 7.1a,b shows the phases observed in an exemplary drum flow ($R_o = 23\,\text{mm}$) and a co-rotating TC flow ($R_o = 23\,\text{mm}$ and $H/R_o = 0.65$) at different rotation rates. For the sake of clarity, the approximate rotation rate ranges associated with the phases shown in Fig. 7.1 are provided in Table 7.1. The ratio of centrifugal-, drag- and gravitational force acting on the particles changes as the rotation rate increases. In analogy to Matson et al. (2003) the rotation rate is devided into three regimes, labeled as I, II and III in Fig. 7.1a,b and indicated with the blue, green and red bars, respectively. While particles remain in a sediment bed within I, they remain dispersed within the fluid most of the time along their trajectory in regime II. Finally at high rotation rates, within regime III centrifugal forces become dominant and particles remain close to the outer wall. Typical particle distribution associated with these phases are shown in Fig. 7.1a for the drum flow and Fig. 7.1b for the TC flow. The images are recorded with the camera perpendicular to the horizontally aligned rotation axis of the cylinder(s) as depicted in Fig. 2.5. Bright regions indicate high local particle volume fractions, while dark regions indicate areas void of particles.

Rotation rate range of phases (rpm)		
Case	TC	Drum
GB	0-28	0-45
FF	28-79	45-94
AX1	79-110	94-105
AZ	110-130	105-130
AX2	130-159	130-175
NP1	159-175	175-180
NP2	175-190	180-185
NP3	190-195	185-200
AX3	195-≈280	200-≈280
CLL	≈350	≈350

Table 7.1: Rotation rate range of the phases for TC-flow and drum-flow associated with the configurations depicted in Fig. 7.1a,b (Drum flow: $R_o = 23\,\text{mm}$, TC-flow: $R_o = 23\,\text{mm}$, $H/R_o = 0.65$)

For region I, we observe the granular bed (GB) (up to 25 rpm) and the fingering flow (FF) (drum: up to 94 rpm, TC: up to 79 rpm), as described by Matson et al. (2003) for the high viscosity drum flow (GB, FF in Fig. 7.1a). Matson et al. (2008) relate the fingering flow to a Rayleigh Taylor-like instability that is induced by a relative movement of individual particles and the granular bed. They further distinguish between two types of fingering flow, associated with a different size of the fingers and a different position where the particles detach from the wall. As the focus of the present work is on the band patterns, such a distinction is not made. Subsequent to the FF the particles tend to distribute homogeneously along the cylinder. However, this state rarely remains stable and the homogeneous distribution develops asymmetries ending up in most of the particles collecting in blobs while a small amount remains uniformly dispersed. Hence, we refer to this phase as unstable homogeneous phase (UH) (UH in Fig. 7.1a,b). Matson et al. (2008) termed this region as homogenous region. However, they also noted that this phase is extremely sensitive to slight misalignments of the cylinder. As the rotation rate is increased the blobs/fingering structures gradually lose stability and disperse into the free flow until around 94 rpm (TC: 79 rpm), when axial bands appear (AX1 in Fig. 7.1a,b). For the drum flow the rotation rate (≈94 rpm) and the axial wavelength ($\lambda^*/R_o \approx 4.12$) matches the values reported by Lipson and Seiden (2002) and analyzed by Seiden et al. (2005). We assume it is the same type of banding here. We call this state axial banding type 1 (AX1).

For the TC-flow it is observed that during AX1 banding the inner cylinder stabilizes the particle bands, as particles land on its surface on one side of the cylinder and get transported in azimuthal direction till they detach on the opposite side. This will be shown hereafter in section 7.2. With a further increase in rotation rate (drum: 105 rpm, TC: 110 rpm), the axial structures reorganize into azimuthal periodic bands

travelling in circumferential direction (AZ in Fig. 7.1a,b). This phenomenon is referred to as azimuthal banding (AZ). Often, depending on the cylinder diameter, AZ is the most dominant phase of the intermediate regime II, occupying the widest rpm range. Nevertheless, the system falls back into axial band formation at higher rotation rates (AX2 in Fig. 7.1a,b). Due to its distinct wavelength and formation characteristics, we refer to this state as axial banding type 2 (AX2). In fact, AX1 and AX2 banding can be distuingished based on the rotation rate with respect to AZ banding. While AX1 banding is associated with rotation rates lower than AZ banding, AX2 occured always at rotations rates higher than AZ banding. Adjacent to the AX2 phase, the

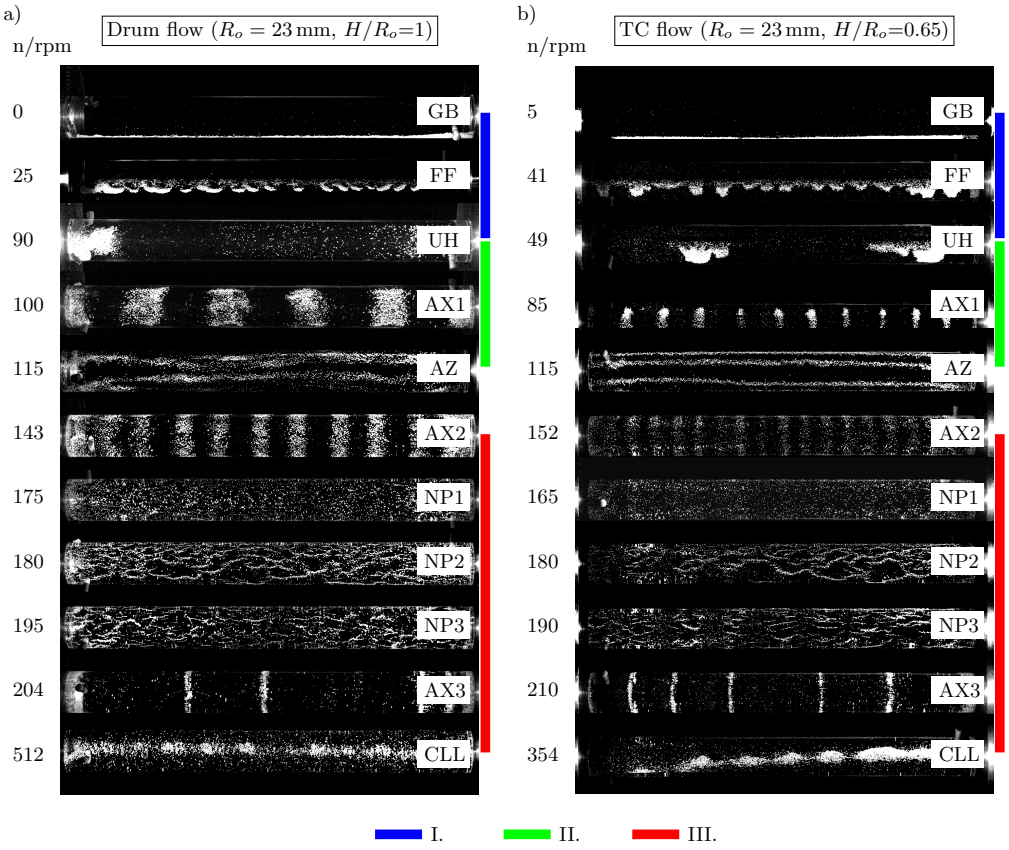

Figure 7.1: Steady state phases observed in an exemplary drum flow and an exemplary TC flow as seen in the front view experiments. Bright areas indicate high concentration of particles. Abbreviations: granular bed (GB), fingering flow (FF), unstable homogenous phase (UH), axial banding of type 1 (AX1), azimuthal banding (AZ), axial banding of type 2 (AX2), net pattern type 1, 2, 3 (NP1, NP2, NP3), axial banding of type 3 (AX3), centrifugal limit line (CL). I.) low rotation rate regime, II.) intermediate rotation rate regime, III.) high rotation rate regime. a) Drum flow ($R_o = 23\,\mathrm{mm}$, H/R_o=1) b) TC flow ($R_o = 23\,\mathrm{mm}$, H/R_o=0.65)

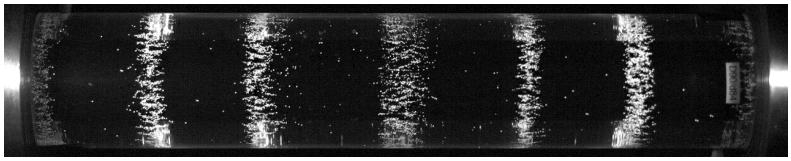

Figure 7.2: Axial banding type 3 (AX3) showing regular wavelength at 154 rpm and $H/R_o = 0.52$ at $R_o = 42$ mm. Time required to reach this state was 60 min.

particles are centrifuged closer to the cylinder wall and accumulate into thin crests surrounded by void areas. The crests appear to be aligned in horizontal direction. Due to its resemblance to a net, we refer to this phase as net pattern (NP1-NP3). Here three sub-types of net patterns occur in a three step progression as the rotation rate increases (NP1-NP3 in Fig. 7.1a,b). First (drum: 175 rpm, TC: 159 rpm) the void areas are small and particles are distributed almost homogeneously over the cylinder walls (NP1). As rotation rate is increased the area between the crests expands (Drum: around 180 rpm, TC: around 175 rpm, NP2). Subsequently, the areas shrink again as the rotation rate is increased further (drum: around 185 rpm, TC: around 190 rpm, NP3). Sometimes it was observed that particles distributed inhomogenously around the circumference during NP1-NP3. A further type of axial banding occurs at rotation rates of about 195 to 200 (AX3 in Fig. 7.1a,b). Due to its distinct wavelength and associated rotation rate we refer to this state as axial banding type 3 (AX3). AX3 banding exhibits peculiar dynamics in comparison to AX1 and AX2 banding, often becoming irregular in spacing in the course of its formation and vice versa. Furthermore, the stabilization period is substantially longer than that of the other phases (30 min to 90 min). An example for AX3 banding with a regular spacing is given in Fig. 7.2. The AX3 bands feature a resemblance to discontinous banding (DB) phase reported by Matson et al. (2008).

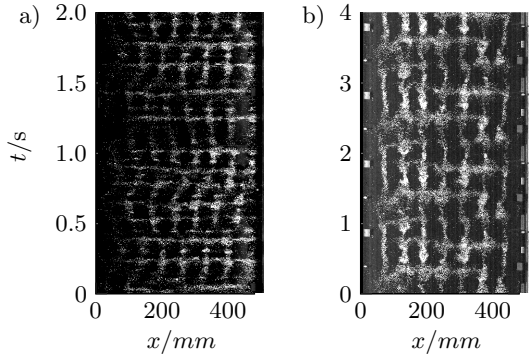

Figure 7.3: Exemplary space-time diagram of square pattern (SQR). Bright areas indicate high concentration of particles. a) $R_o = 112$ mm and H/R_o=0.2 at 41 rpm. b) $R_o = 84$ mm and H/R_o=0.52 at 62 rpm.

However, the bands are much more focused than that reported by Matson et al. (2008). The last phase, consisting of azimuthal lines, is observed at significantly higher rotation rates beyond ≈ 350 rpm and referred to as Centrifugal Limit Line (CLL) (CLL in Fig. 7.1a,b). While a single band is observed for the given example, for larger values of R_o multiple bands randomly distributed along the circumference have been observed. In addition to these phases, in the TC flow, for some combinations of R_o and R_i the coexistence of azimuthal and axial bands is observed between AX1 and AZ as depicted in Fig. 7.3, which is referred to as square pattern (SQR).

Overall, several patterns have been detected with exhibit strikingly different axial patterns. To better understand their dynamics, it is important to extract their radial position, which will be performed in the next section.

7.2 Radial particle distributions

This section considers the radial particle distributions associated with the phases depicted in Fig. 7.1. For this, Fig. 7.4a,b shows the summed up images recorded with the side view setup for GB, FF, AX1, AZ, AX2, NP1 and AX3 for the drum flow and the TC flow, respectively.

As can be seen clearly from Fig. 7.4a,b the particles remain close to the wall within GB and FF. While they are located close to the bottom of the cylinder during GB they seem to allocate further at the left side of the outer cylinder (green and magenta rectangle labeled with “0”) during FF. Within these phases, the drag force can not overcome the gravity which was similarily shown for the numerical single particle trajectories in section 1.2.3.2.

In section 1.2.3.2 it was further shown that single particle trajectories were altered by the presence of the inner cylinder in the TC flow in a certain rotation rate range. A similar behavior is observed here for rotation rates associated with AX1 banding, where multiple particles are present. Figure 7.4a,b reveals that the particles move on an ellipsoid shaped trajectory during AX1 banding, and the additional inner cylinder present in the TC flow affects this trajectory. In fact, the additional inner cylinder widens the diameter of the particle trajectory compared to the drum flow and the scattering of the particles is reduced in the TC flow (AX1 in Fig. 7.4a,b). As can be seen in Fig. 7.4b, within the TC-flow the particles get in contact with the inner cylinder (magenta rectangle labeled with “1”) which then acts as a conveyor belt transporting the particles to the opposite side of the cylinder (magenta rectangle labeled with “2”), similar to the trajectories “R3” reported in section 1.2.3.2. As the particles sediment on the inner cylinder they get focused such that the particles are focused on the trajectory when detaching again from the inner cylinder at point 2 (AX1 in Fig. 7.4b). In contrast, particles follow a widened particle path across the center region inside the drum (green rectangle labeled with “1”, AX1 in Fig. 7.4a). Hence, particles in a drum flow travel

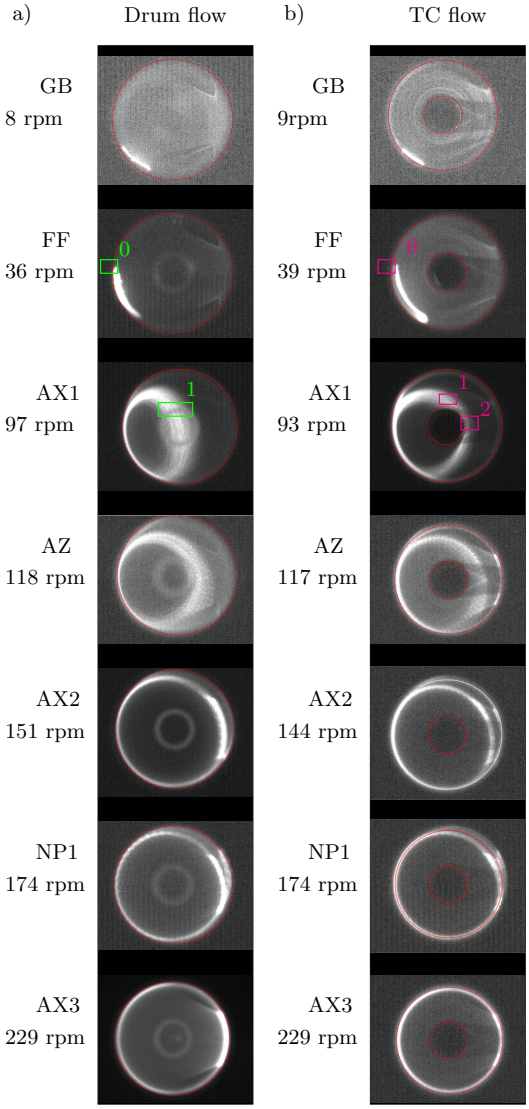

Figure 7.4: Side view recordings analogous to the front view recordings presented in Fig. 7.1. The images presented in a,b are ensemble averages of 1032 recorded frames. Abbreviations are analogous to Fig. 7.1. The system rotates in clockwise direction. Bright areas indicate high concentration of particles. The shaded circle present in Fig. 7.4a represents the groove used to hold the inner cylinder in the TC flow experiments. a) Drum flow ($R_o = 23\,\text{mm}$, H/R_o=1) b) TC flow ($R_o = 23\,\text{mm}$, H/R_o=0.65)

longer distances without contact to the wall and do not get rearranged at point 1. This makes them more susceptible to disturbances induced by interaction with each other and the fluid, which results in an increased scattering compared to the TC flow.

In fact, the effect of the inner cylinder on the particle trajectories during AX1 banding depends both on the rotation rate and the cylinder radius. For illustration of the effect of rotation rate, Fig. 7.5 depicts the particle trajectories in a TC flow with $R_o = 23\,\mathrm{mm}$ and $H/R_o = 0.46$ for different rotation rates associated with AX1 banding. As can be seen at lower rotation rates two trajectories exist (indicated with the blue and green arrow in Fig. 7.5a,b) which are similar to the theoretical single particle trajectories R1 and R3 as discussed in section 1.2.3.2. These two trajectories can coexist in a suspension because particles interact with each other such that individual particles are repelled from one trajectory and fall into the other. When the rotation rate increases these trajectories merge into one trajectory (green arrow in Fig. 7.5c,d). Furthermore, in Fig. 7.5a,b,c,d it can be seen, that the particles are more focused after being transported by the inner cylinder.

During AZ banding the centrifugal force is higher compared to phase AX1 and as a result the trajectory is shifted closer to the right side of the outer cylinder wall (AZ in Fig. 7.4a,b). Also here, a significant difference between drum flow and TC flow becomes evident. Particles appear to be more focused in the trajectory in Fig. 7.4b (AZ) which is an indicator that the inner cylinder leads to a stabilization of the particle band patterns. However, because the trajectory is closer to the right cylinder wall, the effect of the inner cylinder is less pronounced for AZ compared to AX1 banding. In fact, the shape of particle trajectories during AZ banding depends on the rotation rate as depicted exemplarily for a drum flow in Fig. 7.6. As can be seen, with increasing rotation rate the trajectory is shifted closer to the right side of the cylinder wall and gets more focused (Fig. 7.6a-c). At a rotation rate of 125 rpm the trajectory stays out of the area were the inner cylinder would be (shaded bright circle) (Fig. 7.6a-c). Thus, the effect of the inner cylinder on the trajectories depends on rotation rate and radius of the inner cylinder.

During AX2 banding where the rotation rate and hence centrifugal forces are increased further, the particles get closer to the right outer cylinder wall (AX2 in Fig. 7.4a,b). As depicted in Fig. 7.4a,b the maximum distance from the wall of AX2 bands is much less compared to AX1 and AZ bands. Also the trajectories for the TC and the drum flow are essentially identical for AX2 banding as the particles remain away from the inner cylinder. This is in agreement with the findings from the computed single particle trajectories in section 1.2.3.2 where it was shown, that the inner cylinder does not affect the trajectories above a certain rotation rate. Furthermore, within AX2 banding particles scatter much less around the trajectory such that it appears sharper in Fig. 7.4a,b compared to AX1 and AZ banding (see AX1, AZ, AX2 in Fig. 7.4a,b). An

explanation is that particles move faster during AX2 banding and also spend less time attached to the cylinder wall, which makes them more robust against disturbances due to interaction of particles with each other and the fluid.

Regarding the trajectories of AX1, AZ and AX2, an analogy can be drawn to the sedimentation behavior of groups of densely packed particles released in stagnant water. For such scenarios it is known, that the particles start settling as a porous clump. If the interstitial space between particles is small enough water is hindered from flowing through the clump, which then remains stable (Zhao et al. 2014). This interstitial spacing increases during the settling procedure due to interactions between particles with each other and the fluid. When the interstitial space is larger, water easily penetrates the clumps which are destroyed and the particles break up to a cloud (Zhao et al. 2014). Here, the bands could be seen in analogy to a clump. When the particles detach from the wall they have little interstitial space between particles, which then increases when the particle move through the cylinder (as can be seen for AX1 and AZ in Fig. 7.4a). As particles get in contact with outer cylinder or the inner cylinder again, the particles are focused again and the interstitial space is reduced. Hence, the less time particles spend away from the wall, the less the probability for a widening and breakup of the particle band. This could explain the stabilizing effect of the inner cylinder.

In phase NP1 the trajectory is similar to AX2 banding with the particles being even closer to the wall. Similar to AX2 the particles do barely scatter around the trajectory and the trajectories are essentially identical for drum and TC flow (see NP1 in Fig. 7.4a,b).

Finally, for AX3 banding there is no distance visible between particles and wall (AX3 in Fig. 7.4a,b). Obviously, the particles are centrifuged to the wall during AX3 banding. It is concluded, that this is the reason why AX3 banding takes much longer time to develop than AX1, AZ, AX2 banding and NP1-NP3. Strong interactions between particles and wall slow down axial particle movement such that more time is required to form the particle bands.

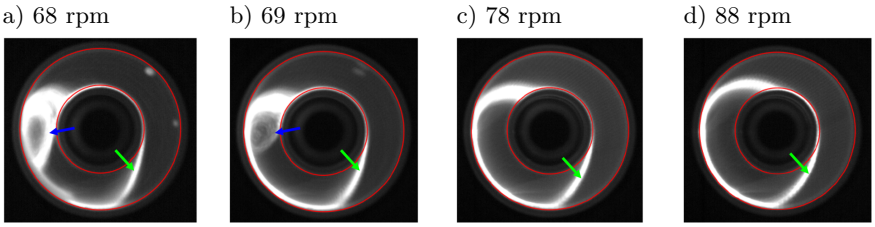

Figure 7.5: Effect of the rotation rate on the trajectories during AX1 banding in TC flow ($R_o = 23\,\text{mm}$ $H/R_o = 0.46$). The system rotates in clockwise direction.

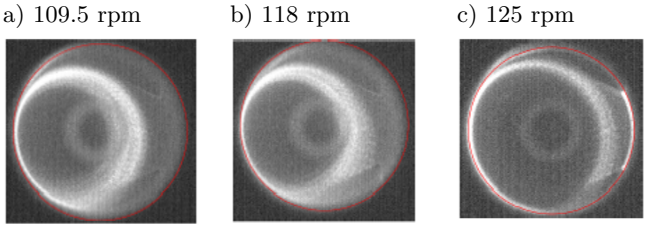

Figure 7.6: Effect of the rotation rate on the trajectories during AZ banding in drum flow ($R_o = 23\,\text{mm}$). The system rotates in clockwise direction. Brighter regions are associated with higher particle concentration.

7.3 Space time diagrams

7.3.1 Drum flow

The space-time diagrams presented in the following are generated by extracting the intensity (MATLAB-improfile) across the rotation axis of the cylinder in each time frame. The space-time diagram is then composed by vertically stacking the individual intensity profiles in an array and presenting it as an image. All results are reported for a volume fraction of $\Phi = 0.11\%$.

In Fig. 7.7 space-time diagrams are shown for the drum flow for different cylinder radii and selected rotation rates. Figure 7.7a,b,c show rotation rates associated with AX1, AZ and AX2 banding, respectively. The cylinder radius increases from the left to the right. Space-time diagrams are shown beginning from an arbitrary time when the band was in a stationary state after the rotation rate was increased as explained in section 2.1.5. The drum radii of $R_o = 48\,\text{mm}$ and $R_o = 52\,\text{mm}$ are an exception as they were not stable. In the latter cases, the space-time diagrams start prior to the begin of band formation.

In Fig. 7.7a, where the space-time diagrams of AX1 banding are shown for the drum flow, it becomes evident that the wavelength increases as the drum radius is increased. It is observed that AX1 banding becomes increasingly unstable if the drum radius increases. No stable bands could be observed for $R_o \geq 26\,\text{mm}$ within the radii considered in our study. For $26\,\text{mm} \leq R_o \leq 32\,\text{mm}$ bands formed, started to oscillate but remained stable for several seconds up to few minutes as can be seen exemplarily for $R_o = 32\,\text{mm}$. For larger drum radii, bands formed and collapsed within a short period of time (about 10 s) as can be seen from Fig. 7.7a for $R_o = 48\,\text{mm}$ and $R_o = 57\,\text{mm}$.

Fig. 7.7b shows space-time diagrams of AZ. The red vertical lines indicate the region of interest, that was considered for the extraction of the wavelength, which will be discussed in section 7.5. Contrary to AX1 banding, AZ banding could be observed for all considered cylinder radii ($7\,\text{mm} \leq R_o \leq 145\,\text{mm}$). Similar to AX1 banding,

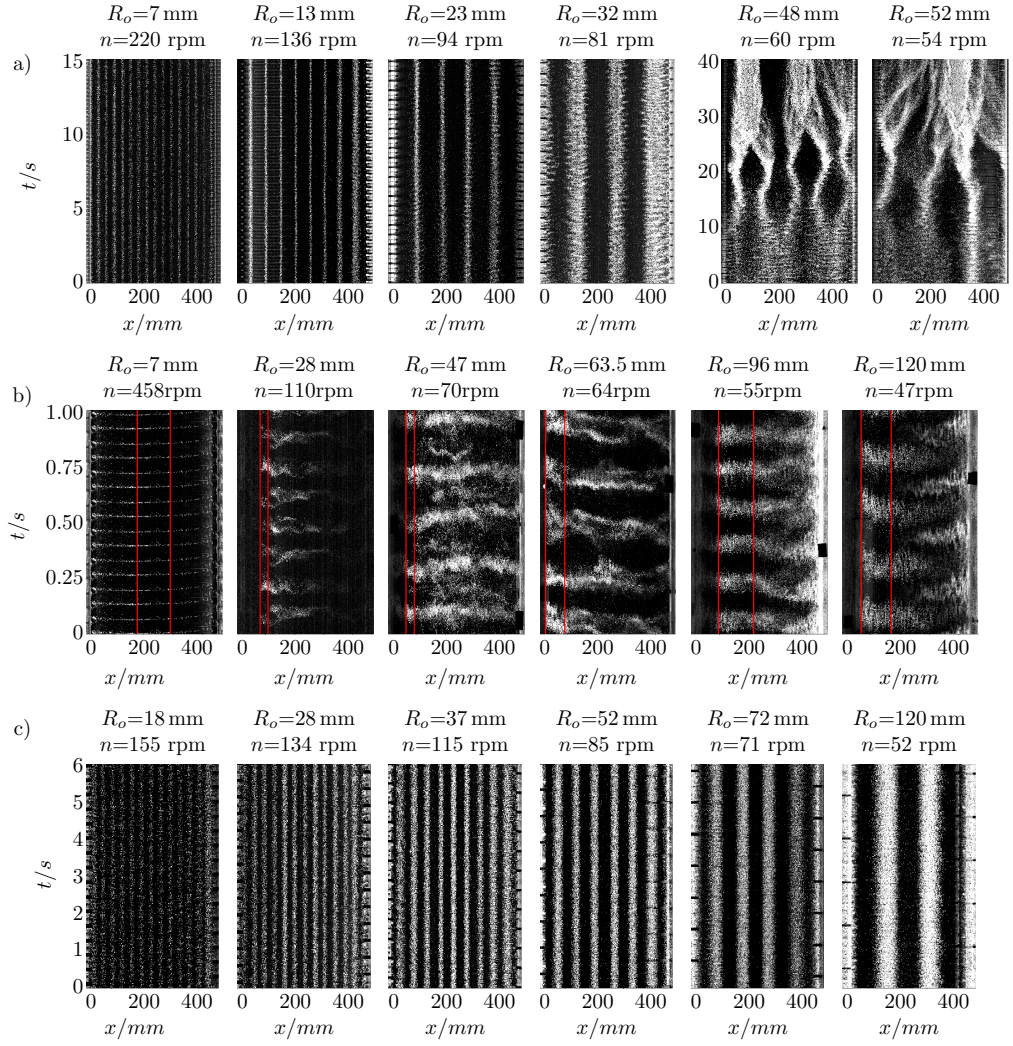

Figure 7.7: a) Time space diagrams of axial banding of type 1 (AX1) for selected R_o in the drum flow. Bands are unstable for $R_o = 32\,\text{mm}$, $R_o = 48\,\text{mm}$ and $R_o = 52\,\text{mm}$. b) Space-time diagrams of azimuthal banding (AZ) for different R_o. Particles are illuminated asymmetrically such that the bands on the backside are invisible to the camera within a specific area of the cylinder (red lines). $R_o = 7\,\text{mm}$: Single band which is visible to camera when located at front or back side of the cylinder. c) Time space diagrams of axial bands of type 2 (AX2) for selected R_o.

the experiments show, that the number of bands and the wavelength of AZ banding depends on the cylinder radius (see Fig. 7.7b). Compared to AX1 banding and AX2, the AZ banding often attain a wavy shape except for small drum radii as can be seen exemplary for $R_o = 7\,\text{mm}$. In general, it is observed that the rotation rate range at which AZ banding can be observed increases with increasing R_o (not shown here).

In Fig. 7.7c space-time diagrams of AX2 banding are depicted. As can be seen, in contrast to AX1, AX2 forms stationary bands even for R_o up to 120 mm. In fact, AX2 banding was observed to be stable for $13\,\text{mm} \leq R_o \leq 145\,\text{mm}$, while for $R_o = 7\,\text{mm}$ no AX2 could be observed. Compared to AZ the bands of AX2 appear to be more regular and do not attain a wavy shape (Fig. 7.7b, Fig. 7.7c). Analogous to AX1 and AZ banding the wavelength of AX2 banding changes with increasing R_o (Fig. 7.7c). Furthermore, it becomes evident from Fig. 7.7c that the width of the particle bands increases as the drum radius increases. Overall, the results indicate that AX2 banding is more stable compared to AX1 and AZ banding in the drum flow. As already explained in section 7.2 the particles scatter much less around the trajectory for AX2 banding than for AX1 and AZ banding. This might be due to the fact that particles are centrifuged closer to the wall during the AX2 banding phase as discussed in Sect. 7.2, such that particle movement is more restricted. In contrast, during AX1 banding or AZ banding the particles experience lower centrifugal forces and hence spend less time on the cylinder walls, which makes them more susceptible to disturbances induced by interaction of particles with the fluid and each other as explained in section 7.2.

7.3.2 Taylor-Couette flow

In Fig. 7.8 space-time diagrams are shown for the TC flow for two selected outer cylinder radii and increasing values of H/R_o for selected rotation rates analogous to Fig. 7.7. Figure 7.8a,b,c show rotation rates associated with AX1, AZ and AX2 banding, respectively. The ratio of gap height and outer cylinder radius H/R_o increases from left to right. Space-time diagrams are shown beginning from an arbitrary time when the band was in a stationary state after the rotation rate was increased.

From Fig. 7.8a, where space-time diagrams for AX1 banding in the TC flow are depicted, it becomes evident that the wavelength changes with increasing H/R_o for fixed R_o. For $R_o = 57\,\text{mm}$ it can be also seen, that the bands become wider as H/R_o increases. Furthermore, Fig. 7.8a, shows that the AX1 bands remain stable for $R_o = 57\,\text{mm}$ while they are unstable for $R_o \geq 32\,\text{mm}$ in the drum flow case (7.7a). In fact, in the TC flow stable bands could be observed for outer cylinder radii up to $R_o = 112\,\text{mm}$ (with a gap width of 12 mm) and gap widths ranging from $H = 5.5\,\text{mm}$ (for $R_o = 72\,\text{mm}$) to $H = 47\,\text{mm}$ (for $R_o = 57\,\text{mm}$). It would be interesting to see, if bands become unstable at larger gap widths, however 47 mm was the maximum gap width considered

in the experiments. It was observed, that the rotation rate range associated with AX1 increased with decreasing gap height. In fact, AX1 banding was the only band pattern that occured at $H = 5.5\,\mathrm{mm}$.

Fig. 7.8b shows the space-time diagrams for AZ banding in the TC flow. For both depicted values of R_o it can be seen, that the spacing and the width of the bands increases as H/R_o increases. Furthermore, the inner cylinder seems to have a stabilizing effect on the AZ bands. These become increasingly wavy as H/R_o increases corresponding to a decreasing inner cylinder radius here (Fig. 7.8b). This reveals, that the presence inner cylinder significantly affects AZ banding. In the TC flow, AZ banding was found to occupy an increasing rotation rate range as the gap height increases. This shows a similarity to the drum flow, where the rotation rate range associated with AZ banding increases with increasing drum radius. AZ banding could be observed for outer cylinder radii up to $R_o = 112\,\mathrm{mm}$ and gap widths ranging from 10 mm to 47 mm.

In Fig. 7.8c the space-time diagrams for AX2 banding in the TC flow are presented. It becomes evident, that the wavelength of AX2 banding changes with increasing H/R_o for fixed R_o (Fig. 7.8c). By comparing the space time diagrams for $H/R_o = 0.38$ and $H/R_o = 0.29$ in Fig. 7.8b and Fig. 7.8c it can be seen, that AX2 banding exhibits bands which are more regular compared to those of AZ banding. The origin for this is the same as in the case of a drum flow: During the AX2 banding particles spend more time close to the wall compared to AZ and hence are less prone to disturbances. Also for the TC flow it was observed, that particles scatter less around the trajectory during AX2 banding compared to AZ and AX1 banding as discussed with regard to Fig. 7.4b. Another detail of AX2 becomes visible for $R_o = 112\,\mathrm{mm}$ in Fig. 7.8c. As can be seen for $H/R_o = 0.29$ the space-time diagram features alternating bands of higher and lower intensity, related to a higher or lower concentration of particles. Thereby, the bands remained stationary and no interchange of particles between bands occured. In fact, for several combinations of H/R_o such alternating bands of high and low concentration could be observed.

7.4 Effect of varying particle volume fraction in the gravity dominated and intermediate regime

Konidena et al. (2019) showed within their simulations of bidisperse suspensions, that the phase boundaries in the gravity dominated regime (comparable to region I here) depend on the ratio of particle settling velocity and circumferential velocity. Based on the work of Dietrich (1982) and Bush et al. (2003) we estimate the particle Reynolds number within our experiments to about $Re_p = d_p|u_p - u_f|\rho_{\mathrm{fluid}}/\mu_{\mathrm{fluid}} \approx 24...35 = O(10^1)$. For such values of Re_p it is known, that the sedimentation velocity of a particle cloud can exceed that of a single particle (Slack 1963; Noh and Fernando 1993; Bush et al. 2003). Therefore, we investigated the fundamental effect of the particle volume fraction in the gravity dominated regime I and the intermediate regime II (GB-AX1, see Fig.

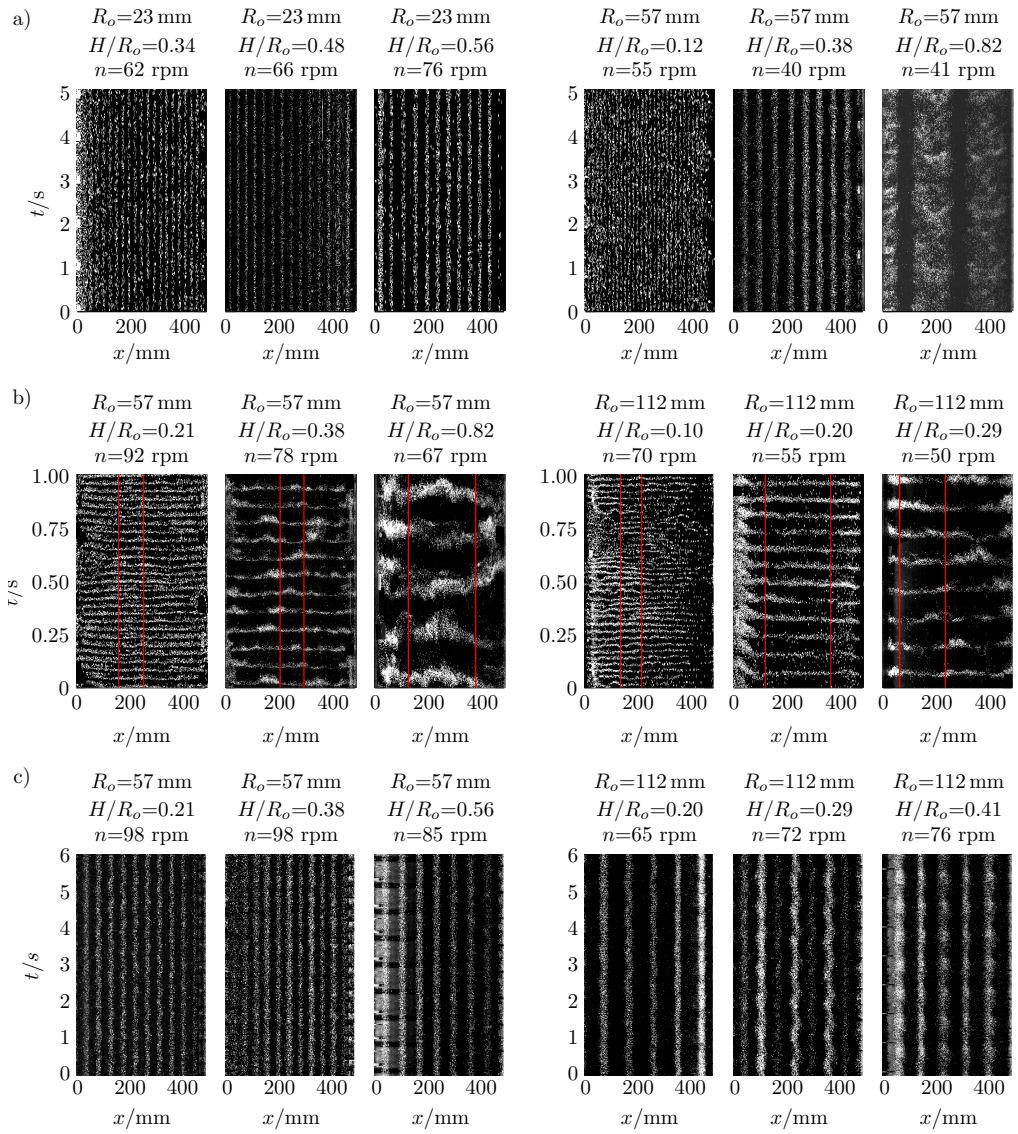

Figure 7.8: Space-time diagrams of AX1, AZ and AX2 banding for selected R_o and H/R_o values in the TC flow. Bright areas indicate high concentration of particles. a) Axial banding of type 1 (AX1) b) Azimuthal banding (AZ) The region of interest for extracting the azimuthal wavelength is highlighted by red rectangles. c) Axial banding type 2 (AX2)

7.1). For this, several phase mapping experiments were performed at R_o =144 mm and $H/R_o = 0.167$ for Φ ranging from 0.07% to 0.5% up to a rotation rate of 60 rpm. As significant effects occured at 0.5% and no stable bands could be observed at the given rotation rate, higher volume fractions were not considered. Figure 7.9 depicts exemplary

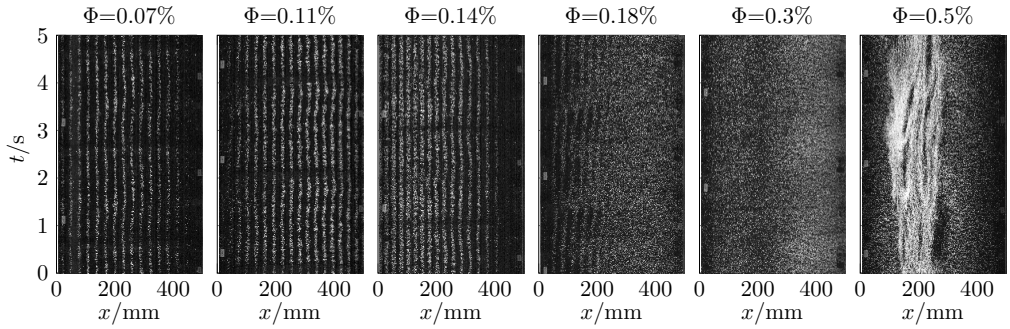

Figure 7.9: Effect of varying the particle volume fraction on the pattern formation. Space-time diagrams at 30 rpm, R_o =144 mm and $H/R_o = 0.167$ for $\Phi = 0.7\%$, 0.11%, 0.14%, 0.18%, 0.30% and 0.5%. Bright areas indicate high concentration of particles.

space-time diagrams for $n = 30$ rpm as a function of Φ. As can be seen for Φ=0.07%, 0.11% and 0.14% a clear AX1 pattern can be observed. Obviously in this range the stability and the wavelength of the bands remains almost unaffected of changes in Φ. However, as Φ is increased further the system begins to fall back to the UH phase ($\Phi =$ 0.18%, 0.3% in Fig. 7.9). As described earlier in the context of Fig. 7.1 the UH phase is associated with a lower rotation rate than AX1 banding. From Fig. 7.9 it can be seen that for $\Phi = 0.18\%$ AX1 banding is present in the left side, while the UH phase is present in the right side of the system. Even though great care was taken for leveling of the system, this indicates a slight gradient of particle concentration in the system. For $\Phi = 0.3\%$ the distribution is approximately homogenous along the cylinder length. This indicates that for $0.18\% \geq \Phi \geq 0.3\%$ particle interactions lead to an enhanced settling velocity such a higher rotatio rate is required to keep the particles on their trajectories. This finding is consistent with the finding of Matson et al. (2008), who concluded that the rotation rate required for each phase boundary increases with increasing Φ. Matson et al. (2008) concluded that the underlying effect is not an increase of effective viscosity but an increase of gravitational driving force due to the increase of particle mass. This is consistent with the scenarios depicted in Fig. 7.9. According to equation 1.5 the effective viscosity changes only by factor 1.01 when Φ is increases from 0.07% to 0.5%. At the same time the overall mass of particles and hence the gravitational force excerted on the suspension increases by factor 7.14.

As Φ is increased even further to Φ =0.5% the system becomes unstable and particles collect in randomly located accumulations, visible as bright wavy lines in Fig. 7.9 for Φ =0.5%. We assume the tendency of UH to form accumulations increases with the particle volume fraction. Overall, in our experiments we observe that within the low rotation regime and the intermediate regime, an increase in particle volume fraction forces the system back to phases which would occur at lower rotation rates. We conclude that increased particle volume fraction leads to increased average particle

settling velocity such that the system falls back to from AX1 banding to a phase that is associated with a lower rotation rate in accordance with the findings of Matson et al. (2008).

7.5 Scaling of Wavelength

In the following, the wavelengths associated with the band patterns (AX1, AZ, AX2) observed in the drum flow and TC flow are compared. To visualize how the wavelengths scale with drum radius as well as with gap height, results are displayed in dimensional presentation in Fig 7.10a,c,e. However, to unravel the asymptotic behavior when the inner cylinder radius decreases a non-dimensional representation of λ^*/R_o is shown as function of the normalized gap width (H/R_o) in Fig. 7.10b,d,f. In Fig. 7.10a the measured wavelength λ^* of AX1 is depicted as a function of the gap height H for the drum (red dots) and the TC-flow (magenta dots). Additionally, linear fit functions are fitted to the data to indicate the scaling behavior.

From Fig. 7.10a it can be seen that λ^* of AX1 increases linearly with H for the drum flow up to a radius of $R_o = 32\,\mathrm{mm}$ (red dots). For the drum flow the wavelength scales approximately linear with a slope of $\lambda^*/H = 3.95$. The corresponding linear fit is labeled with ii in Fig. 7.10a. For the TC-flow the trend is less clear. While the majority of the measured wavelengths (cyan dots) approximately follow linear scaling relations ($\lambda^*/H = 3.95$ labeled with ii, $\lambda^*/H = 2.43$ labeled with i), some points are located inbetween. Obviously, for the TC flow the gap height does not provide an unambiguous correlation for λ^* of AX1.

The geometrical dependence of λ^* of AX1 in the TC flow becomes clear by nondimensionalizing λ^* and H with R_o as depicted in Fig. 7.10b. Here it can be seen that λ^*/R_o increases linearly with a slope of $\lambda^*/H = 2.43$ (i) for $H/R_o < 0.65$. For $H/R_o > 0.65$ the normalized wavelength λ^*/R_o starts to increase sharply as H/R_o increases, till it approximates the linear fit of $\lambda^*/H = 3.95$ (ii) around $H/R_o = 0.8$. For $H/R_o > 0.8$ the data indicates that λ^*/R_o of the TC flow merges smoothly into λ^*/R_o of the drum flow ($H/R_o = 1$) as H/R_o approximates one. We assume this is correlated to the stabilizing effect of the inner cylinder as described in Sect. 7.2. This stabilizing effect faciliates smaller wavelengths ($\lambda^*/H = 2.43$, labeled with i). As the inner cylinder size decreases ($H/R_o \to 1$) its stabilization effect decreases as well. At some point the inner cylinder is too small compared to the outer cylinder to stabilize certain bands and smaller wavelengths disappear. Hence, it is concluded that when there is no stabilizing effect of the inner cylinder, λ^*/R_o is equal for TC and drum flow.

The measured wavelengths of AX2 as a function of H together with linear fit functions are depicted for the drum flow (blue dots) and the TC-flow (cyan dots) in Fig. 7.10c. Here, it can be seen that for both TC and drum flow λ^* of AX2 increases linearly with H but switches between modes with different slopes of λ^*/H, labeled with i, ii, iii and

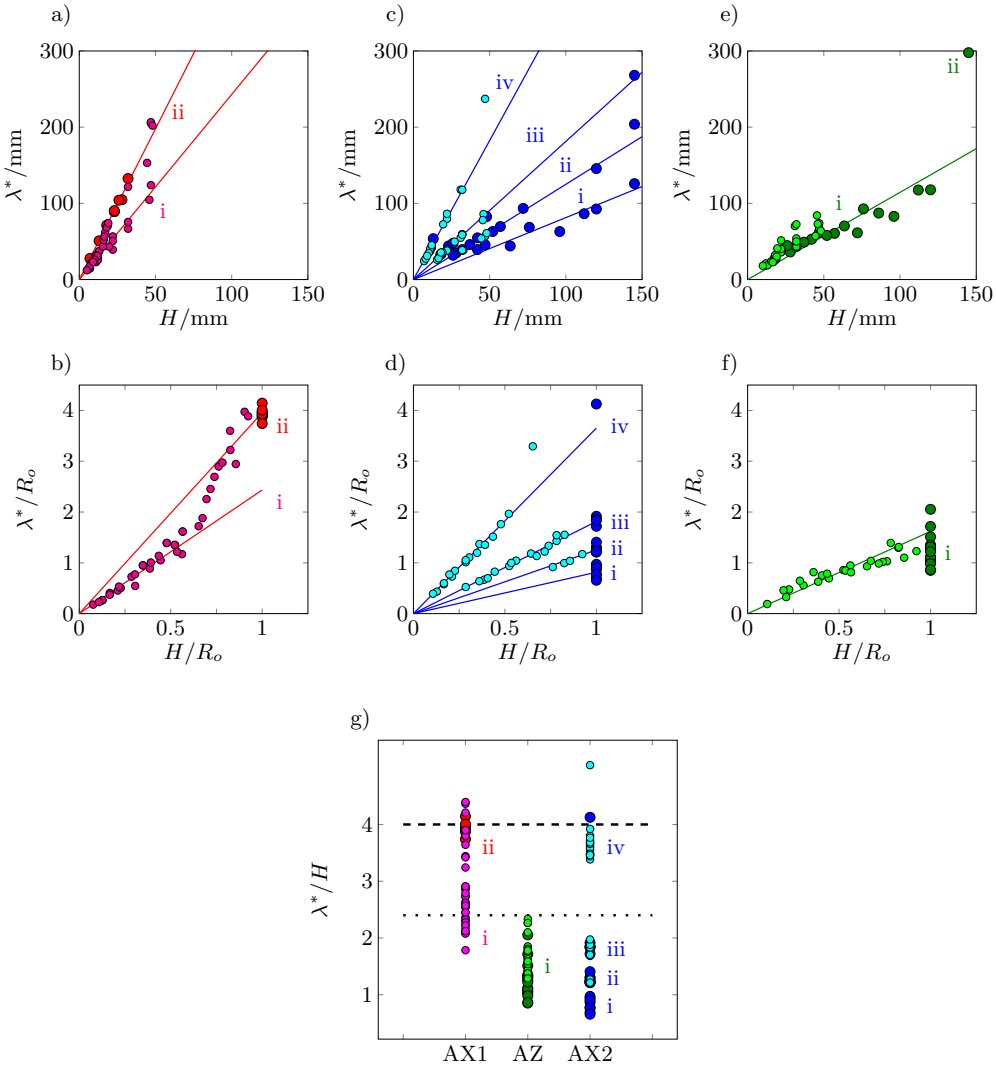

Figure 7.10: Measured wavelengths for AX1, AZ and AX2 banding (Drum flow: $H = R_o$, TC flow: $H = R_o - R_i$). a) λ^* over H for AX1 (magenta dots = TC flow, red dots = drum flow). b) λ^*/R_o over H/R_o for AX1 (magenta dots =TC flow, red dots = drum flow). c) λ^* over H for AX2 (cyan dots = TC flow, blue dots = drum flow). d) λ^*/R_o over H/R_o for AX2 (cyan dots = TC flow, blue dots = drum flow). e) λ^* over H for AZ (green = TC flow, dark green = drum). f) λ^*/R_o over H/R_o for AZ (green = TC flow, dark green = drum). g) λ^*/H for AX1, AZ and AX2. Dashed horizontal line = λ^*/R_o reported by Seiden et al. (2005). Dotted line = λ^*/R_o reported by Matson et al. (2003).

iv, resulting in a fan shaped pattern. Apparently, λ^* can assume multiple values for a given value of H for both the drum as well for the TC flow. In contrast to AX1 banding, no points can be found inbetween those modes for AX2 banding. This fan

shaped pattern becomes also evident from the nondimensionalized presentation which is shown in Fig. 7.10d. The nondimensionalized presentation further reveals how λ^*/R_o of AX2 of the TC flow merges towards the drum flow case as H/R_o approaches one (see Fig. 7.10d).

In comparison to AX1 and AX2 the experimental data of λ^* over H for AZ scatters significantly (see Fig. 7.10e). This is likely because the wavelength of AZ is measured indirectly based on the measured frequency and velocity of the bands, rather than directly as in the case of $AX1$ and $AX2$. Nevertheless, our data clearly shows that λ^* of AZ increases approximately linear as H increases for both the drum flow (dark green) and the TC flow (light green). For the drum flow our data indicates a saw tooth pattern for $55\,\mathrm{mm} < H < 125\,\mathrm{mm}$, however more data points are required here for further conclusions. As already observed for AX1 and AX2 it can be seen in the nondimenzionalized presentation how the data of the TC flow merges to the data of the drum flow as $H/R_o \to 1$ (see Fig. 7.10f).

Figure 7.10g, provides an overview of all measured values of λ^*/H for AX1, AX2 and AZ for all considered values of $0 < H/R_o \leq 1$. It can clearly be seen that the same modes can be triggered in the drum flow (H/R_o<1) and the TC flow (H/R_o=1). The dashed line in Figure 7.10g is λ^*/R_o reported by Seiden et al. (2005) while the dotted line represents λ^*/R_o reported by Matson et al. (2003). As can be seen from Figure 7.10g both AX1 and AX2 exhibit λ^*/H values in agreement with the values reported by Seiden et al. (2005) (dashed line, red ii and blue iv). The wavelength reported by Matson et al. (2003) instead coincides with AX1 for the TC flow (dotted line, red i). AX2 and AZ feature also wavelengths which are different from both the results of Seiden et al. (2005) and Matson et al. (2003).

Overall, the results in Fig. 7.10 reveal significant differences regarding both the dimensionalized wavelength λ^* and the normalized wavelength (λ^*/R_o) for AX1, AX2 and AZ. For AX2 the results indicate that the wavelength can only assume certain values of λ^*/R_o. This suggests that the formation of AX2 is related to a wave motion of the flow resulting into a secondary flow pattern, which exists in the system and can only assume specific wavelengths. Seiden et al. (2005, 2007) explained the formation of particle bands by inertial waves, which are excited by the movement of the particles. According to Seiden et al., the particles accumulate in alternate nodes of the wave excitation. As the (normalized) wavelengths (λ^*/H, λ^*/R_o) appear to be identical for drum and TC flow it is assumed that the same underlying mechanisms are responsible for AX2 formation in both the drum and the TC flow. However, the normalized wavelength of AX1 λ^*/R_o attains different values for the TC flow compared to the drum flow for $H/R_o < 0.6$. For AX1 banding, when R_i decreases compared to R_o the normalized wavelength merges smoothly into that of the drum flow (Fig. 7.10b). This indicates that interactions of particles and inner cylinder play a role in determining the wavelength of AX1 in the TC flow, which is not the case in AX2. This is in agreement with Hou et al. (2014), who concluded that particle interactions are a mechanism that

drives the band formation in drum flows. The fact, that λ^*/R_o apparently can assume arbitary values between the two fits (i, ii) in Fig. 7.10b depending on H/R_o indicates a different underlying mechanism for AX1 compared to AX2.

7.6 Discussion and Conclusion

In this chapter, ten particle patterns were reported for a drum flow and a corotating TC flow with a low viscosity suspension (1 cP) of settling particles. Three types of axial bands (AX1, AX2, AX3) and two types of azimuthal band patterns (AZ, CLL) were discovered for both flow types. Furthermore, a coexistence of axial and azimuthal band structures is revealed for the TC flow, which we denote as square pattern (SQR). Also net shaped particle patterns were discovered, termed as net pattern (NP1-NP3).

With the complete phase range covered from granular bed (GB) to centrifugal limit line (CLL), the results indicate, that the band pattern reported and discussed by Lipson (2001) and Seiden et al. (2005) is axial banding type 1 (AX1). Drum flow experiments reveal that this type of banding (AX1) becomes unstable above a drum radius of approximately $R_o \geq 32\,\text{mm}$, which leads to collapsing of bands after formation. Contrary, for the TC flow the stability of AX1 bands does not depend on the outer radius. In fact, bands could be observed for a TC flow with radii up to $R_o = 112\,\text{mm}$ and gap width up to $H = 47\,\text{mm}$. We conclude, the larger the cylinder radius the longer the particles are suspended within the gap along their trajectories, which make them more susceptible to disturbances induced by interactions of particles with each other and the fluid. This results in a self-reinforcing process which ultimately leads to a collapse of the bands similar to the behavior of particle clouds sedimenting in stagnant water. The additional inner cylinder present in the TC flow configuration can have a stabilizing effect on the band patterns. Investigations on the radial particle position revealed that the inner cylinder strongly alters the particle trajectories of AX1. It is concluded that this effect leads to a stabilization of AX1 bands in the TC flow and facilitates stable bands at large values of R_o. Furthermore, the data reveals that the normalized wavelength λ^*/R_o of AX1 changes smoothly as the geometry changes from TC flow to drum flow with decreasing inner cylinder size ($H/R_o \to 1$).

Most significantly, an azimuthal band pattern (AZ) was discovered that does not resemble any band structure previously discovered. This pattern was observed for gap widths in the range of $7\,\text{mm} \leq H \leq 145\,\text{mm}$. The experiments reveal that the wavelength λ^* (and λ^*/R_o) of AZ increases linearly with H (respective H/R_o). In comparison to AX1 the change in wavelength with the gap width is less pronounced for AZ. As for AX1 we can show for AZ that the wavelength merges smoothly when the geometry changes from the TC flow to the drum flow, as H/R_o approaches $H/R_o = 1$.

The second type of axial banding (AX2) can be observed for drum radii of up to $R_o \approx 150\,\mathrm{mm}$ and appears to be more stable than AX1 banding. Here, particles spend more time on the cylinder walls and less time within the gap such that the bands are more robust against disturbances. It was shown that for both the TC as well as the drum flow, the wavelength of AX2 as a function of H develops a fan shaped pattern where multiple wavelengths can coexist for fixed values of H. Furthermore, the experiments show that the normalized wavelength λ^*/R_o is approximately equal for both drum and TC flow. Similar to AX1 and AZ it was shown for AX2 that the normalized wavelength λ^*/R_o as a function of the normalized gap width H/R_o falls on the same linear fit curves for both drum and TC-flow.

Overall, the present parametric study suggests that the underlying physical mechanism for AX1 and AX2 are different, which comes especially clear in the normalized presentation. While the normalized wavelength λ^*/R_o changes smoothly with H/R_o for AX1, AX2 exhibits an unsteady fan shaped pattern. This indicates that an inertial wavemotion as concluded by Seiden et al. (2005) could be responsible for the AX2 band formation. On the other hand, the irregularities of the AZ bands as well as the unstable behavior of AX1 at higher values of R_o lead us to the conclusion, that here particle interaction may play the key role. It is further concluded that these particle interactions are significantly altered by the presence of the inner cylinder, which results in altered AX1 wavelengths, in the case of the TC flow.

8 Thesis summary and outlook

In this thesis, major physical phenomena relevant to the dynamics of particle laden flows in horizontally aligned Taylor Couette Reactors (TCRs) were thoroughly investigated. These are the stability of the flow, particle migration phenomena as well as the effect of rotation on settling suspensions. In order to reduce the complexity, these phenomena were investigated separately. First, the effect of increasing swirl on the stability of laminar flow in a TCR was studied by means of linear stability analysis. Next, particle migration was investigated in suspension flow of volume fractions up to $\Phi = 9.1\%$ utilizing Astigmatism Particle Tracking Velocimetry (APTV). For this, the application of APTV on large suspension particles was extensively investigated. For reducing the complexity and for benchmarking the results with data from literature, a square duct flow was chosen instead of a TC system, here. Finally, we investigated particle structure formation in horizontally aligned rotating drum and co-rotating Taylor-Couette flows and worked out the effect of the inner cylinder. Hereafter, a summary of the topics and recommendations for future works will be presented.

8.1 Instability mechansims in the Spiral Poiseuille Flow

The flow in a TCR is composed of azimuthal Taylor-Couette (TC) flow and axial Annular Poiseuille Flow (APF) such that the resulting flow is commonly known as Spiral Poiseuille Flow (SPF). In such flows, particle trajectories differ significantly for laminar, bifurcated or turbulent flow. Hence, understanding the stability behavior of the SPF is essential for predicting the particle dynamics. Thus, in the present work the stability of the SPF was analyzed by means of linear stability analyis.

The velocity profile of the SPF is defined by the curvature of the gap $\epsilon = (1-\eta)/(1+\eta)$ where η is the radius ratio of the cylinders (R_i/R_o), as well as the "swirl" which is the ratio of azimuthal and axial flow velocity. According to the Rayleigh criterion the azimuthal flow component is linearly stable (Rayleigh stable) when the ratio of the rotation rate ($\mu = \Omega_o/\Omega_i$) is greater than η^2. Otherwise if $\mu < \eta^2$, the flow is linear unstable (Rayleigh unstable). For the SPF with Rotating Inner cylinder (IRSPF) where $\mu = 0$, it is known that increasing swirl leads to a destabilization of the flow, which has been associated with a transition from a Tollmien-Schlichting to a centrifugal instability. In contrast, for the Spiral Poiseuille Flow with Rotating Outer cylinder (ORSPF, $\mu \to \infty$), it was observed that increasing swirl first destabilizes the flow but also slightly stabilizes the flow as the swirl increases further (Meseguer and Marques

2005). In fact, the underlying mechanisms which lead to a stabilizing or a destabilization of the SPF for both $\mu = 0$ and $\mu \to \infty$ have not been analyzed or quantified in detail and have therefore been investigated in the present study. Furthermore, only a few values of ϵ have been investigated for both IRSPF and ORSPF up to date. Given that, in the present thesis extensive computations on the linear stability behavior were performed for the IRSPF as well as for the ORSPF from low to high swirls and over 77 values of the curvature parameter in the range of $0 < \epsilon < 0.78$. Moreover, an approach was developed to discriminate between different instability mechanisms based on the production terms of the Reynolds Shear Stress Transport Equations (RSSTE) and the budget of the kinetic disturbance energy (K). Detailed phase maps for both cases were generated that describe the stability behavior as quasi-continuous function of ϵ and swirl. It was revealed, that the behavior of the ORSPF strongly depends on ϵ. Three different instability regimes associated with low, intermediate and high swirls could be identified for the ORSPF for $\epsilon > 0.05$ and for the IRSPF for all ϵ considered. Thereby, the swirl values associated with the phase boundaries were found to strongly depend on ϵ for IRSPF as well for ORSPF. In general, it was found that increasing ϵ lowers the swirl values associated with the phase boundaries. Using the approach for identification of instability mechanisms, it was confirmed that in the first regime, associated with low swirls, a Tollmien-Schlichting shear instability is present in both the IRPSF and the ORSPF. Here, the production of shear stresses and of kinetic disturbance energy is due to axial shear. Thereby, based on the distribution of shear stresses and the expression of Vasanta Ram (2019), it was shown that there exists a critical layer, as assumed by Cottrel and Pearlstein (2004). To the authors best knowledge, this is the first time, a critical layer was discussed for non-axissymmetric disturbances in the SPF. Furthermore, it was shown for the first time, that for the ORSPF and small values of ϵ a Tollmien-Schlichting instability can persist even at swirls where the azimuthal flow component is significantly larger than the axial flow component. The second regime is associated with intermediate swirls. Here, for both the IRSPF and the ORSPF the shear stress distributions attain a characteristic shape and the critical Reynolds number Re_c drops sharply with increasing swirl. The decrease of Re_c is well over 90% for all ϵ considered in IRSPF and for $\epsilon \geq 0.2$ in the ORSPF. It was found, that for both the IRSPF and the ORSPF, this drop in Re_c is induced by the same centrifugal instability mechanism, which is characterized by the centrifugal production of τ_{rx} and an axial shear production of kinetic disturbance energy. Here, for the first time, differences as well as common features of the instability mechanism induced by rotation of the outer and the inner cylinder were carefully analyzed. When the swirl is increased further within the second regime, the azimuthal shear production increases in both cases. While in the IRSPF the increasing azimuthal shear production leads to a further destabilization and decrease of Re_c, this leads to stabilization of the ORSPF resulting in a sharp increase of Re_c. This revealed that outer rotation has an ambiguous effect on the stability of the SPF and that there are striking differences between IRSPF and ORSPF. The third regime is associated with relatively large swirls.

For the IRSPF at the beginning of the third regime the axial shear production drops to zero for all ϵ, but overall the shear stresses only change slightly. Instead, for the ORSPF the characteristics of shear stresses and production terms change strikingly here and reveal the existence of a single critical layer close to the inner cylinder. Based on the production terms of the RSSTE it was concluded, that here a Tollmien-Schlichting instability is present which agrees which the presumptions of Deguchi (2017). A striking feature here is, that the centrifugal production terms counteract the shear production terms and hence inhibit shear stress production. For all ϵ considered, the ORSPF is strongly stabilized as the swirl increases within the third regime.

Overall, the results obtained in the present thesis, provide a wide data base which highlights interesting parameter combinations for follow up numerical simulations and experimental works. Even though only pure liquids were considered and also experimental validation is required, some potentially very interesting conclusions can be drawn regarding processing particle laden flows in TCRs. For instance, when high Reynolds numbers or high shear rates are required for the process, while a laminar velocity profile should be maintained, an ORSPF with a low curvature parameter is a promising option. A laminar velocity profile is potentially interesting for particle sorting applications. In contrast, with larger curvature parameters and outer cylinder rotation, instabilities can be induced which potentially leads to transition and turbulence and therefore enhanced diffusion. At the same time, the outer cylinder rotation could prevent heavy particles to form a sediment bed at the outer wall, when the system is horizontally aligned. This could improve the mixing performance in suspensions with heavy particles.

8.2 ATPV and particle migration in suspension flows

Apart from being affected by the structure of the flow, viz the shape of the streamlines, the particles in a TCR flow also undergo cross-streamline migration arising from interaction of particles with each other and the fluid. For instance, in the context of the present work, it was discovered that particles of a tridisperse suspension flowing in a horizontally aligned Taylor-Couette flow with rotating inner cylinder segregate into different particle bands according to their size. As this phenomena cannot be explained based on current literature, one of the main motivations of this work is to extend the understanding of particle migration in mono- and polydisperse suspensions. In general, two mechansims are well known that can cause particle migration in suspension flows and potentially lead to size segregation: Shear induced migration which results from particle interactions and inertial migration which results from inertial effects in suspension flows. In fact, two recent numerical studies revealed, that the interplay of shear induced-migration and inertial migration may result in complex particle distribution patterns (Kazerooni et al. 2017) and even lead to particle size segregation (Chun and Jung 2021).

Therefore, to improve the understanding of separation in TCRs, within this work particle migration phenomena were experimentally investigated, by means of optical measurement techniques. To measure the threedimensional particle distributions and velocities at higher solid volume fractions, a promising, low cost and easy to implement measurement technique is APTV, which is usually applied to small tracer particles ($< 10\,\mu m$) at very dilute conditions. Hence, in the present study, it was thouroughly investigated how APTV can be applied on large suspension particles ($> 10\,\mu m$) at dilute and semi-dilute conditions.

First, an adapted APTV technique was developed which can be applied to large transparent particles in dilute suspensions. Here, the particles act as ball lenses, which focus the light that comes from a background illumination. This results in a bright focal point in front of the particle that is used for the tracking procedure. The technique is referred to as Ball Lens Astigmatism Particle Tracking Velocimetry (BLAPTV). Furthermore, a 3D calibration procedure was developed, which uses the particle image's shape as well as its light intensity to reconstruct the particles depth position. BLAPTV was successfully validated by measuring a planar Poiseuille flow in a rectangular channel. Thereby, it was shown that BLAPTV with large transparent particles can yield comparable accuracies as conventional APTV with small fluorescent particles.

Next, the application of APTV on large fluorescent particles was investigated in monodisperse suspensions of solid volume fractions up to 20 %. Using a refractive index matching (RIM) technique, the suspension was rendered transparent while a few particles were labeled to make them visible for the camera. It was discovered that slight deviations of the refractive index of particles and liquid induce optical distortions, which lead to deformations of the calibration curve that become severe with increasing solid volume fraction. These shape changes were compensated utilizing an interpolation method that was succesfully validated by measuring the laminar velocity profile in a rectangular duct with a $2.550 \times 30\,mm^2$ cross section for six individual volume fractions ranging from $\Phi \leq 0.01\%$ to $\Phi = 19.9\%$. The average standard deviations for the measured in-plane as well as the out-of-plane velocity were found to increase as the volume fraction increased from 0.01% to 19.9%. In fact, the local increase in uncertainty was pronounced for measurement planes closer to the channel bottom as optical distortions were more significant, there. Nevertheless, the averaged velocity profile was found to be in good agreement with the theoretical solution, which confirmed that the proposed interpolation technique is suitable for measuring particle velocities in suspensions beyond the dilute regime.

Finally, the application of APTV on polydisperse suspensions was investigated. Calibration measurements performed for different particle sizes ranging from $15\,\mu m$ to $260\,\mu m$ revealed that the associated calibration curves overlap outside the focal planes leading to ambiguities. It was shown, that these ambiguities can be overcome using the 3D calibration procedure, as the light intensity increases with particle size. Utilizing

the 3D calibration technique, the particle migration in flows of mono- and tridisperse suspensions was investigated in square capillaries of $400\times400\,\mu m^2$ and $600\times600\,\mu m^2$ cross sectional area. The tridisperse suspension contained particles of 30 µm, 40 µm and 60 µm diameter. At a volume fraction of $\Phi = 0.08\%$ and a bulk Reynolds number of $Re_b = 20$ particles were observed to be collected into a Pseudo Segre Silberberg Annulus (PSSA) with no signifcant differences between mono- and polydisperse suspensions. At $\Phi = 9.1\%$ and $Re_b = 20$ particles in monodisperse suspensions scatter around the PSSA. The scattering becomes more pronounced as d_p decreases from 60 µm to 30 µm. When Re_b is increased to $Re_b = 40$ the scattering decreases for all d_p investigated. It was concluded, that inertial migration focusses the particles on the PSSA while shear induced migration counteracts this focussing and disperses particles towards the channel center and walls. An increase in d_p or Re_b enhances inertial migration and hence decreases the scattering in monodisperse suspensions. For polydisperse suspensions, different particle distributions were observed for $\Phi = 9.1\%$ and $Re_b \geq 20$. Compared to the monodisperse case large particles (60 µm) are significantly more focused. In contrast, small and intermediate particles (30 µm and 40 µm) are repulsed by larger particles leading to regions of high concentration close to the channel walls. This size dependent segregation becomes pronounced when Re_b is further increased. It was concluded that inertial forces are pronounced for larger particles such that they reach the PSSA first and screen off smaller particles. At the same time, shear induced migration and hence scattering is less pronounced for larger particles compared to a monodisperse suspension due to the presence of smaller particles which lowers the effect of particle interactions (collisions).

Overall, it was successfully shown that APTV can be applied on large transparent or fluorescent particles in dilute as well as dense suspensions in milimeter sized as well as in sub-millimeter sized geometries. Hence, the technique is promising for investigating the dynamics of mono- and polydisperse suspensions in TCRs with small gap widths and limited optical access. It was further successfully shown that the interplay of inertial migration and shear induced migration can lead to a size segregation of particle species in pressure driven square duct flow. This observation is a further step in untangeling particle segregation phenomena as they are also observed in Taylor Couette devices.

8.3 Pattern formation in particle laden Taylor-Couette flows

Besides the structure of the flow and migration phenomena, the dynamics of particles subjected to the flow in a TCR can also be affected by the interplay of sedimentation and the rotation of the system. In fact, it is known that flows of dilute settling suspensions in horizontally aligned rotating cylinders can give rise to formation of band shaped particle accumulations. This phenomena is also known as particle-banding.

While extensive research on this phenomena has been performed in drum flows, the formation of particle bands in fully liquid filled TC flows has been completely unexplored up to date, such that the effect of an additional inner cylinder is yet unclear. Furthermore, most experiments focused on higher viscosities or on lower rotation rates such that a complete phase mapping for the low viscosity limit is still not available. Therefore, in chapter 7 a comparative study was conducted, considering particle pattern- and band formation in both rotating drum flows as well as in a co-rotating TC flows at solid body rotation. For this, extensive phase mapping was performed over a wide rotation rate range and various cylinder radii as well as radius ratios. Overall, ten different particle structures were observed of which six were previously unknown. These include two types of axial periodic bands (AX2, AX3) and two types of horizontally aligned particle bands (AZ, CLL) which occur in both the drum as well as the TC flow. Furthermore, net shaped particle structures (NP1-NP3) were discovered as well as a coexistence of horizontal and vertical band structures, denoted as square pattern (SQR).

The drum-flow experiments revealed that one type of axial banding (AX1) become temporarily unstable for drum radii above $R_o \gtrapprox 32\,\mathrm{mm}$. Contrary, for the TC-flow the stability of AX1 bands was found to be independent on the outer cylinder radius. In fact, AX1 bands could be observed for a TC flow even for outer cylinder radii up to $R_o = 112\,\mathrm{mm}$ and gap widths up to $H = 46\,\mathrm{mm}$. For the drum flow the wavelength of AX1 banding was found to be in good agreement with that reported by Seiden et al. (2005). It was observed that during AX1 banding the presence of an inner cylinder seems to change the particle trajectories and to stabilize the bands. This allows AX1 bands to be stable even at large values of R_o within a TC flow. Thereby, it was found that the (normalized) wavelength (λ^*/R_o) of AX1 changes smoothly for decreasing inner cylinder size. Based on this, it was concluded that interactions between particles and cylinders play a role in determining the wavelength of AX1 in the flow.

The discovered azimuthal band pattern (AZ) does not resemble any previously discovered band structure and appears to be a robust phenomena which occurs for a wide range of radii and gap widths. It was observed, that the wavelength of AZ banding scales approximately linearly with the drum radius or the gap width, respectively. Also for AZ banding it was observed, that the presence of an inner cylinder can stabilize the particle bands, which indicates that particle interactions play a role in AZ banding. However, the effect is less pronounced compared to AX1 banding as AZ banding is associated with higher rotation rates such that the trajectory is shifted closer to the outer cylinder.

The second type of axial banding (AX2) was observed for drum radii of up to $R_o \approx 150\,\mathrm{mm}$ and appeared to be more stable than AX1 banding. Here, particles spend more time on the cylinder walls and less time within the gap such that the bands are more robust against disturbances induced by interactions of particle with each other and the fluid. In contrast to AX1 banding, the (normalized) wavelength of AX2 banding seems to be unaltered by the presence of an inner cylinder. Regarding the wavelengths AX2

exhibits a striking difference to AX1 banding. It was observed that for AX2 multiple wavelengths could coexist for a given of H/R_o or a given drum radius which is not the case for AX1 banding. Thus, it was assumed, that the wavelength of AX2 is a result of a wavemotion which can attain only specific wavelengths in the system, similar to that discussed by Seiden et al. (2005) for a drum flow. The results indicate that different underlying mechanisms are dominant for AX1 and AX2.

Regarding real life applications the findings of chapter 7 could be applied for TCRs which are operated batch-wise. For instance AZ is a very robust phenomena which could be used to generate a uniform particle distribution in axial direction, prior to the process.

8.4 Outlook

In recent years, the field of suspensions has rapidly gained attention and various numerical and experimental studies provided new insights and revealed several interesting phenomena. Yet, this field of research is far from being completely understood. This accounts especially for the dynamics of particle-laden flows in Taylor-Couette Reactors (TCRs). Combining axial and azimuthal flow, they allow to precisely adjust the mixing conditions and the transport velocity (Schrimpf et al. 2021) and are a promising option for processing suspensions for separation and mixing applications with chemical inert or reactive particles. However, the interplay of axial and azimuthal flow leads to rich dynamics induced by centrifugal effects, gravitational effects and the interactions of particles with the fluid and themselves. Untangling these dynamics is extremely challenging with open questions still too be answered. Some of them are adressed in the following.

By means of linear stability analysis, it was revealed that outer rotation can destabilize and stabilize the flow at intermediate and large swirls, respectively. However, this theory only accounts for infinite small disturbances. For transferring this results to real life applications, it is important to investigate how finite disturbances affect the stability behavior. Therefore, the stability behavior of the ORSPF should be investigated by numerical techniques such as Direct Numerical Simulation (DNS) or experimental techniques, where nonlinear effects are captured. Our phase maps can serve as an initial solution, such that extensive mapping can be avoided. Also, the cases of co- and counter-rotation were not considered in the present computations. Exploring the effect of increasing co- or counter-rotation on the phase maps is surely an interesting task for follow up works.

The application of APTV on suspensions of large particles in dilute as well as dense suspensions was thoroughly investigated. Thereby, it was shown that the interplay of shear-induced and inertial migration lead to segregation of small particles and large particles in pressure driven laminar square duct flows with a parabolic velocity profile.

Further, from literature it is known that linear shear flow can lead to a size segregation of particles in bidisperse suspensions (Chun and Jung 2021). For understanding mixing and separation processes in TCRs, it is important to investigate, which particle distributions arise in polydisperse suspensions when an axial pressure driven flow is combined with an azimuthal shear flow. Hence, future works should investigate particle migration phenomena in Spiral Poseuille flow. Furthermore, the present measurements only considered the motion of large suspension particles which undergo their own dynamics and do not follow the streamlines. Therefore, the present results do not provide fluid velocity information. However, recent numerical studies revealed that particles can induce secondary flows in the carrier liquid (Kazerooni et al. 2017). This could also affect the structure of the flow in TCRs. Hence, future measurements should also utilize small tracer particles to measure the fluid motion such that secondary flow can be resolved and a more complete picture of the underlying physics can be generated.

Also, the structure formation in drum and corotating TC flows was investigated. This allowed to reveal the influence of an additional inner cylinder while maintaining solid body rotation. At solid body rotation the shear tensor equals zero. However, forces on the particle and hence inertial and shear induced migration depend on the shear rate in the flow. Consequently, future works should investigate the effect of increasing relative motion of the cylinders and hence increasing shear on the particle trajectories and the band formation.

A Appendix

A.1 Linear Stability Analysis

A.1.1 Governing equations

The non-dimensionalized set of equations for describing the fluid flow in cylindrical coordinates takes the following form:

- continuity equation

$$\frac{\partial v_x}{\partial x} + \frac{1}{r}\frac{\partial}{\partial r}(r v_r) + \frac{1}{r}\frac{\partial v_\varphi}{\partial \varphi} = 0 \tag{A.1}$$

- x - momentum

$$\frac{\partial u_x}{\partial t} + u_x\frac{\partial u_x}{\partial x} + u_r\frac{\partial u_x}{\partial r} + \frac{u_\varphi}{r}\frac{\partial u_x}{\partial \varphi} + \frac{\partial p}{\partial x} - \frac{1}{Re}\left(\frac{\partial^2 u_x}{\partial x^2} + \frac{1}{r}\frac{\partial}{\partial r}\left(r\frac{\partial u_x}{\partial r}\right) + \frac{1}{r^2}\frac{\partial^2 u_x}{\partial \varphi^2}\right) = 0 \tag{A.2}$$

- r - momentum

$$\begin{aligned}\frac{\partial u_r}{\partial t} + u_x\frac{\partial u_r}{\partial x} + u_r\frac{\partial u_r}{\partial r} + \frac{u_\varphi}{r}\frac{\partial u_r}{\partial \varphi} - \frac{v_\varphi^2}{r} + \frac{\partial p}{\partial r} \\ -\frac{1}{Re}\left(\frac{\partial^2 u_r}{\partial x^2} + \frac{1}{r}\frac{\partial}{\partial r}\left(r\frac{\partial u_r}{\partial r}\right) + \frac{1}{r^2}\frac{\partial^2 u_r}{\partial \varphi^2} - \frac{u_r}{r^2} - \frac{2}{r^2}\frac{u_\varphi}{\partial \varphi}\right) = 0\end{aligned} \tag{A.3}$$

- φ - momentum

$$\begin{aligned}\frac{\partial u_\varphi}{\partial t} + u_x\frac{\partial u_\varphi}{\partial x} + u_r\frac{\partial u_\varphi}{\partial r} + \frac{u_\varphi}{r}\frac{\partial u_\varphi}{\partial \varphi} + \frac{u_\varphi u_r}{r} + \frac{1}{r}\frac{\partial p}{\partial \varphi} \\ -\frac{1}{Re}\left(\frac{\partial^2 u_\varphi}{\partial x^2} + \frac{1}{r}\frac{\partial}{\partial r}\left(r\frac{\partial u_\varphi}{\partial r}\right) + \frac{1}{r^2}\frac{\partial^2 u_\varphi}{\partial \varphi^2} - \frac{u_\varphi}{r^2} + \frac{2}{r^2}\frac{\partial u_r}{\partial \varphi}\right) = 0\end{aligned} \tag{A.4}$$

Where $\frac{1}{r}$ can be expressed as function of y: $\frac{\epsilon}{1+\epsilon \cdot y}$

A.1.2 Nonlinear disturbance equations

For obtaining the non-dimensionalized set of equations for describing the motion of the disturbance velocities the following expressions are substituted into equations (A.1) to A.4) (Gonzales 2013):

$$\begin{aligned} u_x &= V_x + u'_x \\ u_r &= 0 + u'_r \\ u_\varphi &= V_\varphi + u'_\varphi \\ p &= p + p' \end{aligned} \tag{A.5}$$

- Continuity equation (of the disturbance velocities)

$$\frac{\partial u'_x}{\partial x} + \frac{1}{r}\frac{\partial}{\partial r}(r u'_r) + \frac{1}{r}\frac{\partial u'_\varphi}{\partial \varphi} = 0 \tag{A.6}$$

- x - momentum

$$\begin{aligned} &\frac{\partial u'_x}{\partial t} + V_x\frac{\partial u'_x}{\partial x} + u'_r\frac{dV_x}{dr} + \frac{V_\varphi}{r}\frac{\partial u'_x}{\partial \varphi} + \frac{\partial p'}{\partial x} \\ &-\frac{1}{Re}\left(\frac{\partial^2 u'_x}{\partial x^2} + \frac{1}{r}\frac{\partial}{\partial r}\left(r\frac{\partial u'_x}{\partial r}\right) + \frac{1}{r^2}\frac{\partial^2 u'_x}{\partial \varphi^2}\right) = \\ &\qquad -\left(u'_x\frac{\partial u'_x}{\partial x} + u'_r\frac{\partial u'_x}{\partial r} + \frac{u'_\varphi}{r}\frac{\partial u'_x}{\partial \varphi}\right) \end{aligned} \tag{A.7}$$

- r - momentum

$$\begin{aligned} &\frac{\partial u'_r}{\partial t} + V_x\frac{\partial u'_r}{\partial x} + \frac{V_\varphi}{r}\frac{\partial u'_r}{\partial \varphi} - \frac{2V_\varphi u'_\varphi}{r} + \frac{\partial p'}{\partial r} \\ &-\frac{1}{Re}\left(\frac{\partial^2 u'_r}{\partial x^2} + \frac{1}{r}\frac{\partial}{\partial r}\left(r\frac{\partial u'_r}{\partial r}\right) + \frac{1}{r^2}\frac{\partial^2 u'_r}{\partial \varphi^2} - \frac{u'_r}{r^2} - \frac{2}{r^2}\frac{u'_\varphi}{\partial \varphi}\right) = \\ &\qquad -\left(u'_x\frac{\partial u'_r}{\partial x} + u'_r\frac{\partial u'_r}{\partial r} + \frac{u'_\varphi}{r}\frac{\partial u'_r}{\partial \varphi} - \frac{u'_\varphi u'_\varphi}{r}\right) \end{aligned} \tag{A.8}$$

- φ - momentum

$$\begin{aligned} &\frac{\partial u'_\varphi}{\partial t} + V_x\frac{\partial u'_\varphi}{\partial x} + u'_r\frac{dV_\varphi}{dr} + \frac{V_\varphi}{r}\frac{\partial u'_\varphi}{\partial \varphi} + \frac{V_\varphi\, u'_r}{r} + \frac{1}{r}\frac{\partial p'}{\partial \varphi} \\ &-\frac{1}{Re}\left(\frac{\partial^2 u'_\varphi}{\partial x^2} + \frac{1}{r}\frac{\partial}{\partial r}\left(r\frac{\partial u'_\varphi}{\partial r}\right) + \frac{1}{r^2}\frac{\partial^2 u'_\varphi}{\partial \varphi^2} - \frac{u'_\varphi}{r^2} + \frac{2}{r^2}\frac{\partial u'_r}{\partial \varphi}\right) = \\ &\qquad -\left(u'_x\frac{\partial u'_\varphi}{\partial x} + u'_r\frac{\partial u'_\varphi}{\partial y} + \frac{u'_\varphi}{r}\frac{\partial u'_\varphi}{\partial \varphi} + \frac{u'_r\, u'_\varphi}{r}\right) \end{aligned} \tag{A.9}$$

These are the nonlinear disturbance equations. When the nonlinear terms on the right hand sides of A.7 to A.9 are neglected the linearized disturbance equations (2.6 to 2.9) are obtained.

A.1.3 Reynolds shear stress transport equations

In the following the transport equations for the velocity fluctuation products $u'_\varphi u'_r$ and $u'_r u'_x$ are presented. These fluctuations are the shear stresses τ_{rx} and $\tau_{r\varphi}$ when averaged over the wavelengths as described in section 2.2.5.

The transport equation for $u'_\varphi u'_r$ is obtained by the sum of the transport equation of u'_φ (A.9) multiplied with u'_r and the transport equation of u'_r (A.8) multiplied with u'_φ. Within this work the transport equations are spatially averaged over the critical wavelengths (n_c, λ_c) before they are evaluated.

$$
\begin{aligned}
&\underbrace{u'_\varphi \frac{\partial u'_r}{\partial t} + u'_r \frac{\partial u'_\varphi}{\partial t}}_{\text{temp. change}} + \underbrace{u'_\varphi V_x \frac{\partial u'_r}{\partial x} + u'_r V_x \frac{\partial u'_\varphi}{\partial x}}_{\text{convection}} + \underbrace{u'_\varphi \frac{V_\varphi}{r} \frac{\partial u'_r}{\partial \varphi} + u'_r \frac{V_\varphi}{r} \frac{\partial u'_\varphi}{\partial \varphi}}_{\text{convection}} \\
&\underbrace{- u'_\varphi \frac{2 V_\varphi u'_\varphi}{r} + u'_r \frac{V_\varphi u'_r}{r}}_{Z_{\varphi r1}+Z_{\varphi r2}=\text{centr. prod.+ conv.}} + \underbrace{u'_r u'_r \frac{dV_\varphi}{dr}}_{P_{\varphi r}(V_\varphi)=\text{shear production}} + \underbrace{u'_\varphi \frac{\partial p'}{\partial r} + u'_r \frac{1}{r} \frac{\partial p'}{\partial \varphi}}_{P_{D\varphi r}=\text{velocity pressure gradient}} \\
&- \frac{1}{Re} \Bigg(\underbrace{u'_\varphi \frac{\partial^2 u'_r}{\partial x^2} + u'_r \frac{\partial^2 u'_\varphi}{\partial x^2} + u'_\varphi \frac{1}{r} \frac{\partial}{\partial r} \left(r \frac{\partial u'_r}{\partial r} \right) + u'_r \frac{1}{r} \frac{\partial}{\partial r} \left(r \frac{\partial u'_\varphi}{\partial r} \right)}_{\text{viscous effects}} \\
&\quad + \underbrace{u'_\varphi \frac{1}{r^2} \frac{\partial^2 u'_r}{\partial \varphi^2} + u'_r \frac{1}{r^2} \frac{\partial^2 u'_\varphi}{\partial \varphi^2} - u'_\varphi \frac{u'_r}{r^2} - u'_r \frac{u'_\varphi}{r^2} - u'_\varphi \frac{2}{r^2} \frac{\partial u'_\varphi}{\partial \varphi} + u'_r \frac{2}{r^2} \frac{\partial u'_r}{\partial \varphi}}_{\text{viscous effects}} \Bigg) \\
&\quad + \underbrace{u'_\varphi u'_x \frac{\partial u'_r}{\partial x} + u'_r u'_x \frac{\partial u'_\varphi}{\partial x} + u'_\varphi u'_r \frac{\partial u'_r}{\partial r} + u'_r u'_r \frac{\partial u'_\varphi}{\partial r} + u'_\varphi \frac{u'_\varphi}{r} \frac{\partial u'_r}{\partial \varphi} + u'_r \frac{u'_\varphi}{r} \frac{\partial u'_\varphi}{\partial \varphi}}_{\text{triple correlations}} \\
&\quad \underbrace{- u'_\varphi \frac{u'_\varphi u'_\varphi}{r} + u'_r \frac{u'_r u'_\varphi}{r}}_{\text{triple correlations}} = 0
\end{aligned}
\tag{A.10}
$$

The first term is the temporal change of $u'_\varphi u'_r$. In the neutral stable scenario, the disturbance does neither grow nor decay such that this term must be zero when averaged over the wavelength. The centrifugal and shear production terms ($Z_{r\varphi 1}$, $P_{r\varphi}(V_\varphi)$) act as a source or sink depending on the sign of the shear stress. The convection terms describes the convection of the shear stress by the base flow. These terms are zero when averaged over the disturbance wavelengths and hence are not relevant for the present considerations. This does not account for the convection term $Z_{r\varphi 2}$. However this term is always small and negligible. The velocity pressure gradient term accounts for interactions of pressure disturbances and velocity disturbances. The viscous terms

account for the viscous diffusion and dissipation (Rotta 1951; Moser 1984; Moser and Moin 1987; Hanjalić and Launder 2011). The description of the terms also applies for the $u'_r u'_x$ transport equation which is described in the following.

The velocity pressure gradient in equation (A.10) averaged over the wavelength takes the form:

$$\begin{aligned}\overline{P_{Dr\varphi}} &= \frac{\lambda}{2\pi}\frac{n}{2\pi}\int_0^{\frac{2\pi}{\lambda}}\int_0^{\frac{2\pi}{n}}\left(u'_\varphi\frac{\partial p'}{\partial r}+u'_r\frac{1}{r}\frac{\partial p'}{\partial \varphi}\right)dxd\varphi \\ &= A_\varphi\frac{\tilde{A}_p}{\partial y}+\tilde{A}_\varphi\frac{A_p}{\partial y}+A_r\tilde{A}_p(-in)+\tilde{A}_rA_p(+in)\end{aligned} \tag{A.11}$$

The transport equation for $u'_r u'_x$ is obtained by the sum of the transport equation of u'_r (A.8) multiplied with u'_x and the transport equation of u'_x (A.7) multiplied with u'_r.

$$\begin{aligned}&\underbrace{u'_r\frac{\partial u'_x}{\partial t}+u'_x\frac{\partial u'_r}{\partial t}}_{\text{temp. change}}+\underbrace{u'_rV_x\frac{\partial u'_x}{\partial x}+u'_xV_x\frac{\partial u'_r}{\partial x}+u'_x\frac{V_\varphi}{r}\frac{\partial u'_r}{\partial\varphi}+u'_r\frac{V_\varphi}{r}\frac{\partial u'_x}{\partial\varphi}}_{\text{convection}} \\ &\underbrace{-u'_x\frac{2V_\varphi u'_\varphi}{r}}_{Z_{rx}=\text{centrifugal production}}+\underbrace{u'_ru'_r\frac{dV_x}{dr}}_{P_{rx}(V_x)=\text{shear production}}+\underbrace{u'_r\frac{\partial p'}{\partial x}+u'_x\frac{\partial p'}{\partial r}}_{P_{Drx}=\text{velocity pressure gradient}}+ \\ &-\frac{1}{Re}\Bigg(\underbrace{u'_r\frac{\partial^2u'_x}{\partial x^2}+u'_x\frac{\partial^2u'_r}{\partial x^2}+u'_r\frac{1}{r}\frac{\partial}{\partial r}\left(r\frac{\partial u'_x}{\partial r}\right)+u'_x\frac{1}{r}\frac{\partial}{\partial r}\left(r\frac{\partial u'_r}{\partial r}\right)+}_{\text{viscous terms}} \\ &\underbrace{+u'_r\frac{1}{r^2}\frac{\partial^2u'_x}{\partial\varphi^2}+u'_x\frac{1}{r^2}\frac{\partial^2u'_r}{\partial\varphi^2}-u'_x\frac{u'_r}{r^2}-u'_x\frac{2}{r^2}\frac{\partial u'_\varphi}{\partial\varphi}}_{\text{viscous terms}}\Bigg) \\ &+\Bigg(\underbrace{u'_ru'_x\frac{\partial u'_x}{\partial x}+u'_xu'_x\frac{\partial u'_r}{\partial x}+u'_ru'_r\frac{\partial u'_x}{\partial r}+u'_xu'_r\frac{\partial u'_r}{\partial r}}_{\text{triple correlations}} \\ &\underbrace{+u'_r\frac{u'_\varphi}{r}\frac{\partial u_x}{\partial\varphi}+u'_x\frac{u'_{s\varphi}}{r}\frac{\partial u'_r}{\partial\varphi}-u'_x\frac{u'_\varphi u'_\varphi}{r}}_{\text{triple correlations}}\Bigg)=0\end{aligned} \tag{A.12}$$

The velocity pressure gradient in equation (A.12) averaged over the wavelength takes the form:

$$\begin{aligned}\overline{P_{Drx}} &= \frac{\lambda}{2\pi}\frac{n}{2\pi}\int_0^{\frac{2\pi}{\lambda}}\int_0^{\frac{2\pi}{n}}\left(u'_r\frac{\partial p'}{\partial x}+u'_x\frac{\partial p'}{\partial r}\right)dxd\varphi \\ &= \tilde{A}_r\,A_p\,(+i\lambda_x)+\tilde{A}_p\,A_r(-i\lambda_x)+A_x\frac{\tilde{A}_p}{\partial y}+\tilde{A}_x\frac{A_p}{\partial y}\end{aligned} \tag{A.13}$$

A.1.4 Flow velocity profiles for the IRSPF and the ORSPF

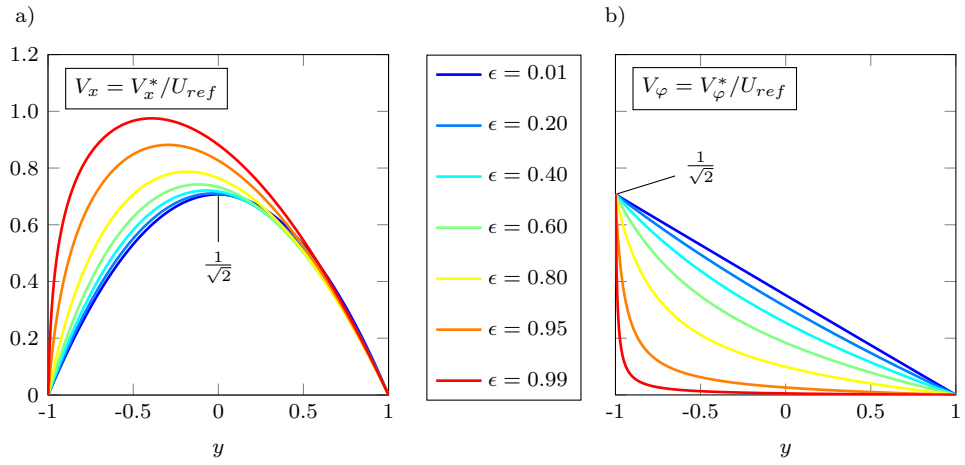

Figure A.1: Normalized velocity profiles for the IRSPF for different ϵ ($S_i = 1$, $U_{\text{ref}} = \sqrt{U_x^2 + U_\varphi^2}$). a) Axial velocity profile. b) Azimuthal velocity profile.

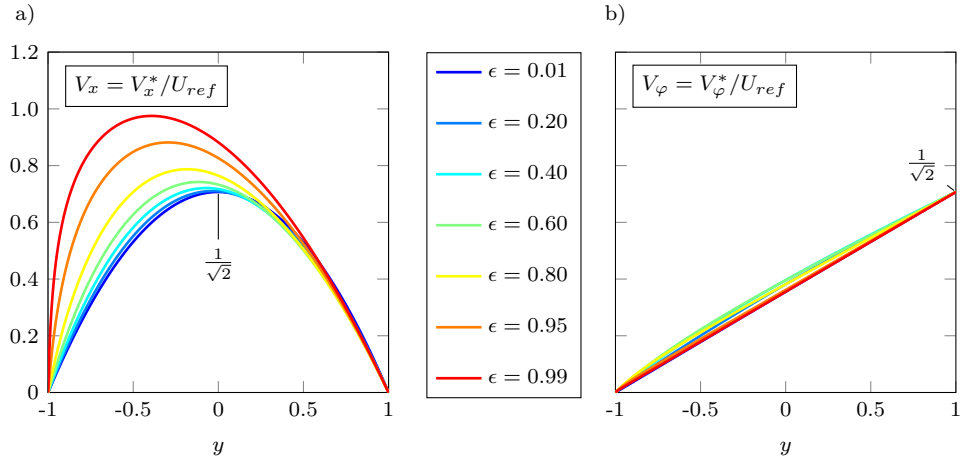

Figure A.2: Normalized velocity profiles for the ORSPF for different ϵ ($S_o = 1$, $U_{\text{ref}} = \sqrt{U_x^2 + U_\varphi^2}$). a) Axial velocity profile. b) Azimuthal velocity profile.

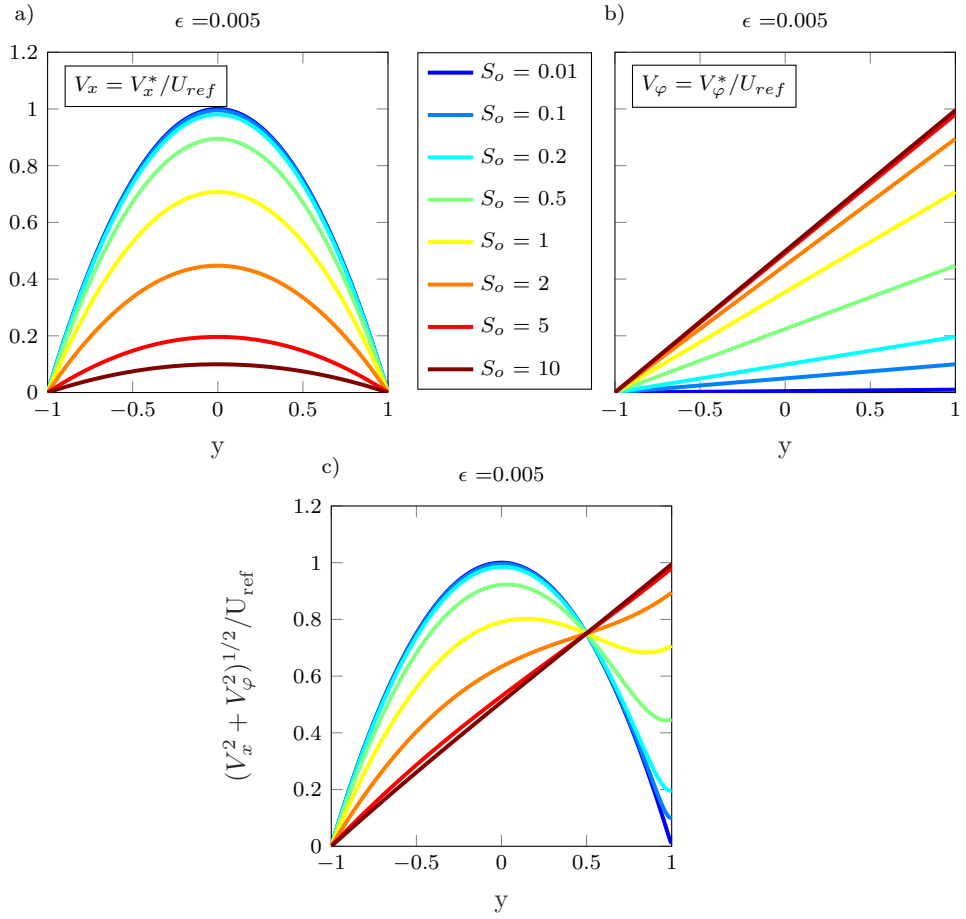

Figure A.3: Normalized velocity profiles for the ORSPF for different values of S_o ($\epsilon = 0.005$, $U_{\text{ref}} = \sqrt{U_x^2 + U_\varphi^2}$). a) Axial velocity profile, normalized with U_{ref}. b) Azimuthal velocity profile, normalized with U_{ref}. c) Resulting velocity profile, normalized with U_{ref}.

A.1.5 Additional plots for the phase maps

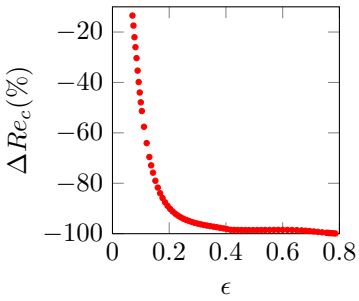

Figure A.4: Change of the critical Reynolds number within region IIO, defined as $(\min(Re_c) - Re_c(S^-_{o,T1}))/Re_c(S^-_{o,T1}) \times 100$. For all $\epsilon > 0.0704$ the minimum critical Reynolds number is achieved in region IIO.

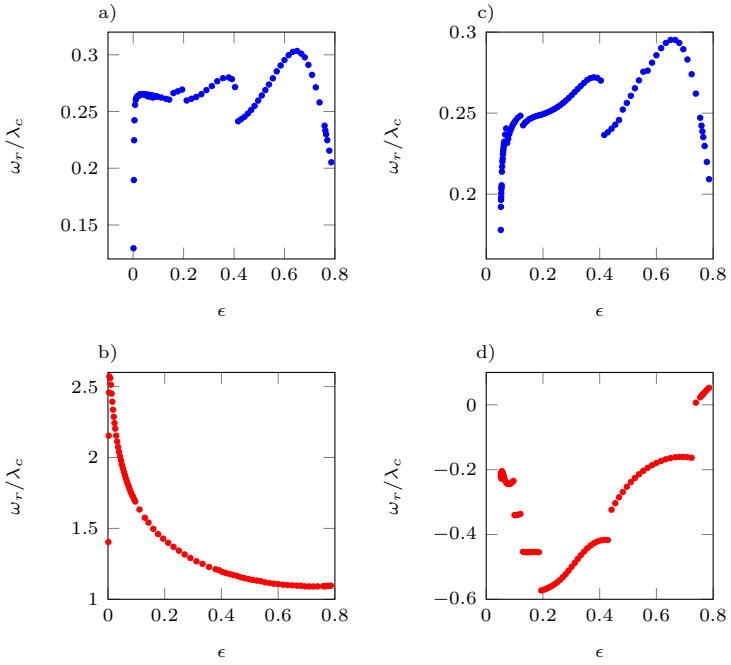

Figure A.5: Axial wavespeed before and behind the first transition for IRSPF and ORSPF. a) ω_r/λ_c at $(S^-_{i,T1})$ b) ω_r/λ_c at $(S^+_{i,T1})$ c) ω_r/λ_c at $(S^-_{o,T1})$ d) ω_r/λ_c at $(S^+_{o,T1})$

A.1.6 Normalized distribution of K, shear stresses and production terms along the gap height

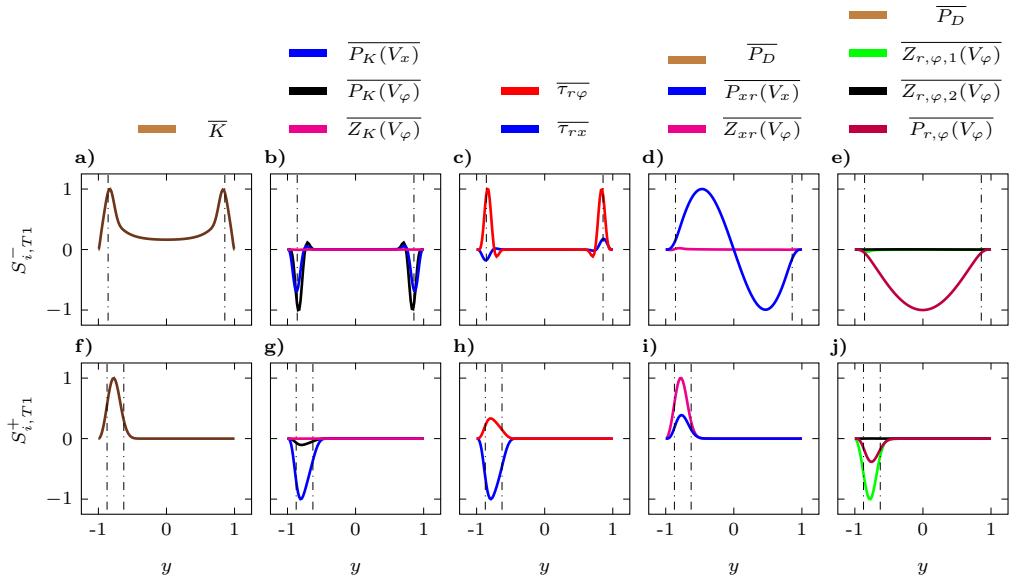

Figure A.6: Normalized radial distributions of kinetic energy, production terms and shear stresses found in the IRPSF at the first transition (I to II) for $\epsilon = 0.0025$. Dash dot line = critical layer. a,f) K over y. b,g) Production of K over y. c,h) τ_{rx}, $\tau_{r\varphi}$ over y. d,i) Production of τ_{rx} over y. e,j) Production of $\tau_{r\varphi}$ over y.

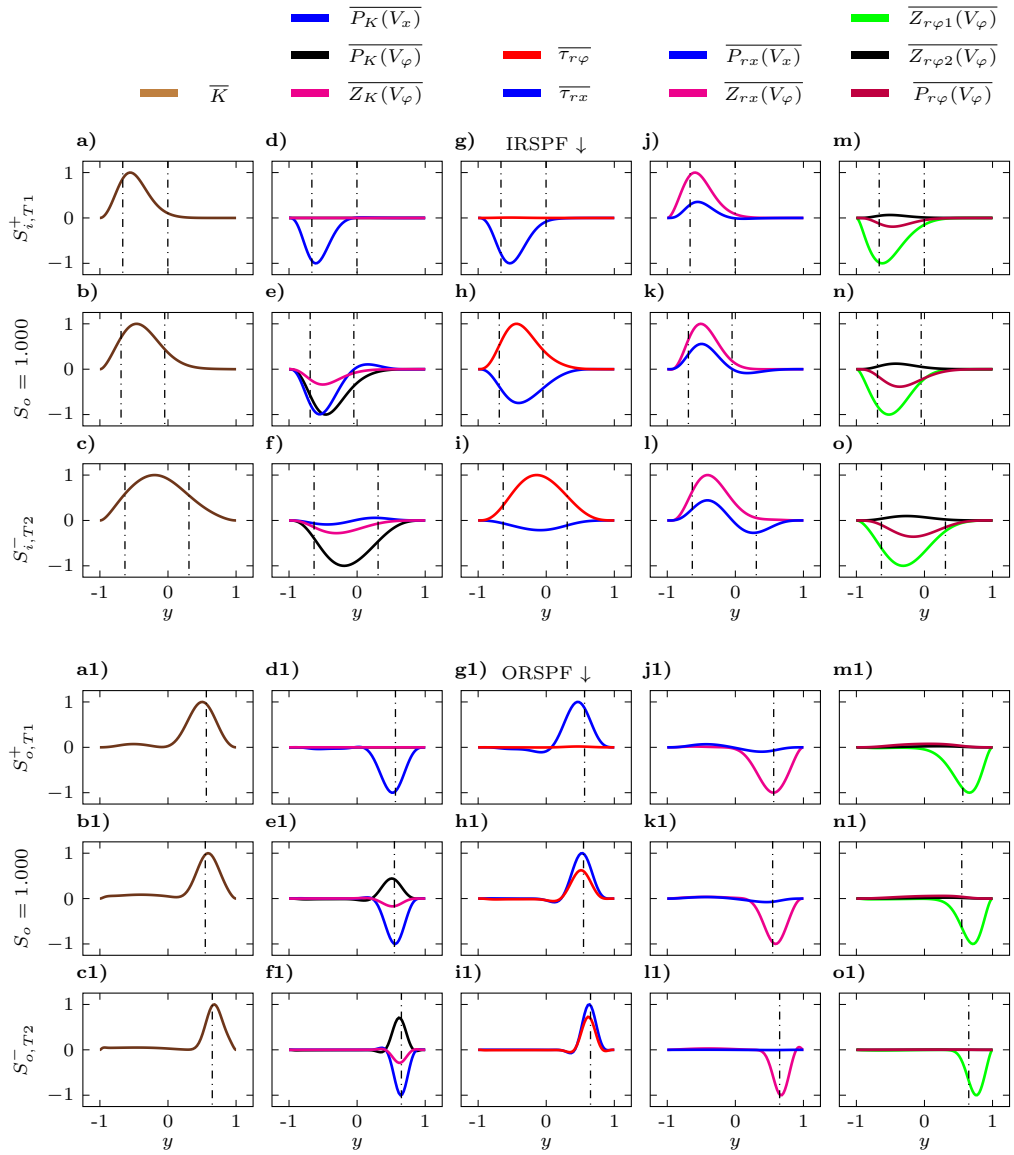

Figure A.7: Normalized Distributions of K, shear stresses and production terms for the IRSPF and ORSPF for different S_i ($S_i = \{S^+_{i,T1}; 1.000; S^-_{i,T2}\}$) and S_o ($S_o = \{S^+_{o,T1}; 1.000; S^-_{o,T2}\}$). Curvature parameter is $\epsilon = 0.25$. a-c, a1-c1) K over y. d-f, d1-f1) K-production terms over y. g-i, g1-i1) τ_{rx} and $\tau_{r\varphi}$ over y. j-l, j1-l1) τ_{rx} production terms over y. m-o, m1-o1) $\tau_{r\varphi}$ production terms over y.

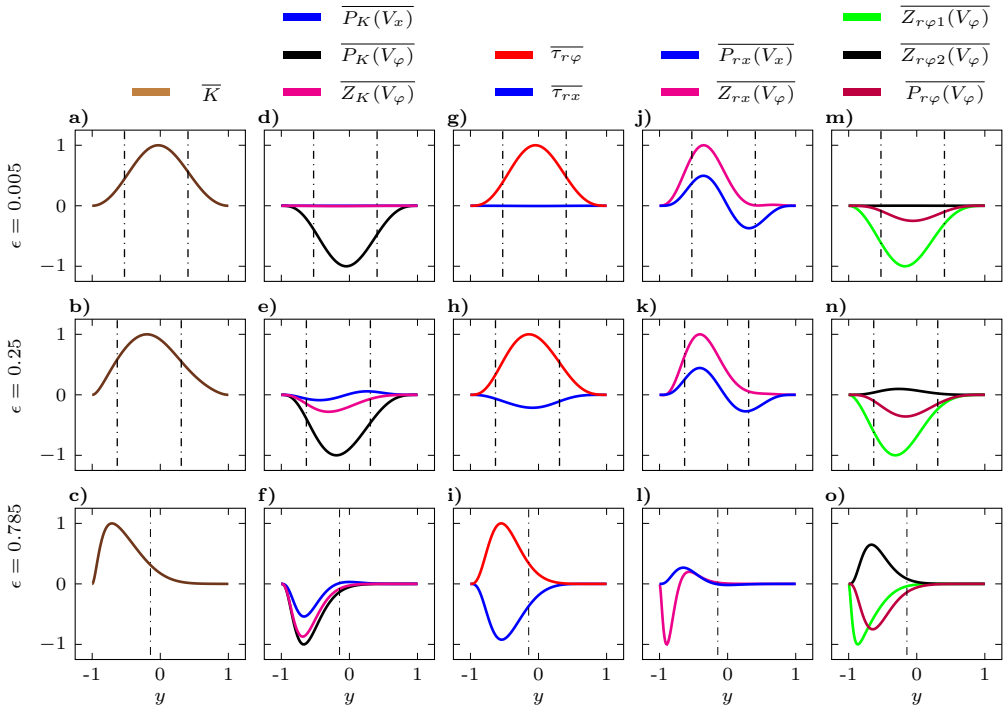

Figure A.8: Normalized radial distributions of kinetic energy, production terms and shear stresses found in the IRSPF before the second transition (end of II) at $S^{-}_{i,T2}$ for $\epsilon = \{0.005; 0.25; 0.78\}$. Dash dot line = position of critical layer according to equation (2.33). a-c) K over y. d-f) Production of K over y. g-i) τ_{rx}, $\tau_{r\varphi}$ over y. j-l) Production of τ_{rx} over y. m-o) Production of $\tau_{r\varphi}$ over y.

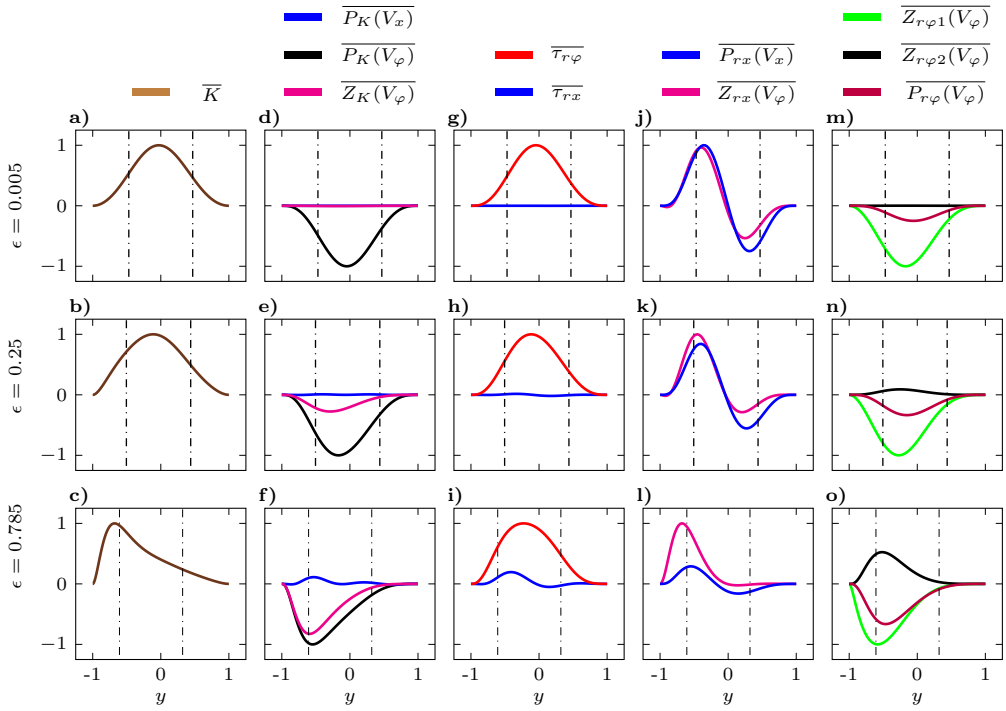

Figure A.9: Normalized radial distributions of kinetic energy, production terms and shear stresses found in the IRSPF behind the second transition (beginning of III) at $S^+_{i,T2}$ for $\epsilon = \{0.005; 0.25; 0.78\}$. Dash dot line = position of critical layer according to equation (2.33). a-c) K over y. d-f) Production of K over y. g-i) τ_{rx}, $\tau_{r\varphi}$ over y. j-l) Production of τ_{rx} over y. m-o) Production of $\tau_{r\varphi}$ over y.

A.1.7 Distribution of velocity pressure gradient and production terms

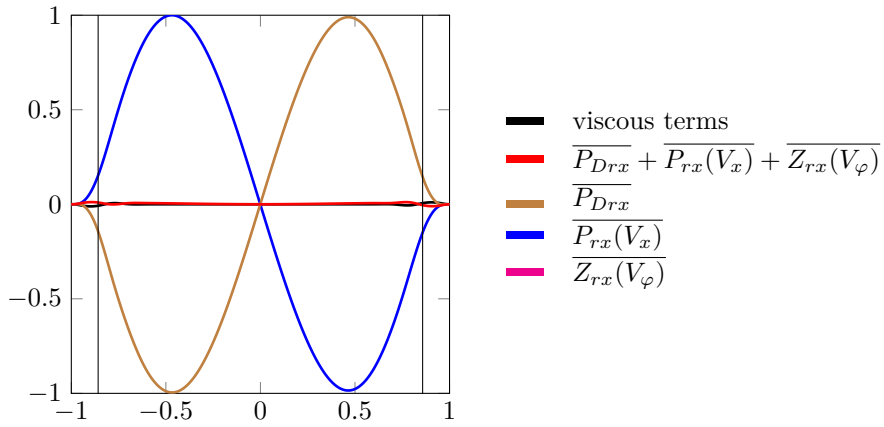

Figure A.10: Demonstration how velocity pressure gradient and shear production cancel out ($\epsilon = 0.005$, $S_i = 10^{-5}$, $N = 500$ (number of collocation points)). $Z_{rx}(V_\varphi)$ is approximately zero (no depicted).

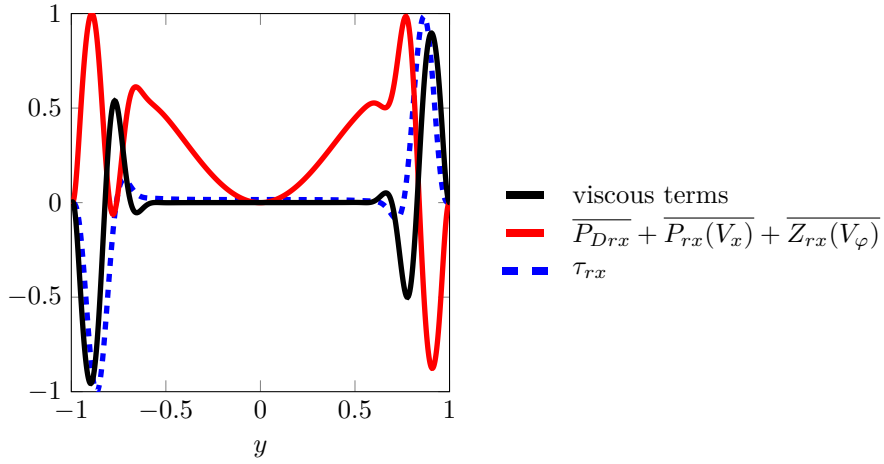

Figure A.11: Close up of Fig. A.10. Explanation of the distribution of τ_{rx} by the sum of velocity pressure gradient and shear production terms ($\epsilon = 0.005$, $S_i = 10^{-5}$, $N = 500$ (number of collocation points). As can be seen while the sum attains peaks close to the peaks of τ_{rx} (and attains and opposed sign which is necessary for production of negative or positive shear stresses) there is a significant deviation left and right of the channel center. These deviations are observed for smaller ϵ and did not occur for larger ϵ as can be seen exemplarily in Fig. A.12 and Fig. A.13

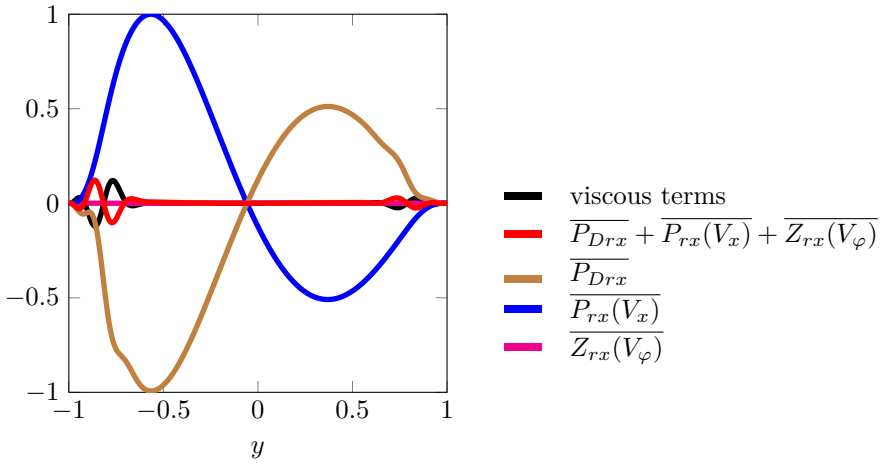

Figure A.12: Demonstration how velocity pressure gradient and shear production cancel out ($\epsilon = 0.333$, $S_i = 10^-5$, $N = 500$ (number of collocation points)).

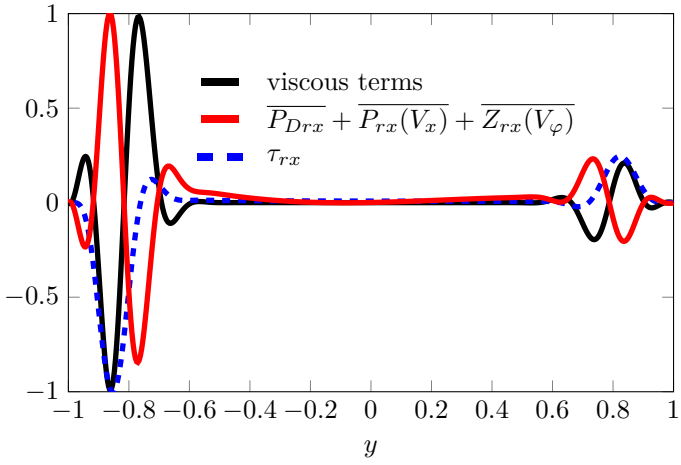

Figure A.13: Close up of Fig. A.12. Explanation of the distribution of τ_{rx} by the sum of velocity pressure gradient and shear production terms ($\epsilon = 0.333$, $S_i = 10^-5$, $N = 500$ (number of collocation points). As can be seen the sum attains peaks close to the peaks of τ_{rx} (and attains and opposed sign which is necessary for production of negative or positive shear stresses).

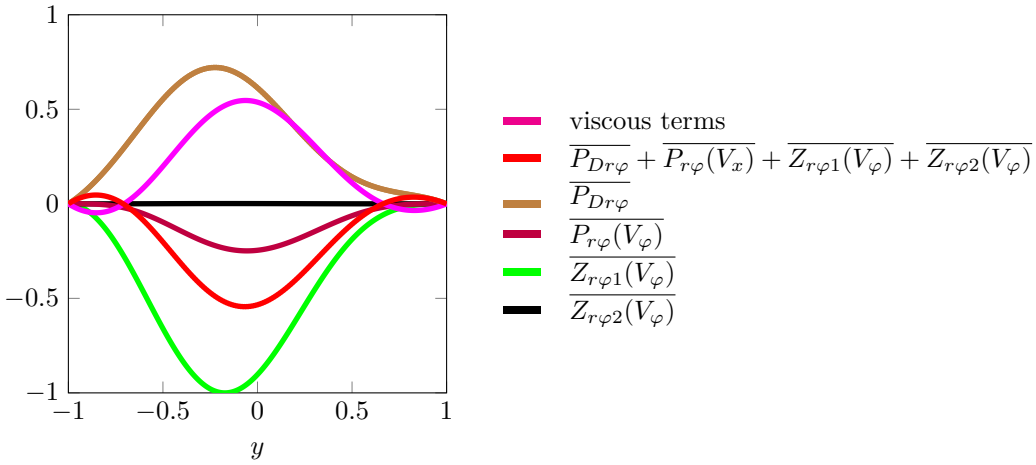

Figure A.14: Complete budget of $\tau_{r\varphi}$ for the TC flow ($S_i = 10^5$, $\epsilon = 0.005$). Red line and magenta line cancel out.

A.1.8 Tables of critical values

ϵ	$S^-_{i,T1}$	Re_c	λ_c	n_c	ω_c	c	c_x
0.0025	0.98061	7914.93	1.021	0	0.1937	0.1895	0.1895
0.0050	0.43939	6252.34	1.021	0	0.2473	0.2422	0.2422
0.0526	0.03782	5887.61	1.013	2	0.2686	0.1198	0.2650
0.25	0.00714	7357.76	0.862	2	0.2266	0.1040	0.2628
0.785	$1.88\text{x}10^{-4}$	140766.82	0.102	-1	0.0211	0.0210	0.2052

Table A.1: Values of Re_c, λ_c, n_c, ω_c, c and c_x at $S^-_{i,T1}$

ϵ	$S^+_{i,T1}$	Re_c	λ_c	n_c	ω_c	c	c_x
0.0025	0.990	7948.72	2.36644	2838	5.09694	0.001795	2.142
0.0050	0.45249	6267.90	0.98885	1191	2.54276	0.002134	2.571
0.0526	0.03838	5850.45	0.07576	61	0.14566	0.002387	1.922
0.25	0.00719	7710.17	0.02257	10	0.03031	0.003031	1.342
0.785	$1.88\text{x}10^{-4}$	131457.91	0.00110	2	0.00121	$6\text{x}10^{-4}$	1.095

Table A.2: Values of Re_c, λ_c, n_c, ω_c, c and c_x at $S^+_{i,T1}$

ϵ	$S^-_{i,T2}$	Re_c	λ_c	n_c	ω_c	c	c_x
0.0025	138.94	292.12	1.563	1	0.0100	0.00543	0.00645
0.0050	72.81	207.18	1.564	1	0.0193	0.01044	0.0123
0.0526	7.92	69.73	1.577	1	0.1814	0.09712	0.1149
0.25	2.55	45.14	1.664	1	0.5981	0.30803	0.3593
0.785	2.87	90.80	3.099	1	1.2845	0.39446	0.4144

Table A.3: Values of Re_c, λ_c, n_c, ω_c, c and c_x at $S^-_{i,T2}$

ϵ	$S^+_{i,T2}$	Re_c	λ_c	n_c	ω_c	c	c_x
0.0025	156.27	291.93	1.563	0	0.00780	0.00499	0.00499
0.0050	74.98	207.11	1.564	0	0.01626	0.01039	0.01039
0.0526	8.04	69.61	1.571	0	0.15097	0.09609	0.09609
0.25	2.57	45.00	1.595	0	0.45208	0.28338	0.28338
0.785	2.96	91.11	1.626	0	0.46066	0.28328	0.28328

Table A.4: Values of Re_c, λ_c, n_c, ω_c, c and c_x at $S^+_{i,T2}$

ϵ	$S^-_{o,T1}$	Re_c	λ_c	n_c	ω_c	c	c_x
0.0526	0.7319	9381.61	1.004	0	0.1989	0.1981	0.198
0.25	0.0232	7433.83	0.856	-2	0.2172	0.0998	0.253
0.785	0.000284	110936.89	0.119	-1	0.0250	0.0249	0.209

Table A.5: Values of Re_c, λ_c, n_c, ω_c, c and c_x at $S^-_{o,T1}$

ϵ	$S^+_{o,T1}$	Re_c	λ_c	n_c	ω_c	c	c_x
0.0526	0.734	9403.81	0.3298	-6	-0.0716	-0.0119	-0.2172
0.25	0.0236	7400.37	0.0139	-4	-0.00763	-0.0019	-0.5478
0.785	$3.0\text{x}10^{-4}$	108214.83	$3.9\text{x}10^{-4}$	-2	$2.07\text{x}10^{-5}$	$1.03\text{x}10^{-5}$	0.0525

Table A.6: Values of Re_c, λ_c, n_c, ω_c, c and c_x at $S^+_{o,T1}$

ϵ	$S^-_{o,T2}$	Re_c	λ_c	n_c	ω_c	c	c_x
0.00502	4.673	79057.11	0.950	1	0.0414	0.0300	0.0436
0.0526	1.401	28431.81	0.957	0	0.1104	0.1152	0.1152
0.111	1.588	34701.70	0.133	-1	-0.0526	-0.0522	-0.3960
0.25	2.754	14259.09	0.0909	-1	-0.154	-0.1537	-1.6966
0.785	37.605	10393.12	0.0312	-3	-1.308	-0.4360	-41.8289

Table A.7: Values of Re_c, λ_c, n_c, ω_c, c and c_x at $S^-_{o,T2}$

ϵ	$S^+_{o,T2}$	Re_c	λ_c	n_c	ω_c	c	c_x
0.0050	4.742	82938.00	0.517	9	0.0285	0.00316	0.0551
0.0526	1.421	29654.94	0.503	3	0.0793	0.02607	0.1576
0.111	1.593	47026.80	0.211	1	0.0383	0.03748	0.1808
0.25	2.764	34370.81	0.381	1	0.0608	0.05682	0.1593
0.785	38.162	10864.63	0.287	1	0.259	0.24943	0.9029

Table A.8: Values of Re_c, λ_c, n_c, ω_c, c and c_x at $S^+_{o,T2}$

A.2 Applying APTV to suspension flows with transparent particles

Table A.9: Accuracies achieved in the literature. MT=method (A=APTV-fluorescent, B=APTV-bright field (non-fluorescent), C=pinhole plate)

Author	MT	d_p	σ_z	Δz	$\frac{\sigma_z}{\Delta z}$	$\frac{\sigma_z}{d_p}$
-	-	µm	µm	µm	%	%
Angarita-Jaimes et al. 2006	A	0.2	0.04	2.5	1.6	20
Buchmann et al. 2014	B	110	140	5100	2.74	-
Chen et al.2009	A	2	2.8	500	0.56	140
Cierpka et al.2010b	A	5	5.6	90	6.2	112
Cierpka et al.2010a	A	2	0.28	35.1	0.78	14
Fuchs et al. 2014b	C	1	133	40000	0.33	13330
Franchini et al. 2019	B	2	7.1*	240	2.95	-
Kao et al. 1994	A	0.093	0.012	120	0.3	12.9
Massing et al. 2018	A	-	0.68	120	0.56	-
Ragan et al.2006	A	0.2	0.04	2.5	1.6	20
Rossi et al. 2014	A	2.24	0.75	102	0.74	33
Rossi et al. 2019	A	0.245	0.2	7	2.85	81
Segura et al. 2015	B	13	1.7	20	8.5	13

Table A.10: Accuarcies for optimized values of c_a, c_I in order to minimize $\sigma_z^*/\Delta z$ (d_p=60 µm, M=20×, water, σ_z=$\sqrt{\sigma_z^{*2} + \min[\sigma(\Delta F_{xz}), \sigma(\Delta F_{yz})]^2}$) (top two rows=CMOS camera, bottom two rows=CCD camera)

Δz	σ_z^*	ΔF_{xz}	ΔF_{yz}	σ_z	$\frac{\sigma_z}{d_p}$	$\frac{\sigma_z}{\Delta z}$	c_a	c_I	c_D	N_{valid}
μm	μm	μm	μm	μm	%	%	-	-	-	-
241	1.97	137.0±7.6	137.9±5.2	5.5	9.2	2.3	0.66	0.37	2	2573
241	2.02	137.0±7.6	137.9±5.2	5.5	9.3	2.3	0.66	0.37	2	2661
162	0.95	134.3±2.3	132.3±2.6	2.5	4.2	1.5	0.44	0.3	3	1683
184	1.09	134.3±2.3	132.3±2.6	2.5	4.3	1.4	0.44	0.26	3	1894

Table A.11: Measured values of the performed parametric study for optimized values of c_a, c_I obtained with 3D calibration procedure (top: PMMA, bottom: PS σ_z=$\sqrt{\sigma_z^{*2} + (\min[\sigma(\Delta F_{xz}), \sigma(\Delta F_{yz})])^2}$), c_D=2)

dp	M	GW	Δz	σ_z^*	ΔF_{xz}	ΔF_{yz}	$\frac{\sigma_z}{d_p}$	$\frac{\sigma_z}{\Delta z}$
μm	-	wt%	μm	μm	μm	μm	%	%
30	20x	0	121.3	4.0	75.4±2.5	60.1±2.6	15.9	3.9
30	20x	25	103.6	1.3	82.4±2.6	65.0±3.0	10.0	2.9
30	20x	50	146.7	5.9	91.4±10.8	78.4 ±2.7	21.7	4.4
60	20x	0	179.9	1.7	136.4±3.3	125.5±2.1	4.5	1.5
60	20x	25	203.2	2.4	148.3±2.3	136.8±1.9	5.2	1.5
60	20x	50	222.2	7.7	159.9±3.1	140.2±2.5	13.6	3.6
60	10x	0	227.9	5.8	111.2±10.4	115.1±5.6	13.5	3.5
60	10x	25	250.9	4.1	126.6±4.8	112.7±15.0	10.6	2.5
60	10x	50	294.9	7.4	183.0±13.4	90.8±15.2	25.6	5.2
124	10x	0	419.8	5.4	226.2±8.1	199.9±8.1	7.9	2.3
124	10x	25	507.4	14.2	252.4±6.0	220.7±6.9	12.4	3.0
124	10x	50	478.1	7.4	259.0±13.3	241.6±11.4	11.0	2.8
124	20x	0	291.9	1.7	236.5±1.8	213.2±1.5	1.8	0.7
124	20x	25	375.1	5.6	273.1±4.8	231.5±3.4	5.2	1.7
124	20x	50	363.4	6.5	323.7±3.4	193.7±1.7	5.5	1.8
80	10x	0	106.6	2.7	114.1±10.3	108.0±8.7	11.5	8.6
80	20x	0	213.2	11.2	135.8±3.8	123.7±3.6	14.7	5.5
124	10x	0	351.9	4.0	186.7±7.6	157.6±7.0	6.5	2.3
124	20x	0	302.5	10.2	185.0±3.6	174.8±2.7	8.5	3.5
140	20x	0	321.2	8.4	211.4±7.1	199.4±4.8	6.9	3.0
140	10x	0	370.5	6.2	209.6±6.1	183.5±6.1	6.2	2.3

Table A.12: ΔF_{xz}, ΔF_{yz}, σ_z^* and σ_z for particles with d_p=80 µm in a 25wt% glycerol-water solution located at the top z=2305 µm and bottom z=0 µm of the channel (c_I=0.575, c_a=0.7, c_D=2)

	z=2305 µm	z=0 µm	Δ
ΔF_{xz}	160.43±9 µm	196.29±7.8 µm	35.86 µm
ΔF_{yz}	145.38±9.1 µm	177.32±10.76 µm	31.94 µm
σ_z^* (2D)	5.4 µm	9 µm	3.6 µm
σ_z^* (3D)	4.6 µm (-15%)	8.12 µm (-10%)	3.52 µm
$\sigma_z(\Delta F_{xz})$ (3D)	10.14 µm	11.25 µm	1.11 µm
$\sigma_z(\Delta F_{yz})$ (3D)	10.23 µm	13.48 µm	3.25 µm
Δz	173.22 µm	201.87 µm	28.65 µm

Nomenclature

Capital Roman letters

A	m^2	area
A_p	-	amplitude of pressure disturbance
$\tilde{A}_p$	-	amplitude of pressure disturbance (conjugated)
A_φ	-	amplitude of azimuthal velocity disturbance
$\tilde{A}_\varphi$	-	amplitude of azimuthal velocity disturbance (conjugated)
A_r	-	amplitude of radial velocity disturbance
$\tilde{A}_r$	-	amplitude of radial velocity disturbance (conjugated)
A_x	-	amplitude of axial velocity disturbance
$\tilde{A}_x$	-	amplitude of axial velocity disturbance (conjugated)
C_{LS}	-	lift coefficient for Saffman force
D_h	m	hydraulic diameter
D_Φ	-	diffusion coefficient
F	m	focal plane in stigmatic system (position)
$\vec{F}_{\mathrm{Buo}}$	kg m s^{-2}	buoyancy force
F_C	-	focusing number
$\vec{F}_D$	kg m s^{-2}	drag force
$\vec{F}_G$	kg m s^{-2}	gravitational force
$\vec{F}_I$	kg m s^{-2}	inertial force
$\vec{F}_p$	kg m s^{-2}	pressure force
$\vec{F}_{\mathrm{Saff}}$	kg m s^{-2}	Saffman force
$\vec{F}_{\mathrm{SG}}$	kg m s^{-2}	shear gradient force
$\vec{F}_{VM}$	kg m s^{-2}	virtual mass force
$\vec{F}_{\mathrm{wall}}$	kg m s^{-2}	wall repulsive force
F_{xz}	m	focal plane in xz plane (position)
F_{yz}	m	focal plane in yz plane (position)
F^*_{xz}	m	z-position where focus point of particle is focused in F_{xz} (position)
F^*_{yz}	m	z-position where focus point of particle is focused in F_{yz} (position)
H	m	channel width / gap between concentric cylinders
I	counts	maximum light intensity of particle image
I	px	maximum light intensity of particle image (scaled)

$I_{\max}$	px	maximum of median of light intensity of multiple calibration particles (scaled)
I_{thr}	counts	intensity threshold
I_{thr}	px	intensity threshold (scaled)
J	-	local Richardson number
K	-	kinetic disturbance energy (non-dimensionalized)
K_c	-	coefficient for collision frequency effect
$K_{\mu_{\text{eff}}}$	-	coefficient for varying viscosity effect
M	-	magnification of microscope
M_{astig}	-	magnification of astigmatic optical system
M_{stig}	-	magnification of stigmatic optical system
N	-	collocation points for discretization
N_{valid}	-	number of valid detected particles
$N_{\text{valid}}(2D)$	-	number of valid detected particles (utilizing 2D reconstruction)
$N_{\text{valid}}(3D)$	-	number of valid detected particles (utilizing 3D reconstruction)
P_{Drx}	-	velocity pressure gradient in the transport equation of the shear stress τ_{rx} (non-dimensionalized)
$P_{Dr\varphi}$	-	velocity pressure gradient in the transport equation of the shear stress $\tau_{r\varphi}$ (non-dimensionalized)
$P_K(V_\varphi)$	-	production of kinetic disturbance energy due to azimuthal shear (non-dimensionalized)
$P_K(V_x)$	-	production of kinetic disturbance energy due to axial shear (non-dimensionalized)
$P_{r\varphi}(V_\varphi)$	-	production of shear stress $\tau_{r\varphi}$ due to azimuthal shear (non-dimensionalized)
$P_{rx}(V_x)$	-	production of shear stress τ_{rx} due to axial shear (non-dimensionalized)
P_{shear}	-	shear Peclet number
R_i	m	radius of the inner cylinder
R_o	m	radius of the outer cylinder
Re	-	Reynolds number
Re_b	-	bulk Reynolds number ($\rho U_b D_h/\mu_{\text{fluid}}$)
Re_c	-	critical Reynolds number
$Re_{\max}$	-	Reynolds number based on maximum velocity of bulk flow ($\rho U_{\max} D_h/\mu_{\text{fluid}}$)
Re_p	-	(shear) particle Reynolds number ($\rho\dot{\gamma}d_p^2/\mu_{\text{fluid}}$)
Re_p	-	(slip) particle Reynolds number ($\rho\lvert u_f - u_p\rvert d_p/\mu_{\text{fluid}}$)
S_i	-	swirl parameter (rotating inner cylinder)
$S_{i,T1}$	-	swirl parameter at transition from region I to II
$S_{i,T2}$	-	swirl parameter at transition from region II to III

S_o	-	swirl parameter (rotating outer cylinder)
$S_{o,T1}$	-	swirl parameter at transition from region IO to IIO
$S_{o,T2}$	-	swirl parameter at transition from region IIO to IIIO
U_b	m s^{-1}	bulk velocity (volume flow rate over crossectional area)
U_φ	m s^{-1}	azimuthal reference velocity
U_{ref}	m s^{-1}	resulting reference velocity
U_{wall}	m s^{-1}	velocity of the wall (linear shear flow)
U_x	m s^{-1}	axial reference velocity
V	m^3	volume
$\dot{V}$	m^3 s^{-1}	volumetric flow rate
V_f	m^3	volume of fluid phase
V_φ	-	base flow velocity in azimuthal direction (normalized)
V_φ^*	m s^{-1}	base flow velocity in azimuthal direction (with dimension)
V_p	m^3	volume occupied by a particle
V_s	m^3	volume of solid phase
V_x	-	base flow velocity in axial direction (normalized)
V_x^*	m s^{-1}	base flow velocity in axial direction (with dimension)
W	m s^{-1}	azimuthal velocity of Taylor Couette flow with independently rotating cylinders
$Z_{r\varphi,1}$	-	production of shear stress $\tau_{r\varphi}$ due to curvature (non-dimensionalized)
$Z_{r\varphi,2}$	-	production/convection of shear stress $\tau_{r\varphi}$ due to curvature (non-dimensionalized)
Z_{rx}	-	production of shear stress τ_{rx} due to curvature (non-dimensionalized)
Z_K	-	production of kinetic disturbance energy due to curvature (centrifugal effects) (non-dimensionalized)

Lowercase Roman letters

a	px	diameter of particle image
a	-	aspect ratio
a_c	-	autocorrelation coefficient
a_D	px	Euclidean distance for outlier detection
a_{st}	px	particle diameter in a stigmatic system
a_x	px	horizontal axis length of particle image
$\overline{a_x}$	px	polynomial fitted to a_x data of calibration particles
a_y	px	vertical axis length of particle image
$\overline{a_y}$	px	polynomial fitted to a_y data of calibration particles
c	-	wave speed (normalized)
c_a	-	autocorrelation coefficient
c_D	-	Euclidean distance factor

c_I	-	intensity coefficient
c_{med}	counts	median of light intensity (of the whole image)
c_{max}	counts	maximum counts of camera
c_{Spr}	kg s^{-2}	spring coefficient
c_s	px counts^{-1}	intensity scale factor
c_s	-	velocity of the disturbance wave front (normalized)
c_x	-	velocity of the disturbance wave in axial direction (normalized)
d_p	m	particle diameter
f	m	focal length of cylindrical lens
f_p	m	focal length of particle (ball lens)
f_{xz}	-	focus function xz plane (Tenengrad variance)
f_{yz}	-	focus function yz plane (Tenengrad variance)
g	m s^{-2}	gravitational acceleration (standard gravity)
h	m	half gap height
m_f	kg	mass of fluid displaced by the particle
m_p	kg	particle mass
n	-	azimuthal wavenumber
n	min^{-1}	rotation rate
n_0	-	refractive index of air
n_c	-	critical azimuthal wavenumber
n_j	-	normal vector
n_L	-	refractive index of liquid
n_p	-	refractive index of particle
n_{RIM}	-	refractive index of RIM liquid
n_w	-	refractive index of water
p	kg m^{-1} s^{-2}	pressure
p'	-	pressure disturbance (normalized)
r	-	coordinate in radial direction (normalized)
r_1	-	arbritary radial position (normalized)
r_2	-	arbritary radial position (normalized)
t	-	temporal coordinate (normalized)
$\vec{u}_f$	m s^{-1}	(theoretical) fluid velocity at particle centroid
$\vec{u}_p$	m s^{-1}	particle velocity at the centroid
u_φ	-	velocity in azimuthal direction (normalized)
u'_φ	-	disturbance velocity in azimuthal direction (normalized)
u_r	-	velocity in radial direction (normalized)
u'_r	-	disturbance velocity in radial direction (normalized)
u_x	-	velocity in axial direction (normalized)
u'_x	-	disturbance velocity in axial direction (normalized)
x	-	coordinate in axial direction (normalized)

y	-	coordinate in annular gap ($-1 \leq y \leq 1$)

Capital Greek letters

Γ	-	ratio of angular speed of outer and inner cylinder ($\mu = \Omega_2/\Omega_1$)
ΔF_{xz}	m	distance from focal point to center of particle (measured in xz plane)
ΔF_{yz}	m	distance from focal point to center of particle (measured in yz plane)
Δn	-	refractive index jump between liquid and particle
Δz	m	measurement volume depth
Φ	-	particle volume fraction/solid volume fraction
Ω	rad s^{-1}	angular velocity
Ω_i	rad s^{-1}	angular velocity (inner cylinder)
Ω_o	rad s^{-1}	angular velocity (outer cylinder)

Lowercase Greek letters

$\dot{\gamma}$	s^{-1}	shear rate
ϵ	-	curvature parameter ($(1 - R_i/R_o)/(1 + R_i/R_o)$)
ϵ	-	threshold value
η	-	ratio of inner cylinder radius and outer cylinder radius ($\eta = R_i/R_o$)
λ	-	axial wavenumber
λ^*	-	wavelength of particle band
λ_c	-	critical axial wavenumber
λ_L	m	wavelength of emitted light
μ	-	ratio of angular speed of outer and inner cylinder ($\mu = \Omega_2/\Omega_1 = \Omega_o/\Omega_i$)
μ_{eff}	kg m^{-1} s^{-1}	effective viscosity of a suspension
μ_{fluid}	kg m^{-1} s^{-1}	dynamic viscosity of the carrier liquid
ν	m^2 s^{-1}	kinematic viscosity
ρ	kg m^{-3}	density of liquid
ρ_f	kg m^{-3}	density of liquid
σ_{ij}	kg m^{-1} s^{-2}	stress tensor
σ_u	m s^{-1}	standard deviation of velocity in x direction (in-plane direction)
σ_v	m s^{-1}	standard deviation of velocity in y direction (in-plane direction)
σ_w	m s^{-1}	standard deviation of velocity in z direction (out-of-plane direction)
σ_z	m	standard deviation of reconstructed depth position

σ_z^*	m	standard deviation of reconstructed depth position of particle focal point
τ_{ij}	-	shear stress obtained by spatial averaging over the disturbance wavelengths (normalized)
φ	-	azimuthal coordinate
ω	-	complex frequency
ω_c	-	critical complex frequency
ω_i	-	imaginary part of complex frequency
$\vec{\omega_f}$	s^{-1}	vorticity of the flow
ω_r	-	real part of complex frequency

Abbreviations

APF	Annular Poiseuille Flow
AX1	Axial Banding type 1
AX2	Axial Banding type 2
AX3	Axial Banding type 3
AZ	Azimuthal Banding
CCD	Charge-Coupled Device
CLL	Centrifugal Limit Line
CMOS	Complementary metaloxidesemiconductor
DOC	Depth of Correlation
FF	Fingering Flow
FVS	Front View Setup
GB	Granular Bed
GDPT	General Defocussing Particle Tracking
IRSPF	Spiral Poiseuille Flow with Rotating Inner cylinder
KTE	Kinetic energy Transport Equation
LVS	Lateral View Setup
NA	Numerical Aperture of objective
NP1-NP3	Net Pattern 1-3
ORSPF	Spiral Poiseuille Flow with Rotating Outer cylinder
PIV	Particle Image Velocimetry
PMMA	Poly(methyl methacrylate) “Acrylic”
PS	Polystyrene
PTV	Particle Tracking Velocimetry
RUB	Ruhr Universität Bochum
SNR	Signal to Noise Ratio
SPF	Spiral Poiseuille Flow
SQR	Square Pattern
TC	Taylor-Couette
TCR	Taylor-Couette Reactor
TUDa	Technische Universität Darmstadt

TSI	Tollmien-Schlichting instability
UH	Unstable Homogenous Region

List of Figures

List of Tables

Bibliography

Abbas, M., Magaud, P., Gao, Y., and Geoffroy, S. (2014). Migration of finite sized particles in a laminar square channel flow from low to high reynolds numbers. *Physics of Fluids*, 26(12):123301.

Abbott, J., Tetlow, N., Graham, A., Altobelli, S., Fukushima, E., Mondy, L., and Stephens, T. (1991). Experimental observations of particle migration in concentrated suspensions: Couette flow. *Journal of rheology*, 35(5):773–795.

Adrian, R. J. (1991). Particle-imaging techniques for experimental fluid mechanics. *Annual review of fluid mechanics*, 23(1):261–304.

Adrian, R. J. and Westerweel, J. (2011). *Particle image velocimetry*. Number 30. Cambridge university press.

Ali, J., Kim, H., Cheang, U. K., and Kim, M. J. (2016). Micro-piv measurements of flows induced by rotating microparticles near a boundary. *Microfluidics and Nanofluidics*, 20(9):1–11.

Amini, H., Lee, W., and Di Carlo, D. (2014). Inertial microfluidic physics. *Lab on a Chip*, 14(15):2739–2761.

Angarita-Jaimes, N., McGhee, E., Chennaoui, M., Campbell, H., Zhang, S., Towers, C., Greenaway, A., and Towers, D. (2006). Wavefront sensing for single view three-component three-dimensional flow velocimetry. *Experiments in fluids*, 41(6):881–891.

Ashwin, P. and King, G. (1997). A study of particle paths in non-axisymmetric taylor–couette flows. *Journal of Fluid Mechanics*, 338:341–362.

Asmolov, E. S. (1999). The inertial lift on a spherical particle in a plane poiseuille flow at large channel reynolds number. *Journal of Fluid Mechanics*, 381:63–87.

Bailey, B. and Yoda, M. (2003). An aqueous low-viscosity density-and refractive index-matched suspension system. *Experiments in fluids*, 35(1):1–3.

Barnkob, R., Cierpka, C., Chen, M., Sachs, S., Mäder, P., and Rossi, M. (2021). Defocus particle tracking: A comparison of methods based on model functions, cross-correlation, and neural networks. *Measurement Science and Technology*.

Barnkob, R., Kähler, C. J., and Rossi, M. (2015). General defocusing particle tracking. *Lab on a Chip*, 15(17):3556–3560.

Barnkob, R. and Rossi, M. (2020). General defocusing particle tracking: fundamentals and uncertainty assessment. *Experiments in Fluids*, 61(4):1–14.

Basset, A. B. (1888). Iii. on the motion of a sphere in a viscous liquid. *Philosophical Transactions of the Royal Society of London.(A.)*, (179):43–63.

Batchelor, G. and Green, J. (1972). The determination of the bulk stress in a suspension of spherical particles to order c 2. *Journal of Fluid Mechanics*, 56(3):401–427.

Batchelor, G. and Van Rensburg, R. J. (1986). Structure formation in bidisperse sedimentation. *Journal of Fluid Mechanics*, 166:379–407.

Bayguinov, P. O., Oakley, D. M., Shih, C.-C., Geanon, D. J., Joens, M. S., and Fitzpatrick, J. A. (2018). Modern laser scanning confocal microscopy. *Current protocols in cytometry*, 85(1):e39.

Bazaz, S. R., Mashhadian, A., Ehsani, A., Saha, S. C., Krüger, T., and Warkiani, M. E. (2020). Computational inertial microfluidics: a review. *Lab on a Chip*, 20(6):1023–1048.

Bhagat, A. A. S., Kuntaegowdanahalli, S. S., and Papautsky, I. (2009). Inertial microfluidics for continuous particle filtration and extraction. *Microfluidics and nanofluidics*, 7(2):217–226.

Bitsch, L., Olesen, L. H., Westergaard, C. H., Bruus, H., Klank, H., and Kutter, J. P. (2005). Micro particle-image velocimetry of bead suspensions and blood flows. *Experiments in fluids*, 39(3):507–513.

Blahout, S., Reinecke, S. R., Kazerooni, H. T., Kruggel-Emden, H., and Hussong, J. (2020). On the 3d distribution and size fractionation of microparticles in a serpentine microchannel. *Microfluidics and Nanofluidics*, 24(3):1–10.

Blahout, S., Reinecke, S. R., Kruggel-Emden, H., and Hussong, J. (2021). On the micro-piv accuracy and reliability utilizing non-gaussian particle images. *Experiments in Fluids*, 62(9):1–23.

Boote, O. and Thomas, P. (1999). Effects of granular additives on transition boundaries between flow states of rimming flows. *Physics of Fluids*, 11(8):2020–2029.

Boussinesq, J. (1903). *Théorie analytique de la chaleur mise en harmonic avec la thermodynamique et avec la théorie mécanique de la lumière: Tome I-[II]...*, volume 2. Gauthier-Villars.

Bradshaw, P. (1973). Effects of streamline curvature on turbulent flow. Technical report, Advisory Group for Aerospace Research and Development Paris (France).

Brenn, G., Durst, F., and Selbach, A. (1998). Experimental investigations of the binary interaction of polydisperse sprays. *Particle & Particle Systems Characterization: Measurement and Description of Particle Properties and Behavior in Powders and Other Disperse Systems*, 15(6):263–273.

Brenner, H. (1966). Hydrodynamic resistance of particles at small reynolds numbers. In *Advances in Chemical Engineering*, volume 6, pages 287–438. Elsevier.

Brenner, M. P. (1999). Screening mechanisms in sedimentation. *Physics of fluids*, 11(4):754–772.

Breu, A. P., Kruelle, C. A., and Rehberg, I. (2003). Pattern formation in a rotating aqueous suspension. *EPL (Europhysics Letters)*, 62(4):491.

Brockmann, P. and Hussong, J. (2021). On the calibration of astigmatism particle tracking velocimetry for suspensions of different volume fractions. *Experiments in Fluids*, 62(1):1–11.

Brockmann, P., Kazerooni, H. T., Brandt, L., and Hussong, J. (2020). Utilizing the ball lens effect for astigmatism particle tracking velocimetry. *Experiments in Fluids*, 61(2):67.

Brown, J. R., Fridjonsson, E. O., Seymour, J. D., and Codd, S. L. (2009). Nuclear magnetic resonance measurement of shear-induced particle migration in brownian suspensions. *Physics of Fluids*, 21(9):093301.

Brücker, C. (1995). Digital-particle-image-velocimetry (dpiv) in a scanning light-sheet: 3d starting flow around a short cylinder. *Experiments in Fluids*, 19(4):255–263.

Buchmann, N., Atkinson, C., and Soria, J. (2012). Ultra-high-speed tomographic digital holographic velocimetry in supersonic particle-laden jet flows. *Measurement Science and Technology*, 24(2):024005.

Buchmann, N., Cierpka, C., Kähler, C., and Soria, J. (2014). Ultra-high-speed 3d astigmatic particle tracking velocimetry: application to particle-laden supersonic impinging jets. *Experiments in fluids*, 55(11):1842.

Budwig, R. (1994). Refractive index matching methods for liquid flow investigations. *Experiments in fluids*, 17(5):350–355.

Bush, J. W., Thurber, B., and Blanchette, F. (2003). Particle clouds in homogeneous and stratified environments. *Journal of Fluid Mechanics*, 489:29.

Butler, J. E. and Bonnecaze, R. T. (1999). Imaging of particle shear migration with electrical impedance tomography. *Physics of fluids*, 11(8):1982–1994.

Buyevich, Y. A. (1996). Particle distribution in suspension shear flow. *Chemical engineering science*, 51(4):635–647.

Chamorro, L. P., Troolin, D. R., Lee, S.-J., Arndt, R., and Sotiropoulos, F. (2013). Three-dimensional flow visualization in the wake of a miniature axial-flow hydrokinetic turbine. *Experiments in fluids*, 54(2):1–12.

Chandrasekhar, S. (1960a). The hydrodynamic stability of inviscid flow between coaxial cylinders. *Proceedings of the National Academy of Sciences of the United States of America*, 46(1):137.

Chandrasekhar, S. (1960b). The hydrodynamic stability of viscid flow between coaxial cylinders. *Proceedings of the National Academy of Sciences of the United States of America*, 46(1):141.

Chandrasekhar, S. (2013). *Hydrodynamic and hydromagnetic stability*. Courier Corporation.

Chang, C. and Powell, R. L. (1994). Effect of particle size distributions on the rheology of concentrated bimodal suspensions. *Journal of rheology*, 38(1):85–98.

Chen, S., Angarita-Jaimes, N., Angarita-Jaimes, D., Pelc, B., Greenaway, A., Towers, C., Lin, D., and Towers, D. (2009). Wavefront sensing for three-component three-dimensional flow velocimetry in microfluidics. *Experiments in Fluids*, 47(4-5):849.

Cheney, M., Isaacson, D., and Newell, J. C. (1999). Electrical impedance tomography. *SIAM review*, 41(1):85–101.

Cheng, N.-S. (2008). Formula for the viscosity of a glycerol- water mixture. *Industrial & engineering chemistry research*, 47(9):3285–3288.

Choi, Y.-S., Seo, K.-W., and Lee, S.-J. (2011). Lateral and cross-lateral focusing of spherical particles in a square microchannel. *Lab on a Chip*, 11(3):460–465.

Chun, B. and Jung, H. W. (2021). Inertia-and shear-induced inhomogeneities in non-brownian mono and bidisperse suspensions under wall-bounded linear shear flow. *Physics of Fluids*, 33(5):053318.

Chun, B. and Ladd, A. (2006). Inertial migration of neutrally buoyant particles in a square duct: An investigation of multiple equilibrium positions. *Physics of Fluids*, 18(3):031704.

Chun, B., Park, J. S., Jung, H. W., and Won, Y.-Y. (2019). Shear-induced particle migration and segregation in non-brownian bidisperse suspensions under planar poiseuille flow. *Journal of Rheology*, 63(3):437–453.

Chung, K. C. and Astill, K. N. (1977). Hydrodynamic instability of viscous flow between rotating coaxial cylinders with fully developed axial flow. *Journal of Fluid Mechanics*, 81(04):641–655.

Cierpka, C. and Kähler, C. (2012). Particle imaging techniques for volumetric three-component (3d3c) velocity measurements in microfluidics. *Journal of visualization*, 15(1):1–31.

Cierpka, C., Lütke, B., and Kähler, C. J. (2013). Higher order multi-frame particle tracking velocimetry. *Experiments in Fluids*, 54(5):1–12.

Cierpka, C., Rossi, M., Segura, R., and Kähler, C. (2010a). On the calibration of astigmatism particle tracking velocimetry for microflows. *Measurement Science and Technology*, 22(1):015401.

Cierpka, C., Rossi, M., Segura, R., Mastrangelo, F., and Kähler, C. (2012). A comparative analysis of the uncertainty of astigmatism-μptv, stereo-μpiv, and μpiv. *Experiments in fluids*, 52(3):605–615.

Cierpka, C., Segura, R., Hain, R., and Kähler, C. J. (2010b). A simple single camera 3c3d velocity measurement technique without errors due to depth of correlation and spatial averaging for microfluidics. *Measurement Science and Technology*, 21(4):045401.

Coëtmellec, S., Buraga-Lefebvre, C., Lebrun, D., and Özkul, C. (2001). Application of in-line digital holography to multiple plane velocimetry. *Measurement Science and Technology*, 12(9):1392.

Cornish, R. J. (1933). Flow of water through fine clearances with relative motion of the boundaries. *Proceedings of the Royal Society of London A: Mathematical, Physical and Engineering Sciences*, 140(840):227–240.

Corrsin, S. and Lumley, J. (1956). On the equation of motion for a particle in turbulent fluid. *Applied Scientific Research, Section A*, 6(2):114–116.

Cotrell, D. L. and Pearlstein, A. J. (2006). Linear stability of spiral and annular poiseuille flow for small radius ratio. *Journal of Fluid Mechanics*, 547:1–20.

Cottrel, D. L. and Pearlstein, A. J. (2004). The connection between centrifugal instability and tollmienschlichting-like instability for spiral poiseuille flow. *Journal of Fluid Mechanics*, 509:331–351.

Cottrel, D. L., Rani, S. L., and Pearlstein, A. J. (2004). Computational assessment of subcritical and delayed onset in spiral poiseuille flow experiments. *Journal of Fluid Mechanics*, 509:353–378.

Craik, A. D. (1988). *Wave interactions and fluid flows*. Cambridge University Press.

Crowe, C. T. (2005). *Multiphase flow handbook*. CRC press.

Dalgarno, P. A., Dalgarno, H. I., Putoud, A., Lambert, R., Paterson, L., Logan, D. C., Towers, D. P., Warburton, R. J., and Greenaway, A. H. (2010). Multiplane imaging and three dimensional nanoscale particle tracking in biological microscopy. *Optics express*, 18(2):877–884.

Deen, N. G., Westerweel, J., and Delnoij, E. (2002). Two-phase piv in bubbly flows: Status and trends. *Chemical engineering & technology*, 25(1):97–101.

Deguchi, K. (2017). Linear instability in rayleigh-stable taylor-couette flow. *Physical Review E*, 95(2):021102.

Di Caprio, G., Gioffre, M. A., Saffioti, N., Grilli, S., Ferraro, P., Puglisi, R., Balduzzi, D., Galli, A., and Coppola, G. (2010). Quantitative label-free animal sperm imaging by means of digital holographic microscopy. *IEEE Journal of Selected Topics in Quantum Electronics*, 16(4):833–840.

Di Carlo, D., Edd, J. F., Humphry, K. J., Stone, H. A., and Toner, M. (2009). Particle segregation and dynamics in confined flows. *Physical review letters*, 102(9):094503.

Di Carlo, D., Irimia, D., Tompkins, R. G., and Toner, M. (2007). Continuous inertial focusing, ordering, and separation of particles in microchannels. *Proceedings of the National Academy of Sciences*, 104(48):18892–18897.

Dietrich, W. E. (1982). Settling velocity of natural particles. *Water resources research*, 18(6):1615–1626.

Dinther, A., Schroën, C., Imhof, A., Vollebregt, H., and Boom, R. (2013). Flow-induced particle migration in microchannels for improved microfiltration processes. *Microfluidics and nanofluidics*, 15(4):451–465.

DiPrima, R. (1960). The stability of a viscous fluid between rotating cylinders with an axial flow. *Journal of Fluid Mechanics*, 9(4):621–631.

DiPrima, R. C. and Pridor, A. (1979). The stability of viscous flow between rotating concentric cylinders with an axial flow. In *Proceedings of the Royal Society of London A: Mathematical, Physical and Engineering Sciences*, volume 366, pages 555–573. The Royal Society.

Discetti, S. and Coletti, F. (2018). Volumetric velocimetry for fluid flows. *Measurement Science and Technology*, 29(4):042001.

Donnelly, R. and Fultz, D. (1960). Experiments on the stability of spiral flow between rotating cylinders. *Proceedings of the National Academy of Sciences of the United States of America*, 46(8):1150.

Drake, J. B., Kenney, A. L., Morgan, T. B., and Heindel, T. J. (2011). Developing tracer particles for x-ray particle tracking velocimetry. In *Fluids Engineering Division Summer Meeting*, volume 44403, pages 2685–2692.

Drazin, P. G. and Reid, W. H. (2004). *Hydrodynamic stability*. Cambridge university press.

Dusting, J. and Balabani, S. (2009). Mixing in a taylor–couette reactor in the non-wavy flow regime. *Chemical Engineering Science*, 64(13):3103–3111.

Einstein, A. (1911). Berichtigung zu meiner arbeit: Eine neue bestimmung der moleküldimensionen. *Annalen der Physik*, 339(3):591–592.

Einstein, A. et al. (1905). On the motion of small particles suspended in liquids at rest required by the molecular-kinetic theory of heat. *Annalen der physik*, 17(549-560):208.

Elsinga, G., Westerweel, J., Scarano, F., and Novara, M. (2011). On the velocity of ghost particles and the bias errors in tomographic-piv. *Experiments in fluids*, 50(4):825–838.

Elsinga, G. E., Scarano, F., Wieneke, B., and van Oudheusden, B. W. (2006). Tomographic particle image velocimetry. *Experiments in fluids*, 41(6):933–947.

Esser, A. and Grossmann, S. (1996). Analytic expression for taylor–couette stability boundary. *Physics of fluids*, 8(7):1814–1819.

Fage, A. (1938). The influence of wall oscillations, wall rotation, and entry eddies, on the breakdown of laminar flow in an annular pipe. *Proceedings of the Royal Society of London. Series A. Mathematical and Physical Sciences*, 165(923):501–529.

Fan, X., Parker, D., and Smith, M. (2006). Labelling a single particle for positron emission particle tracking using direct activation and ion-exchange techniques. *Nuclear Instruments and Methods in Physics Research Section A: Accelerators, Spectrometers, Detectors and Associated Equipment*, 562(1):345–350.

Feng, J., Hu, H. H., and Joseph, D. D. (1994). Direct simulation of initial value problems for the motion of solid bodies in a newtonian fluid. part 2. couette and poiseuille flows. *Journal of fluid mechanics*, 277:271–301.

Ferrand, V., Bazile, R., and Boree, J. (2001). Measurements of concentration per size class in a dense polydispersed jet using planar laser-induced fluorescence and phase doppler techniques. *Experiments in fluids*, 31(6):597–607.

Ferrini, F., Ercolani, D., De Cindio, B., Nicodemo, L., Nicolais, L., and Ranaudo, S. (1979). Shear viscosity of settling suspensions. *Rheologica Acta*, 18(2):289–296.

Fiscaletti, D., Overmars, E., Westerweel, J., and Elsinga, G. (2014). Tomographic long-range micropiv to resolve the small-scale motions in the turbulent region of a jet at high reynolds numbers. In *17th int. symposium on application of laser techniques to fluid mechanics. Lisbon, Portugal*.

Fock, H. and Rasmuson, A. (2008). Near wall studies of pulp suspension flow using piv. *Nordic Pulp & Paper Research Journal*, 23(1):120–125.

Fornari, W., Kazerooni, H. T., Hussong, J., and Brandt, L. (2018). Suspensions of finite-size neutrally buoyant spheres in turbulent duct flow. *Journal of Fluid Mechanics*, 851:148–186.

Franchini, S., Charogiannis, A., Markides, C. N., Blunt, M. J., and Krevor, S. (2019). Calibration of astigmatic particle tracking velocimetry based on generalized gaussian feature extraction. *Advances in Water Resources*, 124:1–8.

Fuchs, T., Hain, R., and Kähler, C. J. (2014a). Macroscopic three-dimensional particle location using stereoscopic imaging and astigmatic aberrations. *Optics letters*, 39(24):6863–6866.

Fuchs, T., Hain, R., and Kähler, C. J. (2014b). Three-dimensional location of micrometer-sized particles in macroscopic domains using astigmatic aberrations. *Optics letters*, 39(5):1298–1301.

Gallagher, A. (1974). On the behaviour of small disturbances in plane couette flow. part 3. the phenomenon of mode-pairing. *Journal of Fluid Mechanics*, 65(1):29–32.

Gao, C., Xu, B., and Gilchrist, J. (2009). Mixing and segregation of microspheres in microchannel flows of mono-and bidispersed suspensions. *Physical Review E*, 79(3):036311.

Gao, Y., Magaud, P., Baldas, L., Lafforgue, C., Abbas, M., and Colin, S. (2017). Self-ordered particle trains in inertial microchannel flows. *Microfluidics and Nanofluidics*, 21(10):1–10.

Gao, Y., Magaud, P., Lafforgue, C., Colin, S., and Baldas, L. (2019). Inertial lateral migration and self-assembly of particles in bidisperse suspensions in microchannel flows. *Microfluidics and Nanofluidics*, 23(7):1–14.

Gatignol, R. et al. (1983). The faxén formulae for a rigid particle in an unsteady non-uniform stokes flow.

Goldstein, S. (1937). The stability of viscous fluid flow between rotating cylinders. In *Proc. Camb. Phil. Soc*, volume 33, pages 41–61. Cambridge Univ Press.

Gonzales, A. (2013). *Merkmale des Umschlags laminar-turbulent in einer drallbehafteten Ringspaltströmung*. PhD thesis, Ruhr-Universität-Bochum, Fakultät Maschinenbau.

Guaus, A. and Bottaro, A. (2007). Instabilities of the flow in a curved channel with compliant walls. *Royal Society of London Proceedings Series A*, 463:2201–2222.

Guazzelli, E. and Morris, J. F. (2011). *A physical introduction to suspension dynamics*, volume 45. Cambridge University Press.

Gurung, A. and Poelma, C. (2016). Measurement of turbulence statistics in single-phase and two-phase flows using ultrasound imaging velocimetry. *Experiments in Fluids*, 57(11):1–12.

Haddadi, H. and Morris, J. F. (2014). Microstructure and rheology of finite inertia neutrally buoyant suspensions. *Journal of Fluid Mechanics*, 749:431–459.

Hampton, R., Mammoli, A., Graham, A., Tetlow, N., and Altobelli, S. (1997). Migration of particles undergoing pressure-driven flow in a circular conduit. *Journal of Rheology*, 41(3):621–640.

Han, M., Kim, C., Kim, M., and Lee, S. (1999). Particle migration in tube flow of suspensions. *Journal of rheology*, 43(5):1157–1174.

Hanjalić, K. and Launder, B. (2011). *Modelling turbulence in engineering and the environment: second-moment routes to closure*. Cambridge university press.

Hasoon, M. A. and Martin, B. W. (1977). The stability of viscous axial flow in an annulus with a rotating inner cylinder. *Proceedings of the Royal Society of London A: Mathematical, Physical and Engineering Sciences*, 352(1670):351–380.

Heaton, C. (2008). Linear instability of annular poiseuille flow. *Journal of Fluid Mechanics*, 610:391–406.

Heindel, T. J. (2011). A review of x-ray flow visualization with applications to multiphase flows. *Journal of Fluids Engineering*, 133(7).

Henderson, K. L., Gwynllyw, D. R., and Barenghi, C. F. (2007). Particle tracking in taylor–couette flow. *European Journal of Mechanics-B/Fluids*, 26(6):738–748.

Hinsch, K. D. (2002). Holographic particle image velocimetry. *Measurement Science and Technology*, 13(7):R61.

Ho, B. and Leal, L. (1974). Inertial migration of rigid spheres in two-dimensional unidirectional flows. *Journal of fluid mechanics*, 65(2):365–400.

Hong, G.-R., Pedrizzetti, G., Tonti, G., Li, P., Wei, Z., Kim, J. K., Baweja, A., Liu, S., Chung, N., Houle, H., et al. (2008). Characterization and quantification of vortex flow in the human left ventricle by contrast echocardiography using vector particle image velocimetry. *JACC: Cardiovascular Imaging*, 1(6):705–717.

Hood, K., Kahkeshani, S., Di Carlo, D., and Roper, M. (2016). Direct measurement of particle inertial migration in rectangular microchannels. *Lab on a Chip*, 16(15):2840–2850.

Hou, S., Pan, T.-W., and Glowinski, R. (2014). Circular band formation for incompressible viscous fluid–rigid-particle mixtures in a rotating cylinder. *Physical Review E*, 89(2):023013.

Howard, L. N. and Gupta, A. (1962). On the hydrodynamic and hydromagnetic stability of swirling flows. *Journal of Fluid Mechanics*, 14(3):463–476.

Huang, B., Wang, W., Bates, M., and Zhuang, X. (2008). Three-dimensional super-resolution imaging by stochastic optical reconstruction microscopy. *Science*, 319(5864):810–813.

Huang, F., Sirinakis, G., Allgeyer, E. S., Schroeder, L. K., Duim, W. C., Kromann, E. B., Phan, T., Rivera-Molina, F. E., Myers, J. R., Irnov, I., et al. (2016). Ultra-high resolution 3d imaging of whole cells. *Cell*, 166(4):1028–1040.

Humphry, K. J., Kulkarni, P. M., Weitz, D. A., Morris, J. F., and Stone, H. A. (2010). Axial and lateral particle ordering in finite reynolds number channel flows. *Physics of Fluids*, 22(8):081703.

Husband, D., Mondy, L., Ganani, E., and Graham, A. (1994). Direct measurements of shear-induced particle migration in suspensions of bimodal spheres. *Rheologica acta*, 33(3):185–192.

Jensen, J. A., Nikolov, S. I., Alfred, C., and Garcia, D. (2016). Ultrasound vector flow imagingpart i: Sequential systems. *IEEE transactions on ultrasonics, ferroelectrics, and frequency control*, 63(11):1704–1721.

Joseph, D. D. (1976). Stability of fluid motions. i, ii. *NASA STI/Recon Technical Report A*, 27:12423.

Kähler, C. J., Scharnowski, S., and Cierpka, C. (2012a). On the resolution limit of digital particle image velocimetry. *Experiments in fluids*, 52(6):1629–1639.

Kähler, C. J., Scharnowski, S., and Cierpka, C. (2012b). On the uncertainty of digital piv and ptv near walls. *Experiments in fluids*, 52(6):1641–1656.

Kalyankar, M. G., Matson, W., Tong, P., and Ackerson, B. J. (2008). Pattern formation in a rotating suspension of non-brownian buoyant particles. *Physics of fluids*, 20(8):083301.

Kang, C. and Mirbod, P. (2020). Shear-induced particle migration of semi-dilute and concentrated brownian suspensions in both poiseuille and circular couette flow. *International Journal of Multiphase Flow*, 126:103239.

Kao, H. P. and Verkman, A. (1994). Tracking of single fluorescent particles in three dimensions: use of cylindrical optics to encode particle position. *Biophysical journal*, 67(3):1291–1300.

Karnis, A., Goldsmith, H., and Mason, S. (1966). The kinetics of flowing dispersions: I. concentrated suspensions of rigid particles. *Journal of Colloid and Interface Science*, 22(6):531–553.

Kaye, J. (1958). Modes of adiabatic and diabatic fluid flow in an annulus with an inner rotating cylinder. *Trans ASME*, 80:753–765.

Kazerooni, H. T., Fornari, W., Hussong, J., and Brandt, L. (2017). Inertial migration in dilute and semidilute suspensions of rigid particles in laminar square duct flow. *Physical Review Fluids*, 2(8):084301.

Kemper, B., Carl, D. D., Schnekenburger, J., Bredebusch, I., Schäfer, M., Domschke, W., and von Bally, G. (2006). Investigation of living pancreas tumor cells by digital holographic microscopy. *Journal of biomedical optics*, 11(3):034005.

Khan, A. and Richardson, J. (1987). The resistance to motion of a solid sphere in a fluid. *Chemical Engineering Communications*, 62(1-6):135–150.

Kiessling, I. (1963). *Ueber das Taylorsche Stabilitätsproblem bei zusätzlicher axialer Durchströmung der Zylinder*. Deutsche Versuchsanstalt für Luft-und Raumfahrt.

Kim, H., Große, S., Elsinga, G. E., and Westerweel, J. (2011). Full 3d-3c velocity measurement inside a liquid immersion droplet. *Experiments in fluids*, 51(2):395–405.

Kim, H., Westerweel, J., and Elsinga, G. E. (2012). Comparison of tomo-piv and 3d-ptv for microfluidic flows. *Measurement Science and Technology*, 24(2):024007.

Kinoshita, H., Kaneda, S., Fujii, T., and Oshima, M. (2007). Three-dimensional measurement and visualization of internal flow of a moving droplet using confocal micro-piv. *Lab on a Chip*, 7(3):338–346.

Kloosterman, A., Poelma, C., and Westerweel, J. (2011). Flow rate estimation in large depth-of-field micro-piv. *Experiments in fluids*, 50(6):1587–1599.

Koh, C. J., Hookham, P., and Leal, L. G. (1994). An experimental investigation of concentrated suspension flows in a rectangular channel. *Journal of Fluid Mechanics*, 266:1–32.

Konidena, S., Lee, J., Reddy, K. A., and Singh, A. (2018). Particle dynamics and pattern formation in a rotating suspension of positively buoyant particles. *Physical Review Fluids*, 3(4):044301.

Konidena, S., Reddy, K. A., and Singh, A. (2019). Dynamics of bidensity particle suspensions in a horizontal rotating cylinder. *Physical Review E*, 99(1):013111.

König, J., Chen, M., Rösing, W., Boho, D., Mäder, P., and Cierpka, C. (2020). On the use of a cascaded convolutional neural network for three-dimensional flow measurements using astigmatic ptv. *Measurement Science and Technology*.

Krishnan, G. P. and Leighton Jr, D. (1995). Dynamic viscous resuspension of bidisperse suspensionsi. effective diffusivity. *International journal of multiphase flow*, 21(5):721–732.

Krueger, E. and Di Prima, R. (1964). The stability of a viscous fluid between rotating cylinders with an axial flow. *Journal of Fluid Mechanics*, 19(4):528–538.

Kühn, J., Charrière, F., Colomb, T., Cuche, E., Montfort, F., Emery, Y., Marquet, P., and Depeursinge, C. (2008). Axial sub-nanometer accuracy in digital holographic microscopy. *Measurement Science and Technology*, 19(7):074007.

Kulkarni, P. M. and Morris, J. F. (2008). Suspension properties at finite reynolds number from simulated shear flow. *Physics of Fluids*, 20(4):040602.

Kumar, A. A. and Singh, A. (2010). Dynamics of bi-dispersed settling suspension of non-colloidal particles in rotating cylinder. *Advanced Powder Technology*, 21(6):641–651.

Landau, L. and Lifshitz, E. (1987). Fluid mechanics. translated from the russian by jb sykes and wh reid. *Course of Theoretical Physics*, 6.

Langehanenberg, P., Ivanova, L., Bernhardt, I., Ketelhut, S., Vollmer, A., Dirksen, D., Georgiev, G. K., von Bally, G., and Kemper, B. (2009). Automated three-dimensional tracking of living cells by digital holographic microscopy. *Journal of biomedical optics*, 14(1):014018.

Lansey, J. C. (2021). Efficient 2d histogram, no toolboxes needed. *MATLAB Central File Exchange*.

Lashgari, I., Picano, F., Breugem, W.-P., and Brandt, L. (2014). Laminar, turbulent, and inertial shear-thickening regimes in channel flow of neutrally buoyant particle suspensions. *Physical review letters*, 113(25):254502.

Lee, J. and Ladd, A. J. (2002). Axial segregation in a cylindrical centrifuge. *Physical review letters*, 89(10):104301.

Lee, J. and Ladd, A. J. (2005). Axial segregation of a settling suspension in a rotating cylinder. *Physical review letters*, 95(4):048001.

Lee, J. and Ladd, A. J. (2007). Particle dynamics and pattern formation in a rotating suspension. *Journal of Fluid Mechanics*, 577:183.

Lee, S. J. and Kim, S. (2009). Advanced particle-based velocimetry techniques for microscale flows. *Microfluidics and Nanofluidics*, 6(5):577–588.

Leighton, D. and Acrivos, A. (1987). The shear-induced migration of particles in concentrated suspensions. *Journal of Fluid Mechanics*, 181:415–439.

Leister, R., Fuchs, T., Mattern, P., and Kriegseis, J. (2021). Flow-structure identification in a radially grooved open wet clutch by means of defocusing particle tracking velocimetry. *Experiments in Fluids*, 62(2):1–14.

Lima, R., Wada, S., Takeda, M., Tsubota, K.-i., and Yamaguchi, T. (2007). In vitro confocal micro-piv measurements of blood flow in a square microchannel: the effect of the haematocrit on instantaneous velocity profiles. *Journal of biomechanics*, 40(12):2752–2757.

Lima, R., Wada, S., Tanaka, S., Takeda, M., Ishikawa, T., Tsubota, K.-i., Imai, Y., and Yamaguchi, T. (2008). In vitro blood flow in a rectangular pdms microchannel: experimental observations using a confocal micro-piv system. *Biomedical microdevices*, 10(2):153–167.

Lima, R., Wada, S., Tsubota, K.-i., and Yamaguchi, T. (2006). Confocal micro-piv measurements of three-dimensional profiles of cell suspension flow in a square microchannel. *Measurement Science and Technology*, 17(4):797.

Lindken, R., Rossi, M., Große, S., and Westerweel, J. (2009). Micro-particle image velocimetry (μpiv): recent developments, applications, and guidelines. *Lab on a Chip*, 9(17):2551–2567.

Lipson, S. (2001). Periodic banding in crystallization from rotating supersaturated solutions. *Journal of Physics: Condensed Matter*, 13(21):5001.

Lipson, S. and Seiden, G. (2002). Particle banding in rotating fluids: a new pattern-forming system. *Physica A: Statistical Mechanics and its Applications*, 314(1-4):272–277.

Ludwieg, H. (1960). Stabilität der strömung in einem zylindrischen ringraum. *Z. Flugwiss*, 8(5):135–140.

Ludwieg, H. (1961). Ergänzung zu der arbeit stabilität der strömung in einem zylindrischen ringraum". *Z. Flugwiss*, 9:359.

Lyon, M. and Leal, L. (1998a). An experimental study of the motion of concentrated suspensions in two-dimensional channel flow. part 1. monodisperse systems. *Journal of fluid mechanics*, 363:25–56.

Lyon, M. and Leal, L. (1998b). An experimental study of the motion of concentrated suspensions in two-dimensional channel flow. part 2. bidisperse systems. *Journal of Fluid Mechanics*, 363:57–77.

Mackrodt, P.-A. (1966). *Spiralströmungen im zylindrischen Ringraum hinter Leiträdern*. Aerodynamische Versuchsanstalt.

Mackrodt, P.-A. (1976). Stability of hagen-poiseuille flow with superimposed rigid rotation. *Journal of Fluid Mechanics*, 73(1):153–164.

Majji, M. V., Banerjee, S., and Morris, J. F. (2018). Inertial flow transitions of a suspension in taylor-couette geometry. *Journal of Fluid Mechanics*, 835:936.

Majji, M. V. and Morris, J. F. (2018). Inertial migration of particles in taylor-couette flows. *Physics of Fluids*, 30(3):033303.

Martel, J. M. and Toner, M. (2014). Inertial focusing in microfluidics. *Annual review of biomedical engineering*, 16:371–396.

Maslowe, S. (1974). Instability of rigidly rotating flows to non-axisymmetric disturbances. *Journal of Fluid Mechanics*, 64(2):307–318.

Maslowe, S. A. (1986). Critical layers in shear flows. *Annual review of fluid mechanics*, 18(1):405–432.

Massing, J., Kaden, D., Kähler, C., and Cierpka, C. (2016). Luminescent two-color tracer particles for simultaneous velocity and temperature measurements in microfluidics. *Measurement Science and Technology*, 27(11):115301.

Massing, J., Kähler, C. J., and Cierpka, C. (2018). A volumetric temperature and velocity measurement technique for microfluidics based on luminescence lifetime imaging. *Experiments in Fluids*, 59(11):163.

Matson, W., Ackerson, B. J., and Tong, P. (2003). Pattern formation in a rotating suspension of non-brownian settling particles. *Physical Review E*, 67(5):050301.

Matson, W., Ackerson, B. J., and Tong, P. (2006). Dynamics of rotating suspensions. *Solid state communications*, 139(11-12):605–616.

Matson, W., Ackerson, B. J., and Tong, P. (2008). Measured scaling properties of the transition boundaries in a rotating suspension of non-brownian settling particles. *Journal of fluid mechanics*, 597:233.

Matson, W., Kalyankar, M., Ackerson, B. J., and Tong, P. (2005). Concentration and velocity patterns in a horizontal rotating suspension of non-brownian settling particles. *Physical Review E*, 71(3):031401.

Maxey, M. R. and Riley, J. J. (1983). Equation of motion for a small rigid sphere in a nonuniform flow. *The Physics of Fluids*, 26(4):883–889.

Medhi, B. J., Reddy, M. M., and Singh, A. (2019). Particle migration of concentrated suspension flow in bifurcating channels. *Advanced Powder Technology*, 30(9):1897–1909.

Mei, R. (1992). An approximate expression for the shear lift force on a spherical particle at finite reynolds number. *International Journal of Multiphase Flow*, 18(1):145–147.

Meinhart, C. D., Wereley, S. T., and Gray, M. (2000). Volume illumination for two-dimensional particle image velocimetry. *Measurement Science and Technology*, 11(6):809.

Meseguer, A. and Marques, F. (2000). Axial effects in the taylor couette problem: Spiral couette and spiral poiseuille flows. In *Physics of Rotating Fluids*, volume 549 of *Lecture Notes in Physics*, pages 118–136. Springer Berlin Heidelberg.

Meseguer, A. and Marques, F. (2005). On the stability of medium gap corotating spiral poiseuille flow. *Physics of Fluids*, 17(9).

Mesequer, A. and Marques, F. (2002). On the competition between centrifugal and shear instability in spiral poiseuille flow. *Journal of Fluid Mechanics*, 455:129–148.

Mewis, J. and Wagner, N. J. (2012). *Colloidal suspension rheology*. Cambridge university press.

Miura, K., Itano, T., and Sugihara-Seki, M. (2014). Inertial migration of neutrally buoyant spheres in a pressure-driven flow through square channels. *Journal of Fluid Mechanics*, 749:320–330.

Morris, J. F. (2020). Toward a fluid mechanics of suspensions. *Physical Review Fluids*, 5(11):110519.

Moser, R. D. (1984). *Direct numerical simulation of curved turbulent channel flow*. PhD thesis, Stanford University.

Moser, R. D. and Moin, P. (1987). The effects of curvature in wall-bounded turbulent flows. *Journal of Fluid Mechanics*, 175:479–510.

Mott, J. and Joseph, D. (1968a). Stability of parallel flow between concentric cylinders. *The Physics of Fluids*, 11(10):2065–2073.

Mott, J. E. and Joseph, D. D. (1968b). Stability of parallel flow between concentric cylinders. *Physics of Fluids*, 11(10):2065–2073.

Müller, P. B., Rossi, M., Marin, A., Barnkob, R., Augustsson, P., Laurell, T., Kaehler, C. J., and Bruus, H. (2013). Ultrasound-induced acoustophoretic motion of microparticles in three dimensions. *Physical Review E*, 88(2):023006.

Murata, S. and Kawamura, M. (1999). Particle depth measurement based on depth-from-defocus. *Optics & Laser Technology*, 31(1):95–102.

Nakagawa, N., Yabu, T., Otomo, R., Kase, A., Makino, M., Itano, T., and Sugihara-Seki, M. (2015). Inertial migration of a spherical particle in laminar square channel flows from low to high reynolds numbers. *Journal of Fluid Mechanics*, 779:776–793.

Nasaba, J. C. and Singh, A. (2018). Axial and radial patterns of a bidispersed suspension in a fully filled horizontal rotating cylinder. *Physical Review E*, 98(5):053102.

Nasaba, J. C. and Singh, A. (2020). Radial patterns and velocity field of non-brownian suspensions in a fully filled horizontal rotating cylinder. *Advanced Powder Technology*, 31(1):448–463.

Nemri, M., Charton, S., and Climent, E. (2016). Mixing and axial dispersion in taylor–couette flows: the effect of the flow regime. *Chemical Engineering Science*, 139:109–124.

Ng, B. S. and Turner, E. R. (1982). On the linear stability of spiral flow between rotating cylinders. *Proceedings of the Royal Society of London A: Mathematical, Physical and Engineering Sciences*, 382(1782):83–102.

Nguyen, N.-T., Wereley, S. T., and Shaegh, S. A. M. (2019). *Fundamentals and applications of microfluidics*. Artech house.

Noh, Y. and Fernando, H. (1993). The transition in the sedimentation pattern of a particle cloud. *Physics of Fluids A: Fluid Dynamics*, 5(12):3049–3055.

Nott, P. R. and Brady, J. F. (1994). Pressure-driven flow of suspensions: simulation and theory. *Journal of Fluid Mechanics*, 275:157–199.

Nouar, C. and Frigaard, I. (2009). Stability of plane couette–poiseuille flow of shear-thinning fluid. *Physics of Fluids*, 21(6):064104.

Oh, S., Song, Y.-q., Garagash, D. I., Lecampion, B., and Desroches, J. (2015). Pressure-driven suspension flow near jamming. *Physical review letters*, 114(8):088301.

Olsen, M. and Adrian, R. (2000). Out-of-focus effects on particle image visibility and correlation in microscopic particle image velocimetry. *Experiments in fluids*, 29(1):S166–S174.

Ortiz-Dueñas, C., Kim, J., and Longmire, E. K. (2010). Investigation of liquid–liquid drop coalescence using tomographic piv. *Experiments in fluids*, 49(1):111–129.

Oseen, C. W. (1927). Neuere methoden und ergebnisse in der hydrodynamik. *Leipzig: Akademische Verlagsgesellschaft mb H.*

Pan, Y., Tanaka, T., and Tsuji, Y. (2001). Direct numerical simulation of particle-laden rotating turbulent channel flow. *Physics of Fluids*, 13(8):2320–2337.

Pan, Z., Zhang, R., Yuan, C., and Wu, H. (2018). Direct measurement of microscale flow structures induced by inertial focusing of single particle and particle trains in a confined microchannel. *Physics of Fluids*, 30(10):102005.

Parker, D., Broadbent, C., Fowles, P., Hawkesworth, M., and McNeil, P. (1993). Positron emission particle tracking-a technique for studying flow within engineering equipment. *Nuclear Instruments and Methods in Physics Research Section A: Accelerators, Spectrometers, Detectors and Associated Equipment*, 326(3):592–607.

Parker, D., Dijkstra, A., Martin, T., and Seville, J. (1997). Positron emission particle tracking studies of spherical particle motion in rotating drums. *Chemical Engineering Science*, 52(13):2011–2022.

Parker, D. J. and Fan, X. (2008). Positron emission particle trackingapplication and labelling techniques. *Particuology*, 6(1):16–23.

Pedley, T. (1968). On the instability of rapidly rotating shear flows to non-axisymmetric disturbances. *Journal of Fluid Mechanics*, 31(3):603–607.

Pereira, F., Gharib, M., Dabiri, D., and Modarress, D. (2000). Defocusing digital particle image velocimetry: a 3-component 3-dimensional dpiv measurement technique. application to bubbly flows. *Experiments in fluids*, 29(1):S078–S084.

Pertuz, S., Puig, D., and Garcia, M. A. (2013). Analysis of focus measure operators for shape-from-focus. *Pattern Recognition*, 46(5):1415–1432.

Phillips, R. J., Armstrong, R. C., Brown, R. A., Graham, A. L., and Abbott, J. R. (1992). A constitutive equation for concentrated suspensions that accounts for shear-induced particle migration. *Physics of Fluids A: Fluid Dynamics*, 4(1):30–40.

Picano, F., Breugem, W.-P., Mitra, D., and Brandt, L. (2013). Shear thickening in non-brownian suspensions: an excluded volume effect. *Physical review letters*, 111(9):098302.

Poelma, C. (2017). Ultrasound imaging velocimetry: a review. *Experiments in Fluids*, 58(1):1–28.

Poelma, C. (2020). Measurement in opaque flows: a review of measurement techniques for dispersed multiphase flows. *Acta mechanica*, 231(6):2089.

Poelma, C., Westerweel, J., and Ooms, G. (2006). Turbulence statistics from optical whole-field measurements in particle-laden turbulence. *Experiments in Fluids*, 40(3):347–363.

Powell, R. L. (2008). Experimental techniques for multiphase flows. *Physics of fluids*, 20(4):040605.

Qian, M., Niu, L., Wang, Y., Jiang, B., Jin, Q., Jiang, C., and Zheng, H. (2010). Measurement of flow velocity fields in small vessel-mimic phantoms and vessels of small animals using micro ultrasonic particle image velocimetry (micro-epiv). *Physics in Medicine & Biology*, 55(20):6069.

Raffel, M., Kähler, C. J., Willert, C. E., Wereley, S. T., Scarano, F., and Kompenhans, J. (2018). Particle image velocimetry: A practical guide.

Ragan, T., Huang, H., So, P., and Gratton, E. (2006). 3d particle tracking on a two-photon microscope. *Journal of fluorescence*, 16(3):325–336.

Ram, S., Prabhat, P., Ward, E. S., and Ober, R. J. (2009). Improved single particle localization accuracy with dual objective multifocal plane microscopy. *Optics express*, 17(8):6881–6898.

Ramesh, P., Bharadwaj, S., and Alam, M. (2019). Suspension taylor–couette flow: co-existence of stationary and travelling waves, and the characteristics of taylor vortices and spirals. *Journal of Fluid Mechanics*, 870:901–940.

Richardson, J. F., Harker, J. H., and Backhurst, J. R. (2002). *Coulson and Richardson's chemical engineering: Particle technology and separation processes*. Butterworth-Heinemann.

Roberts, G. O., Kornfeld, D. M., and Fowlis, W. W. (1991). Particle orbits in a rotating liquid. *Journal of Fluid Mechanics*, 229:555–567.

Rossi, M. and Barnkob, R. (2019). Toward automated 3d ptv for microfluidics. In *13th international symposium on particle image velocimetryISPIV*, pages 22–24.

Rossi, M. and Kähler, C. J. (2014). Optimization of astigmatic particle tracking velocimeters. *Experiments in fluids*, 55(9):1809.

Rossi, M., Marin, A., Cevheri, N., Kähler, C. J., and Yoda, M. (2019). Particle distribution and velocity in electrokinetically induced banding. *Microfluidics and nanofluidics*, 23(5):67.

Rossi, M., Segura, R., Cierpka, C., and Kähler, C. J. (2012). On the effect of particle image intensity and image preprocessing on the depth of correlation in micro-piv. *Experiments in fluids*, 52(4):1063–1075.

Rotta, J. (1951). Statistische theorie nichthomogener turbulenz. *Zeitschrift für Physik*, 129(6):547–572.

Roy, A. and Govindarajan, R. (2010). An introduction to hydrodynamic stability. In *Rheology of Complex Fluids*, pages 131–147. Springer.

Rubinow, S. I. and Keller, J. B. (1961). The transverse force on a spinning sphere moving in a viscous fluid. *Journal of Fluid Mechanics*, 11(3):447–459.

Rudman, M. (1998). Mixing and particle dispersion in the wavy vortex regime of taylor–couette flow. *AIChE journal*, 44(5):1015–1026.

Sadeghi, V. M. and Higgins, B. G. (1991a). Stability of sliding couette–poiseuille flow in an annulus subject to axisymmetric and asymmetric disturbances. *Physics of Fluids A: Fluid Dynamics*, 3(9):2092–2104.

Sadeghi, V. M. and Higgins, B. G. (1991b). Stability of sliding couettepoiseuille flow in an annulus subject to axisymmetric and asymmetric disturbances. *Physics of Fluids A*, 3(9):2092–2104.

Saffman, P. (1965). The lift on a small sphere in a slow shear flow. *Journal of fluid mechanics*, 22(2):385–400.

Salwen, H., Cotton, F. W., and Grosch, C. E. (1980). Linear stability of poiseuille flow in a circular pipe. *Journal of Fluid Mechanics*, 98(2):273–284.

Santiago, J. G., Wereley, S. T., Meinhart, C. D., Beebe, D., and Adrian, R. J. (1998). A particle image velocimetry system for microfluidics. *Experiments in fluids*, 25(4):316–319.

Santiso, E. and Müller, E. A. (2002). Dense packing of binary and polydisperse hard spheres. *Molecular Physics*, 100(15):2461–2469.

Scarano, F. (2012). Tomographic piv: principles and practice. *Measurement Science and Technology*, 24(1):012001.

Scharnowski, S. and Kähler, C. J. (2020). Particle image velocimetry-classical operating rules from todays perspective. *Optics and Lasers in Engineering*, 135:106185.

Schlichting, H. and Kestin, J. (1961). *Boundary layer theory*, volume 121. Springer.

Schmid, P. J. and Henningson, D. S. (2000). *Stability and transition in shear flows*, volume 142. Springer Science & Business Media.

Schmid, P. J. and Henningson, D. S. (2012). *Stability and transition in shear flows*, volume 142. Springer Science & Business Media.

Schrimpf, M., Esteban, J., Warmeling, H., Färber, T., Behr, A., and Vorholt, A. J. (2021). Taylor-couette reactor: Principles, design, and applications. *AIChE Journal*, 67(5):e17228.

Schröder, A. and Willert, C. E. (2008). *Particle image velocimetry: new developments and recent applications*, volume 112. Springer Science & Business Media.

Schröer, K., Kurzeja, P., Schulz, S., Brockmann, P., Hussong, J., Janas, P., Wlokas, I., Kempf, A., and Wolf, D. E. (2017). Dilute suspensions in annular shear flow under gravity: simulation and experiment. In *EPJ Web of Conferences*, volume 140, page 09034. EDP Sciences.

Segre, G. and Silberberg, A. (1961). Radial particle displacements in poiseuille flow of suspensions. *Nature*, 189(4760):209–210.

Segura, R., Rossi, M., Cierpka, C., and Kähler, C. J. (2015). Simultaneous three-dimensional temperature and velocity field measurements using astigmatic imaging of non-encapsulated thermo-liquid crystal (tlc) particles. *Lab on a Chip*, 15(3):660–663.

Seiden, G., Lipson, S. G., and Franklin, J. (2004). Oscillatory axial banding of particles suspended in a rotating fluid. *Phys. Rev. E*, 69:015301.

Seiden, G. and Thomas, P. J. (2011). Complexity, segregation, and pattern formation in rotating-drum flows. *Reviews of Modern Physics*, 83(4):1323.

Seiden, G., Ungarish, M., and Lipson, S. (2005). Banding of suspended particles in a rotating fluid-filled horizontal cylinder. *Physical Review E*, 72(2):021407.

Seiden, G., Ungarish, M., and Lipson, S. G. (2007). Formation and stability of band patterns in a rotating suspension-filled cylinder. *Phys. Rev. E*, 76:026221.

Semwogerere, D. and Weeks, E. R. (2008). Shear-induced particle migration in binary colloidal suspensions. *Physics of Fluids*, 20(4):043306.

Shah, R. K. and London, A. L. (2014). *Laminar flow forced convection in ducts: a source book for compact heat exchanger analytical data*. Academic press.

Shapiro, A. P. and Probstein, R. F. (1992). Random packings of spheres and fluidity limits of monodisperse and bidisperse suspensions. *Physical review letters*, 68(9):1422.

Shapley, N. C., Armstrong, R. C., and Brown, R. A. (2002). Laser doppler velocimetry measurements of particle velocity fluctuations in a concentrated suspension. *Journal of Rheology*, 46(1):241–272.

Shapley, N. C., Brown, R. A., and Armstrong, R. C. (2004). Evaluation of particle migration models based on laser doppler velocimetry measurements in concentrated suspensions. *Journal of Rheology*, 48(2):255–279.

Shichi, H., Yamashita, H., Seki, J., Itano, T., and Sugihara-Seki, M. (2017). Inertial migration regimes of spherical particles suspended in square tube flows. *Physical Review Fluids*, 2(4):044201.

Sinton, S. W. and Chow, A. W. (1991). Nmr flow imaging of fluids and solid suspensions in poiseuille flow. *Journal of Rheology*, 35(5):735–772.

Slack, G. (1963). Sedimentation of a large number of particles as a cluster in air. *Nature*, 200(4913):1306–1306.

Snyder, H. A. (1962). Experiments on the stability of spiral flow at low axial reynolds numbers. *Proceedings of the Royal Society of London. Series A. Mathematical and Physical Sciences*, 265(1321):198–214.

Song, M. S., Choi, H. Y., Seong, J. H., and Kim, E. S. (2015). Matching-index-of-refraction of transparent 3d printing models for flow visualization. *Nuclear engineering and design*, 284:185–191.

Soria, J. and Atkinson, C. (2008). Towards 3c-3d digital holographic fluid velocity vector field measurementtomographic digital holographic piv (tomo-hpiv). *Measurement science and technology*, 19(7):074002.

Steinmann, T., Casas, J., Braud, P., and David, L. (2019). Tomo-ptv measurement of a drop impact at air-water interface. *Munich, Germany*, 14.

Stickel, J. J. and Powell, R. L. (2005). Fluid mechanics and rheology of dense suspensions. *Annu. Rev. Fluid Mech.*, 37:129–149.

Stieß, M. (2008). *Mechanische Verfahrenstechnik-Partikeltechnologie 1*. Springer-Verlag.

Stolz, W. and Köhler, J. (1994). In-plane determination of 3d-velocity vectors using particle tracking anemometry (pta). *Experiments in fluids*, 17(1):105–109.

Synge, J. L. (1938). On the stability of a viscous liquid between rotating coaxial cylinders. *Proceedings of the Royal Society of London A: Mathematical, Physical and Engineering Sciences*, 167(929):250–256.

Takeuchi, D. I. and Jankowski, D. F. (1981). A numerical and experimental investigation of the stability of spiral poiseuille flow. *Journal of Fluid Mechanics*, 102:101–126.

Tanaami, T., Otsuki, S., Tomosada, N., Kosugi, Y., Shimizu, M., and Ishida, H. (2002). High-speed 1-frame/ms scanning confocal microscope with a microlens and nipkow disks. *Applied Optics*, 41(22):4704–4708.

Tatsumi, K., Noguchi, S., Tatsumi, A., Kuriyama, R., and Nakabe, K. (2019). Particle and rigidized red blood cell concentration distributions in microchannel flows. *Physics of Fluids*, 31(8):082006.

Taute, K., Gude, S., Tans, S., and Shimizu, T. (2015). High-throughput 3d tracking of bacteria on a standard phase contrast microscope. *Nature communications*, 6(1):1–9.

Taylor, G. I. (1923). Stability of a viscous liquid contained between two rotating cylinders. *Philosophical Transactions of the Royal Society of London A: Mathematical, Physical and Engineering Sciences*, 223(605-615):289–343.

Tchen, C. (1947). Mean value and correlation problems connected with the motion of small particles suspended in a turbulent fluid.

Thoroddsen, S. and Mahadevan, L. (1997). Experimental study of coating flows in a partially-filled horizontally rotating cylinder. *Experiments in fluids*, 23(1):1–13.

Tirumkudulu, M., Mileo, A., and Acrivos, A. (2000). Particle segregation in monodisperse sheared suspensions in a partially filled rotating horizontal cylinder. *Physics of Fluids*, 12(6):1615–1618.

Tirumkudulu, M., Tripathi, A., and Acrivos, A. (1999). Particle segregation in monodisperse sheared suspensions. *Physics of fluids*, 11(3):507–509.

Tollmien, W. (1930). Über die entstehung der turbulenz. In *Vorträge aus dem Gebiete der Aerodynamik und verwandter Gebiete*, pages 18–21. Springer.

Toloui, M. and Hong, J. (2015). High fidelity digital inline holographic method for 3d flow measurements. *Optics express*, 23(21):27159–27173.

Toprak, E., Balci, H., Blehm, B. H., and Selvin, P. R. (2007). Three-dimensional particle tracking via bifocal imaging. *Nano letters*, 7(7):2043–2045.

Towers, C. E., Towers, D. P., Campbell, H. I., Zhang, S., and Greenaway, A. H. (2006). Three-dimensional particle imaging by wavefront sensing. *Optics letters*, 31(9):1220–1222.

Trefethen, L. N. (2000). *Spectral methods in MATLAB*, volume 10. Siam.

Tropea, C., Yarin, A. L., Foss, J. F., et al. (2007). *Springer handbook of experimental fluid mechanics*. Springer.

Troutman, V. A. and Dabiri, J. O. (2018). Single-camera three-dimensional tracking of natural particulate and zooplankton. *Measurement Science and Technology*, 29(7):075401.

Van Dinther, A., Schroën, C., Vergeldt, F., Van der Sman, R., and Boom, R. (2012). Suspension flow in microfluidic devicesa review of experimental techniques focussing on concentration and velocity gradients. *Advances in colloid and interface science*, 173:23–34.

Vasanta Ram, V. I. (2019). The critical layer during transition of the spiral poiseuille flow in an annular gap. *European Journal of Mechanics-B/Fluids*, 74:50–57.

Vishwanathan, G. and Juarez, G. (2021). Inertial focusing in planar pulsatile flows. *Journal of Fluid Mechanics*, 921.

Wereley, S. T. and Lueptow, R. M. (1999). Inertial particle motion in a taylor couette rotating filter. *Physics of fluids*, 11(2):325–333.

Wereley, S. T. and Meinhart, C. D. (2010). Recent advances in micro-particle image velocimetry. *Annual review of fluid mechanics*, 42:557–576.

Wiederseiner, S., Andreini, N., Epely-Chauvin, G., and Ancey, C. (2011). Refractive-index and density matching in concentrated particle suspensions: a review. *Experiments in fluids*, 50(5):1183–1206.

Willert, C. and Gharib, M. (1992). Three-dimensional particle imaging with a single camera. *Experiments in Fluids*, 12(6):353–358.

Williams, J. C. (1976). The segregation of particulate materials. a review. *Powder technology*, 15(2):245–251.

Windt, C. W. (2007). Nuclear magnetic response imaging of sap flow in plants.

Wright, S. F., Zadrazil, I., and Markides, C. N. (2017). A review of solid–fluid selection options for optical-based measurements in single-phase liquid, two-phase liquid–liquid and multiphase solid–liquid flows. *Experiments in Fluids*, 58(9):1–39.

Yang, C.-T. and Chuang, H.-S. (2005). Measurement of a microchamber flow by using a hybrid multiplexing holographic velocimetry. *Experiments in fluids*, 39(2):385–396.

Yu, X., Hong, J., Liu, C., and Kim, M. K. (2014). Review of digital holographic microscopy for three-dimensional profiling and tracking. *Optical engineering*, 53(11):112306.

Yuan, C., Pan, Z., and Wu, H. (2018). Inertial migration of single particle in a square microchannel over wide ranges of re and particle sizes. *Microfluidics and Nanofluidics*, 22(9):1–13.

Zade, S., Costa, P., Fornari, W., Lundell, F., and Brandt, L. (2018). Experimental investigation of turbulent suspensions of spherical particles in a square duct. *Journal of Fluid Mechanics*, 857:748–783.

Zade, S., Fornari, W., Lundell, F., and Brandt, L. (2019). Buoyant finite-size particles in turbulent duct flow. *Physical Review Fluids*, 4(2):024303.

Zarraga, I. E., Hill, D. A., and Leighton Jr, D. T. (2000). The characterization of the total stress of concentrated suspensions of noncolloidal spheres in newtonian fluids. *Journal of Rheology*, 44(2):185–220.

Zeng, L., Najjar, F., Balachandar, S., and Fischer, P. (2009). Forces on a finite-sized particle located close to a wall in a linear shear flow. *Physics of fluids*, 21(3):033302.

Zhang, J., Yan, S., Yuan, D., Alici, G., Nguyen, N.-T., Warkiani, M. E., and Li, W. (2016). Fundamentals and applications of inertial microfluidics: A review. *Lab on a Chip*, 16(1):10–34.

Zhang, K. and Rival, D. E. (2018). Experimental study of turbulence decay in dense suspensions using index-matched hydrogel particles. *Physics of Fluids*, 30(7):073301.

Zhao, B., Law, A. W.-K., Adams, E. E., and Er, J. (2014). Formation of particle clouds. *Journal of Fluid Mechanics*, 746:193–213.

Zhou, J. and Papautsky, I. (2013). Fundamentals of inertial focusing in microchannels. *Lab on a Chip*, 13(6):1121–1132.

Zhou, W., Tropea, C., Chen, B., Zhang, Y., Luo, X., and Cai, X. (2020a). Spray drop measurements using depth from defocus. *Measurement Science and Technology*, 31(7):075901.

Zhou, W., Zhang, Y., Chen, B., Tropea, C., Xu, R., and Cai, X. (2021). Sensitivity analysis and measurement uncertainties of a two-camera depth from defocus imaging system. *Experiments in Fluids*, 62(11):1–14.

Zhou, Y., Handley, M., Carles, G., and Harvey, A. R. (2019). Advances in 3d single particle localization microscopy. *APL photonics*, 4(6):060901.

Zhou, Z., Kumar, S., Mallery, K., Jiang, W., and Hong, J. (2020b). Holographic astigmatic particle tracking velocimetry (haptv). *Measurement Science and Technology*, 31(6):065202.